Current motion on faults of the San Andreas system in central California inferred from recent GPS and terrestrial survey measurements

Williams, Simon D.P.

Current Motion on Faults of the San Andreas System in Central California Inferred from Recent GPS and Terrestrial Survey Measurements

by

Simon D. P. Williams

A Thesis submitted in partial fulfilment of the requirements for the degree of Doctor of Philosophy

University of Durham

Department of Geological Sciences

June 1995

Declaration

I declare that this thesis, which I submit for the degree of Doctor of Philosophy at the University of Durham, is my own work and is not substantially the same as any which has previously been submitted for a degree at this or another university.

Simon D. P. Williams

University of Durham

June 1995

Acknowledgements

This work was funded by the University of Durham, England and the Crustal Strain project at the U.S. Geological Survey, Menlo Park, California.

I would like to thank Gill Foulger, my supervisor for starting me off on GPS as an undergraduate and for overseeing my postgraduate research and thesis writing. Thanks also to my other two supervisors Will Prescott and Neil Goulty for their help in various forms and all the members of the Crustal Strain project (Mike Lisowski, Jerry Svarc, Mark Murray, Nancy King, Karl Gross, Jim Savage, Will Prescott, Karen Wendt and the field crew) for providing the GPS and trilateration data. In addition, special thanks are in order to Mike Lisowski for help too numerous to mention, Jerry Svarc and Kosuke Heki for teaching me how to process GPS data and Jim Savage and Mark Murray for contributing constructive criticism, advice and some computer code. The many scientists at the USGS were extremely helpful during my two study visits to California, in particular Wayne Thatcher, Ross Stein, Grant Marshall and Bruce Julian. I greatly benefited from working with Michelle Hofton and Kathleen Hodgkinson, my fellow GPS students at Durham. Several people at Stanford University were also of help during my research; Paul Segall, Jeff Freymueller and Tony Mossop.

ABSTRACT

The San Andreas fault system of California comprises dominantly right-lateral strike-slip faults and forms part of the Pacific-North American plate boundary. This fault system has been studied extensively using geological and geophysical methods since it was first brought into prominence by the 1906 $M = 8\frac{1}{4}$ San Francisco earthquake.

Observations of surface deformation thought to define an earthquake deformation cycle have been inferred from terrestrial and space-based geodetic methods. The observed relative motion in these networks has also been used to constrain the distribution of motion across the plate boundary.

Sites in three profiles extending across the fault system in the San Francisco bay region were measured up to 7 times between March 1990 and February 1993 using the Global Positioning System (GPS). The data were processed using the Bernese V3.2 software. The GPS data were combined with trilateration and VLBI data to create a spatially dense sample of the deformation field in the region. Approximately 35±3 mm/yr of fault-parallel (N33°W) shear is distributed across a deforming zone that increases in width northwards from 60 to 100 km and in style from fault-concentrated deformation in the south to near-linear trends in the north. No systematic convergence upon the fault is observed.

Both two- and three-dimensional models of dislocations in an elastic half-space were used to model the deformation and to investigate the effects of structural complexities such as a low-rigidity fault zone, the depth to which surface creep extends, geometrical complexities of the fault system and along-strike variations in slip rate. The models produce a remarkably close fit to the deformation despite such a rheologically simple Earth structure. Approximately half of the observed deformation is accommodated along faults to the east of the San Andreas fault. A zone of concentrated deformation across the San Andreas fault zone in the north of the region may be the result of a 1-2 km wide low-rigidity fault zone there. Surface creep rates, although highly variable, appear to increase to the south. An increase in depth of the surface creep zone to the south may also accompany this. The variations in slip rate at depth along strike are consistent with connectivity between the major faults of the system.

Quasi-steady slip on discrete fault planes or shear zones may occur down to 2-3 times the seismogenic depth and deformation rates are probably almost constant throughout much of the earthquake cycle. The present earthquake potential calculated from the estimated slip rates indicate that several fault segments may have an earthquake potential equivalent in magnitude to the "characteristic" earthquake assumed for that segment. The estimates of relative motion indicate that deformation across the San Andreas fault system, plus that observed to the east of the Sierra Nevada mountains, can account for all of the Pacific-North American plate motion rate.

Contents

Chapter 1

California and the San Andreas Fault System

1.1 Introduction

1.1.1 Definition of the San Andreas Fault System

The term "San Andreas fault system" refers to the network of faults with predominantly right-lateral strike slip that together form the boundary, and accommodate most of the relative motion between, the North American and Pacific plates in California (Figure 1.1). The boundaries of this fault system are not well defined, but it is generally assumed that the term encompasses the set of faults along the western margin of California, on land and offshore. The northern terminus of the San Andreas fault system lies at Cape Mendocino where it forms a branch of the Mendocino triple junction. At its southeast end, the San Andreas fault system merges with a set of *en-echelon* transform faults separated by spreading centres in the Gulf of California. Further south these form a triple junction between the North American, Pacific, and Rivera plates.

Within the fault system there are generally several "fault zones" which are complex zones of sheared rock typically a few kilometres wide and several hundreds of kilometres long that have developed over several million years. A fault zone may be subdivided into smaller elements such as "faults", "fault branches" and "fault strands". The San Andreas fault system consists primarily of the San Andreas, Hayward and Calaveras fault zones in central California (Figure 1.2) and the San Andreas, San Jacinto and Elsinore fault zones in southern California (Figure 1.3).

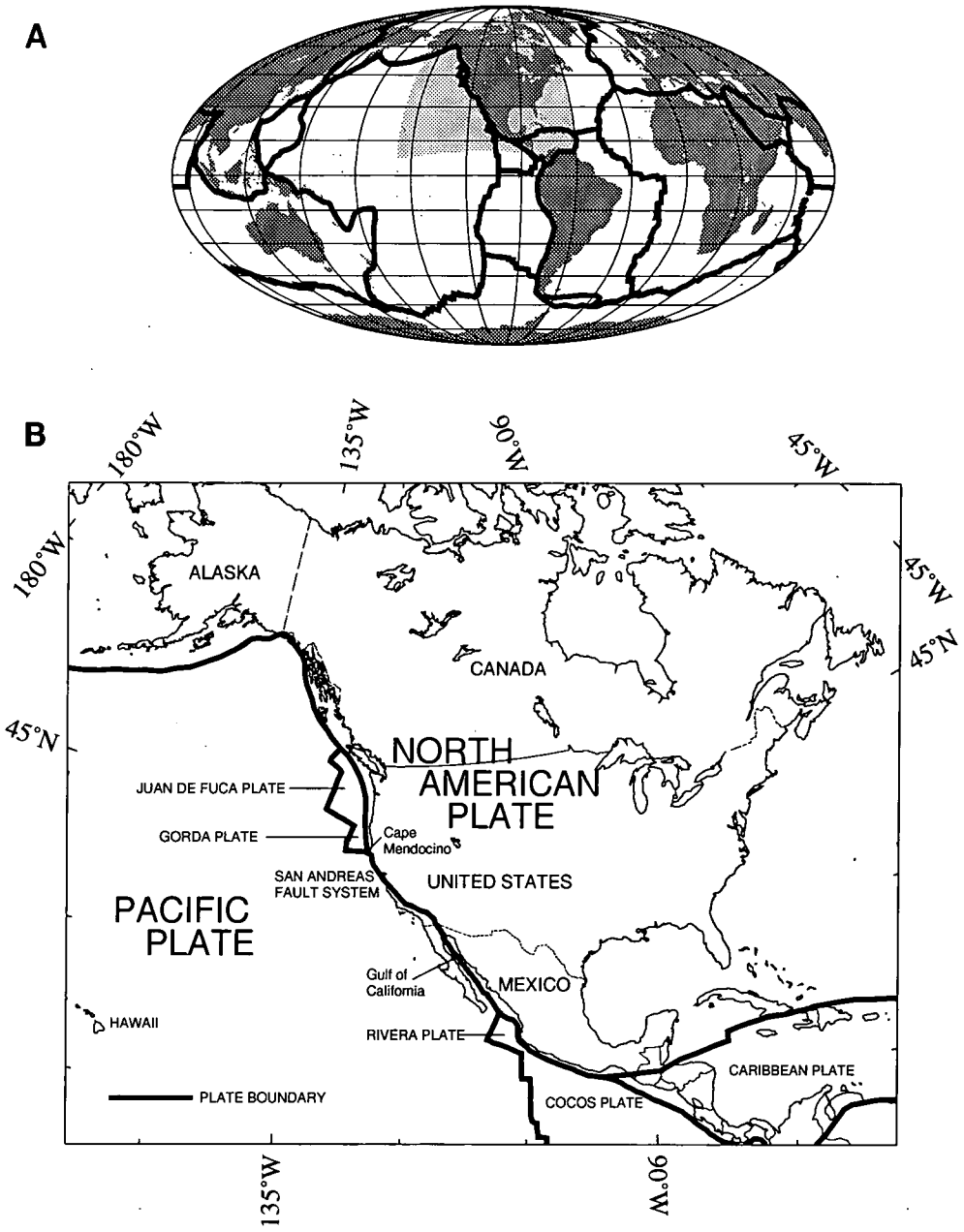

Figure 1.1: Plate tectonic framework. (A) Relation of North America to the global plate tectonic boundaries. Light shaded area indicates approximate area of map shown in B. (B) Simplified diagram showing the San Andreas fault system as a single element forming the complex boundary between the North American and Pacific plates.

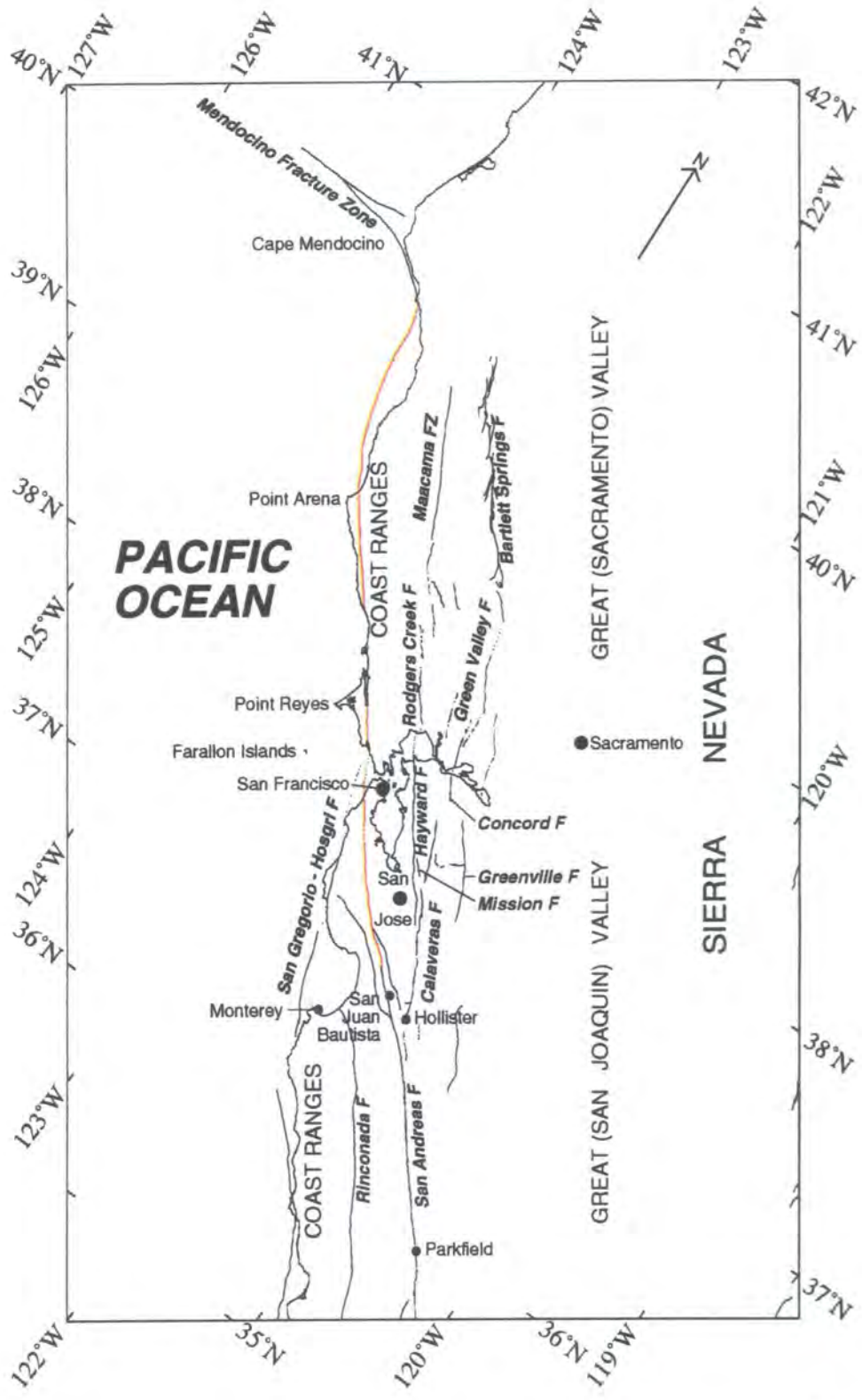

Figure 1.2: The San Andreas fault system in northern California together with place names used in text. Red line indicates extent of fault rupture during the earthquake of 1906. F = fault, FZ = fault zone.

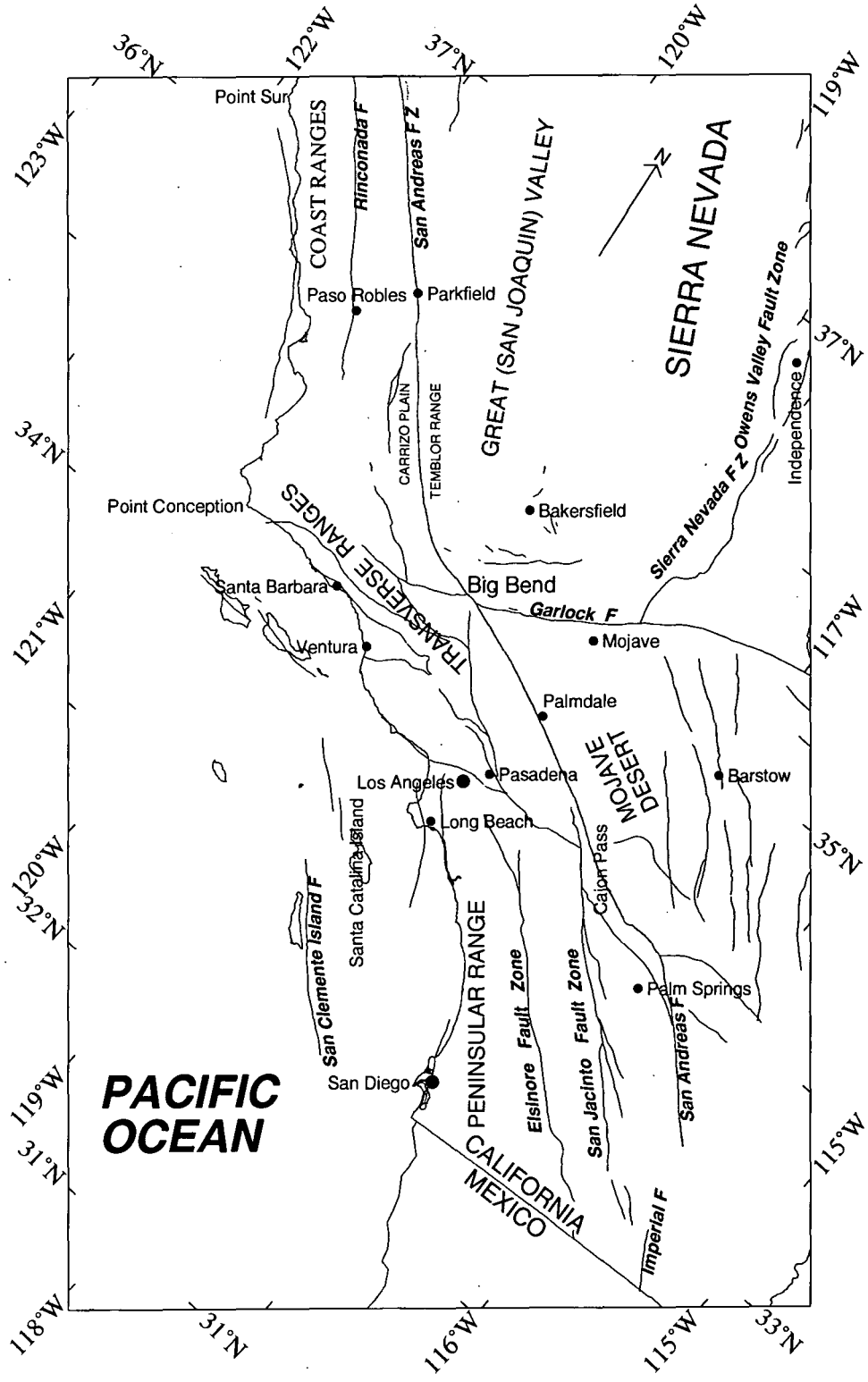

Figure 1.3: The San Andreas fault system in southern California together with places names used in text. F = fault, FZ = fault zone.

1.1.2 Principal Trends

In general the San Andreas fault system trends at about N35°-40°W. In southern California, south of Bakersfield (Figure 1.3), the strike of the San Andreas fault changes sharply at what is known as the "big bend" region. South of the big bend, the fault strikes at about N60°W. In this region, the San Jacinto and Elsinore faults trend at about N50°W and lie southwest of the San Andreas fault. North of the big bend, up to the latitude of Hollister (Figure 1.2), the San Andreas fault system consists of the San Andreas fault only, which is relatively straight and narrow. North of Hollister, the fault strikes at about N50°W and the Calaveras and Hayward faults splay to the east with strikes of between N20°W and N35°W. West of the San Andreas fault, along the San Francisco Peninsula, the San Gregorio-Hosgri fault zone trends at approximately N20°W and joins the San Andreas fault at the southern tip of the Point Reyes peninsula. North of San Francisco bay are extensions of the Hayward and Calaveras faults. The Green Valley and Bartlett Springs faults extend the Calaveras fault and the Rodgers Creek and Maacama faults are the northward extensions of the Hayward fault.

1.1.3 Geomorphic Expression

On aerial photographs and satellite images, the San Andreas fault system appears as a very obvious scar across the landscape. From Point Arena south-eastwards, the San Andreas fault is conspicuous as a series of linear valleys and ridges passing through the Coast Ranges. Between Hollister (Figure 1.2) and the Carrizo plain (Figure 1.3) the fault trace crosses the Coast Ranges at a low angle, the mountain ridges of the latter trending at about 5° to 10° more westerly than the fault. Within the Carrizo plain, the surface expression of the San Andreas fault is well defined and narrow and offset streams are common. Further south, in the big bend region, the San Andreas fault passes through high mountains and so the surface trace rises to a high altitude. Around the Palmdale region the fault is marked by a distinct linear valley together with a contrast between the mountainous terrain of the Transverse Ranges to the west and the low relief region of the Mojave desert to the east. South of Palmdale the fault again cuts across the mountains at a low angle before branching into numerous faults and becoming topographically complex.

On a smaller scale various geomorphic features originate from both lateral and vertical movements between small fault-bounded blocks or slices. These include sag

ponds and depressions, deflected stream offsets, scarps, folds and pressure ridges.

1.1.4 Historical Review

Faults within the San Andreas fault system were first recognised by several geologists in the 1890's [e.g., *Lawson*, 1895]. In that decade, geologists traced the fault zone for 400 miles south of San Francisco [*Fairbanks*, 1907, p. 324]. The San Francisco (M = 8.25) earthquake of 1906 stimulated much geophysical work and drew attention to the fault zone to the north of San Francisco. The name San Andreas, although previously used by *Lawson* [1895, p. 468] to describe a section of the fault along the San Francisco peninsula, was formally applied to the fault and fault zone by the time the final report of the State Earthquake Investigation Commission was published [*Lawson*, 1908]. Furthermore, that report provided a clear account of the fault characteristics and the role of the fault in causing the 1906 earthquake.

After documenting the location and features of the fault, geologists turned their attention for about the following 4 decades to extensive geological mapping of California [*Crowell*, 1962]. Much controversy ensued regarding the cumulative displacement along the fault, the principal direction of slip (i.e., whether movement was primarily strike- or dip-slip), and the age of the fault. For example, *Noble* [1927] described evidence for 39 km of right-lateral displacement, whereas up to 120 km was advocated by *Wallace* [1949] and others.

Hill and Dibblee [1953] produced a landmark paper where they assembled evidence for right-lateral offset along the San Andreas fault of up to 560 km. During the 1960's the theories of sea-floor spreading and plate tectonics were being developed [e.g., *Vine*, 1966; *Morgan*, 1968; *Isacks et al.*, 1968]. The findings of *Hill and Dibblee* [1953] and subsequent studies provided a basis for applying plate tectonic theory to the San Andreas fault system. The proposal that the San Andreas fault was a transform fault connecting two oceanic spreading ridges [*Wilson*, 1965] comprised a further breakthrough in understanding (Figure 1.4). *McKenzie and Morgan* [1969] and *Atwater* [1970] modified the theory of *Wilson* [1965] to account for triple junction migration and plate movements.

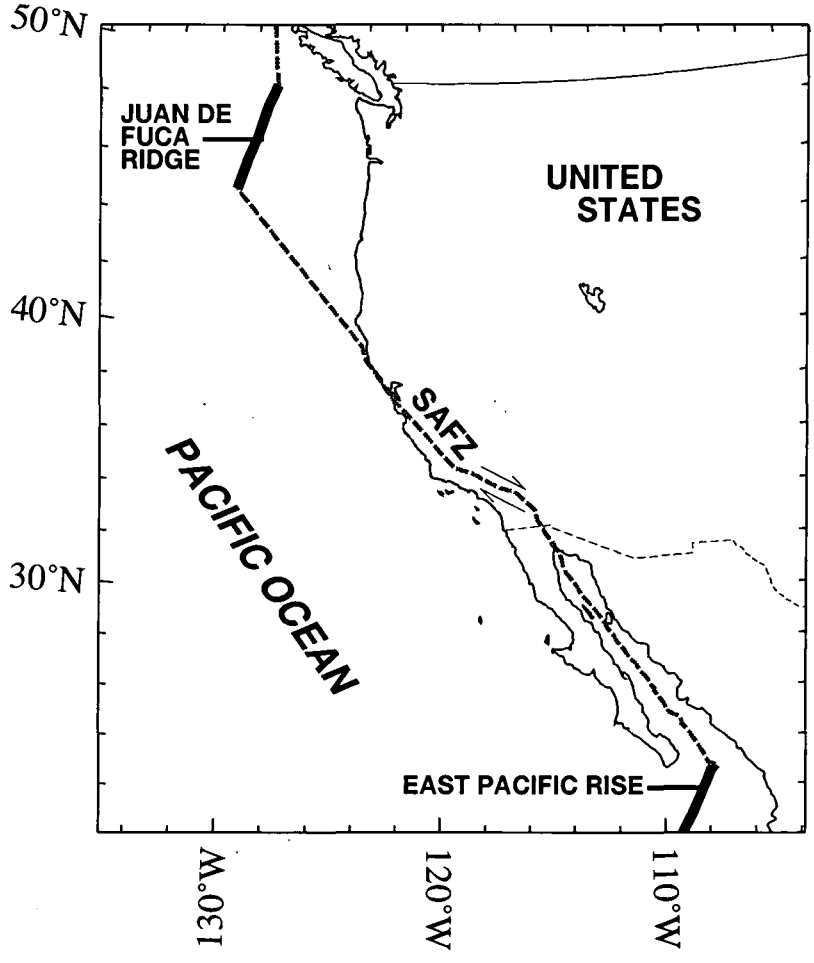

Figure 1.4: The role of the San Andreas fault system as a transform boundary between the Juan de Fuca ridge and the East Pacific Rise as first proposed by *Wilson* [1965]. SAFZ = San Andreas fault zone.

1.1.5 Recent Plate Motion

During the 1970's uncertainties in plate motions were reduced by refined plate tectonic models. Angular velocity vectors (Euler vectors) describing the average relative motions of rigid plates over the past few million years were derived by inverting a combination of ridge spreading rates, transform fault azimuths and earthquake slip vectors. The first comprehensive models were the RM2 model [*Minster and Jordan*, 1978] and the P071 model [*Chase*, 1978]. These models indicated a relative velocity between the Pacific and North American plates of approximately 56 mm/yr at N33°W. Geological studies of displacement during the last 2 Ma, however, gave an average slip rate of about 35 mm/yr for the San Andreas fault system [e.g., *Sieh and Jahns*, 1984]. The discrepancy between these two rates,

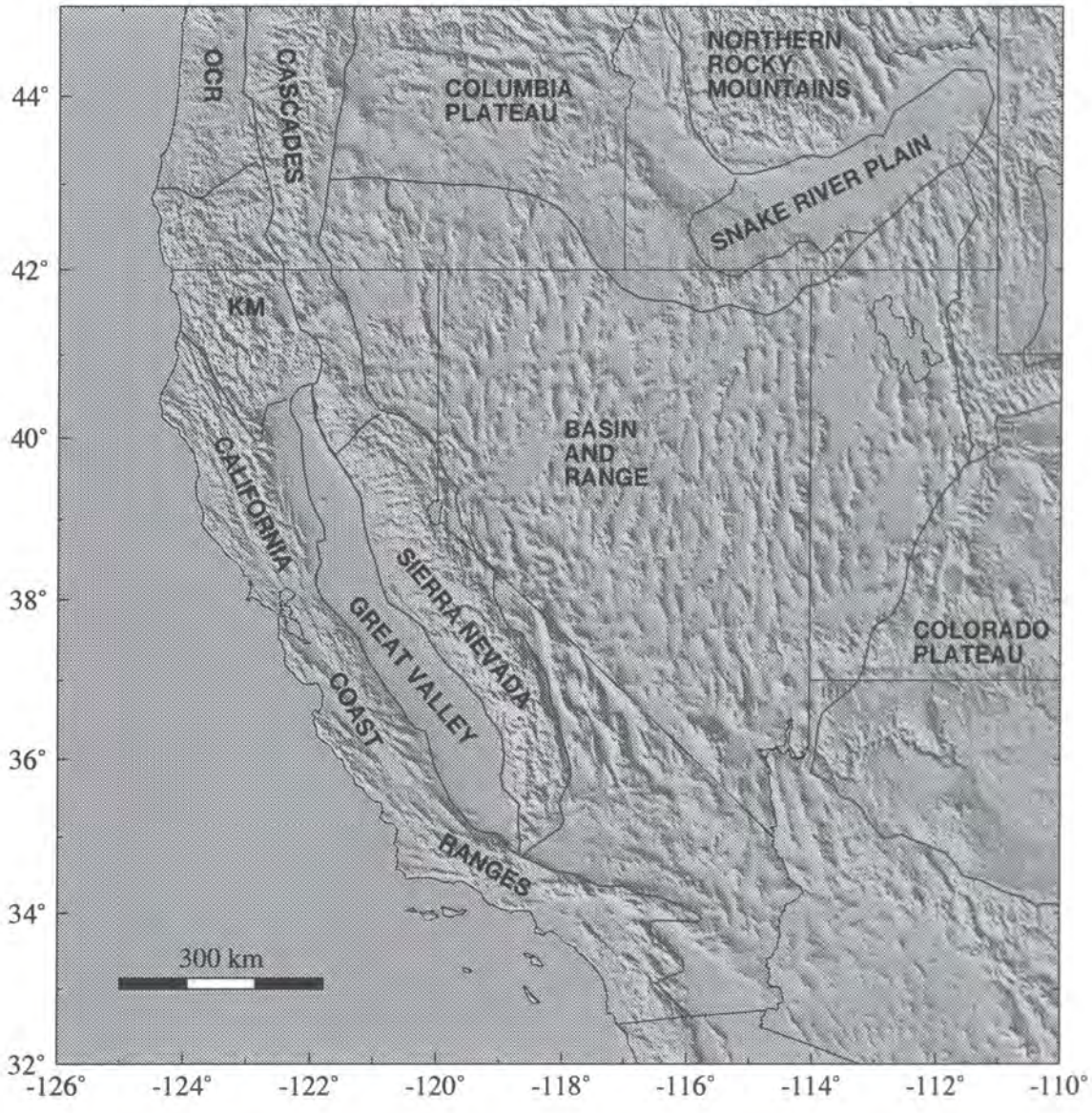

Figure 1.5: Physiographic provinces of the western United States. OCR = Oregon Coast Range, KM = Klamath Mountains.

about 20 mm/yr, has been termed the "San Andreas discrepancy" [*Minster and Jordan*, 1984].

Two explanations have been proposed for the difference between the geological and the plate tectonic rates. First, displacement rates may have varied with time and the present-day slip rate may be higher than the geological rate. The rate has probably varied over time [*Atwater and Molnar*, 1973; *Powell and Weldon*, 1992] and there have been major changes in the plate geometry since its inception at about 30 Ma. However these variations are probably too small to explain the large difference. The second, generally accepted explanation is that the Pacific-North American plate boundary is wide and extends from the continental margin eastwards across the Basin and Range province (Figure 1.5) [*Atwater*, 1970]. The "missing motion" is accommodated on many faults throughout the western United States, concentrated along a few faults outside the San Andreas fault system or by inelastic deformation of the crust.

The most recent and best global plate model, NUVEL-1, uses new data acquired in the 1980's [*DeMets et al.*, 1987a; 1987b; *Stein et al.*, 1988; *Gordon and DeMets*, 1989; *Argus et al.*, 1989; *DeMets et al.*, 1990]. This model predicts a relative velocity of 48 mm/yr at N33°W between the North American and Pacific plates. The model averages velocities over the time since paleomagnetic anomaly number 2A, taken to be at 3.03 Ma on the time scale of *Harland et al.* [1982]. However, recent revision of this time scale suggests that this paleomagnetic reversal is several percent older [e.g., *Hilgen*, 1991] and as a result the NUVEL-1 rates must be scaled by a factor of 0.959 [*Gordon*, 1993; *Feigl et al.*, 1993]. The new global plate model, "rescaled NUVEL-1" or "NUVEL-1A", predicts a Pacific-North American relative plate velocity of 46 mm/yr at N33°W.

The rescaled NUVEL-1 velocity reduces the San Andreas discrepancy to around 10-13 mm/yr at N24°W (Figure 1.6). If the discrepancy can be accounted for by deformations elsewhere, the total relative plate motion should equal the vector addition of the motions in the various provinces of the western U.S. i.e., the San Andreas fault system, the Basin and Range province and the continental margin of California. The motion of the San Andreas fault system is well known. However, obtaining motions for the other regions is more difficult. The Basin and Range province is an 800-km broad region of predominantly normal and strike-slip faulting, resulting in parallel horst-and-graben structures, from the eastern edge of the Sierra Nevada in California to the Wasatch Mountain fault zone in Utah

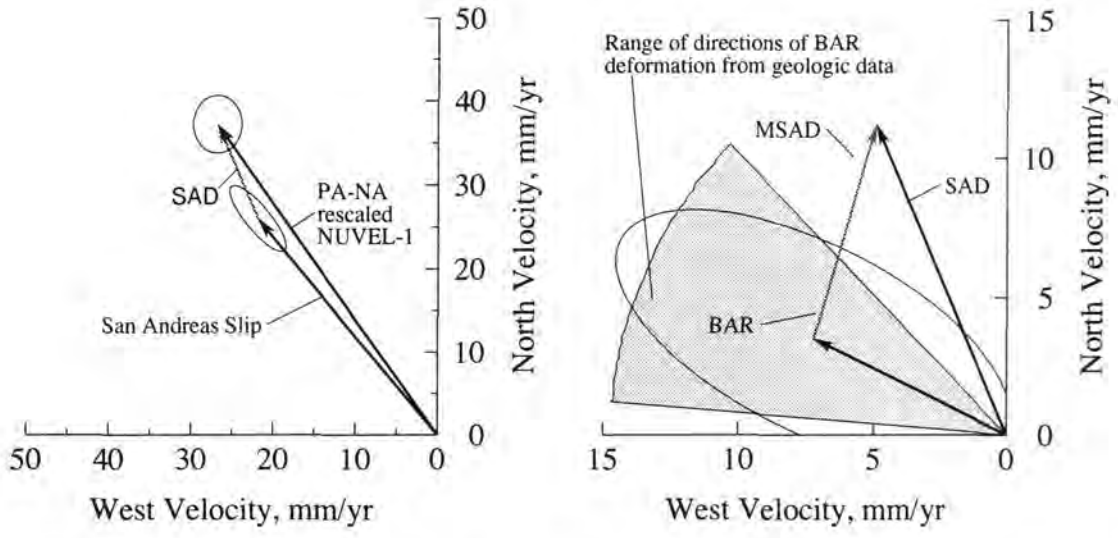

Figure 1.6: Left, Velocity vectors for the San Andreas fault system at latitude 36°N. Slip along the San Andreas fault system takes up only a portion of the Pacific-North American plate motion as predicted by the rescaled NUVEL-1 plate model. The vector difference between the two (SAD, grey arrow) is called the San Andreas Discrepancy. Ellipses indicate 95% confidence limits. Right, vector difference between the San Andreas Discrepancy (SAD) and motion within the Basin and Range province (BAR). The difference between these two, 8 mm/yr at N17°E, is called the modified San Andreas discrepancy (MSAD).

(Figure 1.5). The effect of fault movements in this region is crustal extension orientated roughly west-northwest–east-southeast [*Thompson and Burke*, 1974]. At the latitude of San Francisco the Basin and Range province has about 20 horst-and-graben structures. Although the direction of the vector representing motion in the Basin and Range is well known, estimating the rate of extension from geological data is difficult. Estimates based on geological and geophysical data range from 1 mm/yr to > 20 mm/yr [*Minster and Jordan*, 1984; 1987]. The best geological rate estimates come from paleoseismology, the study of prehistoric earthquakes. Preliminary mapping suggests that extension across the Basin and Range province has not exceeded an average of 12 mm/yr over the past 12,000 years [*Thompson and Burke*, 1973; *Wallace*, 1984; *Minster and Jordan*, 1984; 1987]. In addition, work in the Mojave Desert-Death Valley region suggests the presence of the Eastern California Shear Zone (ECSZ) [*Dokka and Travis*, 1990a; 1990b]. This north-northwest trending shear zone may have carried 9% - 23% of the total relative plate motion since its inception at ~10 to 6 Ma, giving a slip rate of 6-12 mm/yr.

Addition of motion in the Basin and Range province of 8 ±3 mm/yr at N64° ±10°W [*Minster and Jordon*, 1987] to motion along the San Andreas fault system gives a

modified discrepancy of 8 mm/yr at N17°E which must be accommodated within the western USA (Figure 1.6). However, given the uncertainty of the Basin and Range province extension vector, this modified discrepancy is at best a rough estimate.

1.2 Initiation and Evolution of the San Andreas Fault System

The theory of plate tectonics can be used to reconstruct the geological history of the San Andreas using the pattern and timing of magnetic anomalies in the north east Pacific ocean [*Atwater*, 1970]. There was once another plate lying between the North American and Pacific plates, the Farallon plate, *McKenzie and Morgan* [1969]. This plate was consumed by a subduction zone at its boundary with the North American plate. This indicates that spreading at the ridge was slower than the subduction so that eventually the ridge itself was consumed. The San Andreas fault system was initiated during the late Oligocene (approximately 30 Ma) when the ridge impinged upon the subduction zone [*McKenzie and Morgan*, 1969; *Atwater*, 1970] and right-lateral relative motion between the two plates started.

The continental-margin transform lengthened with the simultaneous northward migration of a transform-transform-trench triple junction and a southward migration of a ridge-trench-transform triple junction (Figure 1.7). Outside these triple junctions subduction of the Farallon plate continued. Other evidence for subduction of the Farallon plate includes varied oceanic environments represented in the eugeosynclinal terranes of California [*Hamilton*, 1969]. The rock juxtapositions agree with the model that these materials were scraped off against the North American continent as the oceanic Farallon plate was subducted beneath it. These former Mesozoic subduction zones are now seen as serpentinite belts separating profoundly different rock assemblages.

The models are based mainly on kinematic considerations and oversimplify the geological history of the fault system. *Dickinson* [1981] produced a more realistic model of the evolution of the San Andreas faults system (Figure 1.8), with early transform motion occurring west of the present day San Andreas fault before the opening of the Gulf of California at around 4 to 6 Ma.

Paleogeologic reconstructions indicate that four phases may be discerned after the

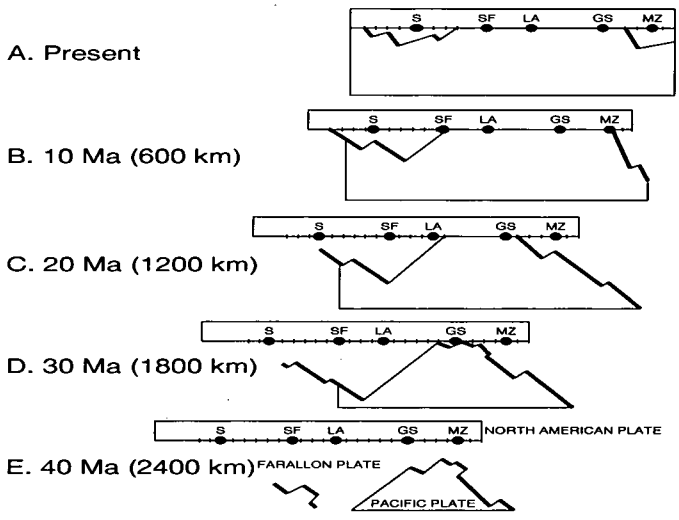

Figure 1.7: Schematic model of plate interactions assuming that the North American and Pacific plates moved with a constant relative velocity of 60 mm/yr parallel to the San Andreas fault system. Captions show the time represented by each sketch in millions of years before present and the distance that the North American plate must be displaced to reach its present position with respect to the Pacific plate. Initials represent cities, S = Seattle, SF = San Francisco, LA = Los Angeles, GS = Guaymas, MZ = Mazatlan. Thin lines are transform faults, thick lines are spreading centres, and hatched lines are subduction zones. From *Atwater* [1970].

intersection of the ridge and subduction zone [*Powell and Weldon*, 1992]. Onshore in California, the earliest phase was a period of transtensional deformation and volcanism between 26 and 22-20 Ma. In the second phase, between 20-17 Ma and 13-12 Ma, the proto-San Andreas fault in southern California accumulated 100 to 110 km of displacement at an average rate of around 20 mm/yr. In the third phase, between 13-12 Ma and 6-4 Ma, faults such as the San Gabriel and San Gregorio-Hosgri developed southwest of the San Andreas fault but with more northerly strikes. These faults accumulated a displacement of 42-45 km at a rate of around 5 mm/yr. In the last phase, spreading in the Gulf of California initiated, and influenced the emergence of the San Andreas fault as the primary element between the migrating triple junctions, and acceleration of strike-slip motion. The San Gabriel fault was largely abandoned, although others such as the San Gregorio-Hosgri fault continued to slip. The slip rate on the San Andreas fault during this phase was about 35 mm/yr [e.g., *Sieh and Jahns*, 1984].

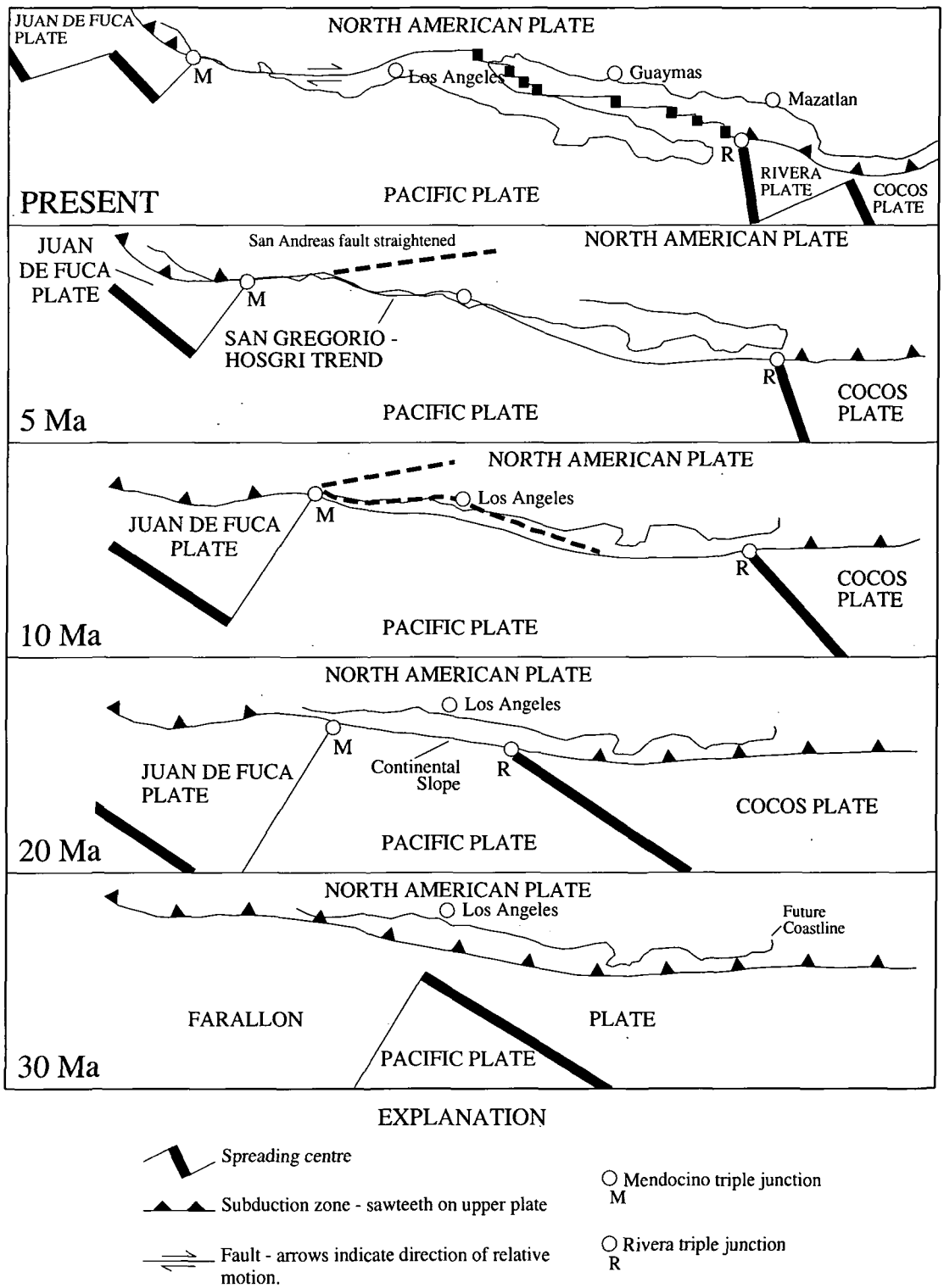

Figure 1.8: Schematic model of interactions between the North American and Pacific plates. From *Dickinson* [1981].

1.3 The Geology of Central California

1.3.1 Geologic Formations

Central California consists of four geological/physiographic provinces: the Coast Ranges, the Great Valley, the Sierra Nevada and the western Basin and Range (Figure 1.5). In the San Francisco bay region there are four principal basement rock types: the Franciscan assemblage, the Coast Range Ophiolite, the Great Valley sequence and the Salinian block (Figures 1.9 and 1.10).

The Franciscan assemblage is largely a melange of dismembered sequences of graywacke interbedded with dark shale and lesser amounts of mafic volcanic rocks, cherts and occasional limestones. Serpentinite and tectonic pods of blueschist also occur and generally separate blocks of the more coherent sequences. Scarce fossils in the Franciscan indicate a general age of Late Jurassic to Cretaceous, but dating of the chert and associated volcanics has yielded an early Jurassic age. The origin of the Franciscan melange is problematical, as much of the material has moved northward by up to 2000 km. The Franciscan is locally overlain by the Coast Range ophiolite and the Great Valley sequence and is separated from them, along the east side of the Coast Ranges, by the Coast Range thrust. This thrust has been inferred to dip eastward through the crust and may be a subduction suture zone [*Hamilton*, 1969]. The upper plate of the thrust (the Coast Range ophiolite and the Great Valley sequence) forms a deformed, antiformal structure over the Franciscan formation in the Diablo Range except for several piercement structures (windows) which expose the lower plate of Franciscan rocks (Figure 1.10). The antiformal structure is truncated to its west by the Hayward and Calaveras faults in the north, and by the San Andreas fault in the south, and it narrows to the southeast as the San Andreas fault converges with the south end of the Great Valley.

The Coast Range ophiolite represents oceanic crust on which much of the Great Valley sequence was deposited. The ophiolite is generally highly sheared, dismembered, thinned and locally missing. Only a few localities display a complete sequence and these indicate a total stratigraphic thickness of 3 to 5 km. Isotopic ages of 165 to 153 Ma indicate that the ophiolite is middle-to-late Jurassic in age. Palaeontological and paleomagnetic evidence indicates an equatorial formation-latitude before subsequent transportation northward prior to accretion to the North

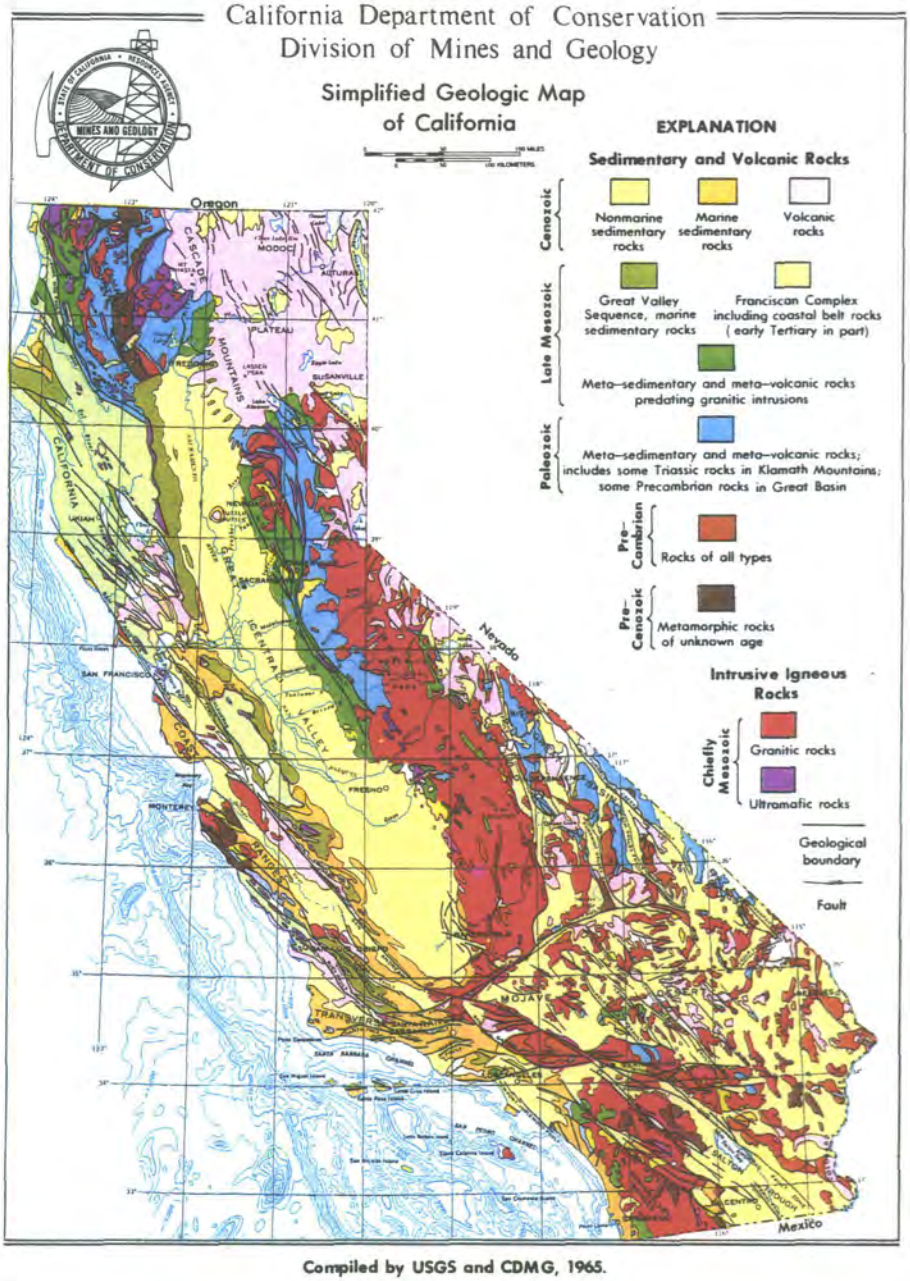

Figure 1.9: Geologic sketch map of central California, showing the distribution of principal basement rocks.

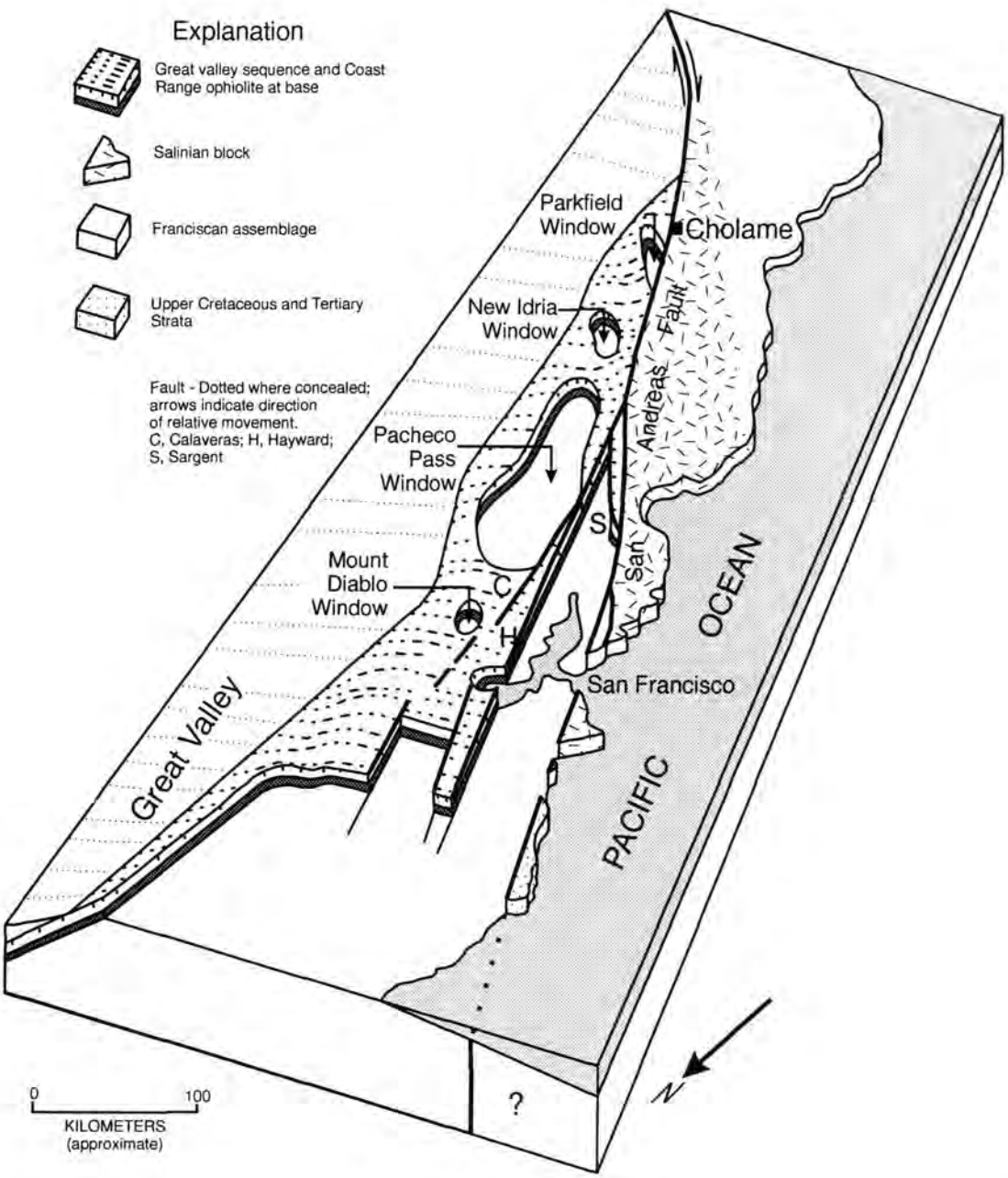

Figure 1.10: Schematic block diagram of central California, showing gross structural relations between principal lithotectonic units cut by the San Andreas fault. The Coast Range ophiolite lies at the base of the Great Valley sequence and is separated from underlying Franciscan rocks by the Coast Range thrust. Blueschist-facies metasedimentary and metavolcanic rocks that form a border zone in the Franciscan immediately below the thrust are not shown. View south-eastward along the San Andreas fault. From *Irwin* [1990].

America plate and overlay of the Great Valley sequence.

The Great Valley sequence consists of a large thickness of miogeosynclinal, interbedded shale, sandstone, mudstone and conglomerate of late Jurassic to Cretaceous age. It is markedly less deformed and more coherent than the Franciscan assemblage. Its aggregate stratigraphic sequence is of the order of 12 km thick and it generally lies depositionally on the Great Valley ophiolite except where disrupted by faults. However, at the north and east end of the Great Valley, the Great Valley sequence onlaps the older basement terranes of the Klamath Mountains and the Sierra Nevada. The great thickness of clastic deposits indicates rapid erosion of the ancestral Klamath Mountains and Sierra Nevada to form submarine fans and turbidity deposits.

The Salinian block generally forms the west wall of the San Andreas fault except in the region of the San Francisco peninsula where it is separated from the San Andreas by a small sliver of Franciscan assemblage. The principal formations of the Salinian block are granitic and metamorphic rocks locally overlain by upper Cretaceous and younger strata. The metamorphic rocks are generally medium to high grade gneiss, granofels and impure quartzite together with minor schists and marbles. These probably represent a metamorphosed, thinly bedded sequence of silt and sandstone. The plutonic rocks are mostly granite and tonalite but range in composition to gabbro. Plutonic activity commenced around 120-105 Ma in the northwest and migrated southeast over a period of 40 Ma. The basement of the Salinian block is similar in composition and age to parts of the Sierra Nevada batholith leading several investigators to conclude that the Salinian originally lay between the Sierra Nevada and the Peninsula Range and has been transported 540 km north-westward along the San Andreas fault [*Page*, 1981; *Ross*, 1984]. More recent paleomagnetic studies support a northward displacement of around 2500 km since the Cretaceous.

The Sierra Nevada is a 600 $\times$ 150 km composite batholith of more than 100 distinct plutons that were emplaced mainly from 180 to 80 Ma. At around 10 Ma the Sierra Nevada, part of the greater Nevadan Mountains, had a lowland landscape with elevations possibly as high as 1800 m. Uplift of the range occurred in Late Cenozoic time primarily due to reactivation of the Sierra Nevada fault on the eastern edge of the Sierra Nevada as the entire block was tilted west. The vertical displacement on this fault is as much as 3350 m and the fault resembles faults of the Basin and Range province, of which it is probably the westernmost member.

The Franciscan assemblage, the Great Valley, and the Sierra Nevada are interpreted as an accretionary prism, a fore-arc basin and a magmatic arc related to the subduction regime in California prior to the development of the transform boundary [*Dickinson*, 1970].

1.3.2 Relation of Geologic Structure to Seismicity

There are differences in seismic behaviour between several major segments of the San Andreas fault system [e.g., *Allen*, 1968; *Wallace*, 1970; *Nason and Tocher*, 1970]. Different segments are characterised by frequent, small magnitude earthquakes, occasional, moderate magnitude earthquakes and aseismic fault creep. Other "locked" segments are characterised by infrequent earthquakes of large magnitude (e.g., the 1906 event) together with a lack of interseismic creep. The seismically-active regions show a remarkably close coincidence with the western faulted edge of the upper plate of the Coast Range thrust i.e., the Great Valley Sequence (Figure 1.9). The virtual restriction of creep and frequent seismic activity to this structural intersection may be because seismic behaviour is influenced by some factor related to this intersection. The presence of the serpentiniferous Coast Range ophiolite at the base of the upper plate may act as a lubricant to aid aseismic creep. Furthermore, the lower plate Franciscan assemblage may yield metamorphic fluids. Natural springs containing metamorphic (especially carbon dioxide rich) fluids are common in the Franciscan terrane and along faults between the Franciscan and Great Valley sequence. The Great Valley sequence may act as a hydraulic cap forcing migrating fluids towards the relatively permeable rock of the fault zone. This will decrease the effective confining pressure, reduce the frictional strength of the fault rocks and therefore increase the potential for aseismic creep [*Irwin and Barnes*, 1975].

1.3.3 Quaternary Deformation

Quaternary deformation processes, faulting, folding and uplift, represent crustal movements that continue today in many places. Study of these processes provides an independent check and data where no historical deformation information is available.

Evidence for Quaternary deformation comes principally from the observed displace-

ment of strata or geomorphic features. If the deformation feature can be dated then an average deformation rate can be calculated. Dating of Quaternary deposits ultimately depends on various forms of geochemical analyses.

Figures 1.2 and 1.3 show faults along which Quaternary displacements have occurred [*Jennings*, 1975]. Although direct geologic evidence of Quaternary slip on faults in the San Andreas fault system is abundant, the age and cross-fault correlation of displaced stratigraphic markers is difficult and Quaternary slip rates are poorly constrained. Despite this, many Quaternary slip rates have now been determined. A summary of many of these rates is given by *Clark et al.* [1984] for the whole of California and by *Kelson et al.* [1992] for the San Francisco bay region.

Throughout the fault system, the rate of right-lateral slip on northwesterly-trending faults typically exceeds, by an order of magnitude, geologically determined rates for other types of deformation such as uplift. The highest observed slip rate is 34 mm/yr for the central creeping portion of the San Andreas fault between latitudes 35° 45′ and 36° 30′ where most of the slip has followed the San Andreas fault. North of latitude 36° 30′ the rate of Quaternary slip along the San Andreas fault, 10-20 mm/yr, is less than observed along the more southerly segments of the fault. Much of this slip deficit can be accounted for by distributed slip on active branch faults. Slip rates on some of these branches may equal or exceed the rate on nearby parts of the San Andreas fault. North of San Francisco bay, estimated slip rates for the San Andreas fault increase from 24±3 mm/yr at Point Reyes [*Niemi and Hall*, 1992] to 26±3 mm/yr at Point Arena [*Prentice*, 1989a, b] (Figure 1.2).

Dominantly northwest-trending folds deform much of the region around the San Andreas fault system except for the relatively undeformed Sebastopol block [*Fox*, 1983] between the San Andreas fault and the Hayward-Rodgers Creek-Maacama fault zone (Figure 1.2). The Sebastopol block is stable, in contrast with the Santa Rosa block to the east which is highly deformed [*Fox*, 1983]. Within the Santa Rosa block and other easterly parts of the Coast Ranges, Quaternary folding and faulting have left uplifted ridges and downwarped basins, the most striking basin being the southern arm of San Francisco bay. Rates of folding and uplift are best calculated for coastal regions where marine terraces between San Francisco and Monterey bay indicate uplift rates of about 0.2 mm/yr [*Brown*, 1990]. Measured uplift and subsidence rates average about 0.5 mm/yr. However no reliable estimates of vertical deformation are available for large parts of the fault system.

1.4 Geophysics in California

1.4.1 Seismic Refraction and Reflection Studies

Seismic refraction and reflection profiles together form a complementary set whose primary product is a model of the seismic P-wave velocity distribution in the crust and upper mantle. From this can be derived maps of crustal thickness and crustal cross sections that summarise the lithospheric structure and tectonics along the San Andreas fault system [*Mooney and Weaver*, 1989] (Figure 1.11).

In central California the crust generally thickens eastward from about 24 km at the coast to 30 km in the central (Great) valley to 55 km underneath the Sierra Nevada before thinning to about 30 km in the Basin and Range province in Nevada. The crust along the San Andreas fault system is everywhere thinner than the 36 km crustal average for the conterminous United States [*Braile et al.*, 1989]. No obvious steps in crustal thickness are detected across the fault system.

Seismic reflection and refraction profiles both indicate pronounced vertical, upper crustal, low velocity zones 1 to 2 km wide and extending to depths of 8 km around faults at several sites in California [*Healy and Peake*, 1975; *Feng and McEvilly*, 1983; *Mooney and Colburn*, 1985]. Similar low velocity zones along faults in the northern Coast Ranges are also detected using three-dimensional velocity inversion of local earthquake arrival times [*Eberhart-Phillips*, 1986].

On the basis of four seismic reflection and refraction profiles across the Coast Range-Great Valley transition, together with surface and borehole geology, gravity and magnetics, *Wentworth et al.* [1984, 1987] concluded that the east margin of the Franciscan assemblage forms a tectonic wedge that overlies Great Valley basement (Figure 1.9). According to this interpretation, the Franciscan tectonic wedge was thrust north-eastward onto the Great Valley basement and uplifting the Great Valley sequence. This contrasts with earlier views of eastward subduction of the Franciscan along the Coast Range thrust, which was proposed to extend down to mantle depths [*Bailey et al.*, 1964]. Uplift of the Franciscan assemblage and extension of the upper plate may have occurred during the Cretaceous and a tectonic wedge of Franciscan assemblage subsequently driven landward with the extended upper plate riding passively on top [*Fuis and Mooney*, 1990]. Modern thrust faulting and folding is still occurring as illustrated by the 1983 Coalinga earthquake [*Eaton*, 1990].

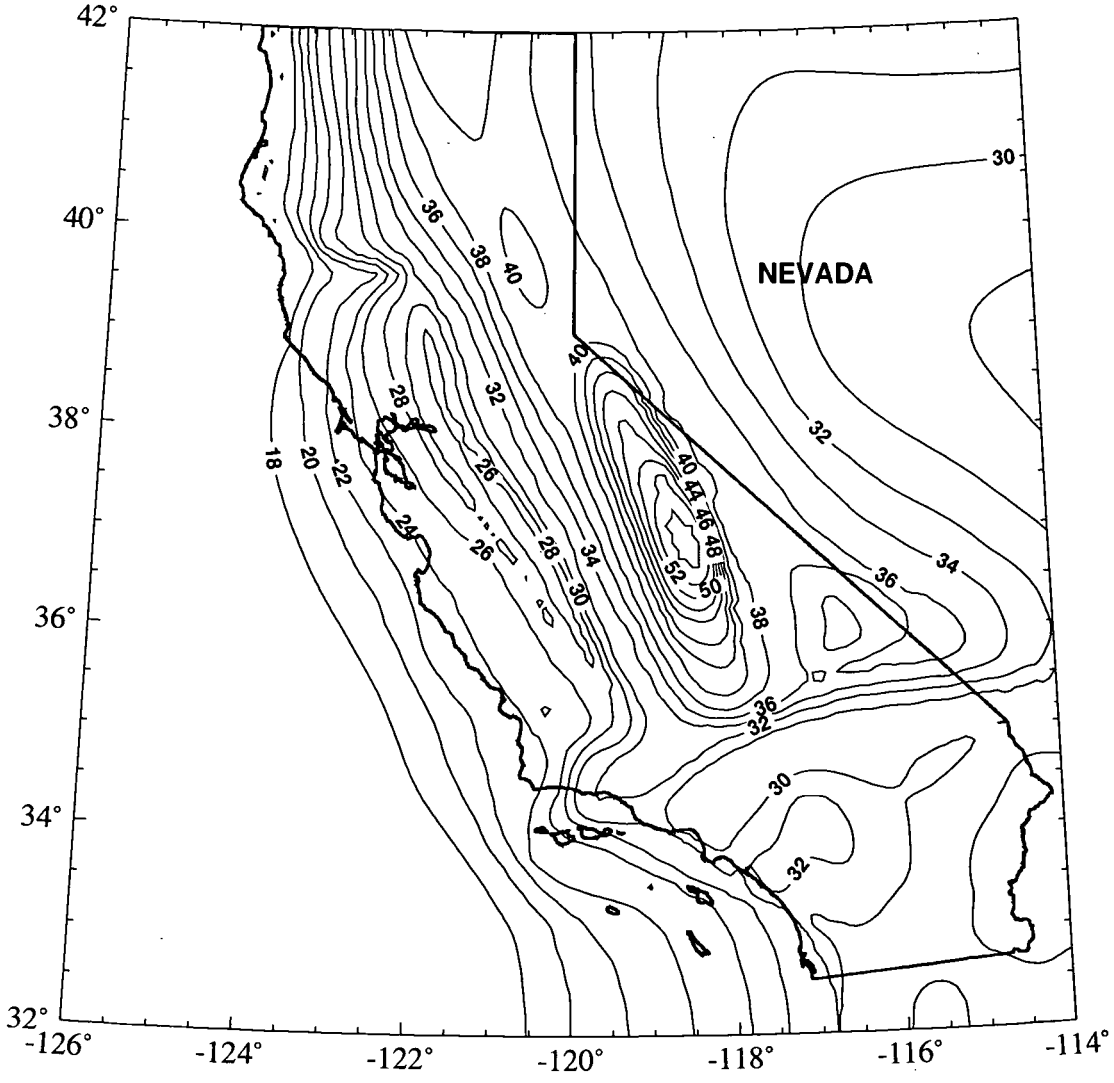

Figure 1.11: Contour map of crustal thickness in km for California and adjacent regions derived from seismic refraction, seismic reflection, seismicity and gravity data. Estimated error is 10%. Adapted from *Mooney and Weaver* [1989]

1.4.2 Seismicity

The high level of seismic activity along the San Andreas fault system (Figure 1.12) reflects brittle accommodation of the crust to the relative motion between the Pacific and North American plates. Although details of the seismicity pattern change over time, the broad pattern has remained stable throughout the entire history of instrumentally recorded earthquakes in California.

Sections of the San Andreas system stand out on seismicity maps as northwest orientated zones of epicentres (Figure 1.12). However, another remarkable aspect of the seismicity pattern is the almost complete lack of seismicity along the section of the San Andreas fault that ruptured in the largest historical earthquake, the great 1906 earthquake (Figure 1.2). Similarly, low seismicity also characterises the ruptured segment of the great 1857 Fort Tejon earthquake in southern California. These two segments appear to be locked at present and show no evidence of aseismic slip (creep). In contrast, other segments exhibit aseismic shallow creep and frequent small to moderate earthquakes.

On the basis of this seismicity pattern, the San Andreas fault system is subdivided into four major divisions [*Allen*, 1968] (1) the quiescent segment that slipped in 1906, (2) branches forming the central California active (creeping) section, (3) the quiescent segment that slipped in 1857, and (4) branches forming the southern California active section. This pattern has persisted since reliable locations became available in the mid 1930's. The largest earthquake to occur in central California recently was the M=7.1, October 1989, Loma Prieta earthquake which ruptured the southernmost 45 km of the 1906 break [*Dietz and Ellsworth*, 1990]. In the San Francisco bay region, the boundary between the first two subdivisions can be seen. Densely aligned epicentres on the San Andreas fault up to latitude 37°10′N mark the south end of the 1906 break. Densely aligned epicentres follow the Calaveras fault northward to a point where the Hayward fault branches to the west and the Greenville fault branches to the east (Figure 1.2). Few epicentres lie along the northward extension of the Calaveras fault north of the branching point except for a diffuse cluster that coincides with the right stepping offset between the north end of the Calaveras fault and its continuation, the Concord fault.

Although the epicentres of small earthquakes coincide closely with the geologically mapped traces in many places [*Eaton et al.*, 1970] there are some exceptions. For example, in the region where the Calaveras fault branches from the main trace of

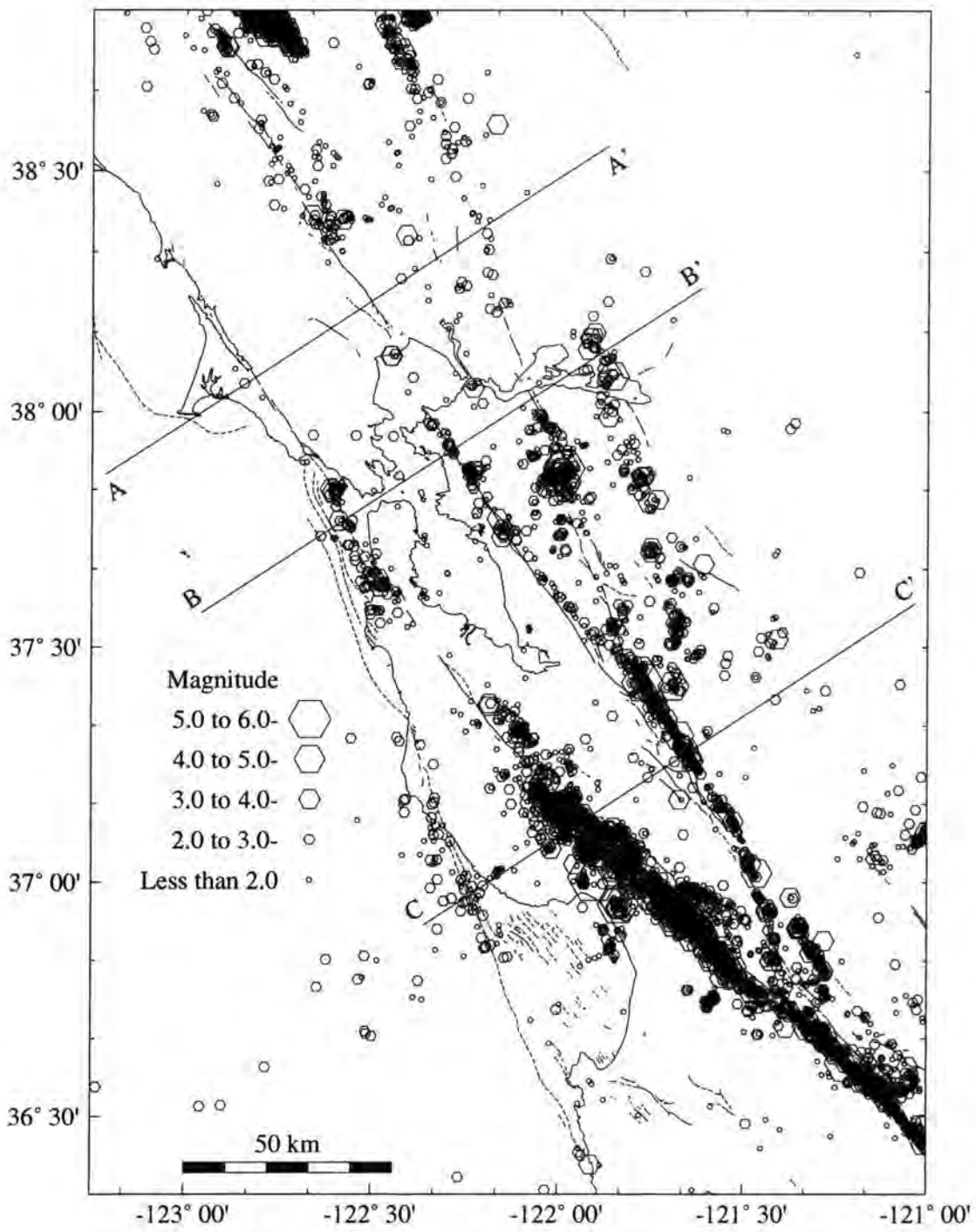

Figure 1.12: Locations of M $\geq$ 1.5 earthquakes recorded by more than 8 seismic stations during the interval 1989-1993 in central California and mapped faults. A-A′, B-B′ and C-C′ define across-strike depth sections of Figure 1.13.

the San Andreas fault the epicentres lie a few kilometres west of the San Andreas fault and a few kilometres east of the Calaveras fault. Most of this offset can be attributed to a contrast in rock type and P-wave velocity across the faults resulting in systematic epicentral errors [*Mayer-Rosa*, 1973]. These offsets are reduced, but not eliminated, when a more appropriate crustal velocity model is used to calculate locations. The remaining offsets may result from the deviation of the faults from vertical. The relation of mapped surface faults to deep seated faults is also obscure at the intersection of the Hayward and Calaveras faults. The mapped surface traces of these faults do not intersect but overlap for about 60 km. Figure 1.12 shows the seismicity in this region to be approximately below the trace of the less prominent Mission fault (Figure 1.2). The Mission fault seismicity then grades into the Hayward fault seismicity, so that the Mission fault appears to transfer strike-slip motion between the Hayward and Calaveras faults [*Andrews et al.*, 1993].

The subparallel epicentre lineations in the Coast Ranges north of San Francisco bay and east of the 1906 break follow the Rodgers Creek-Healdsburg-Maacama, and the Green Valley-Bartlett springs fault zones. These zones are the northern extensions of the Hayward and Calaveras-Concord faults although an aseismic interval obscures the connections. The dense cluster of epicentres in the far north of Figure 1.12 represents industrially induced earthquake activity associated with The Geysers geothermal field [*Eberhart-Phillips and Oppenheimer*, 1984].

Cross sections highlight the across- and along-strike distribution of hypocentres with depth (Figures 1.12, 1.13, 1.14). The northernmost across-strike cross section (Figure 1.13a), shows the concentration of earthquakes around the Rodgers Creek and Green Valley faults. The San Andreas fault, part of the 1906 segment, is virtually aseismic. Further south, the San Andreas, Hayward and Calaveras faults are all clearly delineated by concentrations of hypocentres (Figure 1.13b). The Calaveras fault shows a wider distribution of hypocentres because of the chosen cross-section direction and the right step between the Calaveras and Concord fault. The broad distribution of seismicity across the San Andreas fault in the southern cross-section (Figure 1.13c) results from the abundant cloud of aftershocks following the 1989 Loma Prieta earthquake, which occurred on a westward-dipping fault west of the 1906 break [*Dietz and Ellsworth*, 1990].

The maximum focal depths indicate the thickness of the seismogenic crust. Beneath the San Andreas fault system they range from about 5 km beneath the Geysers geothermal field (north end of Hayward fault depth section, Figure 1.14a)

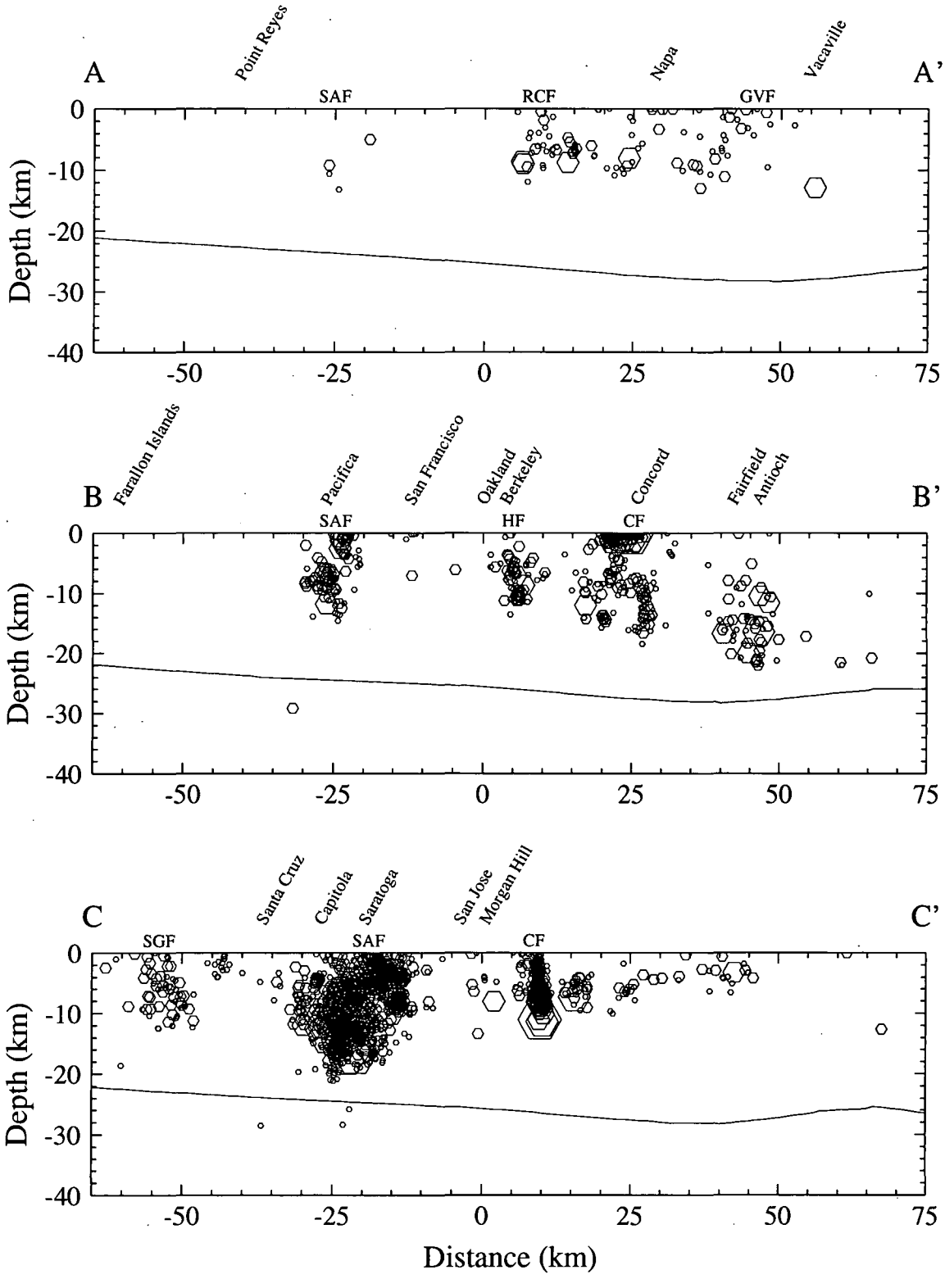

Figure 1.13: Cross sections across the San Andreas fault system in Central California (see Figure 1.12 for lines of sections). Hypocentres are projected onto the plane of the profile for earthquakes within 20 km on either side of the profile. The solid lines represent the crustal thickness (Figure 1.11). SAF = San Andreas fault, RCF = Rodgers Creek fault, GVF = Green Valley fault, HF = Hayward fault, CF = Calaveras fault, SGF = San Gregorio fault.

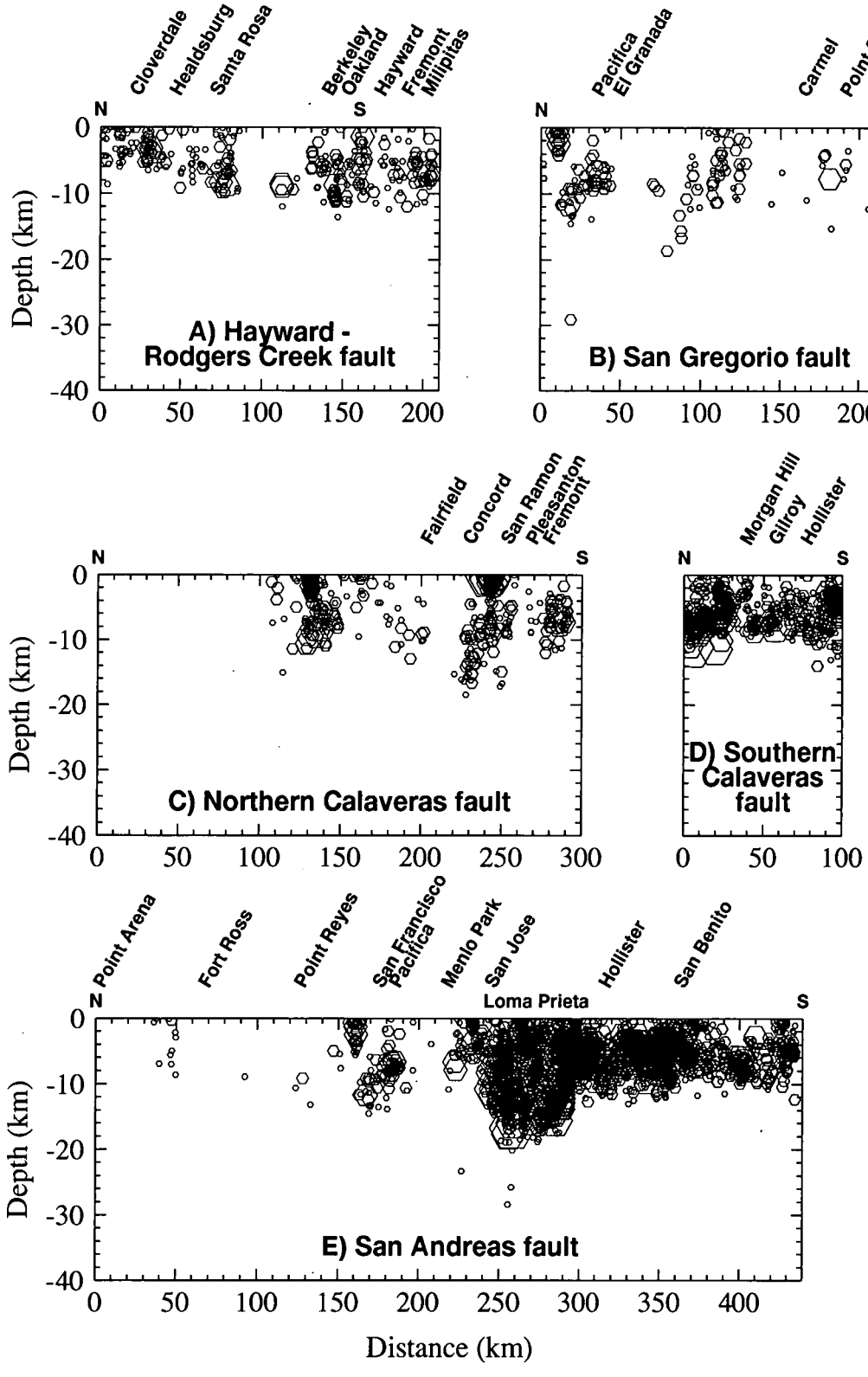

Figure 1.14: Cross sections along the strike of selected faults in the San Andreas fault system in Central California (Figure 1.12). Hypocentres are projected onto the surface trace of the fault for earthquakes within 5 km on either side of the fault. Loma Prieta = extent of aftershocks from 1989, Loma Prieta earthquake.

to just shallower than 20 km beneath San Pablo bay (east end of section B-B′) and along the San Andreas fault where ruptured by the Loma Prieta earthquake (Figure 1.14e). In general, throughout central California, maximum focal depths range from 10 km to 15 km (Figure 1.14a-e). The increased maximum depth along the Loma Prieta segment of the San Andreas fault was observed during that sequence. The main shock initiated at 18 km depth, which is substantially greater than the maximum depth of hypocentres determined prior to the event.

The maximum focal depth along the San Andreas fault system is inversely correlated with surficial heat flow and the maximum depth of earthquakes indicates a temperature-dependent transition from brittle failure in the upper crust to aseismic, quasi-plastic flow in the lower crust and upper mantle [e.g., *Sibson*, 1983; *Scholz*, 1988]. For rocks typical of the upper crust, and deformation rates typical of the San Andreas fault system, the brittle-ductile transition occurs at $\sim 300°C$ [*Sibson*, 1983]. Along "mature" parts of the San Andreas fault system there is a strong correlation between the depth above which 90% of the earthquakes occur and the 300°C isotherm [*Miller and Furlong*, 1988]. In central California the base of the seismogenic crust is everywhere shallower than the base of the crust (Figure 1.13)

Most earthquakes that are located close to the surface traces of the San Andreas fault and its major branches have focal mechanisms that are generally consistent with right-lateral strike slip movement (e.g., events 15, 16, 17, 19, 20, 23, 26-29, 34, 36, 38, 45, 46, Figure 1.15). Exceptions to this pattern appear to be attributable either to regions of fault complexity such as the major bends in the San Andreas fault or, for smaller events close to but not on the major faults, varying conditions along the fault. Earthquakes occurring even a short distance off the faults of the San Andreas system show very different mechanisms. For example, there is a strong component of reverse slip at large angles to the local strike of the fault system for earthquakes on both sides of the Coast Ranges and especially along the Coast Ranges-Great Valley boundary (e.g., events 14, 21, 47-50, 54).

1.4.3 Gravity and Magnetics

The pattern of isostatic gravity anomalies in central California consists of alternating highs and lows that trend subparallel to the major faults in the region. Isostatic residual gravity maps show gravity anomalies that remain after an isostatic cor-

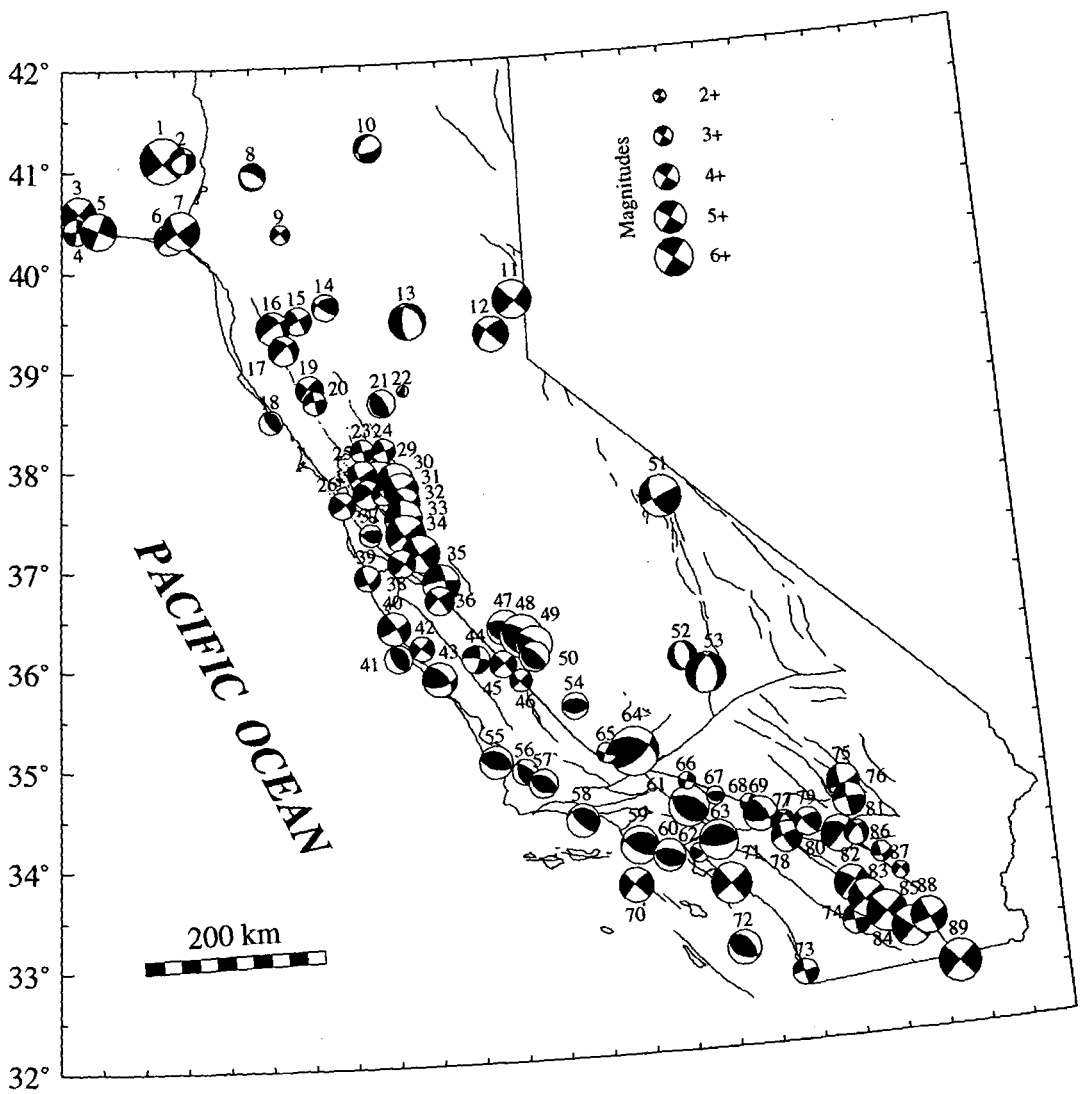

Figure 1.15: Focal mechanisms of selected earthquakes in California 1933-1988. [From *Hill et al.*, 1990]

rection (to correct for structure below sea level) has been made to the Bouguer gravity field [*Simpson et al.*, 1986].

High isostatic residuals in the coastal region occur over the exposed Salinian block southwest of the San Andreas fault and the Franciscan assemblage northeast of the fault. An adjacent low correlates with the Great Valley, where thick accumulations of low density Cenozoic sedimentary rocks cover the Great Valley sequence. The next parallel high occurs over the mafic granitic and metamorphic rocks of the Sierra Nevada. Shallower lows occur over certain large serpentinite bodies within the Franciscan assemblage, over felsic plutons in the granitic terranes of California and over a young concealed granitic pluton associated with The Geysers geothermal field [*Griscom and Jachens*, 1990].

Magnetic anomalies in central California also show linear trends subparallel to the San Andreas fault system. A prominent magnetic high follows the Great Valley axis. To the west a smaller but still prominent high occurs over the western edge of the Great Valley, approximately overlying the position of the Coast Range fault and probably linked to tabular bodies of serpentinite within the Franciscan assemblage.

Gravity lows along a fault may result from an increase in porosity by fracturing [*Stierman*, 1984]. However, some low velocity zones inferred from seismic data have no associated gravity low [e.g., *Trehu and Wheeler* 1987]. Macrofractures within a fault zone can cause large decreases in seismic velocity without an equivalent decrease in density as predicted from standard velocity-density relations [*Griscom and Jachens*, 1990]. Aeromagnetic data along the San Andreas fault from San Francisco and San Bernadino show that the creeping segment of the fault is characterised by broad aeromagnetic anomalies suggesting large concealed bodies of serpentinite [*Hanna et al.*, 1972a, 1972b].

1.4.4 Stress and Heat Flow

1.4.4.1 Stress

Measurements of the magnitude and orientation of crustal stress in the vicinity of the San Andreas fault should provide the most direct evidence of the forces causing interplate motion there. Data on principal stress orientations come from four main sources: earthquake focal mechanisms, elliptical well-bore enlargements or "breakouts", in situ stress measurements (primarily using the hydraulic fracturing

technique) and geological data [*Zoback and Zoback*, 1980].

Stress measurements in central California have been described by *Zoback and Zoback* [1980], *Zoback et al.* [1987], *Mount and Suppe* [1987] and others. Magnitudes of in-situ stress measurements made to depths of 3 km indicate stress consistent with Mohr-Coulomb frictional faulting theory and laboratory derived coefficients of friction. Classical faulting theory predicts the direction of maximum horizontal compression (σ_{Hmax}) to be 30° to 45° from the plane of a vertical strike-slip fault [*Jaeger and Cook*, 1969]. However, the orientation of σ_{Hmax} in central California is nearly perpendicular to the strike, particularly when stress indicators from right-lateral strike-slip focal mechanisms along the San Andreas fault system are ignored [*Zoback et al.*, 1987]. This is supported by observed uplift of the Coast Ranges and current active reverse faulting and folding along nearly the entire length of the west side of the central Great Valley indicating geologically recent, San Andreas fault-normal compression.

1.4.4.2 Heat Flow

Heat flow measurements around the San Andreas fault zone [*Lachenbruch and Sass*, 1980] reveal several contrasting thermal regimes. Average heat flow is high ($\sim$ 2 HFU, $\sim$ 80 mWm^{-2}) throughout the segment of the Coast Ranges that encloses the San Andreas fault system. This broad anomaly falls off rapidly eastwards towards the Great Valley and north-westwards towards the Mendocino triple junction, about 200 km away. A localised region of high heat flow north of San Francisco is associated with the Geysers geothermal field. This broad thermal anomaly has been modelled as the migration of the Mendocino triple junction and the truncation of subduction causing a "hole" in the lithosphere beneath which hot asthenosphere rises, resulting in an increase in surface heat flow by a factor of 2 within 4 Ma of the passage of the triple junction [*Lachenbruch and Sass*, 1980; *Zandt and Furlong*, 1982]. After the initial upwelling of the asthenosphere into the hole, the lithosphere slowly cooled and thickened. This cooling resulted in a lowering of the geotherm and a decrease in surface heat flow and elevation away from the triple junction. Lithospheric strength as a function of time since Mendocino triple junction migration may be calculated [*Furlong et al.*, 1989]. A low-strength region, whose lithospheric strength is less than 20% of the strength of thermally unperturbed lithosphere, extends from near Hollister northwards to past Point Arena (Figure 1.16). The predicted location of minimum strength, and

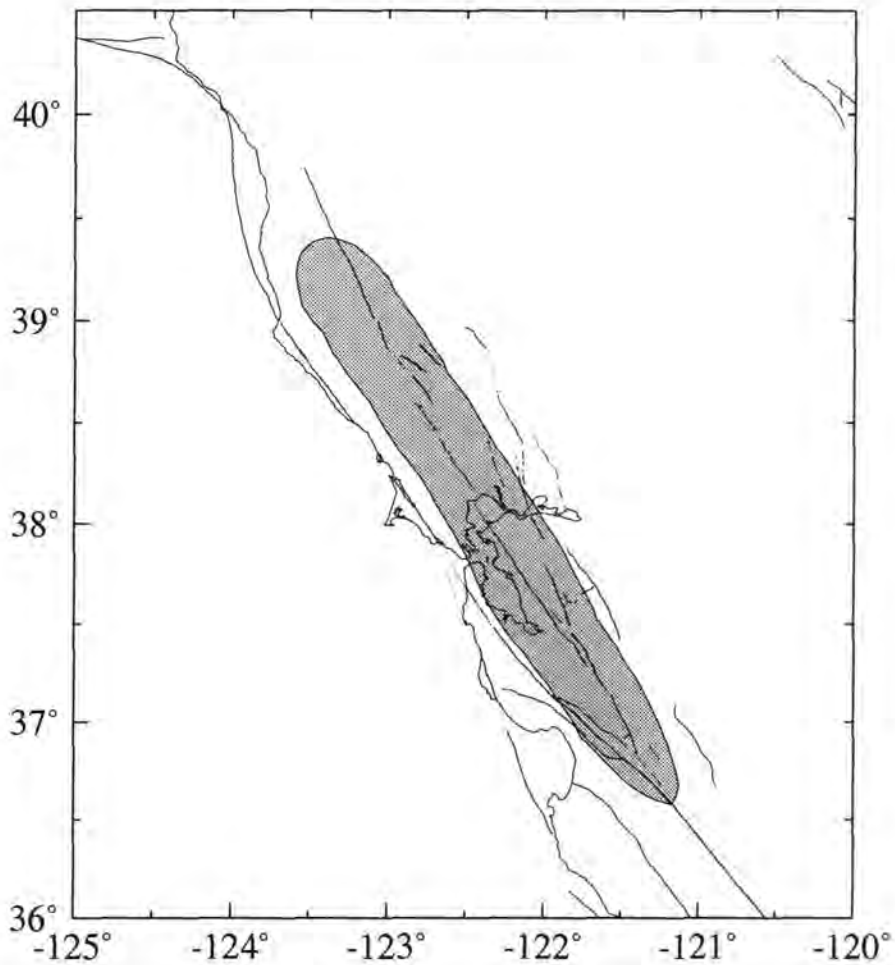

Figure 1.16: Region in Central California (shaded) where lithospheric strength is calculated to be less than 20% of the strength of thermally unperturbed lithosphere [From *Furlong et al.*, 1989]

therefore the preferred location of the plate boundary within the lower lithosphere, is east of the San Andreas fault and dips eastwards. However, dissipative heating due to distributed shear in the strong upper mantle on vertical planes parallel to the San Andreas fault could explain the source of excess heat flow in the Coast Ranges [*Molnar*, 1992].

Another feature of the thermal regime is the absence of any localised heat flow anomaly associated with the San Andreas or other faults that would be expected due to frictional heat generation from long-term, strike-slip motion [*Brune et al*, 1969]. Heat flow measurements imply that the average frictional resistance to fault motion is no greater than about 20 MPa [*Lachenbruch and Sass*, 1981]. For the case of hydrostatic pore pressure, Byerlee's law [*Byerlee*, 1978] predicts levels of shear stress of about 150 MPa at a depth of about 15 km for strike-slip faulting.

However, low permeability in the fault zone could lead to pore fluid pressures that are a significant fraction of the lithostatic pressure [*Rice*, 1992]. This would yield lower levels of shear stress in the fault zone and therefore no localised heat flow anomaly.

1.4.4.3 The Stress-Heat Flow Paradox

There is appreciable evidence that, while the frictional strength of the upper crust is high (in general accordance with simple faulting theory and laboratory-derived coefficients of friction), the frictional resistance to motion along transform plate boundaries is extremely low. In addition, the orientation of principal horizontal stresses along the San Andreas fault system shows shear stresses acting on planes parallel to the San Andreas fault are extremely small. The observed direction of crustal compression in central California suggests that the direction of relative plate motion between the Pacific and North American plates is highly oblique to the San Andreas fault. However, the N35°-40°W fault strike in central California differs by only about 5° from the $\sim$ N35°W relative plate motion direction and this would result in essentially pure shear along the San Andreas and an approximately north-south direction of maximum horizontal compressive stress.

Taken together the above evidence suggests that the San Andreas fault system is weak in a *relative* sense, in that the adjoining crust seems to be mechanically stronger. The fault may also be weak in an *absolute* sense since it may move under shear stresses far smaller than predicted by laboratory friction results unless the fault zone has a high permeability and pore fluid pressures are a significant fraction of the lithostatic pressure.

If a transform plate boundary is considerably weaker than the adjacent crust then principal stresses may re-orientate themselves in order to minimise shear stresses on the planes parallel to the boundary [*Zoback et al.*, 1987; *Zoback*, 1991]. In the case of a transpressional boundary such as the San Andreas, this re-orientation would lead to fault-normal compression. However, the orientations of principal stresses in the upper crust may be a consequence of the partitioning of oblique convergence into pure strike-slip along faults parallel to the boundary between rigid blocks and pure convergence on thrust faults that also have strikes parallel to the boundary [*Molnar*, 1992]. In this case, ignoring stress indicators from focal mechanisms along the major strike-slip faults whilst including focal mechanisms from adjacent thrust faults is biasing the interpretation of stress results. If the orientations are a

consequence of strain partitioning then these orientations provide less insight into the dynamics of crustal deformation than measurements of the full deformation gradient tensor obtained from geodesy.

1.5 Summary

The San Andreas fault system of California is a (~30 Ma years old) system of dominantly right-lateral, strike-slip faults that extends from the Gulf of California to Cape Mendocino and forms part of the boundary between the Pacific and North American plates. Global plate motion models indicate a relative velocity between the Pacific and North American plates of 46 mm/yr at N33°W. However, geological studies indicated a slip rate of only 35 mm/yr. The discrepancy, 10-13 mm/yr, is termed the San Andreas discrepancy. The missing motion is thought to be mainly concentrated in the Basin and Range province either distributed across many horst and graben features or predominantly in the western Basin and Range province along the Eastern California Shear Zone. The geologic assemblages in central California generally reflect the tectonic assemblages of an accretionary prism/fore-arc basin/magmatic arc relating to the subduction regime in California prior to the onset of the transform boundary.

Geophysical studies have revealed many linear features within the system that can be directly related to mapped fault traces at the surface. Earthquake focal mechanisms show that whilst most earthquakes located on active faults show right-lateral strike slip mechanisms, many off-fault earthquakes within the Coast Ranges are consistent with reverse faulting on faults parallel to the general strike of the fault system.

The magnitude and orientation of stress in the crust around the fault system and heat-flow measurements appear to reveal a paradox between these results and theoretical considerations for strike-slip faults and laboratory experiments. Although not fully resolved, this paradox may imply a weak San Andreas fault, high pore fluid pressures and/or a bimodal distribution of stress orientations in the San Andreas fault system that was originally ignored.

Chapter 2

Geodesy and Crustal Deformation in the Western United States

2.1 Overview

Historically, geodesy has been used for two purposes. First, geodesy is used to determine the size and shape of the Earth and the form of its external equipotential surfaces (scientific geodesy). Second it is used in the production of a primary framework of networks (primary arc) for horizontal and vertical ground control on which topographical and cadastral maps could be built (geodetic surveying).

The use of geodesy for surveying purposes in California commenced in 1851-1887 when a primary arc between San Francisco and Lake Tahoe was measured using triangulation. After the initial observation, San Francisco was destroyed in the 1906 earthquake. The 2-4 m of observed displacement along the 450-km long ruptured segment disturbed this primary arc, and by July 1907 repair to the network had been completed. Differencing the pre- and post-earthquake station positions showed that crustal movements extended to many miles on either side of the fault [*Hayford and Baldwin*, 1907]. It was these results that led H. F. Reid to formulate his "elastic rebound" theory of earthquake genesis [*Reid*, 1910].

The value of geodesy for detecting crustal movements was recognised in a report on the 1906 earthquake [*Lawson*, 1908]. Deliberate investigation of crustal deformation then began in California with the re-occupation in 1922-1928 of the sites observed in 1906-1907, together with many more sites occupied in the previous century [*Bowie* 1924, *Bowie*, 1928]. These sites were reoccupied approximately every decade until they were superseded by small networks across the San Andreas fault during the 1940's. Displacements due to earthquakes in both California and Nevada were detected by triangulation networks, and a systematic movement of $\sim$ 50 mm/yr

was observed across the San Andreas fault [e.g., *Whitten*, 1956].

In the 1960's, the use of Electronic Distance Measurements (EDM) to conduct trilateration surveys enabled direct measurement of distance with at least an order of magnitude improvement in accuracy over triangulation. Improved modelling of atmospheric effects along EDM-measured lines increased precision further in the 1970's and trilateration surveys became firmly established as a major tool for studying tectonic processes on local and regional scales [*Savage and Burford*, 1973; *Prescott et al.*, 1979, 1981; *Savage*, 1983]. EDM is limited to measuring line lengths between intervisible stations at spacings of less than $\sim$ 50 km [*Savage and Prescott*, 1973]. Nevertheless, trilateration networks were widely established in the western United States over three decades in order to measure recent plate motions or crustal deformation (Figure 2.1).

The use of space geodetic techniques (measurements using extraterrestrial objects) to monitor both inter- and intra-plate motions was first proposed in the late 1960's [*Shapiro and Knight*, 1970; *Whitten*, 1970]. About fifteen years were required to develop the capability of measuring lines up to the Earth's radius in length with a precision of one centimetre [*Shapiro*, 1983]. In the past decade, techniques such as Satellite Laser Ranging (SLR) [*Christodoulidis et al.*, 1985; *Smith et al.*, 1990] and Very Long Baseline Interferometry (VLBI) [*Herring et al.*, 1986; *Clark et al.*, 1987] have provided precise measurements between points on a continental scale. These observations however, are restricted to relatively sparse networks by the cost of the methods and this limits their use in detailed studies of complex plate boundary systems.

The launch, in 1978, of the first Global Positioning System (GPS) space vehicles (satellites) heralded the next advance in space geodetic measurements. GPS receiving equipment is easily portable and the method thus does not suffer the logistic limitations of SLR and VLBI. The strength of GPS over terrestrial techniques is its ability to yield three-dimensional vector lengths (rather than line distances only) which are not intervisible. It has been widely used during the past decade (e.g., Figure 2.2) and the method will be covered in detail in Chapter 3. However, the results from previous GPS surveys are described in this chapter along with those from the other geodetic methods.

Recently, another technique, Synthetic Aperture Radar interferometry (SAR) was introduced to crustal deformation studies with startling results when *Massonet et al.* [1993] produced a map of displacements that accompanied the magnitude 7.3

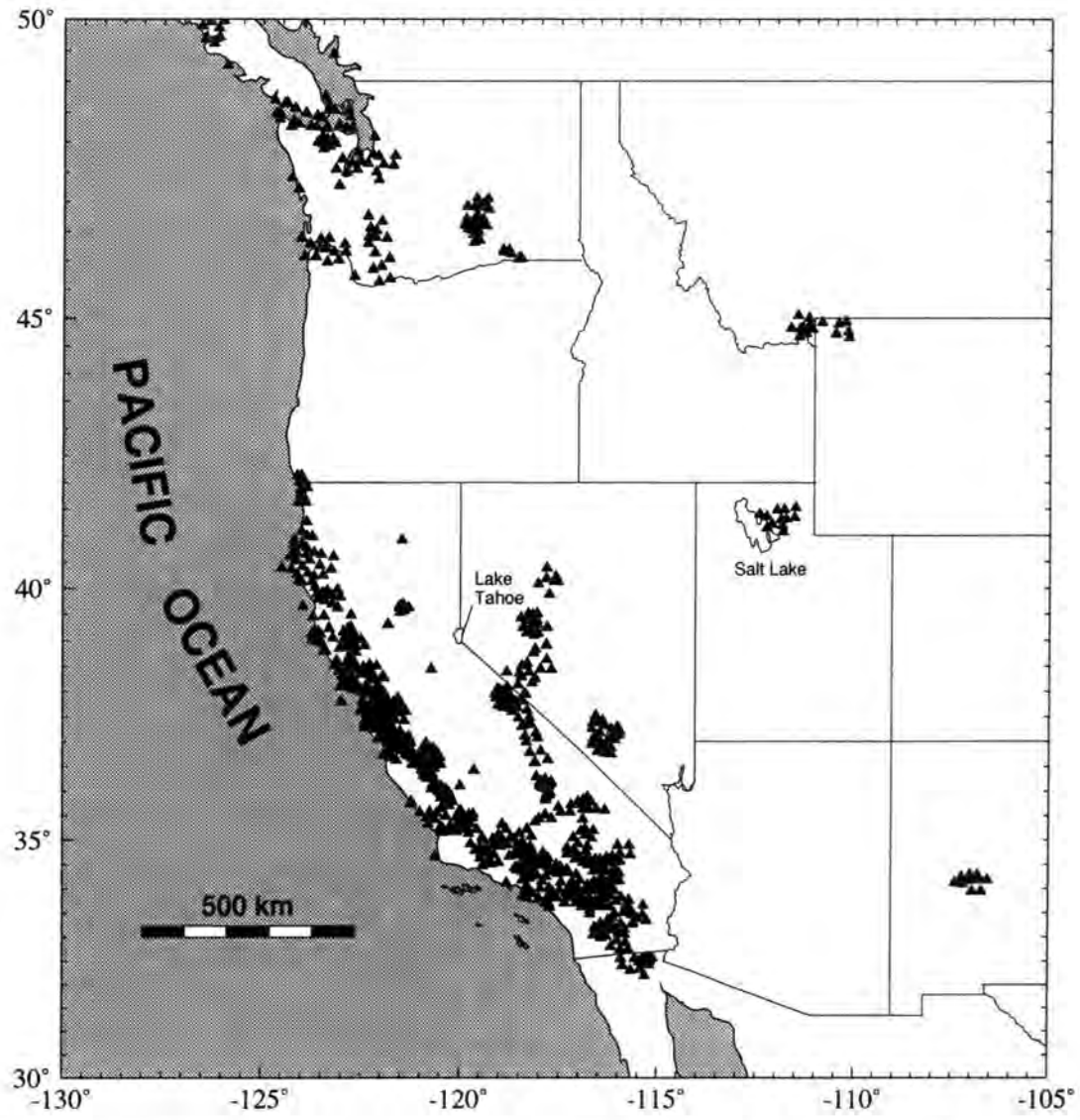

Figure 2.1: Trilateration stations measured by the US Geological Survey for crustal deformation studies in western North America using EDM since the 1960's. Over 2000 stations are plotted.

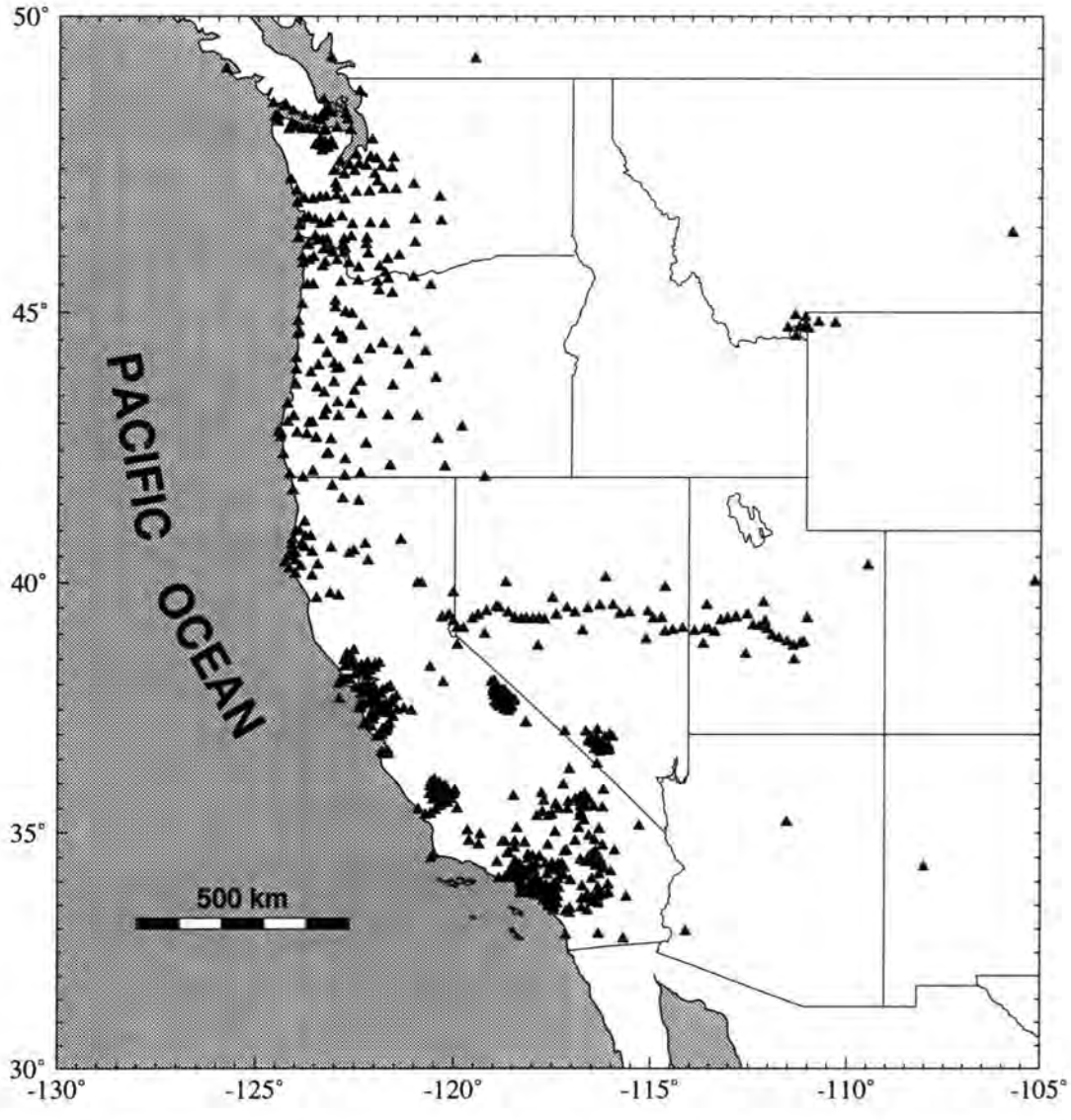

Figure 2.2: GPS stations measured by the US Geological Survey for crustal deformation studies in western North America since the late 1980's.

(M_w) Landers earthquake of June 28, 1992, containing some 300 million measured points. This can be compared with the coseismic displacement field mapped by *Murray et al.* [1993], using GPS, which contained just 28 points over the same area. However, SAR interferometry is still in its infancy and the problems of "uninteresting changes" caused by ground water content, vegetation and cloud cover, low precision ($\sim$ 34 mm; adequate for coseismic displacement detection but at the signal level for aseismic deformation) and measurement of only one component of the deformation field (the component which points towards the satellite) have not yet been solved.

2.2 Geodetic Methods

2.2.1 Triangulation Surveys

Triangulation is the determination of point positions by measurement of the angles between intervisible points using a theodolite. Angle measurements typically have a precision of about 0.1″. However, atmospheric refraction associated with horizontal atmospheric density gradients results in more typical errors of 0.3-0.5″ [*Lambeck*, 1988]. Line lengths are determined by the measurement of the lengths of one or more lines, and the use of these to determine the other distances. Although the accuracy of triangulation surveys is much lower than that of modern geodetic techniques, they have been used for a very long time, and the long time span of the observations has revealed the temporal evolution of the strain field around the San Andreas fault system during most of an earthquake "cycle" [*Thatcher*, 1983; *Gilbert et al.*, 1993].

2.2.2 Trilateration Surveys

Trilateration surveys involve measurements of distance between stations to determine relative positions in the horizontal plane. Pulses of modulated light or microwaves of known frequency are emitted from a device at one end of the line to be measured and reflected back at the other end of the line. The returning pulse is compared with the emitted pulse and the phase difference measured. The distance is an integral number of wavelengths of the light pulse plus the phase difference. The integral number of wavelengths is calculated using measures of the phase dif-

ference at other frequencies. The lengths of the lines measured are limited to about 50 km by station intervisibility and attenuation of the signal. The expected error for EDM lines is $\sigma = \sqrt{a^2 + b^2 L^2}$ where L is the line length. a is a function of calibration and centering errors at the two stations. The length-dependent term b depends on errors in the atmospheric refractive index which in turn come from error in the average temperature used for the path. Typical values of $a \sim 1$ cm and $b \sim 10^{-6}$ cm^{-1} are achieved by measuring the pressure, water vapour pressure and temperature at the two ends of the line. Improved modelling of the atmospheric effects, by flying an aircraft along the line to measure atmospheric properties, can decrease b to about 2 parts in 10^7 [*Savage and Prescott*, 1973].

2.2.3 VLBI and SLR Surveys

VLBI and SLR both rely on cumbersome, observatory-style equipment in order to measure changes in station position. These observations are, therefore, expensive to make and the number of observed sites very limited when compared to terrestrial geodetic techniques. VLBI and SLR experiments have generally concentrated on determining overall plate motions rather than small-scale crustal deformations. Most VLBI and SLR experiments relating to the western United States come under the auspices of the Crustal Dynamics Project (CDP) run by National Aeronautics and Space Administration (NASA). The CDP was formed in 1979 to apply space technology, in the form of VLBI and SLR, to the measurement of tectonic plate motions, regional crustal deformation, polar motion, Earth rotation and other phenomena associated with crustal movements [*Coates et al.*, 1985].

In order to make an SLR measurement, the two-way travel time of a photon pulse from a laser at an observatory to corner cube reflectors on a satellite is measured. This travel time is converted into a range using the speed of light. Repeated range measurements are made to the satellite by a number of different stations. Each range is a constraint on the satellite orbit and the station location. The misclosures between a-priori predicted and observed ranges are minimised to yield the orbit and the three-dimensional coordinates of the tracking stations. The rate of change of the station positions over a long period of time reveal plate motions and local deformation. Errors in the velocities obtained by SLR are generally of the order of 1-10 mm/yr.

In a VLBI experiment, two or more widely-separated radio telescopes simultane-

ously observe and record noise signals from extragalactic radio sources. These signals are cross-correlated in pairs to determine the delay (with respect to local station clocks) between their arrival at the two antennas and the rate of change of this delay. Generally observations are made at two frequencies, the X band (8.4 GHz) and the S band (2.2 GHz) so that corrections for the dispersive effects of the ionosphere can be made. The delays and rates determined are used to estimate geodynamic parameters, including the positions of the radio telescopes and the orientation of the Earth in inertial space. Individual line-length vectors are defined in terms of a length, transverse and vertical component. Expected uncertainties in these components are in the region of 1-2 cm on a 1000 km line and should scale proportionally with line length. The rates of change of these line components can then be used to calculate relative station velocities. Errors in the line rates of change are of the order of 1-10 mm/yr. Specific sets of line length component rate changes obtained from VLBI and SLR experiments under the CDP are regularly published.

2.3 Crustal Deformation in California

2.3.1 Introduction

Geodetic networks for crustal deformation research in California are naturally concentrated along the San Andreas fault system (Figure 2.1 and 2.2). Other network locations are across the Garlock fault (Figure 1.3) and in Owens Valley on the California-Nevada border. About 100 years of triangulation, over 20 years of trilateration and about 10 years of GPS measurements have revealed a significant deformation field around the San Andreas fault system. The focus of this thesis is on the spatial pattern of interearthquake horizontal crustal movements in central California that results from relative motion between the Pacific and North American plates. These movements supply the strain energy which is stored in crustal rocks and released in large earthquakes. Although observations of coseismic offsets and anomalously rapid postseismic deformation have been detected by several networks, these observations are not considered in detail here. The deformation patterns of large strike-slip earthquakes are well-understood consequences of slip in the upper brittle crust. Examples of coseismic movements observed for specific California earthquakes are given, for example, by *Lawson*, [1908] (for the 1906 San

Francisco earthquake), *Segall and Harris*, [1987] (for the 1966 Parkfield earthquake) and *Lisowski et al.*, 1990 (for the 1989 Loma Prieta earthquake).

2.3.2 Strain Rate Variations with Time

Although the accuracy of triangulation surveys is much lower than that of modern geodetic techniques, the long time span of the observations has revealed the non-linear strain buildup within an earthquake cycle. 70 years of observations of the primary arc between San Francisco and Lake Tahoe were used to analyse the strain field associated with the 1906 rupture segment of the San Andreas fault [*Gilbert et al.*, 1993]. Four triangulation surveys between 1922 and 1963 and one GPS survey in 1991 were used. Significant strain associated with the San Andreas fault system is measurable as far as the Great Valley (Figure 1.2) and in the 20-40 years following the 1906 earthquake high strain rates are suggested in both the Coast Ranges and the Great Valley regions. Furthermore, the results imply that the strain rate in the Coast Ranges does not decrease steadily throughout the earthquake cycle, but reaches a constant level with time. Data collected from along the rupture segments of the 1906 and 1857 great earthquakes were combined to illustrate shear strain rates throughout a full earthquake cycle [*Thatcher*, 1983]. Although it may be incorrect to assume that the deformation cycle is similar in both regions, a temporal decline in the shear strain rate that persists for at least 30 years after the event is observed. Decaying strain rates have also been observed after other large earthquakes [e.g., *Savage et al.*, 1994 (for the Loma Prieta earthquake)].

2.3.3 Interseismic Strain Rates Along the San Andreas Fault System

Strain-rate measurements which are consistent with temporally linear strain accumulation can be defined as the background interseismic rate. Principal interseismic strain rates determined from geodetic networks are displayed in Figures 2.3 and 2.4 and in Table 2.1. Some networks span a considerable area, and the strain may vary within that area. The strains shown are averages over the area of the network. In some cases this gives a false picture, for example, in areas where a significant amount of slip occurs as fault creep. In such areas movement is concentrated along the fault and not dispersed throughout the network. Dividing the such areas into

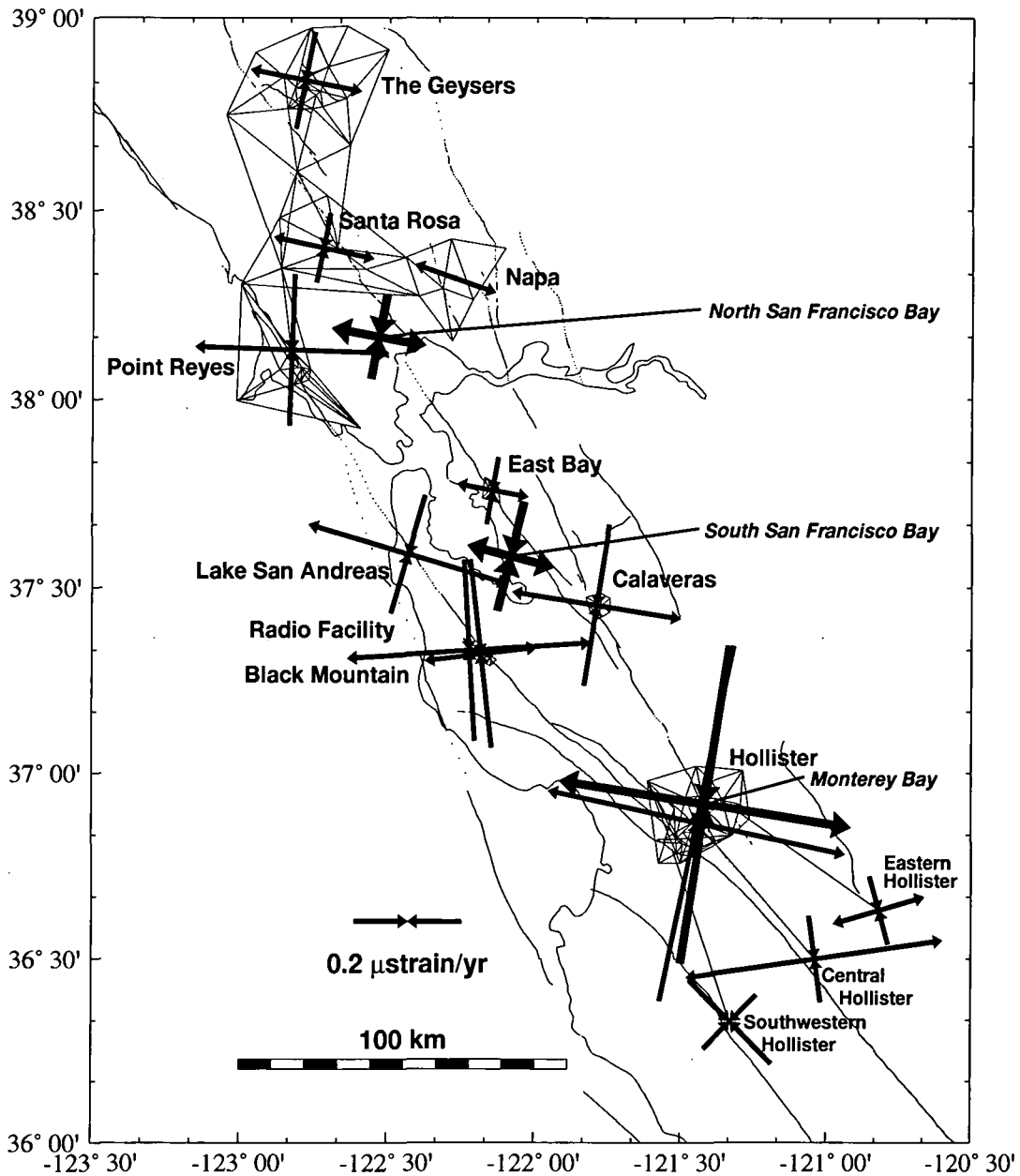

Figure 2.3: Principal strain rate axes determined from geodetic networks in the central California region. Area covered by each network is indicated by triangles. Thick strain rate axes indicate strain rates determined from larger networks (not indicated). See Table 2.1 for details.

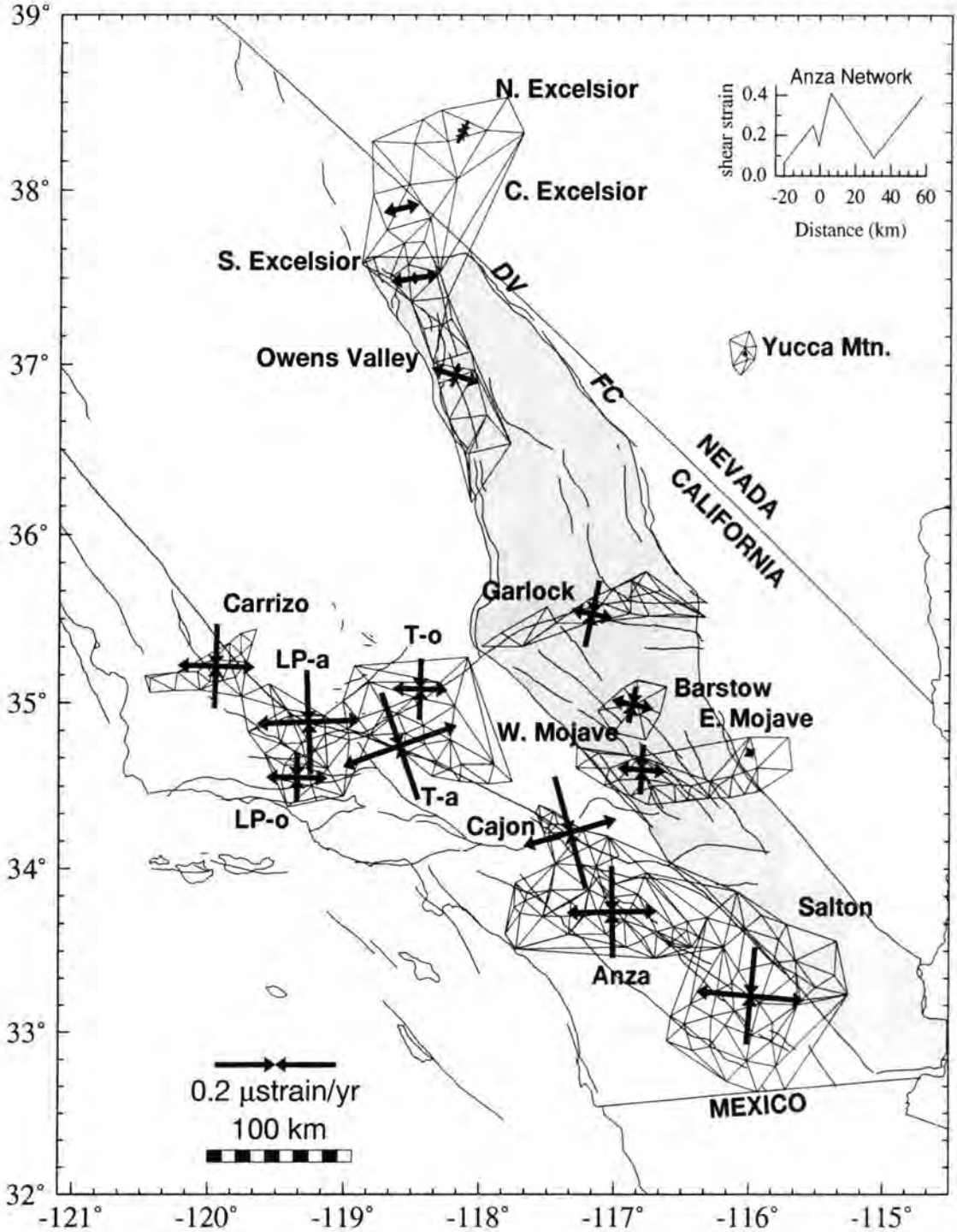

Figure 2.4: Principal strain rate axes determined from geodetic networks in southern California and western Nevada. Area covered by each network is indicated by triangles. Approximate extent of Eastern California shear zone is shown by shading. LP, Los Padres; T, Tehachapi; o, off-fault data; a, along-fault data; DV, Death Valley fault; FC, Furnace Creek fault. Inset, shear strain rates (in μrad/yr) calculated for subregions of the Anza networks plotted against distance perpendicular to the orientation of maximum shear strain for that network. Sources of data are given in Table 2.1

off-fault and on-fault subnetworks may provide a clearer picture.

Along most of the San Andreas fault system the most significant and largest horizontal strain-rate component is shear. The orientation of maximum horizontal shear agrees very well with the surface strike of nearby faults. This agreement is maintained even along major changes of strike such as the big bend of the San Andreas fault in the Transverse Ranges (compare the Los Padre and Tehachapi networks, Figure 2.4) [*Eberhart-Phillips et al.*, 1990; *Lisowski et al.*, 1991; *Gilbert et al.*, 1994]. Significant shear-strain rates are observed as far as about 100 km from the San Andreas fault system. In southern California, just north of the California-Mexico border, most of the crustal deformation is contained within a 40-60 km wide zone centred on the Imperial fault (Figure 1.3) [*Lisowski et al.*, 1991]. To the northwest, the zone of appreciable shear-strain deformation (the "deformation zone") widens to greater than 100 km. In the Anza network (Figure 2.4, main diagram and inset), shear-strain rates calculated for 7 subnetworks show peaks across both the San Jacinto and San Andreas faults [*King and Savage*, 1983]. Shear strains are expected to peak at a fault that is locked, and therefore accumulating strain, in the upper brittle part of the crust. The twin peaks in this network suggest that both the San Jacinto and San Andreas faults are accumulating strain.

North of the big bend region, along the 160-km long central creeping section, a geodetically-derived displacement rate of 33 $\pm$ 1 mm/yr obtained for a 60-km wide network spanning the fault is close to the maximum fault-creep rate of 30 mm/yr measured using alignment arrays and wire extensometers. These data indicate that little strain is accumulating in the crustal blocks on either side of the San Andreas fault in this segment. Most of the relative plate motion is accommodated by rigid-block translation across the San Andreas fault.

North of the central creeping segment, in the San Francisco bay region, the deformation zone once again broadens. Significant shear-strain rates are observed across the seismically active Hayward and Calaveras faults (and their northern extensions, Figure 1.2) to the east of the San Andreas fault (Figure 2.3). In addition fault creep occurs along several segments of the Calaveras and Hayward faults (Figure 2.3). Small (up to 250 m) triangulation triangles are currently being used to measure fault creep in the San Francisco Bay region. About 24 sites have been measured every two to three months since 1979 [*Galehouse*, 1992a; b]. Creep rates are also measured using offset cultural features (curbs, fences, and buildings) [*Lienkaemper et al.*, 1991]. Creep rates of about 13 mm/yr have been measured on the southern

Table 2.1: Average Principal Strain Rates, Strike of Maximum Right-Lateral Shear, and Relative Plate Motion Measured Across Trilateration Networks Along the San Andreas Fault System

Network	Principal Strain Rates $\dot{\varepsilon}_1$ μstrain/yr*	$\dot{\varepsilon}_2$ μstrain/yr	Strike of Maximum Right Lateral Shear deg.†	Relative Velocity mm/yr	Reference
Geyser	0.210	-0.180	N34.0°W ± 2.0°	24.0‡	[*Prescott and Yu*, 1986]
Santa Rosa	0.190	-0.130	N32.9°W ± 1.9°	14.0‡	[*Prescott and Yu*, 1986]
Napa	0.160	-0.010	N26.0°W ± 9.1°	5.0‡	[*Prescott and Yu*, 1986]
North San Francisco Bay	0.179	-0.158	N34.4°W ± 1.5°	31.0	[*Lisowski et al.*, 1991]
Point Reyes	0.360	-0.280	N43.1°W ± 2.3°	23.0‡	[*Prescott and Yu*, 1986]
East Bay	0.135	-0.125	N35.0°W ± 4.0°	2.0‡	[*Prescott et al.*, 1981]
Lake San Andreas	0.385	-0.225	N28.0°W ± 10.0°	2.0‡	[*Prescott et al.*, 1981]
South San Francisco Bay	0.169	-0.206	N31.0°W ± 1.6°	38.0	[*Lisowski et al.*, 1991]
Calaveras	0.320	-0.300	N25.0°W ± 4.0°	4.0‡	[*Prescott et al.*, 1981]
Radio Facility	0.455	-0.335	N47.0°W ± 6.0°	2.0‡	[*Prescott et al.*, 1981]
Black Mountain	0.210	-0.350	N52.0°W ± 6.0°	2.0‡	[*Prescott et al.*, 1981]
Monterey Bay	0.557	-0.593	N36.0°W ± 0.9°	38.0	[*Lisowski et al.*, 1991]
Hollister (all data)	0.570	-0.670	N33.0°W ± 1.0°	23.0‡	[*Savage et al.*, 1979]
Hollister (southwestern)	-0.140	-0.220	N00.0°W ± 3.0°		[*Savage et al.*, 1979]
Hollister (central)	0.490	-0.160	N53.0°W ± 3.0°		[*Savage et al.*, 1979]
Hollister (eastern)	0.180	-0.130	N61.0°W ± 3.0°		[*Savage et al.*, 1979]
Owens Valley	0.082	-0.039	N28.0°W ± 3.0°	6.0‡	[*Savage and Lisowski*, 1995]
Excelsior (northern)	0.002	-0.004	N18.0°W ± 9.0°		[*Savage and Lisowski*, 1984]
Excelsior (central)	0.006	-0.000	N58.0°W ± 12.0°		[*Savage and Lisowski*, 1984]
Excelsior (southern)	0.008	-0.002	N53.0°W ± 14.0°		[*Savage and Lisowski*, 1984]
Yucca Mountain	0.010	-0.009	N45.0°W ± 24.0°		[*Savage et al.*, 1994]
Garlock	0.070	-0.110	N33.0°W ± 3.0°	-12.0‡	[*Savage et al.*, 1990]
Carrizo	0.126	-0.138	N43.3°W ± 2.9°	21.0	[*Lisowski et al.*, 1991]
Tehachapi (along fault)	0.200	-0.185	N64.6°W ± 0.9°		[*Eberhart-Phillips et al.*, 1990]
Tehachapi (off fault)	0.090	-0.100	N43.5°W ± 2.1°		[*Eberhart-Phillips et al.*, 1990]
Tehachapi (all data)	0.150	-0.140	N59.6°W ± 0.8°	24.0‡	[*Eberhart-Phillips et al.*, 1990]
Los Padres (along fault)	0.170	-0.170	N47.0°W ± 1.1°		[*Eberhart-Phillips et al.*, 1990]
Los Padres (off fault)	0.100	-0.080	N43.9°W ± 2.2°		[*Eberhart-Phillips et al.*, 1990]
Los Padres (all data)	0.145	-0.125	N46.7°W ± 0.9°	21.0‡	[*Eberhart-Phillips et al.*, 1990]
Central Transverse Ranges	0.158	-0.151	N61.7°W ± 1.1°	18.0	[*Lisowski et al.*, 1991]
Western Transverse Ranges	0.125	-0.131	N54.4°W ± 1.4°	22.0	[*Lisowski et al.*, 1991]
Barstow	0.070	-0.060	N33.0°W ± 3.0°	6.0‡	[*Savage et al.*, 1990]
W. Mojave (*deviatoric*)	0.080	-0.080	N41.0°W ± 5.0°		[*Savage et al.*, 1990]
E. Mojave (*deviatoric*)	0.020	-0.020	N77.0°W ± 25.0°		[*Savage et al.*, 1990]
Cajon	0.160	-0.190	N61.0°W ± 2.0°	12.0‡	[*Savage et al.*, 1986]
Anza	0.150	-0.150	N46.0°W ± 1.0°		[*Savage et al.*, 1986]
Anza-Joshua	0.113	-0.121	N44.6°W ± 1.1°	31.0	[*Lisowski et al.*, 1991]
Salton	0.180	-0.160	N40.0°W ± 1.0°		[*Savage et al.*, 1986]
Salton	0.141	-0.131	N39.4°W ± 1.3°	37.0	[*Lisowski et al.*, 1991]

* Extension reckoned positive.

† Strike of maximum right-lateral shear is 45° clockwise of the axis of maximum principal extension rate ($\dot{\varepsilon}_1$).

‡ Calculated by multiplying maximum horizontal shear rate by width of network perpendicular to strike of maximum right-lateral shear.

Negative velocity for Garlock network represents left-lateral shear along the Garlock fault.

section of the Calaveras fault. Elsewhere, measured creep rates range from about 1 to 9 mm/yr. To the north, around Point Arena, recent GPS results have indicated strain distributed throughout the Coast Ranges in a deformation zone similar to the northern San Francisco bay region [*J. Freymueller*, personal communication, 1993].

The integrated, right-lateral displacement rates for California are shown in Figures 2.5 and 2.6. These rates constrain the portion of Pacific-North American plate motion accommodated across the San Andreas fault system. Maximum rates for networks spanning the whole of the fault system range from 31 to 37 mm/yr and average 35 mm/yr which is similar to the secular slip rate obtained from geologic studies.

In addition to right-lateral shear strain, fault-normal compression has been detected at several geodetic networks with the Coast Ranges. Fault-normal contraction in the Parkfield region was inferred by *Harris and Segall* [1987] and *Sung and Jackson* [1989] from the misfit of trilateration data to their fault models. Strain rates in a network between the San Andreas fault and the Great Valley in central California displayed the orientation of maximum compressive strain (N16°E $\pm$ 13°) to be similar to the orientations of major fold structures in the region (N25°E) [*Sauber et al.*, 1989]. The measured strain, although not significant at the 95% confidence limit, was attributed to compression across the folds with a shortening rate of around 6 mm/yr. Strain rates obtained from GPS lines spanning the eastern Santa Barbara Channel, the Ventura basin, the Los Angeles basin, and the Santa Maria Fold and Thrust Belt in southern California indicate a component of shortening, up to 5 mm/yr, superimposed on the expected shear strain [*Donnellan et al.*, 1993]. No systematic convergence on the fault was observed between 1973 and 1989 in any of the USGS trilateration networks spanning the fault system (Salton, Anza-Joshua, Transverse Ranges, Carrizo, Monterey Bay, San Francisco Bay) [*Lisowski et al.*, 1991].

2.3.4 Strain Rates Away from the San Andreas Fault System

In addition to deformation measured along the San Andreas fault system, four geodetic networks in eastern California situated between the northern Owens Valley and the Transverse Ranges exhibit simple, right-lateral, shear-strain accumulation

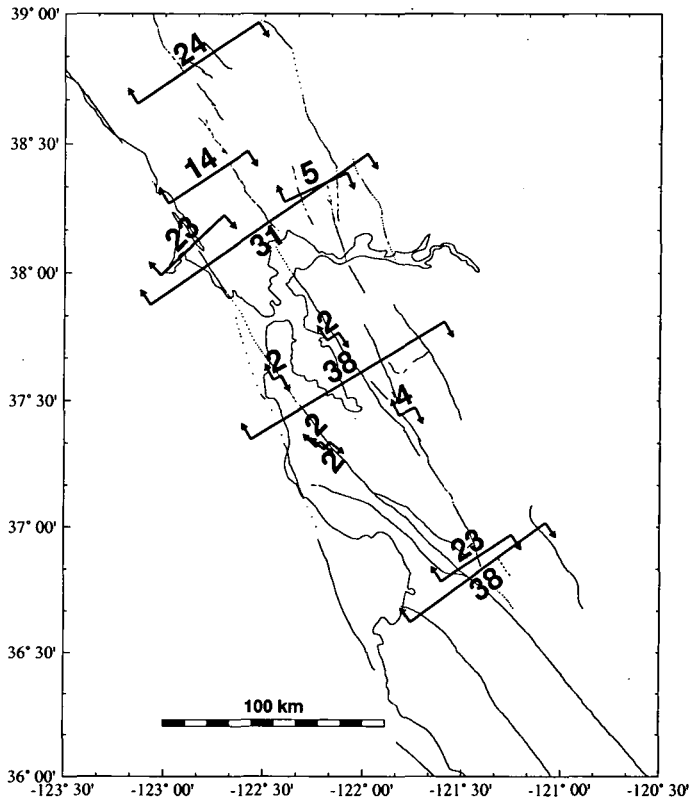

Figure 2.5: Relative strike-slip displacement rates in central California. Values in millimetres per year. Arrows indicate orientation of maximum, right-lateral, shear strain. Lines indicate width of zone measured. See Table 2.1 for details.

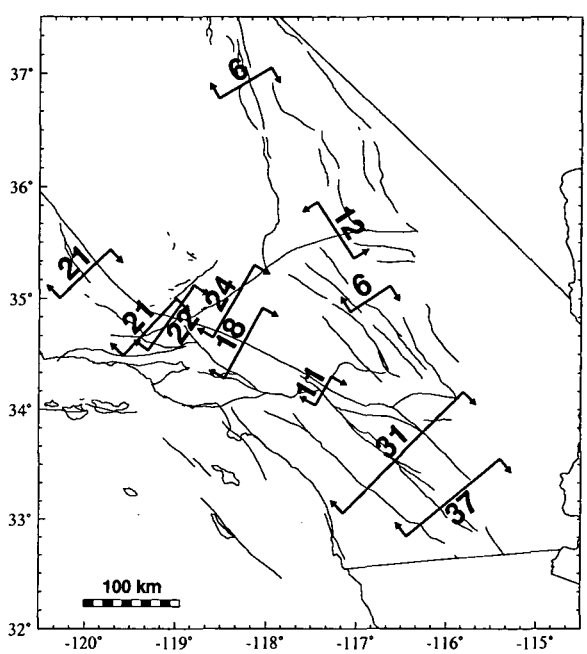

Figure 2.6: Relative strike-slip displacement rates in southern California. Values in millimetres per year. Arrows indicate orientation of maximum, right-lateral, shear strain. Lines indicate width of zone measured. See Table 2.1 for details.

of 0.14 μrad/yr (Figure 2.4) [*Savage et al.*, 1990]. In the White Mountains, just north of Owens Valley, small but resolvable strain rates have been measured. The orientation of the strain field indicates crustal extension perpendicular to the north-south trending normal faults in the area. To the east of Owens Valley, the Yucca Mountain geodetic network in Nevada (Figure 2.4), has shown no significant strain accumulation over the 1983-1993 interval [*Savage et al.*, 1994].

2.3.5 Displacement Patterns in the San Francisco Bay Region

Details of the deformation within this region are best shown by calculating individual station velocities that are then resolved into components parallel and perpendicular to the trend of the fault system. Given the rate of change of length for each line in a trilateration network, station velocities relative to a point at the centre of the network can be determined using a method that minimises the displacements perpendicular to the fault in order to constrain rigid rotation of the network [*Prescott*, 1981]. This provides an appropriate solution for a region deformed by tectonic shear.

Figures 2.7 and 2.8 show the fault-parallel component of velocity for two trilateration networks in the San Francisco bay region. In the Monterey bay region (Figures 2.3 and 2.7), large offsets across the San Andreas and Calaveras faults indicates that a significant fraction of the relative plate motion is being accommodated by fault creep. However, velocity gradients in the blocks to the southwest, northeast and between the faults indicates some internal deformation that could result from locked zones on those faults planes. The integrated displacement rate across the profile, 38 $\pm$ 4 mm/yr [*Lisowski et al.*, 1991], is consistent with the 35 mm/yr of Pacific-North American plate motion attributed to the San Andreas fault system. This suggests that most of the deformation zone has been traversed by the network in the Monterey bay region.

To the north, in the northern San Francisco bay region, 25 $\pm$ 6 mm/yr of relative motion is distributed over about 60 km in the east-west direction (Figure 2.8). To the southwest of the San Andreas fault, the velocity gradient appears to be very small. To the northeast, between the San Andreas and Green Valley faults the station-velocity profile shows a near-linear trend. Between these two trends, within a few km of the San Andreas fault, there is a rapid change in the velocity

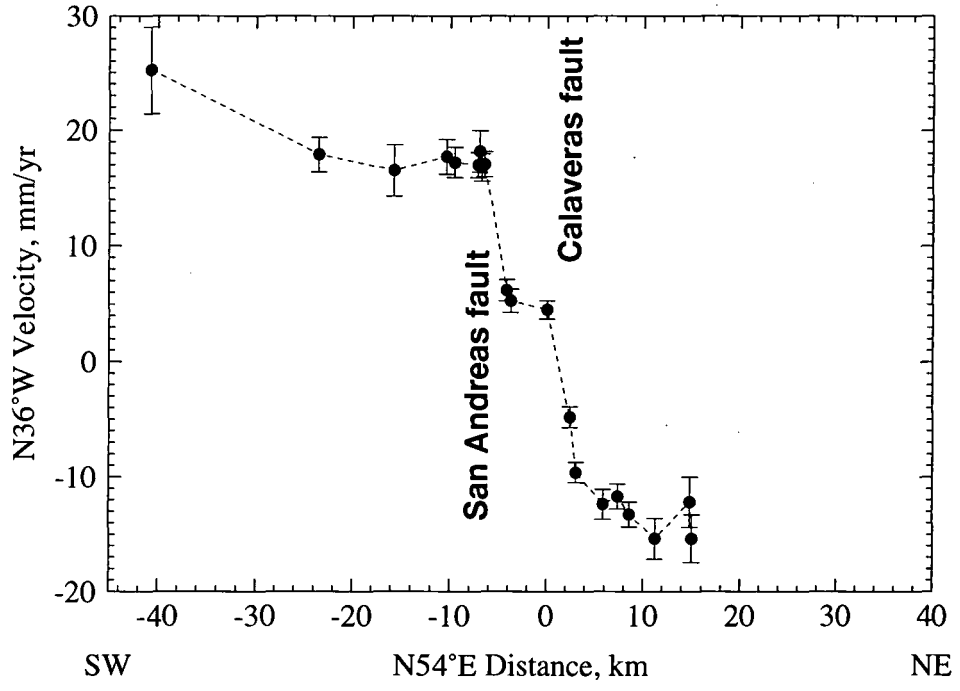

Figure 2.7: Horizontal velocity component perpendicular to a N54°E profile across the Monterey bay region as a function of distance along the profile. The error bars represent one standard deviation on either side of the plotted point. Adapted from *Lisowski et al.* [1991].

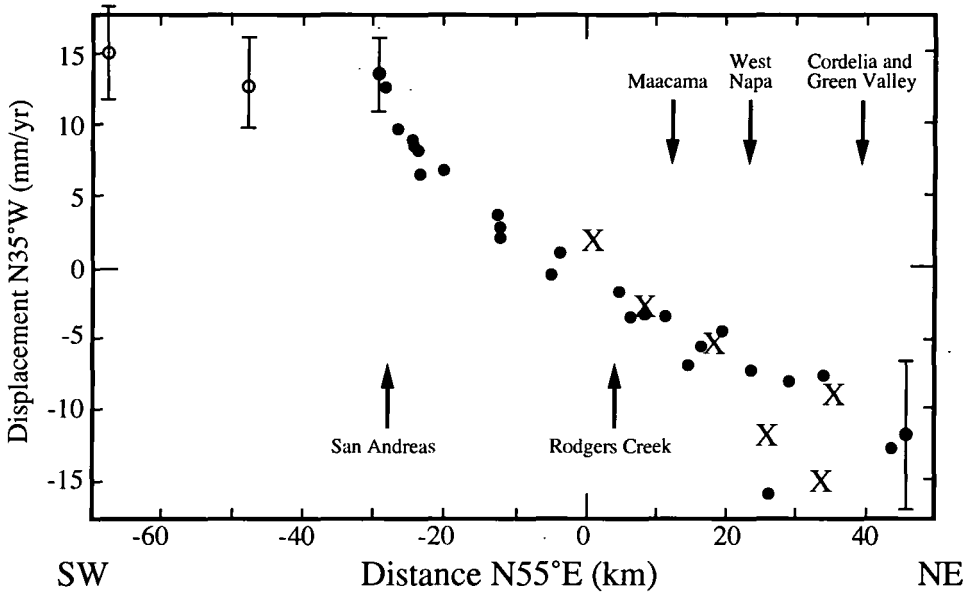

Figure 2.8: Horizontal velocity component perpendicular to a N55°E profile across the north San Francisco bay region from 10 years of trilateration data. Labeled arrows indicate the location of the major fault crossings. Crosses indicate stations further to the north in The Geysers region. Error bars represent one standard deviation. Errors for the other points increase smoothly from zero at the origin to the values shown. From *Prescott and Yu* [1986].

gradient indicating a concentration of strain close to the fault. Only 0.7 mm/yr of fault creep is reported at this locality [*Galehouse*, 1992b] and creep therefore does not appear to explain the near-fault concentration of strain. The continuation of movement to the eastern edge of the profile suggests that the additional 5-10 mm/yr of relative plate motion (35 mm/yr) is occurring further east.

2.4 Plate Tectonics and the San Andreas Discrepancy

In California, local, fault-crossing geodetic surveys have shown that about 35 mm/yr of relative plate motion is accommodated by the San Andreas fault system. There is close agreement between the geodetic data and the findings from geological data which reflect the cumulative effects of many large earthquakes. This agreement between the geologic plate motions averaged over the past 2-3 Ma and the geodetically measured motions averaged over several years indicates that movement at this fault system has remained constant at least 2-3 Ma. Geodetically-derived estimates of plate motion are thus expected to compare well with global plate motion models derived from ridge spreading rates, transform fault azimuths and earthquake slip vectors. The use of ground-based geodetic surveys to measure plate motion is, however, limited in two ways. First, the accuracy of the inferred velocities is often too poor to make quantitatively useful comparisons. Second, geodetic networks are usually less than 100 kilometres wide and are too narrow to span most continental plate boundary zones. These limitations are overcome by space geodetic techniques which are capable of accurate measurements over very long distances.

A velocity solution calculated using SLR results from *Smith et al.* [1990] and VLBI results summarised by *Caprette et al.* [1990] were compared with the rates predicted by the NUVEL-1 model [*Robbins and Smith*, 1990]. The slope of the linear fit is 0.966 $\pm$ 0.009 (1.007 $\pm$ 0.009 when accounting for the recently revised time scale). Therefore, the motion between plates appears to be steady over time spans differing by a factor of 1,000,000.

With sites located throughout North America, VLBI and SLR data can provide constraints on the integrated rate of deformation across sections of the complex Pacific-North American plate boundary especially where geological information is

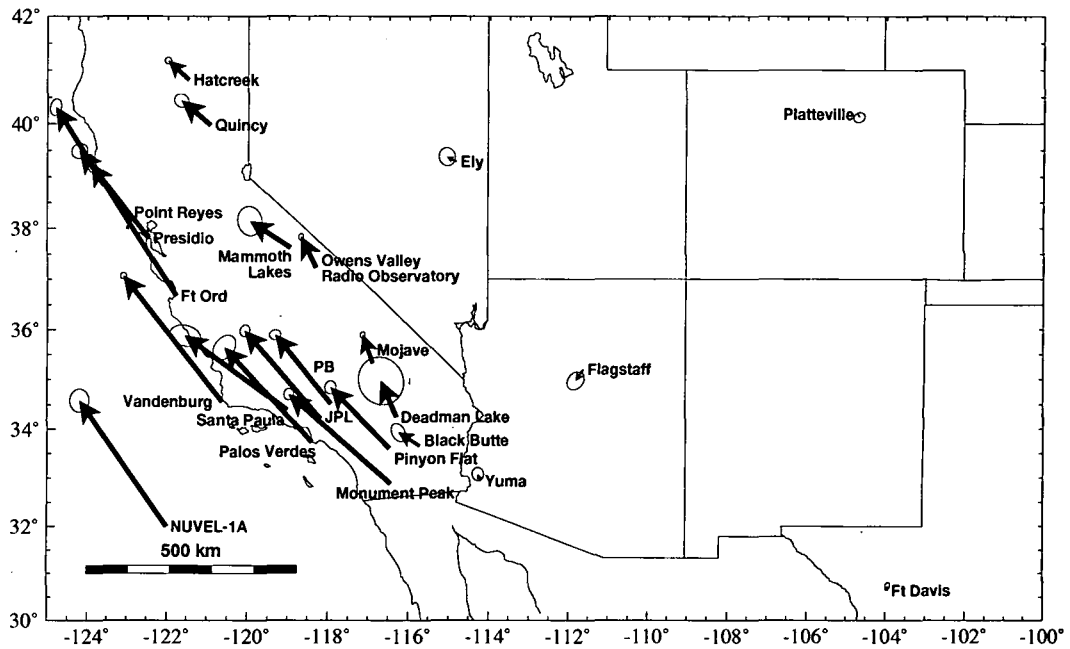

Figure 2.9: Calculated VLBI site velocities for western North America and their 95% confidence ellipses. The observation frame minimises the velocities of six sites in the interior of the North American plate (Ft. Davis, Texas; Flagstaff, Arizona; Platteville, Colorado; Yuma, Arizona; Westford, Massachusetts and Fairbanks, Alaska). PB, Pear Blossom. Vector marked NUVEL-1A indicates Pacific-North American motion as predicted by the NUVEL-1A plate model for central California (at latitude 36°N). Data from *Ward* [1990]

sparse. VLBI sites situated along the central California coast have been found to move at the full Pacific rate consistent with NUVEL-1A predictions [*Clark et al.*, 1987; *Kroger et al.*, 1987; *Ward*, 1990]. The VLBI station YUMA was found to be within the stable interior of the North American plate whereas Fort Ord and Vandenberg are within the stable interior of the Pacific plate (Figure 2.9) [*Ward*, 1990]. The Euler vectors for deformation between several provinces within the western United States were constructed from the VLBI data set. Constructing VLBI plate models allows averaging of the bias and errors of individual site velocities and enables the consistency of specific plate models with the VLBI data set as a whole to be quantified. In central California the plate motion (46.8 $\pm$ 0.5 mm/yr at N36°W $\pm$ 1°) is accommodated by 38.6 $\pm$ 0.4 mm/yr at N36°W $\pm$ 1° on the San Andreas fault system and 8.2 $\pm$ 0.4 mm/yr at N34°W $\pm$ 2° taken up to the east of the San Andreas fault, presumably in the Basin and Range province. This rate for Basin and Range deformation is consistent with previous geological estimates but trends 14-30° more northerly than associated direction estimates. Using a slightly larger VLBI data set the Euler vector for the Sierra Nevada microplate, located

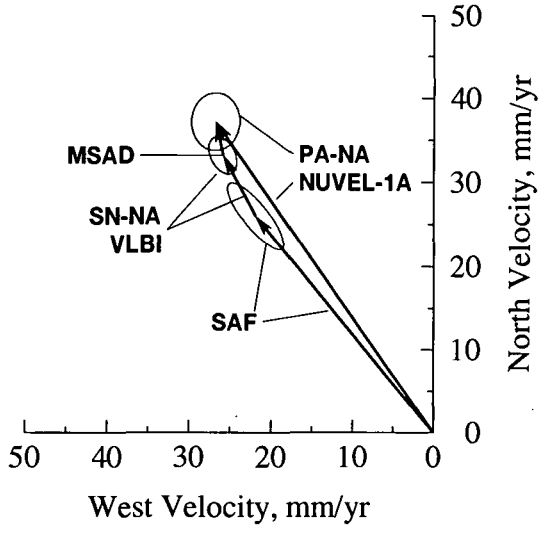

Figure 2.10: Velocity vectors along the San Andreas fault at latitude 36°N. Slip along San Andreas fault takes up only a portion of the Pacific-North American plate motion as predicted by the NUVEL-1A plate model. The vector sum of strike slip along the San Andreas fault system and Sierra Nevada-North America motion (SN-NA) differs little from Pacific-North America (PA-NA) motion. The Modified San Andreas Discrepancy (MSAD) is 4 ±2 mm/yr toward N13°W ±17°W. Ellipses indicate 95% confidence limits for Sierra Nevada-North America motion, Pacific-North American motion and San Andreas fault slip.

between the San Andreas fault system and the Basin and Range province, relative to the North American plate was determined [*Argus and Gordon*, 1990]. The Sierra Nevada-North America Euler vector suggests a velocity of 11 ± 1 mm/yr at N28°W ± 3° at Owens Valley (37.22°N). This velocity is not parallel to the average direction of maximum Basin and Range extension of ~ N60°W, but instead is nearly parallel to the strike of the Sierra Nevada-Basin and Range boundary along the Owens Valley. Using their VLBI-derived Euler vector for Sierra Nevada-North America motion, together with the NUVEL-1A Pacific-North America vector and the observed velocity along the San Andreas fault, a modified San Andreas discrepancy can be calculated (Figure 2.10) [*Argus and Gordon*, 1990]. The difference can be described at 36°N along the San Andreas fault by a vector of 4 ± 2 mm/yr directed toward N13°W.

Deformation measured at several geodetic networks in eastern California indicates shearing with negligible area change that can account for 3-8 mm/yr (and possibly 12 mm/yr, *Sauber et al.*, [1994]) of the plate motion attributed to the Basin and Range province. This motion is carried north-northwest from the Mojave desert along the Eastern California shear zone. North of the Garlock fault, the exact

position of the shear zone is unresolved. Using geodetic data, the shear zone deformation is proposed to transfer to the Owens Valley fault [*Savage et al.*, 1990], whereas on the basis of geologic arguments the shear zone is connected to the Death Valley-Furnace Creek faults (100 km east of Owens Valley, Figure 2.3) [*Dokka and Travis*, 1990a, b]. The observed velocities of VLBI stations Owens Valley Radio Observatory (OVRO) and Mojave (10.0 $\pm$ 0.5 mm/yr at N38°W $\pm$ 3° and 8.6 $\pm$ 0.4 mm/yr at N29°W $\pm$ 4° respectively, *Dixon et al.* [1993]) relative to the North American plate interior seem to require that the shear zone be east of these stations. If the deformation is concentrated solely along Owens Valley these velocities should be only a fraction of the relative motion assigned to the shear zone. The shear strain measured in Owens Valley seems to be too high to be outside of the shear zone proposed by *Dokka and Travis* [1990a, b]. The relative motion carried by the shear zone is probably transferred to the Death Valley-Furnace Creek and Owens Valley faults with 3 mm/yr occurring along the Owens Valley branch [*Savage and Lisowski*, 1995]. The accommodation of 8 mm/yr along the Eastern California shear zone alone can account for the San Andreas discrepancy up to a latitude of about 38°N. If the shear zone continues northwards then it must either be more diffuse or partition into movement north-northwest along the Sierra Nevada mountain front and more northerly along the Nevada seismic zone [*Savage et al.*, 1990].

2.5 Summary

The destruction, by the 1906 San Francisco earthquake, and subsequent repair of the transcontinental geodetic control network provided the first example of the use of geodetic surveying for the detection of crustal movements. Since then an increasing number of sites have been occupied specifically for the deliberate investigation of crustal deformation. More accurate surveying methods have been developed over time, from terrestrial techniques such as triangulation and trilateration to space techniques such as VLBI, SLR and GPS. These have been able to detect increasingly finer details of the distribution of crustal deformation over increasingly larger regions.

Repeated surveys of geodetic networks in the western United States have revealed a significant deformation zone around the San Andreas fault system. This deformation is primarily right-lateral shear with a maximum relative motion of 35-

40 mm/yr across a 50-100 km wide zone. The orientation of maximum horizontal shear agrees with the surface strike of nearby faults. Smaller, but still resolvable, deformation has been measured away from this fault system, particularly along the Owens Valley in eastern California.

In addition to measuring local, plate-boundary deformation, geodetic surveys, especially the more recent space techniques with their ability to measure longer line lengths, have been able to help constrain the distribution of relative plate motion in the wide boundary between the Pacific and North American plates. In particular, geodetic measurements are able to clarify the distribution of deformation where geological and other geophysical information is sparse or uncertain such as within the Basin and Range province. A significant proportion of the San Andreas discrepancy can be attributed to deformation along the Eastern California Shear Zone.

Chapter 3

The Global Positioning System (GPS)

3.1 Introduction

GPS is a worldwide satellite-based radionavigation system, that was developed by the United States Department of Defense (DoD) to "satisfy the requirements for the [U.S.] military forces to accurately determine their position, velocity and time in a common reference system, anywhere on or near the Earth on a continuous basis." [*Wooden*, 1985]. The primary goals were military, but civilian geodesists soon recognised the potential of GPS to produce precise relative positioning at the sub-centimetre level using a method not planned by the designers [*Counselman and Shapiro*, 1979; *MacDoran*, 1979, *Bossler et al.*, 1980]. Such precision suits GPS to application to tectonic problems.

GPS has many advantages over terrestrial and other space techniques. Unlike terrestrial techniques, it does not require intervisibility between measurement points, thus making surveying much more flexible in rugged topography, amongst buildings or in bad weather. GPS data also yield more information. The three dimensional vector separation of points can be obtained, whereas no single terrestrial technique can provide this information. VLBI and SLR, because they involve global networks, are powerful to study global plate motion, Earth orientation and large-scale, boundary-zone deformation [e.g. *Christodoulidis et al.*, 1985; *Kroger et al.*, 1987; *Clark et al.*, 1987]. However, these techniques are cumbersome and impractical for detailed studies of plate boundary zones. Agreement between GPS- and VLBI-derived lines up to 2000 km long has been demonstrated at the several-centimetre level for lines in the western United States [*Blewitt*, 1989]. GPS can therefore provide, to a suitable accuracy, a kinematic description of crustal deformation in broad, complex, plate boundary zones at distances ranging from a few km to 1000 km or more.

3.2 Fundamentals of GPS Surveying

3.2.1 The GPS Segments

3.2.1.1 Introduction

GPS can be thought of as consisting of three segments: The space segment consisting of space vehicles (hereinafter referred to as satellites) which broadcast signals, the ground-based control segment that maintains the system, and the user segment.

3.2.1.2 The Space Segment

The space segment comprises 21 satellites plus three operational spares in six orbital planes, i.e., four satellites in each plane. The satellites occupy near-circular orbits at 20,200 km and inclination angle of 55° to the equator with a period of approximately 12 hours. This configuration provides continuous, four-satellite (or more) coverage worldwide apart from polar regions.

An oscillator on board each satellite generates two carrier signals known as L1 and L2. The frequency of these signals are integer multiples of a fundamental frequency, f_0, which is 10.23 MHz. These carriers are modulated to transmit binary information, performed by bi-phase modulation, to provide satellite identification codes, clock readings and orbital parameters. Two pseudo-random noise (PRN) codes are transmitted. A coarse acquisition (C/A) code with a bit rate of $f_0/10$ is transmitted on L1 and repeated every millisecond. A precision (P) code with a bit rate of f_0 is transmitted on L1 and L2 and repeated every 266.4 days. Each satellite also transmits a navigation message containing its own orbital elements, clock corrections, the system time and status messages together with an almanac which provides approximate data for every active satellite. The navigation message is transmitted over a period of 30 seconds at a frequency of 50 Hz (Table 3.1). The various satellites all transmit on the same frequencies, but with different code assignments. The broadcast signal has spread-spectrum characteristics which provide a large margin of resistance to interference.

The two PRN codes allows GPS to provide two levels of real-time positioning service, a Standard Positioning Service (SPS) and a Precise Positioning Service (PPS). SPS is provided via the C/A code and navigation message and is planned to en-

Table 3.1: Components of the satellite signal. From [*Hoffmann-Wellenhof et al.*, 1993].

	Frequency		
Component		MHz	Wavelength
Fundamental Frequency	f_0	10.23	
L1	$154f_0$	1575.42	19.0 cm
L2	$120f_0$	1227.60	24.0 cm
P code	f_0	10.23	$\sim$ 30 m
C/A code	$f_0/10$	1.023	$\sim$ 300 m
Navigation Message	$f_0/204600$	50.10^{-6}	

able real-time horizontal positioning accuracy within 100 m at 95% probability. The PPS is intended for military positioning and is provided via the P code. PPS is denied to unauthorised (non-military) users by Selective Availability (SA) and Anti-Spoofing (A-S). Selective Availability involves degrading the navigation message, orbit data and satellite clock frequency stability. Anti-Spoofing is switching off of the P code. Authorised military personnel then use the classified Y code. SA has been on sporadically since April 1990, and A-S has been turned on permanently since October 1993.

3.2.1.3 The Control Segment

The control segment consists of five monitor stations at Hawaii, Kwajalein, Ascension Island, Diego Garcia and Colorado Springs, three ground antennas at Ascension Island, Diego Garcia and Kwajalein, and a Master Control Station at Falcon Air Force Base in Colorado. The monitor stations, whose coordinates are known precisely, passively track all the GPS satellites in view. The information is used to determine orbits and to update the SV navigation messages. Updated information is transmitted to each satellite via the ground antennas.

The tracking data are generally not available to the public and independent civilian networks have been established for orbit determination purposes. Such networks include the Cooperative International GPS Network (CIGNET) [*Chin*, 1988], the International GPS Service for Geodynamics (IGS) [*Mueller and Beutler*, 1992] and the Southern California Permanent GPS Geodetic Array (PGGA) [*Lindqwister et al.*, 1991]. The tracking stations are generally co-located at VLBI antennas.

3.2.1.4 The User Segment

The user segment consists of GPS receiving equipment that provides positioning, velocity and precise timing to the user. The basic user equipment is comprised of antenna/pre-amplifier, receiver, microprocessor, power supply and input/output devices. The antenna, in most cases, has a broadbeam characteristic enabling it to receive signals from the zenith to the horizon for one or both frequencies. The actual position measured is the phase centre of the antenna which must be properly related to some position such as a survey mark. The receiver section contains the signal processing electronics and consists of several channels capable of tracking and measuring the GPS signal using a variety of approaches such as code correlation and carrier signal squaring. The microprocessor processes the incoming data, provides a link to the operator and controls any input/ouput devices. The most common output device is a tape recorder or disk drive used to record observations and other information extracted from the signal. When data is collected for post-processing, the receiver makes measurements at regular intervals which are known as epochs.

3.2.2 Positioning from Space

3.2.2.1 Absolute and Relative Point Positioning

GPS can provide both absolute- and relative-point positions. Absolute point positioning is the determination of a position with respect to a well defined coordinate system (Figure 3.1). The coordinates of a satellite relative to the centre of the Earth can be computed from orbital information. From this and the measured range vector between the satellite and the receiver the position of the receiver can be calculated. Absolute positioning is generally undertaken in real-time mode, that is receiver positions are calculated whilst receiving the satellite signals.

Relative point positioning involves the simultaneous observation of a group of satellites by two or more receivers to obtain the three-dimensional vectors connecting all the receivers. These can be used to calculate the coordinates of the points if the location of one or more stations are known a priori. Relative positioning is generally not used in real-time mode but instead the data is stored for processing at a later stage. The accuracy of relative positioning is far superior to that of absolute positioning because all the major errors can be made to cancel out at the data processing stage.

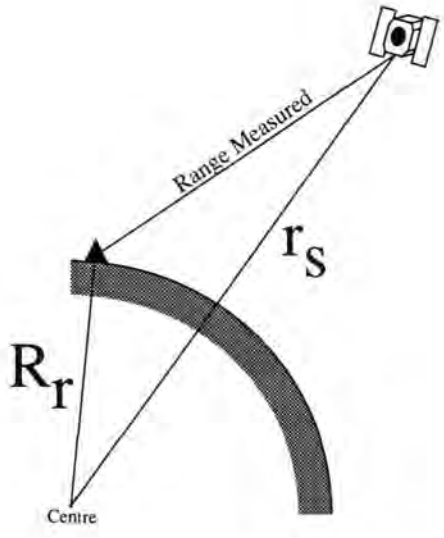

Figure 3.1: Principle of absolute point positioning

3.2.2.2 Ranging

Positioning with GPS is achieved using ranging. The position vector of the receiver is obtained by measuring three, non-coplanar ranges to three satellites of known position. Ranging to three satellites places the receiver at two possible positions formed by the intersection of three spheres with the satellites at the centres and the appropriate ranges as radii. Knowledge that the receiver is on the surface of the Earth eliminates one of these positions. Positioning with GPS is achieved by one-way ranging i.e., the range is measured by the use of one way travel information of the signal from the satellite to the receiver. In the case of absolute, real-time positioning, ranges are calculated and processed in quasi-real time positioning by the receiver. In the case of relative positioning, receiver-calculated ranges are stored and post-processed at a later stage. The rest of this chapter will focus on relative positioning.

3.2.3 Measurements

In order to calculate receiver positions a GPS receiver makes *pseudorange* and *carrier beat phase* measurements. The basic measured quantity is the arrival time of the signal at the receiver. This is achieved by correlating a replica of the code (P or C/A) generated in the receiver with the code received from the satellite (Figure 3.2a). The calculated range, ρ, between the satellite and the receiver is

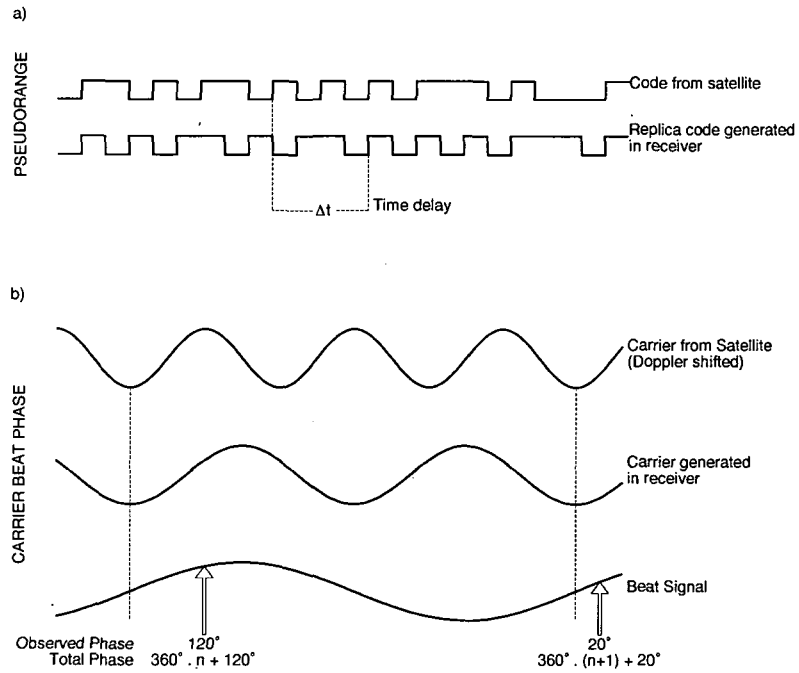

Figure 3.2: Types of measurement available for positioning with GPS. a) Pseudorange measurements. b) Carrier beat phase measurements.

then

$$\rho = c(t_r - t_s), \tag{3.1}$$

where c is the speed of light, t_r is the time the message is received at the receiver and t_s is the time the message was transmitted from the satellite. Errors in the receiver or satellite clocks contaminate these ranges which are therefore called "pseudoranges", p. For absolute positioning, obtaining the pseudorange to a fourth satellite is necessary to obtain a correction to the receiver clock. In addition to clock offsets there are delays in signal propagation through both the ionosphere and troposphere. Taking into account these delays the pseudorange equation becomes

$$p = \rho + c(dt - dT) + d_{ion} + d_{trop}, \tag{3.2}$$

where dt and dT are the offsets from true GPS time of the satellite and receiver clocks and d_{ion} and d_{trop} are the corrections for ionospheric and tropospheric delays.

The precision with which the correlation peak of pseudorange measurements can be measured is about 1% of the wavelength (i.e., the length of one bit of code). This yields a range measurement precision of 30 cm for P-code measurements and 3 m for C/A-code measurements.

A carrier beat phase measurement is the observed difference or "beat" between the incoming, Doppler-shifted satellite carrier phase and a constant frequency gener-

ated in the receiver

$$\phi = \phi_i^k = \phi^k(t) - \phi_i(T), \tag{3.3}$$

where $\phi^k(t)$ is the phase of the signal transmitted by the k^{th} satellite at time t, and $\phi_i(T)$ is the phase at the i^{th} receiver at reception time T (both expressed in cycles) (Figure 3.2b). Including the effects of clock offsets and signal propagation delays gives

$$\phi_{total} = -(f/c) \cdot \rho - f \cdot (dt - dT) - (f/c) \cdot (-d_{ion} + d_{trop}), \tag{3.4}$$

from which the range, ρ, can be calculated.

Since the carrier wavelengths are much shorter than the bit lengths of either codes (Table 3.1) the precision of carrier beat phase measurements is much higher than those for pseudorange measurements. For the L1 carrier signal the precision is about 2 mm.

Carrier beat phase measurements have a fundamental disadvantage. The measured carrier beat phase, $\phi_{measured}$, is the number of phase cycles (the integer number plus the fractional part) from the initial epoch, t_0, (when the receiver began recording) to epoch t, counted by the receiver. However, ϕ_{total}, in equation (3.4) is the total phase which includes an integer number of cycles, N, between the receiver and satellite at the initial epoch t_0

$$\phi_{total} = \phi_{measured} + N(t_0). \tag{3.5}$$

N is unknown and is referred to as the cycle ambiguity. One cycle ambiguity exists per satellite/receiver pair provided the receiver maintains continuous "lock" on the satellite during the observation session. The equation for the instantaneous carrier beat phase measurement for one satellite/receiver pair at one epoch may then be written as

$$\phi_{measured} = -(f/c) \cdot \rho - f \cdot (dt - dT) - (f/c) \cdot (-d_{ion} + d_{trop}) - N, \tag{3.6}$$

Multiplying by the wavelength, $\lambda = c/f$, of the carrier and defining the phase range Φ as

$$\Phi = -\lambda\phi_{total}, \tag{3.7}$$

the carrier beat phase equation in length units is

$$\Phi = \rho + c(dt - dT) + \lambda N - d_{ion} + d_{trop}, \tag{3.8}$$

This observation equation can be compared with the pseudorange equation (3.2). Because the ionosphere causes non-linear dispersion of electromagnetic waves, the

group velocity (associated with the code data) differs from the phase velocity (associated with the phase data). As a result the effect of the ionosphere is to delay code measurements and to advance phase measurements, and thus the delay d_{ion} in equations (3.2) and (3.8) are equal in magnitude but opposite in sign. Unlike the ionosphere, the troposphere, at the frequencies used by GPS, is not dispersive so that the group and phase delays are equal.

3.2.4 Error Sources Affecting GPS Positioning

The code pseudoranges and carrier beat phase ranges are both affected by systematic errors and random noise. Systematic errors, termed "biases", can be classified into three groups: satellite-, receiver-, and propagation/observation-biases. One way to quantify these biases is to project their influence into the range measurement and the sum is called the range bias.

Satellite biases consist of errors in the broadcast satellite clock models and satellite ephemerides (orbits). Receiver biases mainly consist of errors in the receiver clock. Observation/propagation biases are those errors associated with the signal propagation such as ionospheric and tropospheric delays and errors dependent on the observation type such as the cycle ambiguity in carrier beat phase measurements (Table 3.2). The major observational errors are cycle slips and multipath. A cycle slip is a discontinuity of an integer number of cycles in the measured carrier beat phase resulting from a miscount in the GPS receiver (Figure 3.3). Cycle slips can be caused by obstructions of the satellite signal, a low signal-to-noise ratio, failure in the receiver software or malfunctioning satellite oscillators. Multipath results from interference between radiowaves which have travelled between the satellite and receiver via two or more paths of different electrical length (e.g., by reflecting off buildings) [*Bowditch*, 1981].

The magnitude of the receiver position error obtained by GPS is dependent on the magnitude of the range bias and the geometric strength of the satellite configuration observed. The effect of satellite geometry can be expressed by the Geometric Dilution of Precision (GDOP). The value of GDOP is inversely proportional to the instantaneous volume of the body formed by the points of unit vectors from the user to the satellites. A low value of GDOP indicates a well distributed satellite configuration and correspondingly small errors in position.

Table 3.2: Contributions to the range bias [from *Wells*, 1987].

Bias Type	Maximum Contribution
Satellite clock	300,000 m (decreases to 10 m if broadcast clock correction is used)
Receiver clock	10 - 100 m (Depending on type of receiver oscillator)
Orbital	80 m for broadcast ephemerides
Ionospheric delay	150 m at horizon (decreases to 50 m at the zenith)
Tropospheric delay	20 m at 10° above horizon (decreases to 2 m at the zenith)
Carrier beat phase ambiguity	anything

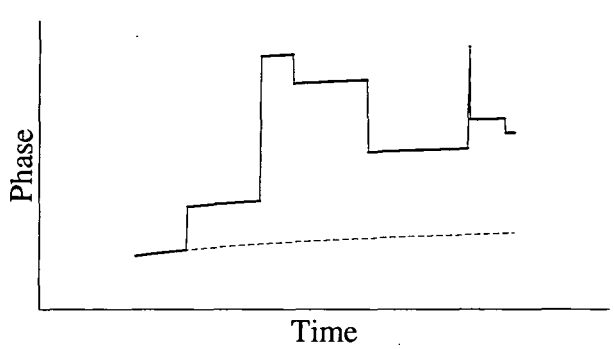

Figure 3.3: Cycle slips in carrier beat phase measurements. Solid line indicates measured phase that has experienced several cycle slips (vertical steps). Dashed line represents measured phase after the cycle slips have been corrected.

3.2.5 Satellite Orbits and Reference Frames

GPS positioning depends substantially on the knowledge of the satellite orbits. Any error in the determination of a satellite orbit will lead to an error in the estimated position of the receiver. From geometrical considerations the precision of an estimated survey line, as a fraction of its length, is roughly proportional to the fractional precision of the orbit used in the analysis [*Murray*, 1991]. In 1991, the broadcast orbit ephemerides provided about 1 part in 10^6 precisions on relative baselines, or an uncertainty of 1 cm along a 10 km baseline, which is inadequate for monitoring crustal motion over a short time interval.

A satellite orbiting the Earth is subject to a force due to the Earth's central, spherically-symmetric component of the gravitational field, and therefore follows Kepler's laws of motion (which are deduced from Newton's laws of motion and gravitation). The equations of motion are best expressed in a quasi-inertial reference frame whose orientation remains fixed with respect to the stars but whose origin is defined as the Earths centre of mass, or geocentre. The satellite orbit will describe an ellipse with one focus at the geocentre. However, other forces acting on the satellite cause departures from this elliptical motion. Gravitational forces such as attractions from the Moon, Sun and other planets and the higher-order harmonics of the Earth's gravity field can be modelled with high accuracy for high-altitude satellites. Non-gravitational forces, such as atmospheric drag, solar radiation pressure, gas emission from the satellite, and magnetic forces, can be much harder to predict a priori.

It is possible to deal with the problem of orbit determination whilst processing GPS data and several approaches may be used. The simplest approach is to assume that the broadcast ephemerides are correct and to hold the orbit fixed to those values during processing. An alternative approach is to begin with an estimate of the six Keplerian orbital elements at some initial epoch and numerically integrate the equations of motion using accurate models for various perturbing forces and resulting accelerations. To account for the somewhat unpredictable perturbing force from solar pressure radiation at least one (although more generally two) additional acceleration parameter is estimated along with the station coordinates in the analysis. This is known as the force model approach. The third alternative is to assume a free orbit and estimate orbital biases at every epoch.

The length of the orbit arc over which the equations are integrated may be only

a few hours (covering the observation period - *short arc*) or may extend up to several days (covering subsequent observation periods - *multiday* or *long arc*). An improvement in orbit accuracy with arc length is not expected since at some point the model used to predict satellite motions will deteriorate because of systematic errors. However, the most successful strategies used for orbit determination have involved multiday arcs [*Lichten and Border*, 1987; *Davis et al.*, 1989]. In relative positioning the effects of certain systematic orbital errors will be removed or reduced thereby requiring less accurate orbital modelling.

Station positions are described in a terrestrial reference frame which is fixed with respect to the Earths surface. A terrestrial reference frame has its origin at the geocentre and the orientation of the axes defined by a right-handed Cartesian system whose z-axis points north along the rotation axis and x-axis that points towards a prime meridian (generally the Greenwich Mean Astronomic Meridian). This, and the quasi-inertial reference frame of the satellites are related by the rotational motions of the Earth such as precession, nutation, polar motion, and by universal time. VLBI and SLR measurements define kinematically a near-ideal inertial reference frame and currently provide the most precise estimates of the Earth's variable rotation.

One method to obtain higher accuracy GPS ephemerides is to tie the orbital system to the terrestrial reference frame. This is achieved by co-locating GPS receivers at VLBI and SLR sites. VLBI and SLR currently provide the most precise global estimates of relative site positions and velocities. If receivers from widely separated sites, whose coordinates have been independently determined from VLBI or SLR, are included in the analysis then the accuracy of the lines joining these "fiducial" sites will be transferred via estimated satellite ephemerides to the lines connecting the non-fiducial sites. Precisions of 2-4 parts in 10^9 have been estimated for continental-scale VLBI-determined baselines [e.g., *Clark et al.*, 1987]. A precision of 4 parts in 10^9 would introduce an approximate uncertainty of 1 mm in a 200 km line. This is called the *fiducial network technique.*

3.2.6 Reducing the Data

The time evolution of the pseudorange or phase observables is primarily a function of the receiver site coordinates, satellite orbits, and the other biases detailed above. Although the primary parameters of concern in crustal deformation studies are the

relative site coordinates, other parameters in the model have to be either estimated, eliminated, or fixed to a well defined value in order to obtain the highest accuracy.

Many of the error sources are correlated amongst the signals received at several receivers simultaneously. If these measurements are combined then various common biases can be eliminated or greatly reduced. Code pseudoranges and carrier beat phase ranges can be differenced between receivers, between satellites and between epochs to create *single differences*. Single differences can be combined further to produce *double* or *triple differences* (Figure 3.4). The most commonly-used single difference is the between-receiver combination. The between-receiver single difference pseudorange is derived by differencing two simultaneously measured pseudoranges (P or C/A) to the same satellite to obtain

$$\Delta p = \Delta\rho - c \cdot \Delta dT + \Delta d_{ion} + \Delta d_{trop}, \tag{3.9}$$

Δ is used here to indicate a between-receiver difference. The satellite clock error (dt) is identical at both receivers and therefore cancels out. Δd_{ion} and Δd_{trop} are the differential ionospheric and atmospheric corrections and ΔdT is the differential receiver clock correction. The corresponding between-receiver carrier beat phase single difference is

$$\Delta\Phi = \Delta\rho - c \cdot \Delta dT + \lambda\Delta N - \Delta d_{ion} + \Delta d_{trop}, \tag{3.10}$$

Providing the line lengths are small compared to the altitude of the satellite then orbit errors and atmospheric delays also partially cancel.

With observations by two receivers of two satellites at the same epoch a receiver-satellite double difference may be obtained. The observation equation is, for pseudorange measurements

$$\Delta\nabla p = \Delta\nabla\rho + \Delta\nabla d_{ion} + \Delta\nabla d_{trop}, \tag{3.11}$$

and for carrier beat phase measurements

$$\Delta\nabla\Phi = \Delta\nabla\rho + \lambda\Delta\nabla N - \Delta\nabla d_{ion} + \Delta\nabla d_{trop}, \tag{3.12}$$

where ∇ indicates between-satellite differences. Double differences thus eliminate, or greatly reduce, both the receiver (dT) and the satellite (dt) clock errors.

Differencing receiver-satellite double differences between epochs gives the receiver-satellite-time triple difference. The observation equations are

$$\delta\Delta\nabla p = \delta\Delta\nabla\rho + \delta\Delta\nabla d_{ion} + \delta\Delta\nabla d_{trop}, \tag{3.13}$$

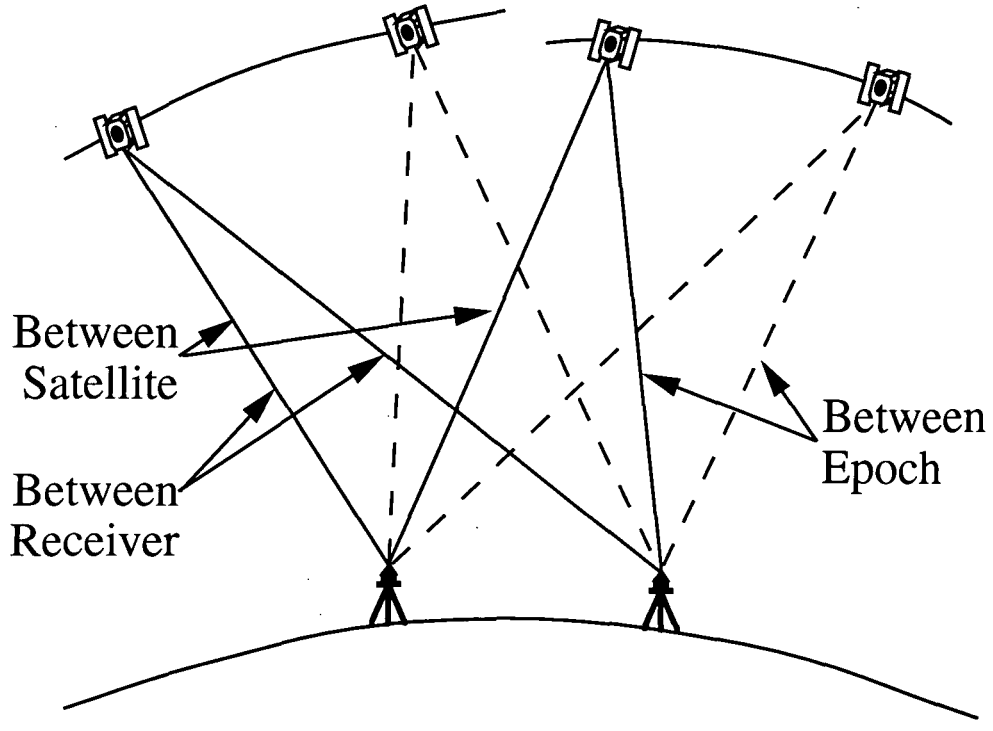

Figure 3.4: Linear combinations of observations. Marked combinations indicate between receiver, satellite and epoch single differences. All dashed or all solid lines represent receiver-satellite double differences. All lines combined represent a receiver-satellite-time triple difference.

and

$$\delta\Delta\nabla\Phi = \delta\Delta\nabla\rho - \delta\Delta\nabla d_{ion} + \delta\Delta\nabla d_{trop}, \tag{3.14}$$

The initial cycle ambiguity in the carrier beat phase measurements is thereby eliminated. Triple differencing the data has the disadvantage of greatly reducing the number of observations and the signal to noise ratio, and point coordinate solutions are thus generally derived using double differences only, and calculating the value of N.

Where dual frequency phase data are available linear combinations of the original carrier phases, Φ_1 and Φ_2 may also be used to isolate or reduce bias effects. They are also used to reduce computational time and aid in the estimation of certain parameters. Three examples of linear combinations of the dual frequency data are the ionosphere-free, geometry-free and wide-lane combinations. These, in conjunction with the original carrier phases, give five data types that can be used in the processing of GPS data (Table 3.3)

Dispersion in the ionosphere is frequency dependent. Therefore its effects can be

Table 3.3: Linear combinations of the carrier phases $L1$ and $L2$ used in the Bernese GPS Software Version 3.2 [From *Rothacher et al.*, 1990].

Carrier	Description	Wavelength cm	Noise $L1 = 1$	Ionosphere $L1 = 1$
L1	Actual Carrier	19.0	1.0	1.0
L2	Actual Carrier	24.0	1.0	1.6
L3	Ionosphere free	10.7	3.0	0.0
L4	Geometry free	5.4	1.4	0.6
L5	Wide Lane	86.2	5.0	1.3

reduced by combining observations at the two frequencies to form the so-called ionosphere free combination, L_3.

$$L_3 = \frac{f_1^2}{f_1^2 - f_2^2} L_1 - \frac{f_2^2}{f_1^2 - f_2^2} L_2, \tag{3.15}$$

where L_1 and L_2 are the phase ranges and f_1 and f_2 are the two carrier frequencies. The effective wavelength of L_3 is $\lambda_3 = c/(f_1 + f_2) \sim 10.7$ cm. This is shorter than the wavelengths of the two carrier phases, making resolution of the cycle ambiguities more complicated. In addition, this combination amplifies the noise, particularly multipath, by approximately a factor of 3.

The L_4, geometry-free combination, is defined as

$$L_4 = L_1 - L_2, \tag{3.16}$$

where the ionospheric wavelength $\lambda_4 = (\lambda_2 - \lambda_1) \sim 5.4$ cm. This combination contains the effects of the ionosphere and cycle ambiguity parameters but is independent of receiver clock and geometry biases. The noise in L_4 is roughly 1.4 times that of L_1 or L_2.

The third linear combination, L_5 is known as the wide-lane combination and is defined by

$$\Phi_5 = \Phi_1 - \Phi_2. \tag{3.17}$$

The phase range observable is

$$L_5 = \frac{f_1}{f_1 - f_2} L_1 - \frac{f_2}{f_1 - f_2} L_2, \tag{3.18}$$

The wide-lane wavelength $\lambda_5 = c(f_1 - f_2) \sim 86.2$ cm is approximately 4 times greater that of the original carriers and therefore ambiguity resolution is easier.

When combining dual frequency phase data the linear combination also has corresponding initial cycle ambiguity. For the wide-lane combination $N_{L5} = N_{L1} - N_{L2}$ where N_{L5} is the wide-lane ambiguity and N_{L1} and N_{L2} are the cycle ambiguities for the L1 and L2 carrier waves. In the case of the ionosphere-free combination the effects of the ionosphere are eliminated at the expense of the corresponding ambiguity N_{L3} being no longer an integer.

There are numerous approaches to analysing GPS data, each involving different combinations of the techniques described above to overcome the main error sources in the model. Most GPS experiments result in overdetermined solutions where the number of data far exceeds the number of unknowns. These problems may be solved using some form of least-squares algorithm. That is, a best estimate, in a least-squares sense, is found for the remaining parameters from the available data (in whatever combined or uncombined form). Prior to the final solution, certain parameters may be estimated and fixed to some value using an iterative procedure.

3.3 GPS in the San Francisco Bay Region

In 1990, the USGS established and measured with GPS a set of 5 geodetic profiles spanning the San Francisco bay region (Figure 3.5). Between March 1990 and February 1993 they measured these profiles a total of 7 times using GPS, together with a few additional sites. The surveys between 1990 and mid-1991 were conducted using Texas Instrument (TI) 4100 dual frequency P-code receivers. These receivers replicate the P-code and can therefore make code and phase observations on both the L1 and L2 frequencies. They can record only four satellites simultaneously, if more than four satellites were visible then those four for which the GDOP was best were chosen. After mid-1991, Ashtech LM-X II receivers were used. These receivers replicate the C/A code only and measure the phase of the L2 carrier by use of the (codeless) squaring technique. The squaring technique consists of multiplying the L2 signal by itself to recover the phase of the carrier at one-half of the original wavelength. During a single observation session 3-5 stations within a profile were occupied for 4-6 hours with measurements taken at 30 s intervals. During the observation session air pressure, temperature and relative humidity near the station were recorded every few hours and the antenna height was typically measured three times. Information such as general weather conditions and possible recording/equipment malfunction were also recorded on a field log sheet.

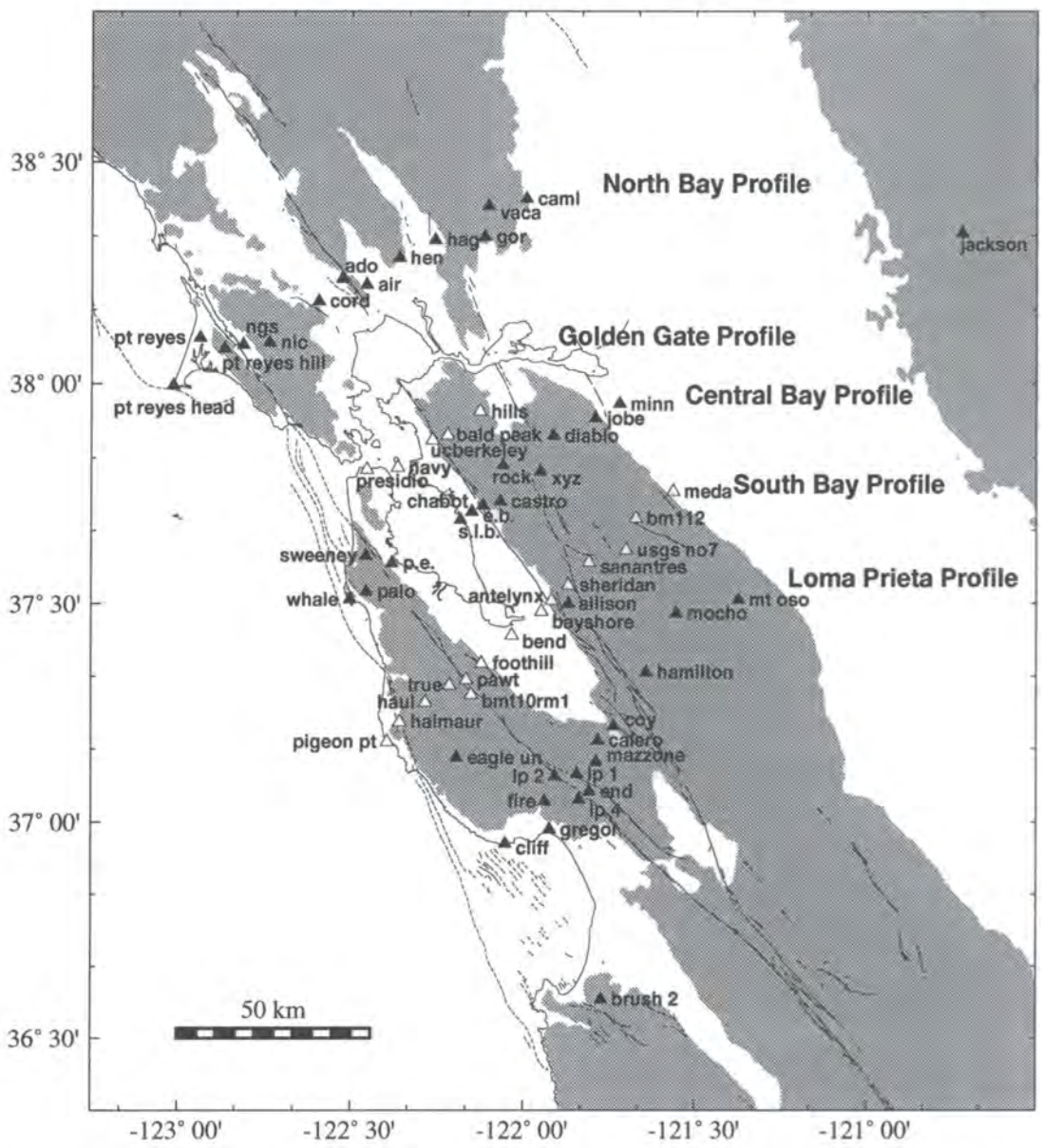

Figure 3.5: USGS GPS profiles in the San Francisco bay region. Grey region (land higher than 100 m) indicates approximate extent of the Coast Ranges and Sierra Nevada.

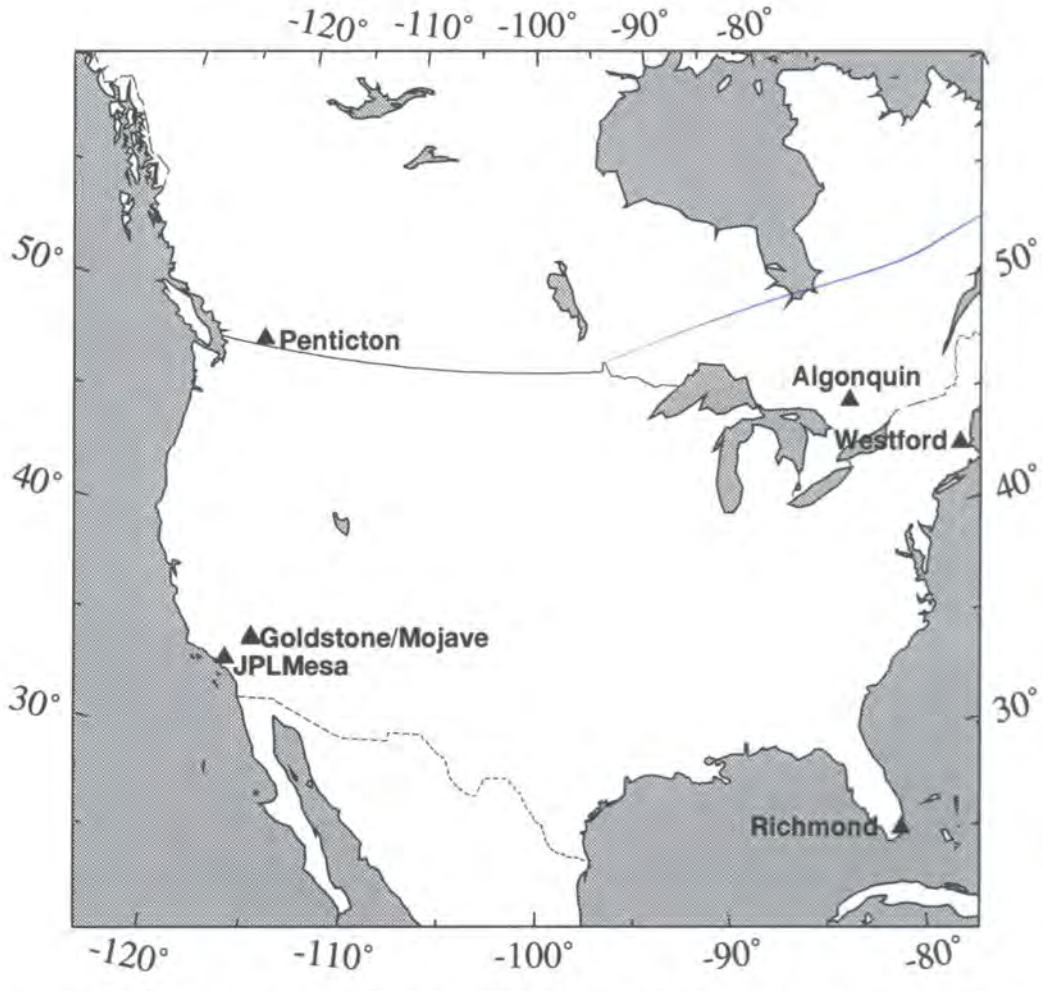

Figure 3.6: Fiducial sites operated by CIGNET, IGS and PGGA and used in the processing of the San Francisco bay region surveys.

A single profile typically took several consecutive sessions to complete, which together are termed a survey. In order to tie points together, at least one site (the "base" site) was occupied during the entire survey. The San Francisco bay profiles were typically measured consecutively so that the individual profile surveys together with "network tie" surveys between adjacent profiles were made, so the profiles could be connected if required.

In this study, data from the three northernmost profiles, North Bay, Golden Gate and South Bay profiles (Figure 3.5) were processed. A list of the stations with identifying codes and approximate positions are given in Table 3.4. Altogether the data set includes usable observations for 41 days and 16 individual surveys between March 1990 and February 1993. A summary of the site occupations together with the fiducial sites used is given in Table 3.5.

Table 3.4: List of Stations.

Station	Lat°N	Lon°W	Height, m †	Stamping
	North Bay Profile			
pt reyes hill	38 04 47.00	122 52 03.00	406.35	pt reyes hill 2 no. 5 1951 [a]
pt reyes head	37 59 47.28	123 00 49.60	185.70	pt reyes head 3 1960 [a]
pt reyes	38 06 12.60	122 56 12.00	-3.15	point reyes ncmn 1981 [b]
ngs	38 05 14.31	122 48 45.52	10.72	1935 1987 [b?]
nic	38 05 33.55	122 44 11.56	30.62	nic [c]
cord	38 11 09.57	122 35 43.03	2.20	cord [c]
ado	38 14 11.12	122 31 38.89	48.10	ado [c]
air	38 13 23.47	122 27 20.43	-29.08	air [c]
hen	38 16 59.55	122 21 42.32	54.84	hen [c]
hag	38 19 25.96	122 15 33.13	-5.03	hag [c]
gor	38 19 52.25	122 06 52.59	72.49	gor [c]
vaca	38 24 04.40	122 06 18.00	859.20	mt vaca 2 1976 [d]
caml	38 25 00.05	121 59 40.96	35.99	caml [c]
jackson	38 20 23.00	120 43 15.83	674.22	jackson 2 1958 [c]
	Golden Gate Profile			
ucberkeley	37 52 18.43	122 15 54.53	36.18	ucg 85 20 [e?]
presidio	37 48 19.09	122 27 18.27	-29.64	JPL 1981
navy	37 48 35.85	122 21 58.16	70.78	navy 1932 [a]
bald peak	37 53 00.85	122 13 19.16	547.99	bald peak 1946(8) [a/f]
hills	37 56 12.83	122 07 41.64	420.20	hills [f]
	Central Bay Profile			
sweeney	37 36 33.99	122 27 29.00	354.06	sweeney rdg 1978 [g]
palo	37 31 36.57	122 27 22.19	357.90	palo [c]
p.e.	37 35 32.05	122 22 55.74	-21.32	unstamped [g?]
chabot	37 43 26.82	122 07 09.08	212.88	chabot 3 1964 [f]
s.l.b.	37 41 26.96	122 11 01.33	-28.99	s.l.b. [c]
e.b.	37 42 34.90	122 09 04.41	-20.17	e.b. [c]
castro	37 43 56.53	122 04 09.25	262.52	castro 2 1948 [f]
rock	37 48 54.06	122 03 41.31	584.64	rock 2 1954 [c]
xyz	37 48 05.09	121 57 11.81	219.96	xyz [c]
diablo	37 52 54.67	121 54 53.10	1137.38	diablo ecc rm2 1962 [h]
jobe	37 55 17.50	121 47 32.85	57.53	jobe [c]
minn	37 57 14.46	121 43 20.61	-3.85	minn [c]
whale	37 30 32.82	122 30 14.03	24.86	unstamped ?

Agencies: *a* USCGS - United States Coast and Geodetic Survey, *b* NGS - National Geodetic Survey, *c* USGS, *d* CDMG - California Division of Mines and Geology, *e* UCB - University of California, Berkeley, *f* EBMUD - ?, *g* NCER - National Center for Earthquake Research, *h* CDWR - Californian Division of Water Resources

† Coordinates are geodetic with respect to WGS 84 ellipsoid.

Table 3.5: Site occupation index for the North Bay, Golden Gate and Central Bay GPS Profiles in the San Francisco bay region together with the fiducial sites used

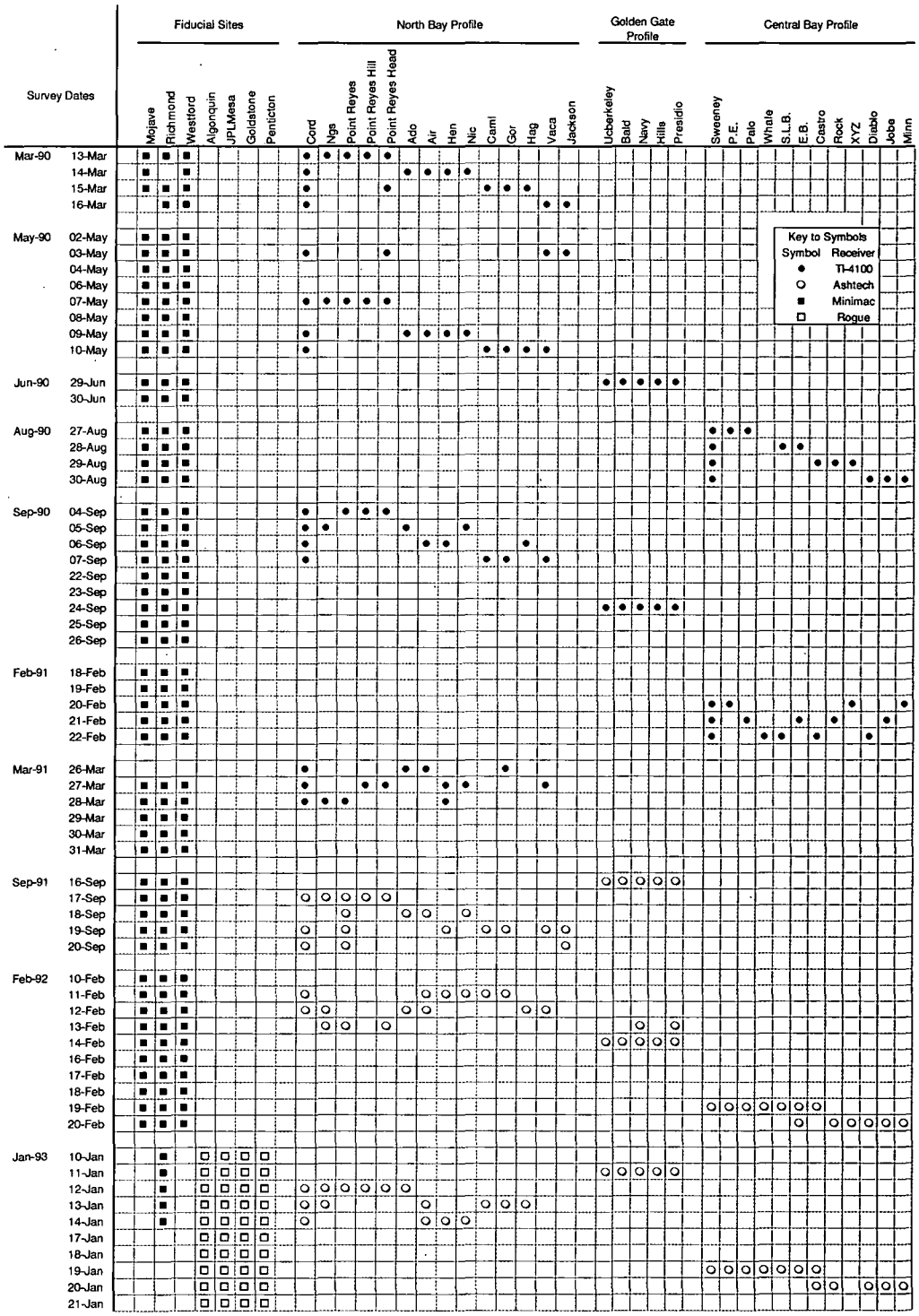

Table 3.6: List of fiducial sites used in the processing of the San Francisco bay region surveys.

Fiducial	Lat°N			Lon°W			Height
Station	°	′	″	°	′	″	m †
Mojave	35	19	53.43	116	53	17.34	904.268
Richmond	25	36	49.75	80	23	03.05	-16.505
Westford	42	36	48.08	71	29	35.97	85.477
Algonquin	45	57	20.88	78	04	16.91	200.873
Penticton	49	19	21.43	119	37	29.94	542.190
JPLMesa	34	12	17.34	118	10	23.59	423.977
Goldstone	35	25	30.56	116	53	21.29	986.582

† Coordinates in WGS 84 system.

The North Bay profile (Figure 3.5) extends for 100 km from Point Reyes Head to the western edge of the Great Valley. This profile crosses all the known active faults within the San Andreas fault system including the San Andreas, Rodgers Creek and Green Valley faults. The Golden Gate profile is shorter, extending for 40 km from Presidio to Hills in the east bay, between the Hayward and Calaveras faults. The Central Bay profile extends eastwards from Whale (within the San Gregorio-Hosgri fault zone), across the San Andreas, Hayward and Calaveras faults, to the eastern edge of the Coast Ranges, a distance of 90 km. Data recorded at Jackson, east of the Great Valley, was included in the North Bay profile for the March 1990, May 1990, and September 1991 surveys.

The three profiles are roughly perpendicular to the strike of the San Andreas fault. In networks of this design, a spurious network rotation would approximate the appearance of fault-parallel shear and a scale error would appear as contraction or extension across the faults. Such errors could result from bias in the satellite orbits or the reference frame. To eliminate this the fiducial network technique was used to obtain higher accuracy satellite orbits and maintain a consistent terrestrial reference frame. Data from several fixed, continuously operating GPS stations run by CIGNET, IGS and PGGA were included in the processing (Figure 3.6, Table 3.6). The equipment used at these permanent tracking stations included Minimac and Rogue receivers.

3.4 Data Analysis

3.4.1 Introduction

The data were processed using the Bernese Version 3.2 Software [*Rothacher et al.*, 1990] with modifications implemented by the USGS [*Davis et al.*, 1989]. The software consists of 37 programs that fall into five categories; Transfer, Orbit, Processing, Simulation and Service. The functional flow diagram for processing is outlined in Figure 3.7. The software uses the receiver-satellite double differences to calculate site coordinates and other parameters.

3.4.2 Processing Procedure

3.4.2.1 Data Transfer

The code and phase data, satellite navigation messages and additional information are recorded in a binary, receiver-dependent format and must be converted into Bernese V3.2 format. The transfer part of the Bernese Software can convert from several receiver formats to or from **RINEX** (Receiver INdependent EXchange format) [*Gurtner et al.*, 1989]. The raw data are separated into files containing phase data, code pseudoranges and broadcast satellite ephemerides.

3.4.2.2 Preprocessing and Orbit Modelling

The broadcast satellite ephemerides from the fiducial and local sites were used to produce a continuous orbit spanning the observation period. The standard strategy used involved combining the data from a single survey into a single network coordinate solution. One continuous orbital arc spanning 5 observation sessions (a multiday arc) was required for this. If a survey lasted less than 3 days, fiducial data from previous and subsequent days were used to compute the full 5 day arc.

The broadcast ephemerides were first checked for satellite shifts (changes in orbit) and outliers (programs **BRDCHK, BRDTST**). If a satellite shift occurred then either the orbital arc was split into two shorter arcs or the data for that satellite discarded from either before or after the shift. The screened ephemerides data were then transformed from the Earth fixed coordinate system into an inertial reference

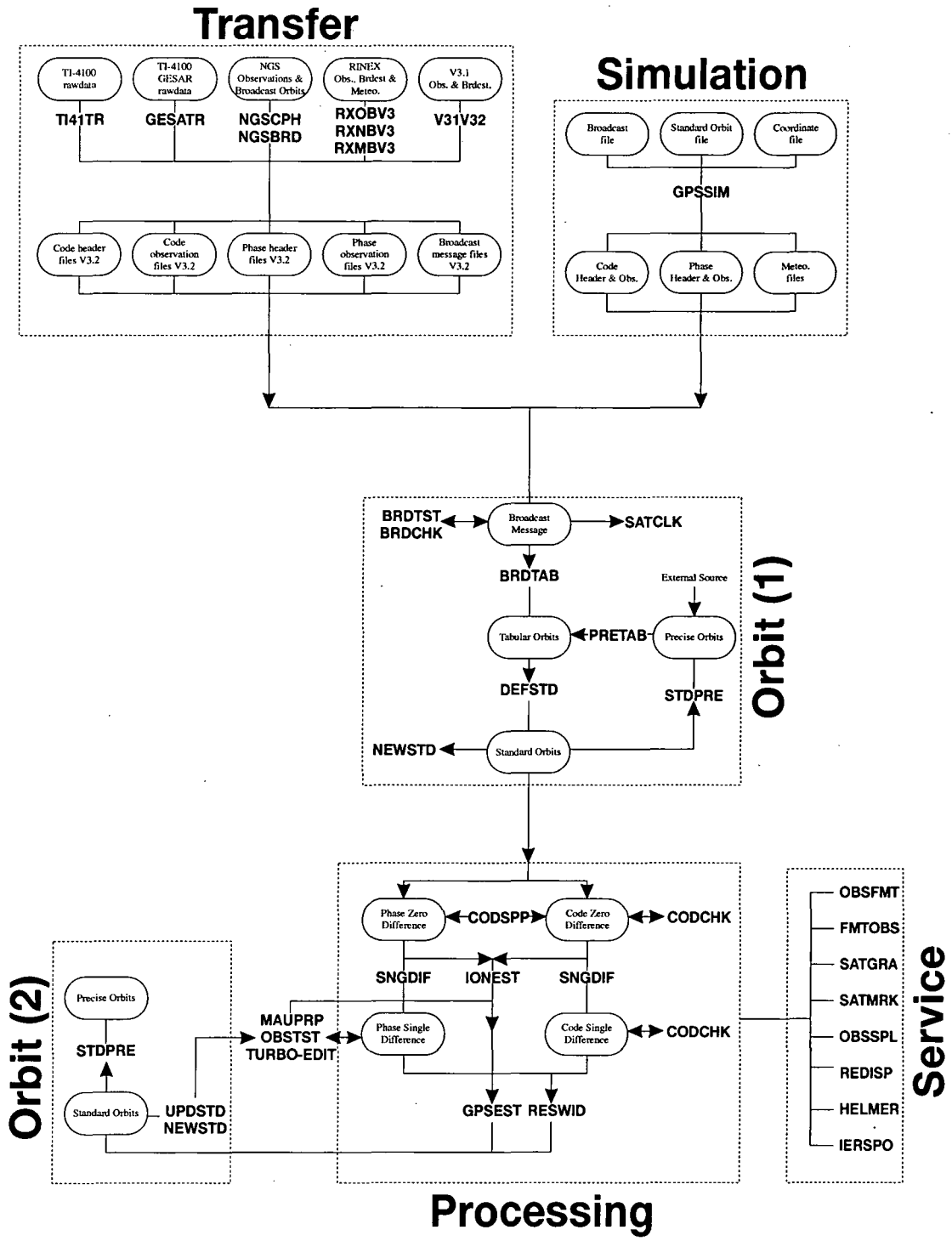

Figure 3.7: Functional flow diagram for the Bernese GPS Software Version 3.2. Names in capital letters indicate individual programs.

frame (**BRDTAB**). Each satellite ephemeris was then treated as a data point to which a "standard" orbit, which accounts for gravitational attraction by the Sun and Moon and solar radiation pressure, was fitted (**DEFSTD**).

The broadcast ephemerides were used along with the pseudorange data, previously checked for outliers (**CODCHK**), to estimate one receiver clock correction per epoch (**CODSPP**). For the fiducial sites measured with Minimac receivers this step was ignored as Minimac receivers automatically calculate and record the receiver clock correction. A set of independent between-receiver, single-difference, phase files were then created between the local sites and the fiducial sites separately (**SNGDIF**). One between-receiver single-difference file was created between the nearest fiducial site and the local base site to tie the local sites to the external reference frame.

The next step involved removing cycle slips and outliers from the single difference phase files. Two cycle-slip detection programs are available, **OBSTST** and **MAUPRP**. Both programs use the residuals from a triple difference solution for coordinates with fixed orbit parameters to detect and repair cycle slips. **MAUPRP** is the descendant of **OBSTST** and was developed when difficulties were experienced in preprocessing dual frequency data recorded during periods of short-period ionospheric variation in the Iceland 1986 survey [*Rothacher et al.*, 1988]. The advantages of **MAUPRP** over **OBSTST** are higher automation and the ability to form and analyse all useful linear combinations in the same processing step. However, from experience it was found that while **MAUPRP** decreased the amount of time spent preprocessing (the most time consuming stage of data processing), **OBSTST**, used in conjunction with a graphics package for examining the residuals, was more reliable.

For fiducial lines, with lengths long enough for errors in the broadcast orbits to hinder cycle slip detection, an iterative technique was used. First, obvious cycle slips and outliers were removed, then a rough orbit adjustment was calculated using the parameter estimation program **GPSEST**. The adjusted orbit parameters were then used to update the standard orbit (**UPDSTD**). Only those satellites for which a statistically significant change in orbital parameters was calculated were updated. These improved orbits were used to scan for cycle slips a second time. Smaller slips were detectable since the residuals for the triple difference solution were thereby reduced. This procedure was repeated until no further cycle slips or outliers in the fiducial or local data single-difference files were detected.

3.4.2.3 Ambiguity Resolution and Processing

Once a value for a cycle ambiguity that is very close to an integer has been determined, the ambiguity is said to be resolved or fixed [*Counselman and Abbot*, 1989]. Ambiguity resolution is not necessary for obtaining station positions, but can improve the results [*Goad*, 1985]. Coordinate solutions where the ambiguities are calculated as floating point numbers and not fixed to integers approach solutions with fixed ambiguities when observation times are long ($>\sim$ 5 hours) [*Rothacher et al.*, 1989]. However, there are many ambiguity parameters in a typical survey (one per satellite per receiver per frequency), and resolving the ambiguities will enable them to be eliminated from the inversion and decrease the formal errors associated with the site coordinates.

Ambiguities are resolved using the parameter estimation program **GPSEST**. They are intitially treated as free parameters together with the other parameters to be estimated which may be station coordinates, orbital parameters (up to 8 per satellite), receiver clock offsets, tropospheric models, ionosphere models and antenna height biases. The chosen parameters are estimated using a least-squares solution. A sigma-dependent strategy is used for the cycle ambiguities. If the error interval surrounding the estimated value contains exactly one integer then the ambiguity is said to be resolved. In order to resolve as many ambiguities as possible the following strategy was employed. First, the wide-lane (L5) ambiguities for the local sites were resolved, usually without difficulty. No attempt was made to resolve the ambiguities for the fiducial stations. The distances separating the fiducial sites was considered too large for successful resolution of ambiguities. In such cases it may be better not to fix an ambiguity than to risk fixing it to a wrong value. Next the L5 ambiguities were held fixed and an attempt was made to resolve the L1 and L2 ambiguities using the ionosphere-free (L3) combination. Once as many ambiguities as possible had been resolved the point coordinates were estimated along with the remaining ambiguities, as floating point values.

All the data from observation sessions on consecutive days were combined, including data from both fiducial and local sites. The coordinates of the local sites were left as free parameters whereas those of the fiducial sites were held fixed. The fixed coordinates of the fiducial sites were obtained from a CDP-VLBI solution in 1988 and corrected for subsequent plate motions as appropriate. For each satellite the six Keplerian elements, and two solar radiation pressure corrections were included as free parameters. A daily, average correction to the a-priori value for the tro-

pospheric delay at the zenith was estimated for each site using the *Saastamoinen* [1972] troposphere model and the CfA-2.2 mapping function [*Davis et al.*, 1985] for mapping the delays to lower elevation angles. A satellite cut-off elevation of 15° was generally used. The advantage of estimating the parameters from all the sessions together in a simultaneous solution which includes all the local and fiducial data (as opposed to using the improved orbit from the fiducial data only) is that the formal errors are propagated correctly, including contributions from ephemeris error [*Lichten and Border*, 1987].

3.5 Summary

GPS is an all-weather, space-based navigation system designed for accurate determination of user position, velocity and time anywhere on or near the Earth. The capability of GPS for accurate relative surveying has proved of great value for crustal deformation studies. The system consists of three segments, the space-, control- and user-segment.

The basic concept behind positioning with GPS is ranging. Two types of measurements are made, code and carrier-phase. Phase data offer the best potential for high-precision positioning. Both measurements are affected by similar error sources (biases) such as clock errors, satellite-orbit errors, and signal delay. Differencing and combining the data can eliminate or reduce various errors and enable the estimation of highly-accurate relative station positions.

This study involved the processing of data from three USGS GPS profiles crossing the San Andreas fault system in the San Francisco bay region. The individual profiles were measured up to 7 times between March 1990 and February 1993.

The data were processed using the Bernese Version 3.2 Software. Data from separate profiles and separated surveys were processed independently. In addition, data from a continental-scale fiducial network were included in the processing as part of the fiducial network technique that provides improved satellite orbit determination and a consistent reference frame.

Chapter 4

Processing Results

4.1 Introduction

Deformation rates in the San Francisco bay region are of the order of a few cm per year. A high accuracy of measurement is therefore required to detect this deformation within a few years. In order to interpret the results of the GPS measurements in a meaningful way it is thus vital to correctly asses the true accuracy.

4.2 Precision, Repeatability and Accuracy

4.2.1 Introduction

Precision is a measure of the scatter in the data used to estimate some parameter. One indicator of precision is repeatability, which is a measure of the scatter of independent estimates of a parameter. Accuracy is a measure of how close the result of the experiment is to the true value. In GPS, the precision of a line-length vector estimate is the formal error calculated in the estimation process and it is based on the scatter of the observed data. However formal errors based on the scatter of the data generally underestimate the true error as they do not account for systematic errors that are constant on the time scale of a single measurement session [*Dixon*, 1991]. Repeatability can be assessed by comparing the scatter in the calculated results for different measurement sessions, and accuracy can be assessed by comparing the GPS results to those obtained from some other more accurate technique (e.g., VLBI). Accuracy cannot be assessed for the results described in this thesis because the only GPS observations at VLBI sites were used in the solution for orbit determination as part of the fiducial network technique and the

site positions were therefore held fixed. Previous estimates of GPS accuracy in the western United States have shown that horizontal rates estimated using GPS agree to within one standard deviation ($\sim$ 1 cm) with those determined by VLBI [*Larson and Agnew*, 1991; *Davis et al.*, 1989, *Larson*, 1993].

GPS surveys are generally conducted as a series of observation sessions over several days separated by months or years. Many errors are highly correlated over one survey such as marker instability, multipath, satellite clock behaviour, fiducial network errors, receiver clock errors, atmospheric and ionospheric conditions and satellite orbit errors. These errors are thus not detectable in surveys involving observations spanning a few adjacent days. However they may vary over long time periods and thus be reflected in the results obtained from surveys separated by months. It is therefore helpful to assess the repeatability of the vectors estimated by GPS over the short- and long-term. Short-term repeatability can be estimated as the weighted variance about the mean of daily estimates, from a single survey. For a vector line-length component (north, east or up) the variance about the weighted mean is

$$\mathbf{S}_{mean} = \sqrt{\frac{\frac{N}{N-1}\sum_{i=1}^{N}\frac{(y_i-\langle y\rangle)^2}{\sigma_i^2}}{\sum_{i=1}^{N}\frac{1}{\sigma_i^2}}}, \tag{4.1}$$

where N is the number of days, y_i is the estimate of the independent component on day i, $\langle y\rangle$ is the weighted mean of y_i's and σ_i is the (formal) standard error. However, in the processing procedure used here, all data from consecutive days were combined in a single solution (i.e., only one estimate for each line-length component during the survey was obtained), and the short-term repeatability (equation 4.1) could not be computed.

Long-term repeatability is indicated by the scatter of the results of a series of GPS surveys performed over years after the effects of crustal deformation are subtracted. This will show the effects of errors that vary from survey to survey. For networks far from active deformational features, zero motion can be assumed and equation (4.1) can be used. For networks deforming at a uniform rate the variance about a best-fit straight line is calculated [*Larson and Agnew*, 1991; *Davis et al.*, 1989].

This is defined as

$$\mathbf{S}_{line} = \sqrt{\frac{\frac{N}{N-2}\sum_{i=1}^{N}\frac{(y_i-(a+bt_i))^2}{\sigma_i^2}}{\sum_{i=1}^{N}\frac{1}{\sigma_i^2}}}, \tag{4.2}$$

where a and b are the intercept and slope of the best-fit straight line, and t_i is the time of the ith measurement. The Reduced χ^2 (or χ^2 per degree of freedom, χ^2_ν) statistic for the best-fit line is given as

$$\chi^2_\nu = \frac{1}{N-2}\sum_{i=1}^{N}\frac{(y_i-(a+bt_i))^2}{\sigma_i^2}. \tag{4.3}$$

χ^2_ν expresses the confidence that we may have in the result. In general, and if the data set is reasonably large, the closer that χ^2_ν approaches unity, the more statistically significant is the result. The magnitude of χ^2_ν is determined by the scatter in the observed parameters, the values assigned to the uncertainties σ_i, and the appropriateness of the fitting function. Therefore a large χ^2_ν may indicate very scattered data, under-assigned uncertainties or the wrong form for the fitting function. If it is assumed that the uncertainties are underestimated then the scatter can be accounted for by multiplying the uncertainties by $\sqrt{\chi^2_\nu}$.

The accuracy of an individual line-length estimate is dependent on several errors. Some of these errors are constant, whilst others will be dependent on the line length. A simple expression describing the accuracy of distance measurements is [*Savage and Prescott*, 1973; *Savage*, 1983]

$$\sigma^2 = a^2 + b^2 l^2, \tag{4.4}$$

where σ is the standard deviation and l is the line length. Equation (4.4) is derived for geodolite measurements where the instrument has a constant error a plus a length-dependent error b introduced by atmospheric refraction along the line. For geodolite data, $a = 3$ mm and $b = 2 \times 10^{-7}$. Although this function has also been applied to GPS measurements [*Hager et al.*, 1991] there is no reason to assume that this is rigorously appropriate. Error sources such as receiver noise, tripod set-up error and multipath are independent of line length. These length-independent errors are typically at the level of 2 mm or less. Other sources of error are proportional to line length. Atmospheric errors are line-length dependent only up to a certain length, after which the error reaches a constant value as the atmospheric variation between the two ends of the line becomes uncorrelated. Errors in estimating the orbits of satellites are almost linearly proportional to line-length. Orbit errors

contribute an error of $l\beta\sigma_{orb}/L$ where L is the receiver - satellite range, σ_{orb} is the error in the satellite orbit and β, a constant, which depends on the geometry of the network. With these factors in mind *Dixon* [1991] proposed the expression

$$\sigma^2 = a^2 + b^2 \left(1 - e^{-l/\lambda}\right)^2 + c^2 l^2, \tag{4.5}$$

where a is the length-independent error, b is the tropospheric contribution to line-length error for lengths exceeding several tropospheric correlation lengths, λ is the tropospheric correlation length, and c is the satellite orbit error. However, equation (4.5) cannot be expressed as a sum of terms with the parameters appearing only as a coefficient of the line-length and error, therefore making estimation of the coefficients difficult. *Larson and Agnew* [1991] use the simple equation

$$\sigma = a + bl, \tag{4.6}$$

in order to approximate the dependence of precision with length.

For the three GPS profiles studied here, the short- and long-term errors are estimated. To express the short-term precision, the formal standard deviations from the GPSEST solution are used and applied to equation (4.6). The long-term repeatability is calculated using equation (4.2) and then applied to equation (4.6). The coefficients a and b in equation (4.6) are estimated using a least-squares algorithm. For the long-term repeatability the reduced χ^2 statistic is also calculated.

4.2.2 Results

4.2.2.1 Short-Term Precision

The short-term precisions of the north-south, east-west, and vertical line-length components for each survey were summarised using equation (4.6) (Table 4.1). In addition, equation (4.6) was applied to all the results for each profile and to all the profiles combined. As an example, the short-term precisions of individual lines plotted as a function of line length for the February 1992 North Bay survey together with the least-squares fit (solid line) are shown in Figure 4.1. There are no previous published estimates of short-term precision (although *Larson and Agnew*, [1991] calculated short-term repeatability and called it short-term precision) and therefore these results are compared with previous estimates of short-term repeatability. Previous estimates of short-term repeatability calculated from vectors

between stations in southern California separated by distances of 50-450 km [*Larson and Agnew*, 1991] are also plotted in Figure 4.1. *Larson and Agnew*, [1991] found a short-term repeatability of 1.9 mm + $0.6 \times 10^{-8} l$ for the north-south component, 2.1 mm + $1.3 \times 10^{-8} l$ in the east-west component and 17 mm + 0 l for the vertical component. In the case of the North Bay profile data, all three components show a line-length dependence (Figure 4.1). For the total combined, short-term precision (bottom, Table 4.1) the north-south component has the least dependence on line-length ($0.4 \times 10^{-8} l$). The east-west component, with a precision of 1.0 mm $+0.7 \times 10^{-8} l$, has a larger line-length dependence than the north-south component. The precision of the vertical component is 8.0 mm $+1.6 \times 10^{-8} l$. The results from the individual surveys shows that the greatest variation in length-dependent errors occurs in the vertical component, from $-0.3 \times 10^{-8} l$ to $43.2 \times 10^{-8} l$ (last column, Table 4.1).

The difference in line-length dependence between the two horizontal components can be explained partly by satellite geometry. Before full satellite coverage was available, the GPS constellation over California was orientated mainly north-south, giving better coverage in that direction and smaller errors in that component [*Dixon*, 1991]. As satellite coverage improves with time this difference should lessen. Variations of line-length dependence between individual surveys show that whilst the north-south precision tends to remain about the same, the east-west precision tends to approach that of the north-south by January 1993. The constant terms for both horizontal components are similar.

The constant terms are about half those estimated for lines in southern California [*Larson and Agnew*, 1991] which were calculated using equation (4.1) for data from several consecutive days. As described above, the short-term precisions used here are based on the phase data scatter determined by the Bernese GPS solution and therefore these disagreements simply illustrate the well known fact that the precision calculated from the data scatter underestimate the actual repeatability and true accuracy.

The vertical component is nearly an order of magnitude less precise than the horizontal components. No significant dependence on line-length was reported for the vertical component for GPS data collected in southern California [*Blewitt*, 1989; *Larson and Agnew*, 1991]. A line-length dependence of $6 \times 10^{-8} l$ was reported for the vertical component for 14 stations in southern California [*Dong and Bock*, 1989]. These differences were possibly the result of different fiducial networks used

Table 4.1: Summary of the short-term precisions of the GPS profiles.

	North		East		Up	
Survey	a	$b \times 10^{-8}$	a	$b \times 10^{-8}$	a	$b \times 10^{-8}$
Date	mm	mm	mm	mm	mm	mm
North Bay Profile						
March 1990	1.4	0.9	1.5	1.3	11.9	5.9
May 1990	1.0	0.2	1.0	0.6	9.7	0.0
Sept. 1990	0.8	0.4	1.1	0.8	6.1	3.2
March 1991	1.5	0.5	1.5	0.8	12.9	1.8
Sept. 1991	1.4	0.2	0.9	0.8	9.8	0.1
Feb. 1992	0.9	0.3	0.8	0.4	6.0	1.7
Jan. 1993	0.7	0.2	0.6	0.2	4.4	1.5
Combined	1.1	0.3	1.1	0.7	8.8	1.3
Golden Gate Profile						
June 1990	0.9	0.4	1.1	0.5	8.2	3.1
Sept. 1990	1.1	0.6	1.1	0.6	9.2	12.1
Sept. 1991	1.3	14.4	0.7	17.2	12.3	43.2
Feb. 1992	0.9	-0.1	8.1	-0.1	6.6	-0.2
Jan. 1993	0.8	0.1	0.7	0.1	5.5	1.9
Combined	1.1	0.0	1.0	0.4	8.7	2.1
South Bay Profile						
Aug. 1990	1.0	0.3	1.2	0.8	7.2	2.1
Feb. 1991	1.2	0.0	1.2	0.0	8.6	-0.3
Feb. 1992	0.9	0.3	0.7	0.6	5.9	1.7
Jan. 1993	0.9	0.3	0.7	0.4	6.0	1.7
Combined	1.0	0.2	1.0	0.4	7.1	1.0
All three profiles						
Combined	1.0	0.4	1.0	0.7	8.0	1.6

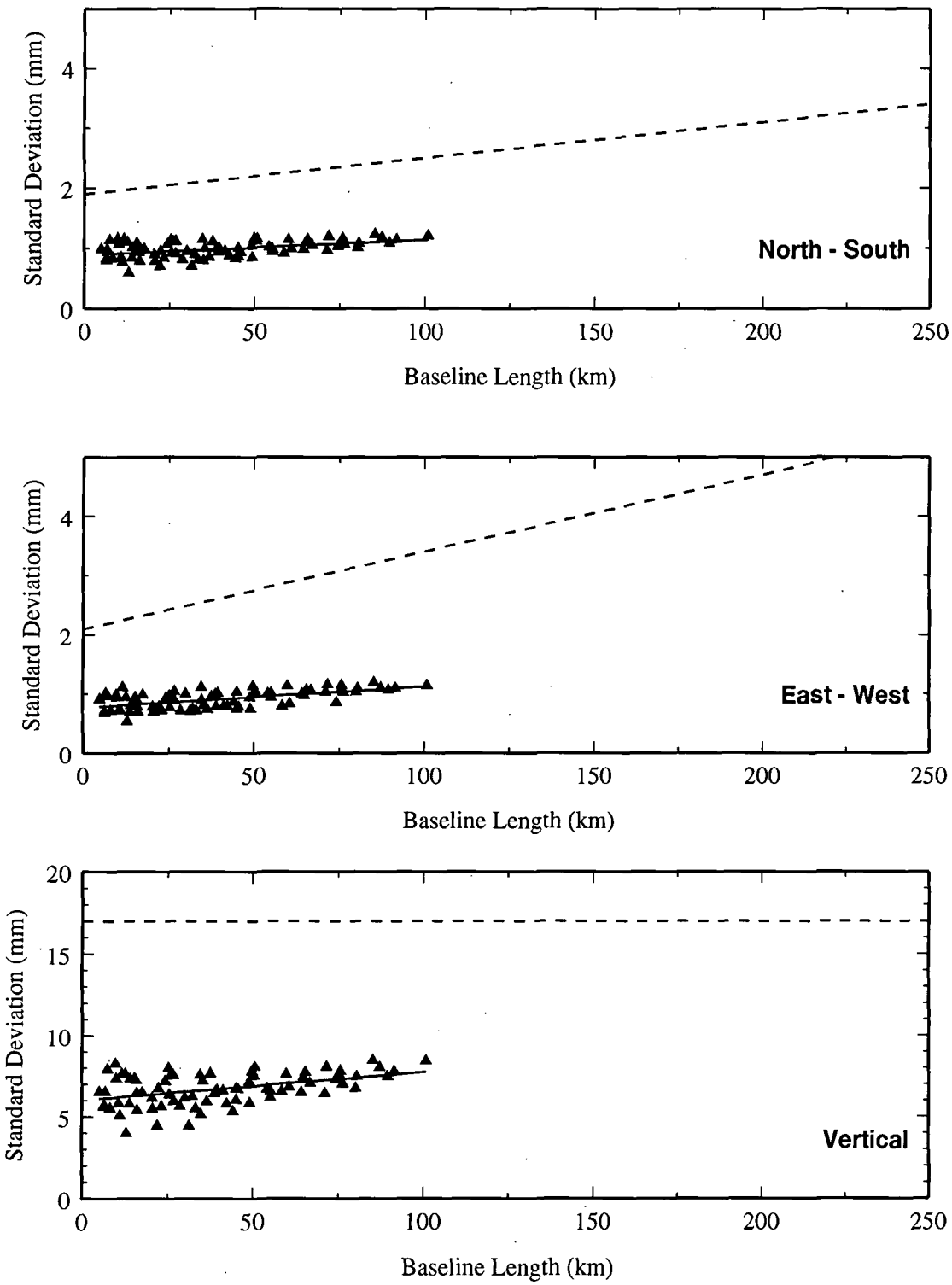

Figure 4.1: Short-term precision for individual lines of the February 1992 North Bay profile. The solid triangles are the formal standard deviations from the GPSEST solution. Solid lines are the least-squares best fits through the data.. Dotted lines are the estimates of short-term repeatability derived by *Larson and Agnew* [1991].

in the analyses [*Larson et al.*, 1991]. However, except for the January 1993 surveys, the fiducial network used for the profiles studied in this thesis was kept the same and therefore cannot be responsible for the large variations calculated (Table 4.1). One of the largest sources of error in the vertical component is the effect of the nondispersive atmosphere, in particular the "wet" component of the tropospheric delay [*Tralli et al.*, 1988]. In this analysis a simple strategy was employed, which was to model the delay at the zenith by a single parameter for each day and for each site in the network. The zenith wet delay can vary by 20-50 mm over several hours [*Davis et al.* 1989]. Ignoring these variations can lead to significant errors in the vertical component. Tropospheric delay is probably the dominant error source for lines up to several hundred kilometres long, [equation (4.5); Figure 12, *Dixon*, 1991]. The vertical error estimates reported by *Larson and Agnew* [1991] are for lines ranging in length from 50 to 400 km, the range where tropospheric errors no longer dominate, whereas lines in the San Francisco bay region profiles are in the range 5 to 165 km, where the troposphere is a large error source.

4.2.2.2 Long-Term Repeatability

Long-term repeatability of GPS interstation vectors from the profiles are summarised in Table 4.2 and Figure 4.2. The best-fit lines used in equation (4.2) are the weighted least-squares station velocities relative to a fixed site as described in Section 4.3 below. The long-term repeatabilities are plotted against line length in Figure 4.2 along with the best-fit lines (equation 4.6) through this data set and the relationship reported by *Larson and Agnew* [1991]. The long-term repeatability in the north-south was estimated using the data indicated by the solid triangles. Apart from the longest line, the data shown by open triangles are all from the Central Bay profile. The time series for this profile indicate that the February 1992 results are anomalous and probably in error. The longest line, Jackson-Cord, is also removed from the calculation. This line has an anomalously poor long-term repeatability in the north component which can be attributed to error in the first survey, March 1990. The long-term repeatability in the north-south is then 4 mm + $2.2 \times 10^{-8} l$. In the east-west direction, all the data were used and the repeatability is 4 mm + $3.5 \times 10^{-8} l$. The repeatability of the horizontal components are similar to estimates made by *Larson and Agnew* [1991] for southern California using the same calculation technique (straight dashed line, Figure 4.2). However in both directions the line-length dependent component estimated here is slightly larger than for their results. The maximum line length for the profiles is 150 km.

Table 4.2: Long-Term Repeatability of the GPS results.

Stations		Length	North	χ^2_ν	East	χ^2_ν	Vertical	χ^2_ν	Obs. Span†	No. of
from	relative to	km	mm		mm		mm		yrs.	Obs.
				North Bay Profile						
Ado	Cord	8	5.9	68.4	3.1	18.7	39.0	53.6	2.8	7
Air	Cord	13	5.2	70.9	2.7	21.0	29.0	42.1	2.8	7
Nic	Cord	16	4.2	47.9	3.0	9.9	14.5	7.3	2.8	7
Ngs	Cord	22	4.8	61.2	5.5	82.2	26.9	38.3	2.8	6
Hen	Cord	23	4.9	51.0	4.7	51.8	27.9	31.2	2.8	6
Pt Reyes Hill	Cord	27	4.6	34.6	2.2	8.1	38.9	46.4	2.8	7
Pt Reyes	Cord	32	4.9	43.4	3.9	31.4	22.6	19.5	2.8	7
Hag	Cord	33	4.8	67.2	7.1	147.0	37.6	74.8	2.8	5
Pt Reyes Head	Cord	42	8.7	119.5	7.1	72.6	18.1	29.3	2.8	8
Gor	Cord	45	4.4	34.6	8.2	123.8	32.7	35.5	2.8	7
Vaca	Cord	49	4.7	37.0	7.3	78.5	36.6	38.5	1.9	6
Caml	Cord	58	5.9	69.2	8.4	141.9	25.9	24.1	2.8	6
Jackson	Cord	165	32.6	682.4	8.7	11.8	47.0	206.5	1.5	3
				Golden Gate Profile						
Bald	Ucberkeley	4	2.6	11.3	1.3	3.3	15.4	6.7	2.5	5
Navy	Ucberkeley	11	6.1	57.3	6.9	84.3	28.7	19.2	2.5	5
Hills	Ucberkeley	14	1.6	4.6	1.4	3.8	38.9	42.5	2.5	5
Presidio	Ucberkeley	18	6.0	42.5	8.1	87.2	13.9	3.4	2.5	4
				Central Bay Profile						
P.E.	Sweeney	7	8.3	98.9	2.3	7.7	20.1	10.7	2.4	4
Palo	Sweeney	9	1.6	67.5	5.6	54.6	14.6	6.8	2.4	4
Whale	Sweeney	12	5.4	44.4	11.6	267.7	79.2	206.2	1.9	3
S.L.B.	Sweeney	26	3.6	18.2	3.9	24.3	75.8	162.4	2.4	4
E.B.	Sweeney	29	10.0	137.8	6.4	55.9	67.5	127.4	2.4	4
Castro	Sweeney	37	9.7	123.4	5.1	31.4	28.6	23.2	2.4	4
Rock	Sweeney	42	9.6	88.1	5.2	21.9	63.7	83.8	2.4	4
Xyz	Sweeney	49	12.7	178.6	5.7	27.1	79.8	146.2	1.5	3
Diablo	Sweeney	57	9.7	89.2	7.1	40.3	49.3	50.1	2.4	4
Jobe	Sweeney	68	13.8	192.0	4.6	16.9	50.7	56.8	2.4	4
Minn	Sweeney	75	19.4	358.7	5.9	26.4	88.4	159.8	2.4	4

† time in years between the first and last survey.

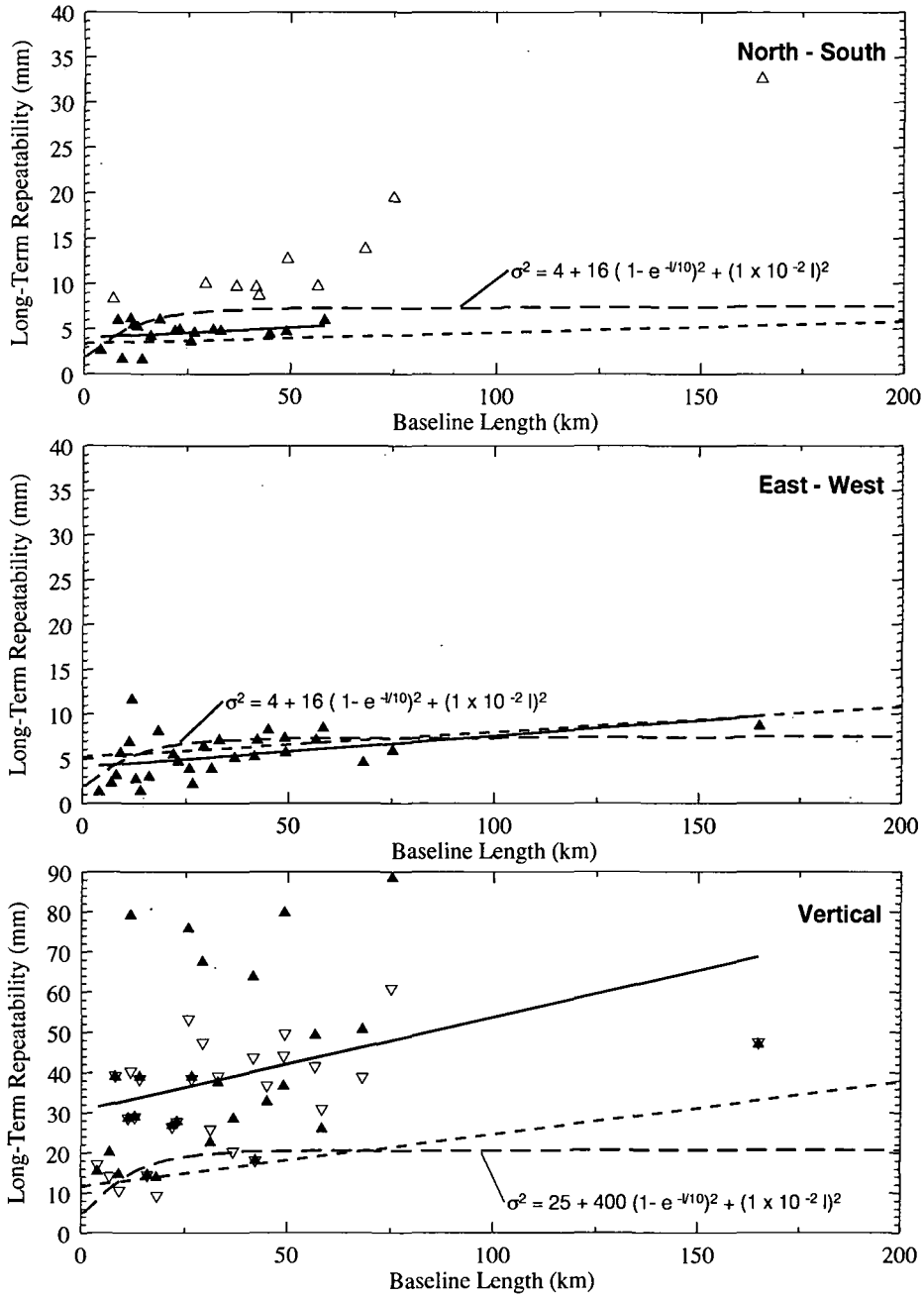

Figure 4.2: Long-term repeatability of interstation vector components for the San Francisco bay region profiles. Solid lines represent the least-squares best fits through the data. Straight dashed line is the long-term repeatability calculated by *Larson and Agnew* [1991] for GPS stations in southern California. Curved dashed line is the error model proposed by *Dixon* [1991] (equation 4.5). Open triangles in the north-south component indicate data deleted when calculating the best-fit line. Open triangles in the vertical component are the long-term repeatabilities calculated assuming no vertical motion.

The vertical component shows poorer repeatability than either horizontal component (31 mm + $23 \times 10^{-8} l$). If no motion in the vertical is assumed then an improved repeatability of 28 mm + $10 \times 10^{-8} l$ is obtained (compare open triangles and closed triangles in the vertical component of Figure 4.2). This is partially a result of different techniques used to calculate the two estimates. The results of the long-term repeatability assuming motion in the vertical were calculated whilst estimating the station velocities, which takes account of the full position covariance matrix for each survey. The long-term repeatability assuming no motion were only calculated using the partial covariance matrix for each line individually and therefore the least-squares and repeatability estimates are different. The error model proposed by *Dixon* [1991] (equation 4.5) agrees well with the data in the east-west component but overestimates the errors in the north-south and greatly underestimates them in the vertical.

The long-term repeatability is approximately a factor of 4 worse than the short-term precision. This is a typical result and illustrates the effect of errors that vary systematically over a long time scale compared with a single survey.

4.3 Estimation of Station Velocities

4.3.1 Introduction

Relative station velocities were obtained using a simple, weighted least-squares procedure. The Cartesian position of each station was assumed to vary linearly with time. A common station for all surveys was chosen, and then, for each survey, the relative vectors of all other stations with respect to that common station were calculated. Then, for each station, a mean relative vector corresponding to the mean measurement time of the station, a linear rate of change and the corresponding uncertainties in the Cartesian components were estimated. The intersite relative vectors and corresponding variance-covariance matrix were then projected onto a Cartesian coordinate system located at one end of the line, whose north is coincident with the local north, and vertical with the normal to the ellipsoid. The uncertainties of the position and velocity estimates are determined by propagation of the full position covariances in the GPSEST solutions, with one exception necessary in order to accommodate singularities introduced by fixed stations which have zero position covariances. The fixed sites were downweighted by assigning 10 m

Table 4.3: Statistics determined from estimating station velocities.

Profile	Fixed Station	Number of data used[a]	Number of parameters estimated[b]	$\sqrt{\chi^2_\nu}$
North Bay	Cord	351	138	5.5
Golden Gate	Ucberkeley	150	99	4.9
Central Bay	Sweeney	177	108	7.2

[a] = ($\sum$ number of stations per survey - 1) $\times$ 3

[b] = ($\sum$ number of common stations) $\times$ 3 + ($\sum$ number of stations in more than one survey) $\times$ 3

variances to their position coordinates, which renders the solution non-singular and insensitive to the coordinates of the fixed sites.

The reduced chi squared, χ^2_v, of the solution was also estimated. If the standard deviations calculated as part of the Bernese solutions correctly represent the long-term repeatability, then χ^2_v would be 1. The χ^2_v obtained from various Bernese solutions provides a factor by which the Bernese formal standard deviations can be scaled so that χ^2_v is 1 i.e. $\sigma_{new} = \sigma_{old}\sqrt{\chi^2_\nu}$. The above method for calculating station velocities has the advantage that the least-squares procedure is always over-determined and therefore a solution is generally simple to calculate [*Menke*, 1984]. However, because there must be a common station for all the surveys, nearby networks cannot be combined to give an overall velocity solution unless they have a common station that has been measured during every survey of both networks. This may even be problematic in a single network as measurements are often lost through problems in the field.

4.3.2 Results

In obtaining the station velocities for the San Francisco bay region profiles, each profile was treated separately. The fixed station for each profile was chosen primarily on a basis of measurement frequency, that is, the station that had the greatest number of observations overall was chosen. A summary of the data used, number of parameters estimated, stations chosen as fixed sites and χ^2_v for the 3 profiles is given in Table 4.3. The station velocity standard deviations were rescaled by a factor of $\sqrt{\chi^2_\nu}$ in order to obtain errors that reflect both precision and repeatability, and are the best possible estimates of accuracy available.

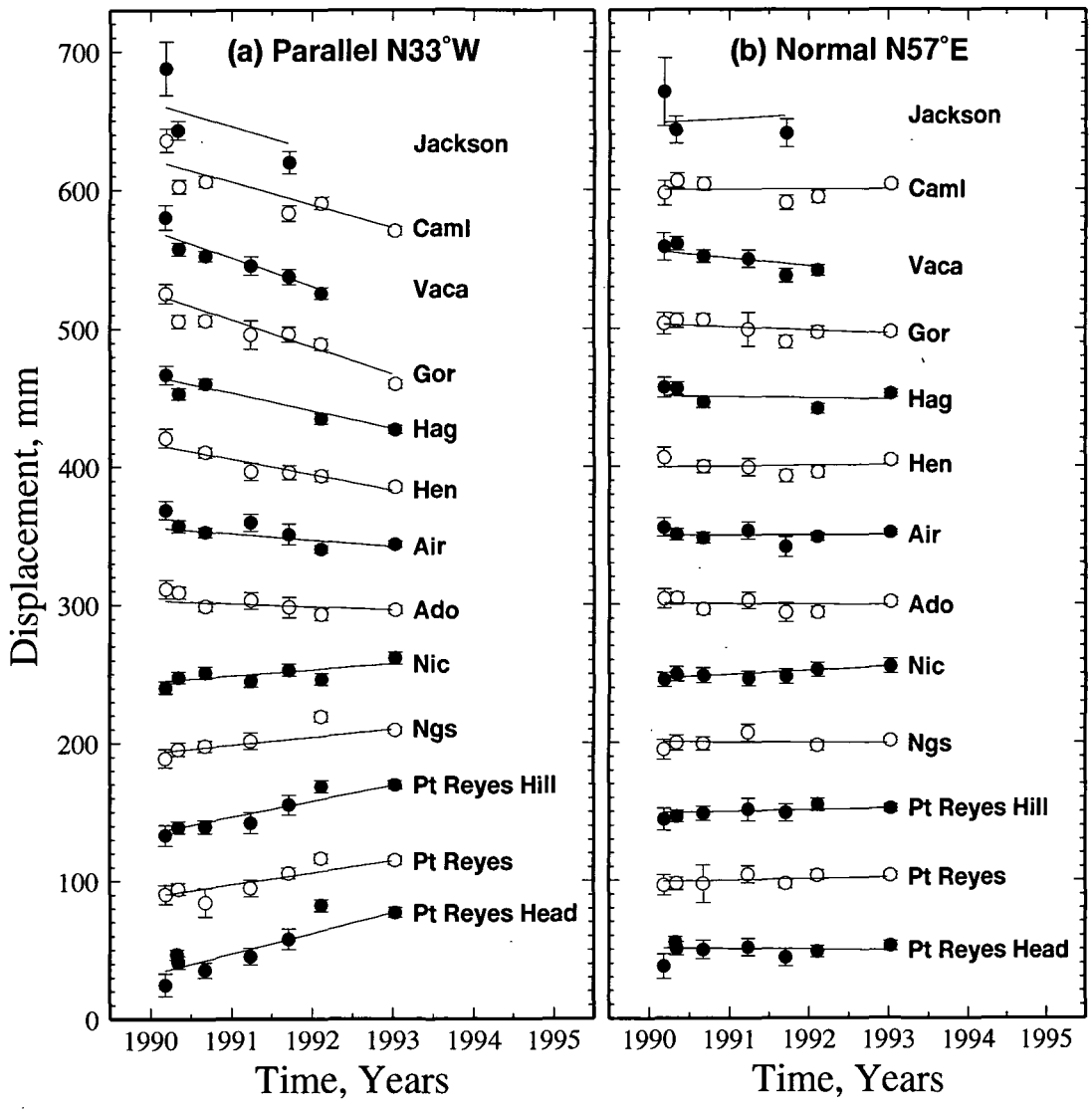

Figure 4.3: Displacement relative to station Cord (a) parallel (N33°W) and (b) normal (N57°E) to the trend of the San Andreas fault as a function of time for the North Bay profile. Error bars represent the 1σ scaled formal standard deviations.

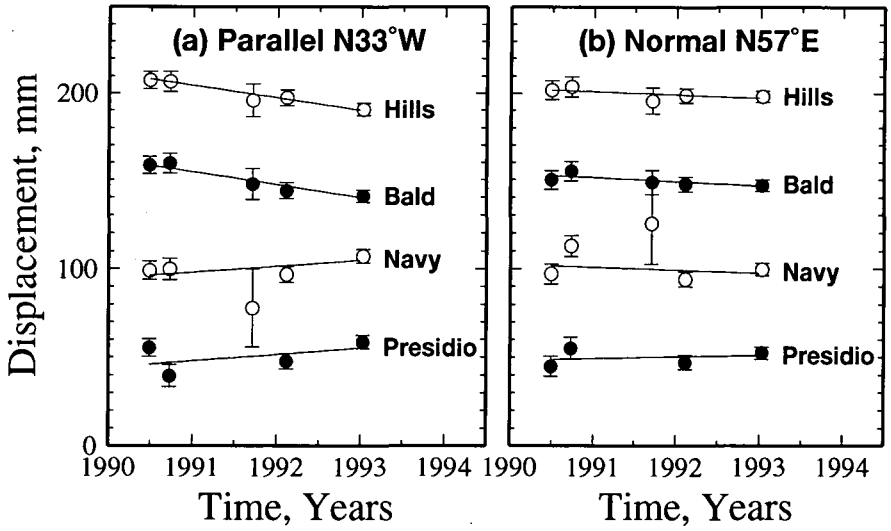

Figure 4.4: Displacement relative to station Ucberkeley (a) parallel (N33°W) and (b) normal (N57°E) to the trend of the San Andreas fault as a function of time for the Golden Gate profile. Error bars represent the 1σ scaled formal standard deviations.

The changes in the fault-parallel (N33°W) and fault-normal (N57°E) line-length components relative to the fixed station as a function of time for the 3 profiles are shown in Figures 4.3 to 4.5. The data are well fit by a linear rate of change. The rate of fault-parallel displacement generally increases with the distance from the fixed station while the fault-normal displacements show little or no significant motion.

The horizontal velocities relative to the fixed station for the 3 profiles are listed in Table 4.4 and shown as vectors in Figure 4.6. The dominant pattern exhibited in all three profiles is right-lateral shear parallel to the trend of the San Andreas fault system. The distribution of deformation is best shown by plotting the fault-parallel and fault-normal velocities along a fault-perpendicular profile (Figures 4.7 to 4.9). The vertical velocities relative to their respective fixed point are shown as vectors along a fault-perpendicular profile in Figure 4.10.

4.3.3 Discussion

4.3.3.1 Fault-Normal Velocities

Fault-normal velocity profiles in a region of shear-strain accumulation are expected to be mainly flat and featureless [*Prescott*, 1981]. The fault-normal (N57°E) velocities (Figures 4.7b, 4.8b and 4.9b) for all three profiles indicate no systematic convergence upon the fault and are generally flat and featureless. Only the velocities of stations Nic and Vaca in the North Bay and s.l.b. in the Central Bay

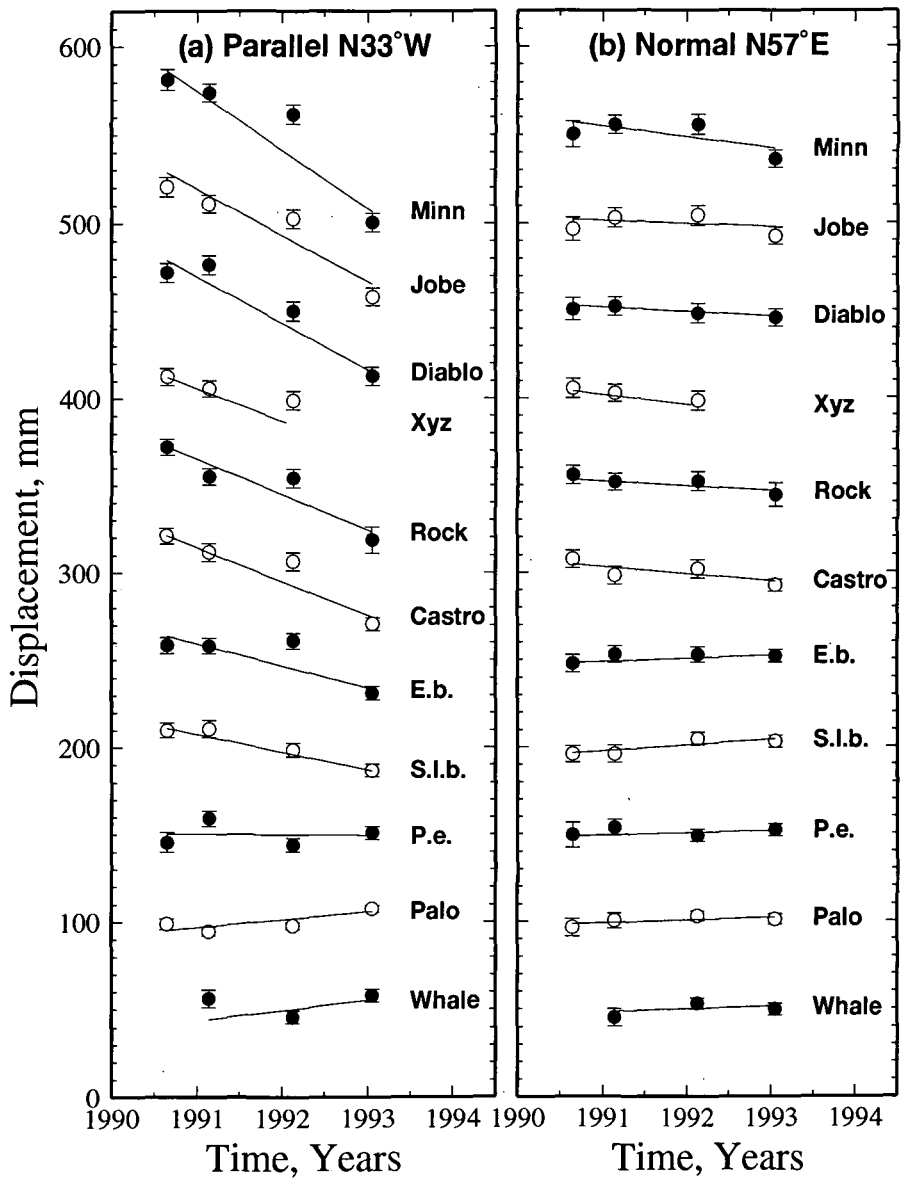

Figure 4.5: Displacement relative to station Sweeney (a) parallel (N33°W) and (b) normal (N57°E) to the trend of the San Andreas fault as a function of time for the Central Bay profile. Error bars represent the 1σ scaled formal standard deviations.

Table 4.4: Average fault parallel (N33°W) and fault normal (N57°E) relative station velocities for the North Bay, Golden Gate and South Bay profiles for 1990 to 1993

Station	Relative to	N57°E Distance from fixed station, km	N33°W Velocity mm/yr†	N57°E Velocity mm/yr†
		North Bay Profile		
Pt Reyes Head	Cord	-42.3	14.8 ± 1.6	-2.7 ± 1.4
Pt Reyes	Cord	-30.1	8.6 ± 1.6	0.3 ± 1.4
Pt Reyes Hill	Cord	-26.5	11.4 ± 1.6	0.0 ± 1.4
Ngs	Cord	-22.0	5.7 ± 1.3	-1.2 ± 1.3
Nic	Cord	-16.0	4.3 ± 1.5	3.4 ± 1.4
Ado	Cord	8.0	-2.3 ± 1.5	-0.4 ± 1.3
Air	Cord	12.5	-4.8 ± 1.2	0.7 ± 1.2
Hen	Cord	23.0	-11.3 ± 1.6	2.1 ± 1.6
Hag	Cord	33.0	-13.0 ± 1.4	0.2 ± 1.4
Gor	Cord	44.0	-19.6 ± 1.6	-1.0 ± 1.5
Vaca	Cord	48.9	-20.7 ± 2.6	-5.8 ± 2.3
Caml	Cord	58.0	-16.5 ± 1.7	1.9 ± 1.5
Jackson	Cord	146.1	-17.3 ± 6.0	6.4 ± 9.5
		Golden Gate Profile		
Presidio	Ucberkeley	-18.0	3.6 ± 2.3	1.0 ± 2.1
Navy	Ucberkeley	-11.2	3.4 ± 2.3	-2.6 ± 2.1
Bald	Ucberkeley	3.9	-7.5 ± 2.1	-2.2 ± 2.1
Hills	Ucberkeley	14.0	-7.3 ± 2.1	-1.5 ± 2.1
		South Bay Profile		
Whale	Sweeney	-9.5	5.8 ± 2.9	1.4 ± 2.6
Palo	Sweeney	-4.8	4.5 ± 2.1	1.6 ± 2.1
p.e.	Sweeney	4.6	-0.5 ± 2.3	1.8 ± 2.3
s.l.b	Sweeney	25.2	-10.2 ± 2.1	6.0 ± 2.1
e.b.	Sweeney	28.8	-12.7 ± 2.1	4.1 ± 2.1
Castro	Sweeney	36.2	-19.3 ± 2.1	-3.5 ± 2.0
Rock	Sweeney	41.8	-20.3 ± 3.0	-1.4 ± 2.9
Xyz	Sweeney	48.9	-18.7 ± 3.7	-5.8 ± 3.5
Diablo	Sweeney	56.6	-26.7 ± 2.8	-0.4 ± 2.6
Jobe	Sweeney	68.0	-26.3 ± 2.8	0.8 ± 2.6
Minn	Sweeney	75.2	-33.2 ± 2.8	-4.6 ± 2.7

† Uncertainties are 1σ

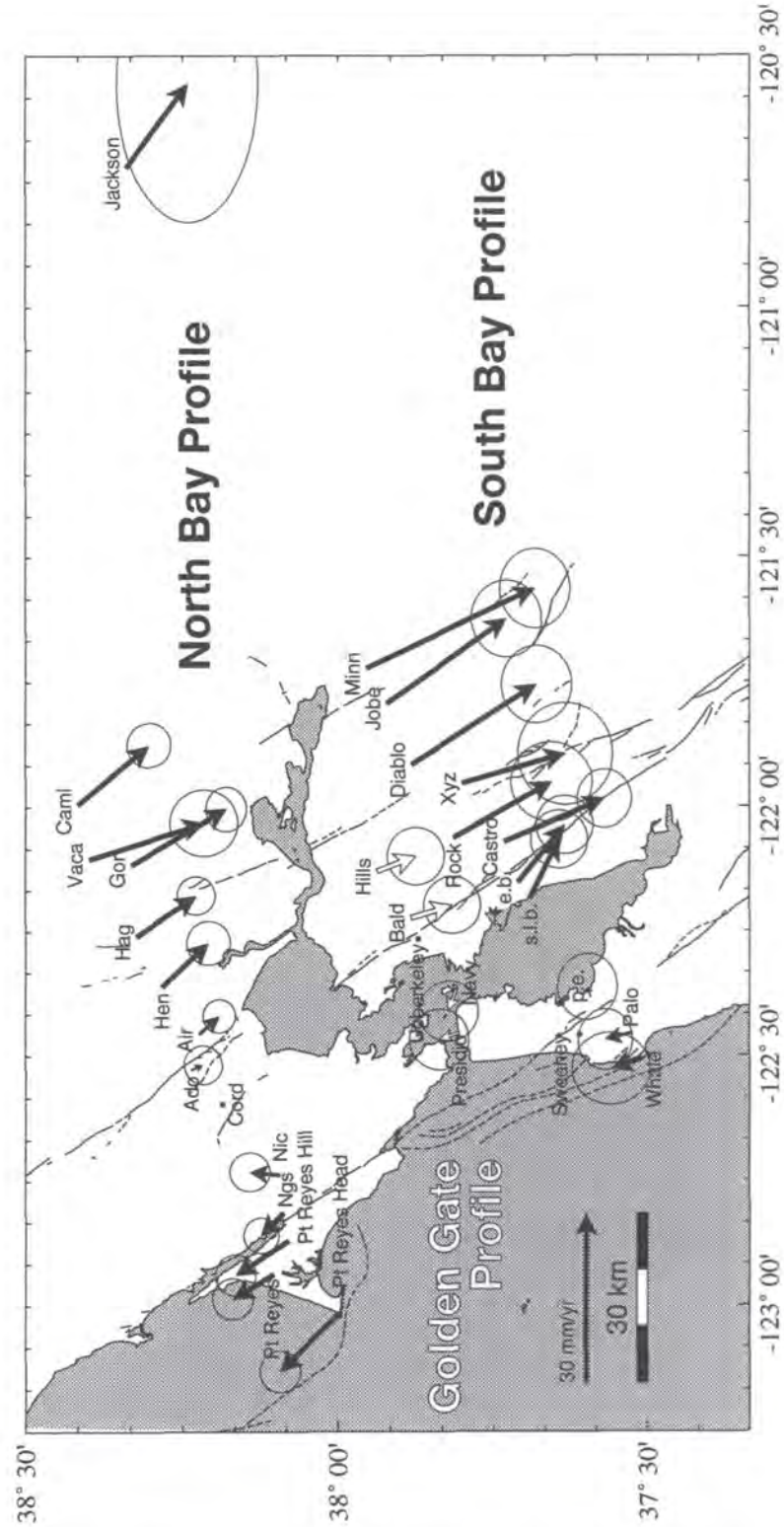

Figure 4.6: Horizontal relative velocities for the North Bay, Golden Gate and Central Bay profiles. 95% confidence ellipses ($\sim 2.45\sigma$) are shown.

(Table 4.4) are significantly different from a null velocity at the 95% confidence level. Station positions are directly measured with GPS, and the fault-normal velocities are thus not dependent on any arbitrary assumptions about network rotations. This contrasts with trilateration surveying which was used prior to GPS. Trilateration velocities are ambiguous because the network lacks a tie to an external reference frame and, as a result, rigid-body motions (translations and rotations) of the network as a whole are not determined. Strain analysis of the 1973-1989 trilateration data from the bay region, which is independent of reference frame, also indicates no regional contraction across the fault, and the GPS results confirm this finding.

4.3.3.2 Fault-Parallel Velocities

Fault-parallel velocity profiles in a region of shear-strain accumulation are expected to exhibit some form of sigmoidal shape (i.e. flattening of the velocity gradient at both ends of the profile) [*Savage*, 1990]. The fault-parallel (N33°W) velocities in general vary linearly along the profiles (Figures 4.7a, 4.8a and 4.9a). In the North Bay (Figure 4.7a) the velocities are adequately described by a straight line with a gradient of -0.33 $\pm$ 0.04 μstrain yr^{-1}. Only three stations differ from this straight line at the 2σ level. These are Point Reyes Hill, Gor and Jackson. The residual at Gor is almost significant at the 3σ level. The residual at Jackson however is significant at the 5σ level. This either indicates that the velocity of Jackson is incorrect or that the velocity gradient decreases to the east of the Green Valley fault. The NUVEL-1A-predicted North American-Pacific relative plate motion is 46 mm/yr. The relative motion between Point Reyes Head and Jackson predicted by the straight line would be 63 mm/yr, 17 mm/yr greater than the expected deformation across the width of this plate boundary zone. Therefore it seems likely that the velocity gradient does decrease to the east of the Green Valley fault. The persistence of significant motion right to the western edge of the profile suggests that additional motion is being accommodated west of Point Reyes Head. A maximum of 36 $\pm$ 3 mm/yr of fault-parallel relative motion across the North Bay profile is observed, which is not significantly different than the 31 $\pm$ 3 mm/yr reported for the trilateration network by *Lisowski et al.* [1991].

The Golden Gate profile (Figure 4.8a) crosses only a small portion of the San Andreas fault system, the Hayward fault. A total of 11 $\pm$ 3 mm/yr of shear is detected and the best-fit straight line has a gradient of -0.37 $\pm$ 0.17 μstrain yr^{-1}.

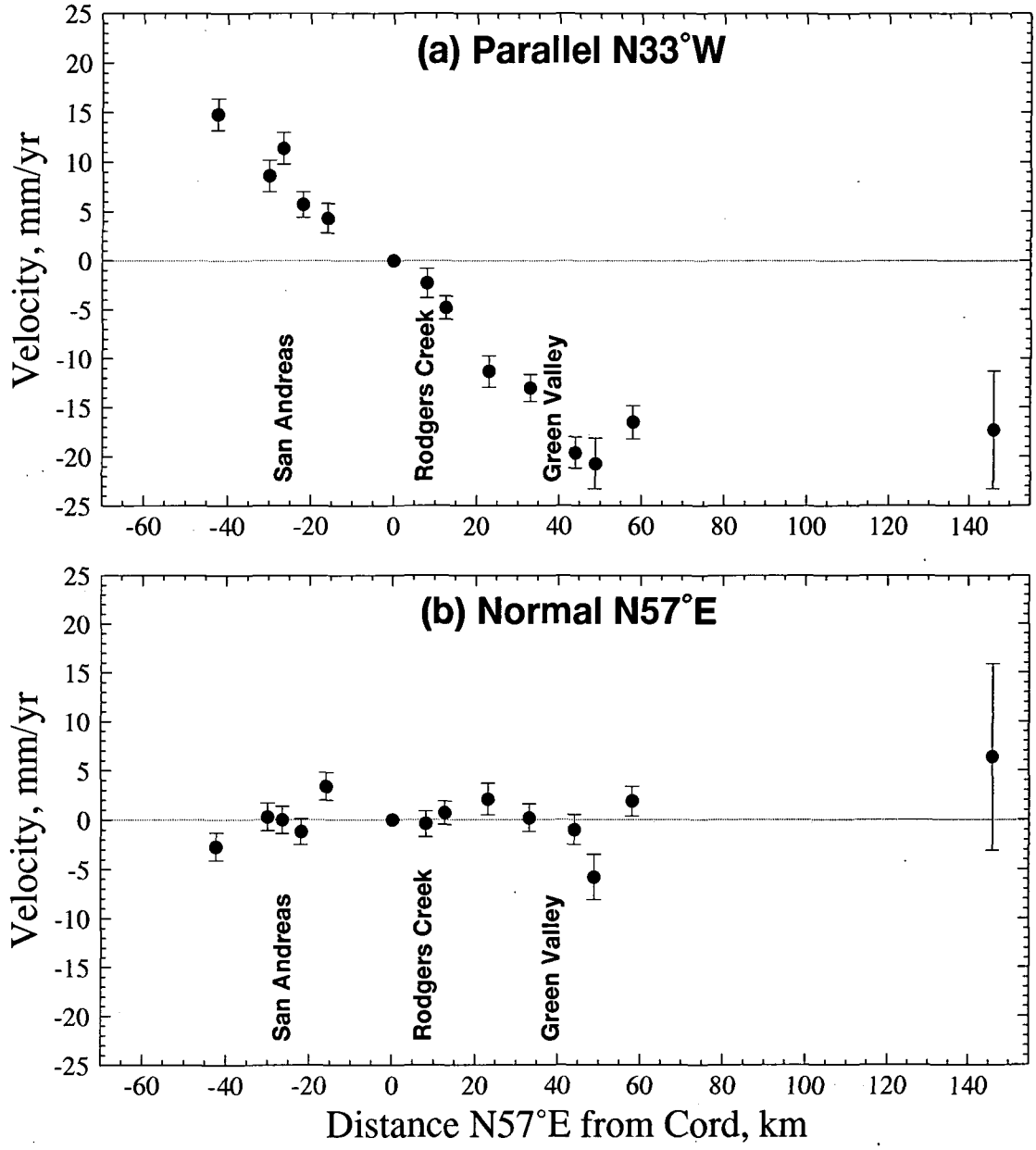

Figure 4.7: Station velocities for the North Bay profile relative to Cord resolved into components (a) parallel and (b) normal to the local trend (N33°W) of the San Andreas fault and plotted as a function of distance from the fault. Error bars represent one standard deviation (1σ).

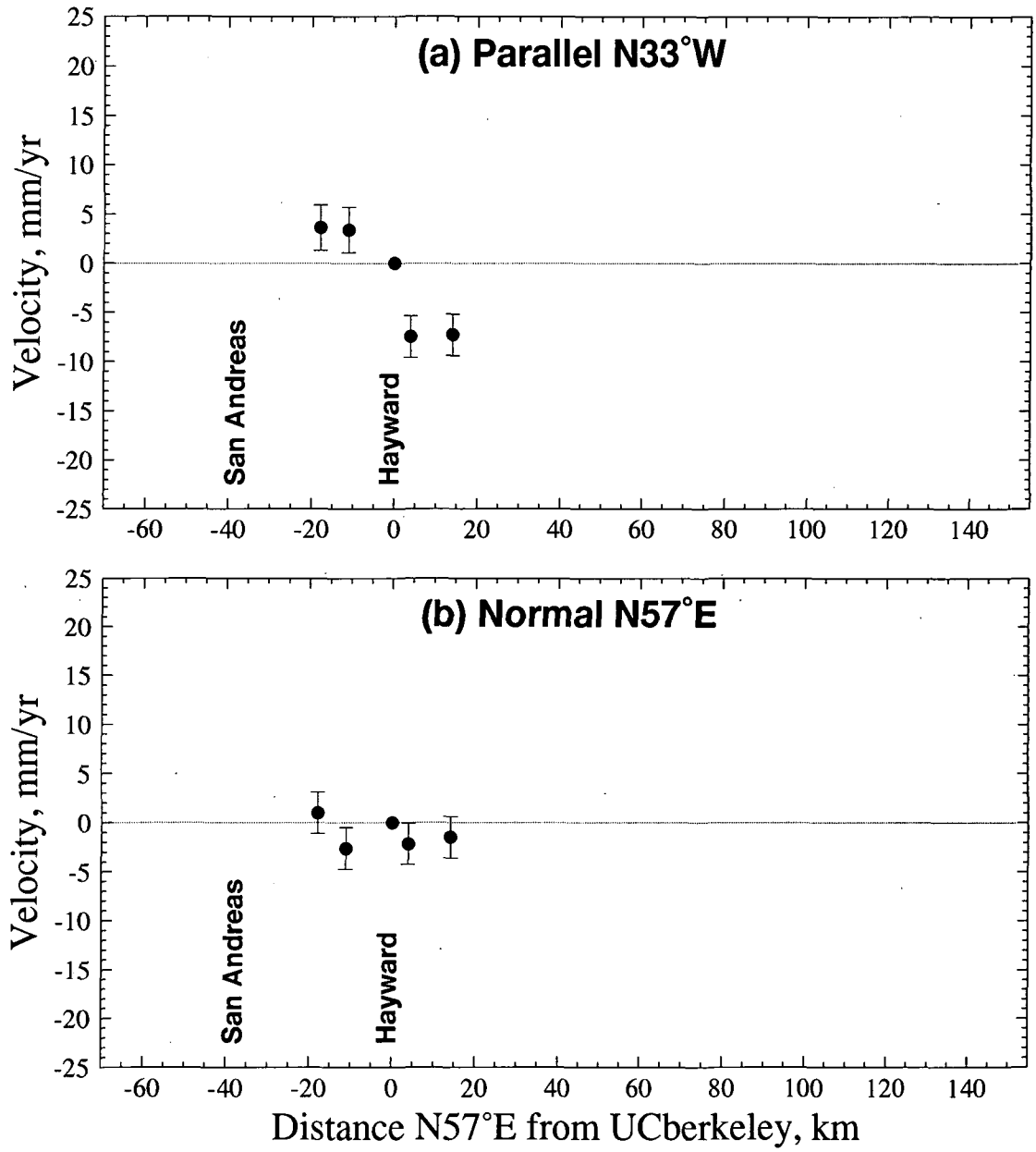

Figure 4.8: Station velocities for the Golden Gate profile relative to Ucberkeley resolved into components (a) parallel and (b) normal to the local trend (N33°W) of the San Andreas fault and plotted as a function of distance from the fault. Error bars represent one standard deviation (1σ).

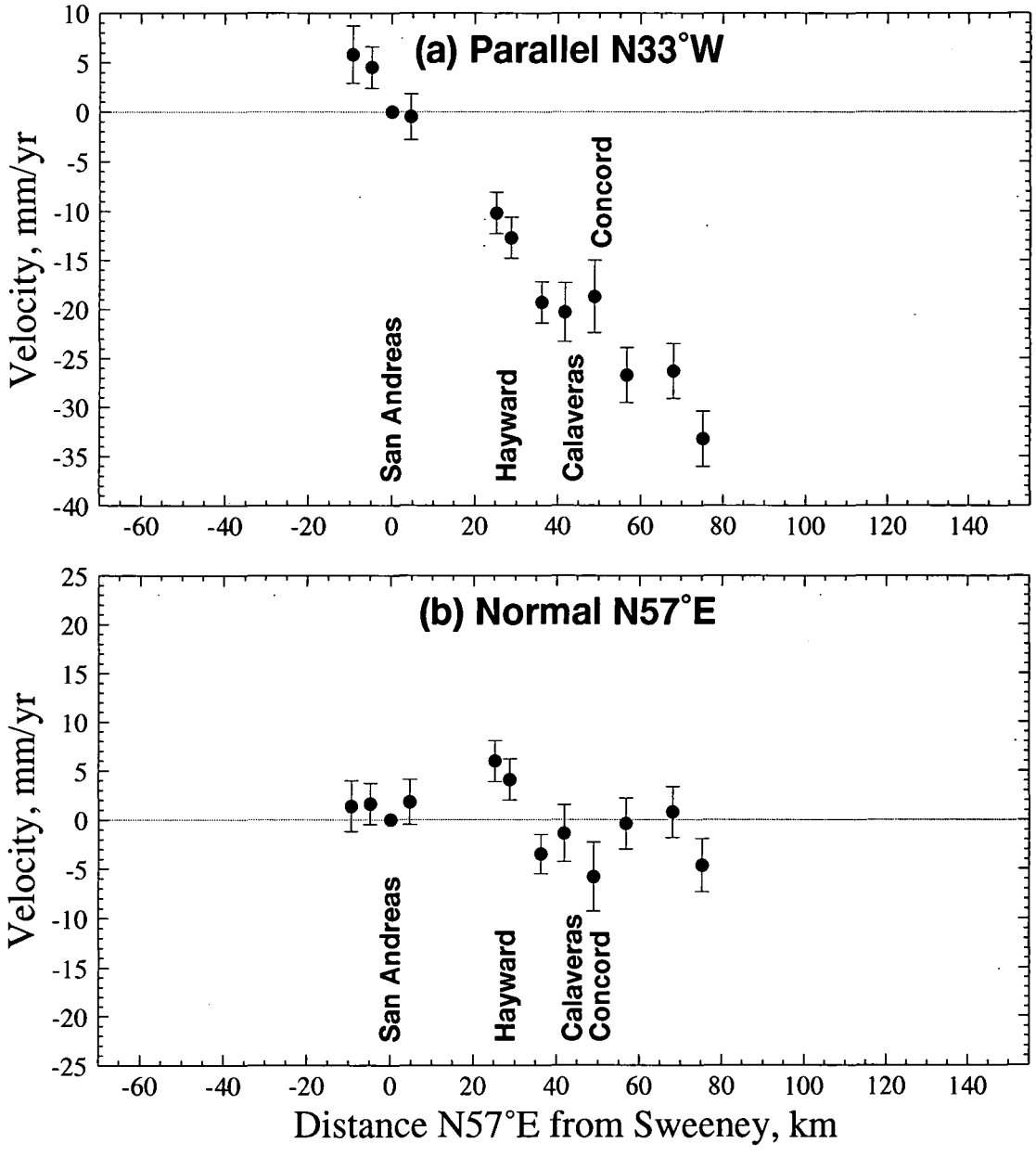

Figure 4.9: Station velocities for the Central Bay profile relative to Sweeney resolved into components (a) parallel and (b) normal to the local trend (N33°W) of the San Andreas fault and plotted as a function of distance from the fault. Error bars represent one standard deviation (1σ).

However the velocity profile appears to be better described as a linear, right-lateral step offset across the Hayward fault with near-zero velocity gradients on either side.

In the Central Bay profile (Figure 4.9a) the velocities appear to vary linearly with distance with a gradient of -0.44 $\pm$ 0.02 μstrain yr^{-1}. This gradient is significantly greater than that of the North Bay profile. No decrease in the velocity gradient is apparent either to the west of the San Andreas fault or east of the Concord-Calaveras fault. A maximum of 39 $\pm$ 4 mm/yr of right lateral shear is detected on the Central Bay profile, which is consistent with the 35 $\pm$ 3 mm/yr estimated by *Lisowski and Savage* [1992] mainly from trilateration data.

4.3.3.3 Vertical Velocities

The relative vertical velocities for all three profiles are shown in Figure 4.10. Only one station, Jackson, has a relative velocity significant at greater than the 2σ level. However, the calculated velocity of Jackson relative to Cord, -120 $\pm$ 22 mm/yr, appears to be too large to be explained by tectonic deformation. Simple explanations for the large velocity determined may be an incorrect measurement of the antenna height during one survey or some error during processing. Although the velocities are insignificant, there does seem to be a positive correlation between those stations that show relative uplift and the highs in topography. Measured rates of uplift in the Coast Ranges around San Francisco bay are about 0.2 to 0.4 mm/yr [*Brown*, 1990].

4.4 Summary

The data from 16 independent GPS surveys distributed between 3 profiles over a time span of around 2.8 years have been processed and analysed in order to measure crustal deformation rates in the San Francisco bay region. In order to interpret the results meaningfully the short-term precision and long-term repeatability were assessed. The short-term horizontal precision is about 1-2 mm in both horizontal components. The vertical short-term precision of about 8-10 mm is almost an order of magnitude worse than the horizontal components. Long-term horizontal repeatability has a constant bias of 4 mm, with a length dependence of $2.2 \times 10^{-8} l$ for the north-south and $3.5 \times 10^{-8} l$ for the east-west components. The vertical

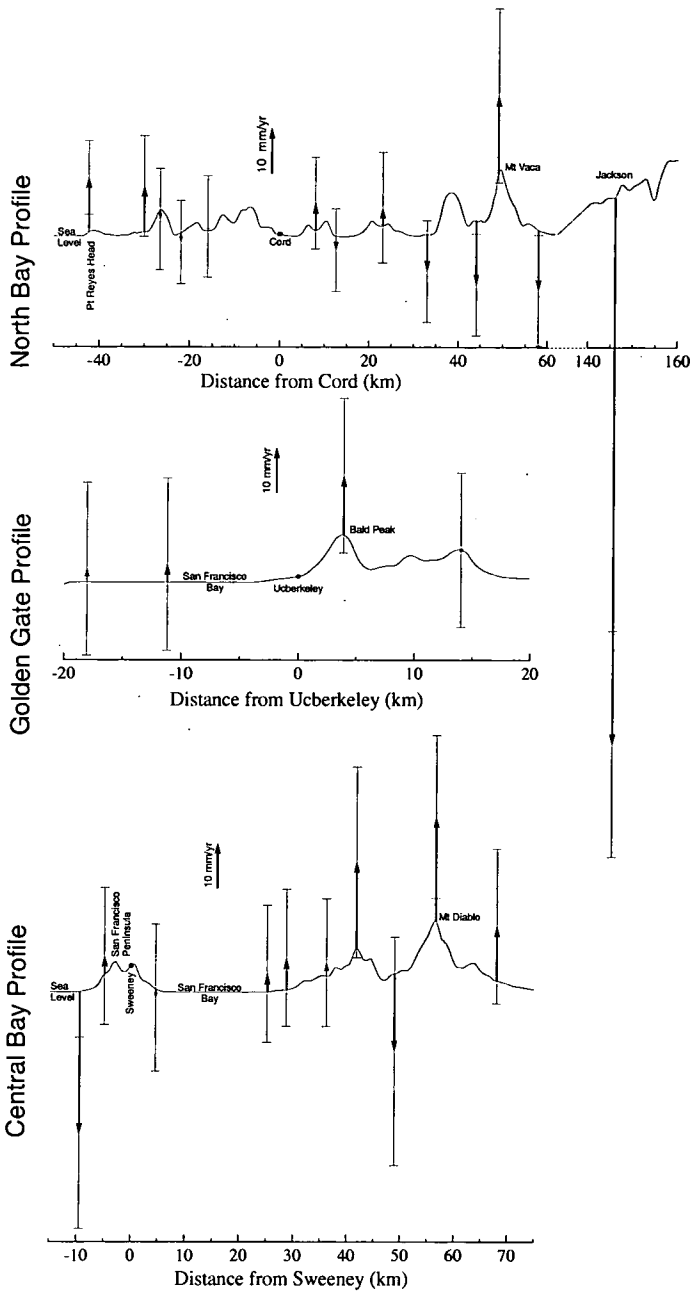

Figure 4.10: Vertical relative station velocities for the North Bay, Golden Gate and Central Bay profiles relative to their respective fixed sites plotted along a line trending N57°E. Sinuous line represents generalised surface topography between the adjacent stations projected onto the line of the profile.

measurements are much less repeatable than the horizontal measurements and are 28 mm + $20 \times 10^{-8} l$ (assuming variation about a mean instead of about a best fitting line).

GPS measurements in the bay region are of sufficient accuracy, in the horizontal components, to detect crustal deformation within a time span of less than 3 years. Velocities parallel to the trend of the San Andreas fault vary linearly along the profiles. The maximum, relative, right-lateral shear rates are 33 $\pm$ 2 mm/yr for the North Bay profile, 11 ± 3 mm/yr for the Golden Gate profile and 35 ± 3 mm/yr for the Central Bay profile. No significant convergence upon the fault is detected in any of the profiles. Apart from station Jackson, which is well outside the bay region the vertical velocities are not significant at the 2σ level.

Chapter 5

Integration of Trilateration, VLBI and GPS Results

5.1 Introduction

The three GPS San Francisco bay region profiles, comprising 31 stations, provide an accurate description of the deformation field around the San Andreas fault system in the San Francisco bay region. However, these data represent only a portion of the total available geodetic information. Data from a century of triangulation, more than two decades of precise trilateration and other space geodetic techniques such as VLBI and SLR are available. Combining all the best geodetic information into one velocity solution provides the best possible picture of the spatial distribution of deformation in the region. In the San Francisco and Monterey bay region, measurements from three geodetic techniques, trilateration GPS and VLBI, are used to calculate the full velocity field (Figure 5.1).

5.2 Method

5.2.1 Introduction

All station velocities estimated from geodetic data are arbitrary to some extent such that any additional motion generated by a rigid translation or rotation of the network cannot be detected. This ambiguity must also be resolved when combining the three different geodetic data sets. The translational ambiguity, which is often removed by either constraining the centre of mass of the network to zero velocity, fixing a station to zero velocity or minimising the velocities of a set of stations

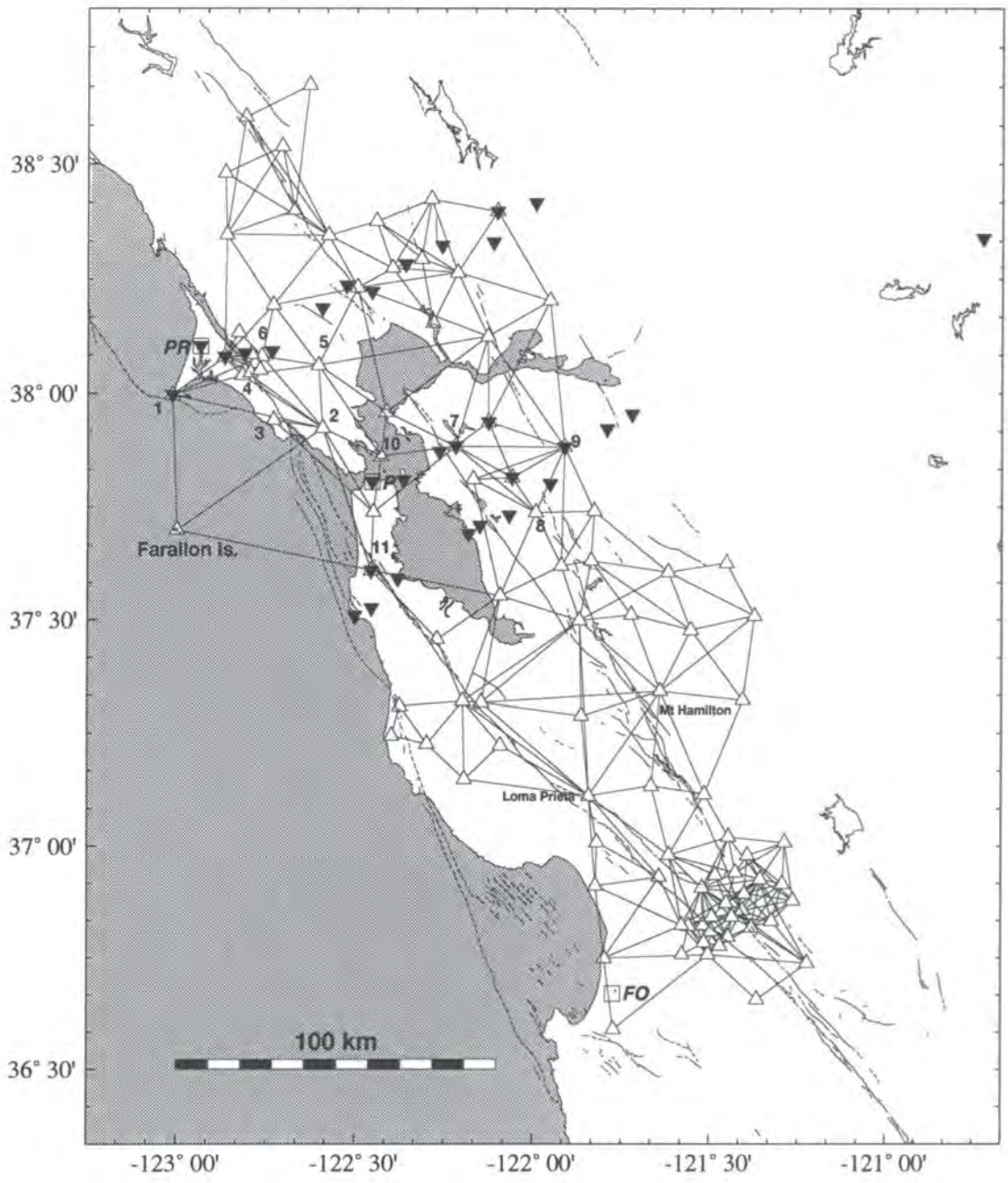

Figure 5.1: Trilateration, GPS and VLBI points in the San Francisco and Monterey bay regions. Trilateration networks are shown by open triangles. The lines connecting stations indicate actual line lengths measured. Inverted solid triangles indicate GPS stations. VLBI stations are shown by open squares (FO, Fort Ord; P, Presidio; and PR, Point Reyes). Numbers 1-11 identify trilateration stations referred to in Figure 5.2.

assumed to move together, is not a serious problem for local crustal deformation studies where only motion within the network is required. The most convenient approach when studying relative motion between the Pacific and North American plates is to hold the interior of one of these plates fixed.

The rotational ambiguity, especially in regions of simple shear, is more problematical since simple shear may be an artefact of a wrong rotational constraint. The VLBI data, since it is used to define a precise terrestrial reference frame, is ideally suited to constrain both the translational and rotational ambiguities. VLBI stations, are deployed, albeit sparsely, across North America and the Pacific margin and can therefore provide precise velocities relative to a fixed plate interior by minimising the velocities of stations in the interior of that plate. Fixing a reference plate also provides a rotational constraint. Since a terrestrial reference frame is usually defined by a set of station coordinates and velocities [*Murray*, 1991] then the VLBI "global frame" station velocities can be chosen as an external reference frame for the GPS and trilateration data provided there are common stations.

The three data sets are combined here by using the VLBI data to establish a global reference frame to which the GPS and trilateration data are tied. The changes in line length of trilateration data, the Cartesian station velocities from GPS derived in the Chapter 4 and the station velocities from VLBI, $\mathbf{d}$ are related to the "global frame" station velocities $\mathbf{u}$ by

$$\mathbf{d} = \mathbf{G}\mathbf{u} + \epsilon, \tag{5.1}$$

where $\mathbf{G}$ is a matrix of linear trigonometric functions defined below for various geodetic data types and ϵ is the positive definite measurement error matrix with zero mean. Obtaining relative site velocities is therefore a discrete inverse problem where equation (5.1) is in explicit linear form [*Menke*, 1984]. Inverting equation (5.1) is achieved using least-squares solutions since they are easy to compute and because they provide the maximum likelihood solution when the measurement errors ϵ are normally distributed [*Segall and Mathews*, 1988].

Out of 122 stations there are a total of 10 common stations (Figure 5.1), that is, stations that have been surveyed by more than one technique. The trilateration network and the Central Bay GPS profile have no common sites with the VLBI data. However, since all three GPS profiles have common stations with the trilateration network, the North Bay and Golden Gate profiles provide a tie between the trilateration and VLBI, which subsequently provides a tie to the Central Bay profile. One VLBI site, Fort Ord (FO in Figure 5.1), is not part of a GPS profile

or the trilateration network. This is not a problem however since the trilateration sites are tied to the VLBI velocities via the ties further north. However, since the ties to the VLBI sites are in the north of the region, errors may accumulate in the network which may distort the displacement pattern. Therefore, the closest station to Fort Ord, is assumed to have the same "global frame" station velocity as Fort Ord. As a result the velocity solution may be slightly biased since the velocities should vary with distance from the fault and the closest trilateration station is approximately 5 km further from the San Andreas fault than Fort Ord.

5.2.2 Trilateration Data and Observation Equations

Since the early 1970's the USGS repeatedly surveyed trilateration networks in central California until the mid 1980's when the use of GPS began. This study uses the same trilateration data used by *Lisowski et al.* [1991] to calculate solutions for the San Francisco bay and Monterey bay regions. The network comprises 98 stations and 300 lines, and the data set contains 2587 line-length measurements recorded mainly during the period 1973 - 1989 (Figure 5.1).

Let $L(a^1, a^2)$ be the length of the line connecting stations a^1 and a^2, i.e.,

$$L(a^1, a^2) = [(x^2 - x^1)^2 + (y^2 - y^1)^2 + (z^2 - z^1)^2]^{1/2}, \tag{5.2}$$

where x, y and z are the station coordinates in the east, north and up directions respectively. The change in line length, $\delta L(a^1, a^2) = L(a^1 + \delta a^1, a^2 + \delta a^2) - L(a^1, a^2)$ can be approximated by taking the first two terms in the Taylor series expansion of $L(a^1 + \delta a^1, a^2 + \delta a^2)$, as long as the line length is large compared with the change in length. This gives

$$\delta L(a^1, a^2) = \frac{1}{L}[(x^2 - x^1)(u_x^2 - u_x^1) + (y^2 - y^1)(u_y^2 - u_y^1) + (z^2 - z^1)(u_z^2 - u_z^1)]. \tag{5.3}$$

In most cases the elevation difference between stations is small relative to the horizontal distances. If the vertical displacements are also small, the third term can be neglected. To obtain station velocities instead of displacements one can simply substitute for the appropriate terms by the corresponding time-dependent variables such that

$$\delta L(t)(a^1, a^2) = \frac{1}{L'}[(x'^2 - x'^1)(v_x^2 - v_x^1) + (y'^2 - y'^1)(v_y^2 - v_y^1)], \tag{5.4}$$

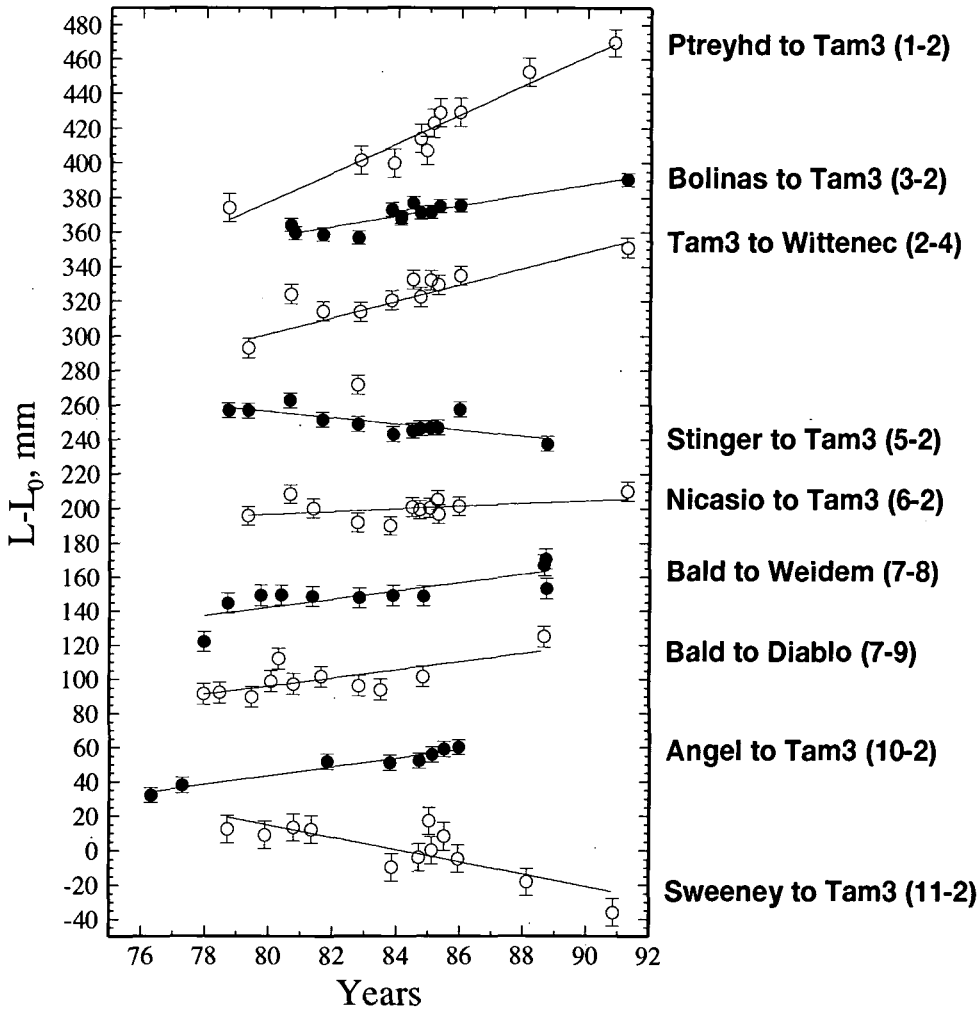

Figure 5.2: Line length L minus a nominal constant L_0 as a function of time for several lines in the north-bay trilateration network. The error bars represent one standard deviation on either side of the plotted point. The straight lines indicate least-squares linear fits to the data. Numbers beside station names are used to identify their positions in Figure 5.1.

where $\delta L(t)$ is the rate of change in line length, L' is the mean line length, $(x'^2 - x'^1)$ and $(y'^2 - y'^1)$ are the mean line length components and $(v_x^2 - v_x^1)$ and $(v_y^2 - v_y^1)$ are the relative velocity components.

For a network of N lines connecting M stations equation (5.1) will be of the form

$$\begin{bmatrix} \delta L_1(t) \\ \vdots \\ \delta L_j(t) \\ \vdots \\ \delta L_N(t) \end{bmatrix} = \begin{bmatrix} -\sin\theta_1 & -\cos\theta_1 & & \\ \vdots & \vdots & \ddots & \\ 0 & 0 & \cdots -\sin\theta_1 & -\cos\theta_1 \; 0 \cdots \sin\theta_j \; \cos\theta_j \cdots \\ \vdots & \vdots & & \end{bmatrix} \begin{bmatrix} u_x^1 \\ u_y^1 \\ \vdots \\ u_x^k \\ u_y^k \\ \vdots \\ u_x^M \\ u_y^M \end{bmatrix}, \quad (5.5)$$

where θ is the line orientation measured clockwise from the y axis and u_x^k and u_y^k are the M "global frame" velocities. The line rate changes (left hand side of equation 5.5) in **d** are obtained by least-squares linear fits to the distance versus time plots for each line and examples of some plots are given in Figure 5.2. If the time series exhibits a clear coseismic step offset, the secular rate of change is estimated from a linear fit to either the pre-seismic or post-seismic observations together with a step offset at the time of the earthquake.

5.2.3 GPS Data and Observation Equations

The three GPS profiles, consisting of a total of 31 stations, described in Chapters 3 and 4 were used. The relative velocity components, calculated in Chapter 4, are used as input into the inversion. For a network of M stations and M-1 independent relative vectors equation (5.1) will take the form

$$\begin{bmatrix} v_x^1 \\ v_y^1 \\ \vdots \\ v_x^j \\ v_y^j \\ \vdots \\ v_x^{M-1} \\ v_y^{M-1} \end{bmatrix} = \begin{bmatrix} -1 & -1 & & & & & & & \\ \vdots & \vdots & \ddots & & & & & & \\ 0 & 0 & \cdots & 1 & 1 & \cdots & -1 & -1 & \cdots \\ \vdots & \vdots & & & & & & & \end{bmatrix} \begin{bmatrix} u_x^1 \\ u_y^1 \\ \vdots \\ u_x^k \\ u_y^k \\ \vdots \\ u_x^M \\ u_y^M \end{bmatrix}, \quad (5.6)$$

where v_x^j and v_y^j are the $M-1$ relative velocity components and u_x^k and u_y^k are the M "global frame" velocities.

5.2.4 VLBI Data and Observation Equations

Three sites in the San Francisco bay region have been measured using VLBI by the NASA Crustal Dynamics Project [*Clark et al.*, 1987]. These VLBI stations are located at Point Reyes, Presidio and Fort Ord (Figure 5.1). The velocities of these and other VLBI stations measured relative to the stable interior of the North American plate were calculated by *Ward* [1990]. The velocities were calculated by reducing the line length velocities parallel to the line azimuth and line transverse velocities normal to the line azimuth from the GLB511 solution to a set of vector site velocities. The transverse velocities are tied to the Polaris - IRIS Earth orientation series [*Robertson and Carter*, 1985] derived using the assumption that the azimuth from Westford, Massachusetts to Richmond, Florida is fixed. The transverse velocities are therefore uncertain within a rigid body rotation of the whole network and hence a rotation can be subtracted from all the velocities without violating the VLBI observations. *Ward* [1990] removed the rigid body rotation of the network when calculating the site velocities by minimising the velocities of six interior North American stations. This is equivalent to the "stationary station" solution of *Gu and Prescott* [1986] and the "special station" solution of *Segall and Mathews* [1988]. These calculated velocities, relative to the (assumed) stable North American interior, are shown as arrows in Figure 2.9 and listed in Table 5.1. In this case equation (5.1) for M sites becomes

$$\begin{bmatrix} v_x^1 \\ v_y^1 \\ \vdots \\ v_x^j \\ v_y^j \\ \vdots \\ v_x^M \\ v_y^M \end{bmatrix} = \mathbf{I} \begin{bmatrix} u_x^1 \\ u_y^1 \\ \vdots \\ u_x^j \\ u_y^j \\ \vdots \\ u_x^M \\ u_y^M \end{bmatrix}, \tag{5.7}$$

where $\mathbf{I}$ is the Identity matrix, i.e., $v_x^j = u_x^j$ and $v_y^j = u_y^j$.

5.2.5 Is the Velocity Field Constant Over Time?

A fundamental assumption underlies the modelling done in this thesis. This assumption is that the *elastic strain rate between major earthquakes is constant.* This

Table 5.1: Velocities of VLBI Stations Relative to the North American interior from *Ward* [1990]

VLBI Station	Longitude	Latitude	North Velocity mm/yr	East Velocity mm/yr
Fairbanks, Alaska	-147.49	64.98	-2.4 ± 0.7	-1.0 ± 0.7
Hatcreek, California	-121.47	40.82	5.7 ± 0.4	-6.3 ± 0.4
Kashima, Japan	-219.33	35.95	2.4 ± 1.3	-2.7 ± 1.2
Kauai, Hawaii	-159.67	22.13	55.5 ± 1.0	-53.6 ± 0.9
Kwajalein, Marshall Islands	-192.52	9.40	45.3 ± 1.8	-60.9 ± 1.7
Mojave, California	-116.89	35.33	8.5 ± 0.4	-3.0 ± 0.3
Vandenberg, California	-120.62	34.56	37.5 ± 0.4	-30.1 ± 0.4
Black Butte, California	-115.72	33.66	4.0 ± 1.1	-6.4 ± 0.9
Deadman Lake, California	-116.28	34.25	10.7 ± 2.9	-4.8 ± 2.8
Ely, Nevada	-114.84	39.29	1.4 ± 1.1	-2.7 ± 1.0
Flagstaff, Arizona	-111.63	35.21	-3.4 ± 1.1	-2.3 ± 1.1
Fort Davis, Texas	-103.95	30.64	1.3 ± 0.5	0.0 ± 0.3
Fort Ord, California	-121.77	36.67	39.7 ± 1.1	-26.0 ± 0.6
JPL, California	-118.17	34.21	26.1 ± 0.7	-23.1 ± 0.6
Mammoth Lakes, California	-118.94	37.64	7.8 ± 1.8	-12.3 ± 1.5
Monument Peak, California	-116.42	32.89	26.5 ± 0.7	-31.0 ± 0.6
Owens Valley, California	-118.29	37.23	9.3 ± 0.4	-4.7 ± 0.3
Pearblossom, California	-117.92	34.51	20.6 ± 0.6	-17.0 ± 0.7
Pinyon Flat, California	-116.46	33.61	18.1 ± 0.8	-17.9 ± 0.7
Platteville, Colorado	-104.73	40.18	-0.9 ± 0.6	0.4 ± 0.7
Point Reyes, California	-122.94	38.10	34.6 ± 1.0	-22.7 ± 0.7
Presidio, California	-122.45	37.81	26.1 ± 0.9	-21.3 ± 1.0
Palos Verdes, California	-118.40	33.74	28.1 ± 1.5	-26.4 ± 1.4
Quincy, California	-120.94	39.98	7.2 ± 0.8	-8.8 ± 0.9
Santa Paula , California	-119.00	34.39	22.1 ± 1.3	-31.0 ± 1.9
Westford, Massachusetts	-71.49	42.61	-3.6 ± 0.9	1.1 ± 0.5
Yuma, Arizona	-114.20	32.94	2.0 ± 0.8	-0.8 ± 0.7

Quoted uncertainties are one standard deviation

assumption is implicit in fitting straight lines to the changes in line length with time determined using the three data types separately. The same assumption must also be made if the combination of the results is treated in the same way. However, the three data sets were not determined during the same time interval. Long-term variations in deformation rate may occur as a result of post-seismic viscoelastic transients that follow major earthquakes. The largest and most readily-discernible transients are of relatively short duration, a few years or less [*Okada and Nagata*, 1953; *Savage et al.*, 1994].

A number of earthquakes have occurred in the San Francisco bay region during the time period spanned by the data. Previous studies suggest that geodetic strain accompanying earthquakes is undetectable at the levels of accuracy relevant here for magnitudes of around 5.0 or less [*Savage and Kinoshita*, 1971, *Savage and Prescott*, 1978b]. The only events substantially larger than this in the San Francisco bay region during the monitoring period were the 1979 Coyote Lake (M_s=5.7), the 1984 Morgan Hill (M_s=6.1) and the 1989 Loma Prieta (M_s=7.1) events. Figure 5.3 shows the timing of these earthquakes with respect to the observation intervals of the three data types used in the velocity solution. The epicentres of those events are show in Figure 5.4.

The Coyote Lake earthquake affects only the trilateration data to the south of the region [*King et al.*, 1981] (Figure 5.3). A model for the coseismic deformation predicted displacements in excess of 20 mm for only four stations. No pre-seismic anomalies were detected. Post-seismic changes produced detectable changes in three lines. However for two of those lines the post-earthquake observations had a negligible effect on the overall rate calculated. The third line, although seemingly affected by afterslip, had few observations, with large uncertainties, and the afterslip again had little affect on the overall rate.

The Morgan Hill earthquake produced coseismic offsets on many lines in the Mt. Hamilton area. The geodolite line Loma Prieta to Hamilton, which crosses the Morgan Hill rupture zone, was part of a network which had been monitored roughly monthly since August 1981. Approximately 40 mm of coseismic offset on that line can be attributed to the Morgan Hill earthquake [Figure 3, *Lisowski et al.*, 1990b; *Bakun et al.*, 1984]. However, no pre-seismic or post-seismic changes in rate affected the long term averaged rate.

The most recent earthquake, the 1989 Loma Prieta event, was the largest on the San Andreas fault since 1906. It provided an opportunity to measure how deformation

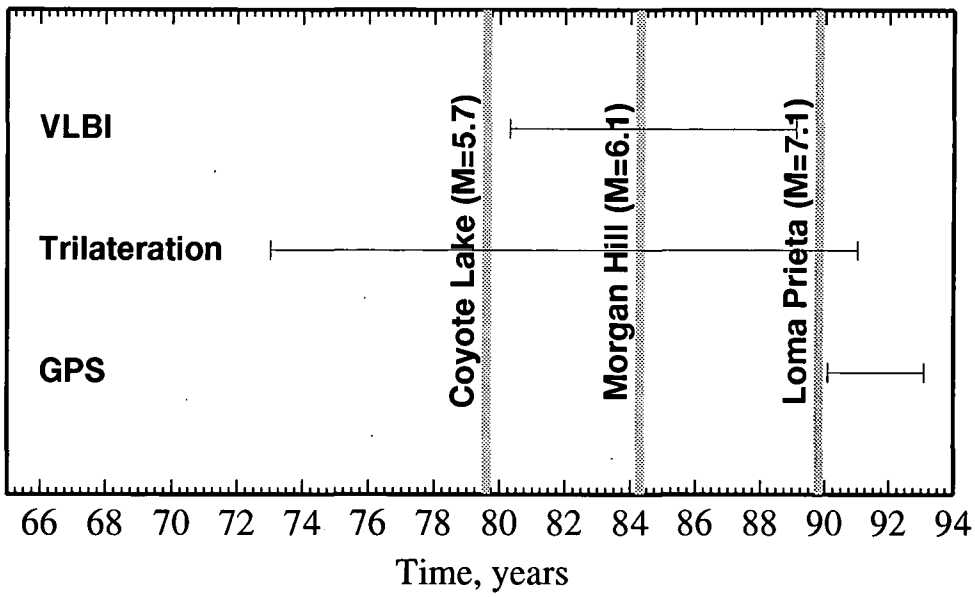

Figure 5.3: Timing of the three major earthquakes in the San Francisco bay region compared with the observation time intervals of the geodetic data.

is distributed in space and time around a large earthquake. GPS, VLBI and trilateration data were used to determine a fault rupture model that accounts for the measured offsets [*Lisowski et al.*, 1990a]. Geodetic data measured at frequent intervals prior to the earthquake were used to seek precursors to the event [*Lisowski et al.*, 1990b]. Anomalous changes in rate for two of three frequently measured lines near Loma Prieta preceded the earthquake. However, the rate for the third line and the only one to cross the imminent rupture zone showed no anomalous changes, bringing the possibility of a regional strain precursor into question. GPS data recorded since 1989 were used to study the effects of post-seismic transients [*Savage et al.*, 1994]. Anomalies were only detectable in the fault-normal surface displacements for a profile crossing the projected surface plane of the coseismic rupture. The fault normal components of the nearest GPS profile in this survey, the Central Bay profile, show no significant affect (Figure 4.5). The Loma Prieta earthquake therefore has no detectable effect on the GPS results used in this thesis.

The geodetic observations thus suggest that a steady, linear strain rate can be assumed to dominate the deformation rates seen in the data. Theoretical considerations support this. For time periods that are short in comparison with the relaxation time of any viscous elements present in the system, the velocity field can be thought of as stationary, that is, independent of time [*Prescott and Yu*, 1986]. *Thatcher* [1983] calculated that peak strain rates (measured close to the fault), during the time interval of the geodetic measurements, would decline by only around

0.04 μstrain/yr per decade. Average strain rates (calculated over the whole region) would be expected to have even smaller changes in strain rate. However, *Thatcher* [1983] suggests that temporal declines in the deformation rate persist for decades following major earthquakes and because of this, no short term geodetic observations will, except by happenstance, reflect the long-term average over many earthquake cycles shown by geological data. Early in the cycle the rate will be higher than average, and later lower. Therefore, although elastic strain build-up measured over short time intervals may be assumed to be constant, fault slip rates determined by inversion of such data may reflect the behaviour of the fault segments at a particular time in their earthquake cycles rather than any average, long-term rate.

5.3 Results

5.3.1 The Velocity Field

The velocity field produced by combining GPS, trilateration and VLBI data in the San Francisco and Monterey bay regions relative to the "stable" North American plate interior is shown in Figure 5.4 and appendix B. The fit of the velocity solution to the data is indicated by the reduced χ^2 fit of 1.4. The dominant feature in the velocity field is the consistent northwesterly movement over the whole region coupled with an increase in amplitude of the motion from east to west. Indeed, at this scale, it is difficult to discern any other features. Stations west of the San Andreas and San Gregorio faults show velocities consistent with the rescaled NUVEL-1 Pacific-North American relative plate velocity [*De Mets et al.*, 1990]. However, the easternmost stations exhibit velocities that are inconsistent with being in the stable interior of the North American plate. The discrepancy, between those points and those in the stable interior is termed the "San Andreas Discrepancy" [*Argus and Gordon*, 1991] and can be attributed mainly to motion across the Great Basin (Section 1.1.5). The motion across the Great Basin at this latitude may be approximated by the 10.0 ± 0.5 mm/yr N38°W velocity of the VLBI station OVRO (Figure 2.9) [*Dixon et al.*, 1993, Table 3], located 300 km east of the San Andreas fault in Owens Valley. Station OVRO is within a tectonically active zone east of the Sierra Nevada Mountains (Figure 1.5) and its velocity is likely 1-2 mm/yr lower than points in the Sierra Nevada Mountains [*Argus and Gordon*, 1991]. In order to obtain

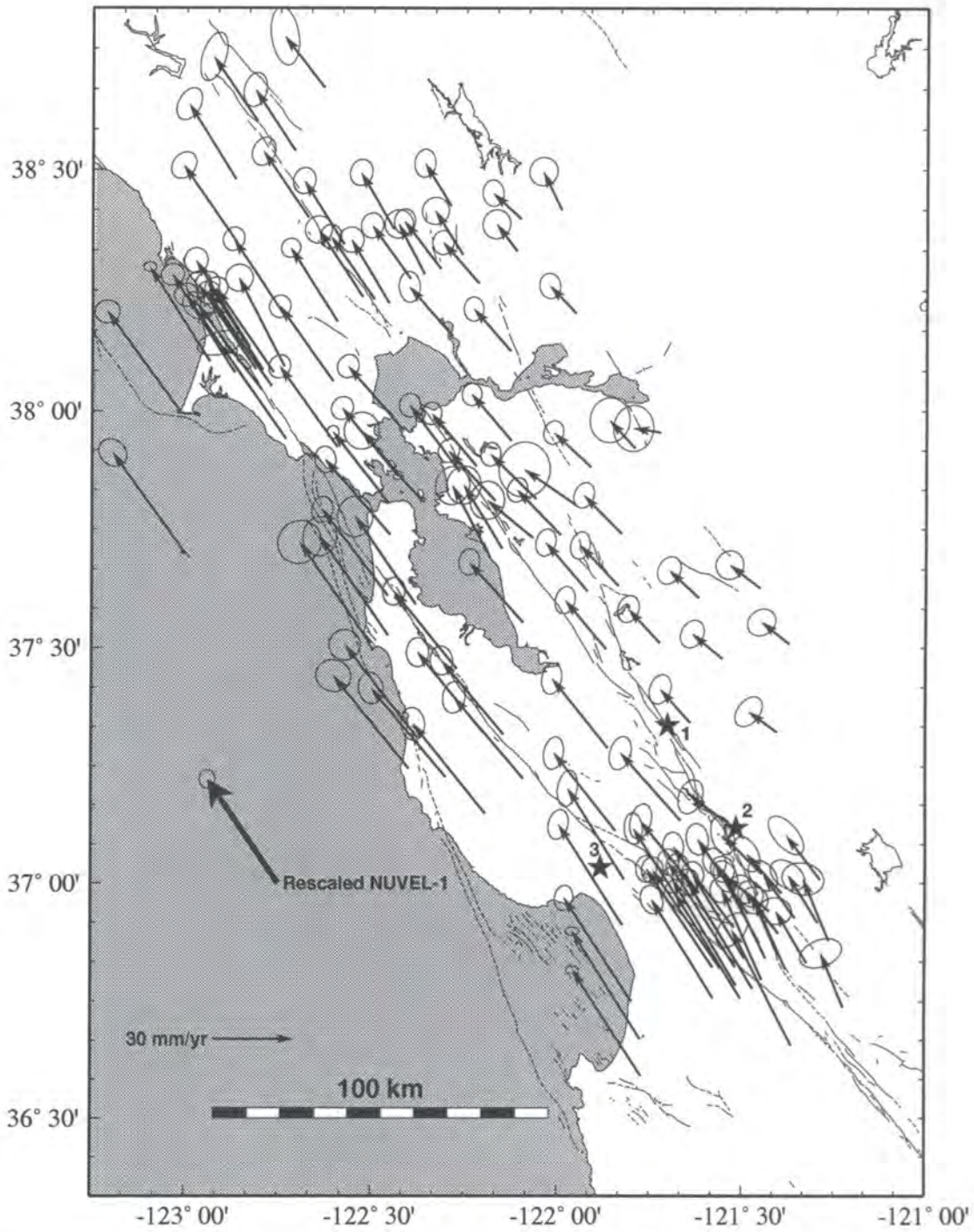

Figure 5.4: Velocity field in the San Francisco and Monterey bay regions relative to the North American plate interior, west of Colorado, which is assumed fixed. The ellipse at the end of each velocity vector represents the 95% confidence interval. The heavy arrow represents the rescaled NUVEL-1 Pacific - North American relative plate velocity for the region. The three stars indicate the epicentres of the Morgan Hill (1), Coyote Lake (2) and Loma Prieta (3) earthquakes.

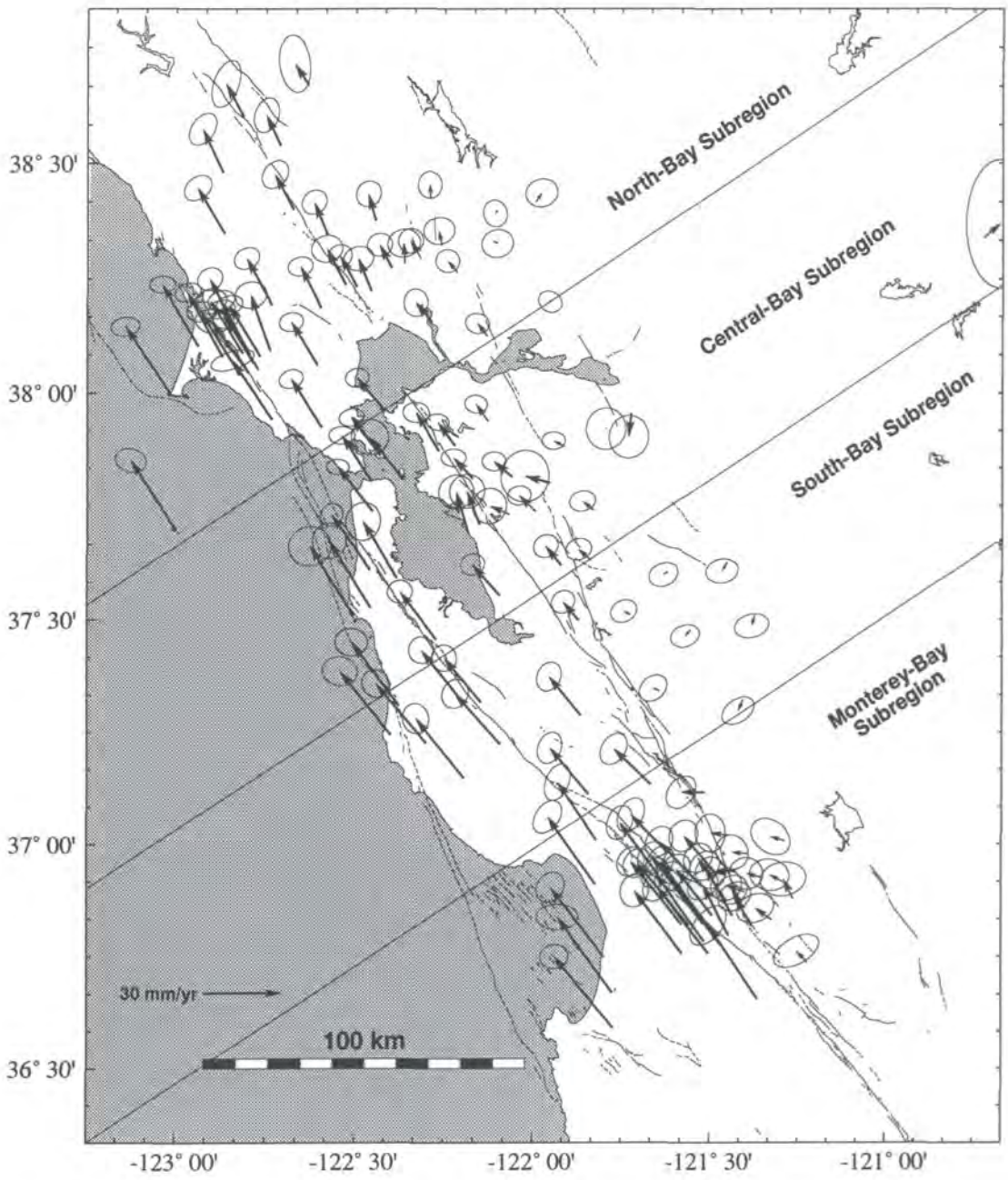

Figure 5.5: Velocity field in the San Francisco and Monterey bay regions. Velocities are relative to the VLBI site OVRO located 300 km east of San Francisco. The ellipse at the end of each velocity vector represents the 95% confidence interval. Diagonal lines separate four subregions described in the text.

position changes that represent deformation around the San Andreas fault system the motion of OVRO is subtracted from the site velocities.

The resultant velocity field around the San Andreas fault system is shown in Figure 5.5. The westernmost points move up to 35 mm/yr relative to the continent 300 km inland from the coast. The easternmost stations in the network show very little motion relative to OVRO. Therefore, nearly all the deformation in northern California is concentrated in a ~100 km wide zone around the San Andreas fault system.

The velocity field in Figure 5.5 has been divided into four subregions: north-bay, central-bay, south-bay and Monterey-bay. Because the GPS observations are restricted to the two northernmost subregions, the deformation in the south-bay and Monterey-bay subregions are derived purely from the trilateration data and are essentially the same as the results presented by *Lisowski et al.* [1991, Figures 6 and 7]. The distribution of deformation across the fault system is best shown by projecting the station velocities onto profiles constructed perpendicular to the plate boundary (Figures 5.6 - 5.9). The parallel and perpendicular velocity components are plotted as a function of distance perpendicular to the plate boundary in the upper and lower parts of these Figures. The magnitude of deformation and width of the zone changes along the strike of the San Andreas fault system (i.e., from profile to profile). This along-strike variation shows the varying complexity of the fault system from south to north.

Velocity profiles for the north-bay subregion are shown in Figure 5.6. The fault-parallel velocity profile (upper part of Figure 5.6) shows that about 32 $\pm$ 2 mm/yr of relative motion is detected by that part of the network. The most distinct feature of the profile is a linear trend with gradient -0.34 $\pm$ 0.01 μstrain/yr between the San Andreas and Green Valley faults. To the southwest of the San Andreas fault and northeast of the Green Valley fault the gradient appears to flatten out. This flattening at both ends of the profile suggests that the entire boundary zone has been spanned and that it is $\sim$ 120 km wide. There appear to be small offsets in the profile across both the San Andreas fault (3.3 $\pm$ 2.8 mm/yr) and the Green Valley fault (5.9 $\pm$ 3.0 mm/yr). No offset across the Rodgers Creek fault is indicated by the observations. The fault-normal velocity profile (lower part of Figure 5.6) shows no significant velocities for most of the stations and no systematic trend.

The velocity profiles for the central-bay subregion are shown in Figure 5.7. The profile of the fault-parallel velocity component shows a near-linear trend over most

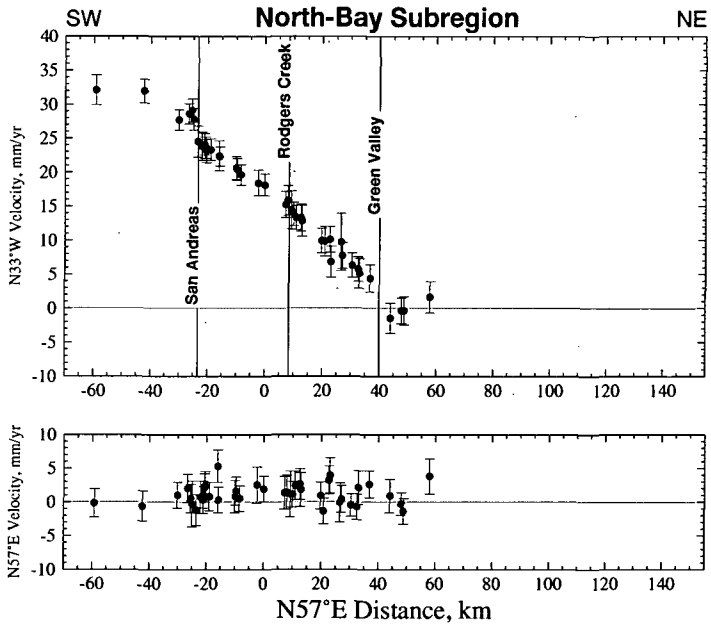

Figure 5.6: Horizontal station velocities for the north-bay subregion resolved into components perpendicular (top) and parallel (bottom) to a N57°E profile and plotted as a function of distance along the profile. Error bars represent one standard deviation.

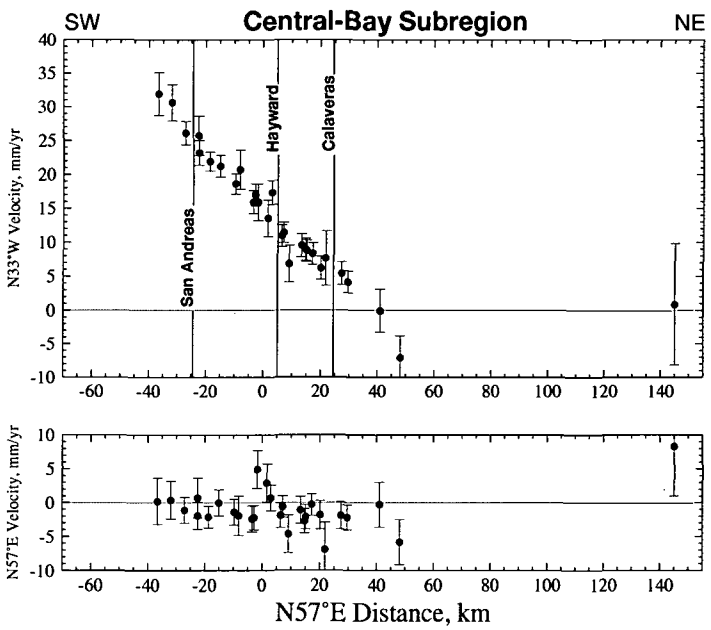

Figure 5.7: Horizontal station velocities for the central-bay subregion resolved into components perpendicular (top) and parallel (bottom) to a N57°E profile and plotted as a function of distance along the profile. Error bars represent one standard deviation.

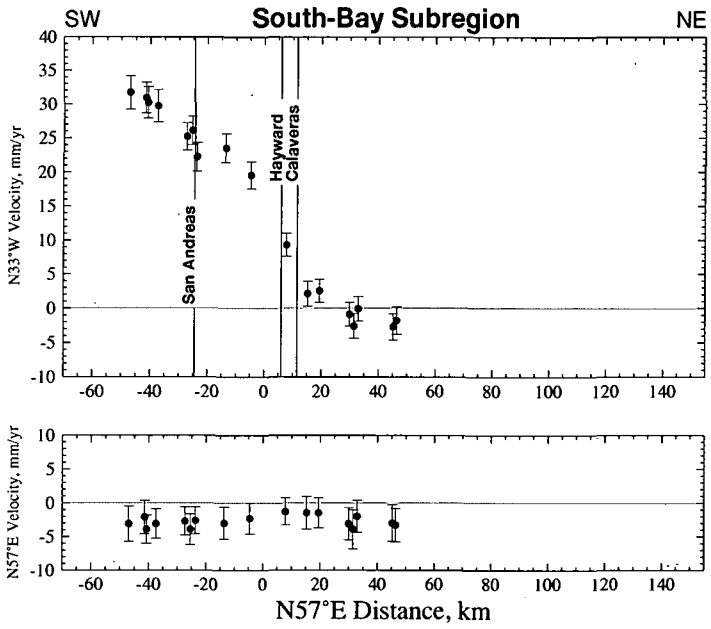

Figure 5.8: Horizontal station velocities for the south-bay subregion resolved into components perpendicular (top) and parallel (bottom) to a N57°E profile and plotted as a function of distance along the profile. Error bars represent one standard deviation.

of the profile (best-fit gradient of -0.38 $\pm$ 0.02 μstrain/yr). The three easternmost points of the profile show no significant motion with respect to OVRO at the 2σ level and suggests that the gradient to the northeast of the Calaveras fault is zero. This suggests that the eastern edge of the deformation zone associated with the San Andreas fault system is covered by the profile. No flattening of the velocity gradient is evident at the southwestern end of the profile. Allowing for the flattening at the eastern end of the profile then the central portion of the profile between the San Andreas and Calaveras fault is fit by a best-fit line with a gradient of -0.41 $\pm$ 0.02 μstrain/yr. A total of 32 $\pm$ 2 mm/yr of plate motion is measured within a zone of $\sim$ 100 km wide. No obvious offsets can be detected across the three faults crossed by the profile. None of the stations have a velocity component in the fault-normal direction that exceeds 2 standard deviations.

Figure 5.8 shows the velocity profiles for the south-bay subregion. All of the fault-parallel velocities in the south-bay subregion can be fit with a straight line of gradient $-0.42\pm$ 0.02 μstrain/yr at the 3σ level. However, at the 2σ level the distribution of observation points are sparse such that any offsets that occur across any of the faults spanned by the profile are unresolvable. As for the north- and central-bay subregions the fault-normal profile shows no significant deviations from a zero velocity. However the negative offset in the fault-normal velocities indicates

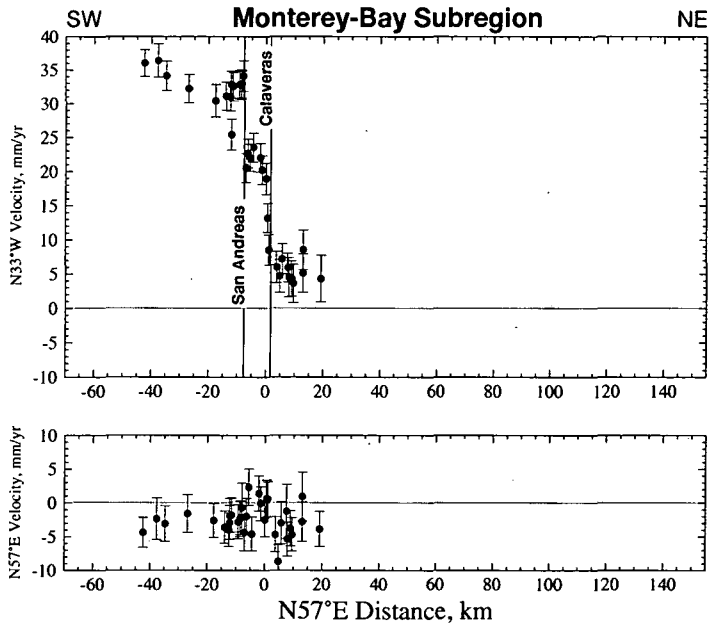

Figure 5.9: Horizontal station velocities for the Monterey-bay subregion resolved into components perpendicular (top) and parallel (bottom) to a N57°E profile and plotted as a function of distance along the profile. Error bars represent one standard deviation.

that all the stations are moving west with respect to the chosen N33°W azimuth in this subregion. That offset is possibly an artefact of the bend of the San Andreas fault in the south-bay subregion (Figure 5.5).

Velocity profiles for the Monterey-bay subregion are shown in Figure 5.9. The fault geometry in this region is relatively complex, with the Calaveras fault merging with the San Andreas fault in the south of the region (Figure 5.5). Both the fault-normal and the fault-parallel velocity components reflect this complexity. The fault-parallel velocity component is not satisfactorily described by a straight line. Large offsets occur across both the San Andreas fault (13.6 $\pm$ 3.1 mm/yr) and the Calaveras fault (11.7 $\pm$ 3.1 mm/yr). Within the blocks on either side, and between these faults, the observations show appreciable scatter and little internal deformation. Only the block to the southwest of the San Andreas fault has a significant velocity gradient (-0.11 $\pm$ 0.05 μstrain/yr) which is less than one-third the gradient detected in the other subregions. The scatter is a result of projecting the station velocities onto a profile in an area where the San Andreas and Calaveras faults are not parallel. Thus for the stations in the north of the subregion the San Andreas fault is located further west and the Calaveras fault further east than is depicted in Figure 5.9. A total of 30 $\pm$ 3 mm/yr is detected over a width of $\sim$ 60 km. This is equal to an average gradient of -0.5 μstrain/yr. The fault-normal velocity component shows

appreciable scatter but no net contraction perpendicular to the trend of the fault.

5.3.2 The Velocity Gradient Tensor

The velocities have been used to estimate the two-dimensional velocity gradient tensor [*Malvern*, 1969] for various triangles of the network using the program of *Feigl et al.* [1993]. The triangles are designated using "Delaunay triangulation" such that they are optimally close to equilateral [*Watson*, 1982]. The symmetric part of this tensor is the strain rate tensor, whilst the antisymmetric part gives a measure of the rate of rotation. The observed values of the symmetric part are shown in terms of their principal compressional and extensional axes for triangles with significant rates in Figure 5.10. Also shown are the average strain rate tensors calculated for the four subregions. These indicate the overall pattern of deformation in the region.

Very high rates of strain occur in the south of the region. This corresponds to the Monterey-bay subregion where large offsets are detected across both the San Andreas and Calaveras faults. For most of the triangles the strain rate shows nearly pure shear with the axes of principal compression directed north-northeast-south-southwest and the axes of principal extension normal to this. This is consistent with right-lateral shear along northwest striking planes. The rate of dilation, or change in area per unit area, is zero at the 2σ level for 98.7% of the triangles. The lack of significant dilation indicates that this area is not dominated by compressional or extensional deformation. Maximum shear-strain rates range from 0.2 to 6.2 μstrain/yr for individual triangles and for the four subregions from 0.3 μstrain/yr in the north-bay to 0.5 μstrain/yr in the Monterey-bay. The direction of maximum right-lateral shear for triangles where the uncertainty in the orientation of the axes are less than 30° are shown in Figure 5.11. Although there is much variation, the direction of maximum right-lateral shear generally agrees with the local fault strike. This is most evident for the Calaveras fault, and near the junction between the Calaveras and San Andreas faults. In contrast, the direction of maximum right-lateral shear for the average subregion strain tensors are around N31°E to N36°E, consistent with the plate motion direction calculated from the NUVEL-1A model.

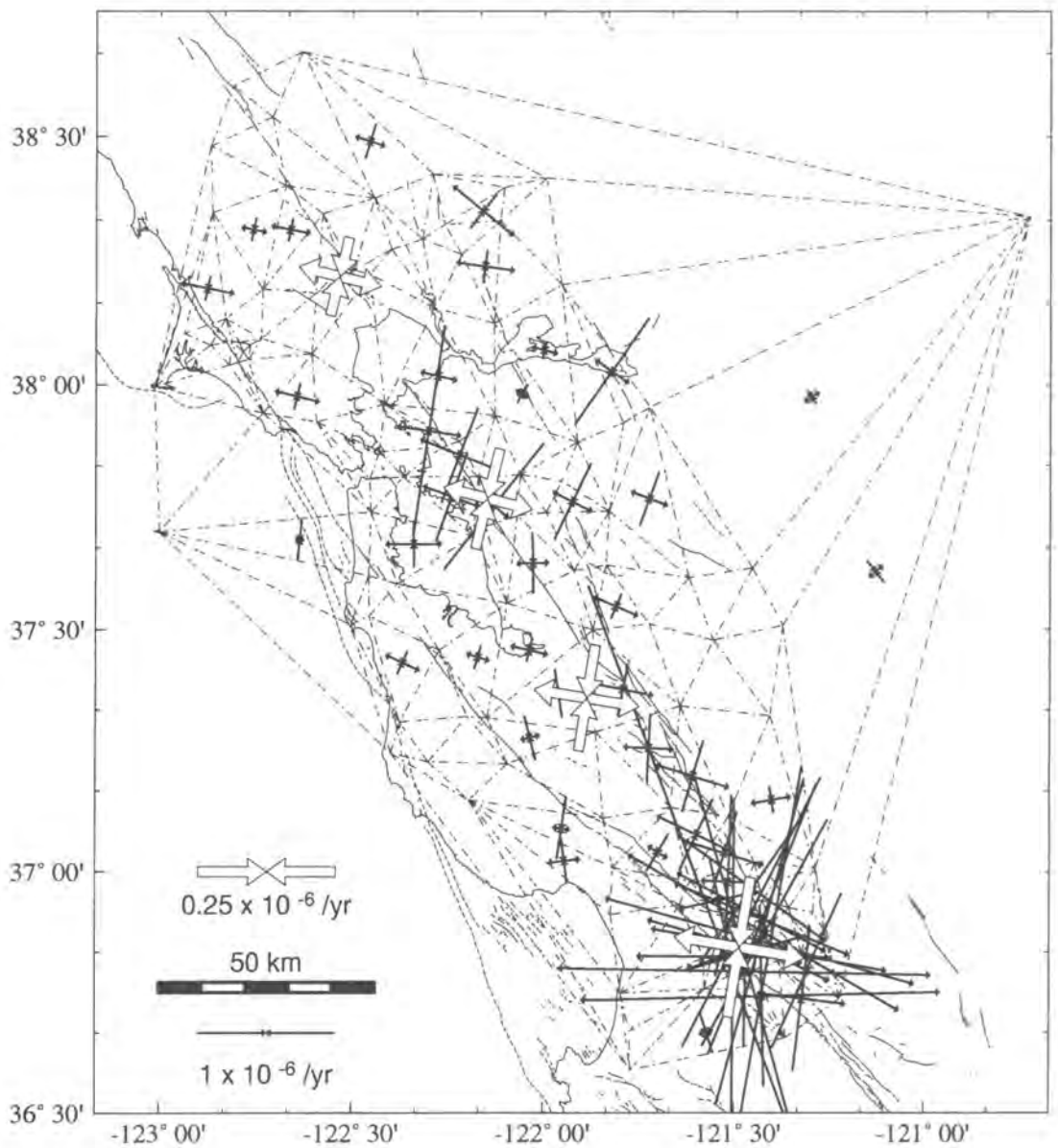

Figure 5.10: Principal axes of the horizontal strain-rate tensor in the San Francisco and Monterey bay regions, calculated from the combined horizontal velocity field shown in Figure 5.5. In each Delaunay triangle (dashed lines), the inward pointing arrow represents compression and the outward pointing arrow represents extension. Large white strain rate tensors are the average rates calculated for the four subregions. If the uncertainty in the orientation of the axes is greater than 30°, and if neither principal strain rate is larger in magnitude than its uncertainty, then the axes are not plotted.

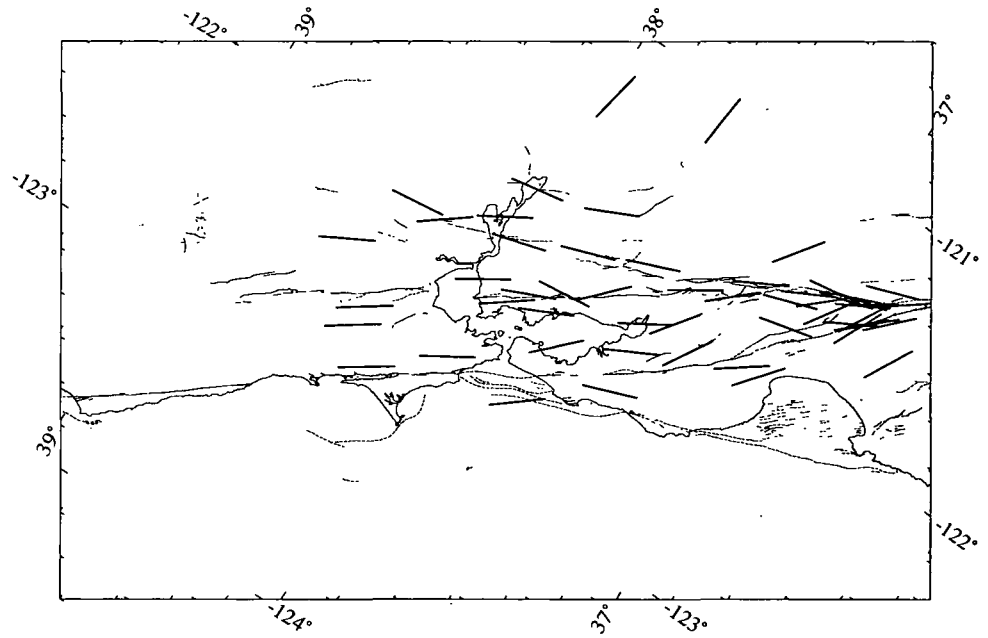

Figure 5.11: Orientation of maximum right-lateral shear in the San Francisco and Monterey bay regions, for the Delaunay triangles of Figure 5.10. This map is plotted in an oblique Mercator projection about the Pacific-North American pole of rotation. A horizontal line would indicate a shear direction parallel to the relative plate motion direction.

5.4 Summary

GPS data in the San Francisco bay region represent only a fraction of the total available geodetic data for calculating the deformation field. Combining different geodetic data using least squares solutions for the inverse of equation (5.1), yields a spatially dense sample of station velocities. The velocity field across the San Andreas fault system between latitudes 36°30′ and 38°40′ has been calculated using trilateration, VLBI and GPS measurements. The measurements show about 35 mm/yr of distributed right lateral shear relative to VLBI station OVRO in eastern California. The width of the deforming zone increases from around 60 km in the south to over 100 km in the north. Fault-normal profiles of the fault-parallel component of velocity indicate a change in the distribution of shear from deformation concentrated on the faults in the south to distributed deformation in the north. Considering that the relative motion measured across the system is similar to geological estimates of slip rate and that motion between the plates appears to be steady over a long time then the data also indicate that the deformation due to the San Andreas fault system occurs primarily northeast of the San Andreas

fault. Little fault-normal motion is detected indicating no significant convergence across the faults. The local orientations of maximum right-lateral shear agree with the surface strikes of nearby faults whereas the orientations averaged over larger regions, i.e., the four subregions, agrees well with the plate-motion direction.

Chapter 6

Geophysical Models of Crustal Deformation

6.1 Introduction

Surveying measurements made in California sample the surface deformation that results from relative, right-lateral translation of the Pacific and North American plates. Within a plate tectonic framework this motion can be approximated to continuous translation of surface plates that are assumed to be rigid. However, varying deformation rates provide evidence for a recurring sequence of interearthquake strain accumulation, coseismic strain release and postseismic readjustment, known as the *earthquake deformation cycle.* Observations along the San Andreas fault system also suggest a range of mechanical fault behaviour from planes completely locked from the surface throughout seismogenic depths (10-15 km) except for abrupt slip in occasional large earthquakes, to free sliding planes at all depths with only minor seismicity.

Most models for earthquakes involve some mechanism where shear stress gradually increases across a fault plane to failure level. At shallow depths corresponding to the seismogenic crust, the rocks behave in an elastic and brittle manner. The frictional strength of faults is thought to increase linearly with depth and faulting is thought to be controlled by Coulomb failure. The fault plane is usually locked so that stress accumulates and is released predominantly in the form of occasional large earthquakes. Below the brittle layer, where temperatures are sufficiently high, plastic, aseismic slip on a downward continuation of the fault zone, or distributed shear flow, occurs continuously. This aseismic deformation concentrates stress in the locked zone above.

The process of strain accumulation and faulting for a transform fault is shown in

Figure 6.1. At the time of an earthquake, only that part of the fault slips which has not moved earlier aseismically and so slip does not extend into the lower, plastic layer. If the depth d is small then continuous, aseismic slip is observed, strain is released more or less continuously and the probability of large earthquakes is low. Fault segments where steady-state creep is observed at the surface but large earthquakes have been documented may indicate transitional behaviour. Fault segments may also slip freely in the upper few kilometres, be in locked frictional contact at mid-crustal depths and slip freely below. Because of the complexities observed in crustal deformation, many models have now been developed for strain accumulation and release on faults embedded in linear elastic, linear viscoelastic or more complex structures.

6.2 Models for Strike-Slip Faulting

6.2.1 Models from Dislocation Theory

Deformation along a strike-slip fault, where the fault is long and straight and the deformation uniform along strike is easy to model using a simple, two-dimensional model (Figure 6.2). The plane $z = 0$ represents the free surface of the Earth, and the fault lies in the $x - z$ plane at $y = 0$. In an infinite, elastic space a discrete-dislocation model can be constructed using two parallel screw dislocations with equal and opposite Burger's vector b [*Weertman and Weertman*, 1964; *Savage*, 1980]. The faulted or slipped area is generally taken as the plane area joining the two dislocations. The displacement and stress field can be calculated from the superposition of the fields from the two screw dislocations parallel to the x-axis but with opposite Burger's vector at depths $z = d_1$ and $z = d_2$. For an elastic half-space, the boundary condition imposed at the free surface can be satisfied by introducing in the lower half-space the field which would be generated by image dislocations at depths $z = -d_1$ and $z = -d_2$ in the absence of the free surface. The complete displacement field is then

$$u_x(y,z) = \frac{b}{2\pi}\left[\tan^{-1}\left(\frac{y}{z-d_1}\right) - \tan^{-1}\left(\frac{y}{z+d_1}\right) - \tan^{-1}\left(\frac{y}{z-d_2}\right) + \tan^{-1}\left(\frac{y}{z+d_2}\right)\right]. \tag{6.1}$$

At the free surface ($z = 0$) this can be simplified to

$$u_x(y) = \frac{-b}{\pi}\left[\tan^{-1}\left(\frac{y}{d_1}\right) - \tan^{-1}\left(\frac{y}{d_2}\right)\right]. \tag{6.2}$$

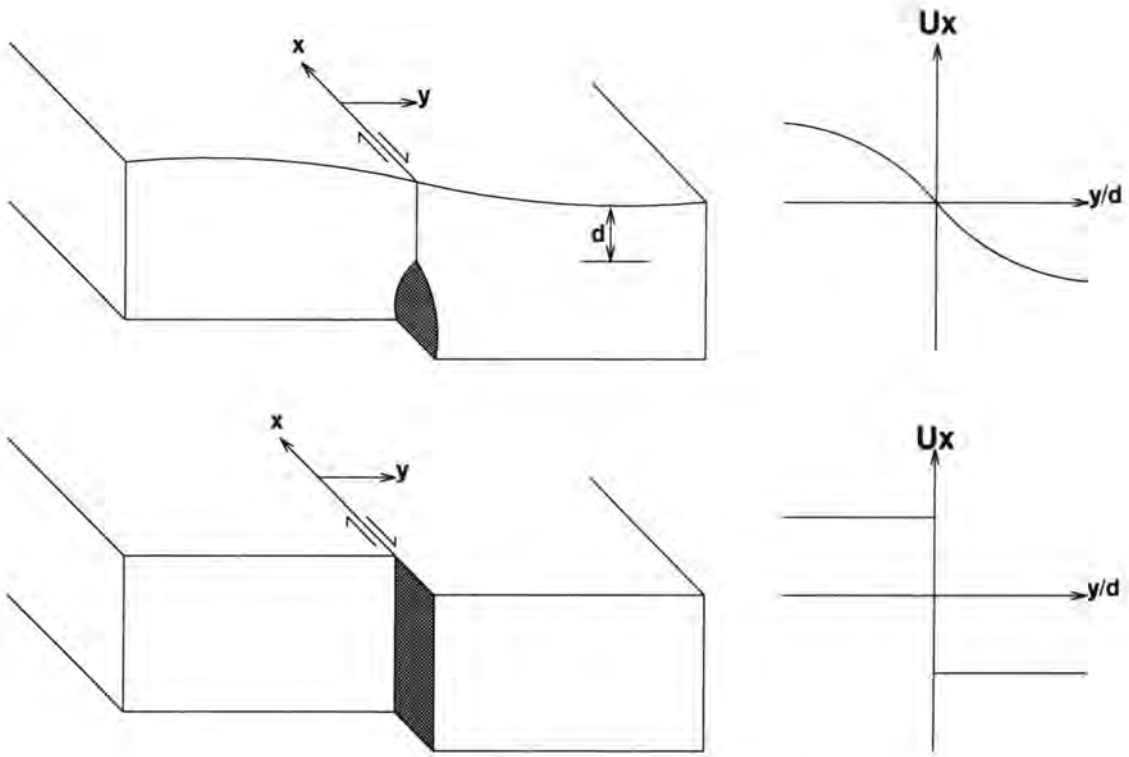

Figure 6.1: Accumulation and release of strain along a strike-slip fault. The upper sketches illustrate the surface motion resulting from strain accumulation on a fault locked above depth d. The lower sketches illustrate the surface displacements after strain release/failure of the fault.

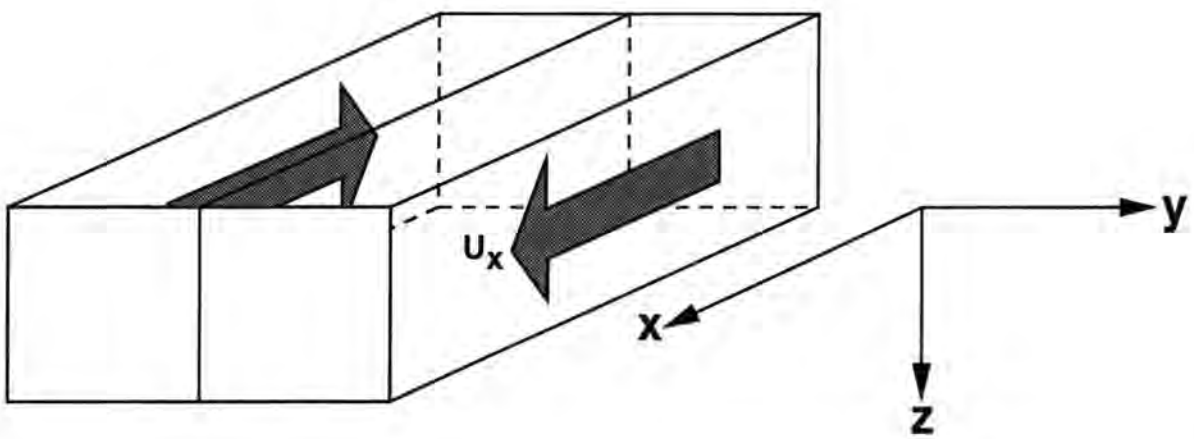

Figure 6.2: Orientation of the coordinate system relative to a fault in the $x - z$ plane at $y = 0$

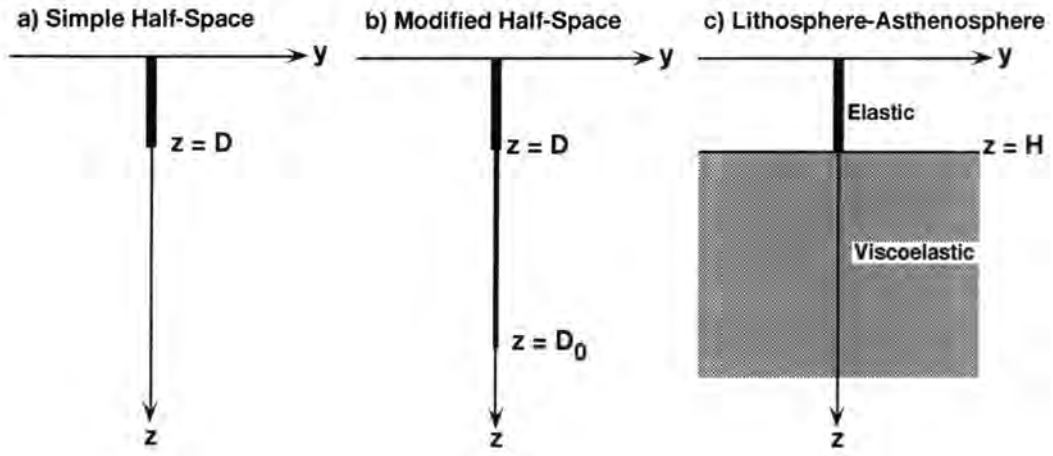

Figure 6.3: (a) Simple elastic half-space, (b) modified elastic half-space, and (c) lithosphere-asthenosphere Earth models. The heavy vertical line segment represents the fault segment that ruptures seismically. From *Lisowski et al.* [1991]

The simplest model that approximates the deformation associated with a long, straight, strike-slip fault is shown in Figure 6.3a. The zero-order motion is rigid block motion, equal to the long-term average plate velocity, V, at the boundary. However, the upper portion of the fault ($z < D$) is locked and slips only during earthquakes by an amount VT at intervals of time T. In the interseismic period the surface deformation can be calculated by subtracting the amount that is taken up in earthquakes from the rigid plate motion. That is

$$\dot{u}_x(y) = \mp\frac{V}{2} + \frac{V}{\pi}\left[\tan^{-1}\left(\frac{y}{d_1}\right) - \tan^{-1}\left(\frac{y}{d_2}\right)\right]. \tag{6.3}$$

Setting $d_1 = 0$ and $d_2 = D$ gives

$$\begin{aligned} \dot{u}_x(y) &= \mp\frac{V}{2} + \frac{V}{\pi}\left[\pm\frac{\pi}{2} - \tan^{-1}\left(\frac{y}{D}\right)\right], \\ &= \mp\frac{V}{2} \pm \frac{V}{2} - \frac{V}{\pi}\tan^{-1}\left(\frac{y}{D}\right), \\ &= -\frac{V}{\pi}\tan^{-1}\left(\frac{y}{D}\right). \end{aligned} \tag{6.4}$$

Equation (6.4) can also be obtained from equation (6.2) by setting $d_1 = D$ and $d_2 = \infty$ and assuming the fault is slipping at a rate, V, at depth. However, although mathematically equivalent, these two methods for obtaining equation (6.4) illustrate different views of the same physical phenomena. The first method suggests slip deficit accumulating on a locked patch as a result of some loading mechanism at greater depth whereas the second method suggests slip on a freely-slipping zone beneath a locked patch.

Where two or more subparallel faults are responsible for the deformation, the total field can be obtained by summing the individual fields from each fault. In this case V is replaced by the slip deficit accumulating along each fault b or conversely by the deep-slip rate on each fault. The surface deformation produced by several screw dislocations is described completely by the dislocations themselves, and is independent of the position and orientation of the slipping surfaces at depth [*Lisowski et al.*, 1991]. It is also possible that at depths where plastic behaviour occurs, the deformation is distributed evenly across a broad lateral zone [*Prescott and Nur*, 1981; *Lachenbruch and Sass*, 1973]. This is the distributed shear case, and can be treated by distributing infinitesimal screw dislocations with Burger's vector density $b/2\omega$ over a zone of width 2ω at depth d. Replacing b with $b/2\omega\ dy'$, y with $y - y'$ in equation (6.2) and integrating over y' from $-\omega$ to $+\omega$ the result is

$$\dot{u}_x(y) = \frac{\dot{b}}{2\pi\omega}\left[(y-\omega)\tan^{-1}\left(\frac{y-\omega}{d}\right) - (y+\omega)\tan^{-1}\left(\frac{y+\omega}{d}\right) - \frac{d}{2}\ln\left(\frac{d^2+(y-\omega)^2}{d^2+(y+\omega)^2}\right)\right]. \tag{6.5}$$

Although the distributed shear zone is modelled as lying within an elastic half-space, it is a reasonable approximation to the velocity distribution that would be produced from viscous tractions at the base of a brittle layer [*Prescott and Yu*, 1986].

One complication that may be important when interpreting observations is the effect of structural inhomogeneity. The effect of layering in a half-space may be modelled using the method of images where the overall deformation is calculated as a large (essentially infinite) sum of terms that represent images of many dislocations in the half-space. The images are required to satisfy boundary conditions at the layer interfaces because of the contrasting elastic properties. The effect of horizontal layering was investigated by *Rybicki* [1971]. For geologically interesting cases, where the rigidity increases with depth, the displacements are concentrated closer to the fault compared with the homogeneous half-space case. A more interesting case of layering, that of an elastic layer over a viscoelastic half-space produces a time-dependent surface deformation [*Nur and Mavko*, 1974]. Lateral inhomogeneity has been studied by *McHugh and Johnston* [1977] and *Rybicki and Kasahara* [1977]. The effect of rigidity contrasts in vertical blocks is to concentrate deformation in the blocks of lower rigidity.

The simple, two-dimensional, screw-dislocation model for strike-slip faulting lacks the ability to model the postseismic transients that follow large earthquakes [*Thatcher*, 1983]. Two contrasting models of the earthquake deformation cycle on strike-

slip faults that predict postseismic movements have been proposed. The first model (the modified elastic half-space model, Figure 6.3b) attributes postseismic deformation to exponentially-decaying aseismic slip on a downward continuation of the fault directly below the coseismic rupture. The slip rate is given by

$$\dot{b} = \alpha VT[\exp(-\alpha t)]/[1 - \exp(-\alpha T)], \tag{6.6}$$

where t is time since the preceding earthquake and α is a time constant [*Thatcher*, 1983]. The second model (the lithosphere-asthenosphere coupling model, Figure 6.3c), assumes post-seismic viscoelastic relaxation in the asthenosphere. A method for calculating the total kinematic motion of the plates is proposed by *Savage and Prescott* [1978a]. The interseismic motion is the sum of (1) uniform block motion, (2) the elastic response to steady shallow "backslip", (3) the viscous response to the steady backslip, and (4) the viscoelastic response to prior periodic step offsets on the fault.

Although geophysical observations of time-varying deformation rates do serve to limit some extreme models, no data sufficiently good to distinguish between these two models are available at present. Furthermore, it can be shown that the deformation for the simple lithosphere-asthenosphere model can be exactly reproduced by a selected distribution of slip on vertical faults in an elastic half-space at various depth intervals for infinite strike-slip faults [*Savage*, 1990] and this suggests that it may be very difficult to resolve this question using crustal deformation observations. Except for the immediate postseismic period, the locking depth and slip rates derived from simple half-space models do not differ significantly from those obtained using more complicated Earth models [*Savage*, 1987]. Inversion of even high quality geodetic data for a distribution of slip at depth is highly unstable [*Weertman*, 1965]. These results illustrate well the inherent extreme insensitivity of crustal deformation to Earth structure.

For many strike-slip faults, variations in strike are too great to allow good deformation modelling using two-dimensional geometries and so three-dimensional geometries must be used. These were first used by *Steketee* [1958] who adopted a mathematical model of a displacement dislocation surface, Σ, i.e., one across which there is a discontinuity in some or all components of the displacement vector u_i. The dislocation is assumed to be such that the discontinuity, Δu_i has the nature of a rigid body displacement satisfying the equations

$$\begin{aligned} \Delta u_i &= u_i + \Omega_{ij} x_j, \\ \Omega_{ij} &= -\Omega_{ji}, \end{aligned} \tag{6.7}$$

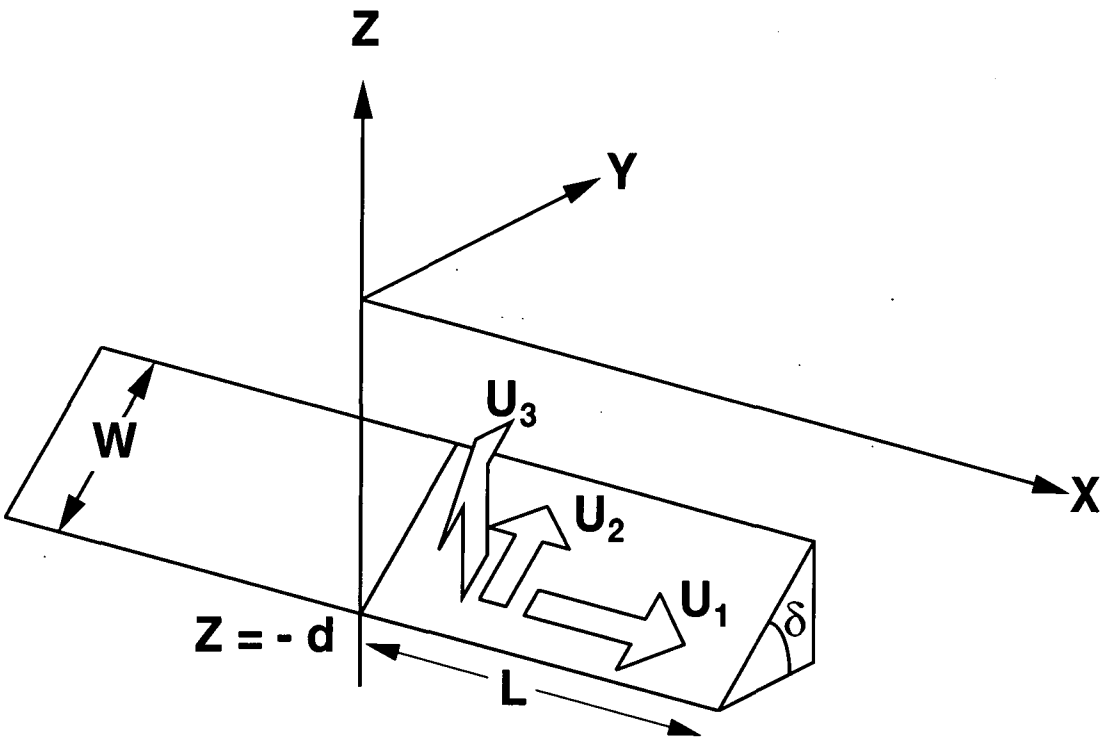

Figure 6.4: Geometry of the source model for three-dimensional faulting at depth. After *Okada* [1985].

where u_i and the rotation matrix Ω_{ij} are constants. Six sets of Green's function are required for the general solution of the problem of a dislocation in a semi-infinite medium, and were determined for a strike-slip fault by *Steketee* [1958]. The five sets of functions describing thrust faulting, normal faulting and dilation in three planes were derived by *Maruyama* [1964]. A complete set of closed analytical expressions for the surface displacements, strains and tilts due to shear and tensile faults in a half-space for point and finite rectangular sources was presented by *Okada* [1985]. The expressions are free from the singularities that were inherent in previous expressions [e.g., *Maruyama*, 1964] and are in compact form. The expressions for the horizontal surface deformation of a finite rectangular fault with length $2L$, width W (Figure 6.4) and a strike-slip dislocation U_1 are

$$\begin{aligned} u_x &= -\frac{U_1}{2\pi}\left[\frac{\xi q}{R(R+\eta)} + \tan^{-1}\frac{\xi\eta}{qR} + I_1 \sin\delta\right]\Big\|, \\ u_y &= -\frac{U_1}{2\pi}\left[\frac{\tilde{y} q}{R(R+\eta)} + \frac{q\cos\delta}{R+\eta} + I_2 \sin\delta\right]\Big\|, \end{aligned} \tag{6.8}$$

where $\|$ represents the substitution

$$f(\xi,\eta)\| = f(x+L,p) - f(x+L,p-W) - f(x-L,p) + f(x-L,p-W),$$

and

$$
\begin{aligned}
I_1 &= \frac{\mu}{\lambda+\mu}\left[\frac{-1}{\cos\delta}\frac{\xi}{R+\tilde{d}}\right] - \frac{\sin\delta}{\cos\delta} I_5, \\
I_2 &= \frac{\mu}{\lambda+\mu}\left[-\ln(R+\eta)\right] - I_3, \\
I_3 &= \frac{\mu}{\lambda+\mu}\left[\frac{1}{\cos\delta}\frac{\tilde{y}}{R+\tilde{d}} - \ln(R+\eta)\right] + \frac{\sin\delta}{\cos\delta} I_4, \\
I_4 &= \frac{\mu}{\lambda+\mu}\frac{1}{\cos\delta}\left[\ln(R+\tilde{d}) - \sin\delta\,\ln(R+\eta)\right], \\
I_5 &= \frac{\mu}{\lambda+\mu}\frac{2}{\cos\delta}\tan^{-1}\frac{\eta(X+q\cos\delta)+X(R+X)\sin\delta}{\xi(R+X)\cos\delta},
\end{aligned}
\tag{6.9}
$$

with

$$
\begin{aligned}
p &= y\cos\delta + d\sin\delta, \\
q &= y\sin\delta - d\cos\delta, \\
\tilde{y} &= \eta\cos\delta + q\sin\delta, \\
\tilde{d} &= \eta\sin\delta - q\cos\delta, \\
R^2 &= \xi^2+\eta^2+q^2 = \xi^2+\tilde{y}^2+\tilde{d}^2, \\
X^2 &= \xi^2+q^2,
\end{aligned}
\tag{6.10}
$$

and λ, μ are the Lamé elastic moduli of the halfspace. For the case of a vertical, strike-slip fault, $\cos\delta = 0$ (taking care of the two cases of $\sin\delta = \pm 1$). Then

$$
\begin{aligned}
I_1 &= -\frac{\mu}{2(\lambda+\mu)}\frac{\xi y}{(R+\eta)^2}, \\
I_2 &= \frac{\mu}{2(\lambda+\mu)}\left[\frac{\eta}{R+\eta} + \frac{y^2}{(R+\eta)^2} - \ln(R+\eta)\right], \\
I_4 &= -\frac{\mu}{\lambda+\mu}\frac{y}{R+\eta}, \\
I_5 &= -\frac{\mu}{\lambda+\mu}\frac{\xi}{R+\eta},
\end{aligned}
\tag{6.11}
$$

with $R^2 = \xi^2+\eta^2+y^2$. In these expressions some terms become singular for special conditions and the following rules avoid them

(i) when $q = 0$ set $\tan^{-1}(\xi\eta/qR) = 0$ in equation (6.8)

(ii) when $\xi = 0$ set $I_5 = 0$ in equation (6.9)

(iii) when $R+\eta = 0$ (occurs only when $\sin\delta < 0$ and $\xi = q = 0$) set all the terms which contain $R+\eta$ in their denominators to be zero in equations (6.8) to (6.11), and replace $\ln(R+\eta)$ to $-\ln(R+\eta)$ in equations (6.9) and (6.11).

Three-dimensional solutions for a rectangular, strike-slip fault in an elastic layer overlying a linearly-viscoelastic half-space have also been constructed both approximately [*Rundle and Jackson*, 1977] and exactly [e.g., *Singh*, 1970; *Cohen*, 1980, 1982].

6.2.2 Models using Two-Dimensional Edge Cracks

Despite the complexities that can be incorporated into discrete dislocation models there are some restrictions. The presence of stress singularities at the dislocation lines is clearly unrealistic although this difficulty can be overcome by introducing a continuous distribution of dislocations. A further objection is that these dislocation models are semiempirical since the slip is imposed on the fault arbitrarily without satisfying any particular boundary condition on the stress. A two-dimensional, elastic, edge crack model (Figure 6.5b) was proposed by *Turcotte and Spence* [1974] to analyse near-fault surface deformation. Loading is from remote edges of surface plates which are decoupled from the asthenosphere below and as a result the loading cannot be directly related to deep-seated motion which limits its application. This inconsistency was remedied by introducing a viscoelastic region beneath the elastic surface plate [*Spence and Turcotte*, 1979; *Turcotte et al.*, 1979]. A vertical, strike-slip fault loaded by tractions at the base of the elastic plate (Figure 6.5a and b) was modelled by *Li and Rice* [1987] using a "line spring" approximation method. *Li and Lim* [1988] produced two new versions of the physical base-traction model in order to include geometric complexities such as shallow fault creep and parallel faults. These models combine features of both the modified elastic half-space and lithosphere-asthenosphere models. However, what is gained in realism of the Earth model is lost, due to mathematical complexity, in ability to include geometric fault variations.

6.2.3 Comment on Structural Geometries

The orientation of the maximum, near-field, right-lateral strain accumulation from published geodetic results throughout the San Andreas fault system has been used to place constraints on the geometries of fault-loading mechanisms [*Gilbert et al.*, 1994]. The orientation of maximum, shear-strain accumulation is better predicted by the orientation of the local faulting direction than by the regional plate motion direction. This is clearest in the Big Bend region of the San Andreas fault

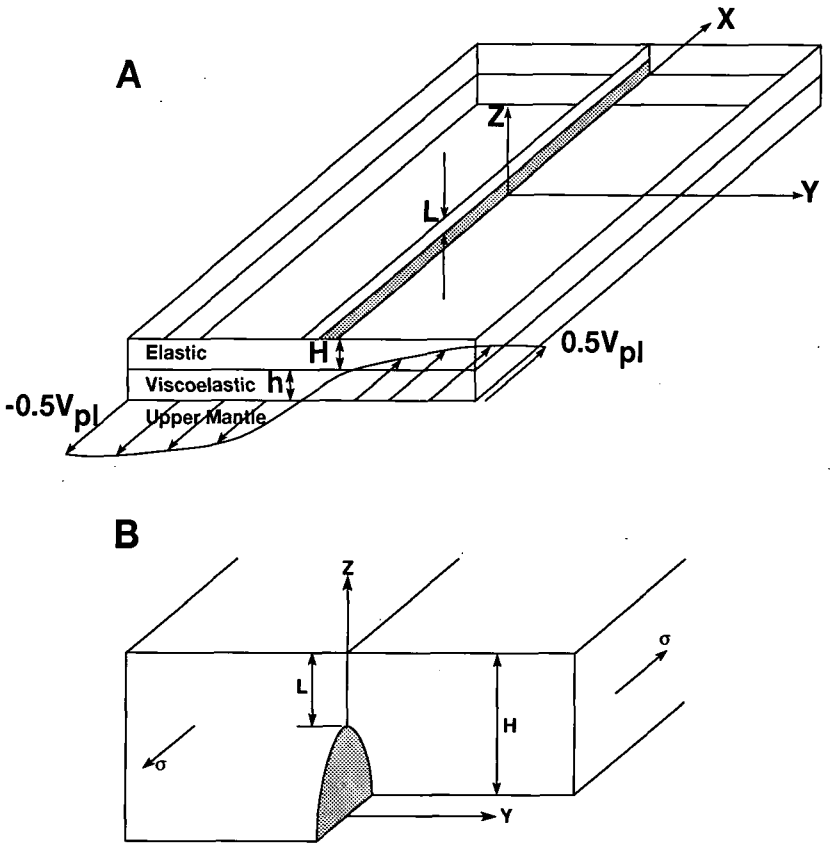

Figure 6.5: (a) Elastic lithosphere coupled to a viscoelastic asthenosphere driven by deep mantle movement. The shaded area indicates the shear zone sliding at constant resistive shear stress below a shallow locked brittle zone. (b) A cross-sectional view of the lithosphere at the plate boundary, modelled as a two-dimensional edge crack under stress. After *Li and Rice* [1987]

(Figures 1.3, 2.4). Here, the maximum, right-lateral shear-strain orientation of N54.4°W is much closer to the local fault direction, N60°W, than the orientation of plate motion, N37°W.

This form of strain localisation can be explained using both lithosphere-asthenosphere models, which are dominated by horizontal layering of the crust, and modified elastic half-space models which have predominantly vertical geometries. The lithosphere-asthenosphere models can accommodate the observed results only if the post-seismic relaxation time of the system is similar to the recurrence times of large earthquakes. However, studies have shown that this is generally not true for the San Andreas fault system [*Thatcher*, 1983].

Vertical geometries produce strain fields that are parallel to the fault direction at all times. Base-traction models show that strain concentration throughout the

earthquake cycle can occur if the elastic layer thickness is 2-3 times larger than the fault-locking depth. Geologic evidence from ancient transcurrent fault zones show that they extend into the middle and lower continental crust as ductile shear zones that mimic the surface patterns of strike-slip faulting presently active [*Sibson*, 1983; *Gilbert et al.*, 1994]. These observations suggest that near-fault strain accumulation is a product of geometries dominated by vertical structures in continental crust. Models whose geometries are predominantly vertical are therefore favoured here for predicting surface deformations.

6.3 Previous Models used in the San Francisco Bay Region

Several different models have been used to explain the surface deformation pattern in the San Francisco bay region. Most assume that the data can be adequately modelled using two dimensional models, with one axis vertical and the other normal to the general strike of the faults.

Several estimates of interseismic slip rates and contrasting models have been produced to describe the deformation in the northern San Francisco bay region [*Prescott and Yu*, 1986; *Li and Rice*, 1987; *Kroger et al.*, 1987 and *Lisowski et al.*, 1991]. The trilateration data from 4 networks measured by the USGS in the interval 1972-1983 were used along with data from VLBI measurements spanning 1980 to 1986. A series of five forward models were used to study the amount and distribution of slip at depth that is consistent with the surface observations (Figure 6.6) [*Prescott and Yu*, 1986]. The observations were poorly modelled with slip at depth on only the San Andreas fault (Figure 6.6, models A and B). A better fit was obtained for slip at depth on three faults (Figure 6.6, model C) or with motion distributed across the whole zone from the San Andreas fault to the Napa Valley fault (Figure 6.6 model D). The best model involved distributed slip, plus additional shallow slip between 6 and 10 km depth on the San Andreas fault to account for the apparent increase in strain rate seen within the Point Reyes network (at -25 km along the profile) (Figure 6.6 model E). The distributed slip models were motivated by observations of heat flow which suggest that the brittle, surface layer is transported by tractions at its base and is decoupled from material beneath [*Lachenbruch and Sass*, 1980].

Modelling of the thermal-mechanical evolution of the plate boundary suggested

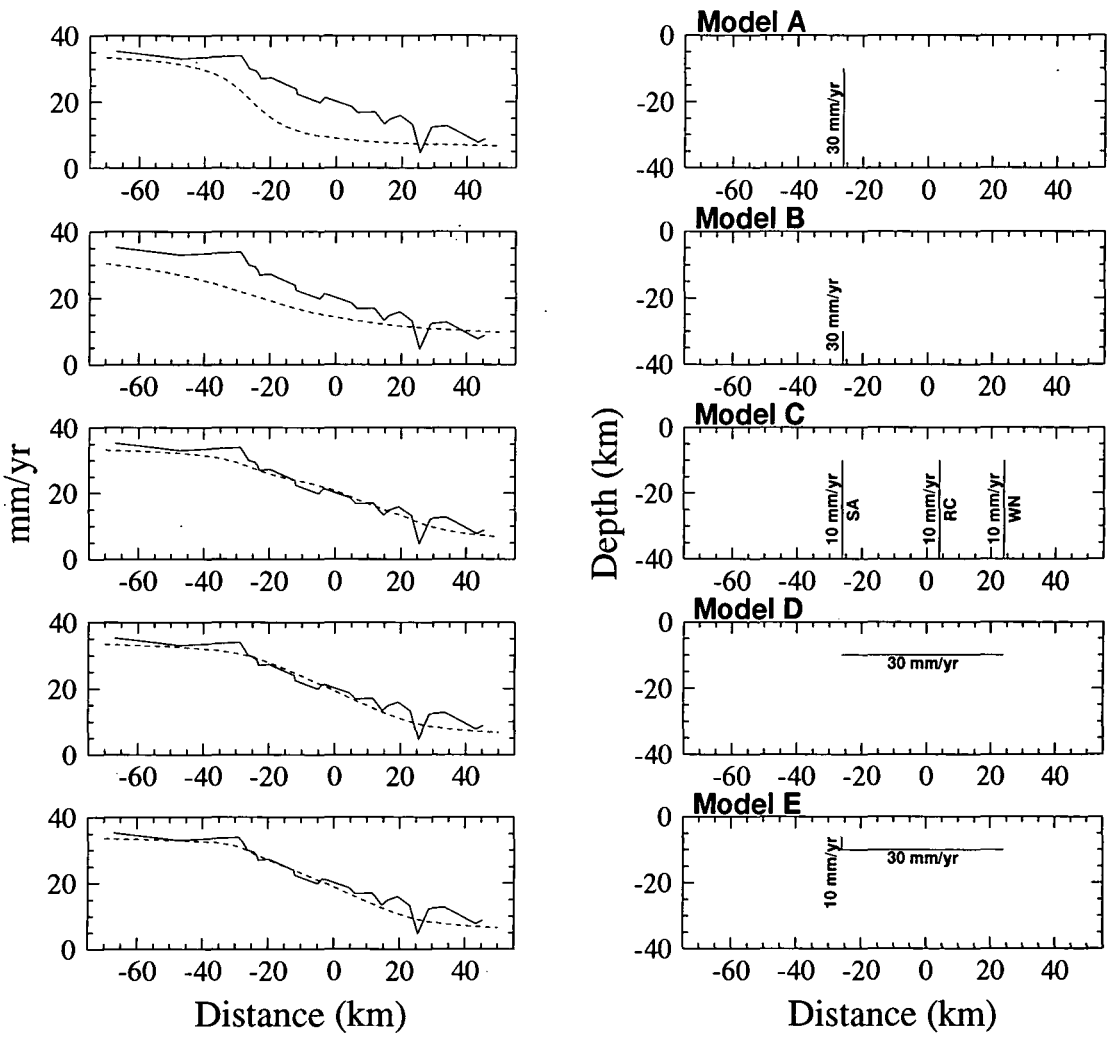

Figure 6.6: The interseismic deformation for various models for the northern San Francisco bay region. Superimposed on the theoretical profiles (dashed line) is the observed velocity profile (solid line). Right-hand column of plots show the models. Vertical lines indicate the location, depth and deep slip rate on the San Andreas (SA), Rodgers Creek (RC) and West Napa (WN) faults. Horizontal lines indicate the width of uniformly distributed vertical shear from the plotted depth to infinity. Modified from *Prescott and Yu* [1986].

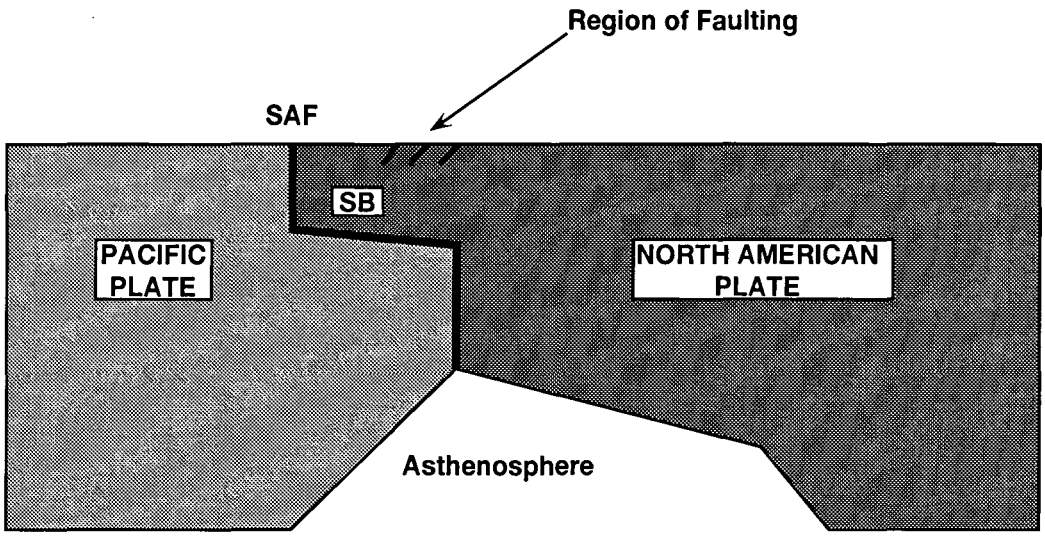

Figure 6.7: Schematic diagram of the fault zone and lithosphere in the San Francisco bay region. The San Andreas fault (SAF) still serves as the principal surface boundary between the Pacific and North American plates. Below seismogenic depths the boundary is $\sim$ 40 km east of the San Andreas fault. A sub-horizontal shear zone connects the San Andreas fault to the deep eastern segment and underlies the Sebastapol Block (SB). Recently formed faults lie above the deeper eastern plate-boundary segment. Modified from *Furlong et al.* [1989].

that the strength minimum at depth, beneath the brittle, surface layer is offset by approximately 40 km northeast of the San Andreas fault (Figure 6.7) [*Furlong et al.* 1989]. From this a model was proposed whereby the San Andreas fault is connected to a vertical shear zone at depth by distributed vertical shear underlying the Sebastapol block (Figure 6.8). In the central San Francisco bay region, distributed vertical shear connects the San Andreas fault to the vertical shear zone at depth underneath the surface location of the Hayward fault. Aseismic creep was included on the Hayward and Calaveras faults (Figure 6.9). Another model based on such a structure involved a slipping plate boundary represented by a screw dislocation 25 km to the east of the San Andreas fault at a depth of 25 km [*Lisowski et al.*, 1991]. The San Andreas fault was represented by a vertical zone of low rigidity (a consequence of past activity on the fault) separating blocks to the left and right of different rigidities (Figure 6.10). This model reproduces several features of the observations, e.g., the flattening of the velocity profile to the west of, and the high strain rate across, the San Andreas fault.

The observed deformation in the northern San Francisco bay region was modelled using theoretical curves from the physical base traction model [*Li and Rice*, 1987].

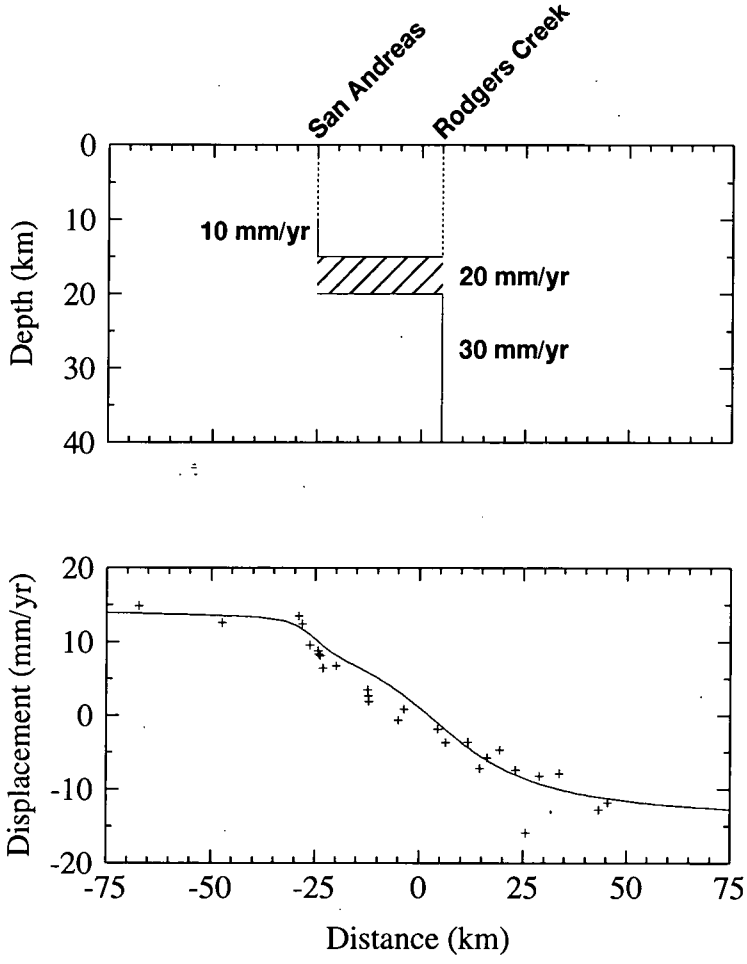

Figure 6.8: The interseismic deformation model for the northern San Francisco bay region of *Furlong et al.* [1989]. Upper part shows the structure. Lower part shows the theoretical profile (line) and the observed velocity data (+) from *Prescott and Yu* [1986]. Faults creeping during observation period are shown as solid lines, the distributed shear zone as a ruled region and locked faults as dashed lines. The slip rates used in the modelling are indicated.

The parameters used (time since the previous earthquake, earthquake repeat time, overall plate velocity, locking depth, elastic plate thickness and relaxation time) were deduced from seismological, geological and strain-rate decay data. However the predicted profiles showed clear deviations from the observed data west of the San Andreas fault and to the east of the West Napa fault (Figure 6.11). The misfit in the southwest block was attributed to a rigidity contrast across the San Andreas fault with the southwest block having a greater thickness-averaged rigidity than the northeast block. However, ignoring the effects of other sub-parallel faults in the region, and locating the mantle flow boundary directly underneath the San Andreas fault, will also have contributed to the misfit.

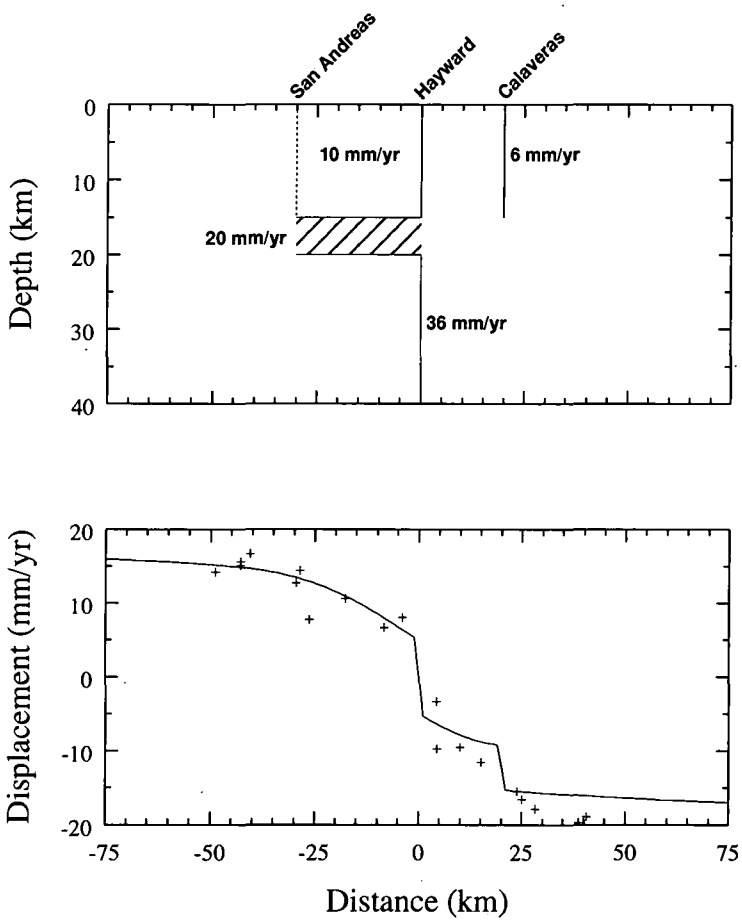

Figure 6.9: The interseismic deformation model for the central San Francisco bay region of *Furlong et al.* [1989]. Upper plot shows the structure. Lower plot shows the theoretical profile (line) and the observed velocity data (+) from *Prescott et al.* [1981]. Faults creeping during observation period shown as solid lines, the distributed shear zone as a ruled region and locked faults as dashed lines. The slip rates used in the modelling are indicated.

Two-dimensional, finite-element methods [e.g., *Melosh and Raefsky*, 1981] were used to model geodetic and VLBI data in the western United States [*Kroger et al.*, 1987]. The model was intended to approximate a lateral slice through a multiply-faulted transform system. The model simulated the time-dependent evolution of displacements and stress in an elastic lithosphere overlying a viscoelastic asthenosphere. For the northern San Francisco bay region activity on the San Andreas fault was supplemented by the Rodgers Creek-Maacama fault (Figure 6.12). The location of the basal flow boundary, 30 km northeast of the San Andreas fault, was based on seismicity and extrapolation of a small circle about the Pacific-North American pole (which is located at 76.6°W, 49.6°N) that fits the fault system in

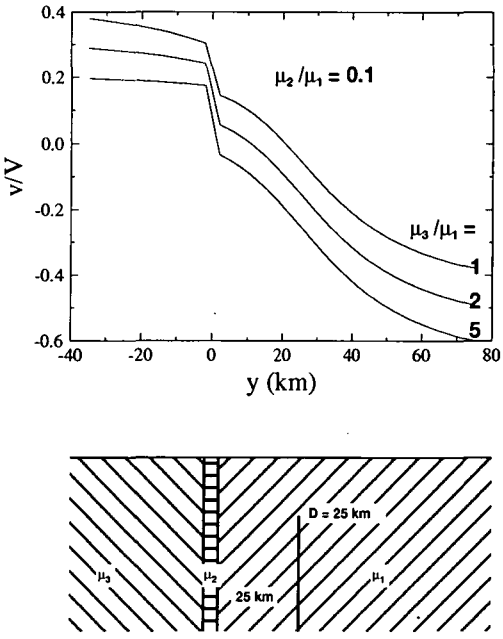

Figure 6.10: Normalised velocity v as a function of distance from the San Andreas fault for a half-space model in the case where the plate boundary is offset from the trace of the principal transform fault. The half-space is made up of two quarter-spaces separated by a 4 km wide fault zone, all with different rigidities. The heavy vertical line (lower plot) represents the plate boundary which slips at rate V. [From *Lisowski et al.*, 1991].

central California. The VLBI velocity gradients were consistent with the model although the agreement would have been improved by a translation of the model origin roughly 20 km to the northeast (Figure 6.13). The results suggest that, in terms of present day tectonic motion, the fault zones east of the bay may be more significant than the San Andreas fault itself. The VLBI results were best explained by the models with a driving rate of 48 mm/yr although models with values of 56 and 41 mm/yr could not be ruled out [*Kroger et al.* 1987].

In the central San Francisco bay region, along the Hayward and Calaveras faults, the lack of strain accumulation in the crust adjacent to the faults was modelled by rigid block motion with a slip rate of 7 $\pm$ 1 mm/yr across both faults [*Prescott et al.*, 1981]. Half of the Calaveras fault slip was distributed over a 5-km wide zone to account for the inelastic deformation of weak, near-surface material. Small trilateration networks from the San Francisco peninsula and networks further south were used to model the deformation of the San Andreas fault on the peninsula [*Prescott et al.*, 1981]. The simplest model, a single screw dislocation in an elastic half space, yielded a slip rate of 12.2 mm/yr at a depth of 6.7 km. However, in order

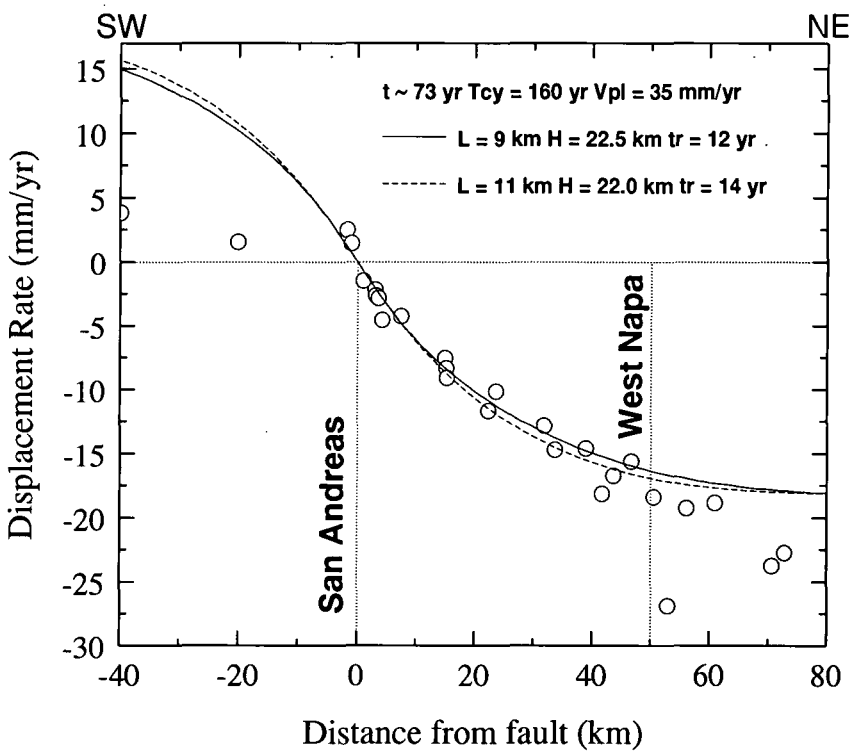

Figure 6.11: Comparison of theoretical displacement rate profiles from the base-traction model [*Li and Rice*, 1987] to geodetic results [*Prescott and Yu*, 1986]. t, time since last earthquake, T_{cy}, earthquake repeat time; V_{pl}, plate boundary velocity; L, fault locking depth; H, elastic plate thickness; t_r, relaxation time.

to obtain this *Prescott et al.* [1981] assumed that the network at the southern end of the peninsula was sufficiently broad to encompass all of the deformation from the San Andreas fault. If, however, the velocity at 20 km from the fault is constrained to be half of the total velocity of 12.2 mm/yr across the 40-km wide network, then a slip rate of 16.8 mm/yr at a depth of 9.2 km is obtained. This is more consistent with estimates of the thickness of the brittle crust from earthquake hypocentres and geologic slip rates for the peninsula. Best-fit models for a distributed shear zone at depth below the San Andreas fault were also calculated. The data are most consistent with a concentration of slip at depth near the San Andreas fault. A larger data set was used to address the problem of strain accumulation along the Hayward and Calaveras faults [*Prescott and Lisowski*, 1983]. After correcting for line-length changes due to surface creep, the strain accumulation rate was calculated and found to be below that of other areas along the fault system, suggesting that a large part of the strain in the area is being relieved by creep. However, the Hayward fault has ruptured in two moderate earthquakes (M $\sim$ 6.8) within the last century which indicates that strain is accumulating.

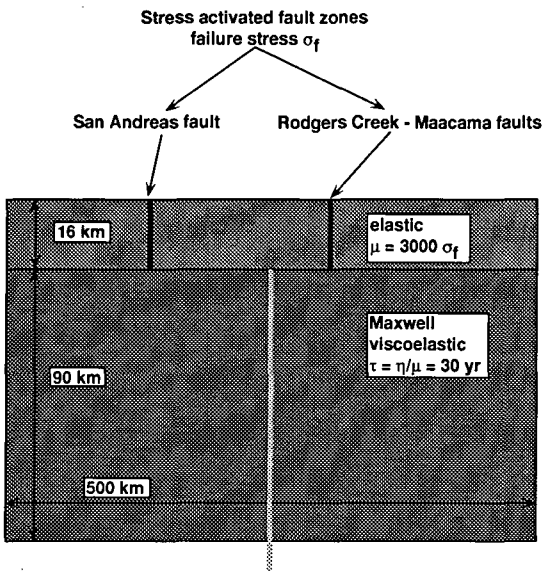

Figure 6.12: Schematic diagram of the "out of plane", two-dimensional, finite-element model of the San Andreas fault [*Kroger et al.*, 1987]. Kinematic parameters are the rates of far-field boundary displacement. Geometric parameters control the number and activity of faults. Light-grey line shows the axis of the basal flow boundary and origin of the model. The stress and time scales are governed by the choices of rheological parameters. Modified from *Kroger et al.* [1987].

Using trilateration data across the San Francisco bay and the measured creep rate at the Hayward fault trace, a model of a fault in frictional contact implied a depth of 5 $\pm$ 1 km for the creeping zone (Figure 6.14) [*Savage and Lisowski*, 1993; *Weertman*, 1964].

The relative block motion and aseismic slip rates along the San Andreas fault system in the Hollister area were estimated by *Thatcher* [1979], *Savage et al.* [1979] and *Matsu'ura et al.* [1986]. Data included triangulation, trilateration and one astronomical azimuth over the interval 1885 to 1976, trilateration data from the Hollister network surveyed by the USGS 1971-1978 and additional trilateration observations between 1978 and 1983. In this region the Calaveras fault diverges from the San Andreas and the fault system was approximated to three-dimensional fault geometries. The data were used to invert for slip rates on vertical, strike-slip segments divided into shallow and deep slip zones [*Thatcher*, 1979; *Savage et al.*, 1979]. A Bayesian inversion procedure to invert the geodetic data allows more parameters such as slip angle, dip angle, locking depth and rigid-block velocities to be resolved in addition to the usual slip rate [*Matsu'ura et al.*, 1986]. Block motion was well resolved in the inversion and agreed well with geological observations of long-term slip rates.

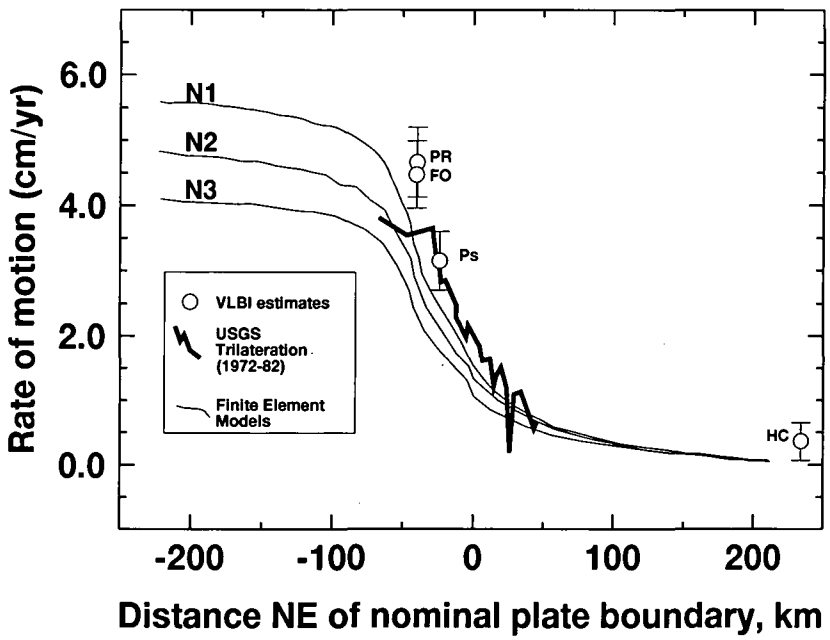

Figure 6.13: Comparison of predicted displacements from the northern California finite-element models [*Kroger et al.*, 1987] with geodetic data [*Prescott and Yu*, 1986] and VLBI results. PR, Point Reyes, FO, Fort Ord, Ps, Presidio, HC, Hat Creek. VLBI results and model plots are relative to stationary North America (neglecting Basin and Range activity) and the VLBI station OVRO respectively. From *Kroger et al.* [1987].

Two models for the whole San Francisco bay region have been studied. A regional dislocation model was used to test the hypothesis that the Hayward fault was locked at depth as opposed to creeping [*Lienkaemper et al.*, 1991]. The velocities predicted were compared with the observed velocities from the San Francisco bay trilateration network [*Lisowski et al.*, 1991]. The slip rates used in the model were derived from geological slip rates, historical creep rates and previous geodetic results. The fit from the models was good near the Hayward fault but the velocities were underestimated near the edges of the network. The excellent fit close to the Hayward fault was a consequence of the model coordinate solution used to calculate the velocities [*Segall and Mathews*, 1988]. In such a solution the velocities are calculated relative to the centre of mass of the network, and in the San Francisco bay network this is close to the Hayward fault. Since the observed and calculated velocities are relative to the same centre of mass, and misfit to the data will increase with distance from this point, the velocities should show good agreement in this region so long as reasonable estimates of the slip rate are used. From a total of 63 observation stations, 60 gave nearly identical velocities ($\pm$ 0.6 mm/yr) for the two

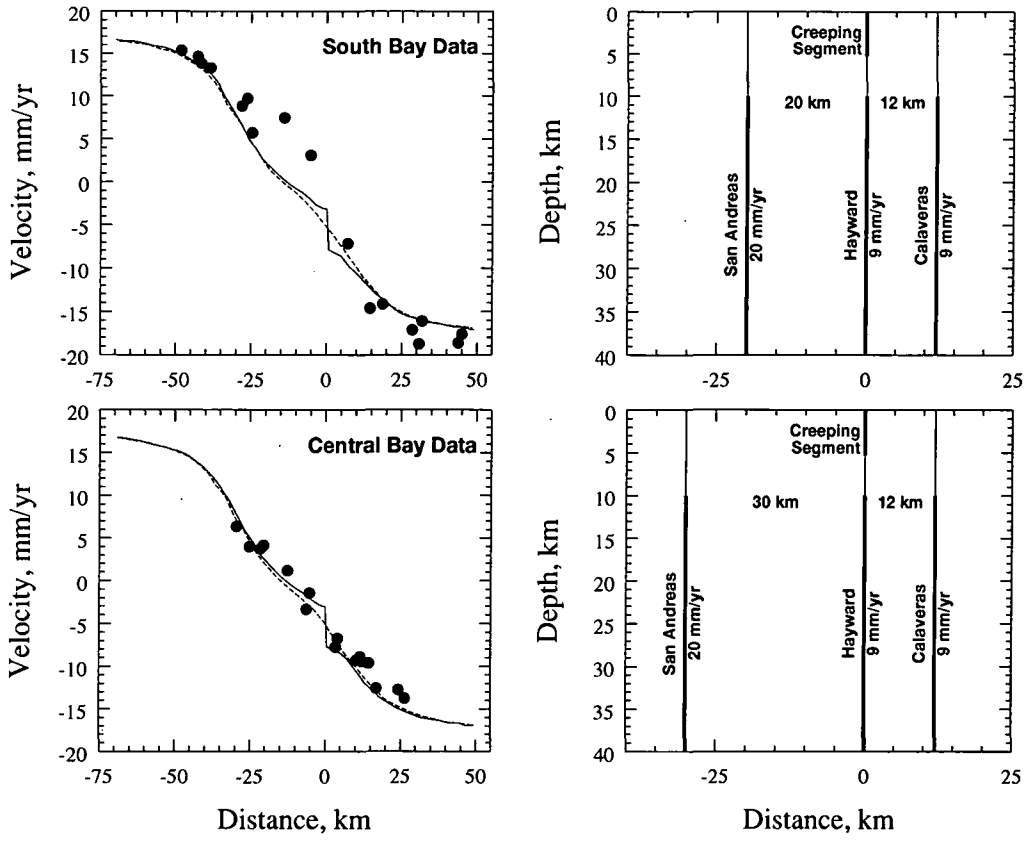

Figure 6.14: Comparisons of predicted displacements for the central and southern San Francisco bay with geodetic data [*Lisowski et al.*, 1991]. Right-hand plots show model cross-sections showing the San Andreas, Hayward and Calaveras faults. The deeper segments of the faults indicated by heavy lines are modelled as slipping continuously at the rates indicated. The surface creeping segment of the Hayward fault is also indicated by a heavy line. Continuous lines in left-hand plots show the predicted profiles with (solid line) and without (dashed line) fault creep on the Hayward fault. Adapted from *Savage and Lisowski* [1993].

hypotheses (locked and unlocked fault at depth). For the three that did not agree, the locked hypothesis provided a marginally better fit to the observed velocities.

The second model for the whole San Francisco bay region explored the relationship of fault zone connectivity to slip rates on faults [*Bilham and Bodin*, 1992]. Faults were modelled as vertical, frictionless dislocations in an elastic plate of uniform thickness. This plate was subjected to antisymmetric displacements that were consistent with the azimuth and rate of the inferred local plate vector. Boundary-element methods [*Crouch and Starfield*, 1989] were used to determine the slip rate along each fault that would minimise within-plate stresses. The calculated slip distribution depended on the way the fault segments were connected (Figure 6.15). The geological slip rates of faults in the San Francisco bay region were most con-

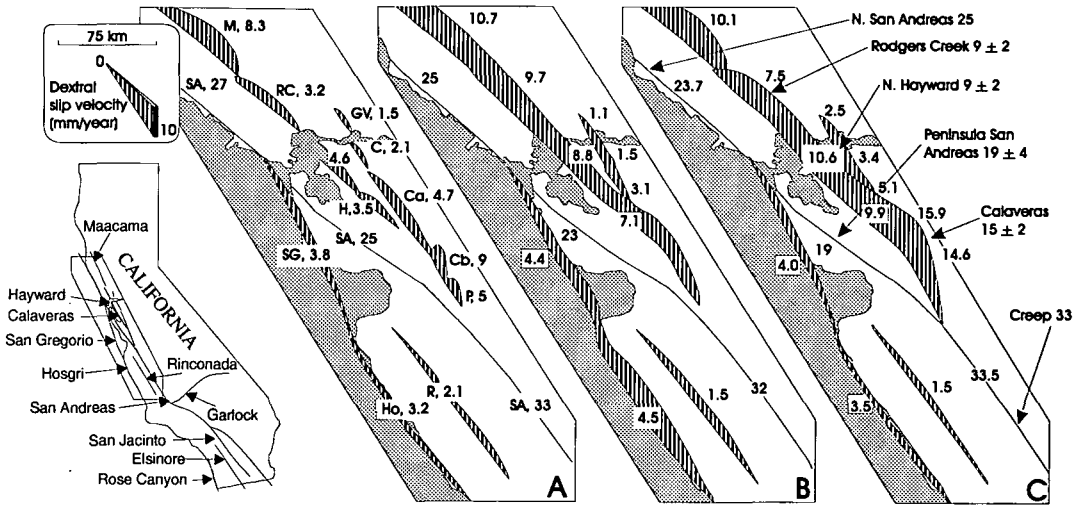

Figure 6.15: The California plate boundary showing fault zones and boundary-element models for slip in the bay region (inset). Faults: M, Maacama; RC, Rodgers Creek; H, Hayward; SG, San Gregorio; Ho, Hosgri; R, Rinconada; SA, San Andreas; GV, Green Valley; C, Concord; Ca, Northern Calaveras; Cb, Central Calaveras; P, Pacines. Shaded regions show variations of slip rates estimated from the boundary-element models. Rates on the San Andreas fault are indicated but not drawn to avoid obscuring the eastern faults. Slip rates lower than observed characterise the isolated faults shown in (A). Increased fault zone connectivity modelled in (B) and (C) results in increased slip rates on the Hayward, Calaveras, and San Gregorio fault zones. The Mission fault links the Hayward and Calaveras faults. (B) and (C) differ only in the connectivity between the Maacama and Hayward fault zones and between the Calaveras and San Andreas fault zones. Values used in estimating probabilities of large earthquakes *WGCEP* [1990] are indicated in the margin to the right of (C). From *Bilham and Bodin* [1992].

sistent with connectivity between the Hayward, Calaveras and San Andreas fault zones (Figure 6.15c).

6.4 Summary

Geophysical observations of coseismic, postseismic and interseismic movements suggest that deformation is cyclic close to the San Andreas fault system and point to a range of mechanical behaviour along the system from fully locked at the surface to freely sliding. Most models of crustal deformation use dislocation theory and prescribe the deformation on the fault plane. Models of dislocation with two- and three-dimensional geometries in an elastic half space have been developed to include the effects of a more realistic Earth model. However, these models are restricted

by their semiempirical nature. A second class of models relate crustal movements to tectonic loading of the lithospheric plates. These are restricted to simple, two-dimensional structures because of the increase in mathematical complexity. The orientation of near-fault strain, together with geological evidence shows that the faulting is dominated by vertical geometries. Surface deformation is therefore most appropriately modelled by structures whose geometries are vertical and whose locking depths are much less than the elastic-layer thickness.

Despite advances in modelling, the analysis of actual observations is still mostly based upon the simplest assumption of an isotropic, homogeneous half space with a simple fault configuration. Most models developed for the San Francisco bay region are based on two-dimensional dislocation models in an elastic half space. Other modelling approaches for this region include base-traction, finite-element, three-dimensional dislocation, and boundary-element models.

Chapter 7

Modelling the Deformation

7.1 Introduction

The discussions in the previous chapters suggest that most of the interseismic deformation occurring in the San Francisco bay region can be explained by continuous relative motion between crustal blocks in the presence of stick-slip resistance in the upper, brittle zone. In addition, since the geodetic data provide no evidence of velocity variations with time, modelling may be restricted to elastic half space Earth models. However, I do not imply that the whole Earth really is elastic but only that for the present data set there is not necessarily a difference, from a kinematic, observational standpoint, between purely elastic models and those with viscous elements.

7.2 The Fundamental Model

I assume that the observed, surface deformation is due entirely to strain accumulation on right-lateral, vertical, strike-slip faults in an elastic half-space (Figure 7.1). Beneath some locking depth, D, which may be the base of the surface, brittle layer, continuous aseismic slip (hereinafter known as "slip at depth" or "deep slip") occurs on a downward continuation of the fault at a rate that is invariant over the geodetic observation period. Above this, the fault segment is either fully locked to the surface (Figure 7.1C) or locked to the base of a shallow surface creeping zone (Figure 7.1A). A shallow, surface creeping zone is included in the model where continuous fault slip at the surface ("surface creep") is observed at the fault trace. If this surface creeping zone extends throughout the brittle layer to the locking depth, slip on the fault is accommodated wholly by continuous slip and only small

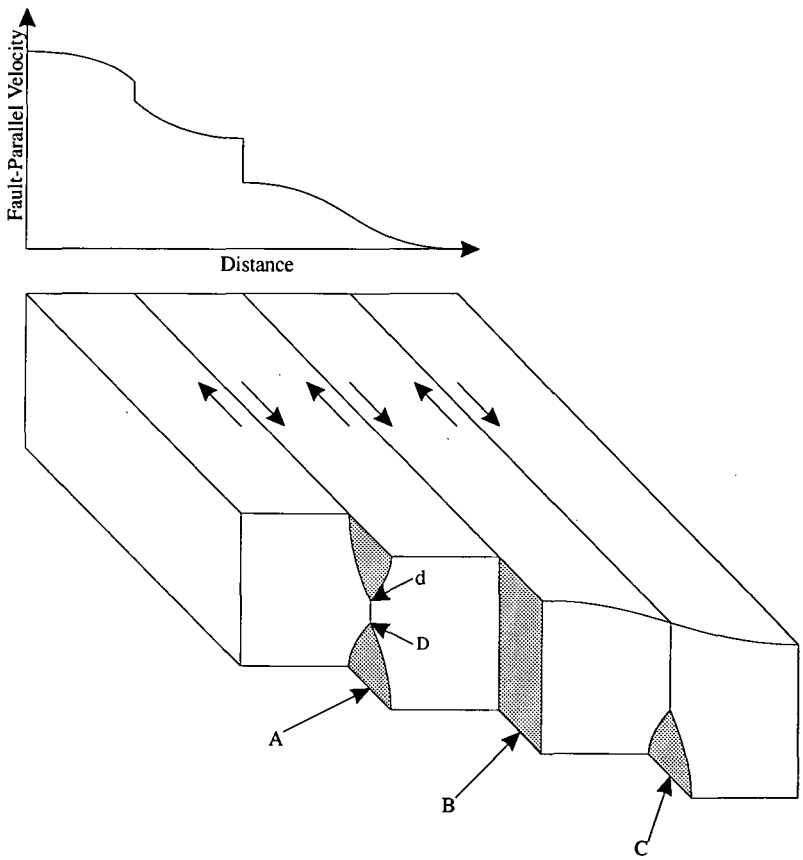

Figure 7.1: Schematic diagram for strike-slip faulting modes. (A) Fault is freely slipping in a shallow, surface creep zone to a depth d, and freely slipping beneath some locking depth D. The fault-parallel velocity profile shows some strain accumulation together with an offset at the fault trace. (B) Fault is slipping freely throughout the brittle layer (rigid block motion). The fault-parallel velocity field shows an offset at the fault trace. (C) Fault is freely slipping beneath some locking depth and locked up to the surface. The fault-parallel velocity field shows the effects of elastic-strain accumulation.

amounts of elastic strain may accumulate (Figure 7.1B). This is thought to occur on the San Andreas fault between Parkfield and San Juan Bautista (Figure 1.2). However if the surface creeping zone is confined to shallow depths ($d < D$, where d is the depth to which the shallow surface creeping zone extends) the fault is locked at mid-crustal depths and accumulates strain.

Formulae for the displacement fields due to slip on finite and infinite fault planes (and shear zones) in an elastic half-space have been given in Chapter 6. In these equations the slip rate $\dot{b}$ is related to a component of velocity, v, at some point (e.g., the horizontal velocity parallel to the strike of the fault plane) by

$$v = \dot{b}U, \tag{7.1}$$

where U is a function of the spatial orientation of the fault plane and the position of the observation point. For the more complicated case where n stations are affected by a system consisting of m fault segments then the velocity of the i^{th} station is

$$v^i = \sum_{k=1}^{m} \dot{b}_k U_k^i. \tag{7.2}$$

Equation (7.2) may be represented as a linear matrix equation of the form

$$\mathbf{v} = \mathbf{U}\mathbf{b}, \tag{7.3}$$

where the velocity vector $\mathbf{v}$ is a $n \times 1$ column vector, $\mathbf{U}$ is an $n \times m$ matrix of functions that are calculated from the fault geometries, and $\mathbf{b}$ is an $m \times 1$ column vector whose values are the slip rates along the m fault segments. Once the position and size of each active fault segment has been specified, the site motions are exact linear functions of the slip rates on each fault segment.

Measured geodetic data (e.g., trilateration, triangulation and GPS) are linear trigonometrical functions of the point motions,

$$\mathbf{d} = \mathbf{A}\mathbf{v}, \tag{7.4}$$

where $\mathbf{d}$ is an $n \times 1$ column vector of the measured geodetic data and $\mathbf{A}$ is an $n \times n$ matrix of trigonometric functions that are dependent on the type of geodetic measurement. Equations (7.3) and (7.4) can be combined to link the observations and model by

$$\mathbf{d} = \mathbf{G}\mathbf{b}, \tag{7.5}$$

where $\mathbf{G}$, the displacement matrix, is the product of the two matrices $\mathbf{A}$ and $\mathbf{U}$.

Two approaches may be adopted towards modelling the deformation. The first is the forward (or simulation) approach. All model parameters are obtained from independent geological and geophysical investigations and are held fixed. This approach is not intended to fit rigorously the geodetic data but rather to test the agreement of independent estimates of the model parameters with the geodetic data. Second, the geodetic data may be inverted to estimate slip rates. This inverse problem has the desirable property of being linear and can thus be solved using a classical least squares procedure.

Many features of the observed surface deformation may be reproduced using a simple, two-dimensional model with one axis vertical and the other normal to the general strike of the faults. This approach considers fault configurations which

are infinitely long, parallel and which neglect along-strike variations. Only the fault-parallel component of velocity is calculated, and the fault-normal component is assumed to be zero. Whilst the fault-normal velocity components (Figure 5.6 to 5.9) are indeed very small, the fault-parallel components do show along-strike variation between the subregions as the fault system changes from being single-fault dominated in the south to being dominated by three principal faults in the north (Figure 1.2). In order to account for this, either separate, two-dimensional models for each subregion, or a regional dislocation model using three-dimensional fault geometries must be used.

Two-dimensional models are both mathematically and geometrically simple and the inverse problem is over-determined and easy to formulate. Furthermore, the effects of additional complexities such as structural inhomogeneities are relatively straightforward to test. A three-dimensional model, whilst able to model best all the components of motion, requires many fault segments, including ones situated outside of the study region, in order to model locally-significant fault complexities and to eliminate edge effects. Inverting the geodetic data for model parameters using a three-dimensional model is an ill-conditioned (or mixed-determined) problem since, in most cases, the stations are unevenly distributed and relatively sparse, the data noisy, and there are many parameters to estimate. A mixed-determined, linear inverse problem can be reduced to an over-determined problem by the inclusion of a-priori model parameters [*Jackson*, 1979; *Menke*, 1984].

Both two-dimensional and three-dimensional models are used here. Forward and inverse models are first produced for the four subregions using the two-dimensional approach. The results from this work are then used as prior parameters (i.e., fixed) in a forward, three-dimensional model and as a-priori parameters (i.e., initial values) in an inverse, three-dimensional model.

7.3 The Two-Dimensional Models

7.3.1 The Data

In order to minimise along-strike variations, the San Francisco and Monterey bay regions are divided into four subregions (Figure 5.5) for the purpose of modelling. Two-dimensional models only predict the fault-parallel velocity component and the

appropriate data are therefore the fault-parallel relative velocities (Figures 5.6 to 5.9). Along-strike variations in relative motion within a subregion would appear as departures from the overall trend. Such variation is absent in all but the Monterey-bay subregion indicating no major changes in fault behaviour within the three most northerly subregions. Greater variation is to be expected in the Monterey-bay subregion since it spans the junction of the Calaveras and San Andreas faults. For this reason the Monterey-bay subregion has been further split into three parts, the northern, central and southern Monterey-bay subregions.

The fault-parallel velocities relative to the VLBI site OVRO, in the Owens Valley (Figure 1.3) are used, in preference to velocities relative to some point within the fault system, to help constrain the far-field motion to the east of the fault system. An additional hypothetical point situated $\approx$ 150 km to the west of the fault system and moving at 35 $\pm$ 2 mm/yr is used to constrain the far-field motion to the southwest. For a locking depth of around 10-12 km, 95% of the maximum relative velocity due to slip at depth on the San Andreas fault system is expected to occur between points at distances of x from the fault system, where $x = \pm 12.7D$, where D is the fault locking depth, i.e., $x = \pm 127$ to 191 km.

7.3.2 Model Parameters

7.3.2.1 Faults and Fault Geometries

The distribution of seismicity in the San Francisco bay region (Figure 1.12) reveals many active faults. To simplify the model only faults which have time-averaged slip rates that exceed 1 mm/yr are used (class A and AA faults [*Matsuda*, 1975]). In the San Francisco bay region, class A and AA faults are the San Gregorio, San Andreas, Hayward, Rodgers Creek, Calaveras, Concord and Green Valley faults.

The strike of the faults in the San Francisco bay region is constrained in the modelling to be N33°W. This direction is consistent with the strikes of the San Andreas fault northwards from the San Francisco peninsula and the Hayward and Rodgers Creek faults and almost parallel with the strike of the southern Calaveras fault. It is also consistent with the direction of predicted motion of the Pacific plate with respect to the North American plate from the NUVEL-1A plate-motion model and with the cumulative geologic slip vector across the fault system [*Kelson et al.*, 1992]. The fault segments are assumed to be located beneath their mapped surface

traces. Where a fault strike deviates substantially from N33°W such that its assumed location is substantially inaccurate, then a position for that fault is chosen that is optimum for the stations closest to the fault.

7.3.2.2 Slip Rates

Slip-rate estimates are made from the ages of offset geological features, the record of large historical earthquakes, previous results from geodetic measurements, data from creep-meters and offset cultural features (Sections 1.3.3, 1.1.5 and Chapter 2). These estimates are divided into those that indicate surface creep and those that indicate the slip rate at depth. For this simple, time-invariant model, geological slip-rate estimates which are averaged over many earthquake cycles are assumed to represent the deep-slip rate. Estimates from inversions of previous geodetic data where rigid block motion is assumed are interpreted either as surface creep rates or lower-bound, long-term slip rates, depending on whether significant surface creep on the fault occurs or not.

A compilation of published slip-rate estimates is given listed in Table 7.1 and they are plotted as a function of distance along the individual faults which are assumed to strike at N33°W in Figure 7.2. These slip rates, in particular the surface-creep rates, appear to vary systematically along-strike rather than randomly and therefore polynomials were fitted through the data. The number of polynomial terms used was minimised by using only terms that are significant i.e., the number of polynomial terms was increased until the reduction in the misfit between the polynomial and the data was not significant at the 1σ (68.3% confidence) level. These polynomials are not based on any physical model and are simply used empirically to quantify these rates.

For each subregion, appropriate values that reflect the surface creep and long-term slip rates were calculated by taking the mean, within each subregion, of the polynomial fit. However there is one exception to this. The polynomial fit to the surface creep-rate data along the San Andreas fault is a line with zero slope and intercept of 0.6 mm/yr (Figure 7.2). Considerably more surface creep is detected along the San Andreas fault to the south of San Juan Bautista (at distances of -55 to 0 km, Figure 7.2) [*Burford and Harsh*, 1980] and therefore the surface creep rates for the Monterey-bay subregion are derived from the mean of those slip-rate data rather than the polynomial fit. For faults where the surface creep rate is less than 1 mm/yr the fault is assumed to exhibit no creep and the value is set

Table 7.1: Geologic and surface-creep rate information for the San Francisco bay region compiled from various sources. Start and end coordinates represent the fault extent over which the slip-rate estimate applies. If no end coordinates are specified then the slip-rate estimate applies to a single point on the fault.

		Start	Start	End	End			
		Longitude	Latitude	Longitude	Latitude	Slip		
Fault	Code	(°W)	(°N)	(°W)	(°N)	(mm/yr)	Type	Source
Antioch	ANT01	121:47:31	37:59:05			1.7 ± 1.7	SC:al. ar.	*Galehouse*, 1992a, b
Antioch	ANT02	121:48:25	37:59:54			0.3 ± 0.3	SC:al. ar.	*Galehouse*, 1992a, b
Antioch	ANT03	121:50:38	38:02:03			0.0 ± 0.0	LT	*Kelson et al.*, 1992
Antioch	ANT04	121:50:38	38:02:03			0.0 ± 0.0	SC	*Kelson et al.*, 1992
Concord	CON01	122:01:44	37:57:42			3.5 ± 0.1	SC:al. ar.	*Galehouse*, 1992a, b
Concord	CON02	122:02:20	37:59:06			2.6 ± 0.1	SC:al. ar.	*Galehouse*, 1992a, b
Green Valley	GVA01	122:05:00	38:10:00			5.0	LT,gl	*Frizzell and Brown*, 1976
Green Valley	GVA02	122:08:02	38:11:19			5.5 ± 0.3	SC:al. ar.	*Galehouse*, 1992a, b
Greenville	GRE01	121:36:50	37:37:43			0.6 ± 0.1	LT,gl	*Kelson et al.*, 1992
Hayward	HAY01	121:55:05	37:29:15	121:55:44	37:30:23	4.0 ± 0.5	SC:various	*Lienkaemper et al.*, 1991
Hayward	HAY02	121:56:31	37:29:56			-0.7 ± 0.2	SC:al. ar.	*Galehouse*, 1992a, b †
Hayward	HAY03	121:55:00	37:30:00	122:07:42	37:44:00	9.0 ± 2.0	LT:various	*WGCEP*, 1990
Hayward	HAY04	121:55:44	37:30:23	121:57:38	37:32:32	9.0 ± 0.5	SC:various	*Lienkaemper et al.*, 1991
Hayward	HAY05	121:58:41	37:31:48			4.9 ± 0.1	SC:al. ar.	*Galehouse*, 1992a, b
Hayward	HAY06	121:57:38	37:32:32	121:58:14	37:33:08	5.1 ± 0.5	SC:various	*Lienkaemper et al.*, 1991
Hayward	HAY07	121:58:14	37:33:08	121:59:22	37:34:51	5.4 ± 0.5	SC:various	*Lienkaemper et al.*, 1991
Hayward	HAY08	121:59:22	37:34:51	122:06:53	37:42:24	5.8 ± 0.5	SC:various	*Lienkaemper et al.*, 1991
Hayward	HAY09	122:00:54	37:34:51			4.6 ± 0.1	SC:al. ar.	*Galehouse*, 1992a, b
Hayward	HAY10	122:01:01	37:36:30	122:21:56	38:00:11	9.0 ± 2.0	LT:estimate	*Lienkaemper et al.*, 1991
Hayward	HAY11	122:01:01	37:36:30	122:21:56	38:00:11	6.8 ± 1.0	LT,gd:rbm	*Prescott et al.*, 1981
Hayward	HAY12	122:04:33	37:39:04			4.6 ± 0.1	SC:al. ar.	*Galehouse*, 1992a, b
Hayward	HAY13	122:05:38	37:40:19			4.8 ± 0.1	SC:al. ar.	*Galehouse*, 1992a, b
Hayward	HAY14	122:06:53	37:42:24	122:07:28	37:43:28	6.6 ± 0.5	SC:various	*Lienkaemper et al.*, 1991
Hayward	HAY15	122:07:28	37:43:28	122:09:35	37:45:53	6.2 ± 0.5	SC:various	*Lienkaemper et al.*, 1991
Hayward	HAY16	122:07:42	37:44:00	122:25:00	38:07:00	9.0 ± 2.0	LT:various	*WGCEP*, 1990
Hayward	HAY17	122:09:35	37:45:53	122:11:18	37:47:41	4.0 ± 0.5	SC:various	*Lienkaemper et al.*, 1991
Hayward	HAY18	122:11:18	37:47:41	122:12:38	37:49:45	4.0 ± 0.5	SC:various	*Lienkaemper et al.*, 1991
Hayward	HAY19	122:12:38	37:49:45	122:14:28	37:51:38	4.7 ± 0.5	SC:various	*Lienkaemper et al.*, 1991
Hayward	HAY20	122:14:28	37:51:38	122:18:07	37:56:14	5.8 ± 0.5	SC:various	*Lienkaemper et al.*, 1991
Hayward	HAY21	122:18:07	37:56:14	122:19:32	37:57:24	6.1 ± 0.5	SC:various	*Lienkaemper et al.*, 1991
Hayward	HAY22	122:19:32	37:57:24	122:21:56	38:00:11	5.6 ± 0.5	SC:various	*Lienkaemper et al.*, 1991
Hayward	HAY23	122:19:55	37:58:04			4.3 ± 0.2	SC:al. ar.	*Galehouse*, 1992a, b
Hayward	HAY24	122:21:56	38:00:11	122:26:42	38:06:04	2.8 ± 0.5	SC:various	*Lienkaemper et al.*, 1991
Maacama	MAC01	123:21:00	39:25:00			5.0	SC:al. ar.	*Galehouse*, 1992a, b
Mission	MIS01	121:48:54	37:27:06	122:01:01	37:36:30	9.0 ± 2.0	tr. jun. ki	*Andrews et al.*, 1993
N. Calaveras	NCA01	121:48:54	37:27:06			8.0 ± 2.0	LT,gl	*Kelson et al.*, 1992
N. Calaveras	NCA02	121:49:43	37:29:48	122:00:00	37:48:04	7.0 ± 1.0	LT,gd:net	*Prescott et al.*, 1981
N. Calaveras	NCA03	121:49:43	37:29:48	122:00:00	37:48:04	2.6 ± 0.6	SC,gd:net	*Prescott et al.*, 1981
N. Calaveras	NCA04	121:58:19	37:45:51			0.2 ± 0.1	SC:al. ar.	*Galehouse*, 1992a, b
Rodgers Creek	RCR01	122:25:00	38:07:00	122:45:00	38:30:00	9.0 ± 2.0	LT:various	*WGCEP*, 1990
Rodgers Creek	RCR02	122:32:42	38:16:12			0.0 ± 0.0	SC:al. ar.	*Galehouse*, 1992a, b
Rodgers Creek	RCR03	122:32:00	38:17:00			2.1 - 5.8	LT,gl:min	*Budding et al.*, 1991
Rodgers Creek	RCR04	122:41:52	38:26:09			0.0 ± 0.0	SC:al. ar.	*Galehouse*, 1992a, b
Rodgers Creek	RCR05	122:43:00	38:30:00			8.0 ± 2.0	LT,gl	*Kelson et al.*, 1992

Table 7.1: (Continued)

Fault	Code	Start Longitude (°W)	Start Latitude (°N)	End Longitude (°W)	End Latitude (°N)	Slip (mm/yr)	Type	Source
S. Calaveras	SCA01	121:24:14	36:49:28			7.1 ± 0.2	SC:al. ar.	*Galehouse*, 1992a, b
S. Calaveras	SCA02	121:23:53	36:49:49	121:48:54	37:27:06	7.0 ± 1.0	LT,gd:rbm	*Prescott et al.*, 1981
S. Calaveras	SCA03	121:23:53	36:49:49	121:48:54	37:27:06	17.0 ± 2.0	LT,gd:rbm	*Savage et al.*, 1979
S. Calaveras	SCA04	121:23:53	36:49:49	121:48:54	37:27:06	14.4 ± 2.2	LT,gd:in.5	*Savage et al.*, 1979
S. Calaveras	SCA05	121:23:53	36:49:49	121:48:54	37:27:06	14.9 ± 1.8	SC,gd:in.5	*Savage et al.*, 1979
S. Calaveras	SCA06	121:23:53	36:49:49			12.0 ± 3.0	LT,gl	*Kelson et al.*, 1992
S. Calaveras	SCA07	121:25:00	36:50:00	121:48:00	37:28:00	15.0	Speculation	*Herd*, 1979
S. Calaveras	SCA08	121:25:01	36:50:45			11.4 ± 0.2	SC:al. ar.	*Galehouse*, 1992a, b
S. Calaveras	SCA09	121:24:30	36:52:00	121:27:00	36:56:30	13.0 ± 10.0	LT,gd:in.6	*Matsu'ura et al.*, 1986
S. Calaveras	SCA00	121:24:30	36:52:00	121:27:00	36:56:30	19.0 ± 10.0	SC,gd:in.6	*Matsu'ura et al.*, 1986
S. Calaveras	SCA11	121:27:00	36:56:30	121:30:00	37:02:00	13.0 ± 3.0	LT,gd:in.12	*Matsu'ura et al.*, 1986
S. Calaveras	SCA12	121:30:00	37:00:00			15.0	SC	*Nason*, 1971
S. Calaveras	SCA13	121:35:00	37:08:00			1.4 - 7.1	LT,gl:min	*Nakata*, 1977
S. Calaveras	SCA14	121:43:00	37:22:00			9.4 ± 0.4	LT,gd:net	*Prescott et al.*, 1984
S. Calaveras	SCA15	121:18:00	36:42:00	121:24:30	36:52:00	13.0 ± 2.0	LT,gd:in.0	*Matsu'ura et al.*, 1986
S. Calaveras	SCA16	121:18:00	36:42:00	121:24:30	36:52:00	-5.0 ± 5.0	SC,gd:in.0	*Matsu'ura et al.*, 1986
S. Calaveras	SCA17	121:25:48	36:54:36	121:32:24	37:06:00	14.0 ± 3.0	SC,gd:in.15	*Thatcher*, 1979
S. Calaveras	SCA18	121:21:36	36:46:48	121:27:00	36:54:00	12.0 ± 1.0	SC,gd:in.15	*Thatcher*, 1979
S. Calaveras	SCA19	121:08:24	36:36:00	121:21:36	36:46:48	13.0 ± 3.0	SC,gd:in.15	*Thatcher*, 1979
San Andreas	SAN01	119:49:36	35:16:18			33.0 - 37.0	LT,gl	*Clark et al.*, 1984
San Andreas	SAN02	121:10:24	36:34:54			30.0 - 39.0	LT,gl	*Clark et al.*, 1984
San Andreas	SAN03	121:13:00	36:38:30	121:18:00	36:42:00	37.0 ± 3.0	LT,gd:in.11	*Matsu'ura et al.*, 1986
San Andreas	SAN04	121:13:00	36:38:30	121:18:00	36:42:00	17.0 ± 9.0	SC,gd:in.11	*Matsu'ura et al.*, 1986
San Andreas	SAN05	121:18:00	36:42:00	121:33:00	36:51:00	25.0 ± 3.0	LT,gd:in.11	*Matsu'ura et al.*, 1986
San Andreas	SAN06	121:18:00	36:42:00	121:33:00	36:51:00	11.0 ± 5.0	SC,gd:in.11	*Matsu'ura et al.*, 1986
San Andreas	SAN07	121:28:16	36:48:14			22.0 ± 6.0	LT,gl	*Kelson et al.*, 1992
San Andreas	SAN08	121:28:16	36:48:14			11.0 ± 3.0	SC	*Kelson et al.*, 1992
San Andreas	SAN09	121:29:52	36:48:23			14.5 ± 1.3	SC:al. ar.	*Galehouse*, 1992a, b †
San Andreas	SAN10	121:32:45	36:50:11			-0.4 ± 0.3	SC:al. ar.	*Galehouse*, 1992a, b †
San Andreas	SAN11	121:33:00	36:51:00	121:40:00	36:56:00	26.0 ± 3.0	LT,gd:in.9	*Matsu'ura et al.*, 1986
San Andreas	SAN12	121:33:00	36:51:00	121:40:00	36:56:00	0.0 ± 6.0	SC,gd:in.9	*Matsu'ura et al.*, 1986
San Andreas	SAN13	121:18:00	36:42:00	122:33:00	36:51:00	13.0 ± 2.0	LT,gd:rbm	*Savage et al.*, 1979
San Andreas	SAN14	121:18:00	36:42:00	122:33:00	36:51:00	22.2 ± 3.1	LT,gd:in.5	*Savage et al.*, 1979
San Andreas	SAN15	121:18:00	36:42:00	122:33:00	36:51:00	8.9 ± 1.5	SC,gd:in.5	*Savage et al.*, 1979
San Andreas	SAN16	121:44:00	36:58:00	122:01:00	37:12:00	33.0 ± 1.0	LT,gd:rbm	*Thatcher*, 1979
San Andreas	SAN17	121:44:00	36:58:00	122:01:00	37:12:00	38.0 ± 3.0	LT,gd:in.15	*Thatcher*, 1979
San Andreas	SAN18	121:44:00	36:58:00	122:01:00	37:12:00	33.0 ± 2.0	LT,gd:in.10	*Thatcher*, 1979
San Andreas	SAN19	121:44:00	36:58:00	122:01:00	37:12:00	19.0 ± 4.0	LT:various	*WGCEP*, 1990
San Andreas	SAN20	122:01:00	37:12:00	122:12:00	37:24:00	10.0 - 30.0	LT,gl	*Cummings*, 1968
San Andreas	SAN21	122:01:00	37:12:00	122:11:00	37:20:00	12.2 ± 4.0	LT,gd:net	*Prescott et al.*, 1981
San Andreas	SAN22	122:01:00	37:12:00	122:11:00	37:20:00	21.5 ± 1.3	LT,gd:in.10	*Prescott et al.*, 1981
San Andreas	SAN23	122:01:00	37:12:00	122:11:00	37:20:00	13.3 ± 0.8	LT,gd:in.5	*Prescott et al.*, 1981
San Andreas	SAN24	122:01:00	37:12:00	122:11:00	37:20:00	35.9 ± 2.2	LT,gd:in.20	*Prescott et al.*, 1981
San Andreas	SAN25	122:01:00	37:12:00	122:24:00	37:34:00	26.0 - 32.0	LT,gd:in.14	*WGCEP*, 1990
San Andreas	SAN26	122:01:00	37:12:00	122:11:00	37:20:00	19.0 ± 4.0	LT:various	*WGCEP*, 1990
San Andreas	SAN27	122:11:00	37:20:00	122:24:00	37:34:00	19.0 ± 4.0	LT:various	*WGCEP*, 1990
San Andreas	SAN28	122:12:00	37:24:00	122:30:00	37:40:00	6.0 - 22.0	LT,gl	*Addicott*, 1969

Table 7.1: (Continued)

Fault	Code	Start Longitude (°W)	Start Latitude (°N)	End Longitude (°W)	End Latitude (°N)	Slip (mm/yr)	Type	Source
San Andreas	SAN29	122:17:05	37:26:07			1.0 ± 0.3	SC:al. ar.	*Galehouse*, 1992a, b
San Andreas	SAN30	122:19:54	37:29:18			6.9 - 12.0	LT,gl:min?	*Clark et al.*, 1984
San Andreas	SAN31	122:23:36	37:33:42			31.0 - 48.0	LT,gl:max?	*Clark et al.*, 1984
San Andreas	SAN32	122:23:36	37:33:42			7.1 - 15.2	LT,gl:min?	*Clark et al.*, 1984
San Andreas	SAN33	122:24:00	37:34:00	124:30:00	40:17:00	19.0 ± 4.0	LT:various	*WGCEP*, 1990
San Andreas	SAN34	122:24:00	37:35:00	122:30:00	37:40:00	17.0 ± 10.0	LT,gl:min	*Brown*, 1990
San Andreas	SAN35	122:25:00	37:35:00			>12.0	LT,gl:min	*Hall*, 1984
San Andreas	SAN36	122:25:00	37:35:00			>7.5	LT,gl:min	*WGCEP*, 1990
San Andreas	SAN37	122:26:56	37:36:42			-0.1 ± 0.0	SC:al. ar.	*Galehouse*, 1992a, b
San Andreas	SAN38	122:46:01	38:02:36			0.7 ± 0.1	SC:al. ar.	*Galehouse*, 1992a, b
San Andreas	SAN39	122:45:00	38:05:00			24.0 ± 3.0	LT,gl:min	*Niemi and Hall*, 1992
San Andreas	SAN40	123:45:00	38:50:00			26.0 ± 3.0	LT,gl:max	*Prentice*, 1989
San Andreas	SAN41	123:45:00	38:50:00			1.0 ± 0.1	SC:al. ar.	*Galehouse*, 1992a, b
San Gregorio	SGR01	122:18:12	37:07:06			7.0 -11.0	LT,gl	*Clark et al.*, 1984
San Gregorio	SGR02	122:20:00	37:07:30			6.0 - 11.0	LT,gl	*Weber and Cotton*, 1981
San Gregorio	SGR03	122:20:00	37:07:30			6.3 - 13.0	LT,gl	*Weber and Lajoie*, 1977
San Gregorio	SGR04	122:20:00	37:07:30			1.0	LT,gl	*Hamilton et al.*, 1979
San Gregorio	SGR05	122:21:50	37:14:18			0.0 ± 0.5	SC:al. ar.	*Galehouse*, 1992a, b
San Gregorio	SGR06	122:25:00	37:20:00			0.0 ± 0	SC	*Kelson et al.*, 1992
San Gregorio	SGR07	122:29:16	37:30:24			0.0 ± 0.5	SC:al. ar.	*Galehouse*, 1992a, b
Vacaville	VCA01	121:58:18	38:18:48			0.3 - 4.0	LT,gl	*Clark et al.*, 1984
West Napa	WNP01	122:18:07	38:16:49			0.0 ± 0.4	SC:al. ar.	*Galehouse*, 1992a, b

Codes used in type column: SC - surface-creep rate; al. ar. - alignment array; LT - Long-term; gl - geological; gd - from geodetic data; rbm - assuming rigid block motion across fault; tr. jun. ki. - triple junction kinematics; net - minimum estimate from total measured motion across a geodetic network; min - minimum; in. - from inversion (number after indicates locking depth); max - maximum;

† creep rate estimates obtained after Loma Prieta that may not represent the long-term average.

to 0 mm/yr. Values of less than 1 mm/yr may be attributable to slip at depth rather than surface creep. If the surface-creep rate in a subregion is found to be larger than the deep-slip rate then both the creep and deep-slip rate are set to the mean of the two estimates. It seems unlikely that over a reasonable period of time the surface-creep rate will be larger than the deep-slip rate beneath. Any inconsistencies in the observations are more likely the result of temporal variations (different observational time-spans), measurement noise, or short-term variations that may preceed some tectonic event [e.g., *Galehouse*, 1992a, b]. The average surface-creep rates are used as prior (fixed) surface-creep rates for both the forward and inverse models and the averaged long-term slip rates are used as fixed deep-slip rates for the forward models. The rates used are listed in Table 7.2.

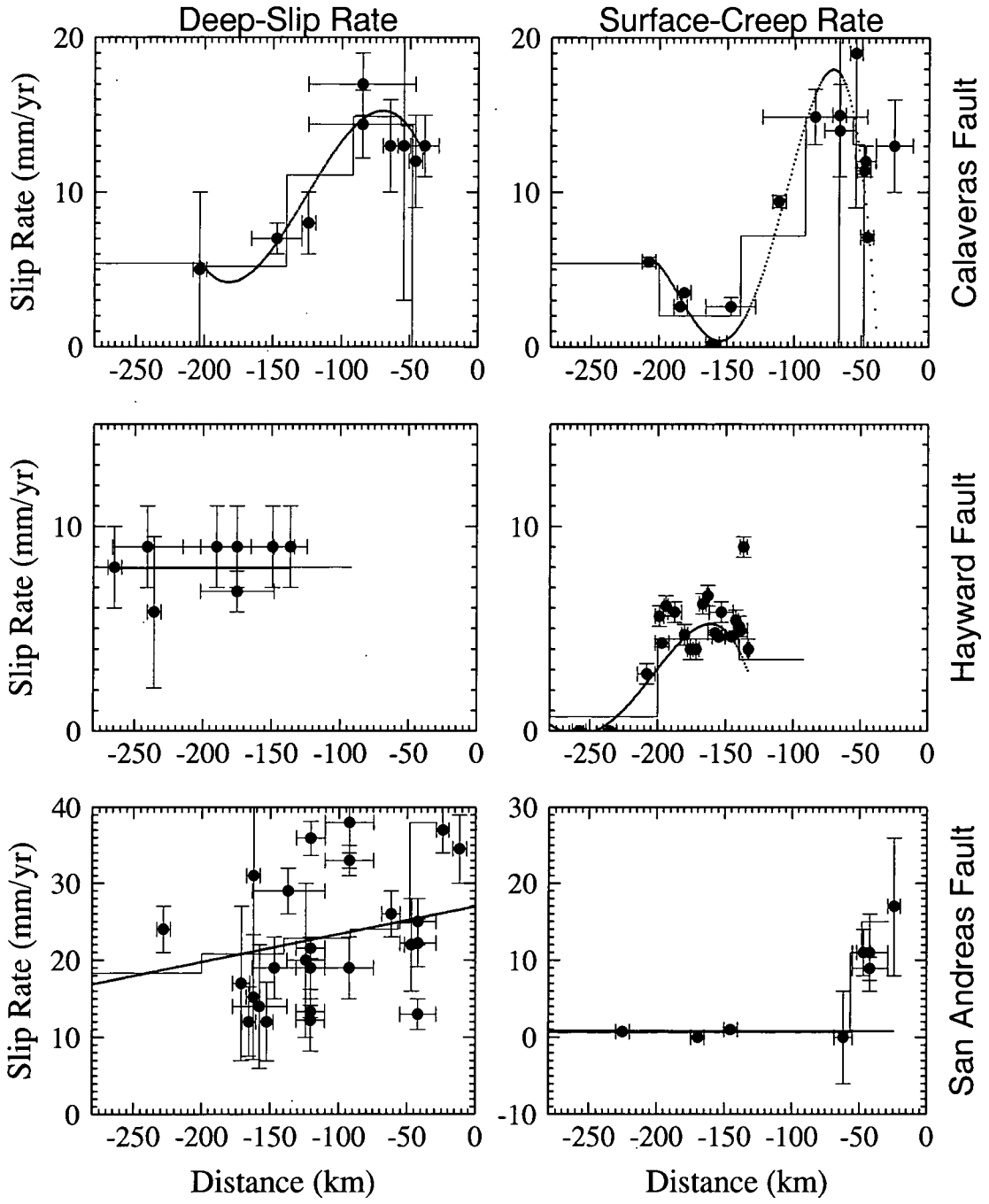

Figure 7.2: Deep-slip and surface-creep rates along the San Andreas, Hayward and Calaveras faults from various sources plotted as a function of distance in the direction N33°W. The origin is the point where each profile crosses 36°N. Vertical bars show ± 1 standard deviation errors. Horizontal bars indicate the projected extent over which the slip-rate estimates apply. Chains of dots represent the minimum-coefficient polynomial fit to the data (see text). Solid lines indicate the slip rates adopted for the four subregions studied in the two dimensional analysis. Chain of dots and solid lines are coincident for the deep-slip rate on the Hayward fault and the surface-creep rate on the San Andreas fault. See Table 7.1 for data.

7.3.2.3 Fault Depths

The depth to the base of the brittle surface layer (the locking depth), where deep slip may be assumed to begin, can be constrained by the distribution of seismicity with depth. Histograms illustrating the depth distributions for well-located events along the major active faults within the area, normalised to percentages, are shown in Figure 7.3. The location of the sampling segments, the sample size and the depth above which 90% of the activity occurs (the 90% depths) are also indicated. The aftershock sequence following the 1989 Loma Prieta earthquake is included in segments SA2 and SA3. There is some evidence that aftershocks propagate down some distance into the quasi-plastic regime [*Sibson*, 1983]. Hence, for segments SA2 and SA3, a depth of 12 km is adopted as a cut-off depth, in agreement with those calculated for other areas. The statistical errors in the 90% depths can be estimated from the sampling frequency in each segment, and they are equal to $d_{90}/\sqrt{n}$ where n is the number of samples in the segment and d_{90} is the 90% depth. The locking depths used for each subregion are also listed in Table 7.2.

The maximum depth to which surface creep extends is harder to constrain. A relation between the creep rate at the surface trace of the fault, the depth to the bottom of the creeping zone, and the rate of stress accumulation on the fault in an elastic half-space was derived by [*Savage and Lisowski*, 1993]. A depth of 5 $\pm$1 km to the base of the creeping zone on the Hayward fault was estimated from the measured surface creep rate (5 mm/yr) and the rate of stress increase on the upper fault trace calculated from a dislocation model based on geodetic measurements in the San Francisco bay region. Similar values (3-5 km) have been proposed for the depth of the creeping zone based on the distribution of microearthquakes along the fault zone [e.g., *Lienkaemper et al.*, 1991]. The depth of creep on other faults within the area has been little investigated. Here the formula of *Savage and Lisowski* [1993] is used to calculate the depth of creep for each fault that exhibits surface creep from the fixed and estimated parameters. The creep-rate distribution with depth is given by

$$\begin{aligned} \dot{s}(z) &= 2\left(\frac{\tau}{\mu}\right)(d^2 - z^2)^{1/2} + \frac{\dot{b}}{\pi}\tan^{-1}\frac{d^2 - Dz}{((D^2 - d^2)(d^2 - z^2))^{1/2}} \\ &+ \frac{\dot{b}}{\pi}\tan^{-1}\frac{d^2 + Dz}{((D^2 - d^2)(d^2 - z^2))^{1/2}}, \end{aligned} \tag{7.6}$$

where τ is the tectonic shear stress imposed by deep slip on adjacent faults, μ is the rigidity of the half-space, $\dot{b}$ is the deep slip rate below the locking depth D on

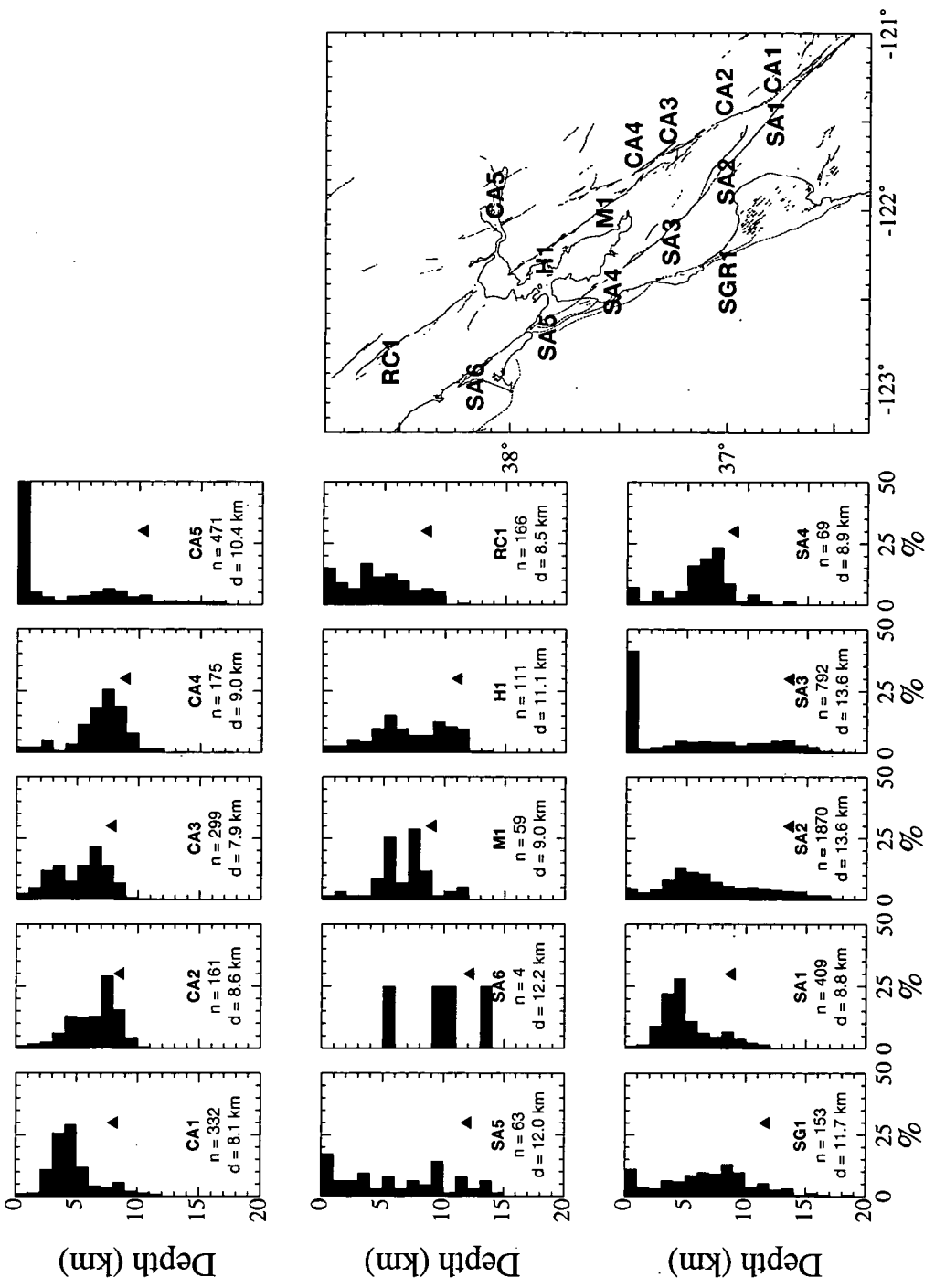

Figure 7.3: Depth distributions of earthquakes in the San Francisco and Monterey bay regions (see map for locations). Bases of solid triangles indicate depths above which 90% of the activity occurs. This depth is specified along with the sample size at the base of each histogram.

Table 7.2: Fixed fault parameters and slip rates for each subregion of the San Francisco bay region

Subregion	Fault	Distance from San Andreas (km)	Deep Slip Rate (mm/yr)	Locking Depth (km)	Creep Rate (mm/yr)
North-Bay					
	San Andreas	0.0	21.9	12.2 ± 6.1	0.0
	Rodgers Creek	33.9	8.0	8.5 ± 0.7	0.0
	Green Valley	64.4	5.4	10.5 ± 0.7	5.4
Central-Bay					
	San Gregorio	-10.3	3.6	11.7 ± 0.9	0.0
	San Andreas	0.0	20.8	10.0 ± 0.9	0.0
	Hayward	29.9	8.0	11.1 ± 1.1	4.5
	Calaveras	44.3	5.2	10.4 ± 0.5	2.0
South-Bay					
	San Gregorio	-20.0	3.6	11.7 ± 0.9	0.0
	San Andreas	0.0	22.8	12.0 ± 1.0	0.0
	Calaveras	32.8	11.1	8.3 ± 0.4	7.2
Monterey-Bay					
	San Gregorio	-48.0	3.6	11.7 ± 0.9	0.0
(Northern part)	San Andreas	0.0	24.0	11.9 ± 0.2	0.0
	Calaveras	17.1	14.9	8.2 ± 0.3	14.9
	San Gregorio	-56.5	3.6	11.7 ± 0.9	0.0
(Central part)	San Andreas	0.0	24.8	11.9 ± 0.2	11.0
	Calaveras	8.2	14.3	8.2 ± 0.3	13.1
	Plate Boundary	4.1	38.0	8.5 ± 0.4	-
(Southern part)	San Gregorio	-65.0	3.6	11.7 ± 0.9	0.0
	Plate Boundary	0.0	38.0	8.5 ± 0.2	15.0

the fault that creeps and d is the depth to which surface creep extends. Therefore the measured creep rate at the surface ($z = 0$) is given by

$$\dot{s}(0) = 2(\tau/\mu)d + (2\dot{b}/\pi)\tan^{-1}\left[d/(D^2 - d^2)^{1/2}\right], \tag{7.7}$$

from which the depth d to which surface creep extends can be calculated.

7.3.3 Modelling Procedure

7.3.3.1 The Forward Calculation

The displacement matrix, **G** that relates the fault-parallel velocities **d**, to the slip rates **b** in equation (7.5) is given by

$$G(i,k) = U(y_i - l_k, D_k) - U(-l_k, D_k), \tag{7.8}$$

where y_i is the position of the i^{th} station, l_k and D_k are the position and locking depth of the k^{th} fault and the origin is at the station whose velocity is fixed at zero.

7.3.3.2 The Forward Model

The forward models are based entirely on fixed model parameters that are estimated from independent geological and geophysical investigations. These make no use of the current geodetic data for estimating the model. The prior model parameters, fault position, deep slip rate, locking depth and surface creep rate used in the forward models are listed in Table 7.2 and explained in Section 7.3.2. The predicted displacements are derived in three stages. First, the displacements due to deep slip on the principal faults are found. Next, the depth to which surface creep extends is calculated from equation (7.7). Finally, the effects on the profile due to surface creep are superimposed onto the predicted displacements from slip at depth to give the complete predicted velocities.

7.3.3.3 The Linear Inversion

The inverse problem posed here is to estimate the deep slip rates from the observed site velocities. However, the depth to which surface creep extends is also unknown. Ideally this depth could be calculated simultaneously with the deep slip rates. Unfortunately the inverse problem would then become non-linear. To overcome this, the calculated depth to which creep extends, estimated from the fixed model parameters, could be used. If the fixed deep slip rates are significantly different from the true values, then this depth, and possibly the estimated slip rates at depth, would be incorrect. Alternatively, the slip rates at depth could be estimated from a linear inversion ignoring the effects of creep. Surface creep only significantly affects points close to the fault, and so ignoring these effects should make little difference

to the estimated slip rates at depth. The depth to which the surface creep zone extends can then be calculated from the fixed model parameters, together with the deep slip rates estimated from inversion, using equation (7.7). If surface creep makes a major contribution to the site velocities, the slip rates at depth and the depth to which surface creep extends can be altered by trial and error to minimise the difference between the observed and calculated velocities. In the following models the depth extent of the surface-creep zone is calculated using the fixed locking depths, surface creep rates and fault positions, and the slip rates at depth estimated by the inversion.

Due to the simplicity of these models, the number of data is greater than the number of unknowns and the matrix equation (7.5) is completely overdetermined. Therefore the slip rates at depth may be estimated using the method of least squares which minimises $(e^i)^2$, the sum of the squares of the data misfit, where $e^i = d^i_{obs} - d^i_{pre}$ and d^i_{obs} and d^i_{pre} are the the observed and predicted relative site velocities. In order to account for the error associated with each individual observation point, a weighted least squares procedure is used. The solution is

$$\dot{\mathbf{b}}^{\mathbf{est}} = \left[\mathbf{G}^{\mathbf{T}}\mathbf{C}_{\mathbf{d}}^{-\mathbf{1}}\mathbf{G}\right]^{-\mathbf{1}}\mathbf{G}^{\mathbf{T}}\mathbf{C}_{\mathbf{d}}^{-\mathbf{1}}\mathbf{d}, \tag{7.9}$$

where $\dot{\mathbf{b}}^{\mathbf{est}}$ is an $m \times 1$ column vector of estimated slip rates and $\mathbf{C}_{\mathbf{d}}^{-\mathbf{1}}$ is the inverse of the $n \times n$ matrix of the covariance of the velocity vectors. In addition, the uncertainties in the slip estimates are calculated using

$$\mathbf{C}_{\dot{\mathbf{b}}\mathbf{est}} = \left[\mathbf{G}^{\mathbf{T}}\mathbf{C}_{\mathbf{d}}^{-\mathbf{1}}\mathbf{G}\right]^{-\mathbf{1}}, \tag{7.10}$$

where $\mathbf{C}_{\dot{\mathbf{b}}\mathbf{est}}$ is the $m \times m$ covariance matrix of the estimated deep-slip rates. These uncertainties are conditional uncertainties mapped from the data uncertainties to the estimated model parameters. A more realistic assessment, used here, scales these uncertainties by the misfit of the model to the data.

A positivity constraint is applied to the inversion in order to stop left-lateral (negative) slip rates being predicted. If the best-fit model predicts a negative slip rate for a fault then that slip rate is constrained to zero and the inversion repeated without that fault included, since none of the class A and class AA faults in the San Francisco bay region exhibit left-lateral movement as indicated by earthquake focal mechanisms (Figure 1.15).

7.3.4 The North-Bay Subregion

The observed displacement pattern in the northern subregion is modelled by dislocations along the San Andreas, Rodgers Creek and Green Valley faults. The model faults are shown in plan view and cross-section in Figure 7.4. The surface projections of the San Andreas and Rodgers Creek faults coincide well with the mapped traces of these faults. The location of the Green Valley fault, which is not closely parallel to the general strike, is based on the location of the mapped surface trace within the southern part of the subregion, the location of the offset seen in the observed velocity profile (Figure 5.6) and the distribution of seismicity along the fault (Figures 1.12 and 1.13). The locus of surface creep is expected to be coincident with the surface trace and the observed velocity offset. However, the seismicity occurs primarily to the west of the mapped trace. To account for the apparent complexity of this fault, the creeping segment is offset about 4 km east of the deeper segment.

The predicted velocity profile with (solid line) and without (dashed line) the effects of creep on the Green Valley fault are shown for the forward model (Figure 7.5a) and for the best-fit model to the geodetic data (Figure 7.5b). Table 7.3 summarises the results of the forward and best-fit models for each subregion. A quantitative measure of the quality of the fit to the data is given by the reduced Chi-squared statistic χ^2_ν [*Bevington and Robinson*, 1992], given by

$$\chi^2_\nu = \frac{\sum_{i=1}^{N} \left(\frac{v^i_{obs} - v^i_{pre}}{\sigma_i} \right)^2}{\nu}, \tag{7.11}$$

where v^i_{obs} is the observed, fault-parallel velocity, v^i_{pre} is the predicted velocity, σ_i is the standard error for v^i_{obs}, N is the number of data points, and $\nu = N - M$ is the number of degrees of freedom where M is the number of adjustable model parameters. Values of χ^2_ν much larger than 1 indicate that the measurement errors cannot account for all of the data misfit, and suggest either an incorrect representation of the physical situation (incorrect model or model parameters) or incorrect estimates of the standard errors of the observed velocities. Very small values of χ^2_ν may imply either that measurement noise is being modelled or that the calculated errors are overestimated. The values for χ^2_ν for the forward and best-fit models with surface creep are 2.1 and 0.5 respectively. The best-fit model is thus consistent with the observed velocities and is an improvement over the forward model.

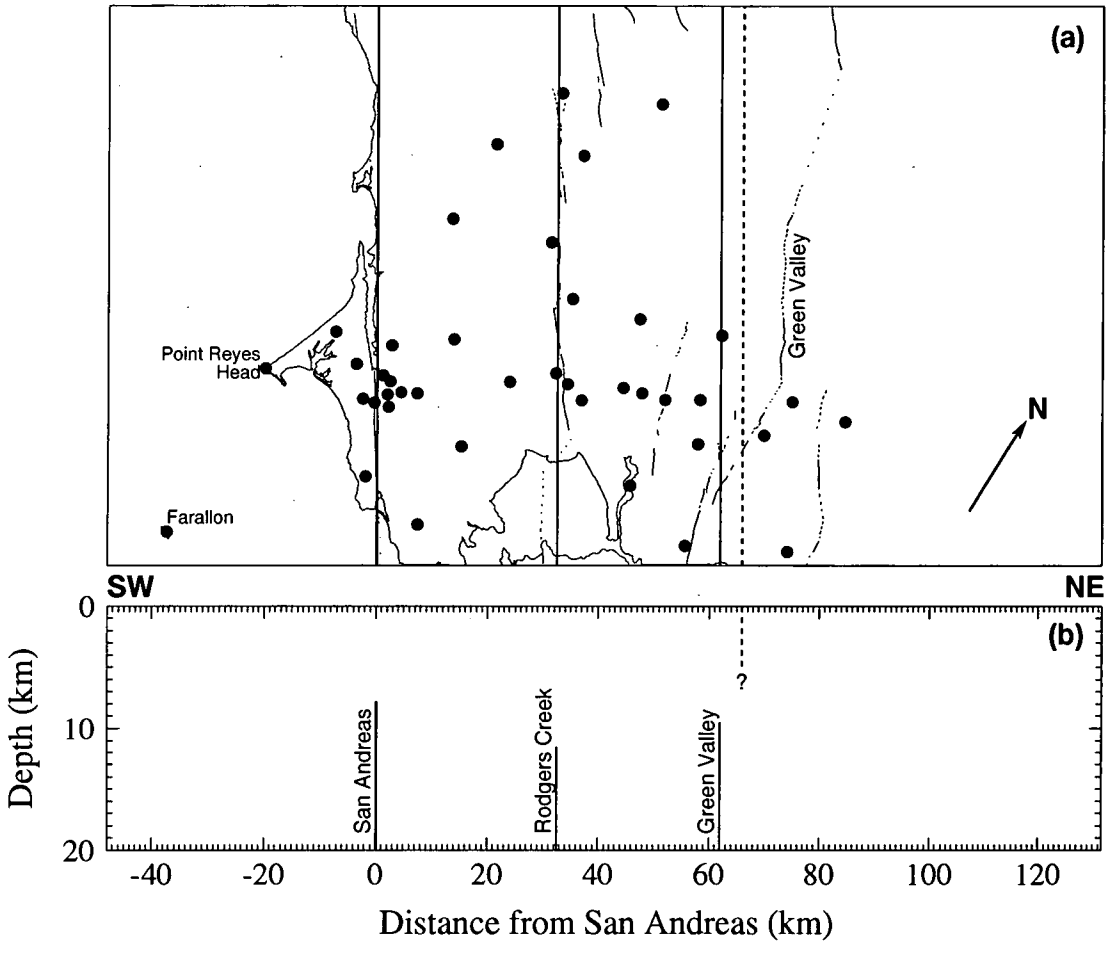

Figure 7.4: (a) Surface projections of the vertical, infinitely-long planes used to model the San Andreas, Rodgers Creek, and Green Valley faults in the north-bay subregion. The map is projected so that vertical lines correspond to the direction N33°W. Solid lines represent positions of the slipping faults at depth. Dashed line represents the locus of the surface creep on the Green Valley fault. (b) Cross section trending at N57°E across the north-bay subregion showing the idealised fault segments used to predict the deformation field. ? indicates unknown, prior to calculating, depth to base of the shallow surface creep zone on the Green Valley fault.

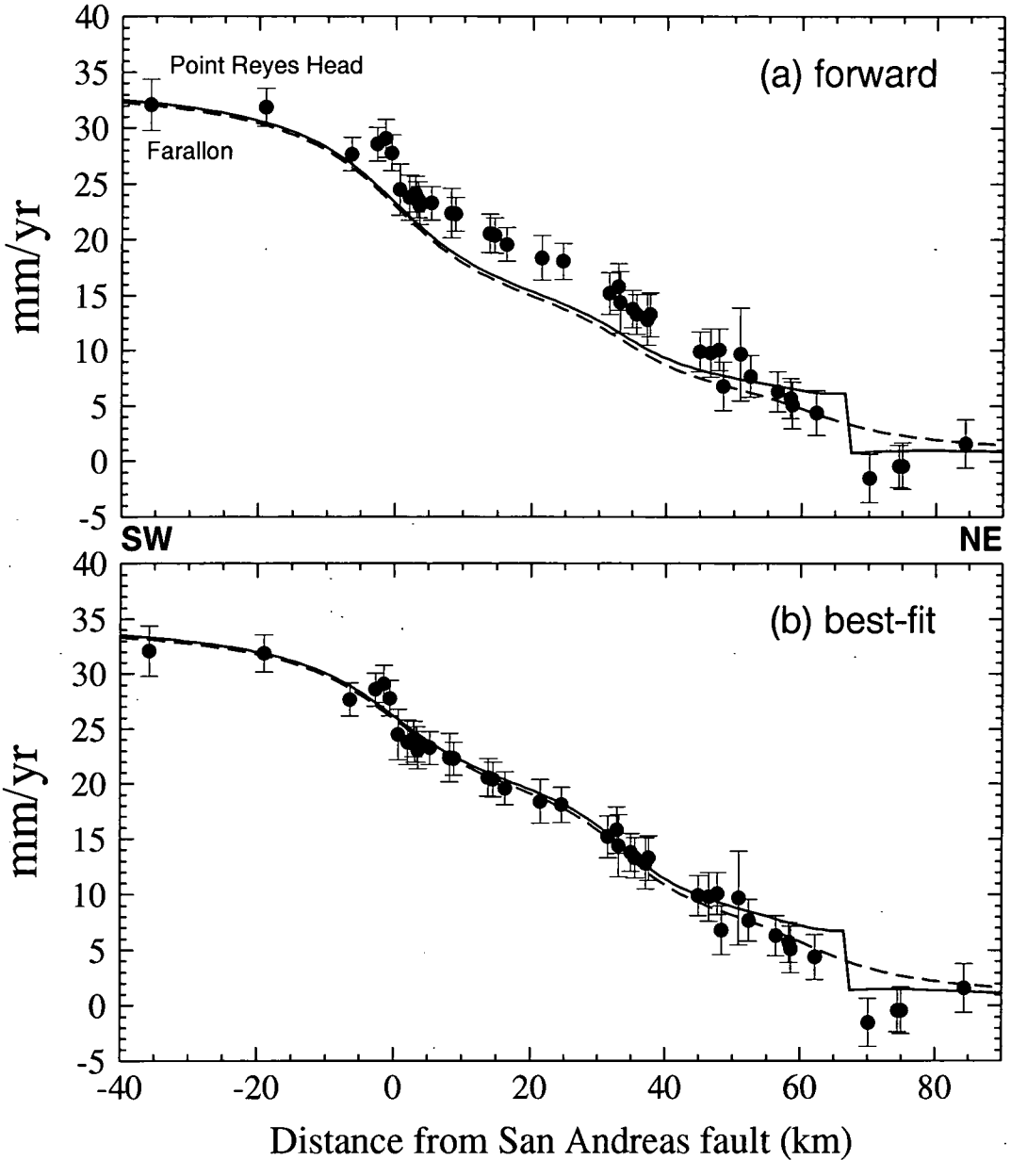

Figure 7.5: Fault-parallel relative velocities predicted for the north-bay subregion along a line trending N57°E by (a) the forward and (b) the best-fit models with (solid line) and without (dashed line) surface creep on the Green Valley fault. Superimposed on the theoretical profiles are the observed data. The error bars represent one standard deviation on either side of the plotted point.

Table 7.3: Slip rates at depth on the San Gregorio, San Andreas, Hayward, Rodgers Creek, Calaveras, Concord and Green Valley faults estimated from the geodetic data. Slip rates presented for the forward models are the fixed estimates adopted in Table 7.2. Also shown is a measure of the quality of the fit to the data given by the reduced Chi-squared statistic.

		Slip rate at depth, mm/yr					
Subregion	Model	San Gregorio Fault	San Andreas Fault	Hayward - Rodgers Creek Faults	Calaveras - Concord - Green Valley Faults	Cumulative Slip across Fault System	χ^2_ν ◇
North-Bay	Forward	-	21.9	8.0	5.4	35.3	2.1
	Best-fit	-	16.7 ± 1.4	12.3 ± 1.2	7.0 ± 0.7	36.0 ± 2.0	0.5
	Compliant fault	-	15.7 ± 0.7	13.1 ± 0.6	7.0 ± 0.4	35.8 ± 1.0	0.4
	Shear Zone	-	-	-	-	31.1 ± 0.4	0.9
Central-Bay	Forward	3.6	20.8	8.0	5.2	34.0	3.0
	Best-fit	0.6 ± 5.9	16.4 ± 5.7	12.2 ± 3.0	7.3 ± 1.9	36.5 ± 8.9	0.7
	Shear Zone	-	-	-	-	33.0 ± 0.8	1.4
South-Bay	Forward	3.6	22.8	-	11.1	37.5	3.6
	Best-fit 1	0.6 ± 5.1	13.5 ± 5.3	-	22.3 ± 2.3	36.4 ± 7.7	1.2
	Best-fit 2	0.0*	19.7 ± 3.7	-	17.6 ± 2.7	37.3 ± 4.6	0.9
	Shear Zone	-	-	-	-	36.6 ± 1.2	2.0
Monterey-Bay							
	Forward	3.6	24.0	-	14.9	42.5	1.4
(Northern)	Best-fit	0.0*	18.4 ± 3.0	-	18.2 ± 2.1	36.6 ± 3.7	0.7
	Shear Zone	-	-	-	-	37.0 ± 0.9	0.8
	Forward	3.6	38.0†	-	-	41.6	1.9
(Central)	Best-fit	0.0*	40.7 ± 1.4 †	-	-	40.7 ± 1.4	2.8
	Forward	3.6	38.0†	-	-	41.6	1.8
(Southern)	Best-fit	0.0*	38.2 ± 1.5 †	-	-	38.2 ± 1.5	1.3

◇ χ^2_ν for the models that include the effects of surface creep.

* set to zero by positivity constraint.

† indicates rates for the "plate boundary" fault (see text).

Simple comparison of the two values of χ^2_ν does not reveal whether the improvement is statistically significant. To test whether the best-fit model is a significant improvement over the forward model an F-test is used [*Bevington and Robinson*, 1992, p.205] where F is the ratio of χ^2_ν for the two models, that is

$$F = \frac{\chi^2_{\nu 1}}{\chi^2_{\nu 2}}. \tag{7.12}$$

If the value of F for the two candidate models is greater than some critical value that is dependent on the number of degrees of freedom then the improvement in χ^2_ν can be reasonably attributed to a significant difference between the models. For example, with 100 degrees of freedom, F must be greater than ~ 1.4 to be significant at the 95% confidence level. The ratio F between the forward and best-fit model is 4.2 which is significant at a confidence level of 99.7%.

The forward model predicts poorly the relative site velocities within the fault system. However, the model does present an acceptable fit to the relative velocities of the most westerly points, Farallon and Point Reyes Head indicating that the breadth of the deforming zone, which is related to the locking depth, and the summed slip rates at depth from the forward model are reasonably consistent with the geodetic data. Where the forward model is inconsistent with the data is in the distribution of motion throughout most of the deforming zone.

The best-fit values for the slip rates at depth are given in Table 7.3, and they yield a cumulative deep slip rate of 36.0 $\pm$ 2.0 mm/yr across the whole San Andreas fault system. The depth to the base of the shallow, surface creep zone on the Green Valley fault is estimated to be 10 km using the fixed deep-slip rates and 9 km using the best-fit deep-slip rates.

Both the best-fit model and the forward model fail to explain the apparent offset across the San Andreas fault (at 0 km, Figure 7.5) of 3 mm/yr. This offset could be accounted for either by a shallow locking depth, surface creep or low rigidity within the fault zone. The lack of seismicity and therefore the large uncertainty in the 90% depth estimate along this segment of the San Andreas fault would allow a much shallower locking depth than the 12.2 km used in the models. However, the offset is so localised that this is not a viable explanation unless in conjunction with this the present deep slip rate on the San Andreas fault is much smaller (corresponding to the size of the offset) than any geological estimates. Furthermore the depth to which coseismic slip extended during the 1906 earthquake is thought to be 10 $\pm$ 2 km, [*Thatcher*, 1975] close to the 90% depth estimate. Less than

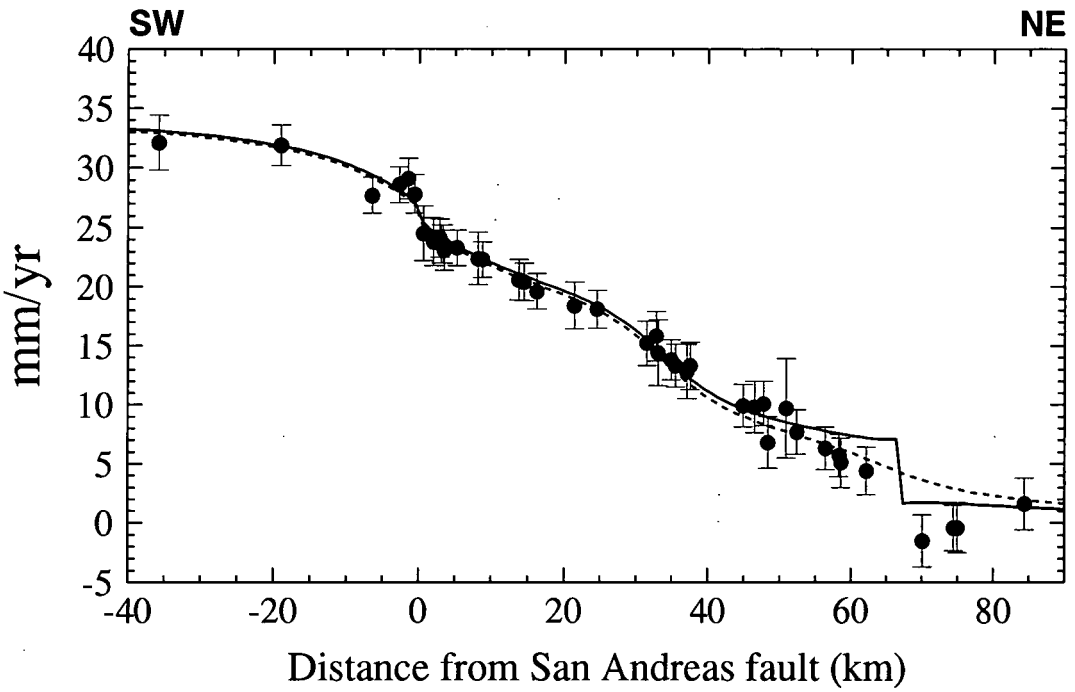

Figure 7.6: Fault-parallel, best-fit, relative velocities predicted for the north-bay subregion along a line trending N57°E using a model which includes the effects of a 1.5-km wide low-rigidity fault zone around the San Andreas fault. The zone has a rigidity contrast of 0.25 with respect to the surrounding quarter spaces. The predicted profile is shown with (solid line) and without (dashed line) the effects of surface creep on the Green Valley fault. Superimposed on the theoretical profiles are the observed data. The error bars represent one standard deviation errors.

1 mm/yr of surface creep along the 1906 trace of the San Andreas fault is reported within this subregion (Table 7.1, Figure 7.2) and therefore surface creep across the main fault trace does not appear to be a viable explanation either. To the north of San Francisco bay, the San Andreas fault occupies a 0.5 to 1.5-km wide fault valley [*Niemi and Hall*, 1992]. Surface creep could occur on a number of subparallel traces within the valley with each trace contributing a small portion to the total offset seen.

Material with low seismic velocities extending to at least 6 km depth has been identified along the San Andreas [*Feng and McEvilly*, 1983], Calaveras [*Mooney and Colburn*, 1985], Maacama and Healdsburg-Rodgers Creek [*Eberhart-Phillips*, 1986] fault zones in central California. Shear wave velocity in the fault zones may be as low as half its value in the material outside the fault zones [*Bakun and Bufe*, 1975] suggesting a shear modulus contrast of up to 0.25 [*McHugh and Johnston*, 1977]. Figure 7.6 shows a best-fit model to the north-bay subregion using a more complex model (compliant fault model) which includes lateral inhomogeneity. A

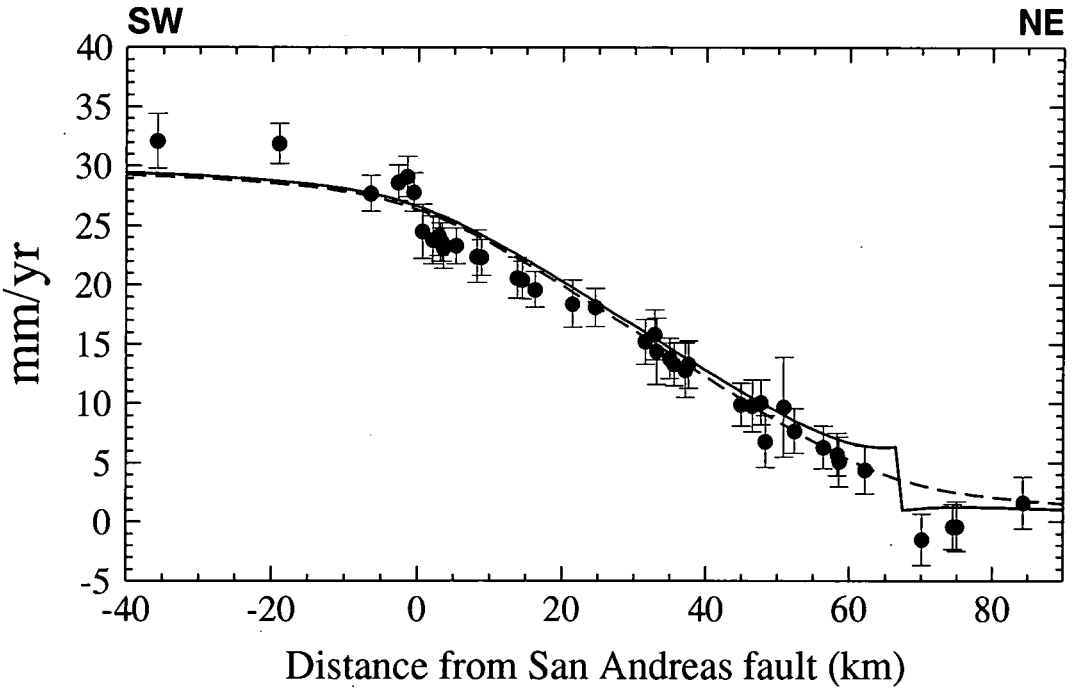

Figure 7.7: Same as for Figure 7.6 except using a model with a vertical shear zone 65 km wide between the San Andreas and Green Valley faults, below a depth of 10 km.

1.5-km wide, low-rigidity fault zone is located around the San Andreas fault. The zone has a rigidity contrast of 0.25 (the low end of realistic contrasts) with the surrounding material. Comparison of Figures 7.5 and 7.6 shows that the effect of the low-rigidity (compliant) fault zone is to concentrate deformation across the San Andreas fault. The χ^2_ν for this model is 0.4, which is a small improvement over the best-fit model using a homogeneous structure. The F-test indicates that this improvement is significant at the 75% confidence level.

Another area where the models fail to explain the geodetic data adequately is around the Green Valley fault. The predicted curve for deformation without creep (e.g., Figure 7.6) fits the points to the immediate southwest of the Green Valley fault better than when surface creep is incorporated, though the latter curve predicts the data northeast of the fault best.

To test whether the geodetic data are consistent with a model of distributed shear rather than deep slip localised on individual faults, a best-fit model for the data was calculated using equation (6.5). In this model, shear is distributed evenly across the fault system between the San Andreas and Green Valley faults below a depth of 10 km. As for the previous models, the locking depth of 10 km is based on the 90% depths. This depth is reasonable as it corresponds to the thickness of

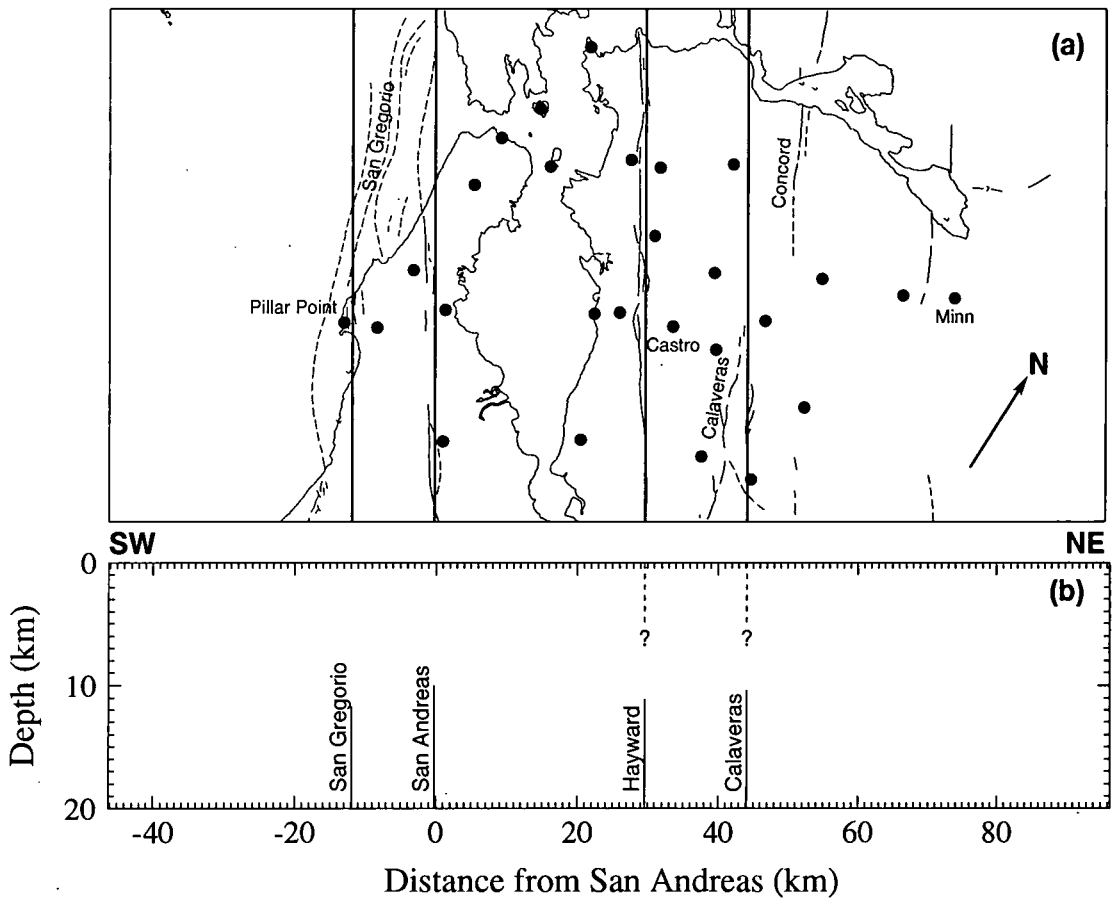

Figure 7.8: Same as for Figure 7.4 except for the San Gregorio, San Andreas, Hayward, and Calaveras-Concord faults in the central-bay subregion.

the locked layer in the modified half space model and the minimum depth of onset of viscoelasticity in lithosphere-asthenosphere type models. The best-fit model predicts 31.1 $\pm$ 0.4 mm/yr of relative, right-lateral motion across the fault system (Figure 7.7, Table 7.3). χ^2_ν for this model is 0.9, which is worse than that of the best-fit model for slip on the principal faults. The data in the southwestern half of the profile are most poorly fit by this model, which predicts velocities that are too low southwest of the San Andreas fault and too high to the northeast.

7.3.5 The Central-Bay Subregion

The principal faults in the central-bay subregion are the San Gregorio, San Andreas, Hayward and Calaveras-Concord faults. These faults, together with the idealised model faults, are shown in plan view and cross section in Figure 7.8. The

surface projections of the model San Andreas and Hayward faults coincide well with their mapped traces. The location of the San Gregorio fault is chosen to be coincident with the mapped surface trace of that fault at Pillar Point between the two southwestern-most stations on the profile (Figure 7.8). The Calaveras-Concord fault is placed so that it separates the sites southwest of the surface trace from those to the northeast. Surface creep on the Hayward and Calaveras faults is assumed to occur immediately above the deep slipping fault planes.

The predicted velocity profiles are shown in Figure 7.9 and the results are summarised in Table 7.3. The values of χ^2_ν for the forward and best-fit models with creep to the geodetic data are 3.0 and 0.7 respectively and F is 4.3 which indicates an improvement significant at the 99% confidence level.

χ^2_ν for the best-fit model without surface creep is 0.7 and the ratio F between the best-fit models with and without creep is 1.0. Therefore, assuming the rest of the model is correct, this analysis suggests that creep is equally likely to be occurring as to be not occurring. Surface creep that has been constant for decades has been documented along at least 66 km of the Hayward fault [*Lienkaemper et al.*, 1991] (Figure 7.2) and along parts of the Calaveras-Concord fault [*Galehouse*, 1992a, b]. This creep is however, not detectable in the geodetic data studied here probably because the noise level of the data is presently too large and the station spacing too broad.

As is the case for the north-bay subregion, the data most poorly fit by the forward model are from points within the fault system indicating that the proportions of deep-slip assigned to the faults are distributed incorrectly . The depths to which the surface creep zones extend calculated from equation (7.7) and the fixed parameters are 6.2 km for the Hayward fault and 3.9 km for the Calaveras fault.

The best-fit values obtained for slip at depth are given in Table 7.3, and the cumulative slip rate at depth across the San Andreas fault system is 36.5 $\pm$ 8.9 mm/yr. As a consequence of the high uncertainties in the slip rates for individual faults (up to 5.9 mm/yr), the best-fit deep slip rates do not differ significantly from those of the forward model at the 1-2σ level. However, the estimates for the San Andreas, Hayward and Calaveras-Concord faults agree remarkably well with those obtained for the San Andreas, Rodgers Creek and Green Valley faults for the north-bay subregion. Surface creep is calculated to extend to 4.7 km on the Hayward fault and 2.8 km on the Calaveras fault.

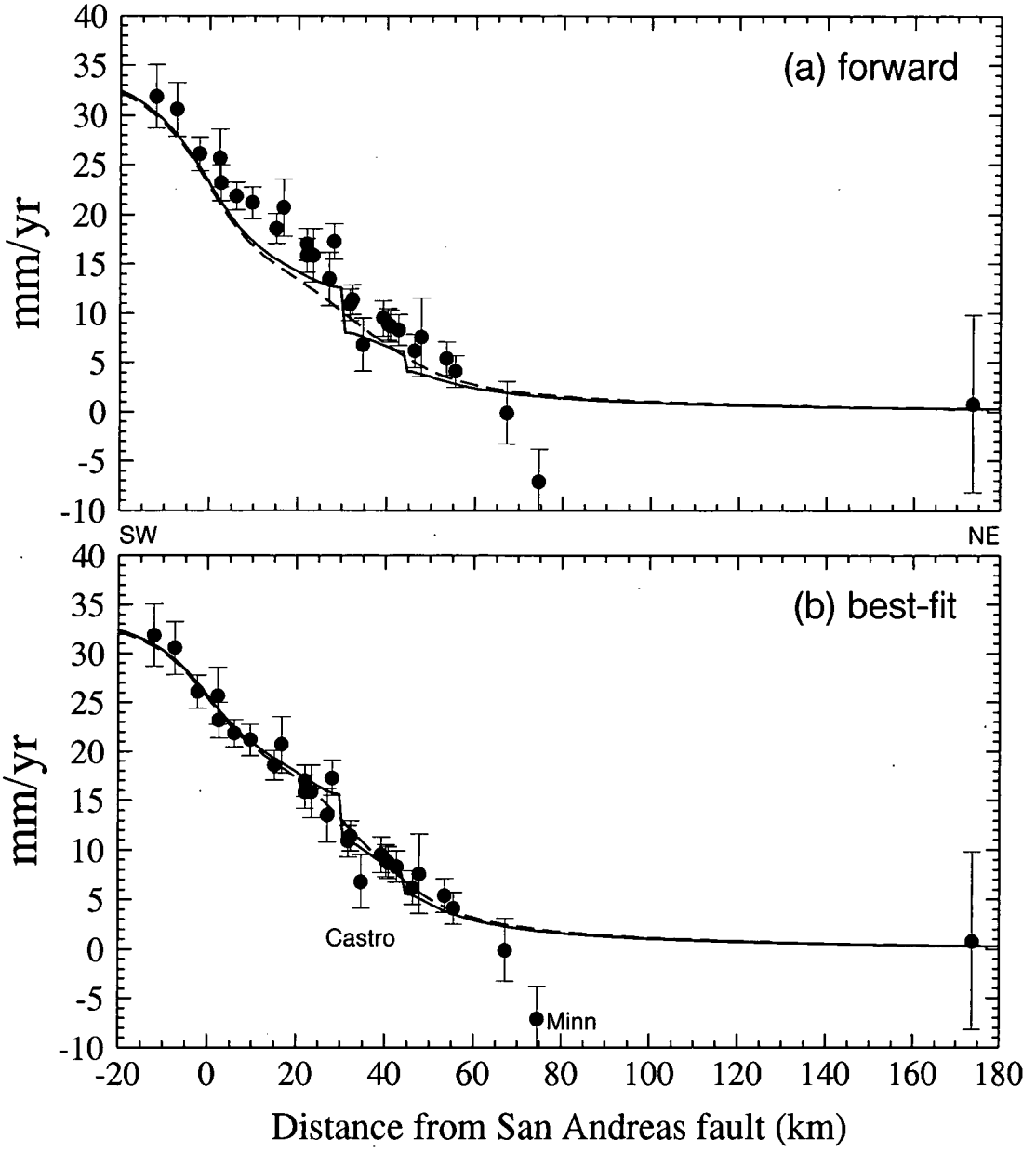

Figure 7.9: Same as Figure 7.5 except for central-bay subregion with (solid lines) and without (dashed lines) surface creep on the Hayward and Calaveras-Concord faults.

Small, San Andreas fault-crossing networks along the San Francisco peninsula indicate high strain rates, in agreement with the offset across that fault seen in the data for the north-bay subregion [*Prescott et al.*, 1981]. However no fault-local offset is evident in the geodetic data for the central-bay subregion (Figure 7.9) and thus a low-rigidity zone around the San Andreas fault, although probably present, is not required by the data modelled here.

In the case of the best-fit model, only two stations show residuals greater than one standard deviation. These are Castro (velocity misfit -3.3 $\pm$ 2.7 mm/yr) and Minn (velocity misfit -8.9 $\pm$ 3.3 mm/yr). Minn is the only station whose residual exceeds 2 standard deviations. The calculated fault-parallel velocity of Minn is heavily dependent on the 1993 survey (Figure 4.5) and if this survey were disregarded the velocity calculated would be substantially less and more consistent with the modelled results. The measured velocity of station Minn may thus simply be in error.

7.3.6 The South-Bay Subregion

The south-bay subregion is mostly south of the junction between the Hayward and Calaveras faults. The fault system in this subregion is therefore considered to consist of the San Gregorio, San Andreas and Calaveras faults. The model faults used are shown in plan view and cross section in Figure 7.10. As only one station, Allison, is close to the junction of the Hayward and Calaveras faults, neglecting motion on the Hayward fault affects only one observation point. The model position of the San Gregorio fault is coincident with the mean position of its surface trace between the two southwestern-most points, Dump and Pom, located on either side of this fault. Similarly, for the San Andreas fault, which changes strike from N44°W to N36°W within this subregion, the model position is midway between the two closest stations. Most of the individual observation points close to the San Andreas fault are situated along the segment that strikes at N36°W and it is these close sites that are more sensitive to the fault position. A consequence of neglecting the change in strike in this simple model is that station Loma, which is $\sim$ 4 km from the mapped surface trace of the San Andreas fault, is at least 10 km from the model fault and its velocity is expected to be poorly modelled.

Figure 7.11 and Table 7.3 show the modelling results. Two best-fit velocity profiles are shown in Figure 7.11b. The upper dashed and solid lines represent the

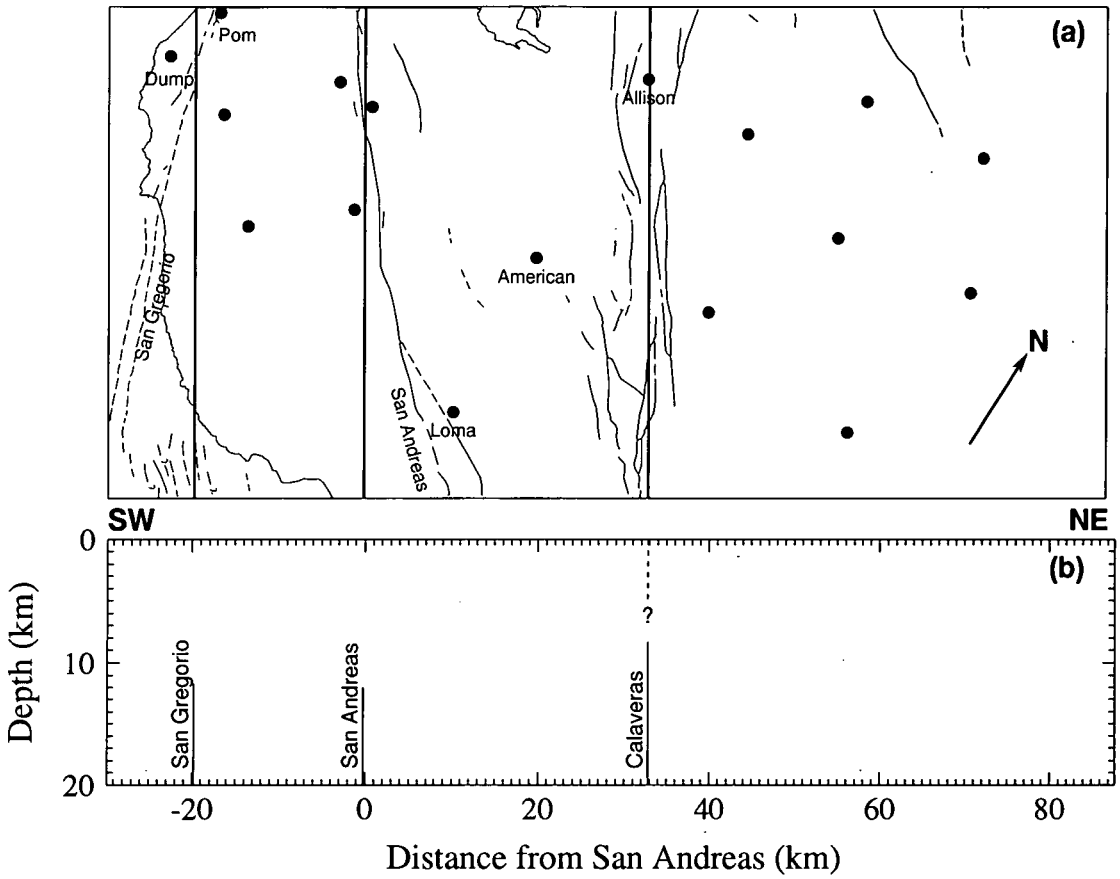

Figure 7.10: Same as Figure 7.4 except for the San Gregorio, San Andreas, and Calaveras faults in the south-bay subregion. Dashed line represents the position of surface creep on the Calaveras fault.

best-fit model obtained from an inversion with all the observed velocities included (model 1). The lower dashed and solid lines represent the best-fit model with the velocities of stations Loma and American omitted (model 2). Only three observation points lie between the San Andreas and Calaveras faults. As a consequence, the inversion relies heavily on those points in distributing slip between the two faults. Because the model is unrealistic for stations Loma and American, their exclusion from the inversion is justified. χ^2_ν for model 1 is 1.2. The slip rate at depth of 13.5 $\pm$ 5.3 mm/yr determined for the San Andreas fault is lower than the estimates obtained from the north-bay and central-bay subregions, but not significantly at the 1σ level.

The slip rates for model 2 yield a χ^2_ν of 0.9, and are marginally more consistent with previous estimates of slip from the north- and central-bay subregions. Both

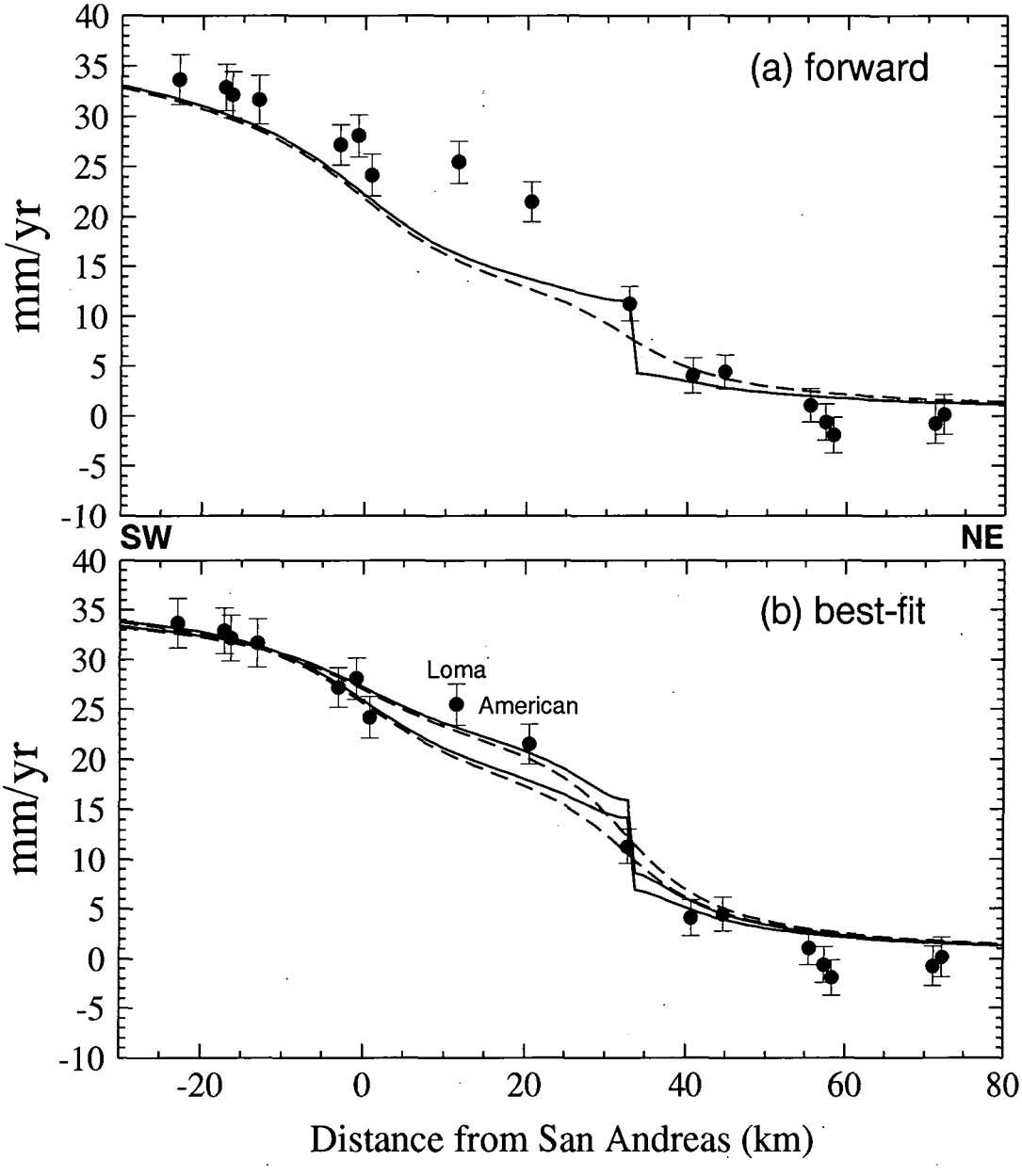

Figure 7.11: Same as Figure 7.5 except for the south-bay subregion with (solid lines) and without (dashed lines) surface creep on the Calaveras fault. For explanation of (b) see text.

model 1 and model 2 are significant improvements over the forward model at a confidence level greater than 98%. The depth to which surface creep extends on the Calaveras fault is 6.4 km from the forward model, 3.9 km from best-fit model 1 and 4.6 km from best-fit model 2.

7.3.7 The Monterey-Bay Subregion

The Monterey-bay subregion has been subdivided into three parts in order to minimise the effects of the significant three-dimensionality of this subregion. The model geometries for the northern, central and southern parts are shown in Figure 7.12. In the northern part, the model San Gregorio, San Andreas and Calaveras faults are located at the midpoints of the surface traces of the faults within that part. For the central and southern parts, the San Andreas and Calaveras faults are not separately distinguished. Instead, slip at depth is modelled as a single "plate boundary" fault midway between the surface traces of the two faults. This is because of the variable strikes of the two faults within this part, which cause slip rates obtained from an inversion to depend critically on the chosen fault positions. Furthermore, it is realistic to assume that distributed deformation occurs at depth as motion is progressively transferred from the San Andreas fault to the Calaveras fault towards the north [*Ellsworth*, 1975]. The deep slip rate estimated for the "plate boundary" fault then approximately represents the sum of the slip on the two faults. The locking depth on this fault is restricted to 8.5 km, an average of the 90% depths close to the junction of the San Andreas and Calaveras faults (Figure 7.3). Surface creep along the San Andreas and Calaveras faults is located where offsets occur in the observed velocity profiles.

The predicted velocity profile for the northern part is shown in Figure 7.13. χ^2_ν for the forward and best-fit models with surface creep are 1.4 and 0.7 respectively. The F-ratio of 2.0 indicates an improvement on the forward model at a confidence level of 87%. The largest difference between the predicted velocities (and thus the residuals) of the forward and best-fit models is at the hypothetical Pacific plate site (not shown). The forward model over-predicts the velocity at this point by nearly 6 mm/yr. If the total relative motion across the San Andreas fault system at this latitude is larger than the 35 mm/yr prescribed then the improvement may not be so large. The depth to which surface creep extends on the Calaveras fault, calculated from the parameters of the forward model, is 7.7 km. No observation points disagree with the best-fit model at the 2σ level. The cumulative deep slip

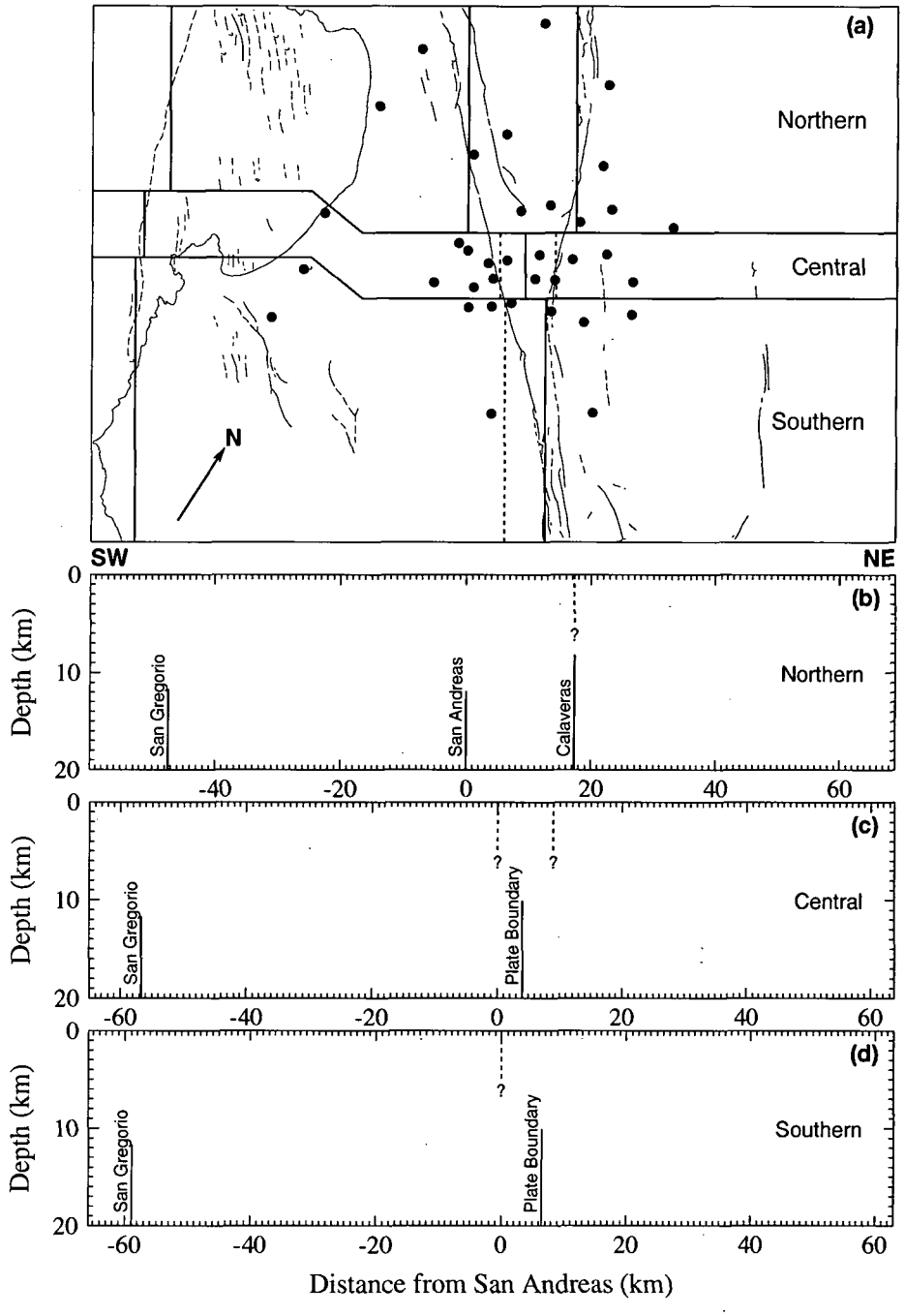

Figure 7.12: (a) Same as for Figure 7.4(a) except for the San Gregorio, San Andreas, and Calaveras faults in the northern, central and southern parts of the Monterey-bay subregion. Dashed lines represent the positions of the surface creep on the San Andreas and Calaveras faults. (b) to (d) Same as for Figure 7.4(b) except for the northern, central and southern parts of the Monterey-bay subregion. In the central and southern subregions, slip at depth is approximated by a single "plate boundary" fault.

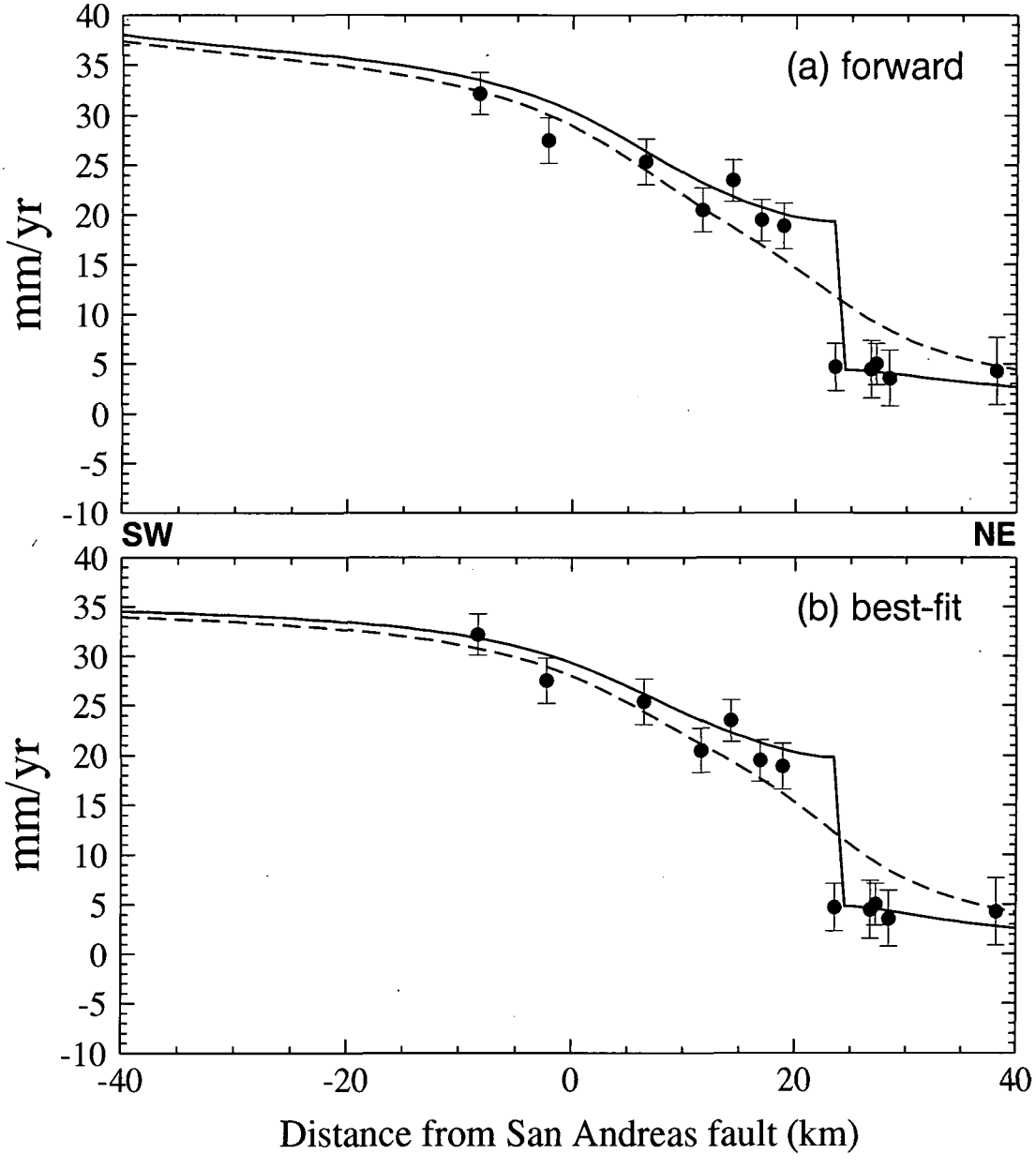

Figure 7.13: Same as for Figure 7.5 except for the northern part of the Monterey-bay subregion.

rate across the fault system estimated from the best-fit model is 36.6 ± 3.7 mm/yr and the depth to which surface creep extends on the Calaveras fault, calculated from the parameters of this model, is 7.2 km.

Figure 7.14 shows the predicted velocity profiles for the central part of the Monterey-bay subregion. For both the forward and best-fit models, the predicted profiles with creep are a substantial improvement over the profiles without creep. χ^2_ν for the forward and best-fit models with surface creep are 1.9 and 2.8 respectively. The best-fit model is therefore not an improvement over the forward model. The most probable explanation for this surprising result lies in the method used in the inversion. As explained above the effects of surface creep are ignored when calculating the best-fit slip rates at depth. This method is reasonable where surface creep accounts for a small part of the motion only. However, where the contribution of surface creep to the point velocities is large, inversion values of the slip rates at depth are biased. A more appropriate method for this case would therefore be to use repeated iterations to improve the fit. The depth extent of surface creep from the forward model is 5.8 km on the San Andreas fault and 6.7 km on the Calaveras fault. From the best-fit model these depths are 5.3 km and 6.2 km. The slip rates obtained from the best-fit model are 0 mm/yr for the San Gregorio fault and 40.7 ± 1.4 mm/yr for the "plate boundary" fault.

The predicted velocity profiles for the southern part of the Monterey-bay subregion are shown in Figure 7.15. As for the other parts of the subregion the predicted profiles that include surface creep are a significant improvement over those without. χ^2_ν for the forward and best-fit models with surface creep are 1.8 and 1.3. This improvement is only marginally significant (68%). The major difference between the two models is the slip rate at depth on the San Gregorio fault (Table 7.3). The slip rate for this fault is not well constrained by the data as there are no points close to the fault in the Monterey-bay subregion. However, in the central- and south-bay subregions (sections 7.3.5 and 7.3.6) where observation points do lie close to this fault the estimated slip rate is not significantly different from zero either. A slip rate of 0 mm/yr is therefore more consistent with the results from other subregions than the prior estimate of 3.6 mm/yr. For both the forward and best-fit models, the depth to which the surface creep zone extends is estimated to be 8.0 km.

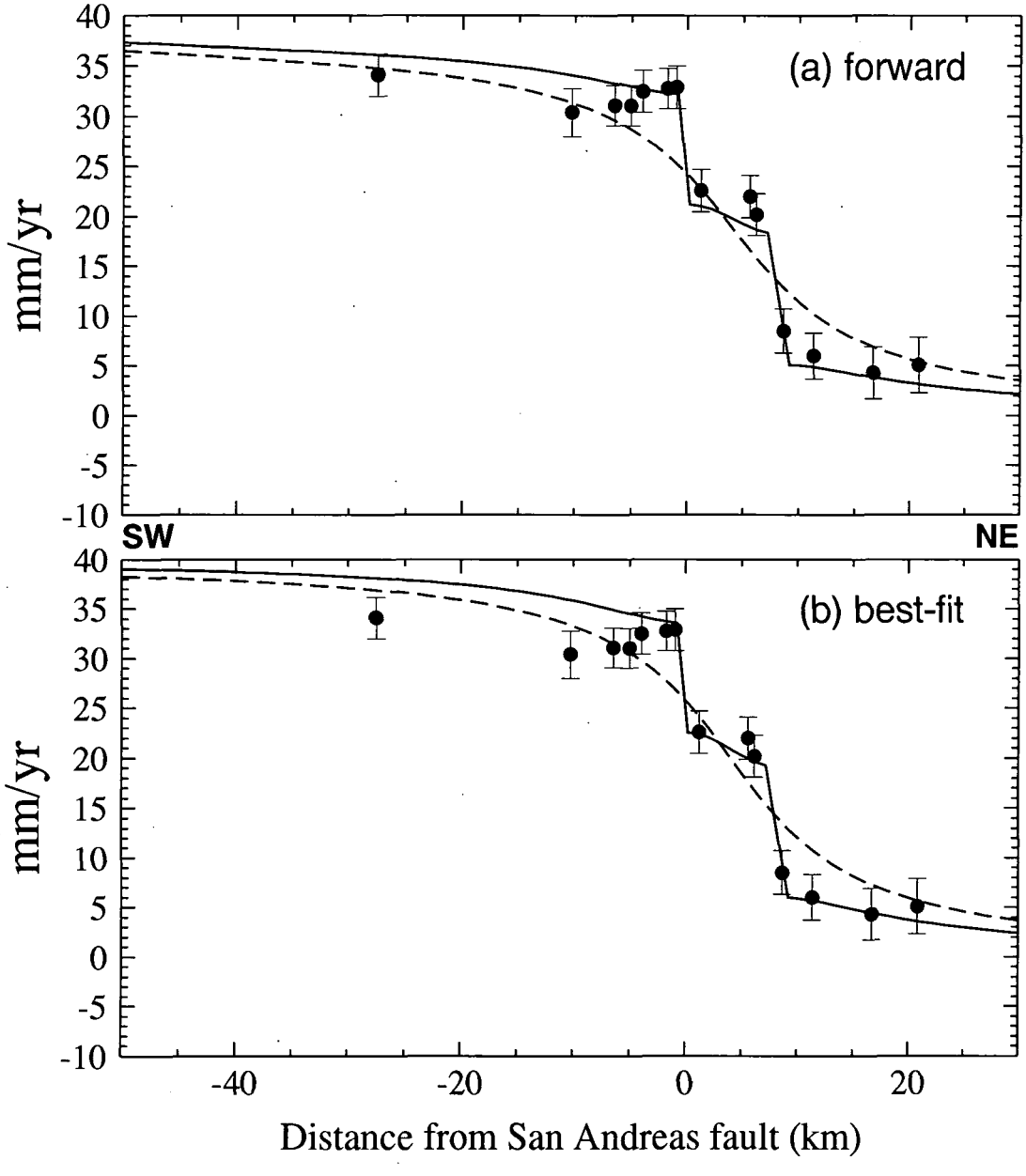

Figure 7.14: Same as for Figure 7.5 except for the central part of the Monterey-bay subregion with (solid lines) and without (dashed lines) surface creep on the San Andreas and Calaveras faults.

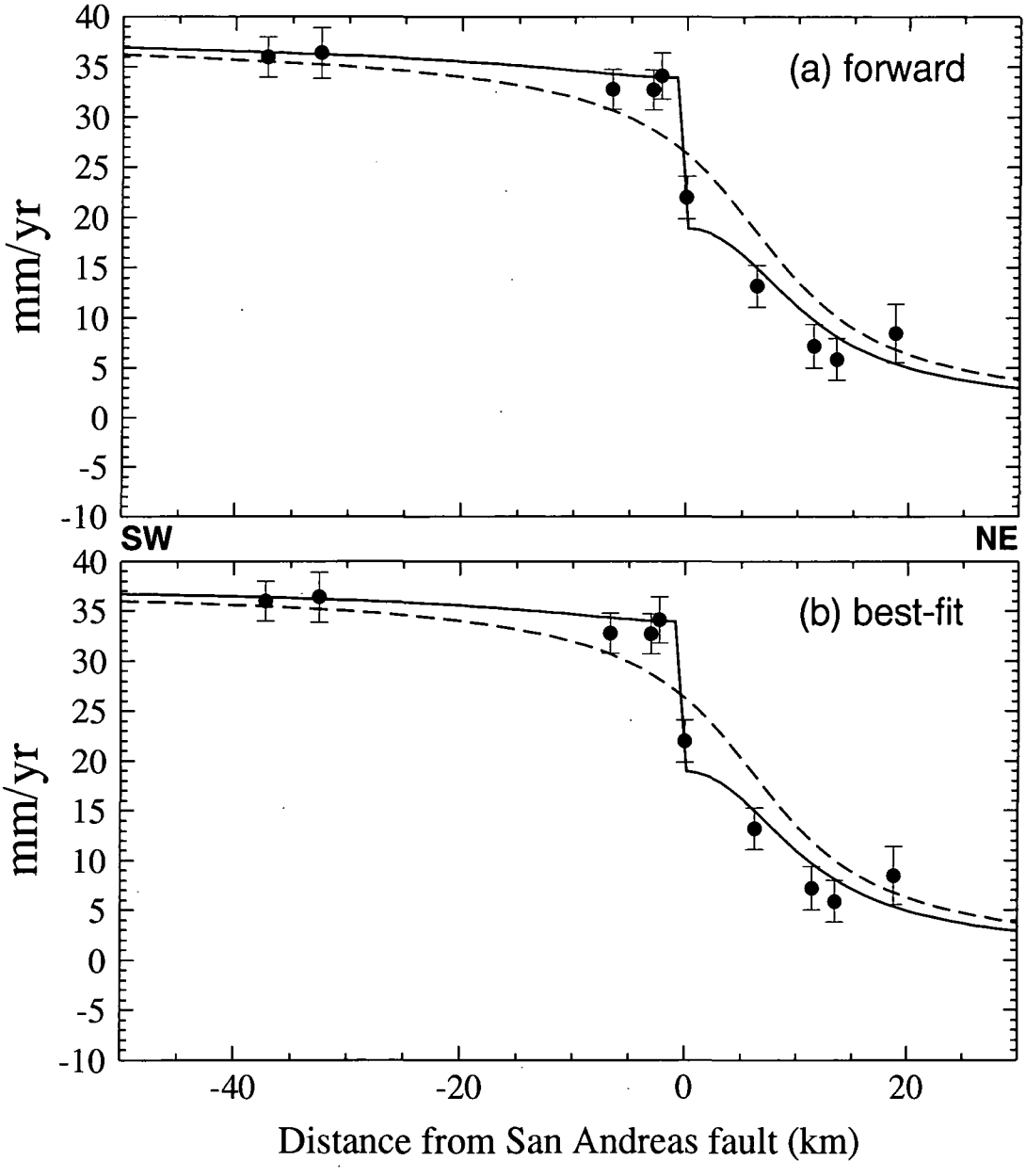

Figure 7.15: Same as for Figure 7.5 except for the southern part of the Monterey-bay subregion with (solid lines) and without (dashed lines) surface creep on the San Andreas fault.

7.4 The Three-Dimensional Model

7.4.1 The Data

In contrast to the two-dimensional models described above, one regional three-dimensional model is able to model the deformation in the San Francisco and Monterey bay regions. This three-dimensional model is able to predict the full three-dimensional velocity field and there is no need to divide the region up into smaller sub-regions. The model is directly fit to the observed line-length change rates from the San Francisco bay trilateration network (Chapter 5) and the horizontal relative velocities from the GPS profiles (Chapter 4) rather than to relative velocities derived from these data. The trilateration data consists of 300 line-length change rates and the GPS data consist of 28 relative horizontal velocities (or 56 observations). The vertical relative velocities from the GPS data are not included since their contribution to constraining the deformation is statistically insignificant due to their large uncertainties. In total there are 356 observations available for analysing the deformation in the San Francisco bay region. The uncertainties in the trilateration data are obtained from the residuals of the linear regression of the line-length estimates with time. The uncertainties in the GPS data are obtained from the least-squares inversion for the relative velocities (Chapter 4). In this modelling, each observation is weighted by the inverse of its standard deviation.

7.4.2 Model Parameters

The surface creep rates compiled from the polynomial fits (Figure 7.2) and the slip rates at depth obtained from the best-fit two-dimensional models are used as fixed parameters in a forward model. These slip rates are also used as a-priori data in the three-dimensional inversion. For all models, the depth to the base of the brittle layer is calculated from the distribution of seismicity (Figure 7.3).

The general geometry of the fault model is shown in Figure 7.16. The principal faults are digitised from the fault map of California [*Jennings*, 1975] and divided along strike into multiple segments averaging 10 km in length. In several cases assumptions had to be made as to the position of the faults because either the position of the fault is not clearly distinguished, there were several mapped traces or the fault was highly segmented. The results do not depend strongly on minor

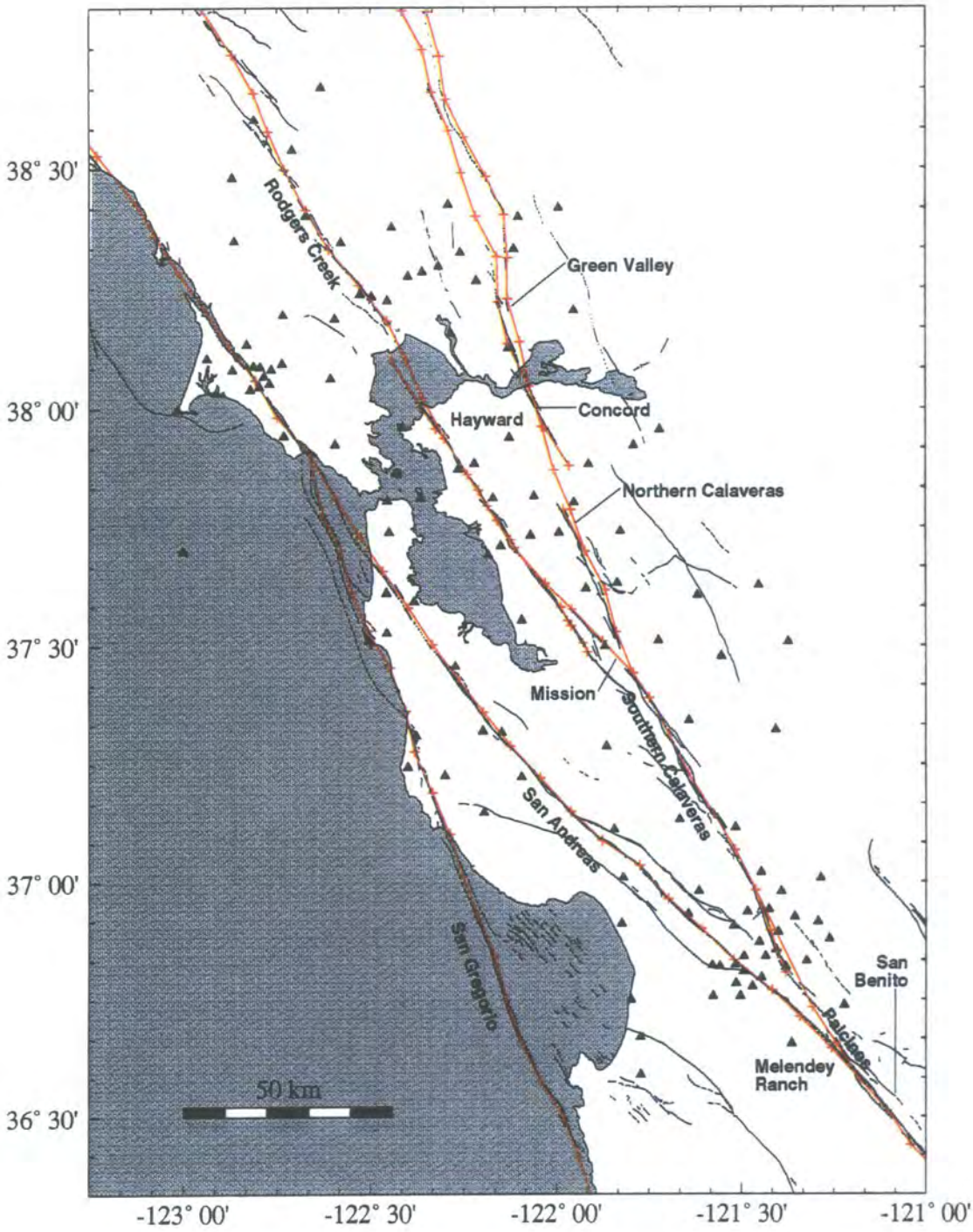

Figure 7.16: Location of the fault segments (red lines and crosses) used to model the deformation in the San Francisco and Monterey bay regions, superimposed on top of mapped surface traces. Triangles represent the positions of the geodetic stations.

changes in fault location for those faults which are locked to the base of the brittle layer but fault location can be important for faults that exhibit surface creep.

Slip beneath the brittle layer on the principal faults is considered to be continuous along strike. That is, where mapped surface traces show offsets such as the right-stepping offset between the Hayward and Rodgers Creek faults and the right-stepping offset between the Northern Calaveras and Concord faults, a straight connection between the faults beneath the brittle layer is assumed (Figure 7.16). The few earthquakes within the right stepover between the Hayward and Rodgers Creek faults seem to deepen to the northeast and location of the deepest events suggest a straight connection at depth [*Lienkaemper et al.*, 1991]. At the left stepover between the Calaveras and Hayward faults, earthquake activity occurs along the Mission fault (Figure 1.2) [*Andrews et al.*, 1993]. Slip is thus considered to be transferred from the Southern Calaveras to the Hayward fault along the Mission fault and the Hayward fault to the south of the Mission fault is considered to be inactive apart from surface creep.

At fault junctions such as the San Andreas-Calaveras, the Calaveras-Hayward and the San Gregorio-San Andreas, the faults at depth are assumed to be connected at a nodal point. The San Andreas-Calaveras junction near Hollister is a complex zone of subparallel faults. The San Andreas fault continues through the area without interruption and without significant splays to connect it with the subparallel faults to the northeast. The Calaveras fault is considered to be the principal member of these subparallel faults. It passes through the town of Hollister (Figure 1.2) and probably continues southwards along the Paicines and San Benito faults. Transfer of slip between the San Andreas and Calaveras faults has been inferred to occur close to the Melendy Ranch (Figure 7.16) [*Ellsworth*, 1975]. Therefore the model Calaveras fault south of Hollister is projected along the strike of the Paicines and San Benito faults and connects with the San Andreas fault at Melendy Ranch. The northward continuation of the northern Calaveras fault comprises the Concord, Green Valley and Bartlett Springs faults [*Castillo and Ellsworth*, 1993]. The mapped surface traces of these faults show en-echelon steps (Figure 1.2), but earthquake epicentres show a continuous, straight connection at depth which the modelled fault follows.

Where surface creep is observed the model fault locations are taken as the mapped surface traces. Appreciable creep on the San Andreas fault occurs only southeast of San Juan Bautista. On the Calaveras fault, creep increases significantly from Seventh Street in Hollister northwestwards to a maximum just north of Hollister

where it gradually decreases to virtually zero near the northwestern terminus of the fault [*Galehouse*, 1992a, b]. Creep is also detected on the Concord fault and the southwestern segment of the Green Valley fault. Whether creep continues or dies out further north along this fault is unknown but it is assumed here to decrease to zero. This affects the results little since these segments are all outside the modelled region. The spatial variation of surface creep along the Hayward fault has been extensively investigated and both the surface creep rates and fault segment coordinates used are taken from the regional dislocation model produced by *Lienkaemper et al.* [1991].

The depths to which surface creep extends calculated from the inverse two-dimensional models are used. The systematic variation of creep rate along the faults within each subregion was not accounted for in those models. Whether these variations are associated with equivalent variations in the depth of the creeping zone is not known. The principal relation between surface-creep rate, the depth extent of surface creep and the rate of stress accumulation (equation 7.7) has not yet been extended to three-dimensional geometries and so the depth to which surface creep extends cannot be estimated here. The depths estimated within each subregion from the two-dimensional models can be regarded as approximations to the average true depths based on averages of the observed surface creep rate and calculated stress accumulation. Where fault segments cross the boundary between two subregions an average from the two subregions for the locking depth and depth to the base of the surface creep zone is adopted. Similarly, northwards along the Green Valley fault, the depth to the base of surface creep is tapered to zero along with the assigned slip rate.

Beyond the region shown in Figure 7.16, additional segments following the general strike of the fault system (N33°W) are included for the San Andreas, Rodgers Creek and Green Valley faults to the north and the San Andreas and San Gregorio faults to the south. The slip rates are constrained to be identical with those on the closest segment. These faults are assigned semi-infinite lengths in order to eliminate edge effects. A table of the fault segments used in the three-dimensional model is given in Appendix A.

7.4.3 Modelling Procedure

7.4.3.1 The Forward Calculation

The exact form of the elements of the displacement matrix, **G**, are dependent on the type of geodetic data used. For trilateration data the rate of change of line length is given by

$$l^{ij} = (v_x^j - v_x^i)\sin\theta^{ij} + (v_y^j - v_y^i)\cos\theta^{ij}, \tag{7.13}$$

where l^{ij} is the rate of line-length change between the i^{th} and j^{th} stations and θ^{ij} is the azimuth of the line clockwise from north. Equation (7.13) is valid under the condition that $\mid v^j - v^i \mid \ll L^{ij}$ where L^{ij} is the line length. This condition is always satisfied since line lengths are usually of the order of several kilometres and the magnitude of displacement less than a few metres. Substituting (7.2) into (7.13) gives

$$l^{ij} = \sum_{k=1}^{m} \dot{b}_k \left[\left[U(x)_k^j - U(x)_k^i \right] \sin\theta^{ij} + \left[U(y)_k^j - U(y)_k^i \right] \cos\theta^{ij} \right], \tag{7.14}$$

which can be written in the form of (7.5) with

$$\begin{aligned} d^p &= l^{ij}, \\ G^{p,k} &= \left[U(x)_k^j - U(x)_k^i \right] \sin\theta^p + \left[U(y)_k^j - U(y)_k^i \right] \cos\theta^p, \end{aligned} \tag{7.15}$$

where p indicates the line between stations i to j.

For GPS data, the relative velocity of station j with respect to station i is

$$\begin{aligned} V(x)^{ij} &= \sum_{k=1}^{m} \dot{b}_k \left[U(x)_k^j - U(x)_k^i \right], \\ V(y)^{ij} &= \sum_{k=1}^{m} \dot{b}_k \left[U(y)_k^j - U(y)_k^i \right], \end{aligned} \tag{7.16}$$

which can be written in the form of (7.5) with

$$\begin{aligned} d(x)^{ij} &= V(x)^{ij}, \\ d(y)^{ij} &= V(y)^{ij}, \\ G(x)^{ij,k} &= U(x)_k^j - U(x)_k^i, \\ G(y)^{ij,k} &= U(y)_k^j - U(y)_k^i. \end{aligned} \tag{7.17}$$

The $d(x)$, $d(y)$ and $G(x), G(y)$ indicate that there are two data for every measured GPS line.

For both trilateration and GPS data, the displacement vector U_k^i for vertical strike-slip faults is determined by eight parameters,

$$U^i = U(x_o, y_o, L, \phi, d, W, x_i, y_i), \tag{7.18}$$

where (x_o, y_o) are the coordinates of the origin of the fault segment, L is the length of the fault segment, ϕ is the strike of the fault segment, d is the depth of the upper fault edge, W is the vertical fault width and (x_i, y_i) are the coordinates of the i^{th} station.

7.4.3.2 The Inversion Method

In theory the inverse problem to find the solution to (7.5) is overdetermined if the number of data exceeds the number of unknown slip rates. However, in practice this may not be the case for real station-segment configurations. If the stations are unevenly distributed the slip rates of some segments may be overdetermined, but those of others undetermined either because there are no nearby points or because lines cross more than one fault segment. This sort of problem is said to be mixed-determined [*Menke*, 1984]. Since the slip rates on individual fault segments can be thought of as representing a discretised continuous function of slip rate on an individual fault that varies with position, several segments can be combined together and the resultant average slip rates thus rendered overdetermined. However combining segments will reduce the variance of the estimated parameters at the expense of resolution of smaller features. If the inverse problem is considered to be mixed-determined then it can be solved using weighted-damped least squares [*Jackson*, 1979; *Menke*, 1984]. The estimate of the solution is

$$\dot{\mathbf{b}}^{\mathrm{est}} = \langle \dot{\mathbf{b}} \rangle + \left[\mathbf{G}^{\mathrm{T}} \mathbf{C}_{\mathbf{d}}^{-1} \mathbf{G} + \mathbf{W}_{\mathbf{m}} \right]^{-1} \mathbf{G}^{\mathrm{T}} \mathbf{C}_{\mathbf{d}}^{-1} \left[\mathbf{d} - \mathbf{G} \langle \dot{\mathbf{b}} \rangle \right], \tag{7.19}$$

where $\langle \dot{\mathbf{b}} \rangle$ is a column vector of a-priori values of the slip rates and $\mathbf{W_m}$ is a matrix of weighting factors which quantifies some measure of simplicity. For a discretised continuous function such as slip rates, along-strike variations are likely to be gradual and the weighting matrix $\mathbf{W_m}$ can be used to impose smoothness on the final result.

7.4.3.3 Obtaining Station Velocities from the Predicted Data

To facilitate comparison the predicted station velocities are best expressed in the same reference frame as the observations. This is achieved by calculating the

predicted trilateration line-length change rates and GPS relative velocities and then combining them with the observed VLBI velocities using the method presented in Chapter 5 for combining the different geodetic data types. Calculating the predicted station velocities in this manner, as opposed to simply estimating them in the modelling software, eliminates the calculation of the motion at the fixed point. If this fixed point is some distance away from the modelled fault system then it is likely that it will be affected either by edge effects or effects from other unmodelled tectonic movement. For example, to correctly calculate the velocities relative to the VLBI station OVRO, the deformation due to the Owens Valley shear zone would have to be included in the model. The mechanisms involved in the deformation in Owens Valley are as yet unresolved [*Savage and Lisowski*, 1995]. Using the same VLBI data to calculate the observed and predicted station velocities relative to some distant point eliminates this bias.

7.4.4 The Forward Model using the results from the Two-Dimensional Analysis

The forward model uses the slip rates and the depths to which the surface creep zones extend from the best-fit two-dimensional models (Figure 7.17). Each coloured rectangle represents a modelled fault segment slipping at the rate indicated. The lower segments extend from the locking depths shown (upper edges of rectangles) to a depth of 9000 km. The choice of 9000 km is arbitrary, and any value large enough to be considered infinite with respect to the dimensions of the region modelled would suffice. The upper segments represent the shallow surface creeping zones.

Figure 7.18 shows the observed and predicted site velocities relative to the VLBI station OVRO. In addition profiles for the four subregions are shown for the fault-parallel (Figure 7.19a-d) and the fault-normal (Figure 7.19e-h) cases. χ^2_ν, calculated from the observed minus the predicted trilateration line-length changes and GPS relative velocities, is 5.8. However, since the geodetic network is geometrically redundant (i.e., the number of intersite observations is greater than the number of sites) some of the misfit may be attributable to measurement noise that is unaccounted for in the data uncertainties rather than misfit of the model [*Segall and Mathews*, 1988]. Geometric redundancy in the GPS observations has already been accounted for during the estimation of the relative site velocities (Chapter 4). No such scaling of the uncertainties in the trilateration data is performed. The average error found in fitting the line-length change rates by dislocation models was found

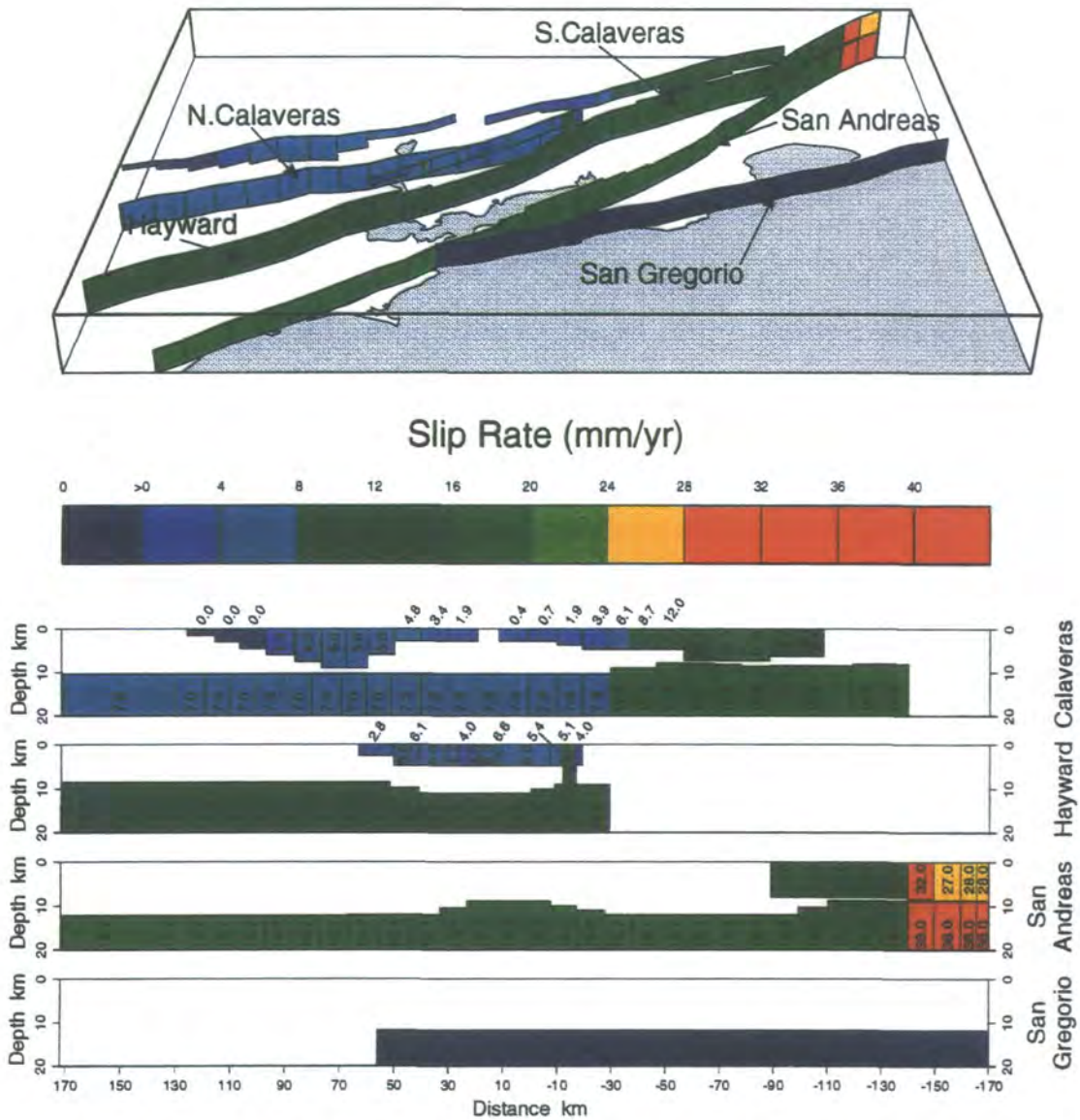

Figure 7.17: The San Andreas fault system showing fault segments and slip rates used in the forward model. Top, perspective view of the fault system looking from the west. Box represents the upper 20 km of the elastic half-space in which the slipping fault segments are buried. The Californian coast is plotted at a depth of 20km. Bottom, along-strike depth sections of the individual faults. Each rectangle represents a single fault segment slipping at the rate indicated by the colour and number. The lower rectangles, extend from the locking depth shown (upper edge) to a depth of 9000 km. The upper rectangles represent zones of shallow surface creep.

to be twice the standard deviation in the rate for a subset of the data near Hollister [*Savage et al.*, 1979]. The uncertainties in the trilateration data are therefore rescaled by a factor of 2 prior to using them in the three-dimensional analysis. Selective reweighting of the trilateration data will attenuate the effect of outliers on any parameters estimated and should lead to an improvement in χ^2_ν at the expense of increasing the uncertainties in the calculated slip rates. After scaling the uncertainties in the trilateration data, χ^2_ν becomes 1.6.

Alternatively, χ^2_ν can be calculated from the derived relative velocities. In this case the uncertainties in the observed data have already been rescaled by the misfit due to geometrical redundancy (observational error). χ^2_ν calculated from the observed minus the predicted velocities is 0.95.

The calculated fault-parallel velocity field (Figures 7.19a-d) agrees closely with the observed data. Much of the apparent scatter in the observed velocities, especially within the Monterey-bay subregion (Figure 7.19d), that cannot be modelled in the two-dimensional analysis, can be explained by along-strike complexities in the fault system. The largest residuals occur for sites located around the Green Valley fault in the north-bay subregion and sites between the San Andreas and Calaveras faults in the Monterey-bay subregion. The largest residual is at station Minn ($-9.1\pm$ 3.3 mm/yr) already identified as an outlier (Figures 7.19b and 7.9).

The residuals from the fault-normal velocity field are consistent with a normal distribution with zero mean but there appear to be systematic discrepancies within the subregions. In the north-bay subregion the observed fault-normal velocities are consistently greater than the predicted velocities (Figure 7.19e) whilst in the south-bay subregion they are consistently lower (Figure 7.19g). Significant changes in the predicted fault-normal velocities would require altering the strikes of the faults. The fault strikes are well-constrained by the surface traces and seismicity, and a more likely explanation for the discrepancy is a systematic direction bias between the trilateration and GPS results.

In order to summarise the model misfit, strain rates are calculated from the residual horizontal velocity field and shown in terms of their principal axes in Figure 7.20. To the north and east of San Francisco bay the residual strain is dominated by compression or extension sub-perpendicular to the fault strike (e.g., at 1 in Figure 7.20). However, there are appears to be no systematic variation to the strain-rate pattern to suggest fault-normal effects. Fault-normal compression or extension in a region would appear as some form of sinusoid in a fault-normal velocity profile not

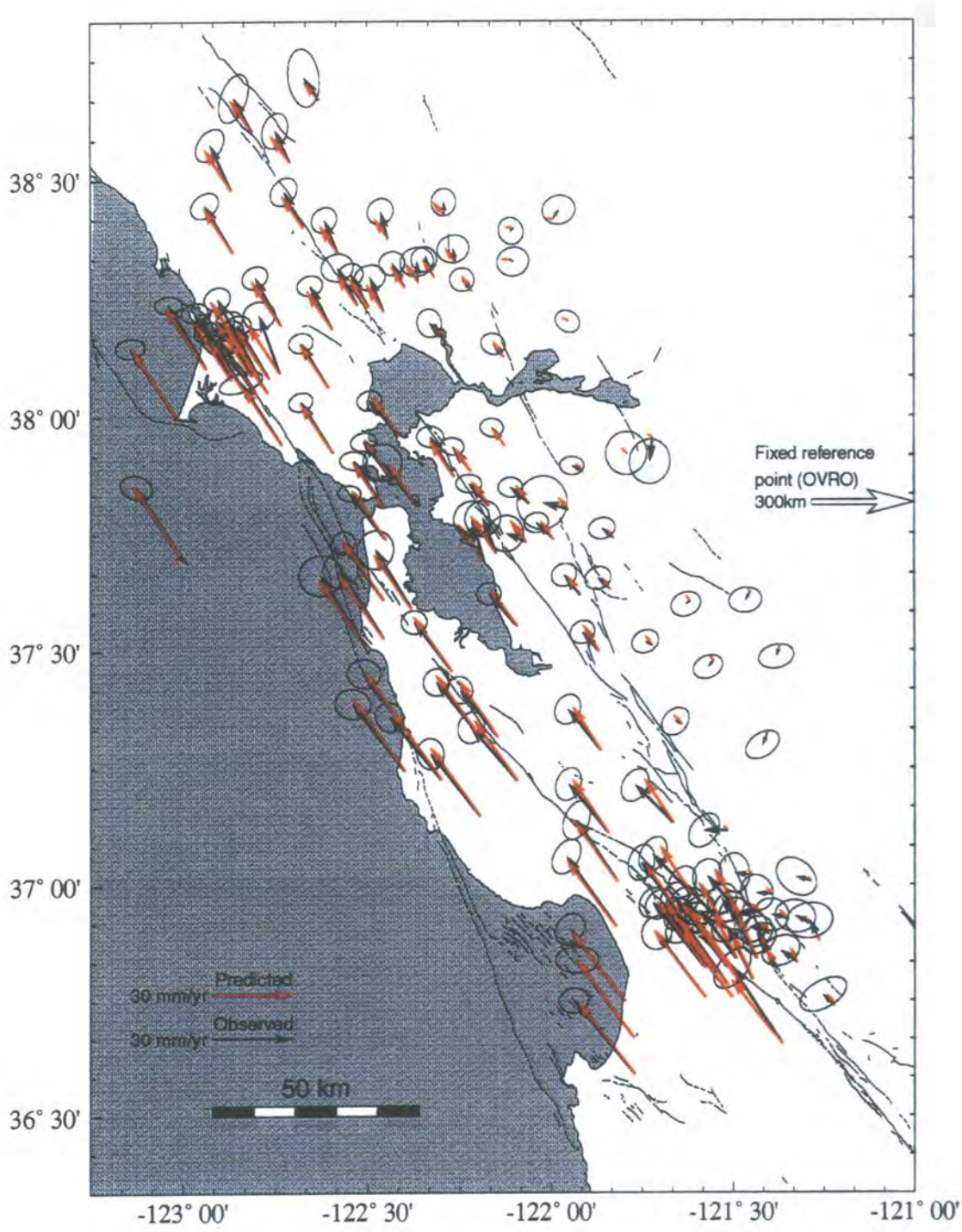

Figure 7.18: Comparison of the observed relative site velocities (black arrows) with those predicted by the forward model (red arrows). Velocities are calculated relative to station OVRO, 300 km east of the fault system. Error ellipses are 95% confidence ellipses around observed velocities.

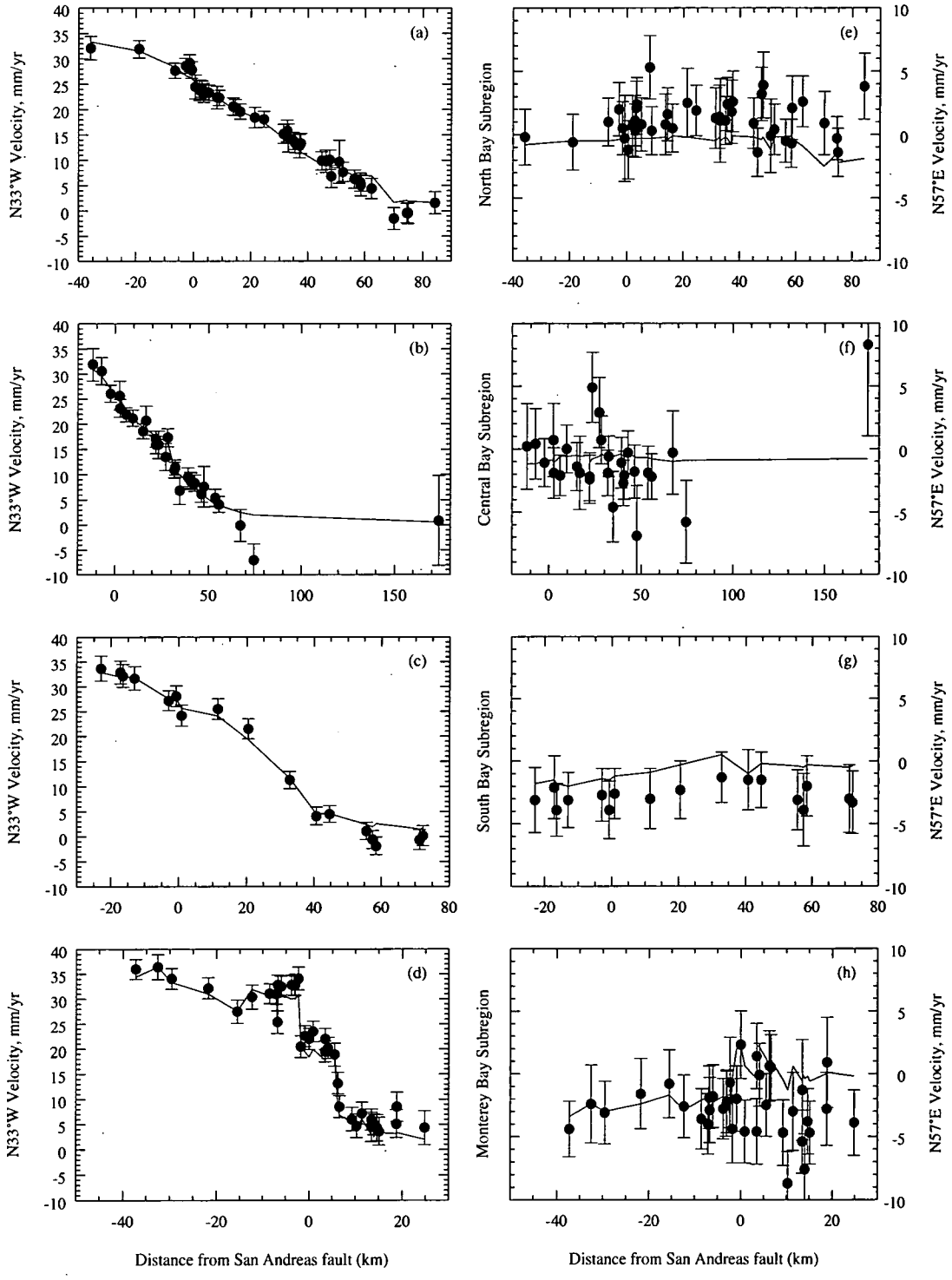

Figure 7.19: N33°W fault-parallel (a-d) and N57°E fault-normal (e-h) velocity profiles predicted for the four San Francisco and Monterey bay subregions by the forward model. Superimposed on the theoretical profiles are the observed data. The error bars represent one standard deviation.

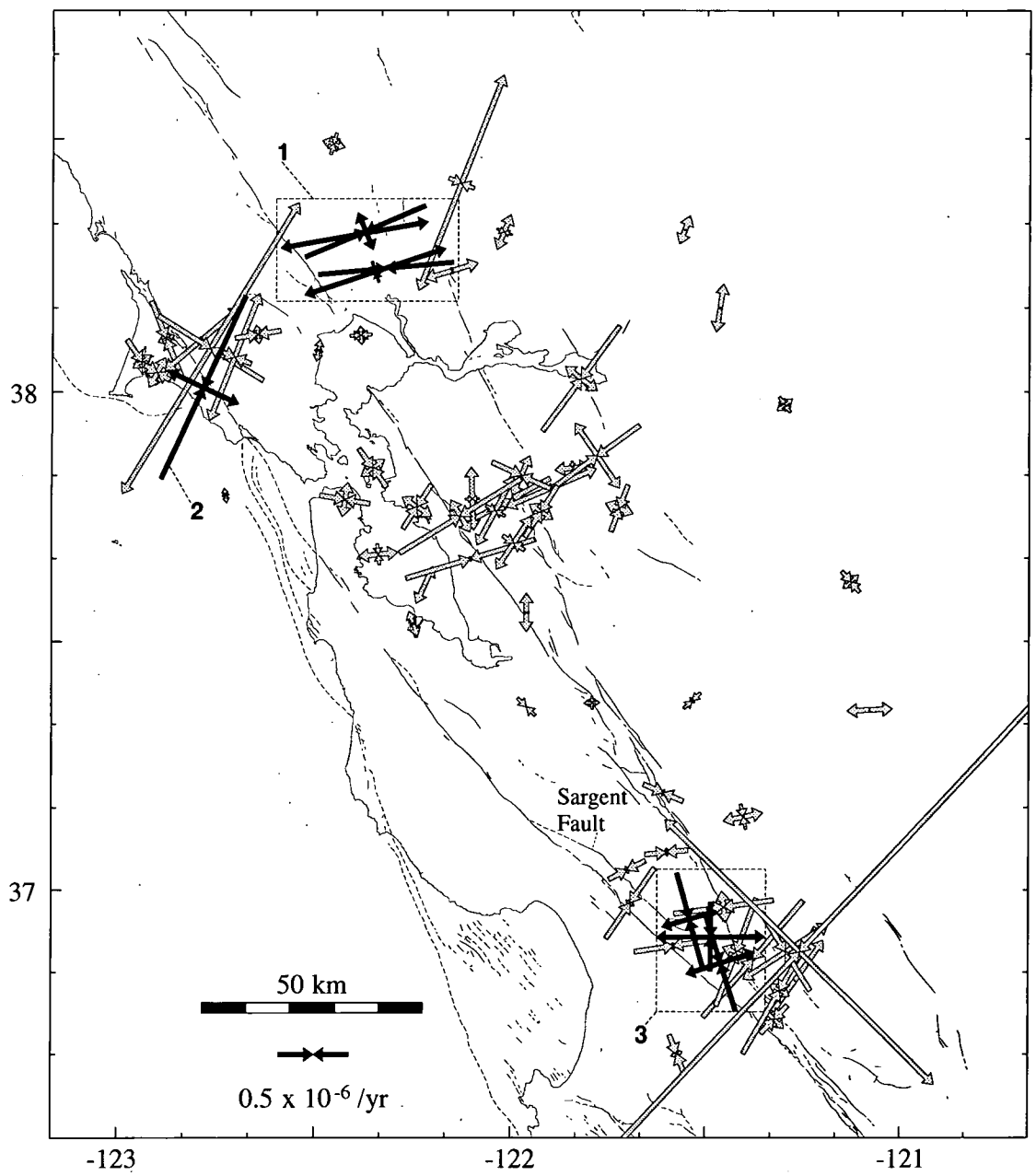

Figure 7.20: Principal axes of horizontal strain-rate tensors calculated for the residual deformation unmodelled by the forward model. Inward pointing arrows represent compression; outward pointing arrows represent extension. Only strain-rates axes whose orientation have an uncertainty less than 30° are plotted. Dark arrows represent strain-rate tensors mentioned in text.

as a systematic offset. The fault-normal compression and extension strain residuals, like the systematic offset seen in the fault-normal velocity field, are probably the result of observational errors. Along the San Andreas fault near the Point Reyes peninsula, there is some residual shear-strain parallel to the fault strike (at 2 in Figure 7.20). This may be attributed to the localised motion described in section 7.3.4, which may be the result of an unmodelled compliant fault zone or surface creep distributed throughout the fault valley. East of Monterey bay, the residuals cluster east of the San Andreas fault and again predominantly indicate compression or extension sub-perpendicular to the local fault strike. Between the San Andreas fault and the Calaveras fault (3 in Figure 7.20), three residuals show shear strain of about 1.2 μstrain/yr that is parallel to the strike of the Sargent fault. Shear strain of 1.2 μstrain/yr across a 5 km wide zone corresponds to 6 mm/yr of right-lateral motion. A possible explanation for these residuals is unmodelled slip on the Sargent fault. Slip of 3 mm/yr has been measured along this fault [*Prescott and Burford*, 1976]. The large strain rate seen east of the Calaveras fault is from the Delaunay triangle between sites Brown, Bolsarm, and Pachecho. These are located almost in a straight line orientated along the shear direction of this residual. The strain-rate tensor is a function of both the magnitude and distribution of the deformation. This large residual is therefore a result of small areal extent rather than large residual deformation.

7.4.5 The Three-Dimensional Inversion

The best-fit three-dimensional model was calculated using a weighted, damped, least-squares procedure. The slip rates used in the forward model were used here as a-priori rates for the inversion. Four segments extending from the surface to a depth of 8 km along the Sargent fault from the Calaveras fault to the San Andreas fault, and one segment extending from the surface to 6.2 km depth at the southern end of the southern Calaveras fault were added to the model. The additional segment on the Calaveras fault is introduced to account for the creep of 6 mm/yr detected on the Paicines fault [*Harsh and Pavoni*, 1978]. Rather than attempting to calculate the slip rate on each segment, several neighbouring segments on the same fault were combined. The number of segments combined was chosen on the basis of trial and error such that along-strike slip variations could be resolved without the inversion becoming "unstable". This instability was characterised by slip rates fluctuating between left- and right-lateral slip on adjacent segments.

Slip rates on fault segments lying outside the network are poorly constrained by the data. In such cases the slip rates were either fixed at a specified value and not varied in the inversion or the segments were combined with neighbouring segments that are within the network. In addition, the surface-creep rates obtained from creep-meter measurements, alignment arrays etc., which are of higher quality than rates predicted by the geodetic data, were used to fix creep rates not estimated in the inversion. Exceptions to this are the surface creep zones along the southern end of the Calaveras fault and along the San Andreas fault near Hollister. These creep rates are estimated as they are constrained by a high concentration of line-length data and also exhibit large variability (Figure 7.2). An incorrect creep rate in this region could seriously degrade the inversion since surface creep plays a dominant role in the deformation here. Therefore it seems reasonable to estimate the creep rates. Altogether 25 slip rates are estimated in the inversion, 14 of which are slip rates at depth and 11 are surface creep rates.

χ^2_ν from the best-fit model is 1.5 after scaling the trilateration errors (0.9 if calculated from the derived velocities). The F-test[1] shows that the best-fit model is a significant improvement from the forward model at the 81% confidence level. The degree to which the model fits the data is illustrated by a histogram of normalised residuals (Figure 7.21). The histogram is approximately symmetric about zero although there is a slight bias towards overpredicting the motion. 71% of the predicted data lie within 1σ of the observed values and 90% within 2σ. These are close to the expected percentages for normally-distributed data with zero mean and correctly-assessed variances.

The predicted velocities derived from the best-fit model are shown as horizontal vectors in Figure 7.22 and as profiles of the fault-parallel and fault-normal velocity components in Figure 7.23. As for the forward model, the best-fit model predicts poorly the fault-parallel relative velocities of sites around the Green Valley fault in the north-bay subregion (Figure 7.23a). There appears to be a systematic misfit such that the velocities of sites west of the fault are overestimated and those east of the fault are underestimated. The systematic offsets in the fault-normal velocities are still evident. However the misfit has been reduced slightly by the inversion. Relative vertical velocities were also predicted for the GPS sites and ranged within ± 0.3 mm/yr.

[1]The F-test removes the ambiguity in the χ^2_ν test by separating the effect of observational error from the model misfit and is therefore independent of the different methods used above for calculating χ^2_ν. The F-test will be the same regardless of which χ^2_ν is used.

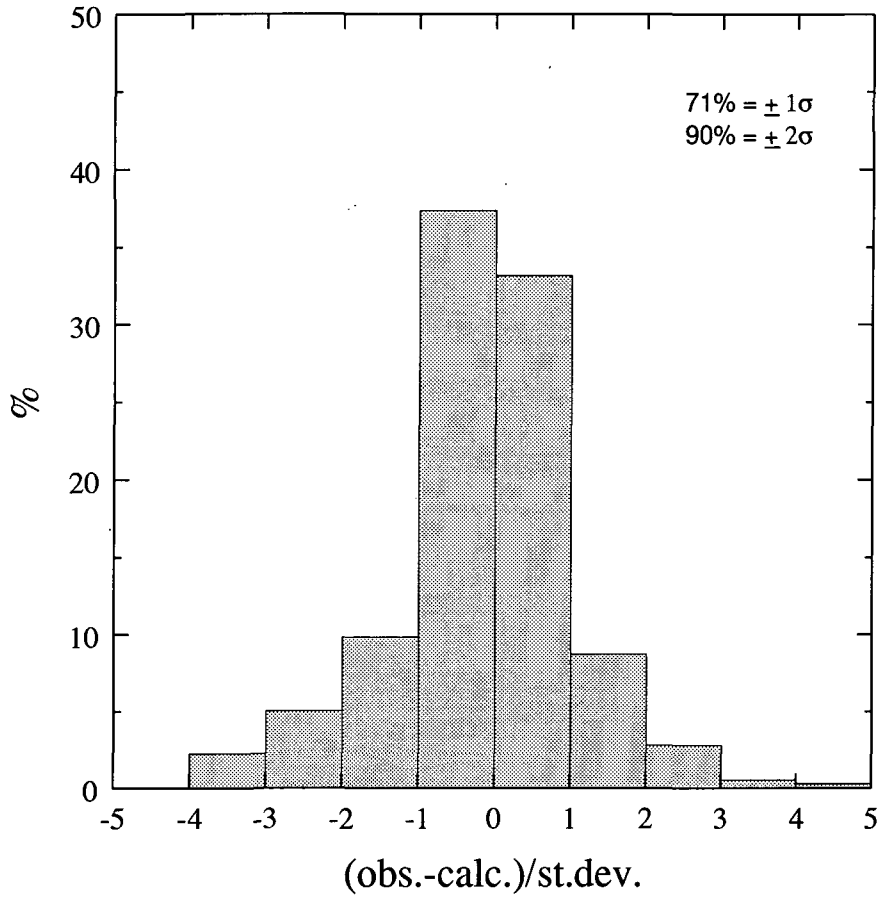

Figure 7.21: Histogram of the normalised residual distribution for the best-fit three-dimensional model.

As for the forward model, the residual strain-rates were calculated to highlight model misfit (Figure 7.24). The largest reduction in the residuals, when compared with the forward model, occurs in the Monterey-bay subregion between the San Andreas and Calaveras faults and is probably a result of allowing surface creep on the Sargent fault. The surface creep rate on the Sargent fault was estimated to be 2.1 ± 0.3 mm/yr, slightly lower than the measured value of 3 mm/yr [*Prescott and Burford*, 1976].

Fault-normal compression is seen in some of the residuals but it is highly variable and associated with an equal amount of fault-normal extension. Several residuals indicate right-lateral shear sub-parallel to the strike of the local faults. Some of these are located close to modelled faults and possibly indicate unmodelled shear-strain on that fault. For a right-lateral shear-strain residual this would indicate either a slip rate too low or a locking depth too deep. The residual shear strain along the Point Reyes peninsula may be once again associated with unmodelled

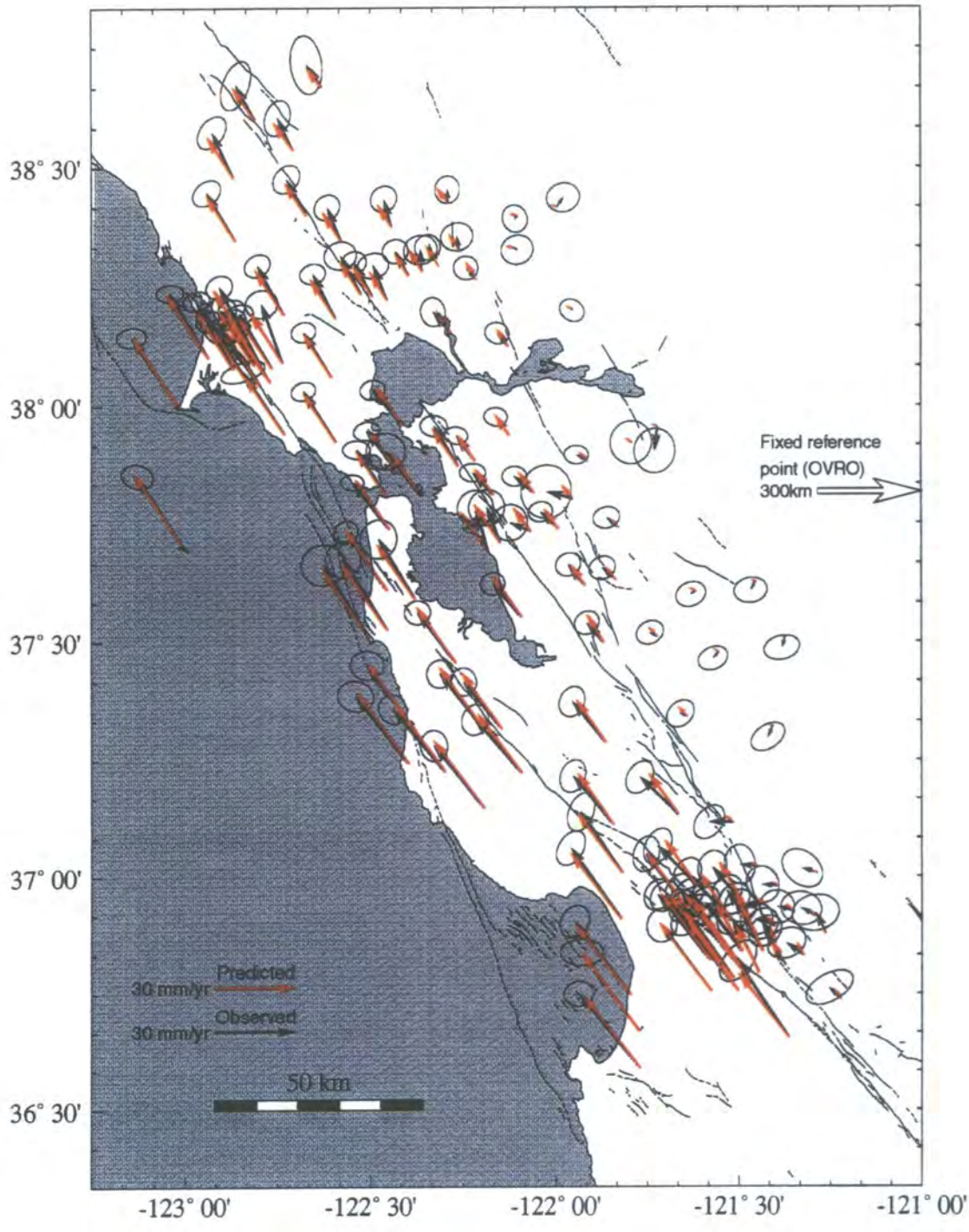

Figure 7.22: Same as Figure 7.18 except for the best-fit three-dimensional model.

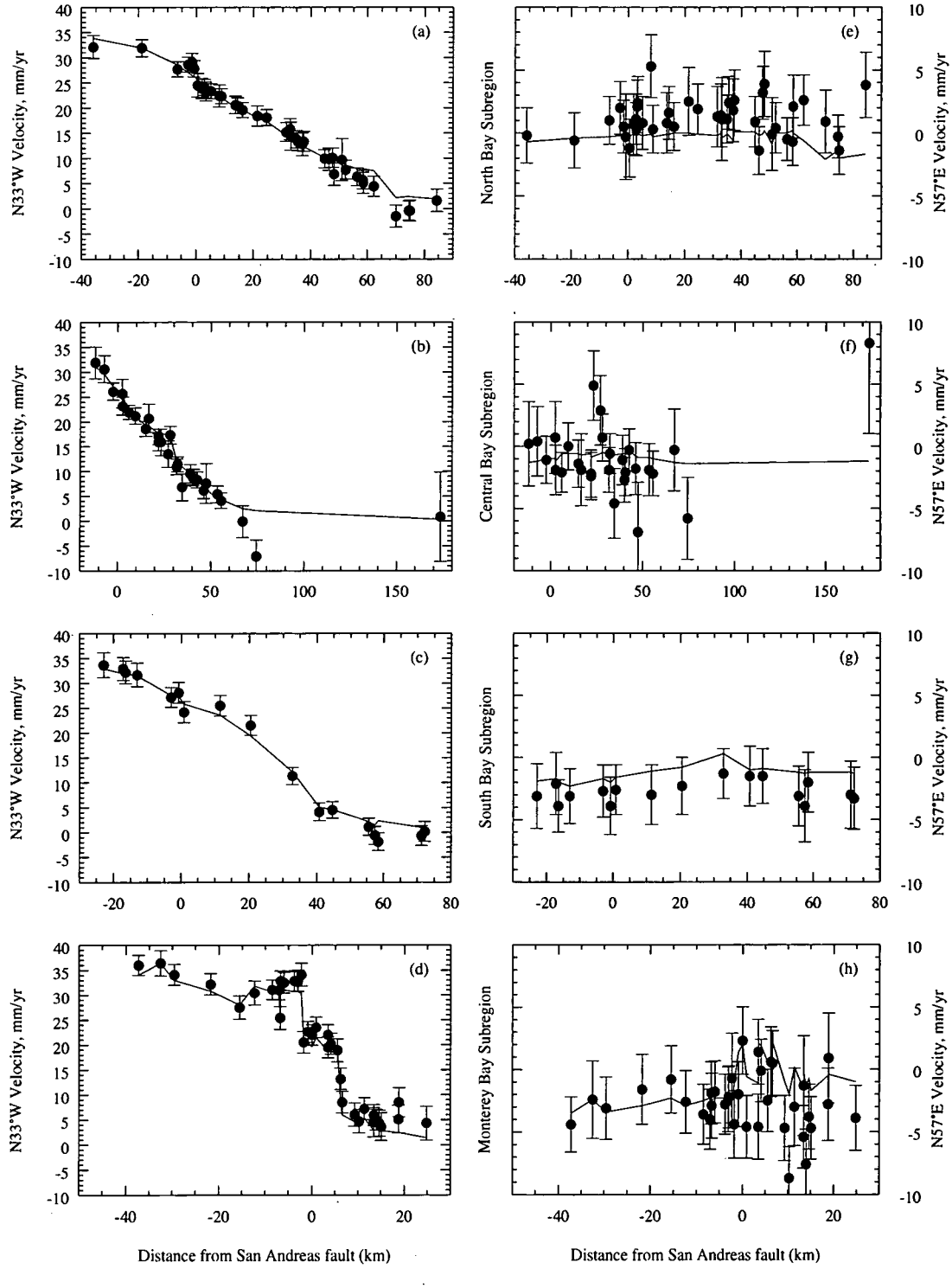

Figure 7.23: Same as Figure 7.19 except for the best-fit three-dimensional model.

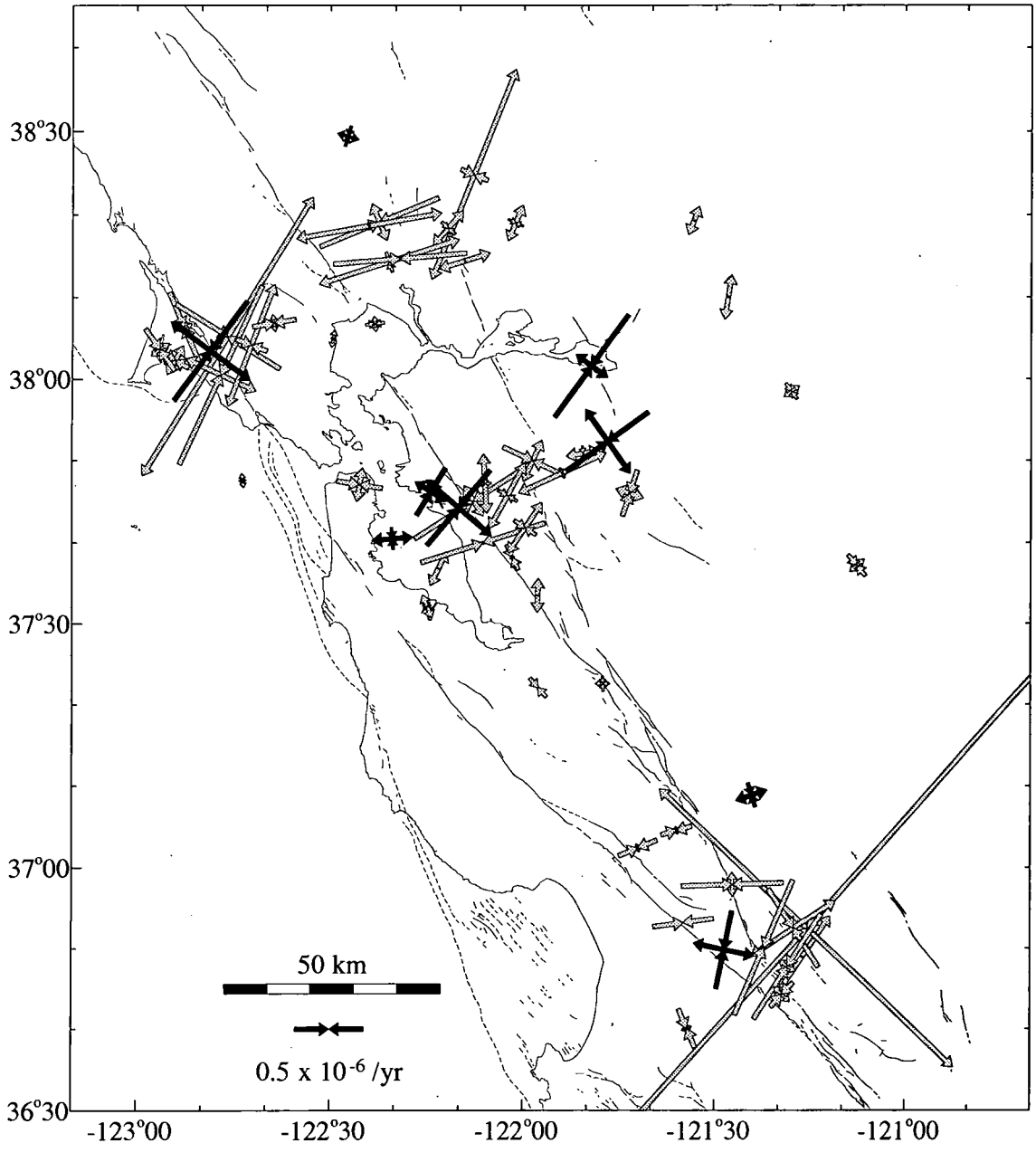

Figure 7.24: Same as Figure 7.20 except for the best-fit three-dimensional model.

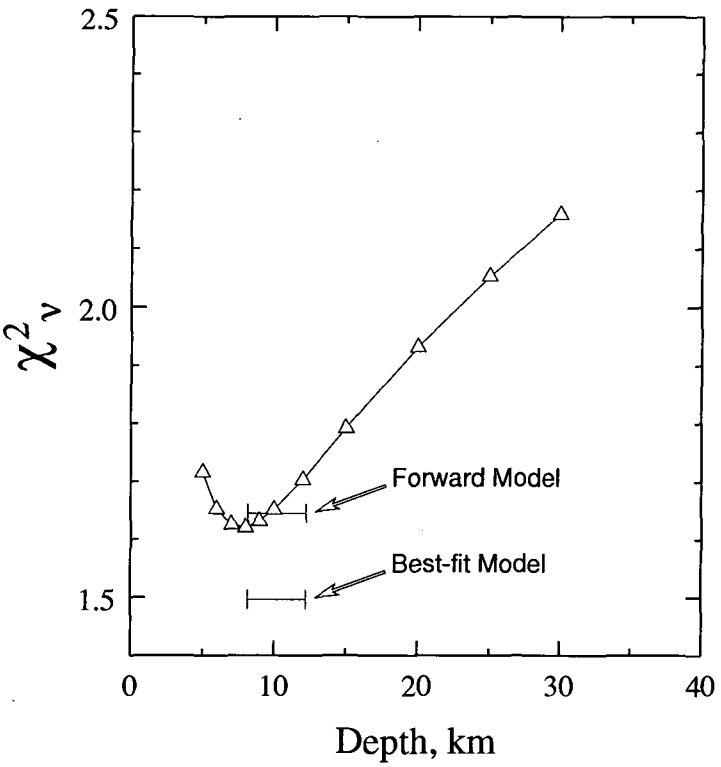

Figure 7.25: χ^2_ν as a function of locking depth for a series of inversion models. Triangles represent the estimated χ^2_ν for each inversion. Horizontal bars represent the forward and best-fit models whose locking depths are fixed using the 90% depths of seismicity.

distributed surface creep or a compliant fault zone. Two shear-strain residuals are situated close to Vaca-Antioch fault just south of the northern arm of San Francisco bay. Geologic slip on this fault has been estimated at 0.3-4.0 mm/yr [*Clark et al.*, 1984] and the residuals may indicate unmodelled movement on this fault during the observation period.

For comparison, a series of solutions were calculated whereby the locking depths on all the faults were varied from 5 to 30 km. In the cases where the locking depth was reduced to less than the estimated base of the surface creeping zone, the depth of surface creep was altered to the locking depth. Figure 7.25 shows the locking depth versus χ^2_ν. There is clearly a minimum at a locking depth of 8 km. This minimum is lower than χ^2_ν for the forward model that has locking depths based on the 90% seismicity depths, but significantly higher than χ^2_ν for the best-fit model. The locking depth primarily effects the slip rate required to fit the data. For example, on the San Andreas fault near San Juan Bautista, a locking depth of 8 km requires a deep slip rate of 15 $\pm$ 1.6 mm/yr, while a depth of 30 km requires

Table 7.4: Slip rates estimated in the three-dimensional inversion. Segment codes refer to those listed in Appendix A.

	Deep Slip					Surface Creep			
	Segment		Rate	Error		Segment		Rate	Error
Fault	From	To	mm/yr	mm/yr	Fault	From	To	mm/yr	mm/yr
San Gregorio	-	-	1.4	2.0	Sargent	SRc1	SRc4	2.1	0.3
San Andreas	SA4	SA8	17.6	1.3	San Andreas	SAc5	SAc7	12.3	1.3
San Andreas	SA9	SA13	15.6	1.2	San Andreas	SAc8	SAc8	11.1	0.4
San Andreas	SA14	SA17	16.7	1.4	San Andreas	SAc9	SAc9	9.4	0.9
San Andreas	SA18	SA22	16.0	1.4					
San Andreas	SA23	SA31	18.1	1.2					
Hayward	HA1	HA6	7.8	1.3					
Hayward	HA7	HA11	9.4	1.3					
Rodgers Creek	HA12	HA19	10.8	1.0					
S. Calaveras	CA1	CA5	23.3	1.1	S. Calaveras	CAcb	CAcb	3.7	1.4
S. Calaveras	CA6	CA10	21.3	1.2	S. Calaveras	CAca	CAca	7.3	0.4
					S. Calaveras	CAc1	CAc1	14.3	0.5
N. Calaveras	CA11	CA14	10.3	1.2	S. Calaveras	CAc2	CAc2	16.9	0.8
					S. Calaveras	CAc3	CAc3	15.3	1.1
Concord	CA15	CA20	9.0	1.2	S. Calaveras	CAc4	CAc4	13.1	1.3
					S. Calaveras	CAc5	CAc8	6.5	1.2
Green Valley	CA21	CA29	7.5	1.1					

a rate of 39.8 $\pm$ 4.5 mm/yr. The uncertainty in the estimated slip rate increases with locking depth, primarily because χ^2_ν increases with increasing depth and the variance is proportional to $\sqrt{\chi^2_\nu}$, but also because surface-strain measurements are increasingly insensitive to the distribution of slip as depth increases.

The 25 estimated slip rates are summarised in Table 7.4 and shown schematically in Figure 7.26. The slip rate on the San Andreas fault, north of the junction with the Calaveras fault, decreases northward from 18 mm/yr to about 16 mm/yr along the San Francisco peninsula. North of the junction with the San Gregorio fault, the slip rate increases to 18 mm/yr, presumably due to the transfer of 1-2 mm/yr of slip from the San Gregorio fault at their junction. Along the Southern Calaveras fault, the estimated deep slip rate is 21-23 mm/yr, up to 10 mm/yr greater than previous estimates along this segment. North of its junction with the Hayward fault, the slip rate on the northern Calaveras-Concord-Green Valley fault steadily decreases from 10 mm/yr to 7.5 mm/yr. The slip rate on the Hayward-Rodgers Creek fault appears to increase northwards from 7.8 to 9.4 mm/yr. Given the uncertainties in the slip rate, this indicates no significant change along fault-strike at a rate that is

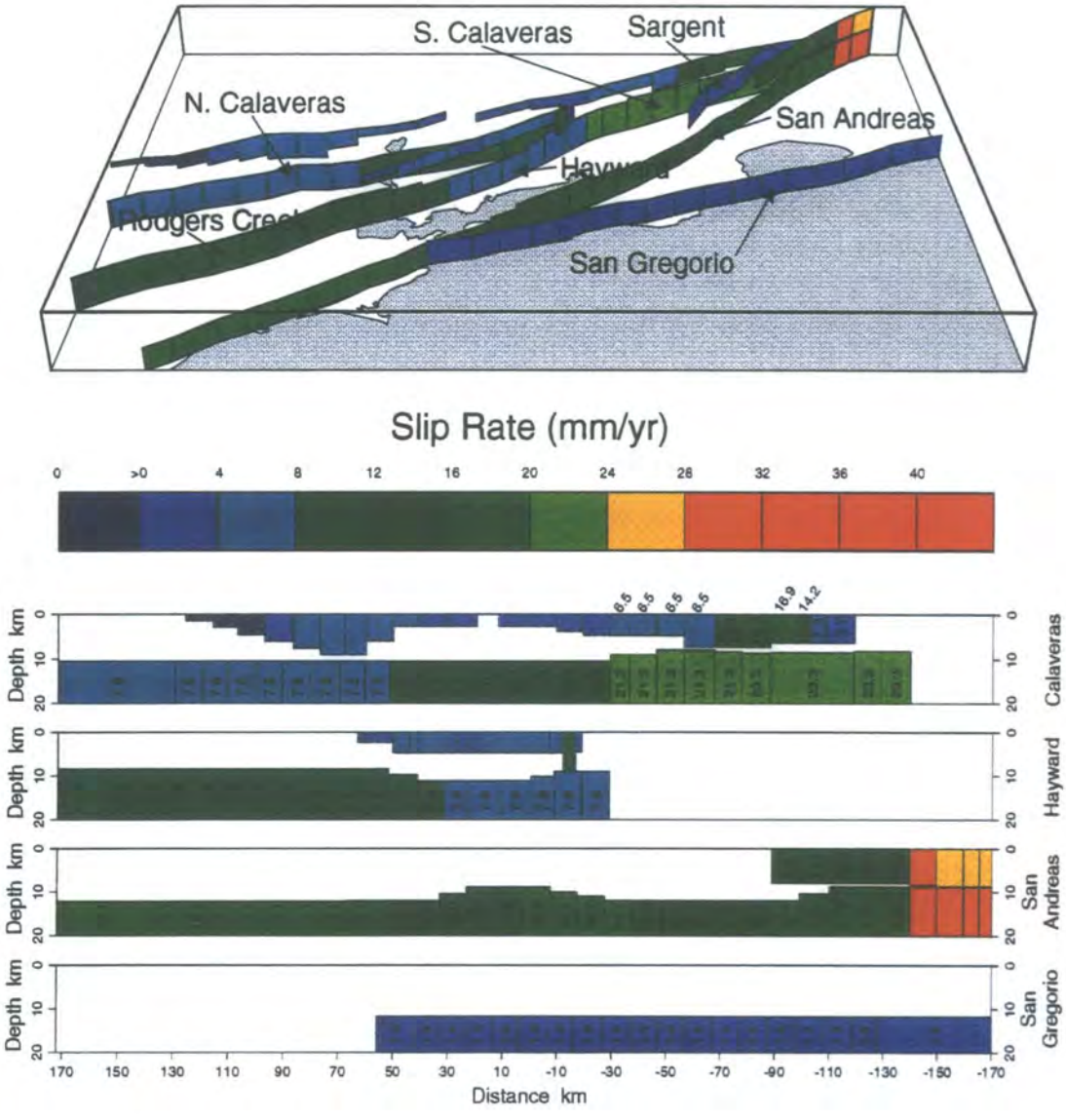

Figure 7.26: Same as Figure 7.17 except showing the results of the three-dimensional inversion. Only slip rates estimated are displayed in the rectangles of the cross-sections.

consistent with previous estimates. Surface creep decreases northward on the San Andreas fault from 12 mm/yr north of the junction with the Calaveras fault to 9 mm/yr just north of San Juan Bautista. Along the southern Calaveras fault, in the Hollister region, the surface creep rate increases from 4 mm/yr to a maximum of 17 mm/yr 10 km north of Hollister, and then decreases to 6-7 mm/yr along the rest of the fault.

7.5 Summary

Measured velocity fields in the San Francisco and Monterey bay regions were modelled using two- and three-dimensional models in an elastic half-space. In the two-dimensional analysis, the faults were assumed to be vertical, infinitely long and parallel. Only the fault-parallel component of the velocity field was studied, and fault-normal motion was assumed to be zero. The region was subdivided into four subregions in order to reduce the effect of the true three-dimensional variation. The Monterey-bay subregion was further subdivided into the northern, central and southern parts because of the extreme variation of fault strike there. Two approaches were used. First, a forward model was calculated using fault slip rates based on estimates from published geologic and geophysical studies. Second, the slip rates at depth were estimated from the geodetic data using a linear, weighted, least-squares procedure. In addition, the depth to which surface creep extends was estimated using both the prior and estimated deep-slip rates.

Whilst most of the features in the fault-parallel velocity field are well-modelled by the two-dimensional model, the region clearly contains numerous fault segments with variable strike. For this reason a three-dimensional model incorporating many fault segments was developed. The positions of the faults were taken from their mapped surface traces. The locking depths were taken from the 90% seismicity depths, and the depths to which surface creep extends were taken from the results of the two-dimensional modelling. A forward model, using the slip rates from the best-fit two-dimensional model, produced a reasonable fit to the data. The residuals from this model highlighted the probability that unmodelled slip was occurring on the Sargent fault. A weighted, damped, least-squares inversion that also solved for surface creep on this fault resulted in a significant reduction in the residuals.

Chapter 8

Discussion of the Results

8.1 The GPS Results

The GPS data processed from the North Bay, Golden Gate and Central Bay profiles were collected over a period of 3 years. The average, short-term precisions, using the formal errors from the Bernese GPS solutions, are 1-2 mm in the horizontal components and 8-10 mm in the vertical component. These precisions are about half those estimated from the scatter in the results for lines in southern California [*Larson and Agnew*, 1991]. Their small sizes illustrate the well known fact that precisions calculated purely from the scatter in the measured data underestimate the true accuracy. Long-term repeatability, obtained from the scatter of the calculated results about about a best-fit straight line, is 4-8 mm in the horizontal components and 30-50 mm in the vertical component. Typical scaled formal errors for the calculated relative velocities were $\sim$2 mm/yr in the horizontal and up to 22 mm/yr in the vertical. These uncertainties were determined by propagation of the full position covariances from each GPS solution, rescaled by the χ^2_ν fit of the data to the least-squares solution. Typical scaling factors for Bernese GPS solutions are around 5 [*M. Murray*, personal communication, 1993].

The smallest errors were found for the North Bay profile and the largest for the Central Bay profile, which is largely attributable to the number of surveys used to calculate the site velocities. 4-7 GPS surveys within a time span of 3 years are sufficient to allow the detection of horizontal crustal deformation. This is less than the $\sim$10 year time span required for terrestrial geodetic measurements. The vertical component is not sufficiently accurate to detect vertical motion in the short time span for which results are available at present. The measured relative horizontal velocities indicate shear flow about the fault system and the measured vertical velocities, although insignificant, mimic the Coast Range topography.

8.2 Integration of the Geodetic Data

The results from the San Francisco bay region GPS profiles were integrated with previous trilateration surveys and VLBI data, using a least-squares procedure, to obtain spatially dense samples of crustal deformation that could be tied to an external reference frame, in this case, the stable interior of a plate. Integrating different geodetic data can only be achieved if there are sufficient sites in common. In the GPS, trilateration and VLBI data there are a total of 10 common sites that were surveyed by more than one technique. Unfortunately most of the ties are in the north of the region which could lead to a distortion of the deformation pattern in the south, and for this reason the closest trilateration point to the VLBI site Fort Ord was assigned the same VLBI velocity as Fort Ord (Section 5.2.1). This biased the velocities in the region slightly because the trilateration point is closer to the San Andreas fault than Fort Ord and therefore probably has a slightly different velocity.

This method of combining the data is not the most rigorous of the techniques available. For example the "simultaneous reduction" technique used by DYNAP [*Drew and Snay*, 1989] is superior in theory because it uses the original data rather than the derived velocities and line-length change rates to estimate the parameters. However the relative simplicity of the former technique, the uncertainties in the data and the inability of the DYNAP program to output velocities, are the reasons why it was used for these data. Any substantial corruption of the results would appear in the calculated velocities as inconsistencies in the velocities or velocity gradients between adjacent sites observed with different techniques. That the observational misfit was relatively low, (χ^2_ν of 1.4) and the velocities at adjacent sites consistent, are evidence that the method worked well.

8.3 The San Andreas Discrepancy

The geodetic measurements of crustal deformation in the San Francisco bay region can be used to constrain the partitioning of Pacific-North America relative plate motion. The maximum motion across the velocity profiles of Figures 5.6 to 5.9 impose a lower bound on the relative plate motion across the San Andreas fault system since the network may not be wide enough to detect the entire zone of deformation. The total relative motion for the four velocity profiles ranges from

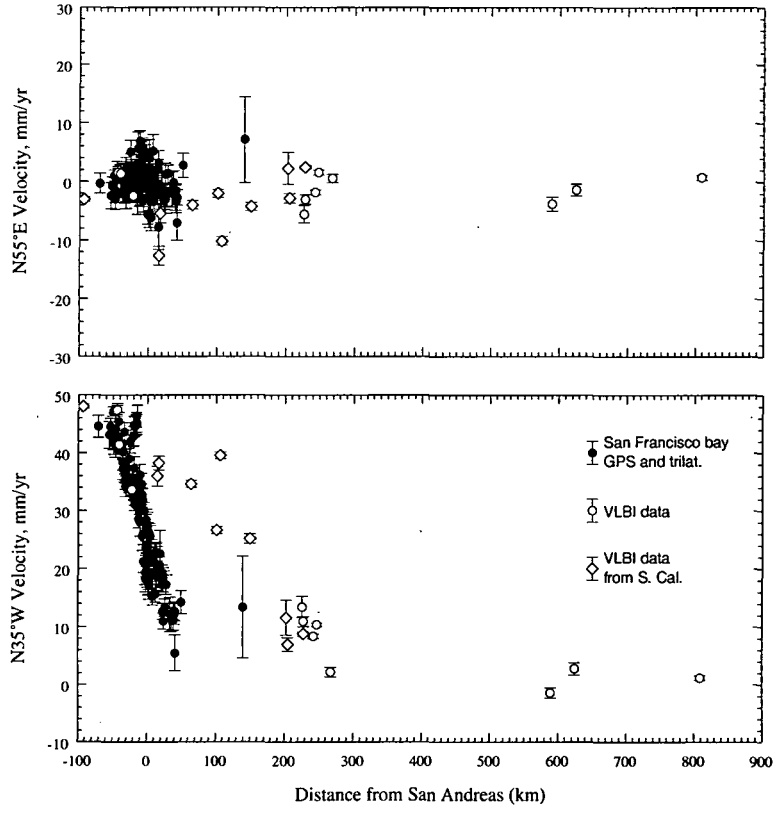

Figure 8.1: Horizontal site velocities for the San Francisco bay region and VLBI sites for the western United States from *Ward* [1990] resolved into components perpendicular (top) and parallel (bottom) to the average, relative, Pacific-North American plate motion direction in central California (N35°W) plotted as a function of distance along a N55°E profile. Error bars represent one standard deviation

30-34 ± 3 mm/yr. These are comparable with the geological slip rate for the San Andreas fault along the central portion of the fault system of 34 ± 3 mm/yr at N41° ± 2° W [*Minster and Jordan*, 1984] but lower than the geologic slip rates across the fault system in the San Francisco bay region of 40-43 ± 4 at N31-38° ± 6° W [*Kelson et al.*, 1992]. The difference could be due to an insufficient width of the network, the effect of elastic stress accumulation and time-dependent complications due to the several orders of magnitude difference in time span between the geodetic and the geologic observations. To account for elastic strain accumulation and the limited width of the network the total, cumulative slip rates across the fault calculated from the two-dimensional models can be compared with the geological estimates. From the best-fit models the cumulative slip rate at depth is approximately 36 ± 4 mm/yr (Table 7.3) which is within 1σ of both geological estimates.

To map the distribution of relative plate motion across the western United States, the San Francisco bay region site velocities relative to the interior of North America were used (Figure 5.4), together with the VLBI site velocities for the western United States (Figure 2.9; from *Ward*, 1990). Since both data sets are relative to the interior of North America then the VLBI data can provide extra control on the distribution of motion outside of the San Francisco bay region. The plate-motion parallel and plate-motion perpendicular velocity components are plotted as a function of distance from the San Andreas fault perpendicular to the plate-motion direction in Figure 8.1. Throughout the western United States the plate-motion perpendicular velocities are scattered evenly about 0 mm/yr. No obvious systematic effect occurs along any part of the profile. The plate-motion parallel velocities in the San Francisco bay region show a near-linear trend from 12 mm/yr in the east to about 46 mm/yr in the west. The VLBI data in southern California clearly define a separate trend that is a product of the more easterly position of the San Andreas fault and a broader distribution of the faults when compared with northern California. If the northern-California velocity gradient continued eastwards then the full NUVEL-1A rate for Pacific-North America motion (46 $\pm$ 2 mm/y, N36° $\pm$ 2°W) would be reached within another 30-50 km east of the Coast Ranges. This is clearly incompatible with the deformation seen in Figure 8.1. Instead the gradient flattens out at around 10-12 mm/yr for approximately 250 km to the western edge of the Basin and Range province (VLBI sites between 200-250 km distance). To the east, the data are unable to distinguish whether the deformation is distributed throughout the Basin and Range province or concentrated along some specific zone. Sites west of the San Andreas fault are moving at a rate comparable to the predicted NUVEL-1A rate and so deformation appears to end abruptly within a few tens of kilometres west of the San Andreas fault system.

Plotting site velocities as a function of distance is not the ideal way of characterising plate boundary deformation. Alternatively, the observed velocities for a series of stations in the western United States may be plotted relative to the interior of either plate. However, partitioning of relative motion is then affected by possible biases and errors of the velocities of the individual sites. A third method is to calculate Euler poles for several hypothetical "microplates" across the plate boundary upon which several (at least two) sites are situated [*Argus and Gordon*, 1990; *Ward*, 1990]. In this approach the velocities of individual sites are averaged out. However, this approach assumes rigid plates. Since, in general, the plate boundaries coincide with the locations of major faults, velocities of stations close to the edge of the plate boundary will be affected by strain accumulation. If the sites are well distributed

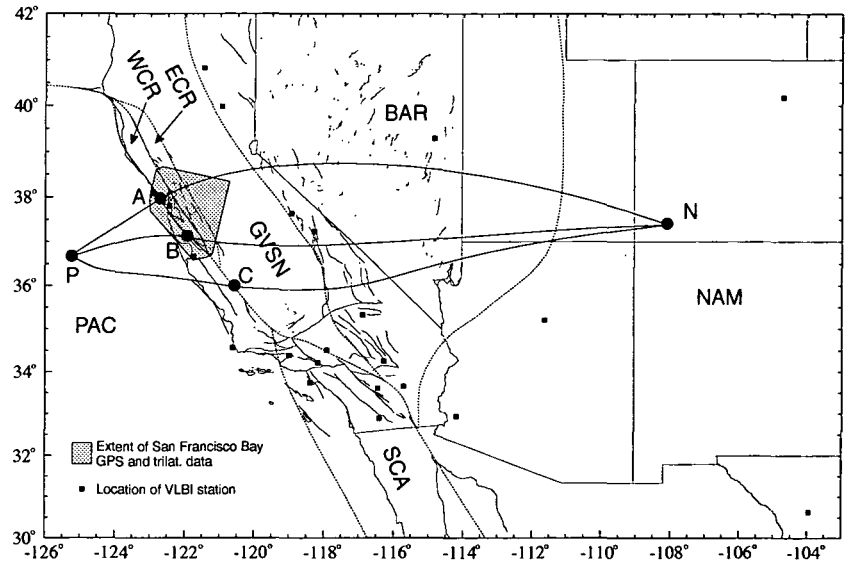

Figure 8.2: The six hypothetical "microplates" in the western United States used to characterise components of the Pacific-North American plate boundary deformation (NAM, North America; BAR, Basin and Range; GVSN, Green Valley-Sierra Nevada; ECR, Eastern Coast Ranges; WCR Western Coast Ranges; PAC, Pacific; SCA, Southern California). Grey polygon indicates the extent of the San Francisco bay GPS and trilateration networks and squares indicate the locations of VLBI sites used to calculate the Euler poles. The Euler poles for these plates are used to estimate integrated deformation rates along paths NAP, NBP and NCP. The Euler pole for SCA is estimated by *Ward* [1990].

across the plate then this bias will average out. In the case of this study, the sites are all distributed along one edge of the plate (west of the San Andreas fault system) and the results are likely to be biased.

Nevertheless, the San Francisco bay region data, and the VLBI data from *Ward* [1990], have been used to find Euler poles for 6 hypothetical "microplates" across the western United States (Figure 8.2). From these, integrated deformation vectors along three paths between the North America plate and the Pacific plate (path NP) through 3 points A (38°N, 122.8°W), B (37.1°N, 121.8°W) and C (36°N, 120.6°W) have been calculated (Figure 8.3). The Euler poles for plates NAM and BAR are the same as those calculated by *Ward* [1990] since no new information is available here. The Great Valley-Sierra Nevada (GVSN) plate only contains one site which is insufficient to calculate a Euler pole. The sites along the western edge of the Coast Ranges are not included in the GVSN plate since their velocities are influenced by strain accumulation around the San Andreas fault system. Therefore GVSN is combined with the Basin and Range province (BAR) to estimate an average Euler

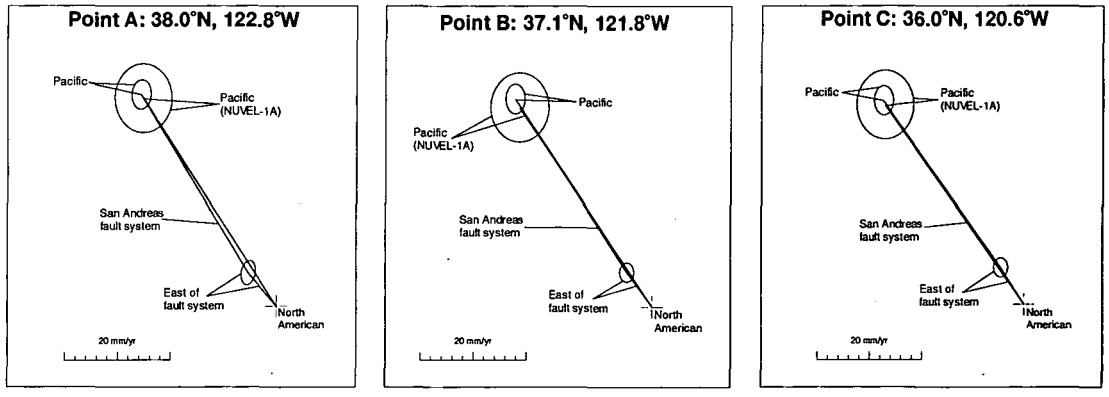

Figure 8.3: Summed plate motion vectors for the San Andreas fault system and deformation east of the fault system and a comparison to the NUVEL-1A prediction at points A, B and C.

pole for deformation east of the San Andreas fault system. The area within the fault system has been divided into two hypothetical plates, the western Coast Ranges (WCR) and the eastern Coast Ranges (ECR). These can be equated with the Sebastapol and Santa Rosa blocks [*Fox*, 1983]. The addition of the San Francisco bay region data eliminates the bias in the results of *Ward* [1990] caused by including the Point Reyes VLBI site in a Northern California plate east of the San Andreas fault. Within the Pacific plate (PAC), only the westernmost sites are included to reduce the effects of strain accumulation.

The relative motion vectors are summarised in Table 8.1. The summed plate motion vectors at sites A, B and C are plotted in Figure 8.3 together with the predicted velocity from the NUVEL-1A model. The full Pacific-North America relative vectors agree to within 1σ with the rates predicted by the NUVEL-1A model for all three points. The plate motion is divided up into 38-39 mm/yr across the San Andreas fault system and 8 mm/yr to the east of the San Andreas fault system. No deformation is required to the west of the fault system. The velocity to the east of the San Andreas fault system is likely to be a few mm/yr higher than estimated because the VLBI stations at the western edge of the Basin and Range province are within tectonically active areas. For example, OVRO lies to the east of the mainly right-lateral Owens Valley fault zone and the normal-slip Independence fault and its velocity is estimated to be 1-2 mm/yr lower than if it were located in the Sierra Nevada Mountains [*Argus and Gordon*, 1991]. As a result the slip rate across the San Andreas fault is likely to be a few mm/yr lower than estimated.

Table 8.1: Summary of relative plate velocities at points A, B and C along the San Andreas fault system in central California together with the NUVEL-1A prediction.

Point	Pacific - N. America (NUVEL-1A)	Pacific - N. America	San Andreas Fault System	Pacific - W. Coast Ranges	W. Coast Ranges - E. Coast Ranges	E. Coast Ranges - East of SAFS	East of SAFS - N. America
A							
38.0°N	46.2±1.4	47.0±0.4	38.9±0.6	13.8±0.6	13.5±0.6	11.6±0.6	8.2±0.4
122.8°W	N33°±2°W	N33°±1°W	N31°±1°W	N29°±2°W	N31°±2°W	N35°±3°W	N41° ± 3°W
B							
37.1°N	46.0±1.4	46.9±0.4	38.7±0.6	13.8±0.6	13.5±0.6		8.2±0.4
121.8°W	N34°±2°W	N34°±1°W	N33°±1°W	N30°±2°W	N29°±3°W		N37°±2°W
C							
36.0°N	45.9±1.4	46.6±0.4	38.4±0.5				8.2±0.4
120.6°W	N36°±2°W	N35°±1°W	N36°±1°W				N33°±2°W

The N33°W direction of motion for the Basin and Range-Sierra Nevada relative to North America at point C is nearly parallel to the N30°$^{+5}_{-10}$W strike of the Eastern California Shear Zone [*Dokka and Travis*, 1990a; 1990b] and the geodetic estimate of N31°W ± 3° for maximum right-lateral shear-strain accumulation in Owens Valley [*Savage et al.*, 1990; *Savage and Lisowski*, 1995]. This has been taken as evidence that the Eastern California Shear Zone accommodates 60-100% of the relative plate motion east of the San Andreas fault system [*Dokka and Travis*, 1990b; *Ward*, 1990; *Savage et al.*, 1990; *Argus and Gordon*, 1990; *Feigl et al.*, 1993; *Sauber et al.*, 1994]. However, to the north (points B and A) the deformation trends 4-8° degrees more westerly and aligns more closely to the models predicted by *Minster and Jordan* [1987] (see Chapter 2) which combined geodetic data with directional data from the Basin and Range province.

This change in azimuth with latitude possibly reflects the changing importance in the type of deformation from primarily right-lateral shear in southern California to a combination of right-lateral shear and extension orientated N60-65°W in northern California, Nevada and Utah. Geodetic data have been unable to define the Eastern California Shear Zone to the north of Owens Valley [*Savage and Lisowski*, 1984]. Across the Owens Valley, measured strain rates imply extension perpendicular to the valley axis and right-lateral shear across the axis. To the north, this deformation probably becomes more diffuse and possibly extends from the Sierra Nevada mountain front to the Nevada seismic zone which has been the locus of several large earthquakes this century [*Ellsworth*, 1990]. The focal mechanisms of

these earthquakes show an increasing proportion of dip-slip movement with respect to strike-slip movement with increasing latitude.

These estimates of relative motion between hypothetical "microplates" indicate that the San Andreas discrepancy can be resolved to within the uncertainties of the global plate motion model NUVEL-1A. Motion on structures offshore of the central California coast is no longer required to explain the discrepancy although a few mm/yr of motion is allowed by the uncertainties. The discrepancy can be attributed wholly to motion in the Basin and Range province, in particular, the Eastern California Shear Zone. If 75-100% of the 10-12 mm/yr attributed to motion east of the San Andreas fault system is accommodated in the Eastern California Shear Zone (and its more diffuse northern extension) then only 0-3 mm/yr is required on faults in the eastern half of the Basin and Range province. This motion may be distributed between many faults in the province or along one fault such as the Wasatch fault forming the eastern edge of the province. This prediction may be tested when the Basin and Range GPS network [*Foulger*, 1994] is resurveyed in the future. That the style and location of the major components of deformation in the Pacific-North America boundary vary along its length precludes the use of one vector diagram to summarise the motion. Several vector diagrams along different paths or a table of Euler vectors are a more complete description of the style of deformation. The azimuth of motion across the San Andreas fault system (Table 8.1) trends slightly more northerly than the strike of the faults in the San Francisco bay region. This may indicate a small component of shortening perpendicular to the faults of up to $\sim$2 mm/yr.

8.4 Deformation in the San Francisco Bay Region

8.4.1 Two- versus Three-Dimensional Models

The fault-parallel component of the geodetically-observed deformation field along the San Andreas fault system can be adequately modelled using two-dimensional elastic dislocation models involving slip at depth approximately below each of the active faults. However, two-dimensional models are unable to describe the fault-normal component of deformation and are inadequate where the faults are not

parallel to one another. In the south-bay subregion, the San Andreas fault changes strike from N44°-36°W. Neglecting this change in strike and including all sites in the inversion resulted in slip-rate estimates for the San Andreas and Calaveras faults that differed by up to 6 mm/yr from slip rates estimated using data that omitted two sites that were not well represented by the chosen fault strike and position (Table 7.3). The variation of fault strike in the Monterey-bay subregion required splitting of that subregion into three separate parts in order to minimise the geometric variation and provide reasonable fits to the data. Nevertheless, despite the obvious geometrical inadequacies, two-dimensional models do offer some advantages for the modelling of deformation across a fault system. Two-dimensional models are more tractable mathematically, and it is easier to invert for various parameters and include structural and rheological complexities, for example, lateral inhomogeneities, shear zones and time dependence.

The three-dimensional model is able to predict both the fault-parallel, fault-normal and the vertical deformation associated with a geometrically complex fault system. The results of the three-dimensional models show that much of the detail in the deformation, which could be attributed to noise in the two-dimensional models, can be explained as resulting from the three-dimensional nature of the fault system. Three-dimensional models are better for exploring the changes in the deformation along fault strike, the effect of smaller, discontinuous faults and fault complexities such as bends and offsets. However, three-dimensional models are harder to formulate and extend to incorporate structural and rheological complexities. A comparison between the slip rates estimated using the two-dimensional models and those estimated using the three-dimensional model is given in Section 8.4.9.

8.4.2 Lateral Inhomogeneities

Despite the absence of fault creep along the San Andreas fault north of San Juan Bautista, the fault-parallel velocity component exhibits a steep gradient across the fault in the north-bay subregion (Figure 5.6). Several explanations have been proposed to explain this offset [*Lisowski et al.*, 1991] such as a shallow locking depth, previously undetected surface creep along the main fault trace, a low-rigidity (compliant) fault zone or surface creep on a number of subparallel traces within the fault valley. A shallow locking depth and surface creep on the main fault trace have previously been discounted as possibilities. Low rigidity within the 1-2 km wide fault zone does produce the required concentration of deformation across the

fault (Figure 7.6). However, distributed surface creep would also produce the same distribution of motion, and indeed these two processes have the same effect from the point of view of relatively sparse surveying measurements. The low-velocity zone, concentrated deformation and 1-2 km wide fault zone together suggest that lateral inhomogeneity influences the deformation close to the fault. However, if low rigidity is the sole cause for the observed offset then some explanation must be found for why an offset is absent around the Rodgers Creek fault which has a similar low-rigidity zone associated with it [*Eberhart-Phillips*, 1986]. Perhaps that velocity contrast is lower, the zone smaller in width and the slip rate lower making the offset undetectable with the current data.

8.4.3 The Green Valley Fault

The models fit poorly the observed geodetic data around the Green Valley fault. In the case of the two-dimensional models, numerous models were tested, varying the position of both the fault at depth and the surface creep zone but none were entirely successful.

Although most of this complexity is accounted for in the three-dimensional model, the fit is still inadequate (Figure 7.23) and of particular note is the asymetry of the misfit about the offset. The surface traces of faults to the north of San Francisco bay and east of the San Andreas fault are more complex than their southern counterparts which is indicative of a young fault [*Castillo and Ellsworth*, 1993]. Within the north-bay subregion the Cordelia fault branches out from the Green Valley fault (Figure 7.4) [*Helley and Herd*, 1977] and creep on the Green Valley fault appears to die out in the north. Seismicity along the Calaveras-Concord-Green Valley-Bartlett Springs fault zones defines a fault plane that is near vertical along the Calaveras fault and dipping 50° to 75° to the northeast along the Green Valley and Bartlett Springs fault. A dip to the northeast of the Green Valley fault could explain the observed asymmetry in the velocity profile.

8.4.4 The Shallow, Surface, Creeping Zone

The depth to which surface creep extends has implications for seismic risk. If the entire seismogenic layer creeps at the plate rate then little or no strain would accumulate and the fault would present a low seismic risk. However if surface

creep is confined to shallow depths and the fault is locked at greater depths, it accumulates stress. The depth to which surface creep extends increases to the south along with the creep rates.

The depth to which surface creep extends was calculated using both the prior slip rates and those estimated in the least-squares inversions. The best-fit slip rates at depth were estimated from the geodetic data assuming that surface creep on near-vertical faults, which produces a symmetrical deformation field that only significantly affects points close to the fault, can be ignored. This assumption appears valid only if the surface creep is small in comparison to the slip rate at depth and is unlikely to bias either the estimate of depth or the slip rate at depth. Where surface creep is considered significant a more appropriate method may be to calculate the depth to which surface creep extends and the slip rate at depth simultaneously using a least-squares iterative procedure.

8.4.5 Fault Locking Depths

During the modelling the fault locking depths were constrained using the distribution of seismicity with depth (Figure 7.3). It is widely accepted that there is a strong correlation between the base of the seismogenic layer and the transition from dominantly brittle to dominantly ductile behaviour [*Meissner and Strehlau*, 1982; *Sibson*, 1983; *Scholz*, 1988]. This transition can be interpreted as the base of the locked layer and the depth beneath which steady aseismic slip occurs (slip at depth).

Inverting the geodetic data for locking depth as well as other parameters is relatively straightforward [e.g., *Matsu'ura et al.*, 1986]. Whether the estimated depths are reliable is, however, the subject of speculation. I believe that 90% depths in seismicity are a better indicator of locking depths than those determined from geodetic data, which are relatively insensitive to the distribution of slip at depth [*Weertman*, 1965]. An example of where an anomalous locking depth would result from the geodetic data is along the San Andreas fault in the north-bay subregion. The steep velocity gradient across this fault, which is probably due to low rigidity within the fault zone, would yield a shallow locking depth and a very low slip rate for the San Andreas fault, together with an large increase (to ~30 mm/yr) in the slip rate estimated for the Rodgers Creek fault, to compensate for the effect of a lower slip rate on the San Andreas fault. Whilst a shallow locking depth

and low slip rate on the San Andreas fault cannot be rejected, especially for fault segments late in their earthquake cycle [*Li and Rice*, 1987; *Tse and Rice*, 1986], the predicted three-fold increase on the Rodgers Creek fault compared to previous, long-term historical rates seems unlikely especially since it is also late in its earthquake cycle.

The three-dimensional model showed that a least-squares inversion using locking depths based on the 90% seismicity depths produced a significantly better fit than any inversion where the locking depths on all the faults were set to some arbitrary value (Figure 7.25). 90% seismicity depths do appear to indicate some fundamental transition depth between brittle behaviour above and more ductile behaviour below which is modelled as continuous aseismic slip at depth.

8.4.6 Shear Zones at Depth

It has been proposed that the plate boundary at depth is better represented by a broad shear zone than by discrete slip planes [*Prescott and Nur*, 1981]. To test this a series of shear zones were considered that extended across the fault system beneath some locking depth. The locking depths were set to the average 90% depths in the region, but deeper or shallower depths did not furnish better fits.

The fits of the shear zone models to the data were generally significantly better than the forward models but significantly worse than the best-fit models. Although the shear-zone model describes the deformation field within the errors, it cannot account for the second-order sinuousity in the velocity profiles (compare Figures 7.5 and 7.7) which suggests some concentration of strain around each fault. However the presence of a shear zone at depth could not necessarily be rejected by the data.

The use of a "mixed model" [*Gilbert et al.*, 1994] could account for the misfit. In such a model the predicted motion results from the superposition of slip along faults beneath the seismogenic layer and tractions at the base of the elastic layer due to motion in a viscoelastic substratum. This model is similar to the base traction model [*Li and Rice*, 1987] when the base of the elastic layer is at least 2-3 times deeper than the fault locking depth. However, surface deformation becomes increasingly insensitive to variations in slip distribution as depth increases and this lack of resolution prevents meaningful inversion of surface data to estimate the relative motion across a shear zone at depths of greater than about 30 km. The results obtained here are most consistent with models where vertical geometries

are dominant and extend far below the brittle-plastic transition.

8.4.7 Fault-Normal Compression

The search for evidence of fault-normal contraction across the fault system was prompted by estimates of a significant component of fault-normal motion in past studies of the modified San Andreas discrepancy (see Chapters 1 and 2), the low shear strength attributed to the fault system [*Mount and Suppe*, 1987; *Zoback et al.*, 1987] and late Cenozoic shortening across the Coast Ranges in southern California, estimated to be between 9 and 15 mm/yr [*Namson and Davis*, 1988; *Argus and Gordon*, 1991]. However, more recent estimates for motion perpendicular to the Pacific-North America plate boundary have revised that estimate downward to around 2 ± 2 mm/yr [*Argus and Gordon*, 1991] or less (see section 8.3).

Spatially-uniform, fault-normal compression was found necessary to fit the trilateration measurements across the San Andreas fault near Parkfield (Figure 1.2) [*Harris and Segall*, 1987]. However, if such compression was required by the San Francisco bay region data studied here, but left unmodelled, the residuals would highlight an almost uniaxial regional compression field (e.g., as observed across the Santa Barbara channel and Ventura Basin in southern California by *Feigl et al.* [1993]). The horizontal strain-rate tensors calculated for the residual velocity field from the best-fit three dimensional model (Figure 7.24) provide no convincing evidence for compression across the fault system. There appears to be no reason why deformation associated with convergence should concentrate around a near-vertical fault such as the San Andreas fault that is hardly, if at all, capable of accommodating compression across it [*Lisowski et al.*, 1991]. A more likely candidate for accommodating convergence would be the Coast Range thrust along the eastern edge of the Coast Ranges, and the search for fault-normal compression in the Coast Ranges should concentrate on sites along its eastern edge.

8.4.8 The Vertical Component of Deformation

Maximum uplift/subsidence rates in the San Francisco bay region, predicted by the three-dimensional model, are of the order of 0.2 mm/yr, similar in magnitude to geological uplift/subsidence rates. The similarity in magnitude of these rates suggests that most of the uplift and subsidence in the area could be explained as the

result of local interactions between active faults (i.e., bends and offsets) without the need to invoke widespread, systematic fault-normal compression across the region. Some additional uplift may occur along more easterly parts of the Coast Ranges due to motion along the Coast Range thrust. This would be consistent with the higher summit elevations in the eastern Coast Ranges and the highly deformed nature of the Santa Rosa block [*Fox*, 1983], east of the Hayward-Rodgers Creek fault, compared to the Sebastapol block to the west.

For GPS measurements, a typical error in the vertical is $\pm$ 20 mm/yr. Significant vertical rates of $\sim$ 0.2 mm/yr will thus be detectable only over $\sim$100 years. Although not very encouraging, the accuracy in the vertical in future surveys should improve with better modelling of the tropospheric path delay and from permanent GPS sites where antenna-height mismeasurement errors are eliminated. In that case, it may be possible to use GPS to study the vertical deformation field in the future. At the present, levelling surveys appear to be the most appropriate technique for studying the vertical deformation field.

8.4.9 Comparison of Calculated Slip Rates to Other Modelling Results

Comparing the estimated slip rates with those predicted using the boundary element method of *Bilham and Bodin* [1992] can provide constraints on the amount of connectivity between the active faults within the system. The estimated slip rates are most consistent with some form of connectivity between all of the class A and class AA faults within the region. That is, the estimated slip rates agree best with those predicted from geometric considerations, if there is connectivity between the San Andreas and Calaveras faults near Hollister, the Hayward and Calaveras faults (along the Mission fault) near Calaveras reservoir, the San Gregorio and San Andreas faults near Point Reyes (Figure 6.15c) and the Rodgers Creek and Maacama faults near Santa Rosa (Figure 6.15b). However, the agreement between rates along the Calaveras-Concord-Green Valley faults is very poor. Slip rates obtained for the Calaveras branch of the fault system would increase if that branch was extended northwards [*Bilham and Bodin*, 1992]. Increasing the slip rates on the Calaveras branch would improve the agreement between the two slip-rate estimates and this suggests that the Calaveras continues northwards as opposed to terminating just north of San Francisco bay.

There is a slight bias between the slip rates estimated from the two- and three-dimensional models, resulting in an overestimate for the two-dimensional slip-rate estimates for the Hayward-Rodgers Creek fault and an underestimate along the Calaveras-Concord-Green Valley faults, compared with the three-dimensional results. This bias is within the uncertainties of the estimate and is presumably a direct result of simplification of the fault system to parallel faults in the two-dimensional model. However, the slip rates estimated from the two-dimensional models provide good initial parameters in the three-dimensional model.

The slip rates at depth and the surface creep rates along the fault system in the Hollister region have been previously estimated using trilateration and triangulation data (See Chapter 6, *Savage et al.*, 1979; *Thatcher*, 1979; *Matsu'ura et al.*, 1986). Those results agree poorly with those estimated here. The older estimate for slip on the San Andreas fault just north of its junction with the Calaveras fault is 4-20 mm/yr greater than the estimate from the three-dimensional inversion. However, the 38 $\pm$ 3 mm/yr estimated by *Thatcher* [1979] was affected by the use of only one fault plane to represent the combined effects of the San Andreas and Calaveras faults, and is more comparable to, and consistent with, the two-dimensional "plate boundary" slip rate of 38.2 $\pm$ 1.5 mm/yr calculated here for the southern part of the Monterey-bay subregion (Table 7.3). The earlier estimates for the southern Calaveras fault are 9-10 mm/yr lower than the present estimate. These differences may be related to the more simplified fault geometries and the smaller data sets used in the earlier models.

A more complicated method, using a Bayesian inverse procedure, to calculate many fault parameters including fault width, dip angle and slip angle was attempted by *Matsu'ura et al.* [1986]. In theory this allows greater freedom during the inversion and removes the assumptions of vertical fault planes and only pure strike-slip motion. Alternatively it could be viewed that freeing more parameters can result in modelling noise in the data. The present models aim not to produce a detailed model of one small area but a reasonable regional model. The results are more consistent along fault strike than those of *Matsu'ura et al.* [1986], and are free from the apparent contradictions of that work such as changes in slip sense from right- to left-lateral along the Sargent fault and estimated fault dips that are not consistent with the dip of the fault plane as defined by earthquake hypocentres.

8.4.10 Time Dependent Complications

In the models presented, the Earth is represented as an elastic half space and strain accumulation between large earthquakes as a result of faults slipping with uniform velocity below some locking depth. In this model there is no provision for variation in the strain rate with time. Whilst elastic behaviour of the crust is demonstrated over short periods of time (e.g., the coseismic response) nonelastic behaviour occurs over longer periods. One of the most widely cited pieces of evidence for nonelastic behaviour is the observed postglacial rebound in Scandinavia. One of the predictions of the viscoelastic model is that slip rates estimated using an elastic half space approximation would be expected to change with time, and reflect the position of that fault in its earthquake cycle. Early on in the cycle, relatively high slip rates would be derived, while late in the cycle they would fall and be lower than the geological rate.

The estimated slip rates at depth (Tables 7.3 and 7.4) generally differ significantly from the predominantly geologically-derived prior slip rates (Tables 7.1 and 7.2). The slip rates estimated for the San Andreas and San Gregorio faults are lower than the prior estimates and the slip rates estimated for the Hayward-Rodgers Creek and Calaveras-Concord-Green Valley faults are higher.

Observations of the time-dependent behaviour of crustal deformation near a fault are generally restricted to the immediate postseismic period (a few months to years following an earthquake). Two end-member mechanisms have been invoked: accelerated aseismic slip on the fault beneath the seismogenic layer (the modified half-space model, Figure 6.3b) and coupling between the elastic layer and viscoelastic half space (the lithosphere-asthenosphere model, Figure 6.3c) (see Chapter 6). It is highly unlikely that surface observations of deformation and two-dimensional models will be able to distinguish between the two mechanisms [*Savage*, 1990] and it is probable that the true behaviour of the earth lies somewhere between the two. However, the observations presented earlier and results from other studies may weigh more heavily in favour of one or other mechanism dominating.

A "mixed" model where vertical structures are dominant and both mechanisms are present was proposed on the basis of observations of strain localisation and orientation [*Gilbert et al.*, 1994]. They considered the base traction model [*Li and Rice*, 1987] to be the closest approximation to their interpretation.

Theoretical models produced by the base traction model were compared with ob-

served trilateration data north of San Francisco bay [*Li and Rice*, 1987] (see also Chapter 6). Their model did not produce an acceptable fit to the data (Figure 6.5). The discrepancy was attributed to either changes in lithosphere thickness across the San Andreas fault or the effects of several subparallel faults. No obvious steps have been detected across the fault system from other geophysical studies (see section 1.4). An extension to the base traction model was presented by *Li and Lim* [1988] to account for two or more subparallel faults. Unfortunately they did not attempt to model the observed data in the San Francisco bay region.

Using the extended base traction model *Li and Lim* [1988] modelled the observed surface deformation for the Salton Sea-Coachella Valley region that includes three subparallel faults. They found that available geologic, geodetic and seismicity data did not provide tight constraints on the model parameters and that the disagreement between the modelling results and the observed deformation suggested that southern California is tectonically different from central and northern California in the sense that it may have a larger relaxation time, smaller elastic plate thickness or a shallower locked zone.

Similar conclusions were presented from analysis of a 100-year geodetic record from northern California between San Francisco and Lake Tahoe [*Gilbert et al.*, 1993]. Those results showed that the majority of deformation associated with the San Andreas fault system was confined to the Coast Range region and that the strain rate there does not continue to decrease throughout the cycle but instead reaches a steady-state level in later intervals (in this case 40 years since the 1906 San Francisco earthquake). They postulated that their results required a thicker lithosphere ($>$ 20 km) and larger relaxation times ($>$ 5-30 years) than usually assumed. In light of these observations, southern California may not be so different from central and northern California.

That such a simple model as the elastic half space should predict the observed deformation is remarkable, especially since the slip rates estimated appear realistic. This has been demonstrated along many parts of the San Andreas fault system (see section 6.3). These models predict the observed deformation without the requirement of a complex slip distribution at depth to duplicate the viscoelastic response of a lithosphere-asthenosphere model [*Savage*, 1990]. These models successfully predict the approximate width of the deforming zone and the localisation of strain around each fault.

The San Andreas fault in the north-bay subregion is used as an example to test

Table 8.2: Parameters for the San Andreas fault in northern California for the base traction model.

Parameter	Value	Reference
Plate velocity V_{pl}	24±3 mm/yr	*Neimi and Hall* [1992]
Elastic plate thickness H	30.0±10 km	*Thatcher* [1983]; *Gilbert et al.*, [1993] *Gilbert et al.* [1994]
Fault locking depth L	12.2±6.1 km	Figure 7.3
Earthquake repeat time T_{cy}	220.0±40 yr.	*Neimi and Hall* [1992]
Relaxation time t_r	14.0 years	*Li and Rice* [1987]
Time since least earthquake t	~87 years	Previous earthquake 1906

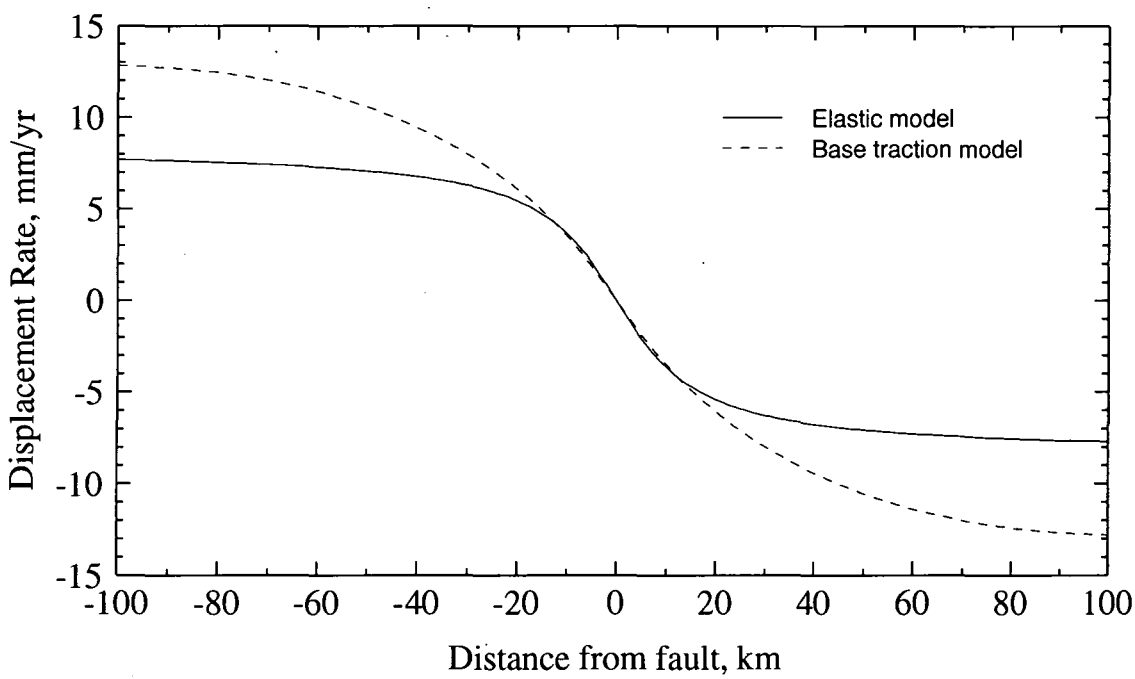

Figure 8.4: Comparison of the velocity profile across the San Andreas fault north of San Francisco bay calculated using the estimated slip rate from the best-fit, two-dimensional, elastic half-space model, and the base traction model using parameters quoted in Table 8.2.

the fit of the base traction model. This model should be able to reproduce the observed deformation across this fault with a similarly good fit as the purely elastic model. A comparison between the velocity profile across the San Andreas fault predicted by the best-fitting elastic model and the base traction model is shown in Figure 8.4. If the fault separation is sufficiently large with respect to the thickness of the elastic layer, then interaction between the faults is weak and predictions of surface deformation can be approximated by the superposition of the velocities calculated for each fault [*Li and Lim*, 1988]. The parameters chosen for the base traction model are provided in Table 8.2. These values were chosen to be consistent with available geological and geophysical evidence. However the uncertainties in these values are large. Within 15 km of the fault the base traction model compares favourably with the elastic model. However beyond 15 km the base traction model predicts too much motion. Assuming that V_{pl} represents the long-term slip rate on the fault, and that the lower rate predicted by the elastic model (16.7 ± 1.4 mm/yr) is a result of the fault being almost mid-way through its earthquake cycle, then the fit can be improved by a combination of increasing the thickness of the lithosphere (elastic layer), increasing the relaxation time and possibly decreasing the locking depth. However there is some trade-off between these parameters such as increasing the relaxation time and lithosphere thickness. Furthermore, increasing the relaxation time and lithosphere thickness broadens the deformation field such that a significant proportion of the deformation lies outside the $\sim$100 km width of the Coast Ranges. Since the only site sufficiently far away from the Coast Ranges is Jackson, which has a high uncertainty associated with its velocity, the results cannot eliminate such a broad zone of deformation. That the maximum relative motion across the profiles (35-38 mm/yr) is very close to the maximum expected across the San Andreas fault system ($\sim$38 mm/yr) suggests, however, that only a minor amount of movement is expected outside the Coast Ranges. It is not clear therefore that both the near- and far-field distribution of deformation, predicted well by the elastic model, can both be simultaneously matched by altering the values of the parameters in the base traction model.

The fit could be improved if V_{pl} is reduced to a similar value to that predicted by the elastic model. The only other change needed to produce a reasonable fit to the data is an increase in the relaxation time to at least half the earthquake repeat time. If this is correct then the slip rates estimated using the elastic models are reasonable approximations to the long-term rate. However, an explanation is then required as to why the geological rates are generally significantly different from the estimated slip rates.

One feature that is common to most observed deformation rates in California is that the motion is nearly linear in time except for the coseismic and immediate postseismic response (up to about 30 years). This has also been demonstrated elsewhere, for example, at subduction zones [*Savage*, 1995]. Lithosphere-asthenosphere models, the modified half-space model and the presently available "mixed" models (e.g., base traction model) all predict changes in the observed rates throughout the earthquake cycle. Time-dependent effects can be decreased in the interseismic period by increasing the asthenosphere relaxation time, introducing a more complex Earth rheology with layers of varying viscoelastic properties or by requiring that there is continuous slip on the down-dip extension of the fault plane that is quasi-steady over the earthquake cycle.

Increasing the relaxation time increases the time over which the viscoelastic effects take place. However, as a result, the time dependence early on in the cycle, during the postseismic period, would be less pronounced and inconsistent with geodetic observations [*Thatcher*, 1983]. Many studies suggest that the Earth is more complex [e.g., *Meissner and Strehlau*, 1982] than a simple elastic layer over a viscoelastic half space and that rock rheology is better represented by a power law as opposed to a linear viscoelastic relationship [e.g., *Kirby*, 1983]. The effects of vertically layered power-law viscoelastic rheology were investigated using a finite-element model of the San Andreas fault in central and southern California [*Williams and Richardson*, 1991]. Several different layering schemes were used, using laboratory results on rock rheology to define the layer properties. These nonlinear models all predicted a smaller time dependence than the linear viscoelastic models. However, in all cases the inclusion of continuous aseismic slip at depth provided a better fit to the observed strain rate than the corresponding model which did not include asesimic slip.

Although the fault plane beneath the locked layer is allowed to slip in response to the imposed stress from an earthquake in the modified half-space and base traction models, the slip rate is predicted to diminish gradually to zero throughout the earthquake cycle. In the base traction model 70% of the total postseismic slip on the fault plane occurs within the first half of the cycle. If, however, the fault plane slips at a steady rate consistent with the average rate, and is only modestly perturbed by the earthquakes occurring above, as predicted by *Tse and Rice* [1986] (e.g., Figure 8.5) then the observed surface deformation, after rapid postseismic motion would be linear throughout the rest of the cycle. This simple modification, which is equivalent to the approach of *Savage and Prescott* [1978], could reproduce

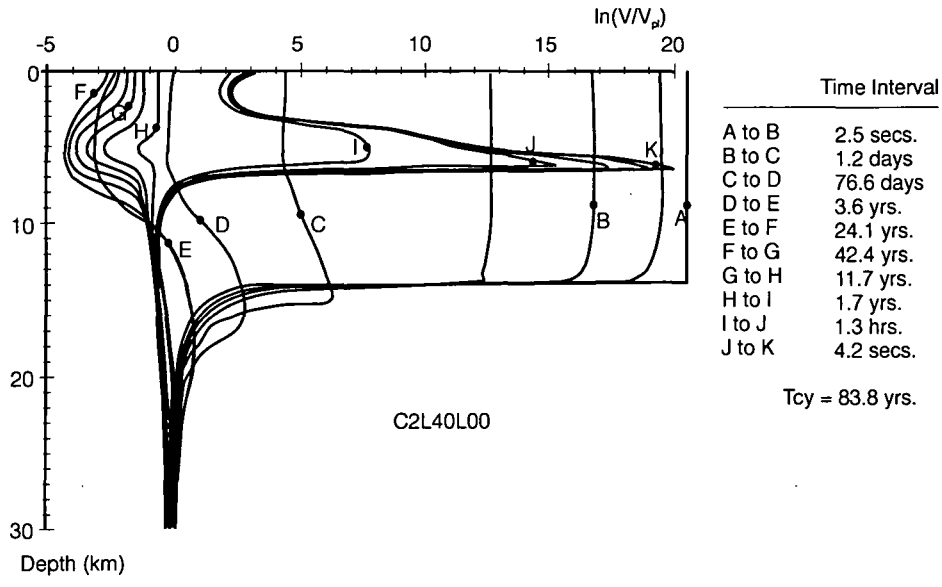

Figure 8.5: Plot of logarithm of normalised slip rate versus depth. Each line represents a constant time, and the time intervals between some lines are listed on the right. Zero on the horizontal axis indicates a slip rate equal to the plate driving rate. Quasi-steady slip from 20 km downwards occurs throughout the earthquake cycle. From *Tse and Rice* [1986].

the basic features seen in the results without requiring model parameters different from previous estimates. The surface deformation would be largely governed by steady slip beneath the seismogenic layer as envisaged in the elastic models but the time dependence would also be significant in the intermediate postseismic period. Interseismic slip rates estimated from elastic models would reflect this quasi-steady slip rate at depth but would not necessarily reflect the geologically inferred rate.

A conceptual model can be proposed based on the above observations (Figure 8.6). In this model the Earth structure consists of several horizontal layers with varying power law viscoelastic rheologies. At increasingly greater depths the effective relaxation time decreases and the material behaves as a fluid on an earthquake-cycle time scale. Along strike-slip faults, an upper, seismogenic, frictional regime gives way at depth to a quasi-plastic regime where largely aseismic, continuous shearing is localised within vertical zones that continue down to 2-3 times the seismogenic thickness. These zones probably broaden with depth to a width of about 20 km at depths of 30-35 km [*Gilbert et al.*, 1994]. Slip on these vertical zones is relatively stable even at shallower levels. Transient, postseismic deformation after a large earthquake results from stress relaxation in the viscoelastic layers and increased aseismic slip below the coseismic fault plane that returns to a stable rate after time.

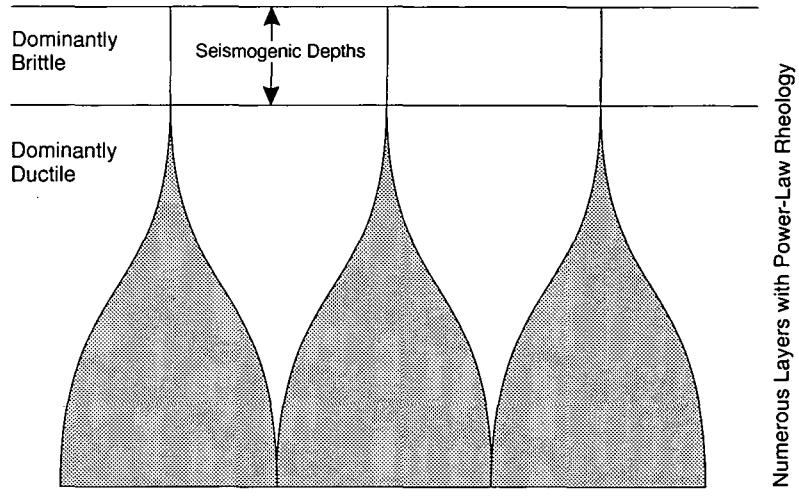

Figure 8.6: A schematic cross section across a transform boundary. The Earth structure consists of several horizontal layers with varying power-law viscoelastic rheologies. The effective relaxation time decreases with depth from greater than, to less than, earthquake-cycle time scales. In the upper brittle layer, relative motion is dominated by earthquakes on discrete fault planes. Below the brittle layer motion is accommodated over a zone that gradually broadens with depth. At depths of around 2-3 times the seismogenic depth these discrete zones merge to form a wide zone in which the medium behaves as a fluid on an earthquake-cycle time scale.

At the present level of accuracy of surface deformation measurements, elastic models provide an adequate first-order approximation to the interseismic deformation. This is because the major influence on the surface deformation is the behaviour of the lithosphere which appears to be, over short time periods, relatively time-independent. However, there are major shortcomings to using the elastic model approach. These models cannot be used to predict the depth to which aseismic slip at depth continues as discrete planes, the variation in surface deformation throughout the whole earthquake cycle or to constrain variations in Earth composition with depth. However they may act as quantitative descriptions of how strain accumulation is partitioned between the major faults in a system. To understand the processes related to repeated earthquakes along transform boundaries a more realistic three-dimensional model of the San Francisco bay region should be developed that includes features of the structure and rheology described above. The model should preferably be dynamic instead of purely kinematic, in the sense that slip on the faults are derived from the boundary conditions applied rather than being specified. Such a complex model is likely to require finite element techniques.

8.5 Earthquake Potential

The San Francisco bay geodetic data provide a means for assessing the potential for future earthquakes in the region. Earthquakes occur as a result of steady accumulation of strain in the Earth's crust which is eventually released by failure along a fault plane. Strain accumulation along interplate boundaries occurs as a result of steady relative plate motions that are more or less constant over geological periods of time. For steady relative motion across the plate boundary to occur, slip on the fault throughout the thickness of the plate must ultimately reach the same total amount. Assuming that the slip rate at depth calculated in the three-dimensional models reasonably represents the long-term or secular slip rate, then, at any depth above the seismogenic depth a slip rate deficit accumulates that is the difference between the total long-term slip and the surface creep. Where the fault does not creep in a shallow, surface zone, i.e., where the fault is fully locked, then a slip deficit is accumulating at the long-term slip rate.

The slip-rate deficit can be converted to the rate of accumulation of potential seismic moment using the derivative of the relationship $M_o = \mu u A$ [*Aki*, 1966], where M_o is the seismic moment, μ is the modulus or rigidity (assumed to be 3×10^{10} Nm^{-2}), A is the fault area and u is the average slip over area A. Figures 8.7 to 8.9 show the slip-rate deficit, the rate of accumulation of seismic moment for a 5 × 5 km square and the history of large earthquake occurrence as a function of position along each fault for the San Andreas, Hayward and Calaveras faults. Where the time of the previous large earthquake on a fault segment is known the total seismic moment accumulated since then can be calculated. From the relation $log M_o = 1.5M + 9$ [*Hanks and Kanamori*, 1979] the equivalent earthquake magnitude M can be found for a given rupture area.

Each fault has been divided into segments based on the pattern of past-seismicity found there and its "characteristic" earthquake [*Schwartz and Coppersmith*, 1984]. For recent and larger earthquakes (e.g., the 1984 Morgan Hill and 1989 Loma Prieta events) the extent of the rupture segment is well documented from various data such as the length of surface break, geodetic data and aftershock sequences. For older and more moderate earthquakes the segment size is based either on prominent geometric irregularities along the fault (e.g., bends or offsets) or using the relationship [*Shimazaki*, 1986],

$$\log L = 0.524 \log M_o - 12.44, \tag{8.1}$$

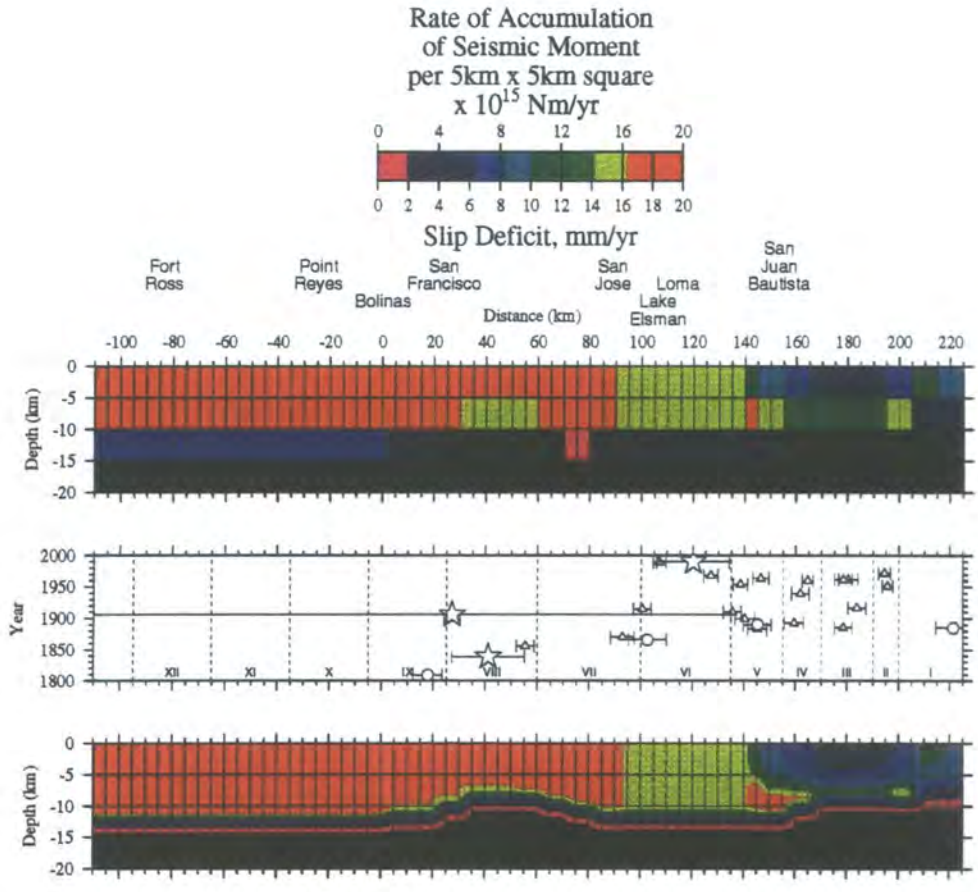

Figure 8.7: Slip-rate deficit and rate of accumulation of seismic moment per 5×5 km square (top and bottom) and past history of earthquakes, $M > 5$, (centre) along the San Andreas fault as a function of distance along that fault. Star, earthquake of magnitude $M \geq 7$; circle, $6 \leq M < 7$; triangle, $5 < M < 6$. Horizontal bar denotes approximate length of rupture zone. Dashed vertical lines divide fault into segments based on "characteristic" earthquakes.

for $M_o \geq 7.5 \times 10^{24}$ N m ($M \geq 6.6$) and

$$\log L = 0.281 \log M_o - 5.98, \tag{8.2}$$

for $M_o < 7.5 \times 10^{24}$ N m ($M < 6.6$). For small to moderate earthquakes the rupture width is proportional to rupture length. For an $M = 5.1$ earthquake the rupture area is expected to be approximately 5×5 km square. For larger earthquakes the rupture width is constrained by the thickness of the seismogenic layer.

The present earthquake potential for the San Francisco bay region is summarised in Table 8.3 based on the results of the best-fit three-dimensional model. It must be emphasised that almost every variable in the calculations is a rough estimate and therefore the results are subject to considerable numerical uncertainty quite apart from any theoretical considerations. Theoretical shortcomings may arise from two

Table 8.3: Predicted earthquake potential for fault segments in the San Francisco bay region based on the slip-rate deficit calculated from the slip rates estimated in the three-dimensional best-fit model.

Fault Segment	Last Earthquake $M > 5$ Year	M	Characteristic Magnitude	Potential Magnitude For Whole Segment Rupture	Potential Maximum Magnitude in 5 km x 5 km Square	Potential Maximum Magnitude in 1 km x 1 km Square
			San Andreas Fault			
I	1885	6.2	6	6.5	6.0	5.1
II	1972	5.1	5	-	5.6	4.7
III	1961	5.6	5	-	5.6	4.7
IV	1960	5.0	5	-	5.7	4.8
V	1963	5.4	5	-	5.7	4.8
VI	1989	7.0	7	6.0	5.2	4.2
VII	1906	8.25	7	6.8	6.0	5.1
VIII	1906	8.25	7	6.8	6.0	5.1
IX	1906	8.25	7-8	6.8	6.0	5.1
X	1906	8.25	7-8	6.8	6.1	5.1
XI	1906	8.25	7-8	6.8	6.1	5.1
XII	1906	8.25	7-8	6.8	6.1	5.1
			Hayward-Rodgers Creek Fault			
I	1868	6.8	6	6.5	5.9	5.0
II	1836	6.8	6	6.8	6.0	5.1
III	1898?	6.2	6	6.5	5.9	5.0
IV	1893	5.1	6	6.5	5.9	5.0
V	?	?	?	?	?	?
Va	1969	5.7	?	5.9	5.5	4.6
Vb	?	?	?	?	?	?
VI	?	?	?	?	?	?
			Calaveras-Concord-Green Valley Fault			
I	1974	5.2	5	-	5.6	4.7
I	1911	5.0	5	-	5.9	5.0
II	1949	5.2	5-6	-	5.9	5.0
III	1979	5.7	5	-	5.5	4.6
IV	1984	6.1	6	6.0	5.4	4.5
V	?	?	5?	?	?	?
VI	1988	5.1	5	-	5.3	4.4
VII	1989	5.2	5	-	5.2	4.3
VIII	?	?	5	?	?	?
IX†	1903?	5.5?	5?		5.9	5.0
IX†	1864	5.7	5?		6.0	5.1
X	1955	5.4	5?		5.6	4.7
XI	?	?	?	?	?	?

† - Two estimates given for this segment. It is unknown whether the 1903 event is associated with this fault.

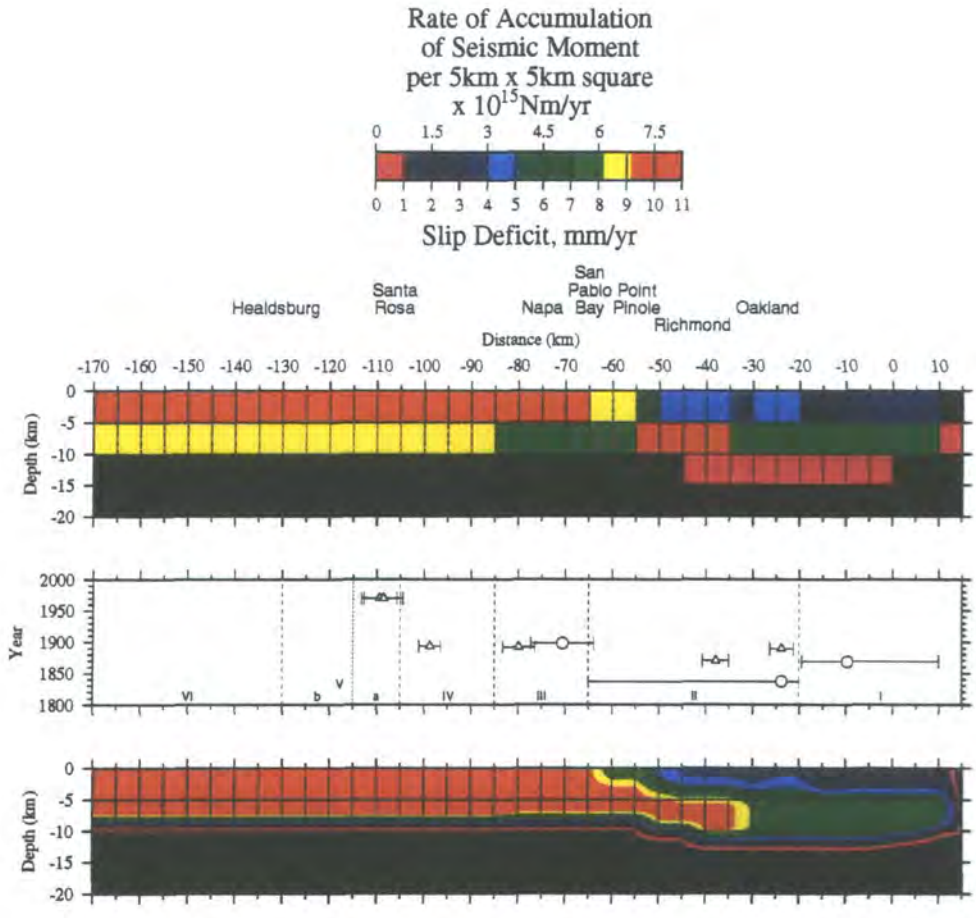

Figure 8.8: Same as Figure 8.6 except for the Hayward-Rodgers Creek faults.

of the main concepts in seismic hazard assessment, "characteristic earthquakes" and "seismic gaps" which are presently under scrutiny [*Jackson and Kagan*, 1995; *Kagan and Jackson*, 1995]. For segments with a characteristic earthquake of magnitude less than 6, the potential magnitude for whole-segment rupture is omitted from Table 8.3 since that segment is not expected to rupture through the entire seismogenic layer in one earthquake.

Whilst it seems from Table 8.3 that almost every fault segment currently has the potential to rupture with a magnitude 5 or larger earthquake, even for segments that have ruptured recently the concern may be misplaced. Take, for example, the Loma Prieta segment (VI on San Andreas fault, Figure 8.7). The present potential on this segment is equivalent to an M 6.0 earthquake despite it being only 5 years since the 1989 earthquake. However, it will take this segment, assuming the present slip rate, a further 150-200 years to reach a potential magnitude of 7.0. During this time some of the strain accumulated may may be released in smaller M 5 earthquakes similar to the M 5.5 (1914) and M 5.3 (1967) events on this segment

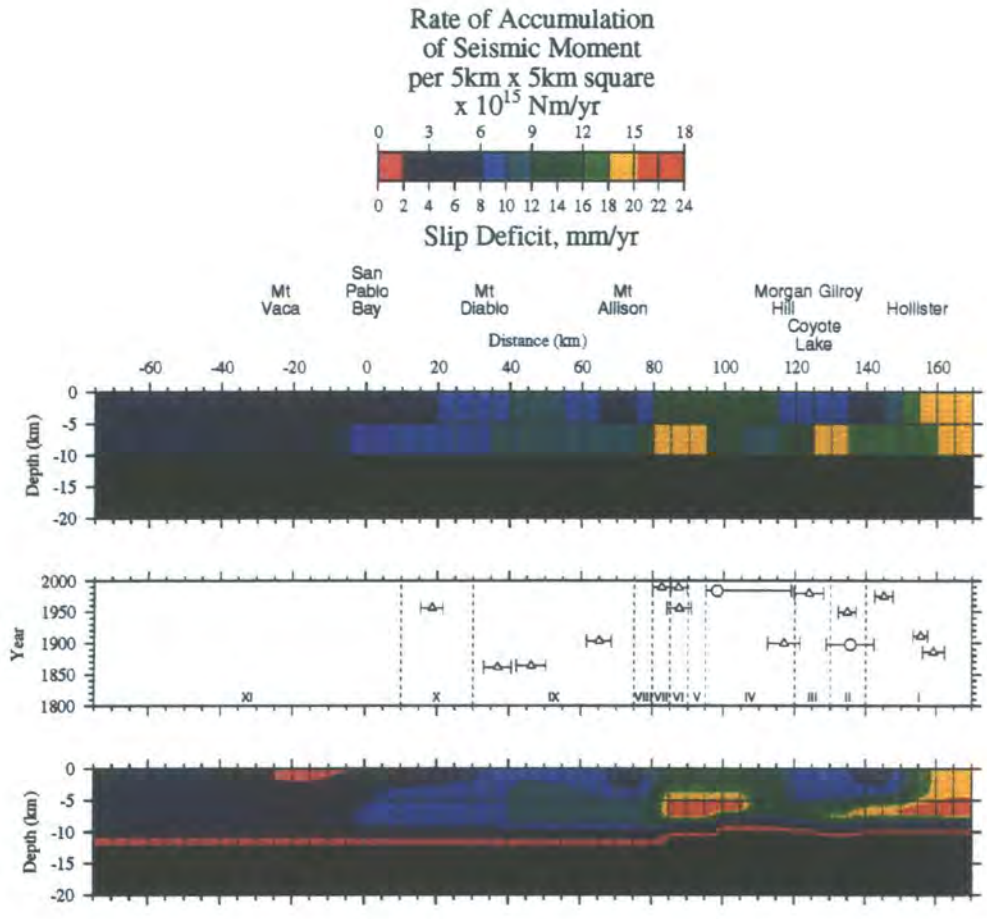

Figure 8.9: Same as Figure 8.6 except for Calaveras-Concord-Green Valley faults.

between the last two "characteristic" earthquakes.

The fault segments considered to have the greatest potential for a "characteristic" earthquake within the coming decades are segments I-IV, VII and VIII along the San Andreas fault, all the segments of the Hayward-Rodgers Creek fault (in particular segment II), and segments I-III, IX, X on the Calaveras-Concord-Green Valley fault. Segments I-V on the San Andreas fault may be considered to be worst-case estimates since these segments are along the creeping section of the San Andreas fault along which some of the strain may be relieved by more frequent but smaller (M 3-4) earthquakes that are not plotted in Figure 8.7. However segment III has been identified as a gap in recent, small-magnitude seismicity that may correspond to a locked patch capable of producing larger (M ~5) earthquakes [*King et al.*, 1990]. Four of the segments identified above (segments VII/VIII on the San Andreas fault and segments I, II and III on the Hayward fault) have previously been identified as having a probability in the range 0.2 to 0.3 of producing a magnitude ~ 7 earthquake in the next 30 years [*WGCEP*, 1990]. Segments II and VII have

previously been identified as the most likely sites for the next $M > 5$ earthquake on the Calaveras fault (equivalent to the zones I and VI of *Oppenheimer et al.* [1990]).

8.6 Summary of the Main Conclusions

1. The deformation revealed by the three San Francisco bay GPS profiles is of sufficiently high accuracy to detect shear flow about the San Andreas fault system. The vertical component is not sufficiently accurate to detect uplift or subsidence in the San Francisco bay region at the present.

2. Combining the GPS results with trilateration and VLBI data yields a spatially dense sample of crustal deformation that can be tied to an external reference frame.

3. The westernmost points of the network have velocities relative to the stable interior of the North American plate that are consistent with the NUVEL-1A prediction. 35-38 mm/yr out of the total 46 mm/yr is accommodated along the San Aandreas fault system. The remaining 8-11 mm/yr is accommodated along structures east of the fault system, particularly the Eastern California Shear Zone. Deformation east of the fault system changes from predominantly strike-slip parallel to the plate motion direction in southern California to a combination of strike-slip and extension in northern California.

4. A northeast-dipping fault plane along the Green Valley fault as defined by seismicity could explain the observed asymmetric offset in the velocity profile across that fault in the north-bay subregion.

5. Low-rigidity within the 1-2 km wide San Andreas fault zone may explain the concentrated deformation close to that fault in the north-bay subregion.

6. Fault locking depths which indicate the transition depth between dominantly brittle behaviour above and dominatly ductile behaviour below may be constrained by the depths above which 90% of the seismicity occurs (the seismogenic depth).

7. Surface creep rates along the San Andreas, Calaveras, Hayward, Concord and Green Valley faults vary considerably along strike. Maximum surface creep rates occur along the Calaveras and San Andreas faults in the south of the region. High creep rates in the south may indicate that the depth to which surface creep extends is close to sesimogenic depths. Lower rates in the north may indicate a locked zone

at depth which is presently accumulating strain.

8. The observed surface deformation is most consistent with slip below seismogenic depths occuring on discrete fault planes rather than broad shear zones.

9. No significant fault-normal compression is detected across the fault system. The small amount of motion allowed by the uncertainties is likely to be concentrated in the eastern Coast Ranges along the Coast Range thrust.

10. The estimated slip rates from the best-fit, three-dimensional model are most consistent with connectivity between all of the class A and AA faults in the system and with the Calaveras-Concord-Green Valley faults continuing north to connect with the Bartlett Springs fault.

11. Quasi-steady, aseismic slip on discrete fault planes probably occurs down to depths of around 2-3 times the seismogenic depth. This, coupled with horizontally layered, power-law viscoelastic rheology of the Earth may account for the almost linear in time deformation rates measured excluding the coseismic and postseismic responses.

12. The estimated slip rates can be used to calculate the present earthquake potential on fault segments in the region. Several segments, in particular those along the Hayward-Rodgers Creek fault, have a potential close to or above the magnitude of the "characteristic earthquake" for those segments and have therefore the greatest potential for a large earthquake in the near future.

8.7 Suggestions for Future Work

• Continued resurveying of the San Francisco GPS profiles in order to increase the accuracy of the observed surface deformation, to constrain second-order deformation features, and to search for temporal variations in the surface deformation rates. In particular to test the hypothesis that the deformation is linear in time except for the coseismic and immediate postseismic response or whether rates continue to decline throughout the earthquake cycle.

• Add more points along the eastern edge of the Coast Ranges to detect possible thrust motion on the Coast Range thrust.

• Add or reoccupy more sites east of the Coast Ranges to help constrain the eastern

edge of the deforming zone around the San Andreas fault system and to search for a broadening of the zone with time.

• Reoccupation, with GPS, of the small (several kilometre wide) fault-crossing networks that were previously measured with trilateration to obtain more recent estimates of fault creep, and for the investigation of compliant fault zones.

• Include the results from the South Bay, Loma Prieta and the Farallon Islands GPS networks into the integrated deformation field and the dislocation models.

• Include the creep rates measured by triangulation [*Galehouse*, 1992] into the regional model.

• Investigate the connectivity of the Calaveras-Concord-Green Valley faults to the Bartlett Springs fault to the north.

• Produce a three-dimensional model that includes viscoelastic rheologies. Investigate further the effects of linear versus power-law viscoelastic rheologies, continuous aseismic slip at depth, and the transition, with depth, from discrete fault planes to shear zones. This may be acheived using finite element techniques.

• Investigate the limits of elastic dislocation models for predicting/modelling interseismic deformation.

References

Addicott, W. O., Late Pliocene mollusks from San Francisco Peninsula, California, and their paleogeographic significance, *California Academy of Sciences Proceedings, Series 4*, 37(3), 57-93, 1969.

Aki, K., Generation and propagation of G waves from the Niigata earthquake of June 16, 1964. Part 2. Estimation of earthquake movement, released energy, and stress-strain drop from G wave spectrum, *Bull. Earthquake Res. Inst. Tokyo Univ., 44*, 73-88, 1966.

Allen, C. R., The tectonic environments of seismically active and inactive areas along the San Andreas fault system, in *Proceedings of the Conference on Geologic Problems of the San Andreas Fault System: Stanford, California* edited by W. R. Dickinson and A. Grantz, Stanford University Publications in the Geological Sciences, 11, 70-82, 1968.

Andrews, D. J., D. H. Oppenheimer, and J. J. Lienkaemper, The Mission link between the Hayward and Calaveras faults, *J. Geophys. Res., 98*, 12083-12095, 1993.

Argus, D. F., R. G. Gordon, C. DeMets, and S. Stein, Closure of the Africa-Eurasia-North America plate circuit and tectonics of the Gloria fault, *J. Geophys. Res., 94*, 5585-5602, 1989.

Argus, D. F., and R. G. Gordon, Pacific-North American plate motion from Very Long Baseline Interferometry compared with motion inferred from magnetic anomalies, transform faults, and earthquake slip vectors, *J. Geophys. Res., 95*, 17315-17324, 1990.

Argus, D. F., and R. G. Gordon, Current Sierra Nevada-North America motion from very long baseline interferometry: Implications for the kinematics of the western United States, *Geology, 19*, 1085-1088, 1991.

Atwater, T., Implications of plate tectonics for the Cenozoic tectonic evolution of western North America, *Bull. geol. Soc. Am., 81*, 3513-3536, 1970.

Atwater, T., and P. Molnar, Relative motion of the Pacific and North American plates deduced from sea-floor spreading in the Atlantic, Indian, and South Pacific Oceans, in *Proceedings of the Conference on Tectonic Problems of the San Andreas Fault System: Stanford, California*, edited by R. L. Kovach and A. Nur, Stanford University Publications in the Geological Sciences, 13, 136-148, 1973.

Bailey, E. H., W. P. Irwin, and D. L. Jones, Franciscan and related rocks, *California Division of Mines and Geology Bulletin, 183*, 154-165, 1964.

Bakun, W. H., and C. G. Bufe, Shear-wave attenuation along the San Andreas fault zone in central California, *Bull. seism. Soc. Am., 65*, 439-459, 1975.

Bakun, W. H., M. M. Clark, R. S. Cockerham, W. L. Ellsworth, A. G. Lindh, W. H. Prescott, A. F. Shakal, and P. Spudich, The 1984 Morgan Hill, California, earthquake, *Science, 225*, 288-291, 1984.

Bevington, P. R., and D. K. Robinson, *Data Reduction and Error Analysis for the Physical Sciences*, McGraw-Hill, 328 pp., 1992.

Bilham, R., and P. Bodin, Fault zone connectivity: Slip rates on faults in the San Francisco Bay area, California, *Science, 258*, 281-284, 1992.

Blewitt, G., Carrier phase ambiguity resolution for the Global Positioning System applied to geodetic baselines up to 2000 km, *J. Geophys. Res., 94*, 10187-10203, 1989.

Bossler, J. D., C. C. Goad, and P. L. Bender, Using the Global Positioning System (GPS) for geodetic positioning. *Bull. Geod., 54*, 553-563, 1980.

Bowditch, N., Useful tables, calculations, glossary of marine navigation, vol. II, *the American Practical Navigator*, pub. no 9, DMAHTC, Washington, D. C., 1981.

Bowie, W., Earth movements in California, *U.S. Coast and Geodetic Survey Special Publication, 106*, 1-22, 1924.

Bowie, W., Comparison of old and new triangulation in California, *U.S. Coast and Geodetic Survey Special Publication, 151*, 1-50, 1928.

Braile, L. W., W. J. Hinze, R. R. B. von Frese, and G. R. Keller, Seismic properties of the crust and upper mantle of the conterminous United States and adjacent Canada, chapter 28 of *Geophysical framework of the continental United States*, edited by L. C. Pakiser and W. D. Mooney, *Geological Society of America Memoir 172*, 655-680, 1989.

Brown, R. D., Quarternary deformation, chapter 4 of *The San Andreas Fault System, California*, edited by R. E. Wallace, *U. S. Geological Survey Professional Paper 1515*, 83-113, 1990.

Brune, J. N., T. L. Henyey, and R. F. Roy, Heat flow, stress and rate of slip along the San Andreas fault, California, *J. Geophys. Res., 74*, 3821-3827, 1969.

Budding, K. E., D. P. Schwartz, and D. H. Oppenheimer, Slip rate, earthquake recurrence, and seismic potential of the Rodgers Creek fault zone, northern California: Initial results, *Geophys. Res. Letts., 18*, 447-450, 1991.

Burford, R. O., and P. Harsh, Slip on the San Andreas fault in central California from alignment array surveys, *Bull. seism. Soc. Am., 70*, 1233-1261, 1980.

Byerlee, J. D. Friction of rocks, *Pure appl. Geophys., 116*, 615-629, 1978.

Caprette, D., C. Ma, and J. W. Ryan, Crustal Dynamics Project Data Analysis-1990: VLBI geodetic results 1979-1989, *NASA Tech. Memo. 100765*, 1990.

Castillo, D. A., and W. L. Ellsworth, Seismotectonics of the San Andreas fault system between Point Arena and Cape Mendocino in northern California, Implications for the development and evolution of a young transform, *J. Geophys. Res., 98*, 6543-6560, 1993.

Chase, C. G., Plate kinematics, the Americas, East Africa, and the rest of the world, *Earth Planet. Sci. Lett., 37*, 355-368, 1978.

Chin, M., CIGNET report, *GPS Bull., 1(1)*, p. 1, Global Positioning System Subcomm. of Comm. VIII, Int. Coord. of Space Tech. for Geod. and Geodyn., Natl Geod. Surv., Rockville, Md., 1988.

Christodoulidis, D. C., D. E. Smith, R. Kolenkiewicz, S. M. Klosko, M. H. Torrence, and P. J. Dunn, Observing tectonic plate motions and deformations from satellite laser ranging, *J. Geophys. Res., 90*, 9249-9263, 1985.

Clark, M. M., K. K. Harms, J. J. Lienkaemper, D. S. Harwood, K. R. Lajoie, J. C. Matti, J. A. Perkins, M. J. Rymer, A. M. Sarna-Wojcicki, R. V. Sharp, J. D. Sims, J. C. Tinsley, and J. I. Ziony, Preliminary slip-rate table and map of late-Quaternary faults of California, *U.S. Geological Survey Open-File Report, 84-103*, 13 pp.; scale 1:1,000,000, 5 sheets, 1984.

Clark, T. A., D. Gordon, W. E. Himwich, C. Ma, A. Mallama, and J. W. Ryan, Determination of relative site motions in the western United States using Mark III very long baseline interferometry, *J. Geophys. Res., 92*, 12741-12750, 1987.

Coates, R. J., H. Frey, G. D. Mead, and J. M. Bosworth, Space-age geodesy: The NASA Crustal Dynamics Project, *IEEE Trans. Geosci. Remote Sens., GE-23*, 360-368, 1985.

Cohen, S. C., Postseismic viscoelastic surface deformation and stress, 1, Theoretical considerations, displacement, and strain calculations, *J. Geophys. Res., 85*, 3131-3150, 1980.

Cohen, S. C., A multilayer model of time dependent deformation following an earthquake on a strike-slip fault, *J. Geophys. Res., 87*, 5409-5421, 1982.

Counselman, C. C., and I. I. Shapiro, Miniature interferometry terminals for Earth surveying, *Bull. Geod. 53(2)*, 139-163, 1979.

Counselman, C. C., and R. I. Abbot, Method of resolving radio phase ambiguity in satellite orbit determination, *J. Geophys. Res., 94*, 7058-7064, 1989.

Crouch, S. L., and A. M. Starfield, *Boundary Element Methods in Solid Mechanics*, Allen and Unwin, London, 1989.

Crowell, J. C., Displacement along the San Andreas Fault, California, *Geological Society of America Special Paper, 71*, 1962.

Cummings, J. C., The Santa Clara Formation and possible post-Pliocene slip on the San Andreas fault in central California, in *Proceedings of the Conference on Geologic Problems of San Andreas fault system: Stanford, California*, edited by W. R. Dickinson and A. Grantz, Stanford University Publications in the Geological Sciences, 11, 191-207, 1968.

Davis, J. L., T. A. Herring, I. I. Shapiro, A. E. E. Rogers, and G. Elgered, Geodesy by radio interferometry: Effects of atmospheric modeling errors on estimates of baseline length, *radio Sci., 20*, 1593-1607, 1985.

Davis, J. L., W. H. Prescott, J. L. Svarc, and K. J. Wendt, Assessment of Global Positioning System measurements for studies of crustal deformation, *J. Geophys. Res., 94*, 13635-13650, 1989.

DeMets, C., R. G. Gordon, and D. F. Argus, Intraplate deformation and closure of the Australia-Antarctica-Africa plate circuit, *J. Geophys. Res., 93*, 11877-11897, 1987a.

De Mets, C., R. G. Gordon, D. F. Argus, and S. Stein, Current plate motions, *Geophys. J. Int., 101*, 425-478, 1990.

DeMets, C., R. G. Gordon, S. Stein, and D. F. Argus, A revised estimate of Pacific-North America motion and implications for western North America plate boundary zone tectonics, *Geophys. Res. Letts., 14*, 911-914, 1987b.

Dickinson, W. R., Relations of andesite, granites, and derived sandstones to arc-trench tectonics, *Reviews of Geophysics and Space Physics, 8*, 813-860, 1970.

Dickinson, W. R., Plate tectonics and the continental margin in California, in *The Geoetctonic Development of California (Rubey volume 1)*, edited by W. G. Ernst, Englewood Cliffs, N. J., Prentice-Hall, 1-28, 1981.

Dietz, L., and W. L. Ellsworth, The October 17, 1989, Loma Prieta, California, earthquake and its aftershocks: Geometry of the sequence for high-resolution locations, *Geophys. Res. Letts., 17*, 1417-1420, 1990.

Dixon, T. H., An introduction to the Global Positioning System and some geological applications, *Rev. Geophys., 29*, 249-276, 1991.

Dixon, T. H., M. Bursik, S. K. Wolf, M. Heflin, F. Webb, F. Farina, and S. Robaudo, Constraints on deformation of the resurgent dome, Long Valley Caldera, California from space geodesy, in *Contributions of Space Geodesy to Geodynamics: Crustal Dynamics (Geodynamics Series, v. 23)*, edited by D. E. Smith and D. L. Turcotte, pp. 193-214, American Geophysical Union, Washington, D.C., 1993.

Dokka, R. K., and C. J. Travis, Late Cenozioc strike-slip faulting in the Mojave Desert, California, *Tectonics, 9*, 311-340, 1990a.

Dokka, R. K., and C. J. Travis, Role of the Eastern California shear zone in accomodating Pacific-North American plate motion, *Geophys. Res. Letts., 17*, 1323-1326, 1990b.

Dong, D., and Y. Bock, Global Positioning System network analysis with phase ambiguity resolution applied to crustal deformation studies in California, *J. Geophys. Res., 94*, 3949-3966, 1989.

Donnellan, A., B. H. Hager, R. W. King, and T. A. Herring, Geodetic measurement of deformation in the Ventura Basin region, southern California, *J. Geophys. Res., 98*, 21727-21739, 1993.

Drew, A. R., and R. A. Snay, DYNAP: Software for estimating crustal deformation from geodetic data, *Tectonophysics, 162*, 331-343, 1989.

Eaton, J. P., The earthquake and its aftershocks from May 2 through September 30, 1983, chapter 8 of *The Coalinga, California, earthquake of May 2, 1983*, edited by M. J. Rymer, and W. l. Ellsworth, *U.S. Geological Survey Professional Paper 1487*, 113-170, 1990.

Eaton, J. P., W. H. K. Lee, and L. C. Pakiser, Use of microearthquakes in the study of the mechanics of earthquake generation along the San Andreas fault in Central California, *Tectonophysics, 9*, 259-282, 1970.

Eberhart-Philips, D., Three-dimensional velocity structure in northern California Coast Ranges from inversion of local earthquake arrival times, *Bull. seism. Soc. Am., 76*, 1025-1052, 1986.

Eberhart-Philips, D., and D. H. Oppenheimer, Induced seismicity in the Geysers geothermal area, California, *J. Geophys. Res., 89*, 1191-1207, 1984.

Eberhart-Phillips, D., M. Lisowski, and M. D. Zoback, Crustal strain near the big bend of the San Andreas fault: analysis of the Los Padres-Tehachapi trilateration networks, California, *J. Geophys. Res., 95*, 1139-1153, 1990.

Ellsworth, W. L., Bear Valley, California earthquake sequence of February-March 1972, *Bull. seism. Soc. Am., 65*, 483-506, 1975.

Fairbanks, H. W., The great earthquake rift of California, in *The California earthquake of 1906: San Francisco*, edited by D. S. Jordan, and A. M. Robertson, 319-338, 1907.

Feigl, K. L., D. C. Agnew, Y. Bock, D. Dong, A. Donnellan, B. H. Hager, T. A. Herring, D. D. Jackson, T. H. Jordan, R. W. King, S. Larsen, K. M. Larson, M. H. Murray, Z. Shen, and F. H. Webb, Space geodetic measurement of crustal deformation in central and southern California, 1984-1992, *J. Geophys. Res., 98*, 21677-21712, 1993.

Feng, R., and T. V. McEvilly, Interpretation of seismic reflection profiling data for the structure of the San Andreas fault zone, *Bull. seism. Soc. Am., 73*, 1701-1720, 1983.

Foulger, G. R., The 1992 Basin and Range province GPS survey: 2. The field survey, *U.S. Geological Survey Open-File Report, 94-286*, 21 pp., 1994.

Fox, K. F., Tectonic setting of Late Miocene, Pliocene, and Pleistocene rocks in part of the Coast Ranges north of San Francisco, California, *U.S. Geological Survey Professional Paper 1239*, 33 pp., 1983.

Frizzell, V. A., and R. D. Brown, Map showing recently active breaks along the Green Valley fault, Napa and Solano Counties, California, scale 1:24,000, *U. S. Geol. Surv. Misc. Field Studies Map, MF-743*, 1976.

Fuis, G. S., and W. D. Mooney, Lithospheric structure and tectonics from seismic refraction and other data, chapter 8 of *The San Andreas Fault System, California*, edited by R. E. Wallace, *U.S. Geological Survey Professional Paper 1515*, 207-236, 1990.

Furlong, K. P., W. D. Hugo, and G. Zandt, Geometry and evolution of the San Andreas fault zone in northern California, *J. Geophys. Res., 94*, 3100-3110, 1989.

Galehouse, J. S., Creep rates and creep characteristics of Eastern San Francisco Bay area faults: 1979-1992, in *Proceedings of the Second Conference on Earthquake Hazards in the Eastern San Francisco Bay Area*, edited by G. Borchardt et al., California Deparment of Conservation, Division of Mines and Geology Special Publication 113, 45-53, 1992a.

Galehouse, J. S., Theodolite measurements of creep rates on San Francisco Bay region faults, in *National Earthquake Hazards Reduction Program, summaries of technical reports, XXXIV*, 292-302, 1992b.

Gilbert, L. E., J. Beavan, and C. H. Scholz, Analysis of a 100 year geodetic record from northern California, in *Contributions of Space Geodesy to Geodynamics: Crustal Deformation, Geodyn. Ser., v. 23*, edited by D. E. Smith and D. L. Turcotte, pp. 215-232, American Geophysical Union, Washington, D.C., 1993.

Gilbert, L. E., H. C. Scholz, and J. Beavan, Strain localization along the San Andreas fault: Consequences for loading mechanisms, *J. Geophys. Res., 99*, 23975-23984, 1994.

Goad, C. C., Precise relative position determination using Global Positioning System carrier phase measurements in a nondifference mode, in *Porceedings of the First International Symposium on Precise Positioning with the Global Positioning System, Rockville, Maryland, April 15-19*, vol 1, 347-356, 1985.

Gordon, R. G., Orbital dates and steady rates, *Nature, 364*, 760-761, 1993.

Gordon, R. G., and C. DeMets, Present-day motion along the Owen fracture zone and Dalrymple trough in the Arabian Sea, *J. Geophys. Res., 94*, 5560-5570, 1989.

Griscom, A., amd R. C. Jachens, Crustal and lithospheric structure from gravity and magnetic studies, chapter 9 of *The San Andreas Fault System, California*, edited by R. E. Wallace, *U.S. Geological Survey Professional Paper 1515*, 239-259, 1990.

Gu, G., and W. H. Prescott, Discussion on displacement analysis: Detection of crustal deformation, *J. Geophys. Res., 91*, 7439-7446, 1986.

Gurtner, W., G. Mader, and D. McArthur, A common exchange format for GPS data, *GPS Bulletin, 2(3)*, 1-11, 1989.

Hager, B. H., R. W. King, and M. H. Murray, Measurement of crustal deformation using the Global Positioning System, *Ann. Rev. Earth Planet. Sci., 19*, 351-382, 1991.

Hall, N. T., Holocene history of the San Andreas fault between Crystal Springs Reservoir and San Andreas Dam, San Mateo County, California, *Bull. seism. Soc. Am., 74*, 281-299, 1984.

Hamilton, W., Mesozoic California and the underflow of Pacific mantle, *Bull. geol. Soc. Am., 80*, 2409-2430, 1969.

Hamilton, D. H., D. L. Fisher, and R. H. Jahns, Evidence of Quaternary right slip and other deformation along the San Gregorio fault, California; another view, *Geol. Soc. Am. Abstr. With Programs, 11(7)*, 437-438, 1979.

Hanks, T. C., and H. Kanamori, A moment magnitude scale, *J. Geophys. Res., 84*, 2348-2350, 1979.

Hanna, W. F., R. D. Brown, D. C. Ross, and A. Griscom, Aeromagnetic reconnaissance along the San Andreas fault between San Francsico and San Bernadino, California, *U.S. Geological Survey Geophysical Investigations Map GP-815*, scale 1:250,000, 1972a.

Hanna, W. F., S. H. Burch, and T. W. Dibblee, Gravity, magnetics, and geology of the San Andreas fault area near Cholame, California, *U.S. Geological Survey Professional Paper 646-C*, 1-29, 1972b.

Harland, W. B., A. V. Cox, P. G. Llewellyn, C. A. Pickton, A. G. Smith, and R. Walters, *A Geologic Time Scale*, Cambridge University Press, New York, 1982.

Harris, R. A., and P. Segall, Detection of a locked zone at depth on the Parkfield, California, segment of the San Andreas fault, *J. Geophys. Res., 92*, 7945-7962, 1987.

Harsh, P. W., and N. Pavoni, Slip on the Paicines fault, *Bull. seism. Soc. Am., 68*, 1191-1193, 1978.

Hayford, J. F., and A. L. Baldwin, The earth movements in the California earthquake of 1906. *US Coast Geod. Surv. Rep. for 1907, App. 3* (Reprinted, 1973, in *Reports on Geodetic Measurement of Crustal Movement 1906-71.* Rockville, Md: Natl. Geod. Surv.) 1907.

Healy, J., and L. Peake, Seismic velocity structure along a section of the San Andreas fault near Bear Valley, California, *Bull. seism. Soc. Am., 65*, 1177-1197, 1975.

Helley, E. J., and D. G. Herd, Map showing faults with Quaternary displacement, northeastern San Francisco Bay region, California, scale 1:125,000, *U. S. Geol. Surv. Misc. Field Study Map, MF-881*, 1977.

Herd, D. G., Neotectonic framework of central coastal California and its implications to microzonation of the San Francisco Bay region, in *Progress on Seismic Zonation in the San Francisco Bay Region*, edited by E. E. Brabb, *U. S. Geol. Surv. Circ. 807*, 3-12, Washington D.C., 1979.

Herring, T. A., I. I. Shapiro and T. A. Clark, Geodesy by radio interferometry: evidence for contemporary plate motion, *J. Geophys. Res., 91*, 8341-8347, 1986.

Hilgen, F. J., Extension of the astronomically calibrated (polarity) time scale to the Miocene-Pliocene boundary, *Earth Planet. Sci. Lett., 107*, 349-368, 1991.

Hill, D. P., J. P. Eaton, and L. M. Jones, Seismicity, 1980-86, chapter 5 of *The San Andreas Fault System, California*, edited by R. E. Wallace, *U.S. Geological Survey Professional Paper 1515*, 115-151, 1990.

Hill, M. L., and T. W. Dibblee, San Andreas, Garlock and Big Pine faults, California - a study of the character, history, and tectonic significance of their displacements, *Bull. geol. Soc. Am., 64*, 443-458, 1953.

Hoffmann-Wellenhof, B., H. Lichtenegger, and J. Collins, Global Positioning System: Theory and Practice, 326 pp., New York: Springer-Verlag, 1993.

Irwin, W. P., Geology and plate-tectonic development, chapter 3 of *The San Andreas Fault System, California*, edited by R. E. Wallace, *U. S. Geological Survey Professional Paper 1515*, 61-80, 1990.

Irwin, W. P., and I. Barnes, Effect of geologic structure and metamorphic fluids on seismic behaviour of the San Andreas fault system in central and northern California, *Geology, 3*, 713-716, 1975.

Isacks, B. L., J. Oliver, and L. R. Sykes, Seismology and the new global tectonics, *J. Geophys. Res., 73*, 5855-5900, 1968.

Jackson, D. D., The use of a priori data to reduce non-uniqueness in linear inversion, *Geophys. J. R. astr. Soc., 57*, 137-147, 1979.

Jackson, D. D., and Y. Y. Kagan, Implications of Characteristic Earthquakes, *Eos Trans. AGU, 76(17)*, Spring Meet. Suppl., S199, 1995.

Jaeger, J. C., and N. G. W. Cook, *Fundamentals of Rock Mechanics*, Metheun, London, 1969.

Jennings, C. W., Fault map of California, with locations of volcanoes, thermal springs, and thermal wells: California Division of Mines and Geology, *Geologic Data Map 1*, scale 1:750,000, 1975.

Kagan, Y. Y., and D. D. Jackson, New seismic gap hypothesis - 5 years after, *J. Geophys. Res., 100*, 3943-3959, 1995.

Kelson, K. I., W. R. Lettis, and M. Lisowski, Distribution of geologic slip and creep along faults in the San Francisco Bay region, in *Proceedings of the Second Conference on Earthquake Hazards in the Eastern San Francisco Bay Area*, edited by G. Borchardt et al., California Department of Conservation, Division of Mines and Geology Special Publication 113, 31-38, 1992.

King, G. C. P., A. G. Lindh, and D. H. Oppenheimer, Seismic slip, segmentation, and the Loma Prieta earthquake, *Geophys. Res. Letts., 17*, 1449-1452, 1990.

King, N. E., and J. C. Savage, Strain-rate profile across the Elsinore, San Jacinto, and the San Andreas faults near Palm Springs, California, 1973-81, *Geophys. Res. Letts., 10*, 55-57, 1983.

King, N. E., J. C. Savage, M. Lisowski, and W. H. Prescott, Preseismic and coseismic deformation associated with the Coyote Lake, California, earthquake, *J. Geophys. Res., 86*, 892-898, 1981.

Kirby, S. H., Rheology of the lithosphere, *Rev. Geophys. Space Phys., 21*, 1458-1487, 1983.

Kroger, P. M., G. A. Lyzenga, K. S. Wallace, and J. M. Davidson, Tectonic motion in the western United States inferred from Very Long Baseline Interferometry measurements, 1980-1986, *J. Geophys. Res., 92*, 14151-14164, 1987.

Lachenbruch, A. H., and Sass, J. H., Thermomechanical aspects of the San Andreas fault system, in *Proceedings of the Conference on Tectonic Problems of the San Andreas fault system: Stanford, California*, edited by R. L. Kovach, and A. Nur, Stanford University Publications in the Geological Sciences, 13, 192-205, 1973.

Lachenbruch, A. H., and J. H. Sass, Heat flow and energetics of the San Andreas fault zone, *J. Geophys. Res., 85*, 6185-6222, 1980.

Lachenbruch, A. H., and J. H. Sass, Corrections to 'Heat flow and energetics of the San Andreas fault zone' and some additional comments on the relation between fault friction and observed heat flow, *J. Geophys. Res., 86*, 7171-7172, 1981.

Lambeck, K., it Geophysical Geodesy: The Slow Deformations of the Earth, Oxford University Press, Oxford, 1988.

Larson, K. M., Application of the Global Positioning System to crustal deformation measurements, 3. Results from the southern California borderlands, *J. Geophys. Res., 98*, 21713-21726, 1993.

Larson, K. M., and D. C. Agnew, Application of the Global Positioning System to crustal deformation measurement, 1. Precision and accuracy, *J. Geophys. Res., 96*, 16547-16565, 1991.

Larson, K. M., F. H. Webb, and D. C. Agnew, Application of the Global Positioning System to crustal deformation measurement, 2, The influence of errors in orbit determination networks, *J. Geophys. Res., 96*, 16567-16584, 1991.

Lawson, A.L., Sketch of the Geology of the San Francisco Peninsula, *U.S. Geological Survey Annual Report, 15*, 439-473, 1895.

Lawson, A. L., The California Earthquake of April 18, 1906, *Report of the State Earthquake Investigation Commission, I*, pp. 451, Carnegie Institution, Washington D.C., 1908.

Li, V. C., and H. S. Lim, Modeling surface deformations at complex strike slip plate boundaries, *J. Geophys. Res., 93*, 7943-7954, 1988.

Li, V. C., and J. R. Rice, Crustal deformation in great California earthquake cycles, *J. Geophys. Res., 92*, 11533-11551, 1987.

Lichten, S. M., and J. S. Border, Strategies for high-precision Global Positioning Systems orbit determination, *J. Geophys. Res., 92*, 12751-12762, 1987.

Lienkaemper, J. J., G. Borchardt, and M. Lisowski, Historic creep rate and potential for seismic slip along the Hayward fault, California, *J. Geophys. Res., 96*, 18261-18283, 1991.

Lindqwister, U. J., G. Blewitt, J. Zumberge, and F. Webb, Few millimeter precision for baselines in the California permanent GPS Geodetic Array, *Geophys. Res. Letts., 18*, 1135-1138, 1991.

Lisowski, M., and J. C. Savage, The velocity field in the San Francisco Bay area and the inferred depth of creep on the Hayward fault, in *Proceedings of the Second Conference on Earthquake Hazards in the Eastern San Francisco Bay Area*, edited by G. Borchardt et al., California Department of Conservation, Division of Mines and Geology Special Publication, 113, 39-44, 1992.

Lisowski, M., W. H. Prescott, J. C. Savage, and M. J. Johnston, Geodetic estimate of coseismic slip during the 1989 Loma Prieta, California, earthquake, *Geophys. Res. Letts., 17*, 1437-1440, 1990a.

Lisowski, M., W. H. Prescott, J. C. Savage, and J. L. Svarc, A possible geodetic anomaly observed prior to the Loma Prieta, California, earthquake, *Geophys. Res. Letts., 17*, 1211-1214, 1990b.

Lisowski, M., J. C. Savage, and W. H. Prescott, The velocity field along the San Andreas fault in central and southern California, *J. Geophys. Res., 96*, 8369-8389, 1991.

MacDoran, P. F., Satellite emission radio interferometric Earth surveying SERIES-GPS geodetic system, *Bull. Geod., 53*, 117-138, 1979.

Malvern, L. E., *Introduction to the Mechanics of a Continuous Medium*, 713 pp., Prentice-Hall, Englewood Cliffs, N.J., 1969.

Maruyama, T., Statical elastic dislocations in an infinite and semi-infinite medium, *Bull. Earthquake Res. Inst., Tokyo Univ., 42*, 289-368, 1964.

Massonet, D., M. Rossi, C. Carmona, F. Adragna, G. Peltzer, K. Fiegl and T. Rabaute, The displacement field of the Landers earthquake mapped by radar interferometry, *Nature, 364*, 138-142, 1993.

Matsuda, T., Magnitude and recurrence intervals of earthquakes from a fault, *Zisin. J. seism. Soc. Japan, 28*, 269-283, 1975.

Matsu'ura, M., D. D. Jackson, and A. Cheng, Dislocation model for aseismic crustal deformation at Hollister, California, *J. Geophys. Res., 91*, 12661-12674, 1986.

Mayer-Rosa, D., Travel-time anomalies and distribution of earthquakes along the Calaveras fault zone, California, *Bull. seism. Soc. Am., 63*, 713-729, 1973.

McHugh, S., and M. Johnston, Surface shear stress, strain and shear displacement for screw dislocations in a vertical slab with shear modulus contrast, *Geophys. J. R. astr. Soc., 49*, 715-722, 1977.

McKenzie, D. P., and W. J. Morgan, Evolution of triple junctions, *Nature, 224*, 125-133, 1969.

Meissner, R. and J. Strehlau, Limits of stress in continental crust and their relation to the depth-frequency relation of shallow earthquakes, *Tectonics, 1*, 73-89, 1982.

Melosh, H. J., and A. Raefsky, A simple and efficient method of introducing faults into finite element computations, *Bull. seism. Soc. Am., 71*, 1391-1400, 1981.

Menke, W., *Geophysical Data Analysis: Discrete Inverse Theory*, 260 pp., Academic, San Diego, California, 1984.

Miller, C. K., and K. P. Furlong, Thermal-mechanical controls of seismicity depth distributions of earthquakes in the continental crust of the United States, *Geophys. Res. Letts., 15*, 1429-1432, 1988.

Minster, J. B., and T. H. Jordan, Present-day plate motions, *J. Geophys. Res., 83*, 5331-5354, 1978.

Minster, J. B., and T. H. Jordan, Vector constraints on Quaternary deformation of the western United Stated east and west of the San Andreas fault, in *Tectonics and Sedimentation along the California Margin*, edited by J. K. Crouch and S. B. Bachman, *Soc. Exp. Petr. Min.: Pacific Section*, Fieldtrip Guidebook 38, 1-16, 1984.

Minster, J. B. and T. H. Jordan, Vector constraints on western U. S. deformation from space geodesy, neotectonics, and plate motions, *J. Geophys. Res., 92*, 4798-4804, 1987.

Molnar, P., Brace-Goetze strength profiles, the partitioning of strike-slip and thrust faulting at zones of oblique convergence, and the stress-heat flow paradox of the San Andreas fault, chapter 18 of *Fault Mechanics and Transport Properties of Rocks*, 435-459, Academic Press, 1992.

Mooney, W. D., and R. H. Colburn, A seismic refraction profile across the San Andreas, Sargent and Calaveras faults, west-central California, *Bull. seism. Soc. Am., 75*, 175-192, 1985.

Mooney, W. D., and C. S. Weaver, Regional crustal structure and tectonics of the Pacific Coastal States: California, Oregon and Washington, chapter 9 of *Geophysical Framework of the Continental United States*, edited by L. C. Pakiser and W. D. Mooney, Geological Society of America Memoir 172, 129-161, 1989.

Morgan, W. J., Rises, trenches, great faults, and crustal blocks, *J. Geophys. Res., 73*, 1959-1982, 1968.

Mount, V. S., and J. Suppe, State of stress near the San Andreas fault: Implications for wrench tectonics, *Geology, 15*, 1,143-1,146, 1987.

Mueller I., and G. Beutler, The International GPS Service for Geodynamics - development and current structure, *Fifth International Symposium on GPS positioning*, Ohio, 1992.

Murray, M. H., Global Positioning System measurements of crustal deformation in central California, Ph.D. thesis, 310 pp., Mass. Inst. of Technol., Cambridge, 1991.

Murray, M. H., J. C. Savage, M. Lisowski, and W. K. Gross, Coseismic displacements - 1992 Landers, California, Earthquake, *Geophys. Res. Letts., 20*, 623-626, 1993.

Nakata, J. K., Distribution and petrology of the Anderson-Coyote Reservoir volcanic rocks, M.S. thesis, 105 pp., San Jose State Univ., Calif., 1977.

Namson, J. S., and T. L. Davis, Seismically active fold and thrust belt in the San Joaquin Valley, central California, *Bull. geol. Soc. Am., 100*, 257-273, 1988.

Nason, R. D., Investigation of fault creep slippage in northern and central California, Ph.D. thesis, Univ. Calif., San Diego, 1971.

Nason, R. D., and D. Tocher, Measurement of movement on the San Andreas fault, in *Earthquake Displacement Fields and the Rotation of the Earth*, edited by L. Mansinha, D. E. Smylie and A. E. Beck, Dordrecht, Netherlands, Reidel, 246-254, 1970.

Niemi, T. M., and N. T. Hall, Late Holocene slip rate and recurrence of great earthquakes on the San Andreas fault in northern California, *Geology, 20*, 195-198, 1992.

Noble, L. F., The San Andreas rift and some other active faults in the desert region of southeastern California, *Bull. seism. Soc. Am., 17*, 25-39, 1927.

Nur, A., and G. Mavko, Postseimic viscoelastic rebound, *Science, 183*, 204-206, 1974.

Okada, A., and T. Nagata, Land deformation in the vicinity of Muroto Point after the Nankaido great earthquake in 1946, *Bull. Earthquake Res. Inst. Tokyo Univ., 31*, 169-177, 1953.

Okada, Y., surface deformation due to shear and tensile fault in a half-space, *Bull. seism. Soc. Am., 75*, 1135-1154, 1985.

Oppenheimer, D. H., W. H. Bakun, and A. G. Lindh, Slip partitioning of the Calaveras fault, California, and prospects for future earthquakes, *J. Geophys. Res., 95*, 8483-8498, 1990.

Page, B. M., The southern Coast Ranges, in *The Geotectonic Development of California (Rubey volume 1)*, edited by W. G. Ernst, Englewood Cliffs, N. J., Prentice-Hall, 329-417, 1981.

Powell, R. E., and R. J. Weldon, Evolution of the San Andreas fault, *Annu. Rev. Earth Planet Sci., 20*, 431-468, 1992.

Prentice, C. S., Earthquake geology of the northern San Andreas fault near Point Arena, California, Ph.D. thesis, California Institute of Technology, Pasadena, 186 pp., 1989a.

Prentice, C. S., The northern San Andreas fault: Russian River to Point Arena, in *The San Andreas Transform Belt*, lead by A. G. Sylvester and J. C. Crowell, International Geological Congress Field Trip, 28th, guidebook T309, 49-51, 1989b.

Prescott, W. H., The determination of displacement fields from geodetic data along a strike slip fault, *J. Geophys. Res., 86*, 6067-6072, 1981.

Prescott, W. H., and R. O. Burford, Slip on the Sargent fault, *Bull. seism. Soc. Am., 66*, 1013-1016, 1976.

Prescott, W. H., and M. Lisowski, Strain accumulation along the San Andreas fault system east of San Francisco Bay, California, *Tectonophysics, 97*, 41-56, 1983.

Prescott, W. H., and A. Nur, The accommodation of relative motion at depth on the San Andreas fault system in California, *J. Geophys. Res., 86*, 999-1004, 1981.

Prescott, W. H., and S.-B. Yu, Geodetic measurement of horizontal deformation in the northern San Francisco Bay region, California, *J. Geophys. Res., 91*, 7475-7484, 1986.

Prescott, W. H., N. E. King, and G. Guohua, Preseismic, coseismic and postseismic deformation associated with the 1984 Morgan Hill, California, earthquake, The 1984 Morgan Hill, California, Earthquake, *Spec. Publ. 68*, 137-148, Calif. Dep. of Conserv., Div. of Mines and Geol., Sacremento, 1984.

Prescott, W. H., M. Lisowski and J. C. Savage, Geodetic measurement of crustal deformation on the San Andreas, Hayward, and Calaveras faults near San Francisco, California. *J. Geophys. Res., 86*, 10853-10869, 1981.

Prescott, W. H., J. C. Savage and W. T. Kinoshita, Strain accumulation in the western United States between 1970 and 1978. *J. Geophys. Res., 84*, 5423-5435, 1979.

Reid, H. F., The mechanics of the earthquake., *The California Earthquake of April 18, 1906, II*, 16-28, Carnegie Institution, Washington D.C., 1910.

Rice, J. R., Fault stress states, pore pressure distributions, and the weakness of the San Andreas fault, chapter 20 of *Fault Mechanics and Transport Properties of Rocks*, Academic Press, 1992.

Robbins, J. W., and D. E. Smith, The role of time scales and plate acclerations in the development of present-day tectonic models (abstract), *EOS Trans. AGU, 71*, 1278, 1990.

Robertson, D. S., and W. E. Carter, Earth orientation determinations from VLBI observations, paper presented at *International Conference on Earth Rotation and the Terrestrial Reference Frame*, Int. Astron. Union, Columbus, Ohio, 1985.

Ross, D. C., Possible correlations of basement rocks across the San Andreas, San Gregorio-Hosgri, and Rinconada-Reliz-King City faults, California, *U. S. Geol. Surv. Prof. Pap., 1317*, 37 pp., 1984.

Rothacher, M., G. Beutler, G. Foulger, R. Bilham, C. Rocken and J. Beaven, Iceland 1986 GPS campaign: A complete network solution with fixed ambiguities, *EOS, Trans. Am. Geophys. Union, 69(43)*, 1988.

Rothacher, M., G. Beutler, W. Gurtner, T. Schildknecht and U. Wild, Results of the 1984, 1986 and 1988 Alaska GPS campaigns, in *Proceedings of the Fifth International Geodetic Symposium on Satellite Positioning, Las Cruces, Mexico, March 13-17, vol. 1*, 554-566, 1989.

Rothacher, M., G. Beutler, W. Gurtner, T. Schildknecht and U. Wild, *Documentation for Bernese GPS Software Version 3.2*, University of Bern, 1990.

Rundle, J. B., and D. D. Jackson, A three dimensional viscoelastic model of a strike slip fault, *Geophys. J. R. astr. Soc., 49*, 575-592, 1977.

Rybicki, K., The elastic residual field of a very long strike slip fault in the presence of a discontinuity, *Bull. seism. Soc. Am., 61*, 79-92, 1971.

Rybicki, K., and K. Kasahara, A strike-slip fault in a laterally inhomogeneous medium, *Tectonophysics, 42*, 127-138, 1977.

Saastamoinen, J., Atmospheric correction for the troposphere and stratosphere in radio ranging of satellites, in *The Use of Artificial Satellites for Geodesy, Geophys. Monogr, Ser., vol. 15*, edited by S. W. Henriksen et al., 247-251, AGU, Washington, D. C., 1972.

Sauber, J., M. Lisowski, and S. C. Solomon, Geodetic measurements of deformation east of the San Andreas fault in central California, in *Slow Deformation and Transmission of Stress in the Earth, Geophysical Monograph 49*, edited by S. C. Cohen and P. Vanicek, 71-86, 1989.

Sauber, J., W. Thatcher, S. C. Solomon, and M. Lisowski, Geodetic slip rate for the eastern California shear zone and the recurrence time of Mojave desert earthquakes, *Nature, 367*, 264-266, 1994.

Savage, J. C., Dislocations in seismology, in *Dislocations in Solids*, vol. 3, edited by F. R. N. Nabarro, pp. 251-339, North-Holland, New York, 1980.

Savage, J. C., Strain accumulation in the western United States. *Annu. Rev. Earth Planet. Sci., 11*, 11-43, 1983.

Savage, J. C., Effect of crustal layering upon dislocation modeling, *J. Geophys. Res., 92*, 10595-10600, 1987.

Savage, J. C., Equivalent strike-slip earthquake cycles in half-space and lithosphere-asthenosphere earth models,*J. Geophys. Res., 95*, 4873-4879, 1990.

Savage, J. C., Interseismic uplift at the Nankai subduction zone, southwest Japan, 1951-1990, *J. Geophys. Res., 100*, 6339-6350, 1995.

Savage, J. C., and R. O. Burford, Geodetic determination of relative plate motion in central California. *J. Geophys. Res., 78*, 832-845, 1973.

Savage, J. C., and W. T. Kinoshita, Absence of observable geodetic strain accompanying the Danville, Calfironia, earthquake sequence, *Bull. seism. Soc. Am., 61*, 1795-1799, 1971.

Savage, J. C., and M. Lisowski, Deformation in the White Mountain seismic gap, California-Nevada, 1972-1982, *J. Geophys. Res., 89*, 7671-7687, 1984.

Savage, J. C., and M. Lisowski, Inferred depth of creep on the Hayward fault, central California, *J. Geophys. Res., 98*, 787-793, 1993.

Savage, J. C., and M. Lisowski, Strain accumulation in Owens Valley, California, 1974-1988, *Bull. seism. Soc. Am., 85*, 151-158, 1995.

Savage, J. C., and W. H. Prescott, Precisions of geodolite distance measurements for determining fault movements, *J. Geophys. Res., 78*, 6001-6008, 1973.

Savage, J. C., and W. H. Prescott, Asthenosphere readjustment and the earthquake cycle, *J. Geophys. Res., 83*, 3369-3376, 1978a.

Savage, J. C., and W. H. Prescott, Geodolite measurements near the Briones Hills, California, earthquake swarm of January 8, 1977, *Bull. seism. Soc. Am., 68*, 175-180, 1978b.

Savage, J. C., W. H. Prescott and G. Gu, Strain accumulation in southern California, 1973-1984, *J. Geophys. Res., 91*, 7455-7473, 1986.

Savage, J.C., M. Lisowski, and W. H. Prescott, An apparent shear zone trending north-northwest across the mojave desert into Owens Valley, eastern California, *Geophys. Res. Letts., 17*, 2113-2116, 1990.

Savage, J.C., M. Lisowski, W. K. Gross, N. E. King, and J. L. Svarc, Strain accumulation near Yucca Mountain, Nevada, 1983-1993, *J. Geophys. Res., 99*, 18103-18107, 1994.

Savage, J. C., M. Lisowski, and J. L. Svarc, Postseismic deformation following the 1989 (M = 7.1) Loma Prieta, California, earthquake, *J. Geophys. Res., 99*, 13757-13765, 1994.

Savage, J. C., W. H. Prescott, M. Lisowski, and N. E. King, Geodolite measurements of deformation near Hollister, California, 1971-1978, *J. Geophys. Res., 84*, 7599-7615, 1979.

Scholz, C. H., The brittle-plastic transition and the depth of seismic faulting, *Geol. Rundsch., 77*, 319-328, 1988.

Schwarz, D. P., and K. J. Coppersmith, Fault behavior and characteristic earthquakes: Examples from the Wasatch and San Andreas fault zones, *J. Geophys. Res., 89*, 5681-5698, 1984.

Segall, P., and R. Harris, Earthquake deformation cycle on the San Andreas fault near Parkfield, *J. Geophys. Res., 92*, 10511-10525, 1987.

Segall, P., and M. V. Mathews, Displacement calculations from geodetic data and the testing of geophysical deformation models, *J. Geophys. Res., 93*, 14954-14966, 1988.

Shapiro, I. I., Use of space techniques for geodesy, in *Earthquakes: Observation, Theory, and Interpretation, Proc. Int. Sch. Phys. Enrico Fermi*, edited by H. Kanamori, pp. 530-568, North-Holland, Amsterdam, 1983.

Shapiro, I. I., and C. A. Knight, Geophysical applications of long baseline radio interferometry. In *Earthquake displacement fields and the rotation of the Earth*, edited by L. Mansinha, D. E. Smyle, and A. E. Beck, pp. 284-301, Reidel, Dordrecht, 1970.

Shimazaki, K., Small and large earthquakes: The effects of the thickness of seismogenic layer and the free surface, in *Earthquake Source Mechanics, Geophysical Monograph 37, Maurice Ewing Vol. 6*, edited by S. Das, J. Boatwright, and C. H. Scholz, 209-216, 1986.

Sibson, R. H., Continental fault structure and the shallow earthquake source, *J. Geol. Soc. Lond., 140*, 741-767, 1983.

Sieh, K. E., and R. H. Jahns, Holocene activity of the San Andreas fault at Wallace Creek, California, *Bull. geol. Soc. Am., 95*, 883-896, 1984.

Simpson, R. W., R. C. Jachens, R. J. Blakely, and R. W. Saltus, A new isostatic residual gravity map of the conterminous United States with a discussion on the significance of isostatic residual anomalies, *J. Geophys. Res., 91*, 8,348-8,372, 1986.

Singh, S. J., Static deformation of a multilayered half-space by internal sources, *J. Geophys. Res., 75*, 3527-3263, 1970.

Smith, D. E., R. Kolenkiewicz, P. J. Dunn, J. W. Robbins, M. H. Torrence, S. M. Klosko, R. G. Williamson, E. C. Pavlis, N. B. Douglas, and S. K. Fricke, Tectonic motion and deformation from satellite laser ranging to LAGEOS, *J. Geophys. Res., 95*, 22013-22041, 1990.

Spence, D. A., and D. L. Turcotte, Viscoelastic relaxation of cyclic displacements on the San Andreas fault, *Proc. R. Soc. London, Ser. A, 365*, 121-144, 1979.

Stein, S., C. DeMets, R. G. Gordan, J. Brodholt, J, F. Engeln, D. A. Wiens, D. Argus, P. Lundgren, C. Stein, and D. Woods, A test of alternative Caribbean plate relative motion models, *J. Geophys. Res., 93*, 3041-3050, 1988.

Steketee, J. A., On Volterra's dislocation in a semi-infinite elastic medium, *Can. J. Phys., 36*, 192-205, 1958.

Stierman, D. J., Geophysical and geological evidence for fracturing, water circulation, and chemical alteration in granitic rocks adjacent to major strike-slip faults, *J. Geophys. Res., 89*, 5,849-5,857, 1984.

Sung, L., and D. D. Jackson, Reply, *Geophys. Res. Letts., 16*, 105-108, 1989.

Thatcher, W., Strain accumulation and release mechanism of the 1906 San Francisco earthquake, *J. Geophys. Res., 80*, 4862-4872, 1975.

Thatcher, W., Systematic inversion of geodetic data in central California, *J. Geophys. Res., 84*, 2283-2295, 1979.

Thatcher, W., Nonlinear strain buildup and the earthquake cycle on the San Andreas fault, *J. Geophys. Res., 88*, 5893-5902, 1983.

Thompson, G. A., and D. B. Burke, Rate and direction of spreading in Dixie Valley, Basin and Range province, Nevada, *Bull. geol. Soc. Am., 84*, 627-632, 1973.

Thompson, G. A., and D. B. Burke, Regional geophysics of the Basin and Range province, *Ann. Rev. Earth Planet. Sci., 2*, 213-228, 1974.

Tralli, D. M., T. H. Dixon, and S. A. Stephens, The effect of wet tropospheric path delays on estimation of geodetic baselines in the Gulf of California using the Global Positioning System, *J. Geophys. Res., 93*, 6545-6557, 1988.

Trehu, A. M., and W. H. Wheeler, Possible evidence for subducted sedimentary materials beneath central California, *Geology, 15*, 254-258, 1987.

Tse, S. T., and J. R. Rice, Crustal earthquake instability in relation to the depth variation of frictional slip properties, *J. Geophys. Res., 91*, 9452-9472, 1986.

Turcotte, D. L., and D. A. Spence, An analysis of strain accumulation on a strike slip fault, *J. Geophys. Res., 79*, 4407-4412, 1974.

Turcotte, D. L., R. T. Clancy, D. A. Spence, And F. H. Kulhawy, Mechanisms for the accummulation and release of stress on the San Andreas fault, *J. Geophys. Res., 84*, 2273-2282, 1979.

Vine, F. J., Spreading of the ocean floor - New evidence, *Science, 154*, 1405-1415, 1966.

Wallace, R. E., Structure of a portion of the San Andreas rift in southern California, *Bull. geol. Soc. Am., 60*, 781-806, 1949.

Wallace, R. E., Earthquake recurrence intervals on the San Andreas fault, *Bull. geol. Soc. Am.81*, 2875-2890, 1970.

Wallace, R. E., Patterns and timing of Late Quaternary faulting in the Great Basin province and relation to some regional tectonic features, *J. Geophys. Res., 89*, 5763-5770, 1984.

Ward, S. N., North America-Pacific plate boundary, an elastic-plastic megashear: Evidence from Very Long Baseline Interferometry, *J. Geophys. Res., 93*, 7716-7728, 1988.

Ward, S. N., Pacific-North America plate motions: new results from very long baseline interferometry, *J. Geophys. Res., 95*, 21965-21982, 1990.

Watson, D. F., ACORD: Automatic contouring of raw data, *Comput. Geosci., 8*, 97-101, 1982.

Weber, G. E., and W. R. Cotton, Geologic investigation of recurrence intervals and recency of faulting along the San Gregorio fault zone, San Mateo County, California, *U. S. Geological Survey Open-file Report 81-283*, 133 pp., 1981.

Weber, G. E., and K. R. Lajoie, Late Pleistocene and Holocene tectonics of the San Gregorio fault zone between Moss Beach and Point Ano Nuevo, San Mateo County, California, *Geol. Soc. Am. Abstr. with Programs, 9(4)*, 524, 1977.

Weertman, J., Continuous distribution of dislocations on faults with finite friction, *Bull. seism. Soc. Am., 54*, 1035-1058, 1964.

Weertman, J., Relationship between displacements on a free surface and the stress on a fault, *Bull. seism. Soc. Am., 55*, 945-953, 1965.

Weertman, J., and J. R. Weertman, *Elementary Dislocation Theory*, 213 pp., Macmillan, New York, 1964.

Wells, D., N. Beck, D. Delikaraoglou, A. Kleusberg, E. J. Krakiwsky, G. Lachapelle, R. B. Langley, M. Nakiboglu, K.-P. Schwarz, J. M. Tranquilla, and P. Vanicek, *Guide to GPS Positioning*, Canadian GPS Associates, Fredericton, N. B., Canada, 1987.

Wentworth, C. M., M. C. Blake, D. L. Jones, and A. W. Walter., Tectonic wedging associated with emplacement of the Franciscan assemblage, California Coast Ranges, in *Franciscan Geology of Northern California (volume 43)*, edited by M. C. Blake, Society of Economic Paleontologists and Mineralogists, Pacific Section Field Trip Guidebook, 163-173, 1984.

Wentworth, C. M., M. D. Zoback, A. Griscom, R. C. Jachens, and W. D. Mooney, A transect across the Mesozoic accretionary margin of central California, *Geophys. J. R. astr. Soc., 89*, 105-110, 1987.

Whitten, C. A., Crustal movement in California and Nevada. *Trans. Am. Geophys. Union, 37*, 393-398, 1956.

Whitten, C.A., Crustal movement from geodetic measurements. In *Earthquake displacement fields and the rotation of the Earth*, edited by L. Mansinha, D. E. Smyle, and A. E. Beck, 255-268, Reidel, Dordrecht, 1970.

Wilson, J. T., A new class of faults and their bearing on continental drift, *Nature, 207*, 343-347, 1965.

Wooden, W. H., Navstar Global Positioning System, in *Proceedings of the First International Symposium on Precise Positioning with the Global Positioning System*, Rockville, Maryland, April 15-19, vol. 1, 403-412, 1985.

Working Group on California Earthquake Probabilities (WGCEP), Probabilities of large earthquakes in the San Francisco bay region, California, *U.S. Geol. Surv. Circ., 1053*, 51 pp., 1990.

Zandt, G., and K. P. Furlong, Evolution and thickness of the lithosphere beneath coastal California, *Geology, 10*, 376-381, 1982.

Zoback, M. D., State of stress and crustal deformation along weak transform faults, *Phil. Trans. R. Soc. Lond.A 337*, 141-150, 1991.

Zoback, M. L., and M. D. Zoback, State of stress in the conterminous United States, *J. Geophys. Res., 85*, 6,113-6,156, 1980.

Zoback, M. D., M. L. Zoback, V. S. Mount, J. Suppe, J. P. Eaton, J. H. Healy, D. H. Oppenheimer, P. Reasenberg, L. Jones, C. B. Raleigh, I. G. Wong, O. Scotti, C. Wentworth, New evidence on the state of stress of the San Andreas fault system, *Science, 238*, 1,105-1,111, 1987.

Appendix A

Table A.1: Segments used for the San Francisco Bay three-dimensional model.

Segment	Start		End		Width, km	Depth Top, km	Slip Rate*, mm/yr
	Longitude	Latitude	Longitude	Latitude			
Free fault segments							
San Gregorio fault - slip at depth							
SGa	∞		-120°41'37.31"	34°51'24.94"	9000.0	11.7	0.0
SGb	-120°41'37.31"	34°51'24.94"	-121°11'24.06"	35°39'36.15"	9000.0	11.7	0.0
SGc	-121°11'24.06"	35°39'36.15"	-121°54'20.85"	36°19'31.33"	9000.0	11.7	0.0
SG1	-121°54'20.85"	36°19'31.33"	-121°56'18.55"	36°24'39.38"	9000.0	11.7	0.0
SG2	-121°56'18.55"	36°24'39.38"	-121°58'51.66"	36°29'55.27"	9000.0	11.7	0.0
SG3	-121°58'51.66"	36°29'55.27"	-122°02'39.45"	36°34'40.18"	9000.0	11.7	0.0
SG4	-122°02'39.45"	36°34'40.18"	-122°05'45.47"	36°39'39.07"	9000.0	11.7	0.0
SG5	-122°05'45.47"	36°39'39.07"	-122°08'07.21"	36°45'02.06"	9000.0	11.7	0.0
SG6	-122°08'07.21"	36°45'02.06"	-122°09'58.56"	36°50'28.76"	9000.0	11.7	0.0
SG7	-122°09'58.56"	36°50'28.76"	-122°12'39.28"	36°55'35.76"	9000.0	11.7	0.0
SG8	-122°12'39.28"	36°55'35.76"	-122°15'04.81"	37°00'46.47"	9000.0	11.7	0.0
SG9	-122°15'04.81"	37°00'46.47"	-122°17'15.15"	37°06'08.99"	9000.0	11.7	0.0
SG10	-122°17'15.15"	37°06'08.99"	-122°20'00.00"	37°11'25.05"	9000.0	11.7	0.0
SG11	-122°20'00.00"	37°11'25.05"	-122°23'00.00"	37°16'36.70"	9000.0	11.7	0.0
SG12	-122°23'00.00"	37°16'36.70"	-122°24'20.39"	37°21'46.98"	9000.0	11.7	0.0
SG13	-122°24'20.39"	37°21'46.98"	-122°26'56.00"	37°27'16.05"	9000.0	11.7	0.0
SG14	-122°26'56.00"	37°27'16.05"	-122°30'31.13"	37°31'56.37"	9000.0	11.7	0.0
SG15	-122°30'31.13"	37°31'56.37"	-122°33'06.79"	37°36'52.50"	9000.0	11.7	0.0
SG16	-122°33'06.79"	37°36'52.50"	-122°34'53.08"	37°42'06.38"	9000.0	11.7	0.0
SG17	-122°34'53.08"	37°42'06.38"	-122°37'40.12"	37°46'38.73"	9000.0	11.7	0.0
SG18	-122°37'40.12"	37°46'38.73"	-122°39'54.26"	37°54'24.37"	9000.0	11.7	0.0
San Andreas fault - slip at depth							
SA4	-121°10'46.40"	36°34'48.00"	-121°15'29.87"	36°38'48.08"	9000.0	8.8	19.0
SA5	-121°15'29.87"	36°38'48.08"	-121°20'34.84"	36°42'50.68"	9000.0	8.8	19.0
SA6	-121°20'34.84"	36°42'50.68"	-121°25'05.00"	36°46'13.34"	9000.0	8.8	19.0
SA7	-121°25'05.00"	36°46'13.34"	-121°31'20.23"	36°50'03.33"	9000.0	10.4	19.0
SA8	-121°31'20.23"	36°50'03.33"	-121°36'29.01"	36°54'00.24"	9000.0	12.0	18.4
SA9	-121°36'29.01"	36°54'00.24"	-121°41'51.69"	36°57'50.85"	9000.0	12.0	18.4
SA10	-121°41'51.69"	36°57'50.85"	-121°46'33.90"	37°02'04.60"	9000.0	12.0	18.4

Table A.1: (Continued)

Segment	Start Longitude	Start Latitude	End Longitude	End Latitude	Width, km	Depth Top, km	Slip Rate, mm/yr
			San Andreas fault - slip at depth (continued)				
SA11	-121°46'33.90"	37°02'04.60"	-121°52'38.36"	37°05'18.30"	9000.0	12.0	18.4
SA12	-121°52'38.36"	37°05'18.30"	-121°57'40.80"	37°09'03.28"	9000.0	12.0	19.7
SA13	-121°57'40.80"	37°09'03.28"	-122°02'38.18"	37°13'19.43"	9000.0	12.0	19.7
SA14	-122°02'38.18"	37°13'19.43"	-122°07'25.45"	37°17'22.20"	9000.0	12.0	19.7
SA15	-122°07'25.45"	37°17'22.20"	-122°11'51.19"	37°21'39.90"	9000.0	11.0	19.7
SA16	-122°11'51.19"	37°21'39.90"	-122°15'54.17"	37°25'49.29"	9000.0	10.0	19.7
SA17	-122°15'54.17"	37°25'49.29"	-122°20'05.99"	37°30'11.53"	9000.0	8.9	16.4
SA18	-122°20'05.99"	37°30'11.53"	-122°23'57.57"	37°34'49.65"	9000.0	8.9	16.4
SA19	-122°23'57.57"	37°34'49.65"	-122°28'06.87"	37°39'27.47"	9000.0	8.9	16.4
SA20	-122°28'06.87"	37°39'27.47"	-122°31'45.79"	37°43'52.94"	9000.0	10.5	16.4
SA21	-122°31'45.79"	37°43'52.94"	-122°35'41.16"	37°48'38.22"	9000.0	12.0	16.4
SA22	-122°35'41.16"	37°48'38.22"	-122°39'54.26"	37°54'24.37"	9000.0	12.0	16.4
SA23	-122°39'54.26"	37°54'24.37"	-122°45'00.00"	37°58'54.95"	9000.0	12.1	16.7
SA24	-122°45'00.00"	37°58'54.95"	-122°48'30.00"	38°03'34.25"	9000.0	12.2	16.7
SA25	-122°48'30.00"	38°03'34.25"	-122°52'55.00"	38°08'03.26"	9000.0	12.2	16.7
SA26	-122°52'55.00"	38°08'03.26"	-122°56'50.00"	38°12'31.99"	9000.0	12.2	16.7
SA27	-122°56'50.00"	38°12'31.99"	-123°00'48.00"	38°17'00.45"	9000.0	12.2	16.7
SA28	-123°00'48.00"	38°17'00.45"	-123°04'30.00"	38°21'31.62"	9000.0	12.2	16.7
SA29	-123°04'30.00"	38°21'31.62"	-123°07'33.29"	38°25'39.60"	9000.0	12.2	16.7
SA30	-123°07'33.29"	38°25'39.60"	-123°13'49.13"	38°31'43.69"	9000.0	12.2	16.7
SA31	-123°13'49.13"	38°31'43.69"	∞		9000.0	12.2	16.7
			San Andreas fault - surface creep				
SAc5	-121°10'46.40"	36°34'48.00"	-121°15'29.87"	36°38'48.08"	8.0	0.0	15.0
SAc6	-121°15'29.87"	36°38'48.08"	-121°20'34.84"	36°42'50.68"	8.0	0.0	15.0
SAc7	-121°20'34.84"	36°42'50.68"	-121°25'05.00"	36°46'13.34"	8.0	0.0	15.0
SAc8	-121°25'05.00"	36°46'13.34"	-121°31'20.23"	36°50'03.33"	8.0	0.0	11.0
SAc9	-121°31'20.23"	36°50'03.33"	-121°36'29.01"	36°54'00.24"	8.0	0.0	4.0
			Hayward-Rodgers Creek fault - slip at depth				
HA1	-121°47'39.70"	37°26'32.33"	-121°52'38.36"	37°30'38.76"	9000.0	9.0	12.2
HA2	-121°52'38.36"	37°30'38.76"	-121°57'33.21"	37°34'37.57"	9000.0	9.0	12.2
HA3	-121°57'33.21"	37°34'37.57"	-122°01'52.63"	37°37'51.88"	9000.0	10.1	12.2
HA4	-122°01'52.63"	37°37'51.88"	-122°06'53.00"	37°42'24.00"	9000.0	11.1	12.2
HA5	-122°06'53.00"	37°42'24.00"	-122°11'18.00"	37°47'41.00"	9000.0	11.1	12.2
HA6	-122°11'18.00"	37°47'41.00"	-122°14'28.00"	37°51'38.00"	9000.0	11.1	12.2
HA7	-122°14'28.00"	37°51'38.00"	-122°18'07.00"	37°56'14.00"	9000.0	11.1	12.2
HA8	-122°18'07.00"	37°56'14.00"	-122°21'38.37"	38°01'16.14"	9000.0	9.8	12.2
HA9	-122°21'38.37"	38°01'16.14"	-122°24'21.61"	38°06'07.29"	9000.0	8.5	12.3
HA10	-122°24'21.61"	38°06'07.29"	-122°27'23.84"	38°10'57.12"	9000.0	8.5	12.3

Table A.1: (Continued)

Segment	Start		End		Width, km	Depth Top, km	Slip Rate, mm/yr
	Longitude	Latitude	Longitude	Latitude			
	Hayward-Rodgers Creek fault - slip at depth (continued)						
HA11	-122°27'23.84"	38°10'57.12"	-122°32'00.00"	38°15'21.68"	9000.0	8.5	12.3
HA12	-122°32'00.00"	38°15'21.68"	-122°36'42.00"	38°19'52.95"	9000.0	8.5	12.3
HA13	-122°36'42.00"	38°19'52.95"	-122°40'30.00"	38°24'49.83"	9000.0	8.5	12.3
HA14	-122°40'30.00"	38°24'49.83"	-122°43'52.00"	38°29'51.34"	9000.0	8.5	12.3
HA15	-122°43'52.00"	38°29'51.34"	-122°46'30.00"	38°34'39.57"	9000.0	8.5	12.3
HA16	-122°46'30.00"	38°34'39.57"	-122°48'50.82"	38°39'29.47"	9000.0	8.5	12.3
HA17	-122°48'50.82"	38°39'29.47"	-122°52'18.35"	38°44'14.09"	9000.0	8.5	12.3
HA18	-122°52'18.35"	38°44'14.09"	-122°57'05.62"	38°49'53.82"	9000.0	8.5	12.3
HA19	-122°57'05.62"	38°49'53.82"	∞		9000.0	8.5	12.3
	Calaveras-Concord-Green Valley fault - slip at depth						
CA1	-121°10'46.40"	36°34'48.00"	-121°14'43.04"	36°39'28.86"	9000.0	8.1	19.0
CA2	-121°14'43.04"	36°39'28.86"	-121°18'37.16"	36°44'01.98"	9000.0	8.1	19.0
CA4	-121°18'37.16"	36°44'01.98"	-121°27'45.10"	36°59'01.93"	9000.0	8.4	19.0
CA5	-121°27'45.10"	36°59'01.93"	-121°31'02.51"	37°04'05.30"	9000.0	8.6	18.2
CA6	-121°31'02.51"	37°04'05.30"	-121°34'32.58"	37°08'43.01"	9000.0	8.2	18.2
CA7	-121°34'32.58"	37°08'43.01"	-121°38'38.08"	37°13'50.80"	9000.0	7.9	17.6
CA8	-121°38'38.08"	37°13'50.80"	-121°41'44.11"	37°18'40.04"	9000.0	7.9	17.6
CA9	-121°41'44.11"	37°18'40.04"	-121°44'55.19"	37°23'26.95"	9000.0	9.0	17.6
CA10	-121°44'55.19"	37°23'26.95"	-121°47'39.70"	37°26'32.33"	9000.0	9.0	17.6
CA11	-121°47'39.70"	37°26'32.33"	-121°50'20.41"	37°31'46.29"	9000.0	10.4	7.3
CA12	-121°50'20.41"	37°31'46.29"	-121°52'10.00"	37°37'04.57"	9000.0	10.4	7.3
CA13	-121°52'10.00"	37°37'04.57"	-121°55'26.66"	37°41'56.33"	9000.0	10.4	7.3
CA14	-121°55'26.66"	37°41'56.33"	-121°57'45.86"	37°47'13.87"	9000.0	10.4	7.3
CA15	-121°57'45.86"	37°47'13.87"	-122°00'27.84"	37°52'11.99"	9000.0	10.4	7.3
CA16	-122°00'27.84"	37°52'11.99"	-122°02'28.06"	37°57'41.82"	9000.0	10.4	7.3
CA17	-122°02'28.06"	37°57'41.82"	-122°04'29.55"	38°02'46.22"	9000.0	10.4	7.3
CA18	-122°04'29.55"	38°02'46.22"	-122°08'00.00"	38°08'07.26"	9000.0	10.4	7.3
CA19	-122°08'00.00"	38°08'07.26"	-122°09'30.00"	38°13'12.93"	9000.0	10.4	7.0
CA20	-122°09'30.00"	38°13'12.93"	-122°09'42.12"	38°18'54.14"	9000.0	10.4	7.0
CA21	-122°09'42.12"	38°18'54.14"	-122°13'10.00"	38°23'59.04"	9000.0	10.4	7.0
CA22	-122°13'10.00"	38°23'59.04"	-122°15'30.00"	38°29'27.46"	9000.0	10.4	7.0
CA23	-122°15'30.00"	38°29'27.46"	-122°17'30.00"	38°34'45.53"	9000.0	10.4	7.0
CA24	-122°17'30.00"	38°34'45.53"	-122°20'15.00"	38°39'35.43"	9000.0	10.4	7.0
CA25	-122°20'15.00"	38°39'35.43"	-122°21'43.43"	38°44'50.76"	9000.0	10.4	7.0
CA26	-122°21'43.43"	38°44'50.76"	-122°25'09.70"	38°49'39.97"	9000.0	10.4	7.0
CA27	-122°25'09.70"	38°49'39.97"	-122°58'27.48"	39°30'44.96"	9000.0	10.4	7.0
CA28	-122°58'27.48"	39°30'44.96"	-123°32'57.21"	40°14'11.90"	9000.0	10.4	7.0
CA29	-123°32'57.21"	40°14'11.90"	∞		9000.0	10.4	7.0

Table A.1: (Continued)

Segment	Start Longitude	Start Latitude	End Longitude	End Latitude	Width, km	Depth Top, km	Slip Rate, mm/yr
			Calaveras-Concord-Green Valley fault - surface creep				
CAcb†	-121°20'34.84"	36°42'50.68"	-121°22'56.58"	36°48'27.69"	6.2	0.0	6.3
CAca	-121°22'56.58"	36°48'27.69"	-121°24'21.81"	36°51'20.98"	6.2	0.0	8.4
CAc1	-121°24'21.81"	36°51'20.98"	-121°25'23.37"	36°53'52.11"	6.2	0.0	12.1
CAc2	-121°25'23.37"	36°53'52.11"	-121°27'45.10"	36°59'01.93"	6.2	0.0	15.7
CAc3	-121°27'45.10"	36°59'01.93"	-121°31'02.51"	37°04'05.30"	7.2	0.0	17.8
CAc4	-121°31'02.51"	37°04'05.30"	-121°34'32.58"	37°08'43.01"	7.2	0.0	17.3
CAc5	-121°34'32.58"	37°08'43.01"	-121°38'38.08"	37°13'50.80"	7.2	0.0	15.1
CAc6	-121°38'38.08"	37°13'50.80"	-121°41'44.11"	37°18'40.04"	4.6	0.0	12.0
CAc7	-121°41'44.11"	37°18'40.04"	-121°44'55.19"	37°23'26.95"	4.6	0.0	8.7
CAc8	-121°44'55.19"	37°23'26.95"	-121°47'39.70"	37°26'32.33"	4.6	0.0	6.1
			Sargent fault - surface creep				
SRc1†	-121°22'56.58"	36°48'27.69"	-121°30'17.41"	36°54'23.13"	8.0	0.0	2.3
SRc2†	-121°30'17.41"	36°54'23.13"	-121°35'10.11"	36°55'47.25"	8.0	0.0	2.3
SRc3†	-121°35'10.11"	36°55'47.25"	-121°44'56.31"	37°03'46.08"	8.0	0.0	2.3
SRc4†	-121°44'56.31"	37°03'46.08"	-121°55'46.42"	37°07'45.49"	8.0	0.0	2.3
			Fixed fault segments				
			San Andreas fault - slip at depth				
SAc	∞		-120°15'36.94"	35°43'10.52"	9000.0	8.8	38.0
SAd	-120°15'36.94"	35°43'10.52"	-120°59'42.03"	36°24'04.60"	9000.0	8.8	38.0
SA1	-120°59'42.03"	36°24' 4.60"	-121°02'31.60"	36°26'21.65"	9000.0	8.8	38.0
SA2	-121°02'31.60"	36°26'21.65"	-121°06'16.86"	36°30'49.41"	9000.0	8.8	38.0
SA3	-121°06'16.86"	36°30'49.41"	-121°10'46.40"	36°34'48.00"	9000.0	8.8	38.0
			San Andreas fault - surface creep				
SAc1	-120°15'36.94"	35°43'10.52"	-120°59'42.03"	36°24'04.60"	8.8	0.0	28.0
SAc2	-120°59'42.03"	36°24'04.60"	-121°02'31.60"	36°26'21.65"	8.8	0.0	28.0
SAc3	-121°02'31.60"	36°26'21.65"	-121°06'16.86"	36°30'49.41"	8.8	0.0	27.0
SAc4	-121°06'16.86"	36°30'49.41"	-121°10'46.40"	36°34'48.00"	8.4	0.0	32.0
			Hayward-Rodgers Creek fault - surface creep				
HAc1	-121°55'05.00"	37°29'15.00"	-121°55'44.00"	37°30'23.00"	4.5	0.0	4.0
HAc2	-121°55'44.00"	37°30'23.00"	-121°57'38.00"	37°32'32.00"	9.0	0.0	9.0
HAc3	-121°57'38.00"	37°32'32.00"	-121°58'14.00"	37°33'08.00"	4.7	0.0	5.1
HAc4	-121°58'14.00"	37°33'08.00"	-121°59'22.00"	37°34'51.00"	4.7	0.0	5.4
HAc5	-121°59'22.00"	37°34'51.00"	-122°06'53.00"	37°42'24.00"	4.7	0.0	5.8
HAc6	-122°06'53.00"	37°42'24.00"	-122°07'28.00"	37°43'28.00"	4.7	0.0	6.6
HAc7	-122°07'28.00"	37°43'28.00"	-122°09'35.00"	37°45'53.00"	4.7	0.0	6.2
HAc8	-122°09'35.00"	37°45'53.00"	-122°11'18.00"	37°47'41.00"	4.7	0.0	4.0
HAc9	-122°11'18.00"	37°47'41.00"	-122°12'38.00"	37°49'45.00"	4.7	0.0	4.0

Table A.1: (Continued)

Segment	Start Longitude	Start Latitude	End Longitude	End Latitude	Width, km	Depth Top, km	Slip Rate, mm/yr
			Hayward-Rodgers Creek fault - surface creep (continued)				
HAc10	-122°12'38.00"	37°49'45.00"	-122°14'28.00"	37°51'38.00"	4.7	0.0	4.7
HAc11	-122°14'28.00"	37°51'38.00"	-122°18'07.00"	37°56'14.00"	4.7	0.0	5.8
HAc12	-122°18'07.00"	37°56'14.00"	-122°19'32.00"	37°57'24.00"	4.7	0.0	6.1
HAc13	-122°19'32.00"	37°57'24.00"	-122°21'56.00"	38°00'11.00"	4.7	0.0	5.6
HAc14	-122°21'56.00"	38°00'11.00"	-122°26'42.00"	38°06'04.00"	2.4	0.0	2.8
			Calaveras-Concord-Green Valley fault - surface creep				
CAc9	-121°47'39.70"	37°26'32.33"	-121°50'20.41"	37°31'46.29"	4.6	0.0	3.9
CAc10	-121°50'20.41"	37°31'46.29"	-121°52'07.98"	37°37'04.57"	3.7	0.0	1.9
CAc11	-121°52'07.98"	37°37'04.57"	-121°55'26.66"	37°41'56.33"	2.8	0.0	0.7
CAc12	-121°55'26.66"	37°41'56.33"	-121°59'00.00"	37°47'13.87"	2.8	0.0	0.4
CAc13	-121°58'00.00"	37°52'44.08"	-122°02'00.00"	37°57'35.81"	2.8	0.0	1.9
CAc14	-122°02'00.00"	37°57'35.81"	-122°04'29.55"	38°02'46.22"	2.8	0.0	3.4
CAc15	-122°04'29.55"	38°02'46.22"	-122°06'00.00"	38°08'17.26"	2.8	0.0	4.8
CAc16	-122°06'00.00"	38°08'17.26"	-122°08'00.00"	38°13'38.89"	5.9	0.0	5.6
CAc17	-122°08'00.00"	38°13'38.89"	-122°08'00.00"	38°18'47.16"	9.0	0.0	5.6
CAc18	-122°08'00.00"	38°18'47.16"	-122°08'30.00"	38°24'13.98"	9.0	0.0	5.6
CAc19	-122°08'30.00"	38°24'13.98"	-122°11'30.00"	38°28'57.63"	7.5	0.0	4.2
CAc20	-122°11'30.00"	38°28'57.63"	-122°15'00.00"	38°33'54.87"	6.0	0.0	1.5
CAc21	-122°15'00.00"	38°33'54.87"	-122°18'00.00"	38°38'41.85"	4.5	0.0	0.0
CAc22	-122°18'00.00"	38°38'41.85"	-122°19'00.00"	38°44'03.18"	3.0	0.0	0.0
CAc23	-122°19'00.00"	38°44'03.18"	-122°21'00.00"	38°49'30.07"	1.5	0.0	0.0

† - not used in the forward three-dimensional model.

* - Slip rates indicated are those used in the forward three-dimensional model and as initial values in the inversion.

∞ - fault segment is semi-infinite in length with an azimuth of N33°W.

Appendix B

Table B.1: Velocities relative the the VLBI site OVRO located 300 km east of San Francisco from the integration of VLBI, trilateration and GPS results.

Longitude	Latitude	V_{east}	V_{north}	σ_{east}	σ_{north}	Cor.	Station
-122.42917	37.86167	-11.3	14.8	2.0	1.4	0.1443	angel
-122.73350	38.19367	-9.8	18.0	2.0	1.7	0.2190	antonio
-122.39900	38.27433	-4.7	8.8	2.0	1.8	0.0501	arrow
-122.22066	37.88383	-6.7	9.2	1.8	1.3	-0.0743	bald ecc
-122.73200	37.94117	-15.4	23.2	3.4	1.7	0.5197	bolinas
-121.91367	37.88200	-4.1	2.2	1.9	1.4	0.0022	diablo 2
-123.00083	37.69933	-17.6	26.8	2.5	1.9	-0.1698	farallon
-122.12717	37.93700	-4.8	6.8	1.8	1.4	-0.0596	hills
-122.13017	38.12433	-3.9	5.0	1.9	1.6	-0.0976	lopez
-122.76500	38.08067	-12.0	20.0	2.1	1.5	0.1700	nicasio
-122.57883	38.34583	-5.2	12.5	2.0	1.9	0.1528	petaluma
-121.95450	38.20267	0.0	-0.5	1.9	1.7	-0.1854	potrero
-122.41500	37.95883	-11.1	13.1	1.9	1.5	0.0905	sanpablo
-122.49650	38.23200	-6.6	12.2	1.9	1.7	0.0663	sleepy
-122.60616	38.06150	-10.2	16.7	1.9	1.5	0.1254	stinger
-122.45750	37.61000	-15.2	21.3	1.8	1.8	0.0990	sweeney
-122.59450	37.92367	-11.9	18.9	1.9	1.5	0.1859	tam 3
-122.21567	38.26433	-3.7	4.4	1.9	1.8	-0.0145	tulucay
-122.82050	38.03950	-15.4	24.7	2.2	1.6	0.0814	wittenec
-122.31750	38.29450	-3.9	6.7	2.0	1.9	0.0256	dan
-122.44366	38.37650	-2.8	10.2	2.0	2.0	0.0989	hooker
-122.29083	38.42433	-0.2	5.1	1.9	2.1	0.0276	rector
-122.28433	38.15467	-6.5	7.5	1.9	2.2	-0.0597	slaught
-122.86383	38.34783	-10.6	17.7	2.2	2.0	0.3230	burnside
-122.78416	38.06617	-12.2	20.8	2.1	1.5	0.1445	garcia
-122.83000	38.13350	-10.6	20.7	2.0	1.8	0.1567	mill
-122.79733	38.04483	-14.3	19.9	2.6	1.9	-0.1471	seic
-122.76984	38.05100	-12.6	19.9	2.1	1.5	0.1660	tacloma
-122.79450	38.08550	-11.1	20.9	2.1	1.6	0.1749	tomasi
-122.70983	38.53833	-5.5	11.7	2.0	2.7	0.2495	mark
-122.67367	38.40067	-7.2	13.4	2.1	2.2	0.2767	taylor
-122.86916	38.48017	-7.9	16.8	2.2	2.5	0.4030	trenton
-122.63233	38.66950	-5.4	8.1	2.5	4.5	-0.1797	helena
-122.81167	38.60083	-6.9	12.7	2.3	3.7	0.4264	weston
-121.87016	37.49900	-6.2	7.1	1.9	1.8	0.1439	allison

Table B.1: (Continued)

Longitude	Latitude	V_{east}	V_{north}	σ_{east}	σ_{north}	Cor.	Station
-121.86483	37.28767	-12.6	15.1	2.0	2.3	0.1944	american
-122.09300	37.22267	-17.5	19.8	2.1	2.3	0.1281	biel
-122.14684	37.31750	-14.3	17.2	2.0	2.1	-0.0414	bmt rf
-122.29984	37.22583	-19.7	23.2	2.2	2.2	-0.0850	butano
-122.27167	37.45700	-14.2	18.4	2.0	1.8	0.0315	crossrm1
-121.82850	37.74117	-4.5	3.5	2.1	1.6	0.1207	doolan 2
-122.39883	37.24383	-19.9	24.9	2.8	2.3	-0.0676	dump
-122.19417	37.14767	-18.8	23.2	2.1	2.4	-0.0382	eagle rk
-121.84333	37.11117	-15.3	18.1	2.0	2.5	0.2299	loma use
-122.19867	37.32017	-16.0	19.7	2.0	2.1	0.0238	mindego
-122.37666	37.30917	-18.6	24.8	2.6	2.2	-0.0140	pom
-122.09367	37.55383	-10.7	12.0	1.9	1.7	0.0370	rdhillec
-122.06033	37.81500	-7.1	6.0	1.9	1.5	0.0058	rock 2
-122.17050	37.81116	-7.5	8.1	2.0	1.4	-0.0064	skyline
-121.92133	37.62017	-6.1	7.4	2.0	1.8	0.1212	sunol 2
-121.83667	37.63117	-4.9	4.2	2.1	1.7	0.1333	vern
-121.99384	37.73833	-6.5	6.2	1.9	1.5	0.0844	weidem 2
-121.45367	37.62617	-1.8	-3.3	2.6	1.9	0.0833	corral
-121.61916	37.60583	-1.6	-1.2	2.3	1.9	0.1843	cranerm1
-121.64200	37.34184	-2.4	1.0	2.2	2.1	0.2759	hamilton
-121.55483	37.47750	-2.1	-2.4	2.3	1.8	0.2453	mochoecc
-121.37383	37.50850	-1.1	-3.9	2.8	1.9	0.1989	mt oso
-121.40750	37.32233	-1.8	-4.3	2.6	2.2	0.4089	mt stake
-121.72383	37.51117	-2.6	1.3	2.1	1.8	0.1879	rose2rm5
-121.64300	36.93100	-15.4	20.3	2.1	2.7	0.2092	chamber
-121.82317	36.91100	-18.9	26.1	2.3	2.6	0.3731	gal
-121.79784	36.74917	-21.2	26.9	2.3	2.4	0.2044	mulligan
-121.81917	37.00834	-15.6	22.6	2.1	2.9	0.3491	vargo
-121.66700	37.13300	-14.5	13.8	2.2	2.5	0.3152	llagas
-121.51550	37.11500	-9.1	0.1	2.4	2.6	0.3519	sheeprm2
-121.22217	36.73817	-4.3	4.2	3.7	2.6	0.4947	browns
-121.36533	36.65667	-19.2	28.2	2.9	3.1	0.5090	mcvail
-121.26283	36.87833	-3.9	7.6	3.7	2.7	0.1048	bolsarm2
-121.44700	37.02033	-7.0	0.8	2.4	3.0	-0.0383	canada
-121.42583	36.94067	-9.8	-0.8	2.4	2.5	0.0209	church
-121.51733	36.82267	-20.2	26.0	2.2	2.3	0.2136	cross
-121.57684	36.75717	-18.7	24.1	2.3	2.6	0.0771	dusty
-121.35616	36.92583	-5.5	1.5	2.7	2.5	-0.0263	fairview
-121.39283	36.97933	-5.9	0.5	2.6	2.7	-0.0903	felipe
-121.32383	36.83183	-6.4	4.4	3.0	2.3	0.2353	foothill
-121.50300	36.75717	-20.3	25.9	2.2	2.4	0.2914	fremont
-121.61517	36.97983	-14.9	14.8	2.2	2.7	0.3523	gilroy
-121.55883	36.82050	-20.2	23.8	2.2	2.3	0.2146	hiway
-121.40067	36.89333	-7.2	2.5	2.5	2.4	0.0972	hollair
-121.40600	36.85583	-4.2	7.4	2.5	2.3	0.1533	hollis
-121.49583	36.80917	-19.8	26.4	2.2	2.4	0.2498	holt
-121.57867	36.82200	-19.9	24.1	2.2	2.3	0.2076	juan
-121.45233	36.87233	-11.1	16.9	2.3	2.3	0.1726	knob

Table B.1: (Continued)

Longitude	Latitude	V_{east}	V_{north}	σ_{east}	σ_{north}	Cor.	Station
-121.29333	36.91533	-5.1	2.8	3.2	2.5	-0.0727	lone t
-121.49300	36.84117	-14.0	17.9	2.3	2.4	0.2544	morse
-121.44600	36.79617	-10.1	19.7	2.4	2.4	0.2910	oak
-121.28667	37.00783	-5.6	1.5	3.2	2.9	-0.3157	pacheco
-121.38067	36.81783	-6.7	11.4	2.6	2.3	0.2600	pereira2
-121.43533	36.84150	-10.8	19.2	2.4	2.3	0.2087	picket
-121.47034	36.77666	-19.8	26.1	2.3	2.4	0.2863	sandy
-121.52100	36.90617	-16.7	17.2	2.2	2.4	0.2346	sargent
-121.48367	36.93550	-12.4	14.5	2.3	2.5	0.1286	shore
-121.51517	36.78367	-19.2	26.3	2.2	2.4	0.2425	yates79
-121.77167	36.58967	-23.3	27.8	2.3	1.9	0.0548	brush 2
-122.45084	37.73917	-13.7	17.2	1.8	1.2	-0.0203	davidson
-122.45500	37.80533	-11.5	17.8	2.1	1.4	-0.0058	presidio
-121.77333	36.66983	-21.8	29.2	3.4	2.0	0.0000	fort ord
-122.10300	38.39783	-0.9	-1.1	1.9	2.1	-0.0810	mt vaca
-122.86867	38.07967	-13.9	25.1	2.1	1.5	0.2213	pt reyes
-123.01483	37.99633	-17.9	26.4	2.3	1.5	0.1104	ptreyhd3
-122.52750	38.23650	-7.4	14.0	2.5	2.1	0.0739	ado
-122.45567	38.22317	-5.1	12.6	2.4	1.9	0.0991	air
-121.99467	38.41667	2.3	3.4	2.6	2.2	0.0708	caml
-122.59534	38.18600	-8.3	16.2	2.0	1.5	0.1223	cord
-122.11467	38.33117	1.6	-0.8	2.5	2.2	0.0632	gor
-122.25916	38.32383	-1.0	5.4	2.5	2.1	0.0739	hag
-122.36183	38.28316	-0.4	7.8	2.6	2.2	0.0708	hen
-120.72100	38.33967	6.5	5.2	5.6	10.1	0.0065	jackson
-122.81267	38.08733	-12.4	20.3	2.4	2.0	0.0772	ngs
-122.73650	38.09267	-7.8	21.7	2.5	2.1	0.0644	nic
-122.93667	38.10350	-14.3	23.8	2.1	1.3	0.0623	pt rvlbi
-122.36617	37.81000	-12.9	16.3	3.0	2.8	-0.0089	navy
-122.26517	37.87183	-8.9	14.9	2.1	1.6	-0.0354	ucberk
-122.50383	37.50917	-17.2	26.9	3.4	3.1	0.0273	whale
-122.15117	37.70967	-4.9	12.9	2.8	2.7	0.0325	e.b.
-122.45617	37.52683	-16.3	25.9	2.7	2.8	0.0272	palo
-122.38216	37.59217	-13.4	21.9	2.8	3.0	0.0483	p.e.
-122.18367	37.69083	-4.6	16.0	2.8	2.7	0.0325	s.l.b.
-122.06917	37.73233	-7.6	3.2	2.7	2.8	0.0358	castro
-121.95333	37.80133	-9.9	2.6	3.9	4.1	0.0235	xyz
-121.79250	37.92150	-0.2	-0.2	3.2	3.3	0.0189	jobe
-121.72234	37.95400	-1.0	-9.1	3.2	3.4	0.0247	minn

Velocities are in millimeters per year

Cor., correlation component between east and north components

Appendix C

Source Code, Explanation and Input Files for BMODEL and SSELF

C.1 Program : BMODEL

C.1.1 Introduction

Program **BMODEL** calculates fault-parallel displacements for two-dimensional (i.e. infinite in length) faults or shear zones using a series of screw dislocations embedded in an elastic half-space. Both forward models and inversions from observed fault-parallel velocities to estimate slip rates can be performed. Slip rates are estimated using a linear, weighted, least-squares inversion. All calculated velocities are fixed relative to some point (at 0 km).

BMODEL accepts two options on the command line e.g. bmodel -I*input* -O*output* where *input* is the input file and *output* is the output file. If no input file is specified the default name is *bmodel.inp*. If no output file is specified the results default to the screen.

C.1.2 Input File

An example input file is shown below:

```
No of stations --> 12
No of faults   --> 4
L Squares (0/1) -> 1
   -59.26   14.0    2.3   -2.0    2.2  farallon
   -30.10    9.6    1.5   -0.9    1.9  pt rvlbi
   -23.39    6.4    2.3   -3.0    2.3  seic
   -21.13    6.0    1.6   -0.8    2.0  garcia
   -15.80    4.2    1.5   -1.5    1.9  tam 3
    -2.35    0.3    2.0    0.7    2.7  trenton
    12.50   -4.8    2.0    0.7    2.4  air
    19.76   -8.2    1.8   -1.0    2.0  arrow
    30.39  -11.8    1.8   -2.4    1.7  lopez
    33.00  -13.0    2.1    0.2    2.5  hag
    48.92  -18.5    2.1   -3.2    1.9  mt vaca
    57.99  -16.5    2.2    1.9    2.6  caml

pos (km)  slip   top    bottom  width
****.*** ***.** ***.*** ****.** ****.*
-24.00    20.00  12.000   30.0     0.0
-24.00    20.00  12.000   30.0    60.0
   9.6    10.00   0.001   30.0     0.0
   9.6     8.00  30.000 -999.0     0.0
```

The first three lines indicate the number of velocities you have, the number of faults to model and whether you require a least-squares inversion (1) or a forward model (0). The next lines (12 in the example file) include the position, fault-parallel velocity, standard deviation and station name with the format `(f9.2,2f7.1,16x,a15)`. Note that the last two number columns relating to the fault-normal velocities are not used. The fault parameters (beneath the row of stars) are unformatted. The second column, slip, is only used if a forward model is required. A value of 0.0 is not allowed in the third and fourth columns, set it to 0.001 instead. -999.0 in the third column indicates that the fault extends to infinity. Setting any value other than 0.0 in the fourth (width) column indicates that you require a shear zone of a certain width centred around the position given in the first (position) column.

C.1.3 Source Code

```
c*
      program bmodel
cc
cc name      : bmodel
cc
cc purpose   : calculates displacement for infinite length
cc             faults or shear zones using screw dislocation.
cc             This program calculates slip on the faults.
cc
cc sr called : getarg getopt lfit greens dgemm
cc             fchisq gaussj covsrt
cc
cc remarks   : getarg and getopt are from the utilsubs.f
cc             from the program dispinvl written by P. Segall
cc             lfit covsrt and gaussj are based on routines in
cc             numerical recipes in fortran
cc             dgemm is part of the blas/lapack library
cc             (which is incorporated into the nag library?)
cc
cc
cc author    : S.D.P. Williams
cc
cc version   : 1.0
cc
cc created   : 12/05/93
cc
cc copyright : S. Williams
cc      1993   Dept. of Geological Sciences
cc             university of Durham
cc                Durham
c*
c
c     declarations
c     ------------
c
      implicit none

      integer maxflt
      integer maxsta

      parameter (maxflt = 10)
      parameter (maxsta = 50)

      integer j,k,l
      integer lnout,leas,ndat
      integer iargc, nflt,nsta
      integer lista(maxflt*3)
      integer index(maxflt*3)
      integer nflt,iadd

      real*8 g(maxsta,maxflt)
      real*8 grow(maxflt)
      real*8 u(maxflt)

      real*8 spos(maxsta)
      real*8 svel(maxsta)
      real*8 serr(maxsta)
      real*8 pred(maxsta)
      real*8 chisq,rchisq
      real*8 dof
      real*8 nrms,omc(maxsta)

      real*8 pi,small

      real*8 coeff(maxflt*4)
      real*8 covar(maxflt,maxflt)

      character*1 ldummy,ans
      character*15 sname(maxsta),model(2)
      character*40 infil,outfil,arg

      data pi/3.141592653589793d0/
      model(1)='Forward'
      model(2)='Least Squares'
      small=1.0

c
c --- Get input features
c     ------------------

      outfil='*'
      infil='*'
      lnout = 6
      do j=1,iargc()
       call getarg(j,arg)
       if (arg(1:2).eq.'-I') then
        infil=arg(3:len(arg))
       else if(arg(1:2).eq.'-O') then
        outfil=arg(3:len(arg))
       endif
      enddo
      if(infil(1:1).eq.'*') then
       infil = 'bmodel.inp'
       open(unit=10,file='bmodel.inp',status='old',err=999)
      else
       open(unit=10,file=infil,status='old',err=999)
      endif
      if(outfil(1:1).eq.'*') then
       lnout = 6
      else
       lnout = 12
       open(unit=lnout,file=outfil)
      endif

c
c --- Read from input file
c     --------------------

      read(10,'(19x,i2)') ndat
      nsta=ndat+1
      read(10,'(19x,i2)') nflt
      read(10,'(19x,i1)') leas
      do k=1,ndat
       read(10,'(f9.2,2f7.1,16x,a15)')
     . spos(k),svel(k),serr(k),sname(k)
      enddo
      read(10,*)
      read(10,*)
      read(10,*)
      do j=1,nflt
c      read(10,'(f8.3,1x,f6.2,1x,f6.2,1x,f7.2,1x,f6.1)')
       read(10,*)
     . coeff(j*4-3),u(j),coeff(j*4-2),coeff(j*4-1),coeff(j*4)
      enddo

      close(10)

c
c --- Forming default list
c     --------------------

10    nflt=nflt
      do j=1,nflt
       lista(j)=j
      enddo
      do j=1,nflt
       do l=1,nflt
        if(lista(l).eq.j) then
         index(j)=l
        endif
       enddo
```

```
      write(0,'(i2,2x,f7.3,2x,i2)')
     . j,u(j),index(j)
      enddo
      call getopt('New Coefficient List?',
     .     'y/n','n',ans)
      if(ans.eq.'y') then
       do j=1,nflt
        lista(j)=0
       enddo
       write(0,'(a)')
     . 'Input new coefficients (0 to end)'
       k=1
 20    read(5,'(i2)') iadd
       if(iadd.gt.0.and.iadd.le.nflt) then
        lista(k)=iadd
        k=k+1
        goto 20
       else if(iadd.eq.0) then
        nfit=k-1
        goto 30
       else
        write(0,'(a)') 'That coefficient is not valid'
        goto 20
       endif
      endif

 30    if(nfit.eq.0.or.nfit.gt.ndat) then
       write(0,'(a)') 'Invalid number in list'
       goto 10
      endif

      dof=ndat-nfit

c
c --- Do least squares inversion
c     ------------------------

      if(leas.eq.1) then
      call lfit(spos,svel,serr,ndat,u,nflt,lista,
     .          nfit,covar,maxflt,chisq,coeff)
      endif

c
c --- Calculate final predicted velocities
c     ----------------------------------

      do k=1,ndat
       call greens(spos(k),grow,nflt,coeff)
       do j=1,nflt
        g(k,j)=grow(j)
       enddo
      enddo
      call dgemm('N','N',ndat,1,nflt,1.d0,g,
     .           maxsta,u,maxflt,0.d0,pred,
     .           maxsta)


c
c --- Output Results
c     --------------

      write(lnout,'(a6,2x,4(a10,2x),a15)')
     . ' D km ',' observed ','obs. error',
     . 'calculated',
     . ' obs-cal  ','station name   '
      do k=1,ndat
       write(lnout,'(f6.1,2x,4(f10.4,2x),a15)')
     . spos(k),svel(k),serr(k),pred(k),
     . svel(k)-pred(k),sname(k)
       if(lnout.ne.6) then
        write(6,'(f6.1,2x,4(f10.4,2x),a15)')
     .  spos(k),svel(k),serr(k),pred(k),
     .  svel(k)-pred(k),sname(k)
       endif
      enddo
      if(leas.eq.0) nfit=0
      call fchisq(ndat,nfit,maxsta,svel,pred,serr,
     .            omc,chisq,rchisq,nrms)
      write(lnout,'(a)') ''
      write(lnout,'(a,i4)') 'dof : ',ndat-nfit
      write(lnout,'(a)') ''
      write(lnout,'(a,f10.4,a,f10.4)')
     . 'Chi Squared : ',chisq,
     . ' Reduced Chi Squared : ',rchisq
      write(lnout,'(a)') ''

      write(lnout,'(a12,2x,a15)')
     . 'Model Type :',model(leas+1)
      write(lnout,'(a)')
     . 'Predicted fault slip rates'

      write(lnout,'(a8,1x,2(a6,1x))')
     . ' flt pos',' slip',' error'
      do j=1,nflt
       write(lnout,'(f8.3,1x,6(f8.2,1x))')
     .  coeff(j*4-3),u(j),sqrt(covar(j,j)),
     .  coeff(j*4-2),coeff(j*4-1),coeff(j*4)
      enddo

      stop

 999  write(6,'(a30,2x,a15)')
     . 'Error: Input file not found : ',infil

      end


      subroutine covsrt(covar,ncvm,ma,lista,mfit)
      implicit real*8 (a-h,o-z)

      dimension covar(ncvm,ncvm),lista(mfit)
      do 12 j=1,ma-1
       do 11 i=j+1,ma
        covar(i,j)=0.
 11    continue
 12   continue
      do 14 i=1,mfit-1
       do 13 j=i+1,mfit
        if(lista(j).gt.lista(i)) then
         covar(lista(j),lista(i))=covar(i,j)
        else
         covar(lista(i),lista(j))=covar(i,j)
        endif
 13    continue
 14   continue
      swap=covar(1,1)
      do 15 j=1,ma
       covar(1,j)=covar(j,j)
       covar(j,j)=0.
 15   continue
      covar(lista(1),lista(1))=swap
      do 16 j=2,mfit
       covar(lista(j),lista(j))=covar(1,j)
 16   continue
      do 18 j=2,ma
       do 17 i=1,j-1
        covar(i,j)=covar(j,i)
 17    continue
 18   continue
      return
      end
      subroutine fchisq(npts,nterm,mdpts,obs,calc,err,
     .                  omc,chi2,rchi2,norm)

      implicit none

      integer npts,nterm,mdpts
      integer k,nfree

      real*8 obs(mdpts),calc(mdpts)
      real*8 err(mdpts),omc(mdpts)
      real*8 chi2,rchi2,norm

      chi2=0.d0
      do k=1,npts
       omc(k)=obs(k)-calc(k)
       chi2=chi2+(omc(k)/err(k))**2
      enddo
      nfree=npts-nterm
      if(nfree.lt.0) then
       rchi2=0.0
       norm=0.0
       goto 10
      endif
      rchi2=chi2/nfree
      norm=sqrt(rchi2)
 10   return
      end

      SUBROUTINE GAUSSJ(A,N,NP,B,M,MP)
      implicit real*8 (a-h,o-z)
      PARAMETER (NMAX=50)
      DIMENSION A(NP,NP),B(NP,MP),IPIV(NMAX),INDXR(NMAX),INDXC(NMAX)
      DO 11 J=1,N
       IPIV(J)=0
 11   CONTINUE
```

```
      DO 22 I=1,N
       BIG=0.
       DO 13 J=1,N
        IF(IPIV(J).NE.1)THEN
         DO 12 K=1,N
          IF (IPIV(K).EQ.0) THEN
           IF (ABS(A(J,K)).GE.BIG)THEN
            BIG=ABS(A(J,K))
            IROW=J
            ICOL=K
           ENDIF
          ELSE IF (IPIV(K).GT.1) THEN
           PAUSE 'Singular matrix'
          ENDIF
   12     CONTINUE
        ENDIF
   13   CONTINUE
        IPIV(ICOL)=IPIV(ICOL)+1
        IF (IROW.NE.ICOL) THEN
         DO 14 L=1,N
          DUM=A(IROW,L)
          A(IROW,L)=A(ICOL,L)
          A(ICOL,L)=DUM
   14    CONTINUE
         DO 15 L=1,M
          DUM=B(IROW,L)
          B(IROW,L)=B(ICOL,L)
          B(ICOL,L)=DUM
   15    CONTINUE
        ENDIF
        INDXR(I)=IROW
        INDXC(I)=ICOL
        IF (A(ICOL,ICOL).EQ.0.) PAUSE 'Singular matrix.'
        PIVINV=1./A(ICOL,ICOL)
        A(ICOL,ICOL)=1.
        DO 16 L=1,N
         A(ICOL,L)=A(ICOL,L)*PIVINV
   16   CONTINUE
        DO 17 L=1,M
         B(ICOL,L)=B(ICOL,L)*PIVINV
   17   CONTINUE
        DO 21 LL=1,N
         IF(LL.NE.ICOL)THEN
          DUM=A(LL,ICOL)
          A(LL,ICOL)=0.
          DO 18 L=1,N
           A(LL,L)=A(LL,L)-A(ICOL,L)*DUM
   18     CONTINUE
          DO 19 L=1,M
           B(LL,L)=B(LL,L)-B(ICOL,L)*DUM
   19     CONTINUE
         ENDIF
   21   CONTINUE
   22  CONTINUE
       DO 24 L=N,1,-1
        IF(INDXR(L).NE.INDXC(L))THEN
         DO 23 K=1,N
          DUM=A(K,INDXR(L))
          A(K,INDXR(L))=A(K,INDXC(L))
          A(K,INDXC(L))=DUM
   23    CONTINUE
        ENDIF
   24  CONTINUE
       RETURN
       END

       subroutine greens(x,p,np,param)

cc     This subroutine calculates the greens function
cc     for either a infinite fault at depth, infinite
cc     fault segment, shear zone, or shear zone segment
cc     for use in the program bmodel
cc
cc     x = site position
cc     p = greens function for each fault
cc     np = number of fault
cc     param = coefficients needed

       implicit none

       integer np,j

       real*8 x,p(np),param(np*4)
       real*8 xx(100)
       real*8 dpt(100),dpb(100)
       real*8 fullwidth(100),hw(100)
       real*8 wka,wkb
       real*8 b,c,d,e
       real*8 pi

       data pi/3.1415926535897 93d0/

       do j=1,np
        hw(j)=param(j*4)/2.d0
        fullwidth(j)=param(j*4)
        dpb(j)=param(j*4-1)
        dpt(j)=param(j*4-2)
        xx(j)=param(j*4-3)
       enddo

       do j=1,np
        b=xx(j)
        c=dpt(j)
        d=dpb(j)
        e=hw(j)
        if (fullwidth(j).eq.0.0) then
         if (x.eq.0.0.and.c.eq.0.0) then
          p(j)=0.d0
         else
          if(d.lt.0.0) then
           p(j)=atan(-b/c)-atan((x-b)/c)
           p(j)=p(j)/pi
          else
           p(j)=atan(-b/c)-atan((x-b)/c)-atan(-b/d)+
     .          atan((x-b)/d)
           p(j)=p(j)/pi
          endif
         endif
        else
         if(d.lt.0.0) then
          p(j)=(x-b-e)*atan((x-b-e)/c)-(x-b+e)*atan((x-b+e)/c)
     .         -(c/2)*log((c**2+(x-b-e)**2)/(c**2+(x-b+e)**2))
     .         -(-b-e)*atan((-b-e)/c)+(e-b)*atan((e-b)/c)+
     .         (c/2)*log((c**2+(-b-e)**2)/(c**2+(e-b)**2))
          p(j)=p(j)/(2*pi*e)
         else
          wka=(x-b-e)*atan((x-b-e)/c)-(x-b+e)*atan((x-b+e)/c)
     .         -(c/2)*log((c**2+(x-b-e)**2)/(c**2+(x-b+e)**2))
     .         -(-b-e)*atan((-b-e)/c)+(e-b)*atan((e-b)/c)+
     .         (c/2)*log((c**2+(-b-e)**2)/(c**2+(e-b)**2))
          wka=wka/(2*pi*e)
          wkb=(x-b-e)*atan((x-b-e)/d)-(x-b+e)*atan((x-b+e)/d)
     .         -(d/2)*log((d**2+(x-b-e)**2)/(d**2+(x-b+e)**2))
     .         -(-b-e)*atan((-b-e)/d)+(e-b)*atan((e-b)/d)+
     .         (d/2)*log((d**2+(-b-e)**2)/(d**2+(e-b)**2))
          wkb=wkb/(2*pi*e)
          p(j)=wka-wkb
         endif
        endif
       enddo

       return
       end

       subroutine lfit(x,y,sig,ndata,a,ma,lista,mfit,covar,ncvm,chisq,
      *coeff)
       implicit real*8 (a-h,o-z)
       parameter (mmax=50)
       dimension x(ndata),y(ndata),sig(ndata),a(ma),lista(ma),
      *  covar(ncvm,ncvm),beta(mmax),afunc(mmax)
       dimension coeff(ncvm*4)
       kk=mfit+1
       do 12 j=1,ma
        ihit=0
        do 11 k=1,mfit
         if (lista(k).eq.j) ihit=ihit+1
   11   continue
        if (ihit.eq.0) then
         lista(kk)=j
         kk=kk+1
        else if (ihit.gt.1) then
         pause 'improper set in lista'
        endif
   12  continue
       if (kk.ne.(ma+1)) pause 'improper set in lista'
       do 14 j=1,mfit
        do 13 k=1,mfit
         covar(j,k)=0.
   13   continue
        beta(j)=0.
   14  continue
       do 18 i=1,ndata
        call greens(x(i),afunc,ma,coeff)
        ym=y(i)
        if(mfit.lt.ma) then
         do 15 j=mfit+1,ma
```

```
          ym=ym-a(lista(j))*afunc(lista(j))
15        continue
        endif
        sig2i=1./sig(i)**2
        do 17 j=1,mfit
          wt=afunc(lista(j))*sig2i
          do 16 k=1,j
            covar(j,k)=covar(j,k)+wt*afunc(lista(k))
16        continue
          beta(j)=beta(j)+ym*wt
17      continue
18    continue
      if (mfit.gt.1) then
        do 21 j=2,mfit
          do 19 k=1,j-1
            covar(k,j)=covar(j,k)
19        continue
21      continue
      endif
      call gaussj(covar,mfit,ncvm,beta,1,1)
      do 22 j=1,mfit
        a(lista(j))=beta(j)
22    continue
      chisq=0.
      do 24 i=1,ndata
        call greens(x(i),afunc,ma,coeff)
        sum=0.
        do 23 j=1,ma
          sum=sum+a(j)*afunc(j)
23      continue
        chisq=chisq+((y(i)-sum)/sig(i))**2
24    continue
      call covsrt(covar,ncvm,ma,lista,mfit)
      return
      end
```

C.2 Program : SSELF

C.2.1 Introduction

Program **SSELF** computes the horizontal displacements at the surface of an elastic half space due to a finite vertical strike slip fault with given orientation and dimensions. The displacement is calculated at specified coordinates corresponding to given GPS and/or trilateration data points and is output in the form of GPS relative velocities and/or trilateration line-length changes. The program requires up to four input files and produces several output files. **SSELF** is also interactive, asking several questions relating to the input data and input/output files.

C.2.2 Input Files

C.2.2.1 Dislocation Geometry File

This is used to specify the parameters of the individual fault segments to be used in the model. Several segments can be combined to produce a single fault i.e. a set of segments that are treated as one and as such have one slip rate assigned and/or estimated to them. Fixed fault segments can also be assigned. The slip rates on these segments are not estimated when performing a least-squares inversion. An example input file is:

```
*start coordinates            end coordinates              width  depth slip err  seg
**** ** **.****,** ** **.**** **** ** **.****,** ** **.**** ****.* ***** **** **** ***
-120 41 37.3092 34 51 24.9372 -119 38 41.6940 32 58  4.1628 9000.0  11.7 0.00 0.60 SGa
-120 41 37.3092 34 51 24.9372 -121 11 24.0612 35 39 36.1476 9000.0  11.7 0.00 0.60 SGb
-121 11 24.0612 35 39 36.1476 -121 54 20.8548 36 19 31.3284 9000.0  11.7 0.00 0.60 SGc
*
-121 10 46.4016 36 34 48.0036 -121 15 29.8656 36 38 48.0804 9000.0  08.8 19.0 3.00 SA4
-121 15 29.8656 36 38 48.0804 -121 20 34.8396 36 42 50.6772 9000.0  08.8 19.0 3.00 SA5
-121 20 34.8396 36 42 50.6772 -121 25  5.0000 36 46 13.3428 9000.0  08.8 19.0 3.00 SA6
*
-121 36 29.0052 36 54  0.2376 -121 41 51.6948 36 57 50.8500 9000.0  12.0 18.4 4.60 SA9
-121 41 51.6948 36 57 50.8500 -121 46 33.8952 37  2  4.5996 9000.0  12.0 18.4 4.60 SA10
-121 46 33.8952 37  2  4.5996 -121 52 38.3556 37  5 18.3012 9000.0  12.0 18.4 4.60 SA11
*
fixed
-120 15 36.9396 35 43 10.5168 -119 34 47.2620 35  2 47.2344 9000.0  08.8 38.0 0.10 SAc
-120 15 36.9396 35 43 10.5168 -120 59 42.0252 36 24  4.6044 9000.0  08.8 38.0 0.10 SAd
-120 59 42.0252 36 24  4.6044 -121  2 31.5996 36 26 21.6528 9000.0  08.8 38.0 0.10 SA1
-121  2 31.5996 36 26 21.6528 -121  6 16.8552 36 30 49.4136 9000.0  08.8 38.0 0.10 SA2
```

The lines in this input file are in free format. The start and end coordinates (columns 1-12) refer to the longitudes and latitudes (in degrees, minutes and sec-

onds) of the end-points of each segment. Note, if a segment is to be made semi-infinite in length then only the start coordinates matter. Be careful to choose the correct start or end point for semi-infinite segments. Width (column 13) indicates the down-dip width of the segment. The bottom of the segment is at depth + width. Column 14, depth, indicates the depth from the surface to the top of the segment. Column 15, slip, indicates either the prior estimate for the slip rate (to be used in some of the inversion methods) or the slip rate for the forward model. Column 16, is the assigned error estimate for the slip rate in column 15. Column 17, seg, is an identifying code for each segment e.g. SG = San Gregorio etc. Individual stars on separate lines slip the individual segments up into segments to be combined as mentioned above. Segments listed after the line marked "fixed" are fixed segments whose slip rates are not estimated in any inversion.

C.2.2.2 Station coordinate file

This file lists the coordinates of all the stations that you wish to calculate displacements for (both GPS and trilateration data). The file may be a general coordinate file containing more station coordinates than actually used. The station coordinate file should be in Menlo Park format. An example of this file is:

```
bayn  angel     n 37 51 42.     -122 25 45.       n  238.05   bb unstamped USCGS mark
bayn  antonio   a 38 11 36.954  -122 44 00.866    a  356.80   bb 'antonio 1930' USGS
bayn  arrow     a 38 16 27.329  -122 23 56.532    h  297.36   bb 'arrowhead 1929' USCGS
bayn  bald ecc  p 37 53 01.6723 -122 13 14.6659   n  583.10   aa 'bald ecc 1977' HCER
gps   mt vaca     38 23 52.36246-122 06 10.52698     820.7210   e
gps   pt reyes    38 04 46.95540-122 52 07.42314     374.4860   e
gps   ptreyhd3    37 59 47.05731-123 00 53.66235     152.1800   e
```

The format of this file is `(6x,a8,5x,i2,1x,i2,1x,f8.5,i4,1x,i2,1x,f8.5)`.

C.2.2.3 Line Length Data File

This is an optional input file containing trilateration data results in Menlo Park format. An example of this file is:

```
rate        arrow    dan       0.000   5  7434.628-0.0005 0.0005  72.9
rate        arrow    hooker    0.000   5 12006.525 0.0007 0.0008 341.3
rate        arrow    rector    0.000   7 19165.043-0.0006 0.0005  29.6
rate        arrow    slaught   0.000   4 16648.361 0.0004 0.0011 143.1
rate        arrow    tulucay   0.000   8 16077.902 0.0014 0.0006  93.9
rate        dan      hooker    0.000   6 14300.937 0.0013 0.0004 309.6
```

The format of this file is `(13x,a8,1x,a8,t44,f10.3,t54,f7.4,1x,f6.4,t69,f5.1)`. The last four columns indicate the line-length, change in line length, the standard deviation, and the lines' azimuth (angle of the second station from the first, clockwise from north).

C.2.2.4 GPS Data File

This is an optional input file containing GPS data results in **DISPINVL** format (written by Paul Segall). An example of this file is:

```
'palo    '      'sweeney '       -.0011 0.0022  0.0046 0.0020  0.0037 0.0148
'p.e.    '      'sweeney '       0.0018 0.0024  0.0006 0.0022  -.0017 0.0162
's.l.b.  '      'sweeney '       0.0106 0.0021  -.0053 0.0021  0.0037 0.0148
'e.b.    '      'sweeney '       0.0103 0.0021  -.0084 0.0021  0.0066 0.0151
```

This file is in free format. The numerical columns indicate (in order) V_e, σ_e, V_n, σ_n, V_u, σ_u in metres. Note that the vertical velocities are not used in the program.

C.2.3 Options in Program

Once the program is running there are several options/questions. Questions that need a brief explanation are

- trilateration data available? - do you want to include trilateration data in the inversion.
- GPS data available? - do you want to include GPS data in the inversion.
- Do you want fault segments printed? Prints out a file of the fault segments (latitude and longitude) in a format suitable for plotting with GMT or other plotting package.
- Output line length change vs azimuth? - Allows you to specify an extra output file containing the observed and predicted line-length changes and the azimuth of the line.
- Make end faults very long? - This option allows you to make some fault segments semi-infinite in length. This is useful for eliminating edge effects. If you answer 'y' then you are presented with a table of which segments you require to make semi-infinite.
- Output graphics file? - Allows the user the option to print a file containing information for plotting three-dimensional pictures of the fault model.

In the program there are six possible modeling methods

- Forward model
- Weighted least squares inversion
- Weighted damped least squares inversion

- Weighted Minimum length inversion
- Stochastic inversion
- Singular value decomposition

See *Menke* [1984] for a description of the different methods. The stochastic inversion uses flatness or smoothing between adjacent segments (an additional menu allows the user to select which segments are physically adjacent) as a type of a priori information. The stochastic inversion was used in the thesis. An additional option in the weighted least squares inversion allows the user to place a positivity constraint on the estimated slip rates (see *Menke* [1984]). However, at the present, this option does not seem to work.

C.2.4 Output files

Many output files are printed including some optional ones described above. The most important of these are the general output file which is mostly self-explanatory and output files that can be used as input into **DISPINVL** which combines different geodetic data. The **DISPINVL** output files are in the same format as the line-length and GPS data input files but instead include the predicted line-length changes and relative velocities.

C.2.5 Source Code

```
*
      program sself
cc
cc name       : sself
cc
cc purpose    : calculating 3d deformation using okada's equations
cc              for: strike slip fault
cc
cc sr called  : poly44,gfvstr,dummy,fchisq,dpoinv,dgemm,dgemv,
cc              srectf,getint,getopt,getfile2,norman,
cc              lsinv,pls,wdlsinv,mlinv,stocinv,svdinv,
cc              add,sub
cc
cc remarks    : This version allows the use of four different
cc              inversion schemes as described in Menke[Geophysical
cc              Data Analysis, Discrete Inverse Theory]
cc              or just a forward model to be calculated.
cc              Subroutines norman, srectf are courtesy of Y.Okada
cc              Subroutines dgemm, dgemv, dpoinv, and dgesvd are
cc              from the blas and lapack libraries which are
cc              also included in the nag library (I think!)
cc              Subroutines getopt, getfile2, getint are from
cc              the utilsubs.f library from P. Segall's dispinvl program
cc              Subroutine poly44 also came from P. Segall's dispnvl
cc              Subroutines pls,add and sub are from W. Menke's book
cc              Part of the subroutine svdinv may have come from
cc              somewhere else but I cant remember!
cc
cc author     : S.D.P. Williams
cc
cc version    : 1.0
cc
cc created    : 1995
cc
cc copyright  : S. Williams
cc      1995     Dept. of Geological Sciences
cc               University of Durham
cc                  Durham
c*
c
c     declarations
c     ------------
c
      implicit none

      integer i,j,k,l,flnum,nflt,n
      integer mpar,m,nsta
      integer ndata,mseg
      integer uot,ust,ugm,udt
      integer numll,numgps,free,nfree
      integer ilatd,ilond,ilatm,ilonm
      integer add,sfl1,sfl2,answer,ierr

      parameter (mpar   = 360)
      parameter (flnum  = 10)

      integer nseg(mpar)
      integer iseg(mpar)

      real*8 latf(mpar,2,3),lonf(mpar,2,3)
      real*8 lat(3),lon(3),staloc(mpar,2)
      real*8 flat(mpar,2),flon(mpar,2)
      real*8 slat,slon
      real*8 xflt(mpar,2),yflt(mpar,2)
      real*8 x1,x2,y1,y2,theta,xx,yy
      real*8 a1,a2,a3,u11,u12,u21,u22,u31,u32
      real*8 b1,b2,b3,bigu,ux,uy
      real*8 xsta(mpar),ysta(mpar)
      real*8 len(mpar),d(mpar)
      real*8 w(mpar),xstart(mpar),xprior(mpar)
      real*8 dep(mpar),dx,dy,dtr
      real*8 origin(2)
      real*8 small,lon_sum,lat_sum

      real*8 pi,alp,azimuth
      real*8 tosec(3)

      real*8 xav,xbdav,xtmp(mpar),xbdtmp(mpar),tmpg(mpar,mpar)
      real*8 xbd(mpar),gbar(mpar,mpar),dbar(mpar)
      real*8 gech(mpar),gesd(mpar),gnch(mpar),gnsd(mpar)
      real*8 guch(mpar),gusd(mpar)
      real*8 llch(mpar),llsd(mpar),distan,azi(mpar)
      real*8 yo(mpar),stdy(mpar)
      real*8 yobs(mpar),yfxd(mpar)
      real*8 covd(mpar,mpar)
      real*8 g(mpar,mpar),gup(mpar,mpar)
      real*8 crchis,cchis,cnrms
      real*8 yc(mpar),yf(mpar),yu(mpar)
      real*8 omc(mpar)
      real*8 covxn(mpar,mpar),xn(mpar)
      real*8 covm(mpar,mpar)
      real*8 gp(mpar,mpar),dp(mpar,mpar),e(mpar)
      real*8 wm(mpar,mpar),matd(mpar,mpar),matdt(mpar,mpar)

      character*8 gpssn(2,mpar),llsn(2,mpar),sta(mpar)
      character*90 line
      character*32 ofile,filenm,dlcnm,dname
      character*1 dataop(6),pos
      character*5 sname(mpar)
      data pi/3.141592653589793d0/
      data tosec/3600.0d0,60.d0,1.d0/
      data small/0.1d-01/
      uot=10
      ust=11
      udt=12
      ugm=13
      dtr = datan(1.0d0)/45.0d0

ccccccccccccccccccccccccccccccccccccccccccccccccccccc
c --- read input information and open output files --- c
ccccccccccccccccccccccccccccccccccccccccccccccccccccc

      Call getfile2(uot,'Output file name','out','formatted',
     +              ofile)

      call getopt('trilateration data available?','y/n','n',dataop(1))
      call getopt('GPS vector data available?  ','y/n','n',dataop(2))
      call getopt('Do you want fault segments printed ? ',
     +            'y/n','n',dataop(3))
      if (dataop(1).eq.'y') then
      call getopt('Output line length change vs azimuth ? ',
     +            'y/n','n',dataop(4))
      endif

      if(dataop(1).eq.'n'.and.dataop(2).eq.'n') then
       write(0,*) 'No input data.....'
       write(0,*) 'exiting.....'
       stop
      endif

      Call getfile2(ust,'Station coordinate file name','in',
     +              'formatted',filenm)

      Call getfile2(ugm,'Dislocation geometry file name','in',
     +      'formatted',dlcnm)

      call getopt('Make end faults very long ?','y/n','n',dataop(6))

ccccccccccccccccccccccccc
c --- Read input data --- c
ccccccccccccccccccccccccc
```

```
      if(dataop(1).eq.'y') then
       call getfile2(udt,'line length data file name',
     +              'in','formatted',dname)
       j=1
 5     read(udt,10,end=20) llsn(1,j),llsn(2,j),distan,llch(j),llsd(j),
     +                    azi(j)
10     format(13x,a8,1x,a8,t44,f10.3,t54,f7.4,1x,f6.4,t69,f5.1)
       llch(j)=llch(j)*1.d03
       llsd(j)=llsd(j)*1.d03
       j=j+1
       goto 5

20     numll = j-1
       close(udt)
      endif
      if(dataop(2).eq.'y') then
       call getfile2(udt,'gps vector data file name','in',
     +              'formatted',dname)
       j=1
25     read(udt,*,end=30) gpssn(1,j),gpssn(2,j),gech(j),gesd(j),
     +                    gnch(j),gnsd(j),guch(j),gusd(j)
       gech(j)=gech(j)*1.d03
       gesd(j)=gesd(j)*1.d03
       gnch(j)=gnch(j)*1.d03
       gnsd(j)=gnsd(j)*1.d03
       guch(j)=guch(j)*1.d03
       gusd(j)=gusd(j)*1.d03
       j=j+1
       goto 25
30     numgps = j-1
       close(udt)
      endif

      ndata=numll+(numgps*2)

      j=1
35    read(ust,40,end=45) sta(j),ilatd,ilatm,lat(3),
     +                    ilond,ilonm,lon(3)
40    format(6x,a8,5x,i2,1x,i2,1x,f8.5,i4,1x,i2,1x,f8.5)
      lat(1)=real(ilatd)
      lat(2)=real(ilatm)
      lon(1)=real(ilond)
      lon(2)=real(ilonm)
      staloc(j,1)=abs(lat(1))+lat(2)/60.d0+lat(3)/3600.d0
      staloc(j,1)=sign(staloc(j,1),lat(1))
      staloc(j,2)=abs(lon(1))+lon(2)/60.d0+lon(3)/3600.d0
      staloc(j,2)=sign(staloc(j,2),lon(1))
      j=j+1
      goto 35
45    nsta=j-1
      close(ust)

ccccccccccccccccccccccccccccccccccccccc
c --- Read in dislocation geometry file --- c
ccccccccccccccccccccccccccccccccccccccc

      read(ugm,'(a)') line
      read(ugm,'(a)') line
      l=1
      free=0
      nflt=1
      nseg(nflt)=1
50    read(ugm,'(a)',end=100) line

      if(line(1:5).eq.'fixed') then
       nfree=l-1
       free=1
       nflt=nflt-1
       goto 50
      else if(line(1:1).eq.'*') then
       nseg(nflt)=nseg(nflt)-1
       nflt=nflt+1
       nseg(nflt)=1
       goto 50
      else if(line(1:1).eq.'#') then
       goto 50
      endif

       read(line,*)
     + (lonf(l,1,i),i=1,3),
     + (latf(l,1,i),i=1,3),
     + (lonf(l,2,i),i=1,3),
     + (latf(l,2,i),i=1,3),
     + w(l),dep(l),xstart(l),xbd(l),
     + sname(l)
       if(free.eq.0) then
        nseg(nflt)=nseg(nflt)+1
       endif

       xprior(l)=xstart(l)
       d(l)=w(l)+dep(l)

       do m=1,2
        flat(l,m) = 0.d0
        flon(l,m) = 0.d0
        do n=1,3
         flat(l,m) =
     +   flat(l,m) + abs(latf(l,m,n))*tosec(n)
         flon(l,m)=
     .   flon(l,m) + abs(lonf(l,m,n))*tosec(n)
        enddo

        flat(l,m) = sign(flat(l,m),latf(l,m,1))
        flat(l,m) = flat(l,m)/tosec(1)
        flon(l,m) = sign(flon(l,m),lonf(l,m,1))
        flon(l,m) = flon(l,m)/tosec(1)
       enddo

       l=l+1
       goto 50
100    close(ugm)
       mseg=l-1

       iseg(1)=1
       do j=2,nflt
        iseg(j)=iseg(j-1)+nseg(j-1)
       enddo

ccccccccccccccccccccccccccccccccccccccccccccccccccccccccccccccc
c --- Let centre of mass of station file be origin for x,y --- c
ccccccccccccccccccccccccccccccccccccccccccccccccccccccccccccccc

      lon_sum=0.d0
      lat_sum=0.d0
      do j=1,nsta
       lat_sum=lat_sum+staloc(j,1)
       lon_sum=lon_sum+staloc(j,2)
      enddo
      origin(1)=(lon_sum/nsta)
      origin(2)=(lat_sum/nsta)
      write(uot,*) 'Origin is at '
      write(uot,'(f12.5,2x,f12.5)') origin(1),origin(2)

ccccccccccccccccccccccccccccccccccccccccccccccccccccccccccccccc
c --- Convert lat/long for faults and stations to x-y(km) --- c
ccccccccccccccccccccccccccccccccccccccccccccccccccccccccccccccc

      write(uot,*) 'Station positions'
      do j=1,nsta
       call poly44(origin,staloc(j,2),staloc(j,1),
     +      xsta(j),ysta(j))
       write(uot,'(2(f8.3,1x),1x,a8,1x,2(f12.5,1x))')
     +     xsta(j),ysta(j),sta(j),
     +     staloc(j,2),staloc(j,1)
      enddo
      write(uot,*) ''
      do l=1,mseg
       do m=1,2
        call poly44(origin,flon(l,m),flat(l,m),
     +       xflt(l,m),yflt(l,m))
       enddo
      enddo

ccccccccccccccccccccccccccccccccc
c --- Compute fault constants --- c
ccccccccccccccccccccccccccccccccc

      do l=1,mseg
       dx=xflt(l,2)-xflt(l,1)
       dy=yflt(l,2)-yflt(l,1)
       len(l)=sqrt(dx**2 + dy**2)
       azi(l)=atan2(dy,dx)
       write(uot,'(5(f8.3,1x),f5.1)')
     + xflt(l,1),yflt(l,1),
     + xflt(l,2),yflt(l,2),
     + len(l),azi(l)/dtr
      enddo

      write(uot,'(a)') ''
      if(dataop(6).eq.'y') then
      write(uot,'(a)') 'Faults whose lengths have been increased'
       do l=1,mseg,4
        write(6,'(4(i3,1x,a4,3x))') (l+j,sname(l+j),j=0,3)
       enddo
       write(6,*) ''
```

```
      write(6,*) 'Enter end faults (0 to finish)'
111   read(5,*) i
      if(i.ne.0) then
       if(i.gt.mseg) goto 111
        len(i)=1.d06
        if(azi(i).gt.0.d0) azi(i)=123.d0*dtr
        if(azi(i).le.0.d0) azi(i)=-57.d0*dtr
        write(uot,'(i3,1x,5(f8.3,1x),f5.1,1x,a4)')
     +    i,xflt(l,1),yflt(l,1),
     +    xflt(l,2),yflt(l,2),
     +    len(l),azi(l)/dtr,sname(i)
       goto 111
      endif
      write(uot,'(a)') ''
      endif


ccccccccccccccccccccccccccccccccccccccccccc
c --- Start calculating greens functions --- c
ccccccccccccccccccccccccccccccccccccccccccc

      if(dataop(1).eq.'y') then
       write(0,*) 'Calculating p.ds for line length data'
       do j=1,numll
        sfl1=0
        sfl2=0
        do k=1,nsta
         if(llsn(1,j).eq.sta(k)) then
          x1=xsta(k)
          y1=ysta(k)
          sfl1=1
         endif
        enddo
        do k=1,nsta
         if(llsn(2,j).eq.sta(k)) then
          x2=xsta(k)
          y2=ysta(k)
          sfl2=1
         endif
        enddo
        if(sfl1.eq.0.or.sfl2.eq.0) then
         write(0,'(a,$)')'Unable to find station(s). '
         if(sfl1.eq.0) write(0,'(a8,1x,$)') llsn(1,j)
         if(sfl2.eq.0) write(0,'(a8,1x,$)') llsn(2,j)
         write(0,*)''
         stop
        endif
        theta=atan2(y2-y1,x2-x1)

        yo(j)=llch(j)
ccccccccccccccccccccccccccccccc
c --- Multiply st.dev. by 2. - c
c --- If required !          - c
ccccccccccccccccccccccccccccccc
        stdy(j)=llsd(j)*2
        covd(j,j)=(llsd(j)*2)**2
c       stdy(j)=llsd(j)

        do l = 1,mseg
         xx=(x1-xflt(l,1))*dcos(azi(l)) + (y1-yflt(l,1))*dsin(azi(l))
         yy=-(x1-xflt(l,1))*dsin(azi(l)) + (y1-yflt(l,1))*dcos(azi(l))
         call srectf(alp,xx,yy,d(l),len(l),w(l),1.d0,0.d0,
     +        -1.d0,0.d0,0.d0,a1,a2,a3,u11,u12,u21,u22,u31,u32)

         ux=a1*cos(azi(l))-a2*sin(azi(l))
         uy=a1*sin(azi(l))+a2*cos(azi(l))
         a1=ux
         a2=uy

         xx=(x2-xflt(l,1))*dcos(azi(l)) + (y2-yflt(l,1))*dsin(azi(l))
         yy=-(x2-xflt(l,1))*dsin(azi(l)) + (y2-yflt(l,1))*dcos(azi(l))
         call srectf(alp,xx,yy,d(l),len(l),w(l),1.d0,0.d0,
     +        -1.d0,0.d0,0.d0,b1,b2,b3,u11,u12,u21,u22,u31,u32)

         ux=b1*cos(azi(l))-b2*sin(azi(l))
         uy=b1*sin(azi(l))+b2*cos(azi(l))
         b1=ux
         b2=uy

         bigu=(b1-a1)*cos(theta)+(b2-a2)*sin(theta)

         g(j,l) = bigu
        enddo
       enddo
      endif
      if(dataop(2).eq.'y') then
       add=0
       if(dataop(1).eq.'y') add=numll

       write(0,*) 'Calculating p.ds for gps data'
       do j=1,numgps
        sfl1=0
        sfl2=0
        do k=1,nsta
         if(gpssn(1,j).eq.sta(k)) then
          x1=xsta(k)
          y1=ysta(k)
          sfl1=1
         endif
        enddo
        do k=1,nsta
         if(gpssn(2,j).eq.sta(k)) then
          x2=xsta(k)
          y2=ysta(k)
          sfl2=1
         endif
        enddo
        if(sfl1.eq.0.or.sfl2.eq.0) then
         write(0,'(a,$)')'Unable to find station(s). '
         if(sfl1.eq.0) write(0,'(a8,1x,$)') llsn(1,j)
         if(sfl2.eq.0) write(0,'(a8,1x,$)') llsn(2,j)
         write(0,*)''
         stop
        endif
        yo(add+j*2-1)  = gnch(j)
        yo(add+j*2)    = gech(j)
        stdy(add+j*2-1) = gnsd(j)
        stdy(add+j*2)  = gesd(j)
        covd(add+j*2-1,add+j*2-1)=gnsd(j)**2
        covd(add+j*2,add+j*2)   =gesd(j)**2
        do l=1,mseg

         xx=(x1-xflt(l,1))*dcos(azi(l)) + (y1-yflt(l,1))*dsin(azi(l))
         yy=-(x1-xflt(l,1))*dsin(azi(l)) + (y1-yflt(l,1))*dcos(azi(l))
         call srectf(alp,xx,yy,d(l),len(l),w(l),1.d0,0.d0,
     +    -1.d0,0.d0,0.d0,a1,a2,a3,u11,u12,u21,u22,u31,u32)

         xx=(x2-xflt(l,1))*dcos(azi(l)) + (y2-yflt(l,1))*dsin(azi(l))
         yy=-(x2-xflt(l,1))*dsin(azi(l)) + (y2-yflt(l,1))*dcos(azi(l))
         call srectf(alp,xx,yy,d(l),len(l),w(l),1.d0,0.d0,
     +    -1.d0,0.d0,0.d0,b1,b2,b3,u11,u12,u21,u22,u31,u32)

         g(add+j*2-1,l)=(a1-b1)*dsin(azi(l))+(a2-b2)*dcos(azi(l))
         g(add+j*2,l)  =(a1-b1)*dcos(azi(l))-(a2-b2)*dsin(azi(l))
         gup(j,l)=a3-b3

        enddo
       enddo
      endif

ccccccccccccccccccccccccccccccccc
c --- Calculating forward model --- c
ccccccccccccccccccccccccccccccccc

      do j=1,ndata
       yf(j)=0.d0
       do l=1,mseg
        yf(j)=yf(j)+g(j,l)*xstart(l)
       enddo
      enddo
      do j=1,numgps
       yu(j)=0.d0
       do l=1,mseg
        yu(j)=yu(j)+gup(j,l)*xstart(l)
       enddo
      enddo

ccccccccccccccccccccccccccccccccccccccccccccccccccccccccc
c --- Remove fixed fault segments from observed data --- c
ccccccccccccccccccccccccccccccccccccccccccccccccccccccccc

      if(mseg.ge.nfree+1) then
      if(dataop(3).eq.'y') then
       open(unit=20,file='fixed_segm')
       write(20,'(a)') '>'
      endif
      write(uot,'(a)') 'Fixed fault segments : ',mseg-nfree-1
      do j=nfree+1,mseg
       write(uot,'(i3,1x,4(f9.4,1x),2(f6.1,1x),2(f5.2,1x))')
     + j,flon(j,1),flat(j,1),flon(j,2),flat(j,2),w(j),d(j),
     + xstart(j),xbd(j)

       if(dataop(3).eq.'y') then
        write(20,'(f9.4,2x,f9.4)')
     + flon(j,1),flat(j,1)
        write(20,'(f9.4,2x,f9.4)')
     + flon(j,2),flat(j,2)
```

```
        write(20,'(a)') '>'
       endif
      enddo

      if(dataop(3).eq.'y') close(20)

      write(0,'(a)') 'Removing fixed fault segments.....'
      do j=1,ndata
       yfxd(j)=0.d0
       yobs(j)=yo(j)
       do l=nfree+1,mseg
        yfxd(j)=yfxd(j)+xstart(l)*g(j,l)
        yo(j)=yo(j)-xstart(l)*g(j,l)
       enddo
      enddo
      else
       do j=1,ndata
        yfxd(j)=0.d0
        yobs(j)=yo(j)
       enddo
      endif

ccccccccccccccccccccccccccccccccccccccccc
c --- Combine columns of the [g] matrix --- c
ccccccccccccccccccccccccccccccccccccccccc

      write(uot,'(a,i3)') 'Free fault segments : ',nflt
      if(dataop(3).eq.'y') then
       open(unit=20,file='free_segm')
       write(20,'(a)') '>'
      endif
      do j=1,nflt
       do k=iseg(j),iseg(j)+nseg(j)-1
        write(uot,'(i3,1x,4(f9.4,1x),2(f6.1,1x),2(f5.2,1x))')
     +  k,flon(k,1),flat(k,1),flon(k,2),flat(k,2),w(k),d(k),
     +  xstart(k),xbd(k)
        if(dataop(3).eq.'y') then
         write(20,'(f9.4,2x,f9.4)')
     +   flon(k,1),flat(k,1)
         write(20,'(f9.4,2x,f9.4)')
     +   flon(k,2),flat(k,2)
         write(20,'(a)') '>'
        endif
       enddo
       write(uot,'(a)') ''
      enddo
      if(dataop(3).eq.'y') close(20)

      write(0,'(a)') 'Combining columns of the [g] matrix'

      do l=1,nflt
       do j=1,ndata
        tmpg(j,l)=0.d0
        do k=iseg(l),iseg(l)+nseg(l)-1
         tmpg(j,l)=tmpg(j,l)+g(j,k)
        enddo
       enddo
      enddo

ccccccccccccccccccccccccccc
c --- clear matrix [g] --- c
ccccccccccccccccccccccccccc

      do j=1,mpar
       do l=1,mpar
        g(j,l)=0.d0
       enddo
      enddo

      do j=1,ndata
       do l=1,nflt
        g(j,l)=tmpg(j,l)
       enddo
      enddo

      do j=1,nflt
       xav=0.d0
       xbdav=0.d0
       do k=iseg(j),iseg(j)+nseg(j)-1
        xav=xav+xstart(k)
        xbdav=xbdav+xbd(k)
       enddo
        xtmp(j)=xav/nseg(j)
        xbdtmp(j)=xbdav/nseg(j)
      enddo

      do j=1,nflt
       xbd(j)=xbdtmp(j)
        xstart(j)=xtmp(j)
      enddo

      write(0,'(a)') 'Done '

ccccccccccccccccccccccccccc
c --- Begin Inversion --- c
ccccccccccccccccccccccccccc

      do l=1,nflt
       covm(l,l)=xbd(l)**2
      enddo

ccccccccccccccccccccccccccccc
c --- Generalise problem --- c
ccccccccccccccccccccccccccccc

      do j=1,ndata
       dbar(j)=yo(j)/sqrt(covd(j,j))
       do k=1,nflt
        gbar(j,k)=g(j,k)/sqrt(covd(j,j))
       enddo
      enddo

ccccccccccccccccccccccccccccccccccccccccccccccccccccc
c --- Weighted Damped or Weighted linear inversion? -- c
ccccccccccccccccccccccccccccccccccccccccccccccccccccc

150   write(6,'(a)') '1. Forward model '
      write(6,'(a)') ''
      write(6,'(a)') '2. Weighted least squares inversion'
      write(6,'(a)') ''
      write(6,'(a)') '3. Weighted damped least squares inversion '
      write(6,'(a)') ''
      write(6,'(a)') '4. Weighted Minimum length inversion'
      write(6,'(a)') ''
      write(6,'(a)') '5. Stochastic inversion'
      write(6,'(a)') ''
      write(6,'(a)') '6. Singular value decomposition'

      call getint('Select method  ',2,answer)

      if(answer.eq.1) then

       continue

      else if (answer.eq.2) then

       call getopt('With or without positivity ? ','y/n','y',pos)

       if(pos.eq.'n') then

        call lsinv(gbar,dbar,xn,covxn,ndata,nflt,mpar)

       else

        call pls(gbar,xn,dbar,ndata,nflt,mpar,mpar,gp,dp,e,mpar,
     +           mpar,0.000001,ierr)

       endif

      else if (answer.eq.3) then

       call wdlsinv(g,yo,covd,xstart,covm,xn,covxn,ndata,nflt,mpar)

      else if (answer.eq.4) then

       call mlinv(gbar,dbar,xn,covxn,ndata,nflt,mpar)

      else if (answer.eq.5) then

       write(6,'(a)') 'using flatness as prior information'
       write(6,*) ''
       do j=1,nflt
        write(6,'(i3,1x,a4,a,a4)') j,sname(iseg(j)),' to ',
     +  sname(iseg(j)+nseg(j)-1)
       enddo
       l=1
       write(6,*) ''
       write(6,*) 'Enter adjacent faults for weighting (0 0 to finish) '
200    read(5,*) i,j
       if(i.ne.0.and.j.ne.0) then
        if(i.gt.nflt.or.j.gt.nflt) goto 200
        matd(l,i)=-1.d0
        matdt(i,l)=-1.d0
        matd(l,j)=1.d0
        matdt(j,l)=1.d0
        l=l+1
```

```
        goto 200
       endif

       call dgemm('N','N',nflt,nflt,l-1,1.d0,matdt,mpar,matd,mpar,
      +      0.d0,wm,mpar)

       call stocinv(gbar,dbar,xstart,covm,xn,covxn,ndata,nflt,mpar,wm)

      else if (answer.eq.6) then

       call svdinv(gbar,dbar,xstart,covm,xn,covxn,ndata,nflt,mpar)

      else

       write(6,'(a)') ''
       write(6,'(a)') 'Unrecognised number '
       write(6,'(a)') ''
       goto 150

      endif

ccccccccccccccccccccccccc
c --- Inversion finished --- c
ccccccccccccccccccccccccc

cccccccccccccccccccccccccccccccccccccccccccccccccccccccccccccccccc
c --- Check wether inversion has predicted negative slip rates --- c
cccccccccccccccccccccccccccccccccccccccccccccccccccccccccccccccccc

      if(answer.ne.1) then
       do k=1,nflt
        if(xn(k).lt.0.0) then
         write(0,'(a,i3)') 'Negative slip rate for ',k
        endif
       enddo

ccccccccccccccccccccccccccccccccc
c --- Calculate predicted motions --- c
ccccccccccccccccccccccccccccccccc

ccccccccccccccccccccc
c --- from inversion --- c
ccccccccccccccccccccc

      call dgemm('N','N',ndata,1,nflt,1.d0,g,
     .           mpar,xn,mpar,0.d0,yc,
     .           mpar)

ccccccccccccccccccccccccccccccccccccccccc
c --- add back effects of fixed segments --- c
ccccccccccccccccccccccccccccccccccccccccc

      do j=1,ndata
       yc(j)=yc(j)+yfxd(j)
      enddo

      call fchisq(ndata,nflt,mpar,yobs,yc,
     .     stdy,omc,cchis,crchis,cnrms)

      else

       do j=1,ndata
        yc(j)=yf(j)
       enddo

       call fchisq(ndata,0,mpar,yobs,yc,
     .     stdy,omc,cchis,crchis,cnrms)

      endif
cccccccccccccccccccccccccc
c --- Print Out Results --- c
cccccccccccccccccccccccccc

      write(uot,'(4x,3(a6,2x))')
     + 'Obs.  ','Calc. ','Resid.'
      write(uot,'(4x,3(a6,2x))')
     + '------','------','------'
      do j=1,ndata
       write(uot,'(i3,1x,3(f6.4,2x))')
     + j,yobs(j)/1.d03,yc(j)/1.d03,
     + (yobs(j)-yc(j))/1.d03
       write(30,305)
     +   yobs(j),yc(j),stdy(j),(yobs(j)-yc(j))**2/(stdy(j)**2)
305   format(4(f6.1,1x))
      enddo

c     if(dataop(1).eq.'y') then
c      do j=1,numll
c       do k=1,nsta
c        if(llsn(1,j).eq.sta(k)) then
c         x1=staloc(k,1)
c         y1=staloc(k,2)
c        endif
c       enddo
c       do k=1,nsta
c        if(llsn(2,j).eq.sta(k)) then
c         x2=staloc(k,1)
c         y2=staloc(k,2)
c        endif
c       enddo
c       write(30,300)
c     +   yobs(j),yc(j),stdy(j),(yobs(j)-yc(j))**2/(stdy(j)**2),
c     +   llsn(1,j),llsn(2,j)
300     format(4(f6.1,1x),a8,1x,a8)
c      enddo
c     endif


      write(uot,'(a)') ''
      write(uot,'(a,1x,f12.5,1x,f12.5)')
     + 'Chi Square : ',cchis,crchis
      write(uot,'(a)') ''

      if(answer.ne.1) then
       write(uot,'(a)') 'Slip Rates'
       write(uot,'(a3,a4,a4,a4,a6,2x,a6,2x,a6)')
     +  'No ','Flt ','Flt ',
     +  ' Orig.',' Calc.',' Error'
       do k=1,nflt
        write(uot,'(i2,1x,a4,a,a4,3(f6.2,2x))')
     +   k,sname(iseg(k)),' to ',
     +   sname(iseg(k)+nseg(k)-1),
     +   xstart(k),xn(k),sqrt(covxn(k,k))
       enddo
      endif

ccccccccccccccccccccccccccccccccc
c --- Output files for dispinvl --- c
ccccccccccccccccccccccccccccccccc

      if (dataop(1).eq.'y') then
      open(unit=23,file='model.geod')
      write(0,*) 'Writing model line length data'
       do j=1,numll
        do k=1,nsta
         if(llsn(1,j).eq.sta(k)) then
          x1=xsta(k)
          y1=ysta(k)
         endif
        enddo
        do k=1,nsta
         if(llsn(2,j).eq.sta(k)) then
          x2=xsta(k)
          y2=ysta(k)
         endif
        enddo
        azimuth=atan2(x2-x1,y2-y1)/dtr
        call norman(azimuth,360.d0)
        distan =sqrt((x2-x1)**2 + (y2-y1)**2)*1.d03
        write(23,120) 'model   +     ',llsn(1,j),llsn(2,j),0.000,1,
     +                distan,yc(j)/1.d03,0.0005,azimuth
        if(dataop(4).eq.'y') then
         write(18,'(f5.1,1x,3(f7.4,1x))') azimuth,yc(j)/1.d03,
     +      llch(j),llsd(j)
        endif
120     format(a13,a8,1x,a8,3x,f6.3,i4,f10.3,f7.4,1x,f6.4,1x,f5.1)
       enddo
       close(23)
      endif
      if(dataop(2).eq.'y') then
       open(unit=24,file='model.gps')
       add=0
       if(dataop(1).eq.'y') add=numll
       write(0,*) 'Writing model gps data'
       do j=1,numgps
        do k=1,nsta
         if(gpssn(1,j).eq.sta(k)) then
          slat=staloc(k,1)
          slon=staloc(k,2)
         endif
        enddo
        write(24,'(1x,2(a1,a8,a1,6x),3(2x,f6.4,1x,f6.4))')
     +   char(39),gpssn(1,j),char(39),char(39),gpssn(2,j),char(39),
     +   yc(add+j*2)/1.d03,0.0005,yc(add+j*2-1)/1.d03,0.0005,0.0,0.000
        write(25,'(f12.5,f12.5,2x,f7.2,a8,2x,a8)')
     +  slon,slat,yu(j),gpssn(1,j),gpssn(2,j)
```

```
      enddo
      close(24)
     endif

ccccccccccccccccccccccccccccccccccccccccccccccccc
c --- Write out fault file for graphics progs --- c
ccccccccccccccccccccccccccccccccccccccccccccccccc

     if(answer.ne.1) then

     call getopt('output graphics file ?','y/n','y',dataop(5))

     if(dataop(5).eq.'y') then

     do j=1,nflt
      do k=iseg(j),iseg(j)+nseg(j)-1
       write(23,500) int(lonf(k,1,1)),
     +  int(lonf(k,1,2)),lonf(k,1,3),
     +  int(latf(k,1,1)),int(latf(k,1,2)),latf(k,1,3),
     +  int(lonf(k,2,1)),int(lonf(k,2,2)),lonf(k,2,3),
     +  int(latf(k,2,1)),int(latf(k,2,2)),latf(k,2,3),
     +  w(k),dep(k),xn(j),sqrt(covxn(j,j)),sname(k)
      enddo
     enddo
     if(mseg.ge.nfree+1) then
      do k=1,nfree+1,mseg
       write(23,500) int(lonf(k,1,1)),
     +  int(lonf(k,1,2)),lonf(k,1,3),
     +  int(latf(k,1,1)),int(latf(k,1,2)),latf(k,1,3),
     +  int(lonf(k,2,1)),int(lonf(k,2,2)),lonf(k,2,3),
     +  int(latf(k,2,1)),int(latf(k,2,2)),latf(k,2,3),
     +  w(k),dep(k),xprior(k),0.0,sname(k)
      enddo
     endif
     endif
     endif

500  format(2(i4,i3,f8.4,i3,i3,f8.4,1x),f6.1,f5.1,f5.2,
    +       f6.2,1x,a4)



999  stop

2000 print*,'Error in reading station file'

     stop
     end

     subroutine dummy(flnum,n)

ccccccccccccccccccccccccccccccccccccccccccccccccc
c --- reads unwanted lines in an input file --- c
ccccccccccccccccccccccccccccccccccccccccccccccccc

     integer n,j,flnum
     do j=1,n
      read(flnum,*)
     enddo

     return
     end


ccccccccccccccccccccccccccccccc
c ---  normalize the angle --- c
ccccccccccccccccccccccccccccccc

     subroutine  norman(ang,n)
c
c      input
c        n   : normalizing range
c      input/output
c        ang : angle normalized within (0 - n)
c
     real*8 n,b,ang
     b=n
    1 if(ang.lt.0.)  then
       ang=ang+b
       go to 1
      elseif(ang.gt.b)  then
       ang=ang-b
       go to 1
      endif
      return
      end

ccccccccccccccccccccccccccccccccccccccccccccccccc

c --- General least squares inversion -- c
ccccccccccccccccccccccccccccccccccccccccccccccccc

     subroutine lsinv(g,d,m,covm,ndata,npar,mpar)

     implicit none

c    INPUT

     integer ndata,npar,mpar

     real*8 g(mpar,mpar),d(mpar)

c    OUTPUT

     real*8 m(mpar),covm(mpar,mpar)

c    INTERNAL

     integer j,k,ipar

     parameter (ipar=360)

     real*8 gt(ipar,ipar)
     real*8 check(ipar),worka(ipar,ipar)
     real*8 gmg(ipar,ipar)

     do j=1,ndata
      do k=1,npar
       gt(k,j)=g(j,k)
      enddo
     enddo

     call dgemm('N','N',npar,npar,ndata,1.d0,
    +     gt,ipar,g,mpar,0.d0,
    +     worka,ipar)

     call dpoinv(npar,worka,ipar,check)

     do j=1,npar
      do k=1,npar
       covm(j,k)=worka(j,k)
      enddo
     enddo

     call dgemm('N','N',npar,ndata,npar,1.d0,
    +     worka,ipar,gt,ipar,0.d0,
    +     gmg,ipar)

     call dgemv('N',npar,ndata,1.d0,
    +     gmg,ipar,d,1,0.d0,m,1)

     return
     end

ccccccccccccccccccccccccccccccccccccccccccccccccc
c --- General minimum length inversion -- c
ccccccccccccccccccccccccccccccccccccccccccccccccc

     subroutine mlinv(g,d,m,covm,ndata,npar,mpar)

     implicit none

c    INPUT

     integer ndata,npar,mpar

     real*8 g(mpar,mpar),d(mpar)

c    OUTPUT

     real*8 m(mpar),covm(mpar,mpar)

c    INTERNAL

     integer j,k,ipar

     parameter (ipar=360)

     real*8 gt(ipar,ipar)
     real*8 check(ipar),worka(ipar,ipar)
     real*8 gmg(ipar,ipar)

     do j=1,ndata
      do k=1,npar
       gt(k,j)=g(j,k)
      enddo
     enddo
```

```
      call dgemm('N','N',ndata,ndata,npar,1.d0,
     +     g,ipar,gt,ipar,0.d0,
     +     worka,ipar)

      call dpoinv(ndata,worka,ipar,check)

      call dgemm('N','N',npar,ndata,ndata,1.d0,
     +     gt,ipar,worka,ipar,0.d0,
     +     gmg,ipar)

      call dgemv('N',npar,ndata,1.d0,
     +     gmg,ipar,d,1,0.d0,m,1)

      return
      end

ccccccccccccccccccccccccccccccccccccccccccccccccccccccccccccccc
c --- Least squares inversion with positivity constraint --- c
ccccccccccccccccccccccccccccccccccccccccccccccccccccccccccccccc

      subroutine pls(g,xm,d,n,m,nst,mst,gp,dp,e,npst,mpst,ierr)

      implicit none

      integer n, m, nst, mst, npst, mpst, ierr
      integer i,j,k,iadd,izmin,nlist

      real*8 g(nst,mst), xm(mst), d(nst), test
      real*8 dp(npst), e(npst), gp(npst,mpst)
      real*8 t,alfa,gmax,zmin

      integer list(360),itr(360),igp(360),mcur

      real*8 grade(360), z(360)
      real*8 u(360)

      common /plscom/ mcur, itr, igp
      common /ucom/ u

      test = 0.000001

       do i=1, n
        dp(i) = d(i)
       enddo
       mcur = 0
       do i=1,m
        itr(i)=0
        igp(i)=0
        xm(i)=0.0
        z(i)=0.0
       enddo

      do i=1, 3*m

       do j=1, n
         e(j) = d(j)
         do k=1, m
          e(j) = e(j) - g(j,k)*xm(k)
         enddo
       enddo

       do j=1, m
         grade(j)=0.0
         do k=1, n
           grade(j) = grade(j) + g(k,j)*e(k)
         enddo
       enddo

       gmax=0.0
       iadd = 0
       do j=1, m
         if( itr(j).eq.0.and.grade(j).gt.gmax ) then
           iadd = j
           gmax = grade(j)
         endif
       enddo

       if(gmax.le.0.0) then
          ierr=0
          print*,"gmax<0"
          return
       endif

       call add(g,z,d,n,m,mst,nst,gp,dp,mpst,npst,test,iadd,ierr)
       if(ierr.ne.0) then
         print*,"after add"
         return
       endif

       zmin = 0.0
       izmin = 0
       do j=1, m
        if (itr(j). ne. 0 .and. z(j). lt. zmin) then
         izmin=j
         zmin = z(j)
        endif
       enddo

       if(zmin.ge.-test) then
        do k=1, m
         if (itr(k).ne.0) then
           xm(k) = z(k)
         endif
        enddo

       else

        do j=1, m

         alfa = 1.e30
         do k=1, m
           if (itr(k).ne.0) then
             t = xm(k) / (xm(k)-z(k))
             if (t.lt.alfa) then
               alfa=t
             end if
           end if
         enddo

         do k=1, m
          if (itr(k). ne. 0) then
           xm(k)=xm(k)+alfa*(z(k)-xm(k))
          end if
         enddo

         nlist=0
         do k=1, m
          if (itr(k).ne.0.and.xm(k).le.test) then
           nlist=nlist+1
           list(nlist)=k
          end if
         enddo

         do k=1, nlist
          call sub(g,z,d,n,m,mst,nst,gp,dp,mpst,
     .             npst,test,list(k),ierr)
          if(ierr.ne.0) then
           print*,"after sub"
           return
          end if
         enddo

         zmin = 0.0
         izmin = 0
         do k=1, m
          if (itr(k).ne.0.and.z(k).le.zmin) then
           izmin=k
           zmin=z(k)
          end if
         enddo
         if(izmin.eq.0.or.zmin.gt.-test) then
          goto 15
         end if

        enddo
15      continue
       end if
       enddo


       ierr=2
       return
       end


       subroutine add(g,xm,d,n,m,nst,mst,gp,dp,npst,mpst,test,iv,ierr)

       implicit none

       integer n, m, nst, mst, npst, mpst, ierr
       integer iv,i,j,k

       real*8 g(nst,mst), xm(mst), d(nst), test, gp(npst,mpst), dp(npst)
       real*8 alfa,beta,gama,t
```

```
 real*8 u(360)

 integer itr(360),igp(360),mcur

 common /plscom/ mcur, itr, igp
 common /ucom/ u

 if(iv.lt.1.or.iv.gt.m) then
  print*,"iv<1 or iv>m"
  ierr=1
  return
 endif

 if(itr(iv).ne.0) then
  print*,"itr(iv).ne.0"
  ierr=1
  return
 end if

 mcur = mcur + 1
 igp(mcur)=iv
 itr(iv)=mcur


 do i=1, n
  gp(i,iv) = g(i,iv)
 enddo


 do j=1, mcur-1
  k = igp(j)
  beta = -u(k) * gp(j,k)
  gama = 0.d0
  do i=j,n
   gama = gama + gp(i,iv)*gp(i,k)
  enddo
  gama = gama / beta
  do i=j,n
   gp(i,iv) = gp(i,iv) - gama*gp(i,k)
  enddo
 enddo

 if(n.gt.mcur) then
  alfa = 0.d0
  do i=mcur, n
   alfa = alfa + gp(i,iv)**2
  enddo

  alfa = sqrt( alfa )

  if(gp(mcur,iv).lt.0.d0) then
   alfa = -alfa
  end if

  u(iv) = -alfa
  t = gp(mcur,iv) + alfa

  if( abs(t) .lt. test ) then
   ierr=1
   print*,"abs(t)<test"
   print*,abs(t),test
   return
  end if

  gp(mcur,iv) = t
  beta = -u(iv) * gp(mcur,iv)
  gama = 0.d0

  do  i = mcur, n
   gama = gama + dp(i)*gp(i,iv)
  enddo

  gama = gama / beta

  do i = mcur, n
   dp(i) = dp(i) - gama*gp(i,iv)
  enddo
 else
  u(iv) = gp(mcur,iv)
 end if

 do i=mcur,1,-1
  t = dp(i)
  do j=i+1,mcur
   k = igp(j)
   t = t - gp(i,k) * xm(k)
  enddo
  xm(igp(i)) = t / u(igp(i))
 enddo

 return
 end

 subroutine sub(g,xm,d,n,m,nst,mst,gp,dp,npst,mpst,test,iv,ierr)

 implicit none

 integer n, m, nst, mst, npst, mpst, ierr
 integer i,iv,ncur,ntr,k,j,jj,kk

 real*8 g(nst,mst), xm(mst), d(nst), test, gp(npst,mpst), dp(npst)
 real*8 beta,gama,alfa,t
 real*8 u(360)

 integer itr(360),igp(360),mcur

 common /plscom/ mcur, itr, igp
 common /ucom/ u

 if( iv.lt.1 .or. iv.gt.m ) then
  print*,"iv<1oriv>m"
  ierr=1
  return
 end if

 ntr = itr( iv )
 if( ntr .eq. 0 ) then
  print*,"ntr=0"
  ierr = 1
  return
 end if

 do i=ntr+1, mcur
  k = igp(i)
  do j=1, n
   gp(j,k) = g(j,k)
  enddo
 enddo

 do i=1, n
  dp(i) = d(i)
 enddo

 do j=1, ntr-1
  k = igp(j)
  beta = -u(k) * gp(j,k)

  do jj=ntr+1, ncur
   kk = igp(jj)
   gama = 0.d0
   do  i=j, n
    gama = gama + gp(i,kk)*gp(i,k)
   enddo
   gama = gama / beta
   do i=j, n
    gp(i,kk) = gp(i,kk) - gama*gp(i,k)
   enddo
  enddo

  gama = 0.d0
  do i=j, n
   gama = gama + dp(i)*gp(i,k)
  enddo
  gama = gama / beta
  do i=j, n
   dp(i) = dp(i) - gama*gp(i,k)
  enddo
 enddo

 do i=ntr+1, mcur
  igp(i-1) = igp(i)
  itr(igp(i-1)) = i-1
 enddo

 itr(iv) = 0
 igp(mcur) = 0
 mcur = mcur - 1
 do j = ntr, mcur

  alfa = 0.d0
  k = igp(j)
  do i=j, n
   alfa = alfa + gp(i,k)**2
  enddo
  alfa = sqrt( alfa )
  if( gp(j,k) .lt. 0.d0 ) then
```

```
          alfa = -alfa
         end if
         u(k) = -alfa
         t = gp(j,k) + alfa
         if( abs(t) .lt. test ) then
          print*,"abs(t)<test"
          print*,abs(t),test
          ierr=1
          return
         end if
         gp(j,k) = t
         beta = -u(k) * gp(j,k)

         do jj = j+1, mcur
          kk = igp(jj)
          gama = 0.d0
          do i=j, n
           gama = gama + gp(i,kk)*gp(i,k)
          enddo
          gama = gama / beta
          do i=j, n
           gp(i,kk) = gp(i,kk) - gama*gp(i,k)
          enddo
         enddo

         gama = 0.d0
         do i = j, n
          gama = gama + dp(i)*gp(i,k)
         enddo
         gama = gama / beta
         do i = j, n
          dp(i) = dp(i) - gama*gp(i,k)
         enddo
        enddo

        xm(iv) = 0.d0
        do i=mcur,1,-1
         t = dp(i)
         do j=i+1,mcur
          k = igp(j)
          t = t - gp(i,k) * xm(k)
         enddo
         xm(igp(i)) = t / u(igp(i))
        enddo

        return
        end

ccccccccccccccccccccccccccccccccccccc
c --- Singular value decomposition --- c
ccccccccccccccccccccccccccccccccccccc

        subroutine svdinv(g,d,xs,covxs,m,covm,ndata,npar,mpar)

        implicit none

c       INPUT

        integer ndata,npar,mpar

        real*8 g(mpar,mpar),d(mpar)
        real*8 xs(mpar),covxs(mpar,mpar)

c       OUTPUT

        real*8 m(mpar),covm(mpar,mpar)

c       INTERNAL

        integer i,j,k,ipar,info,p

        character*1 ans

        parameter (ipar=360)

        real*8 uval(ipar),u(ipar,ipar)
        real*8 vt(ipar,ipar),junk(10096)
        real*8 vlmbda(ipar,ipar)
        real*8 uvalinv(ipar),gmg(ipar,ipar)
        real*8 ident(ipar,ipar),r(ipar,ipar)
        real*8 worka(ipar,ipar)

        call dgesvd('A','A',ndata,npar,g,mpar,
     .      uval,u,ipar,vt,ipar,junk,10096,
     .      info)


        do j=1,npar
         write(6,'(i3,2x,f10.4)') j,uval(j)
        enddo

        write(6,'(a,$)') 'Number of Eigenvalues to retain '
        read(5,*) p

        do j=1,p
         uvalinv(j)=1.d0/uval(j)
         do k=1,npar
          vlmbda(k,j) = uvalinv(j)*vt(j,k)
         enddo
        enddo


        do i=1,npar
         do j=1,ndata
          gmg(i,j) = 0.d0
          do k=1,p
           gmg(i,j) = gmg(i,j)+vlmbda(i,k)*u(j,k)
          enddo
         enddo
        enddo

        do i=1,npar
         m(i) = 0.d0
         do j=1,ndata
          m(i)=m(i)+gmg(i,j)*d(j)
         enddo
        enddo

        do k=1,npar
         covm(k,k)=0.d0
         do j=1,ndata
          covm(k,k)= covm(k,k) + gmg(k,j)*gmg(k,j)
         enddo
        enddo

        write(6,'(a)') 'Do you want minmimise the vectors'
        write(6,'(a,$)') 'with respect to the a priori ? '
        read(5,*) ans

        if (ans.eq.'y') then

         do j=1,p
          do k=1,p
           ident(j,k)=0.d0
          enddo
          ident(j,j)=1.d0
         enddo

         do i=1,npar
          do j=1,npar
           r(i,j) = 0.d0
           do k=1,p
            r(i,j) = r(i,j)+vt(k,i)*vt(k,j)
           enddo
          enddo
         enddo

         do k=1,npar
          do j=1,npar
           worka(k,j) = ident(k,j)-r(k,j)
          enddo
         enddo

         do k=1,npar
          do j=1,npar
           m(k)=m(k)+worka(k,j)*xs(j)
          enddo
         enddo

c        remember to add in estimate for covariance

        endif


        return
        end


ccccccccccccccccccccccccccccccccccccc
c --- weighted generalized inverse --- c
ccccccccccccccccccccccccccccccccccccc

        subroutine wdlsinv(g,d,covd,m,covm,xn,covxn,ndata,npar,mpar)

        implicit none
```

```
c     INPUT

      integer ndata,npar,mpar

      real*8 g(mpar,mpar),d(mpar),covd(mpar,mpar)
      real*8 m(mpar),covm(mpar,mpar)

c     OUTPUT

      real*8 xn(mpar),covxn(mpar,mpar)

c     INTERNAL

      integer j,k,ipar,l

      parameter (ipar=360)

      real*8 check(ipar),worka(ipar,ipar)
      real*8 workb(ipar,ipar)
      real*8 workbinv(ipar,ipar)
      real*8 workc(ipar),workd(ipar),worke(ipar,ipar)
      real*8 workf(ipar,ipar)
      real*8 workg(ipar),workh(ipar,ipar)
      real*8 ident(ipar,ipar),worki(ipar,ipar)
      real*8 workj(ipar,ipar),workk(ipar,ipar)
      real*8 workl(ipar,ipar),workm(ipar,ipar)


ccccccccccccccccccccccccccccccccc
c --- Calculate : Worka=G*[Covm] --- c
ccccccccccccccccccccccccccccccccc

      call dgemm('N','N',ndata,npar,npar,1.d0,
     .           g,mpar,covm,mpar,
     .           0.d0,worka,ipar)

ccccccccccccccccccccccccccccccccc
c --- Calculate : Workb=Worka*G' --- c
ccccccccccccccccccccccccccccccccc

      call dgemm('N','T',ndata,ndata,npar,1.d0,
     .           worka,ipar,g,mpar,
     .           0.d0,workb,ipar)

ccccccccccccccccccccccccccccccccccccccccc
c --- Calculate : workb = {[covd]+G[Covm]G'} --- c
ccccccccccccccccccccccccccccccccccccccccc

      do j=1,ndata
       do l=1,ndata
        workb(j,l)=workb(j,l)+covd(j,l)
        workbinv(j,l)=workb(j,l)
       enddo
      enddo

ccccccccccccccccccccccccccccccccccccccccccccccccc
c --- Calculate : workbinv = {[covd]+G[Covm]G'}^-1 --- c
ccccccccccccccccccccccccccccccccccccccccccccccccc

      call dpoinv(ndata,workbinv,ipar,check)

ccccccccccccccccccccccccccccccccccccccccc
c --- Calculate : G<m> : workc = g*m --- c
ccccccccccccccccccccccccccccccccccccccccc

      call dgemv('N',ndata,npar,1.d0,g,mpar,
     .           m,1,0.d0,workc,1)

ccccccccccccccccccccccccccccccccccccccccccccccccc
c --- Calculate : dobs-G<m> : workd = svel - workc --- c
ccccccccccccccccccccccccccccccccccccccccccccccccc

      do j=1,ndata
       workd(j)=d(j)-workc(j)
      enddo

ccccccccccccccccccccccccccccccccccccccccc
c --- Calculate : [Covm]*G : worke = covm*g --- c
ccccccccccccccccccccccccccccccccccccccccc

      call dgemm('N','T',npar,ndata,npar,1.d0,
     .           covm,mpar,g,mpar,0.d0,worke,
     .           ipar)

ccccccccccccccccccccccccccccccccccccccccccccccccccccc
c --- Calculate : [Covm}G*{[covd]+G[Covm]G'}^-1 : G^-g --- c
c --- workf = worke*workbinv                        --- c
ccccccccccccccccccccccccccccccccccccccccccccccccccccc

      call dgemm('N','N',npar,ndata,ndata,1.d0,
     .           worke,ipar,workbinv,ipar,0.d0,
     .           workf,ipar)

ccccccccccccccccccccccccccccccccccccccccccccccccc
c --- Calculate : G^-g[dobs-G<m>] : workg = workf*workd --- c
ccccccccccccccccccccccccccccccccccccccccccccccccc

      call dgemv('N',npar,ndata,1.d0,workf,ipar,
     .           workd,1,0.d0,workg,1)

ccccccccccccccccccccccccccccccccccccccccccccccccccccccc
c --- Calculate : <m>+G^-g[dobs-G<m>] : xn = xnstart+workg -- c
ccccccccccccccccccccccccccccccccccccccccccccccccccccccc


      do k=1,npar
       xn(k)=m(k)+workg(k)
      enddo

ccccccccccccccccccccccccccccccccccccccccccccccccc
c --- Begin Calculating Covariance of slip estimates --- c
ccccccccccccccccccccccccccccccccccccccccccccccccc

ccccccccccccccccccccccccccccccccccccccc
c --  Calculate : G^-gG : workh = workf*g --- c
ccccccccccccccccccccccccccccccccccccccc

      call dgemm('N','N',npar,npar,ndata,1.d0,
     .           workf,ipar,g,mpar,0.d0,
     .           workh,ipar)

ccccccccccccccccccccccccccccccc
c     Form an Identity matrix --- c
ccccccccccccccccccccccccccccccc

      do k=1,npar
       do l=1,npar
        ident(k,l)=0.d0
       enddo
       ident(k,k)=1.d0
      enddo

ccccccccccccccccccccccccccccccccccccccccccccccc
c     Calculate : [I-R] : worki = ident - workh --- c
ccccccccccccccccccccccccccccccccccccccccccccccc

      do k=1,npar
       do l=1,npar
        worki(k,l)=ident(k,l)-workh(k,l)
       enddo
      enddo

ccccccccccccccccccccccccccccccccccccccccccccccc
c     Calculate : [I-R][Covm] : workj = worki * covm --- c
ccccccccccccccccccccccccccccccccccccccccccccccc

      call dgemm('N','N',npar,npar,npar,1.d0,
     .     worki,ipar,covm,mpar,0.d0,workj,ipar)

ccccccccccccccccccccccccccccccccccccccccccccccccc
c     Calculate : [I-R][Covm][I-R]' : workk = workj * worki' --- c
ccccccccccccccccccccccccccccccccccccccccccccccccc

      call dgemm('N','N',npar,npar,npar,1.d0,
     .     worki,ipar,covm,mpar,0.d0,workj,ipar)

ccccccccccccccccccccccccccccccccccccccccccccccccc
c     Calculate : [I-R][Covm][I-R]' : workk = workj * worki' --- c
ccccccccccccccccccccccccccccccccccccccccccccccccc

      call dgemm('N','T',npar,npar,npar,1.d0,
     .     workj,ipar,worki,ipar,0.d0,workk,ipar)

ccccccccccccccccccccccccccccccccccccccccccccc
c     Calculate : G^-g[covd] : workl = workf * covd --- c
ccccccccccccccccccccccccccccccccccccccccccccc

      call dgemm('N','N',npar,ndata,ndata,1.d0,
     .     workf,ipar,covd,mpar,0.d0,workl,ipar)

ccccccccccccccccccccccccccccccccccccccccccccccc
c     Calculate : G^-g[covd]G^-g' : workm = workl * workf' --- c
ccccccccccccccccccccccccccccccccccccccccccccccc

      call dgemm('N','T',npar,npar,ndata,1.d0,
     .     workl,ipar,workf,ipar,0.d0,workm,ipar)
```

```
ccccccccccccccccccccccccccccccccccccccccccccccccccccccccc
c     Calculate : G^-g[covd]G^-g'+[I-R][Covm][I-R]' -- c
c     covxn = workm + workk                            c
ccccccccccccccccccccccccccccccccccccccccccccccccccccccccc

      do k=1,npar
       do l=1,npar
        covxn(k,l)=workm(k,l)+workk(k,l)
       enddo
      enddo

ccccccccccccccccccccccccccccccccccc
c --- Finish generalised inverse --- c
ccccccccccccccccccccccccccccccccccc

      return
      end

      subroutine stocinv(g,d,xs,covxs,m,covm,ndata,npar,mpar,wm)

      implicit none

c     INPUT

      integer ndata,npar,mpar

      real*8 g(mpar,mpar),d(mpar)
      real*8 xs(mpar),wm(mpar,mpar)
      real*8 covxs(mpar,mpar)

c     OUTPUT

      real*8 m(mpar),covm(mpar,mpar)

c     INTERNAL

      integer j,k,ipar,l

      parameter (ipar=360)

      real*8 gt(ipar,ipar)
      real*8 worka(ipar,ipar)
      real*8 workb(ipar),workc(ipar)
      real*8 workd(ipar),check(ipar)
      real*8 gmg(ipar,ipar)
      real*8 workh(ipar,ipar),ident(ipar,ipar)
      real*8 worki(ipar,ipar)
      real*8 workk(ipar,ipar)
      real*8 workm(ipar,ipar)

      do j=1,ndata
       do k=1,npar
        gt(k,j)=g(j,k)
       enddo
      enddo

      call dgemm('N','N',npar,npar,ndata,1.d0,
     +     gt,ipar,g,mpar,0.d0,
     +     worka,ipar)

      do j=1,ndata
       do k=1,npar
        worka(j,k)=worka(j,k)+wm(j,k)
       enddo
      enddo

      call dpoinv(npar,worka,ipar,check)

      call dgemm('N','N',npar,ndata,npar,1.d0,
     +     worka,ipar,gt,ipar,0.d0,
     +     gmg,ipar)

      call dgemv('N',ndata,npar,1.d0,
     +     g,mpar,xs,1,0.d0,workb,1)

      do j=1,ndata
       workc(j)=d(j)-workb(j)
      enddo

      call dgemv('N',npar,ndata,1.d0,
     +     gmg,ipar,workc,1,0.d0,workd,1)

      do j=1,npar
       m(j)=xs(j)+workd(j)
      enddo

ccccccccccccccccccccccccccccccccccccccccccccccccccccccccc
c --- Begin Calculating Covariance of slip estimates --- c
ccccccccccccccccccccccccccccccccccccccccccccccccccccccccc

ccccccccccccccccccccccccccccccccccccccccccccccccccccccccc

ccccccccccccccccccccccccccccccccccccccccccccccccccccccccc
c --  Calculate : G^-gG : workh = workf*g --- c
ccccccccccccccccccccccccccccccccccccccccccccccccccccccccc

      call dgemm('N','N',npar,npar,ndata,1.d0,
     .           gmg,ipar,g,mpar,0.d0,
     .           workh,ipar)

ccccccccccccccccccccccccccccccccc
c     Form an Identity matrix --- c
ccccccccccccccccccccccccccccccccc

      do k=1,npar
       do l=1,npar
        ident(k,l)=0.d0
       enddo
       ident(k,k)=1.d0
      enddo

ccccccccccccccccccccccccccccccccccccccccccccccccccccccccc
c     Calculate : [I-R] : worki = ident - workh --- c
ccccccccccccccccccccccccccccccccccccccccccccccccccccccccc

      do k=1,npar
       do l=1,npar
        worki(k,l)=ident(k,l)-workh(k,l)
       enddo
      enddo

ccccccccccccccccccccccccccccccccccccccccccccccccccccccccccccccc
c     Calculate : [I-R][Covm][I-R]' : workk = workj * worki' --- c
ccccccccccccccccccccccccccccccccccccccccccccccccccccccccccccccc

      call dgemm('N','T',npar,npar,npar,1.d0,
     .     worki,ipar,worki,ipar,0.d0,workk,ipar)

ccccccccccccccccccccccccccccccccccccccccccccccccccccccccccccccc
c     Calculate : G^-g[covd]G^-g' : workm = workl * workf' --- c
ccccccccccccccccccccccccccccccccccccccccccccccccccccccccccccccc

      call dgemm('N','T',npar,npar,ndata,1.d0,
     .     gmg,ipar,gmg,ipar,0.d0,workm,ipar)

ccccccccccccccccccccccccccccccccccccccccccccccccccccccccccccccccccccccccccccccccccccc
c     Calculate : G^-gG^-g'+[I-R][Covm][I-R]' : covxn = workm + workk --- c
ccccccccccccccccccccccccccccccccccccccccccccccccccccccccccccccccccccccccccccccccccccc

      do k=1,npar
       do l=1,npar
        covm(k,l)=workm(k,l)+workk(k,l)
       enddo
      enddo

      return
      end

      subroutine poly44(ori,lon,lat,x,y)

c  polyconic projection of point lat=p2, diff long=il from arbitrary
c     central meridian. lat of arbitrary origin is p1. x=dist from cm
c     along lat p2. y=dist from p1 to p2. x,y in meters.
c     p1,p2,and il in seconds.

      implicit none

      real*8 il,la,ip,ipr,pr,p1,p2
      real*8 arcone,esq,a0,a2,a4,a6,a8
      real*8 sinp2,cosp2,theta,a,cot,x,y
      real*8 ori(2),lon,lat

      data arcone,esq,la,a0,a2,a4,a6,a8/4.8481368e-6,6.7686580e-3,
     +     6378206.4,6367399.7,32433.888,34.4187,.0454,6.0e-5/

      p1=ori(2)*3600.d0
      p2=lat*3600.d0
      il=(lon-ori(1))*3600.d0
      ip=p2-p1
      sinp2=sin(p2*arcone)
      cosp2=cos(p2*arcone)
      theta=il*sinp2
      a=sqrt(1.0-(esq*(2.*sinp2)))/(la*arcone)
      cot=cosp2/sinp2
      x=(cot*sin(theta*arcone))/(a*arcone)
      ipr=ip*arcone
      pr=((p2+p1)/2.)*arcone
      y= a0*ipr-(a2*cos(2.*pr)*sin(ipr))+(a4*cos(4.*pr)*sin(2.*ipr))-
```

```
     * (a6*cos(6.*pr)*sin(3.*ipr))+a8*cos(8.*pr)*sin(4.*ipr)
      x=x/1.d03
      y=y/1.d03
      return
      end
      subroutine fchisq(npts,nterm,mdpts,obs,calc,err,
     .                  omc,chi2,rchi2,norm)

      implicit none

      integer npts,nterm,mdpts
      integer k,nfree

      real*8 obs(mdpts),calc(mdpts)
      real*8 err(mdpts),omc(mdpts)
      real*8 chi2,rchi2,norm

      chi2=0.d0
      do k=1,npts
       omc(k)=obs(k)-calc(k)
       chi2=chi2+(omc(k)/err(k))**2
      enddo
      nfree=npts-nterm
      if(nfree.le.0) then
       rchi2=0.0
       norm=0.0
       goto 10
      endif
      rchi2=chi2/nfree
      norm=sqrt(rchi2)
 10   return
      end
c***********************************************************************
c*****                                                          *****
c***** surface displacement,strain,tilt due to rectangular fault  *****
c***** in a semiinfinite medium   (Okada,1985 : BSSA,75,1135-1154) *****
c*****                          coded by  y.okada ... jan 1985 *****
c*****                                                          *****
c***********************************************************************
      subroutine  srectf(alp,x,y,dep,al,aw,sd,cd,disl1,disl2,disl3,
     *                   u1,u2,u3,u11,u12,u21,u22,u31,u32)
c*****
c***** input
c*****   alp   : medium constant  myu/(lamda+myu)
c*****   x,y   : coordinate of station
c*****   dep   : source depth
c*****   al,aw : length and width of fault
c*****   sd,cd : sin,cos of dip-angle
c*****           (cd=0.d0, sd=+/-1.d0 should be given for vertical fault)
c*****   disl1,disl2,disl3 : strike-, dip- and tensile-dislocation
c*****
c***** output
c*****   u1, u2, u3      : displacement ( unit= unit of disl     )
c*****   u11,u12,u21,u22 : strain        ( unit= unit of disl /
c*****   u31,u32         : tilt                unit of x,y,,,aw )
c*****
c***** subroutine used...srectg
c*****
      implicit real*8 (a-h,o-z)
      dimension  u(9),du(9)
      data  f0, f1 / 0.d0, 1.d0 /
c*****
      p = y*cd + dep*sd
      q = y*sd - dep*cd
c*****
      do 1111  i=1,9
 1111 u(i)=f0
c*****
      do 5555  k=1,2
       if(k.eq.1)  et=p
       if(k.eq.2)  et=p-aw
       do 4444  j=1,2
        if(j.eq.1)  xi=x
        if(j.eq.2)  xi=x-al
        jk=j+k
        if(jk.ne.3)  sign= f1
        if(jk.eq.3)  sign=-f1
        call srectg(alp,xi,et,q,sd,cd,disl1,disl2,disl3,
     *            du(1),du(2),du(3),du(4),du(5),du(6),du(7),du(8),du(9))
        do 3333  i=1,9
         u(i)=u(i)+sign*du(i)
 3333   continue
 4444   continue
 5555 continue
      u1 =u(1)
      u2 =u(2)
      u3 =u(3)
      u11=u(4)
      u12=u(5)
      u21=u(6)
      u22=u(7)
      u31=u(8)
      u32=u(9)
      return
      end
c***********************************************************************
c*****                                                          *****
c***** indefinite integral of surface displacement,strain,tilt  *****
c*****     due to finite fault    (Okada,1985 : BSSA,75,1135-1154) *****
c*****                            coded by  y.okada ... jan 1985 *****
c*****                                                          *****
c***********************************************************************
      subroutine  srectg(alp,xi,et,q,sd,cd,disl1,disl2,disl3,
     *                   u1,u2,u3,u11,u12,u21,u22,u31,u32)
c*****
c***** input
c*****   alp     : medium constant  myu/(lamda+myu)
c*****   xi,et,q : fault coordinate
c*****   sd,cd   : sin,cos of dip-angle
c*****             (cd=0.d0, sd=+/-1.d0 should be given for vertical fault)
c*****   disl1,disl2,disl3 : strike-, dip- and tensile-dislocation
c*****
c***** output
c*****   u1, u2, u3      : displacement ( unit= unit of disl     )
c*****   u11,u12,u21,u22 : strain        ( unit= unit of disl /
c*****   u31,u32         : tilt                unit of xi,et,q )
c*****
      implicit real*8 (a-h,o-z)
      data  f0,f1,f2/ 0.d0, 1.d0, 2.d0 /
      pi2=6.283185307179586d0
c*****
      xi2=xi*xi
      et2=et*et
      q2=q*q
      r2=xi2+et2+q2
      r =dsqrt(r2)
      r3=r*r2
      d =et*sd-q*cd
      y =et*cd+q*sd
      ret=r+et
      if(ret.lt.f0)  ret=f0
      rd =r+d
      rrd=f1/(r*rd)
c*****
      if( q .ne.f0)  tt = datan( xi*et/(q*r) )
      if( q .eq.f0)  tt = f0
      if(ret.ne.f0)  re = f1/ret
      if(ret.eq.f0)  re = f0
      if(ret.ne.f0)  dle= dlog(ret)
      if(ret.eq.f0)  dle=-dlog(r-et)
      rrx=f1/(r*(r+xi))
      rre=re/r
      axi=(f2*r+xi)*rrx*rrx/r
      aet=(f2*r+et)*rre*rre/r
      if(cd.eq.f0)  go to 20
c*****
c***** inclined fault
c*****
      td=sd/cd
      x =dsqrt(xi2+q2)
      if(xi.eq.f0)  a5=f0
      if(xi.ne.f0)
     *a5= alp*f2/cd*datan( (et*(x+q*cd)+x*(r+x)*sd) / (xi*(r+x)*cd) )
      a4= alp/cd*( dlog(rd) - sd*dle )
      a3= alp*(y/rd/cd - dle) + td*a4
      a1=-alp/cd*xi/rd       - td*a5
      c1= alp/cd*xi*(rrd - sd*rre)
      c3= alp/cd*(q*rre - y*rrd)
      b1= alp/cd*(xi2*rrd - f1)/rd - td*c3
      b2= alp/cd*xi*y*rrd/rd       - td*c1
      go to 30
c*****
c***** vertical fault
c*****
   20 rd2=rd*rd
      a1=-alp/f2*xi*q/rd2
      a3= alp/f2*( et/rd + y*q/rd2 - dle )
      a4=-alp*q/rd
      a5=-alp*xi*sd/rd
      b1= alp/f2*  q  /rd2*(f2*xi2*rrd - f1)
      b2= alp/f2*xi*sd/rd2*(f2*q2 *rrd - f1)
      c1= alp*xi*q*rrd/rd
      c3= alp*sd/rd*(xi2*rrd - f1)
c*****
   30 a2=-alp*dle - a3
      b3=-alp*xi*rre - b2
```


```
      b4=-alp*( cd/r + q*sd*rre ) - b1
      c2= alp*(-sd/r + q*cd*rre ) - c3
c*****
      u1 =f0
      u2 =f0
      u3 =f0
      u11=f0
      u12=f0
      u21=f0
      u22=f0
      u31=f0
      u32=f0
c-------------------------------------
c-----  strike-slip  contribution  -----
c-------------------------------------
      if(disl1.eq.f0)  go to 200
      un=disl1/pi2
      req=rre*q
      u1 =u1 - un*( req*xi +   tt    + a1*sd )
      u2 =u2 - un*( req*y  + q*cd*re + a2*sd )
      u3 =u3 - un*( req*d  + q*sd*re + a4*sd )
      u11=u11+ un*( xi2*q*aet - b1*sd )
      u12=u12+ un*( xi2*xi*( d/(et2+q2)/r3 - aet*sd ) - b2*sd )
      u21=u21+ un*( xi*q/r3*cd + (xi*q2*aet - b2)*sd )
      u22=u22+ un*( y *q/r3*cd + (q*sd*(q2*aet-f2*rre)
     *                         -(xi2+et2)/r3*cd - b4)*sd )
      u31=u31+ un*(-xi*q2*aet*cd + (xi*q/r3 - c1)*sd )
      u32=u32+ un*( d*q/r3*cd + (xi2*q*aet*cd - sd/r + y*q/r3 - c2)*sd )
c-------------------------------------
c-----   dip-slip  contribution   -----
c-------------------------------------
  200 if(disl2.eq.f0)  go to 300
      un=disl2/pi2
      sdcd=sd*cd
      u1 =u1 - un*( q/r              - a3*sdcd )
      u2 =u2 - un*( y*q*rrx + cd*tt - a1*sdcd )
      u3 =u3 - un*( d*q*rrx + sd*tt - a5*sdcd )
      u11=u11+ un*( xi*q/r3            + b3*sdcd )
      u12=u12+ un*( y *q/r3 - sd/r     + b1*sdcd )
      u21=u21+ un*( y *q/r3 + q*cd*rre + b1*sdcd )
      u22=u22+ un*( y*y*q*axi - (f2*y*rrx + xi*cd*rre)*sd + b2*sdcd )
      u31=u31+ un*( d *q/r3 + q*sd*rre + c3*sdcd )
      u32=u32+ un*( y*d*q*axi - (f2*d*rrx + xi*sd*rre)*sd + c1*sdcd )
c-------------------------------------
c-----  tensile-fault contribution  -----
c-------------------------------------
  300 if(disl3.eq.f0)  go to 900
      un=disl3/pi2
      sdsd=sd*sd
      u1 =u1 + un*( q2*rre                        - a3*sdsd )
      u2 =u2 + un*(-d*q*rrx - sd*(xi*q*rre - tt) - a1*sdsd )
      u3 =u3 + un*( y*q*rrx + cd*(xi*q*rre - tt) - a5*sdsd )
      u11=u11- un*( xi*q2*aet             + b3*sdsd )
      u12=u12- un*(-d*q/r3 - xi2*q*aet*sd + b1*sdsd )
      u21=u21- un*( q2*(cd/r3 + q*aet*sd) + b1*sdsd )
      u22=u22- un*((y*cd-d*sd)*q2*axi - f2*q*sd*cd*rrx
     *                - (xi*q2*aet - b2)*sdsd )
      u31=u31- un*( q2*(sd/r3 - q*aet*cd) + c3*sdsd )
      u32=u32- un*((y*sd+d*cd)*q2*axi + xi*q2*aet*sd*cd
     *                - (f2*q*rrx - c1)*sdsd )
c*****
  900 return
      end
```

sume an arbitrary rotation of the network as a whole. The GPS network extends farther northeast than the trilateration network, but there is little deformation apparent in this area. Indeed, there is no additional movement as far east as Jackson, 170 km from the San Andreas fault. The trilateration network includes a site on Farallon Islands, 30 km southwest of the GPS site Point Reyes Head and 40 km from the San Andreas fault. A flattening in the velocity field west of Point Reyes Head is indicated by the trilateration data, with only 1.5 ± 1.1 mm/yr of motion occurring between Point Reyes Head and Farallon Islands. We observe a total of 33 ± 2 mm/yr of fault-parallel relative plate motion across the GPS network, which is not significantly different than the 31 ± 3 mm/yr reported for the trilateration network by *Lisowski et al.* [1991].

The deformation within the GPS network is evenly distributed southwest and northeast of the Rodgers Creek fault. This broadly distributed deformation with concentrations of strain around the faults could simply be explained as a result of loading of the San Andreas, Rodgers Creek, and Green Valley faults by continuous slip at depth on the faults. As discussed by *Lisowski et al.* [1991], the surface velocity field can be reproduced by a wide-range of fault models depending on assumptions about fault geometry and elastic properties of the crust. We do not present a fault model here. In the future we plan to combine the GPS and trilateration data to infer slip on the faults.

The 33 ± 2 mm/yr of deformation within the profile is significantly less than the full plate motion rate at this latitude (46–47 mm/yr N33°W [*De Mets et al.*, 1990; *Gordon*, 1993; *Robaudo and Harrison*, 1993]). The deforming zone along this plate boundary extends well into the interior of North America, and motion is partitioned between the San Andreas fault system and deformation across the Great Basin. The motion across the Great Basin at this latitude is approximated by the 10.0 ± 0.5 mm/yr N38°W velocity of the VLBI station OVRO [*Dixon et al.*, 1993, Table 3], located 200 km east of the San Andreas fault. Station OVRO is within a tectonically active zone east of the Sierra Nevada Mountains and its velocity is likely 1–2 mm/yr lower than it would be if it were located in the Sierra Nevada Mountains [*Argus and Gordon*, 1991]. The part of the motion accommodated by the San Andreas fault zone is then about 34–37 mm/yr. This motion can be accounted for by the 33 ± 2 mm/yr rate of shearing of the GPS network plus the 1.5 ± 1.1 mm/yr rate of shearing offshore of the GPS network. The geodetic data suggest that the full Pacific plate rate of motion is obtained near the Farallon Islands and little deformation occurs between the Great Valley and the Sierra Nevada Mountains.

Conclusion

We present results from 7 GPS surveys within the time span of 2.8 years that provide significant relative displacements across a 100-km-long profile crossing the San Andreas fault system in the North Bay area. Motion parallel to the trend of the San Andreas fault is distributed across the profile. No significant convergence upon the fault was detected. Fault-parallel velocity gradients decrease near the ends of the profile, suggesting that nearly all of the deformation associated with the San Andreas fault system is captured within the profile.

References

Argus, D. F., and R. G. Gordon, Current Sierra Nevada–North American motion from Very Long Baseline Interferometry: Implications for the kinematics of the western United States, *Geology, 19*, 1085–1088, 1991.

Davis, J. L., W. H. Prescott, J. L. Svarc, and K. L. Wendt, Assessment of Global Positioning System measurements for studies of crustal deformation, *J. Geophys. Res., 94*, 13635–13650, 1989.

DeMets, C., R. G. Gordon, D. F. Argus, and S. Stein, Current plate motions, *Geophys. J. Int., 101*, 425–478, 1990.

Dixon, T. H., M. Bursik, S. K. Wolf, M. Heflin, F. Webb, F. Farina, and S. Robaudo, Constraints on deformation of the resurgent dome, Long Valley Caldera, California from space geodesy, in *Contributions of Space Geodesy to Geodynamics: Crustal Dynamics (Geodynamics Series, v. 23)*, edited by D. E. Smith and D. L. Turcotte, pp. 193–214, American Geophysical Union, Washington, D.C., 1993.

Gordon, R. G., Orbital dates and steady rates, *Nature, 364*, 760–761, 1993.

Helley, E. J., and D. G. Herd, Map showing faults with Quaternary displacement, northeastern San Francisco Bay region, California, scale 1:125,000, *U.S. Geol. Surv. Misc. Field Study Map, MF-881*, 1977.

Herd, D. G., and E. J. Helley, Map showing faults with Quaternary displacement, northwestern San Francisco Bay region, California, scale 1:125,000, *U.S. Geol. Surv. Misc. Field Study Map, MF-818*, 1976.

Larson, K. M., and D. C. Agnew, Application of the Global Positioning System to crustal deformation measurement 1. Precision and Accuracy, *J. Geophys. Res., 96*, 16547–16565, 1991.

Lisowski, M., J. C. Savage, and W. H. Prescott, The velocity field along the San Andreas fault in Central and Southern California, *J. Geophys. Res., 96*, 8369–8389, 1991.

Ma., C., J. W. Ryan, D. Gordon, D. S. Caprette, and W. E. Himwich, Reference frames from CDP VLBI data, in *Contributions of Space Geodesy to Geodynamics: Earth Dynamics (Geodynamics Series, v. 24)*, edited by D. E. Smith and D. L. Turcotte, pp. 121–145, American Geophysical Union, Washington, D.C., 1993.

Prescott, W. H., The determination of displacement fields from geodetic data along a strike-slip fault, *J. Geophys. Res., 86*, 6067– 6072, 1981.

Robaudo, S., and C. G. A. Harrison, Plate tectonics from SLR and VLBI global data, in *Contributions of Space Geodesy to Geodynamics: Crustal Dynamics (Geodynamics Series, v. 23)*, edited by D. E. Smith and D. L. Turcotte, pp. 51–72, American Geophysical Union, Washington, D.C., 1993.

Rothacher, M., G. Beutler, W. Gurtner, T. Schildknecht and U. Wild, *Documentation for Bernese GPS Software Version 3.2*, University of Bern, 1990.

M. Lisowski, J. L. Svarc, W. H. Prescott, U.S. Geological Survey, Menlo Park, CA 94025.

S. D. P. Williams, Department of Geological Sciences, University of Durham, England.

(received November 3, 1993; accepted December 11, 1993.)

GEOPHYSICAL RESEARCH LETTERS, VOL. 21, NO. 14, PAGES 1511-1514, JULY 1, 1994

GPS measured rates of deformation in the northern San Francisco Bay region, California, 1990-1993

S. D. P. Williams [1], J. L. Svarc, M. Lisowski, W. H. Prescott

U.S. Geological Survey, Menlo Park, California

Abstract. A 100-km-long, 13-station profile extending across the San Andreas fault system north of San Francisco Bay was measured 7 times between March 1990 and January 1993 with the Global Positioning System (GPS). The data have been processed using the Bernese Version 3.2 software. Data from a continental-scale fiducial network were included in the solutions to aid orbit improvement and provide a consistent reference frame. We find 33 ± 2 mm/yr of fault-parallel (N33°W) shear evenly distributed southwest and northeast of the Rodgers Creek fault and a near linear velocity gradient across the profile. The profile spans most of the zone of active deformation associated with the San Andreas fault system. Shear is negligible at the east end of the profile near the Great Valley. Additional shear of a few millimeters per year is likely beyond Point Reyes Head, the west end of the profile. We observe no systematic convergence upon the fault. The GPS measured velocities are similar to those derived previously from trilateration. The velocity change across the GPS profile (31–35 mm/yr) plus that west of the profile (0-3 mm/yr) and that observed with VLBI east of the Sierra Nevada Mountains (~10-12 mm/yr) accounts for the North American-Pacific plate rate (46–47 mm/yr).

Introduction

The San Andreas fault system north of San Francisco Bay consists of several near parallel faults. The principal active fault is the San Andreas but faults farther to the east (Rodgers Creek and Green Valley) have developed within the last 2–4 Ma [*Helley and Herd*, 1977] and now accommodate a significant fraction of plate motion.

Geodetic surveys used to determine deformation in the region date back to around 1860. The initial surveys used triangulation methods. Since the early 1970's the U.S. Geological Survey (USGS) has repeatedly measured distances between geodetic stations in the San Francisco Bay area using a Geodolite, a laser distance measuring instrument. *Lisowski et al.* [1991] found 31 ± 3 mm/yr of fault parallel motion distributed across a 115-km-wide trilateration network in the North Bay region and no significant convergence upon the fault. These rates, however, are based on an arbitrary assumption about unmeasured rotation of the trilateration network as a whole. During the mid-1980's Geodolite surveys began to be replaced by Global Positioning System (GPS) observations of relative position. In 1990, the USGS established and measured with GPS a set of geodetic profiles spanning the San Francisco Bay Region. One of these, the North Bay profile (Figure 1), extends for 100 km from Point Reyes Head to the western edge of the Great Valley. Possible network rotation is directly measured with GPS. We find that the GPS observed pattern and rate of deformation are in good agreement with those previously estimated by *Lisowski et al.* [1991].

Data

Between March 1990 and February 1993, the USGS measured the North Bay profile 7 times using GPS. The first 4 surveys were conducted with TI-4100 dual frequency P-code receivers, and the last 3 surveys with Ashtech LM-XII receivers (C/A code on L1 and codeless on L2). Each survey consisted of 4 observation sessions and during each session 3–5 of the 13 stations were occupied for 4–6 hours. One station, Cord, was occupied during each session. Data recorded at station Jackson (Figure 1 inset) were included in the March 1990, May 1990, and September 1991 surveys. The data were processed using the Bernese Version 3.2 Software [*Rothacher et al.*, 1990], with modifications and additions to the programs implemented by the USGS [*Davis et al.*, 1989].

The North Bay profile extends in nearly a straight line perpendicular to the strike of the San Andreas fault, across the maximum shear strain gradients associated with tectonic loading of the San Andreas and nearby faults. In a network of this design, a spurious network rotation could approximate the appearance of shear strain and a scale error would appear as contraction or extension across the faults. Such errors could result from error in the satellite orbits or reference frame. We use the fiducial network concept to obtain higher accuracy GPS satellite orbits and maintain a consistent terrestrial reference frame. Data from several fixed GPS stations operated by the Cooperative International GPS Network (CIGNET), the International GPS Service for Geodynamics (IGS) or the Southern California Permanent GPS geodetic Array (PGGA) are included in our

[1]Department of Geological Sciences, University of Durham, England

Paper number 94GL01227
0094-8534/94/94GL-01227$03.00

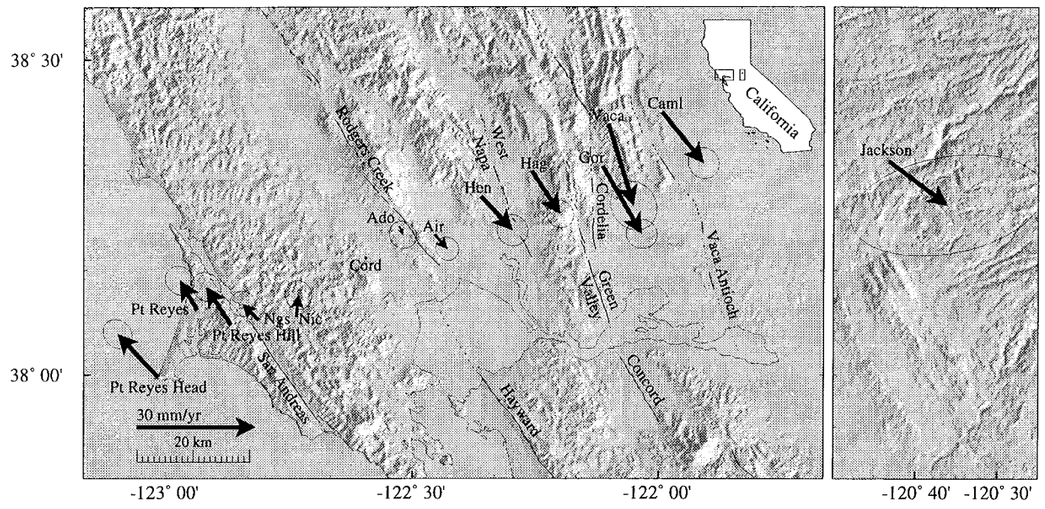

Figure 1. Map showing major faults, North Bay profile GPS stations, and 1990–1993 site velocities relative to station Cord. Velocities are tipped with 95% confidence ellipses. Faults are from *Herd and Helley* [1976] and *Helley and Herd* [1977].

solutions. These fixed stations are colocated with Very Long Baseline Interferometry (VLBI) antennas whose coordinates and velocities, derived from extragalactic quasar radio sources, define a precise terrestrial reference frame [*Ma et al.*, 1993]. A summary of the site occupation together with the fiducial sites used is given in Table 1.

Table 1. Site Occupation Index for North Bay GPS Surveys and Fiducial Stations Used in the Processing

	90.2	90.4	90.7	91.2	91.7	92.1	93.0
Local Stations							
Cord	•	•	•	•	○	○	○
Ngs	•	•	•	•		○	○
Pt Reyes	•	•	•	•	○	○	○
Pt Reyes Head	•	•	•	•	○	○	○
Pt Reyes Hill	•	•	•	•	○	○	○
Ado	•	•	•	•	○	○	○
Air	•	•	•	•	○	○	○
Hen	•		•	•	○	○	○
Nic	•	•	•	•	○	○	○
Caml	•	•	•		○	○	○
Gor	•	•	•	•	○	○	○
Hag	•	•	•		○	○	○
Mt Vaca	•	•	•	•	○	○	
Jackson	•	•			○		
Fiducial Stations							
Mojave	○	○	○	○	○	○	
Richmond	○	○	○	○	○	○	
Westford	○	○	○	○	○	○	
Algonquin							•
Penticton							•
JPLMesa							•
Goldstone							•
Richmond:2							•

• Dual frequency, P – code receiver
○ Dual frequency receiver, no P – code

The standard strategy used to process the North Bay data is similar to that described by *Davis et al.* [1989]. Phase ambiguities for the local sites were resolved where possible. No attempt was made at resolving the ambiguities for the fiducial sites. The coordinates of the local stations were left as free parameters.

Table 2. 1990 to 1993 Average Fault Parallel (N33°) and Fault Normal (N57°E) Station Velocities Relative to Station Cord.

Station	N57°E Distance from Cord, km	N33°W Velocity, mm/yr†	N57°E Velocity, mm/yr†
Pt Reyes Head	−42.3	14.8 ± 1.6	(-2.7 ± 1.4)
Pt Reyes	−30.1	8.6 ± 1.6	(-0.3 ± 1.4)
Pt Reyes Hill	−26.5	11.4 ± 1.6	(0.0 ± 1.4)
Ngs	−22.0	5.7 ± 1.3	(-1.2 ± 1.3)
Nic	−16.0	4.3 ± 1.5	3.4 ± 1.4
Ado	8.0	(-2.3 ± 1.5)	(-0.4 ± 1.3)
Air	12.5	-4.8 ± 1.2	(0.7 ± 1.2)
Hen	23.0	-11.3 ± 1.6	(2.1 ± 1.6)
Hag	33.0	-13.0 ± 1.4	(0.2 ± 1.4)
Gor	44.0	-19.6 ± 1.6	(-1.0 ± 1.5)
Vaca	48.9	-20.7 ± 2.6	-5.8 ± 2.3
Caml	58.0	-16.5 ± 1.7	(1.9 ± 1.5)
Jackson	146.1	-17.3 ± 6.0	(6.4 ± 9.5)

†Uncertainties are 1σ, bracketed rates are not significant at 95% confidence.

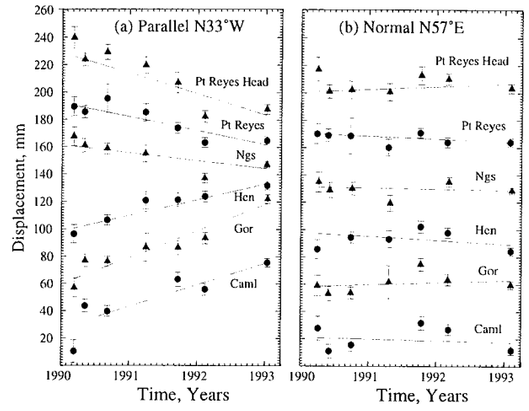

Figure 2. Changes in displacement relative to station Cord (a) parallel (N33°W) and (b) normal (N57°E) to the trend of the San Andreas fault as a function of time. Error bars represent one standard deviation.

Results

We obtain site velocities using a simple least squares procedure. The north, east, and up baseline components relative to a common site are calculated from the GPS position solutions. A linear rate of change in the three components is then calculated. The uncertainties are determined by propagation of the full position covariances. The errors quoted in this paper are the formal standard deviations obtained from the Bernese solutions increased by a factor of 5. This factor brings the formal errors into agreement with the long-term scatter in the data and with GPS error estimates given by *Larson and Agnew* [1991]. The horizontal velocities relative to the station Cord are listed in Table 2 and shown as vectors in Figure 1.

The changes in the fault-parallel (N33°W) and fault-normal (N57°E) displacements relative to station Cord as a function of time are shown for several stations in Figure 2. The data are well fit by a linear rate of change. The rate of fault-parallel displacement (Figure 2a) generally increases with the distance from Cord, while the fault-normal displacements (Figure 2b) show little or no significant motion. The distribution of deformation across the network is best shown by projecting the rates of fault-parallel and fault-normal displacements onto a profile constructed perpendicular to the local strike of the San Andreas fault (Figure 3).

Discussion

Fault-Normal Velocities

The GPS measured fault-normal (N57°E) velocities (Figure 3b) indicate no systematic convergence upon the fault. Only the velocities of stations Nic and Vaca are significantly different from a null velocity at the 95% confidence level. No systematic convergence upon the fault was observed between 1973 and 1989 in a trilateration network spanning the same area [*Lisowski et al.*, 1991, Figure 15]. The trilateration velocities, however, are ambiguous, because the network lacks a tie to an external reference frame and, as a result, rigid-body motions (translations and rotations) of the network as a whole are not determined. The trilateration velocities are from a particular solution (the so-called "outer-coordinate" solution) that adds a network rotation that minimizes the velocities perpendicular to the fault [*Prescott*, 1981]. This provides an appropriate solution for a region deformed by tectonic shear. Strain analysis of the trilateration data, which is independent of the choice of reference frame, also indicates no regional contraction across the fault. Positions are directly measured with GPS and our fault-normal velocities are not biased by arbitrary assumptions about network rotations. Our GPS results and results from trilateration surveys suggest that convergence upon the San Andreas fault is less than a few millimeters per year.

Fault-Parallel Velocities

The GPS measured fault-parallel (N33°W) velocities decrease at nearly a constant rate across the profile and flatten to the east of the Green Valley fault (Figure 3a). We observe steeper velocity gradients across the San Andreas and Green Valley faults, but these features are not well defined because the sites are widely spaced. The relative velocities and gradients in the velocity field are consistent with those derived by *Lisowski et al.* [1991] from trilateration data. As previously discussed, the GPS relative velocities are directly measured, whereas those derived from trilateration data as-

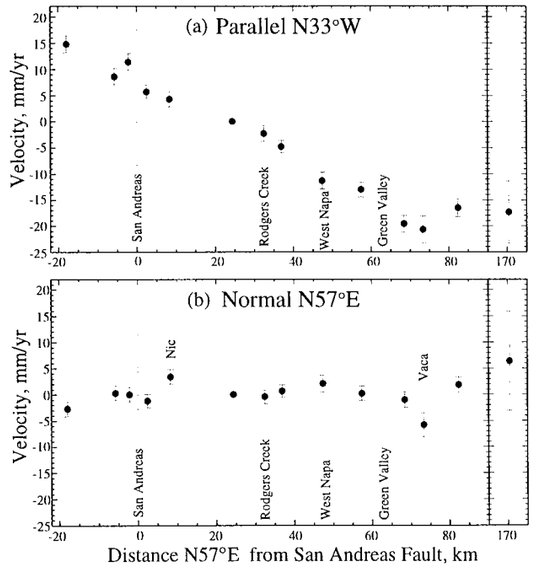

Figure 3. Station velocities relative to Cord resolved into components (a) parallel and (b) normal to the local trend (N33°W) of the San Andreas fault plotted as a function of distance from the fault. Error bars represent one standard deviation.